Nuclear Science

Speciation, Techniques and Facilities for Radioactive Materials at Synchrotron Light Sources

Workshop Proceedings
Grenoble, France
10-12 September 2000

NUCLEAR ENERGY AGENCY
ORGANISATION FOR ECONOMIC CO-OPERATION AND DEVELOPMENT

ORGANISATION FOR ECONOMIC CO-OPERATION AND DEVELOPMENT

Pursuant to Article 1 of the Convention signed in Paris on 14th December 1960, and which came into force on 30th September 1961, the Organisation for Economic Co-operation and Development (OECD) shall promote policies designed:

- to achieve the highest sustainable economic growth and employment and a rising standard of living in Member countries, while maintaining financial stability, and thus to contribute to the development of the world economy;
- to contribute to sound economic expansion in Member as well as non-member countries in the process of economic development; and
- to contribute to the expansion of world trade on a multilateral, non-discriminatory basis in accordance with international obligations.

The original Member countries of the OECD are Austria, Belgium, Canada, Denmark, France, Germany, Greece, Iceland, Ireland, Italy, Luxembourg, the Netherlands, Norway, Portugal, Spain, Sweden, Switzerland, Turkey, the United Kingdom and the United States. The following countries became Members subsequently through accession at the dates indicated hereafter: Japan (28th April 1964), Finland (28th January 1969), Australia (7th June 1971), New Zealand (29th May 1973), Mexico (18th May 1994), the Czech Republic (21st December 1995), Hungary (7th May 1996), Poland (22nd November 1996), Korea (12th December 1996) and the Slovak Republic (14 December 2000). The Commission of the European Communities takes part in the work of the OECD (Article 13 of the OECD Convention).

NUCLEAR ENERGY AGENCY

The OECD Nuclear Energy Agency (NEA) was established on 1st February 1958 under the name of the OEEC European Nuclear Energy Agency. It received its present designation on 20th April 1972, when Japan became its first non-European full Member. NEA membership today consists of 27 OECD Member countries: Australia, Austria, Belgium, Canada, Czech Republic, Denmark, Finland, France, Germany, Greece, Hungary, Iceland, Ireland, Italy, Japan, Luxembourg, Mexico, the Netherlands, Norway, Portugal, Republic of Korea, Spain, Sweden, Switzerland, Turkey, the United Kingdom and the United States. The Commission of the European Communities also takes part in the work of the Agency.

The mission of the NEA is:

- to assist its Member countries in maintaining and further developing, through international co-operation, the scientific, technological and legal bases required for a safe, environmentally friendly and economical use of nuclear energy for peaceful purposes, as well as
- to provide authoritative assessments and to forge common understandings on key issues, as input to government decisions on nuclear energy policy and to broader OECD policy analyses in areas such as energy and sustainable development.

Specific areas of competence of the NEA include safety and regulation of nuclear activities, radioactive waste management, radiological protection, nuclear science, economic and technical analyses of the nuclear fuel cycle, nuclear law and liability, and public information. The NEA Data Bank provides nuclear data and computer program services for participating countries.

In these and related tasks, the NEA works in close collaboration with the International Atomic Energy Agency in Vienna, with which it has a Co-operation Agreement, as well as with other international organisations in the nuclear field.

FOREWORD

The second Euroconference and NEA Workshop on Speciation, Techniques and Facilities for Radioactive Materials at Synchrotron Light Sources, Actinide-XAS-2000, was held in Grenoble, France, on 10-12 September 2000. The meeting focused on the application of synchrotron-based techniques to radionuclide/actinide sciences. Over 70 participants from 12 countries discussed the progress made in this field since the first meeting, Actinide-XAS-98. In particular, the following topics were addressed:

- radionuclides in the environment;
- nuclear waste forms and remediation;
- separation technology;
- general actinide chemistry;
- radiopharmaceutical chemistry;
- actinide interaction with micro-organisms;
- electric and magnetic properties.

Twenty-nine oral presentations, most of them invited talks, contributed to the sections on:

- X-ray absorption spectroscopy of radionuclides;
- application of synchrotron radiation techniques and complementary techniques;
- present and future synchrotron facilities for radionuclide studies.

An additional 27 contributed papers were presented at the poster session.

These proceedings contain the abstracts and some of the full papers presented at the meeting. The editors, Dr. Reich and Dr. Shuh, and other anonymous referees reviewed the full papers. The organising committee wishes to thank these reviewers.

Actinide-XAS-2000 was hosted by the European Synchrotron Radiation Facility (ESRF) and the Institute Laue Langevin (ILL), and organised mainly by the *Forschungszentrum Rossendorf* (FZR), Germany. The European Commission, the NEA and the US Department of Energy co-sponsored the meeting.

TABLE OF CONTENTS

EXECUTIVE SUMMARY

During the last two years since the first Euroconference and NEA Workshop on Speciation, Techniques and Facilities for Radioactive Materials at Synchrotron Light Sources, Actinide-XAS-98, the number of studies on radionuclides and actinides in particular using synchrotron radiation techniques has grown significantly. This is due to the unique properties of synchrotron radiation to provide intense X-ray photons that enable an increasing variety of experiments for obtaining molecular-level information on radionuclide/actinide species. Fundamental knowledge of radionuclide speciation is essential for understanding and predicting the behaviour of these hazardous elements in the environment, for risk assessment of nuclear waste storage, remediation of contaminated sites and development of effective separation technologies. Other important fields, where synchrotron radiation is a powerful tool, are radiopharmaceutical chemistry and general actinide chemistry and physics.

For this reason, the second Euroconference and NEA Workshop Actinide-XAS-2000, which was held in Grenoble, France, from 10-12 September 2000, focused on the scientific progress made in these areas since the Actinide-XAS-98 meeting. Numerous newcomers among the over 70 participants from 10 European countries, USA, Japan and Australia had the opportunity to learn about the type of information that can be obtained using synchrotron radiation from the examples given in the invited lectures. Twenty-four (24) graduate students and post-graduate students benefited from TMR and INCO fellowships by the European Commission.

The meeting was organised into three sessions with 30 oral talks and one evening session with 27 poster presentations. On the first day, G.E. Brown, Jr. opened the session "X-ray Absorption Spectroscopy of Radionuclides" by introducing the US research concept of molecular environmental sciences. His specific examples focused on the near- and medium-range co-ordination environment around the actinides on mineral surfaces and in silicate glass melts. The talk underlined the effects of anharmonicities on distances and co-ordination numbers determined by EXAFS and demonstrated the usefulness of Pauling bond valence theory for the construction of plausible structural models. C. Madic presented EXAFS investigations on the structure of trivalent lanthanide and americium solution complexes that are relevant to extractive separation of minor actinides from nuclear waste. P.G. Allen discussed anomalous background absorption effects and the influence of electronic structure on the XANES of solid actinide metals and oxides. The calculation of and comparison with experimental K-edge XANES spectra of several transition metal compounds, including technetium, with octahedral and tetrahedral symmetry were presented by V.L. Kraizman. Quantum chemical calculations of uranium(VI) species in aqueous solution and comparison of their metrical parameters with those from EXAFS measurements were given by S. Tsushima. L. Soderholm reported on EXAFS data and *ab initio* calculations on Np(VI) and Np(VII) species in alkaline solution. Related to radioactive waste disposal, F. Farges presented *in situ* XAFS studies on metals in silica melts over an extended temperature range. Molecular-level information on the sorption of thorium(IV) on montmorillonite and of uranium(VI) on zircon and zirconia were presented by R. Dähn and C. Lomenech, respectively.

The second day and part of the third day were devoted to "Application of Synchrotron Radiation Techniques and Complementary Techniques". In the first lecture in this session, D.K. Shuh discussed several experimental techniques available for actinide research at the ALS in the vacuum ultraviolet

(VUV)/soft X-ray region, i.e. X-ray photoelectron spectroscopy, NEXAFS spectroscopy and X-ray emission spectroscopy. J. Susini gave an overview of the experimental possibilities and applications of X-ray microscopy in the energy range of 2-10 keV at the ESRF. M. Drakopoulos and B. Salbu presented the principle of synchrotron X-ray microprobe and its application to the speciation of uranium particles, respectively. The characterisation of environmental particles was also the subject of the talk given by M. Betti. As techniques, which are complementary to synchrotron radiation, she applied secondary ion mass spectrometry and nuclear track methods to study particles containing actinides. Several presentations in this session were devoted to new results of XAFS investigations on actinide interactions with bacteria (C. Hennig) and humic substances (M.A. Denecke), of environmental plutonium samples (D.L. Clark), plutonium colloids and alloys (S.D. Conradson) and actinide complexes with hexacyano metallate ions (I. Bonhoure). Yu.A. Babanov introduced the Tikhonov regularisation method as an important alternative to the standard EXAFS analysis methods based on least-square fits. The investigation of X-ray magnetooptics in lanthanides, the pressure behaviour of actinides and the electronic structure of thin actinide films were the topics of talks given by K. Starke, R.G. Haire and T. Gouder, respectively.

In the final session entitled “Present and Future Synchrotron Facilities for Radionuclide Studies”, experimental stations available or planned for actinide research were presented: ALS (D.K. Shuh), APS (L. Soderholm), ESRF-ROBL (T. Reich), SSRL (G.E. Brown, Jr.), HASYLAB (E. Welter), ANKA (M.A. Denecke) and SOLEIL (C. Madic). After these oral presentations, the participants used the opportunity to visit several beam lines at the ESRF including BM 20 (Rossendorf Beamline for radiochemistry and materials research), ID 21 (X-ray microscopy) and ID 22 (X-ray fluorescence microprobe).

During the three days of Actinide-XAS-2000, both the quality and the number of new results in the field of radionuclide/actinide research using synchrotron radiation was impressive. Both the experts in the field and the large number of young scientists benefited from this excellent opportunity for scientific discussion and teaching. New projects for scientific collaborations were discussed. It was, therefore, suggested to keep convening this meeting every two years.

SESSION I

X-ray Absorption Spectroscopy of Radionuclides

Chairs: G. Kaindl, G. Bernhard, D.L. Clark

ACTINIDES IN SILICATE GLASSES AND MELTS AND ON MINERAL SURFACES: INFORMATION ON LOCAL CO-ORDINATION ENVIRONMENTS FROM XAFS SPECTROSCOPY AND BOND VALENCE THEORY

Gordon E. Brown, Jr.,[1,2] **François Farges,**[1,2,3] **John R. Bargar**[2] **and Hillary Thompson Berbeco**[4]
[1]Surface & Aqueous Geochemistry Group
Department of Geological & Environmental Sciences
Stanford University, Stanford, CA 94305-2115, USA
[2]Stanford Synchrotron Radiation Laboratory
P.O. Box 4349, Stanford, CA 94309-0210, USA
[3]Laboratoire des Géomatériaux, Université de Marne-la-Vallée
5, blvd Descartes, Champs s/Marne, 77454 Marne-la-Vallée Cedex 2, France
[4]F.W. Olin College of Engineering
1735 Great Plain Avenue, Needham, MA 02492-1245

Abstract

The impact of actinides on the environment is mitigated by their interaction with particle surfaces and by incorporation into suitable waste forms. In both cases, a fundamental knowledge of the local co-ordination environment of actinide ions is essential for understanding their stability in various near-surface environments under a range of conditions. When actinide ions are sorbed on mineral surfaces, the extent to which the ions are immobilised depends on the type of surface complex or solid precipitate that forms. When incorporated into a glass or crystalline waste form, the stability of the actinide will depend in part on its redox state and local co-ordination environment. In both cases, XAFS spectroscopy can provide unique information on the number and types of first and, in certain cases, more distant neighbours, and their geometric arrangement (including inter-atomic distances and a measure of their disorder). When this structural information from XAFS spectroscopy is combined with Pauling bond valence theory and modern bond valences corrected for bond length variations, it is also possible to develop plausible models for their medium-range co-ordination environments (out to ≈ 4 Å radial distance around the actinide) for both sorbed actinide ions and those present in a silicate glass or melt. We discuss results from several XAFS studies of the naturally occurring actinides uranium and thorium in sorption samples, silicate glasses and silicate melts at high temperature.

Introduction

When XAFS spectroscopy was first introduced as an element-specific method capable of providing quantitative information on the local co-ordination environment around selected atoms in crystalline and amorphous materials [1], few appreciated its potential applications in science and technology. In spite of a variety of early problems, including (1) non-optimised synchrotron sources operating in parasitic mode, (2) the inaccuracy of some XAFS-derived inter-atomic distances and co-ordination numbers due to inadequate model compounds and theoretical methods for deriving accurate phase shifts and backscattering amplitudes, (3) lack of proper experimental procedures and (4) anharmonic effects, this potential has been largely realised in modern XAFS studies. Because of dramatic improvements in XAFS theory, particularly the availability of user-friendly computer codes capable of accurate modelling of XAFS spectra (both XANES and EXAFS) of elements in different co-ordination environments (see e.g. Feff [2,3]), it is now possible to obtain accuracies of ±0.01 Å for first co-ordination shell inter-atomic distances around most absorber atoms and of ±0.04 Å for second-shell distances, even in structurally complex materials [4]. Corresponding improvements in synchrotron light sources [5] and X-ray detectors [6,7] have also had dramatic impacts on XAFS spectroscopy and its many applications. It is now possible to determine first-shell co-ordination environments of elements with atomic number >15 (P) at concentrations of 100 ppm in most types of materials (crystalline and amorphous solids under ambient conditions and aqueous solutions). With improvements in focusing optics at third-generation hard X-ray synchrotrons, X-ray beam diameters of 1-5 μm are now available for micro-XAFS studies of the spatial distribution and speciation of elements in highly heterogeneous samples such as soils and sediments [8,9]. These beams are also useful for the collection of spectra with very low signal-to-noise ratios (i.e. $< 10^{-4}$) required for improved pre-edge, XANES deconvolution, and next-nearest neighbour analyses, especially in natural materials, such as glasses or gels, where a continuum of sites for one specific element may be present. Applications of XAFS spectroscopy in mineralogy and geochemistry [10], environmental geochemistry/chemistry [11,12], interfacial chemistry [13,14], glass science [15,16], materials science and chemistry [11,17], and soil science [18], among other fields of science and engineering, are quite varied and, in many cases, provide unique information not easily obtainable by other means. In the case of actinides, XAFS spectroscopy has been used to obtain unique information about their co-ordination environments when present at mineral-water interfaces, in metamict minerals, or in silicate glasses and melts.

The purpose of this paper is to review several examples of these studies and to demonstrate how XAFS spectroscopy can be combined with Pauling bond valence theory to place constraints on the medium-range co-ordination environments of actinide ions in amorphous materials and at mineral-aqueous solution interfaces. In addition, because positional (or static) and thermal disorder involving actinide ions in solids or liquids at high temperatures can result in significant inaccuracies in inter-atomic distances and co-ordination numbers when using the normal harmonic approximation in EXAFS data analysis, we review the effects of anharmonicity on EXAFS spectra and some of the methods that can be used to account for these effects. Selected applications of XAFS spectroscopy to U and Th ions in metamict minerals, glasses and melts are discussed in a companion paper in this volume [19].

XAFS spectroscopy and anharmonic effects

EXAFS spectra can be modelled accurately, in the absence of multiple-scattering of the photoelectron among different atoms in the vicinity of the absorber, by using the single-scattering formalism [20], where the modulations of the normalised absorption coefficient $\chi(k)$ are given by:

$$\chi(k) = S_0^2 rf \sum_j \frac{N_j |F_{cw}|(k,R)}{k} \int_0^\infty \frac{g(R_j)}{R_j^2} e^{-2R_j/\lambda} \sin\left(2kR_j + \sum \phi(k,R)\right) dR \quad (1)$$

Here S_0^2 is the amplitude reduction factor, and *rf* is the reduction factor for the total central atom loss. Also, for every shell of neighbouring atoms *j*, N_j is the number of backscattering atoms; $|F_{cw}(k,R)|$ is the effective, curved-wave backscattering amplitude; R_j is the average distance between the central and backscattering atoms; $g(R_j)$ is the (partial) radial distribution function of the neighbouring distances around the absorbing element; λ is the photoelectron mean free path; and $\sum \phi(k,R)$ is the sum of the phase shift functions (central and backscattering phase shifts). This formalism is valid for any experimental XAFS data. Eq. (1) can be simplified by using a Gaussian pair distribution function to represent $g(R_j)$ when atomic vibrations are harmonic or when the distribution of inter-atomic distances is relatively symmetrical around the absorbing atom.

The local environment of actinides in many crystalline and amorphous materials at ambient to low temperatures (to 10 K) can be modelled accurately from EXAFS spectra using the harmonic approximation. This was demonstrated in several studies of U co-ordination environments in complex crystalline solids [21,22], metamict minerals [23] and silicate glasses [21]. This has also been demonstrated for Th in crystalline and amorphous materials [24,25]. However, in several of these studies, a quasi-anharmonic approach (two Gaussian shells fit and averaged) was needed for analysing the EXAFS spectra properly.

When positional disorder around an atom in a solid or liquid is large, however, such as for a low-valent, weakly bonded cation in silicate glasses, or when inter-atomic vibrations are anharmonic, such as for a non-framework cation in a silicate melt at high temperature, the harmonic approximation may fail to model the EXAFS data accurately, and EXAFS-derived inter-atomic distances and co-ordination numbers are often too small. In this case, it is necessary to use a $g(R_j)$ function that properly models anharmonicity. There are a number of ways of doing this (see [15] for a review of methods), including the cumulant expansion method [20], empirical anharmonic potential energy functions for a given bond type [26,27], empirical models that utilise known linear thermal expansion coefficients of specific bonds or Pauling bond valence for specific atom pairs [28] and analytical expressions for the anharmonic pair correlation function [29]. When anharmonic effects are large, the cumulant expansion method may be inadequate [30,31]. An example of this is the recent work of Wu and Farges [31], who carried out a high-temperature EXAFS study of crystalline ThO_2 over the temperature range 20 to 1 474°C (see Figure 1 in [19]). They used the analytical expression for anharmonic effects in Winterer's [29] XAFS data analysis code to derive average Th-O distances as a function of temperature that are consistent with known Th-O bond thermal expansion. The resulting average Th-O distances at 1 474°C are 2.44(1) and 2.33(1) Å, respectively, from anharmonic and harmonic fits of Th L_{III}-EXAFS data for ThO_2, in excellent agreement with *in situ* X-ray diffraction experiments.

U and Th co-ordination environments in silicate glasses and melts

Silicate glasses and melts have a special role in the long-term disposal of actinides because of the proposal to incorporate high-level nuclear waste in borosilicate glass [32]. The initial step in the vitrification process involves incorporation of actinides and other radioactive elements in a borosilicate melt, so a knowledge of the medium-range structural environment of the actinides in the melt and the quenched melt as a function of melt composition is important for tailoring the local environment of actinide ions for maximum stability.

Although the structures of silicate glasses and melts lack long-range order, the local co-ordination environments around cations can be relatively undistorted. For example, all available evidence from X-ray scattering and NMR measurements in silicate glasses and melts as well as borosilicate glasses and melts indicates that the silicate tetrahedron (SiO_4^{4-}) and borate tetrahedron (BO_4^{5-}) and triangle (BO_3^{3-}) are stable and relatively undistorted [15,33]. These small, high-valent ions act as network formers, whereas large, low-valent cations like Na^+, K^+ or Ca^{2+}, which have co-ordination numbers of 6 to 8 in silicate glasses [34-38], act as network modifiers or, alternatively, as charge-compensating cations, when cations like Al^{3+} occur in tetrahedral co-ordination in aluminosilicate glasses and melts. Uranium(IV,V) and thorium(IV) are relatively large ions that are typically six-co-ordinated by oxygens in silicate glasses and melts [21,24]. However, when the partial pressure of oxygen is sufficiently high to favour U(VI), uranium typically occurs in a different type of co-ordination environment in silicate glasses and melts, referred to as trans-dioxo, with two axial oxygens forming relatively short double bonds [$d(U = O_{axial}) = 1.77(2)$ to $1.85(2)$ Å]. The U(VI) co-ordination environment is completed by 4 to 5 equatorial oxygens that form longer bonds [$d(U - O_{equatorial}) \approx 2.23(3)$ Å]. Figure 1 shows models of these co-ordination environments in a sodium silicate glass derived from EXAFS spectroscopy and Pauling bond valence theory (see section entitled *Constraints on the medium-range co-ordination environments of cations in silicate glasses and melts and on mineral surfaces from XAFS spectroscopy and Pauling bond valence theory*). A similar co-ordination environment for U(VI) has also been found in naturally occurring Si-Al-Fe gels found in a uranium deposit associated with granitic rocks [39].

Figure 1. Models of medium-range co-ordination environments of (a) U(VI) and (b) U(V) and U(IV) in silicate glasses showing bond valence values for selected bonds (after [21])

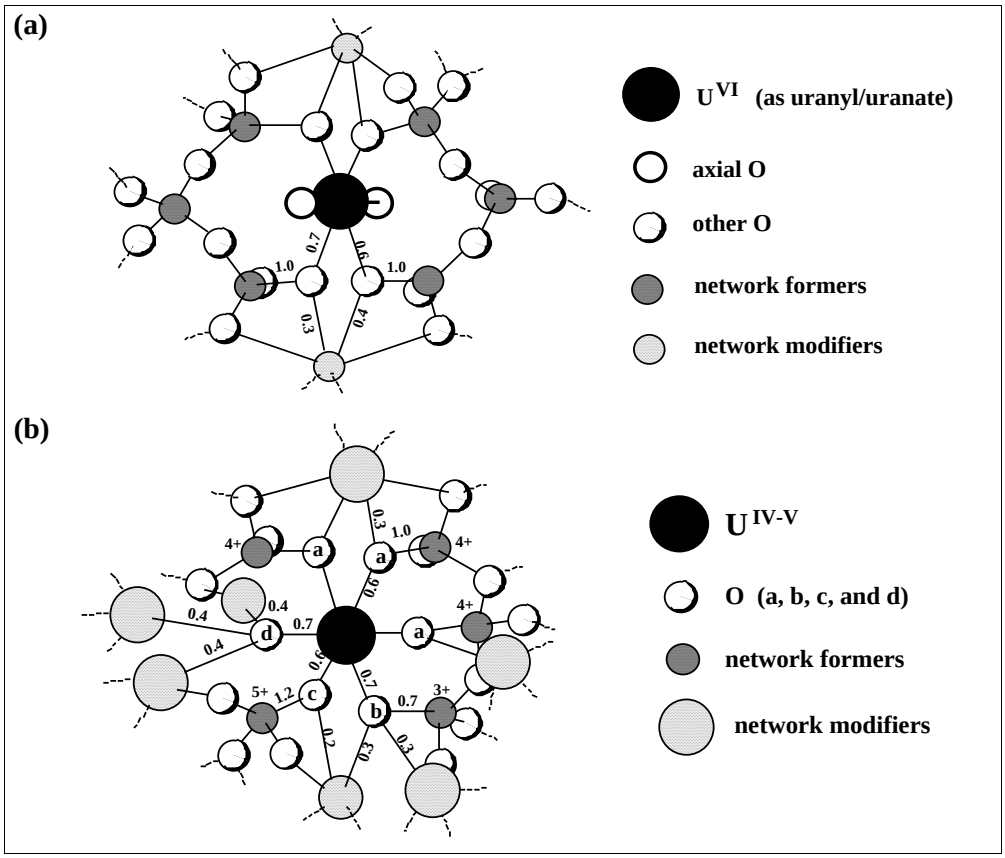

XAFS spectroscopy has also been used to determine the average first-shell co-ordination environments of actinides in silicate melts at high temperature (see [15] and [40] for a discussion of high-temperature EXAFS methods). For example, the local co-ordination environments of 0.2 to 7 wt.% U(VI) in $Na_2Si_2O_5$ and $Na_2Si_3O_7$ composition glasses and melts were studied at temperatures to 1 550 K [41]. U(VI) was found to be present as the uranyl moiety in these glass/melts for all temperatures and compositions examined. The local co-ordination environment of Th(IV) was also determined using high-temperature XAFS methods in the same glass/melt compositions [41]. Th(IV) was found to occur as a mixture of six and eight-co-ordinated Th at the 1-3 wt.% Th level, but as eight-co-ordinated Th when at trace levels (90-1 000 ppm). For these particular glass/melt compositions, neither U nor Th was found to undergo significant co-ordination changes during the glass-to-melt transformation. However, special care in data analysis was needed to account for the effects of anharmonicity (both positional and thermal effects) which tend to artificially increase the (apparent) amount of six-co-ordinated Th.

The co-ordination environments of a number of other selected cations commonly found in silicate, aluminosilicate and borosilicate glasses and melts are discussed in [15]. Many of these ions, including Zr(IV) and Th(IV), are "spectroscopically silent" and cannot be studied by most element-specific spectroscopic methods, including EPR, NMR and UV-vis-NIR spectroscopy. In addition, when at low concentrations, the co-ordination environments of these cations cannot be determined by X-ray or neutron scattering methods. The scattering power of an atom and its positional and thermal disorder are also important limitations. For example, the co-ordination environment of Na^+ in sodium silicate glasses and melts cannot be determined with much accuracy using X-ray scattering methods, even when present at relatively high concentrations, because the Na-O pair correlation function contributes little to the overall radial distribution function due to these effects [15]. This is also true for other important network modifiers like K^+ and Ca^{2+}. For these ions, as well as for the actinides, XAFS spectroscopy provides structural and compositional information about co-ordination environments that often can not be obtained using other structural methods.

Structural classification of cations in silicate glasses and melts

A convenient way of classifying cations among network forming and network modifying types is to examine their average bond strengths (s) in valence units (vu), which are defined in the classical Pauling sense [42] as ion charge/ion co-ordination number. Figure 2 plots bond strength values for many cations found in natural and technologically important silicate, aluminosilicate and borosilicate glasses and melts versus their atomic numbers. Cations in Category I (s = 0.75-1.3 vu) typically act as network formers, whereas those in Category II (s < 0.75 vu) act as network modifiers or charge-compensating cations. Generalised pictures of the linkages for each category of cation (I, II, III or IV) in glass and melts are shown on the right side of Figure 2. The figure to the right of Field I corresponds to two typical network formers (small dark grey atom) bonded to a common "bridging" oxygen (large light grey atom). It depicts more covalent bonds using thicker lines, with bond valences corresponding to 1 ± 0.25 vu for each bond. The figure to the right of Field II shows a network modifying ion (small dark grey atom) bonded to a non-bridging oxygen that is also bonded to a network-former, such as Si, and two other network modifier ions (light grey). The network modifier-oxygen bonds are typically more ionic than network former-oxygen bonds and have individual bond valences of < 0.75 vu). The figure to the right of Field III corresponds to a "complex-forming" ion that can only bond to non-framework oxygens (i.e. neither bridging nor non-bridging) because of the very high bond valence of these bonds (1.25 < s < 2 vu). The oxygens to which these "complex formers" bond are also bonded to an appropriate number of network modifiers required to satisfy Pauling's second rule. Finally, the figure to the right of Field IV shows the unusual case of a non-framework oxygen such as the axial oxygen of a uranyl moiety, with bond valence of 2 vu.

Figure 2. Average bond strength [43] versus atomic number (Z) for a variety of cations occurring in natural and technologically important silicate, aluminosilicate and borosilicate glasses and melts

The two five-co-ordinated values for Ti connected by the bracket between Fields I and III represent the apical Ti = O bond ("titanyl", s = 1.7 vu) and the four Ti-O bonds (s ≈ 0.7-0.8 vu). Similarly, the bond strengths for U(VI)-O_{axial} and U(VI)-$O_{equatorial}$ are located in Fields IV and II, respectively (after [44]).

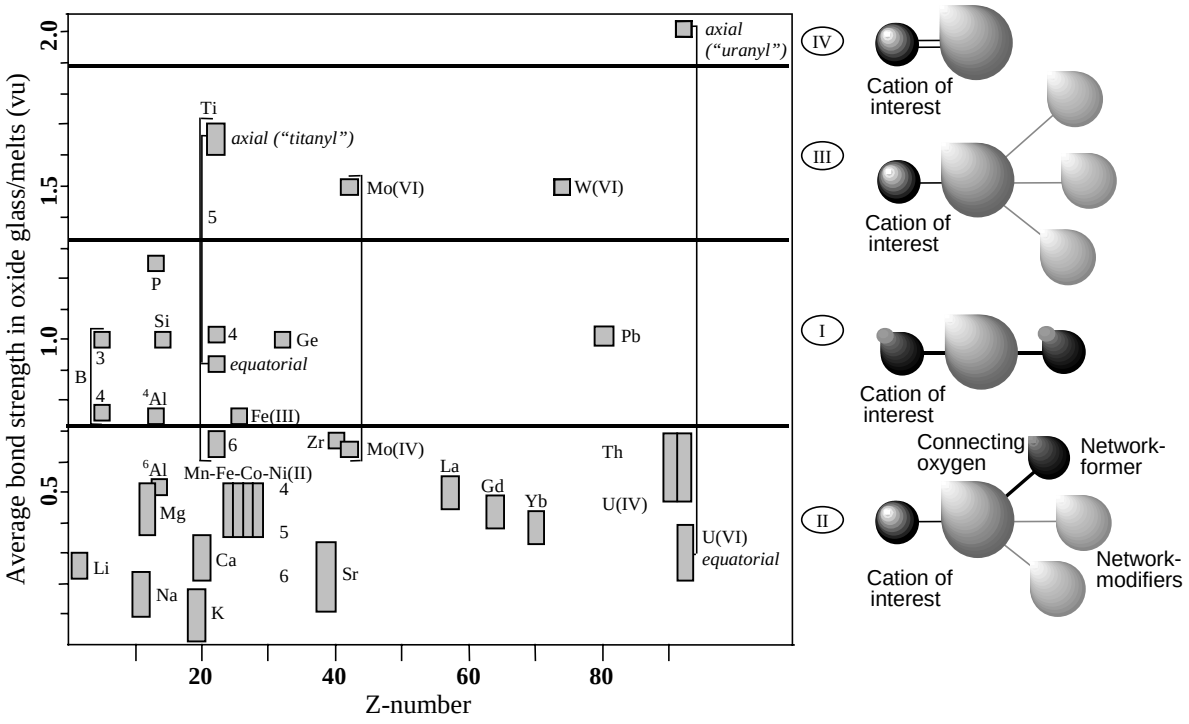

Six-co-ordinated U(IV) and Th(IV) have relatively high individual M-O bond valences (≈ 0.7 vu), which restricts the types of oxygens to which they can bond in silicate glasses and melts. This is also true of U(VI) in the uranyl moiety, in which the $U = O_{axial}$ bond has s ≈ 2 vu, whereas $U\text{-}O_{equatorial}$ bonds have s ≈ 0.62 vu. Some of the implications of the very high bond valence of $U = O_{axial}$ bonds for local and medium-range structure in silicate glasses and melts are discussed further in the following section.

Table 1 lists a number of parameters for selected cations (M), including (1) nominal valences; (2) most common co-ordination numbers in oxide compounds; (3) ionic radius values for different co-ordination numbers [45]; (4) mean linear thermal expansion coefficient of the M-O bond [46]; (5) mean M-O interatomic distance at 298 K (from the sum of Shannon and Prewitt ionic radius values [45]); (6) mean M-O interatomic distance at 1 773 K (calculated using $\bar{\alpha}$ values in Table 1); (7) field strength of the cation at 298 K; (8) the R_0 value used to calculate the Brese and O'Keeffe values of M-O bond valence [43]; (9) M-O bond valence at 298 K; and (10) M-O bond valence at 1 773 K. These parameters are useful for predicting the average co-ordination environments of cations in silicate glasses and melts and in building plausible medium-range structural models for these materials using the approach discussed below.

Table 1. Valence (Z), co-ordination number (CN), ionic radius, mean linear M-O expansion coefficient ($\overline{\alpha}$) ($\times 10^6$ K^{-1}) at 1 773 K, mean d(M-O) at 298 K, mean d(M-O) at 1 773 K, field strength, and bond valences at 298 K and 1 773 K for selected cations occurring in silicate glasses and melts (after [15])

Cation (M)	Nominal valence (Z)[1]	CN (M-O)[2]	Ionic radius (Å)[3]	Mean linear $\overline{\alpha}$ [4]	R_{298K} = D(M-O) (Å)[5]	$R_{1\ 773K}$ = D(M-O) (Å)[6]	Field strength {Z/R²}[7]	R_0 value[8]	M-O bond valence 298 K (vu)[9]	M-O bond valence 1 773 K (vu)[10]
Network modifiers										
Cs	1	8	1.74	32.0	3.10	3.25	0.10	2.42	0.16	0.11
K	1	8	1.51	32.0	2.87	3.01	0.12	2.13	0.14	0.09
Na	1	6	1.02	24.0	2.38	2.47	0.18	1.80	0.21	0.17
Sr	2	8	1.26	16.0	2.62	2.68	0.29	2.118	0.26	0.22
Ca	2	6	1.00	12.0	2.36	2.40	0.36	1.967	0.35	0.31
Mg	2	6	0.72	12.0	2.08	2.12	0.46	1.693	0.35	0.32
		5	0.66	10.0	2.02	2.05	0.49		0.41	0.38
		4	0.57	8.0	1.93	1.95	0.53		0.53	0.50
Fe	2	6	0.78	12.0	2.14	2.18	0.44	1.734	0.33	0.30
		5	0.70	10.0	2.06	2.09	0.47		0.41	0.38
		4	0.63	8.0	1.99	2.01	0.51		0.50	0.47
Pb	2	8	1.29	16.0	2.65	2.71	0.28	2.112	0.23	0.20
Al	3	6	0.535	8.0	1.90	1.92	0.83	1.651	0.51	0.48
		5	0.48	6.7	1.84	1.86	0.89		0.60	0.57
	3	6	0.645	8.0	2.00	2.02	0.75	1.759	0.52	0.49
		5	0.58	6.7	1.94	1.96	0.80		0.61	0.58
Ti	4	6	0.605	6.0	1.965	1.98	1.04	1.815	0.67	0.64
		5	0.34	5.0	1.70	1.71	1.38		1.4	1.32
Zr	4	8	0.84	8.0	2.20	2.23	0.83	1.937	0.49	0.46
		6	0.72	6.0	2.08	2.10	0.92		0.68	0.65
Th	4	8	1.05	8.0	2.41	2.44	0.69	2.167	0.52	0.48
		6	0.94	6.0	2.30	2.32	0.76		0.70	0.66
U	6	2	0.45	1.3	1.82	1.82	1.89	2.075	1.99	1.97
		4	0.89	2.7	2.25	2.26	1.19		0.62	0.61
	4	6	0.89	6.0	2.25	2.27	0.79	2.112	0.69	0.65
Network formers										
B	3	4	0.11	5.3	1.47	1.48	1.39	1.371	0.77	0.74
		3	0.01	4.0	1.37	1.38	1.60		1.00	0.98
Al	3	4	0.39	5.3	1.75	1.76	0.98	1.651	0.77	0.74
Fe	3	4	0.49	5.3	1.85	1.86	0.88	1.759	0.78	0.75
Si	4	4	0.26	4.0	1.62	1.63	1.52	1.624	1.01	0.98
Ti	4	5	0.51	5.0	1.95	1.96	1.05	1.815	0.70	0.67
		4	0.42	4.0	1.78	1.79	1.26		1.10	1.07

Constraints on the medium-range co-ordination environments of cations in silicate glasses and melts and on mineral surfaces from XAFS spectroscopy and Pauling bond valence theory

Medium-range (≤ 4 Å) co-ordination environments of cations in amorphous oxides or of cations sorbed at mineral-aqueous solution interfaces are difficult to determine by most experimental structural methods. This is true even for cases where a given cation is present at high concentrations, and it is especially true when cation concentration is in the parts per million range. Knowledge of medium-range ordering is essential for a fundamental understanding of the physical properties of aluminosilicate glasses and melts, such as their dissolution kinetics. A molecular-level knowledge of speciation is also

essential for understanding why some cations sorbed at mineral-water interfaces are easily desorbed (e.g. when present as weakly-bonded outer-sphere sorption complexes) and why some are more difficult to desorb (e.g. when present as inner-sphere sorption complexes or as three-dimensional precipitates).

Important constraints concerning the structure and composition of medium-range co-ordination environments of cations in such materials can be developed by combining structural and compositional information from XAFS spectroscopy and X-ray or neutron scattering with the concept of Pauling bond valence and Pauling's second rule for complex ionic crystals. Pauling's second rule [42] states that the sum of bond valences to an ion in a stable co-ordination environment should equal the absolute value of the nominal valence of the ion (±0.05 vu). This rule works well for crystalline oxides, including structurally complex silicates and aluminosilicates, and it has also been found to work well for cation environments in amorphous silicates [47] and aqueous solutions [48] and on mineral surfaces [49]. For instance, the bond valence rule can be used to test EXAFS-derived parameters for the short-range environments around cations in silicate glasses and melts. The co-ordination number N_j and first-neighbour distances R_j of a selected cation are obtained from fitting the experimental EXAFS spectra. One can then use the R_j values to determine average s_j values (the average bond valence of the bond studied by EXAFS) and determine if the calculated bond valence sum matches the nominal valence of the central ion probed [50]. Discrepancies between calculated valence sums and nominal valences for the central ion can be explained in most cases by the need for an appropriate anharmonic theory or the use of an improper anharmonic theory in fitting the EXAFS data.

We have used the approach described above to place constraints on the short- and medium-range co-ordination environments of cations in silicate glasses and melts [15,47,50] as well as on mineral surfaces [49,51]. We make use of the fact that the range of variations of M-O bond lengths in oxide materials differs with bond type and bond valence. For example, in a sodium aluminosilicate glass/melt, the classical Pauling bond valences for the ^{IV}Si-O, ^{IV}Al-O and ^{VI}Na-O bonds are 1.0, 0.75 and 0.167 vu, respectively. These values can be adjusted for variations in Si-O, Al-O, and Na-O bond lengths using the empirical bond strength-bond length model of Brown and Shannon [52] (see also [43,53]). An M-O bond with high bond valence should show less length variation than a bond with low bond valence in oxide materials. This is borne out in crystalline sodium aluminosilicates where the lengths of individual Si-O bonds vary between ≈ 1.54 and ≈ 1.70 Å, with bond valences ranging between 1.28 and 0.82 vu, and those of individual Al-O bonds vary between about 1.63 and 1.82 Å, with bond valences between 1.04 and 0.63 vu [54]. Because of their much smaller bond valences, which range between 0.29 and 0.02 vu, Na-O bonds show much larger variations in length in these materials (≈ 2.2 to ≈ 3.4 Å). All evidence to date indicates that similar bond length ranges occur in sodium aluminosilicate glasses, although the first-shell co-ordination environments of network modifying cations such as Na^+ and Ca^{2+} can be more regular in silicate glasses than in crystalline silicates [15,34,35,38,55].

In developing molecular models for the average medium-range co-ordination environment around a cation (M) in a silicate glass or melt or at a sodium aluminosilicate-aqueous solution interface, we fix the average M-O distance for the M cation to that derived from EXAFS spectroscopy and adjust the Si-O, Al-O, and Na-O bond lengths within the bond length ranges indicated above such that the total bond valence to each type of oxygen is near 2.0 vu. A similar approach works for other bond types as well. In the case of cations at mineral-aqueous solution interfaces, hydrogen bonds play an important role and can contribute significant bond valence (0.7-0.9 vu) when hydroxyl groups are present or much less bond valence (0.1-0.2 vu) when longer hydrogen bonds are present [51,56].

Recent molecular dynamics calculations for a variety of silicate glass and melt structures suggest that Pauling's bond valence rule employing Brese and O'Keeffe bond valences [43] is generally satisfied around most of the ions considered (e.g. O, Si, Na, K, Ti and Fe [50]). The few observed

discrepancies (especially around Ca) were found to be related to inaccurate pair potential parameters (Born-Mayer-Huggins type potentials were used), which were modified to yield excellent bond valence sums and more realistic structures.

Examples of the application of this approach to Zr(IV), Th(IV) and U(VI) can be found in [47], [24] and [21], respectively. As shown in Figure 1, the uranyl moiety is bonded to oxygens in the glass through equatorial bonds with bond valences of ≈ 0.6 vu. In addition, these oxygens are bonded to one four-co-ordinated Si rather than two ^{IV}Si. The latter case would result in a bond valence sum of 2.6 vu and "overbonding" of ≈ 0.6 vu, which violates Pauling's second rule; the former results in a bond valence sum of ≈ 1.7 vu, with an "underbonding" of ≈ 0.3 vu. This "underbonding" is satisfied by bonding a six-co-ordinated Na to the oxygen with a relatively short Na-O bond. Thus, U(VI) is predicted to bond only to non-bridging oxygens in an aluminosilicate glass or melt, and the axial oxygens of the uranyl moiety are not bonded to other cations since the bond valence of the $U = O_{axial}$ bond is ≈ 2 vu, which satisfies the bond valence requirements of the axial oxygens. This is tantamount to stating that the non-bonded electron density on the axial oxygens is sufficiently small such that lone pair repulsions between axial oxygens and other nearby oxygen ions do not destabilise the local structure [57]. In the case of U(IV), the first-neighbour oxygens around uranium can be bonded to $^{IV}Al^{3+}$ and two $^{VI}Na^{+}$, or to one $^{IV}Si^{4+}$ and one $^{VI}Na^{+}$, or to three $^{VI}Na^{+}$. Each of these second-neighbour arrangements would result in a bond valence sum near 2 vu.

In the case of uranyl sorption on mineral surfaces, as discussed earlier, the same procedure can be applied to develop plausible models for the extended bonding environment of U(VI). As for the uranyl moiety in silicate glasses, the axial oxygens do not bond to mineral surfaces. Instead, the uranyl ion forms inner-sphere complexes on oxide mineral surfaces by bonding through equatorial oxygens [58].

XAFS studies of the sorption of actinides on mineral surfaces

Sorption of actinides on mineral surfaces provides a natural or "engineered" means of sequestering these ions in groundwater aquifers and vadose zones, thus mitigating their dispersal. There have been a limited number of XAFS studies of aqueous actinide ion sorption on "model" mineral surfaces in controlled laboratory conditions as a function of pH, including U(VI) sorption on montmorillonite [59-62], kaolinite [58], vermiculite and hydrobiotite [63], alumina [61,62], silica [59,61,62], silica gel [64], hematite [65], hydrous iron and manganese oxides [66], ferrihydrite [64,67] and hydrothermally altered concrete [68]; Th(IV) sorption on amorphous silica [69]; and Np(V) sorption on goethite [70]. In each of these studies, evidence was found from EXAFS spectroscopy that the actinide is dominantly bound in an inner-sphere fashion on the mineral surface. In the case of actinide sorption on iron and manganese oxide surfaces, EXAFS spectroscopy revealed that the binding is bidentate, indicating a relatively strong adsorbate-adsorbent bond.

The EXAFS study of Thompson, *et al*. [58] examined the reaction products resulting from the uptake of $U(VI)_{aqueous}$ onto kaolinite (KGa-2) particles over the pH range 6.0 to 7.9 and in the presence and absence of CO_2 in air. Under all conditions examined, the sorbed uranyl moiety is characterised by two short axial bonds ($d(U = O_{axial})$ = 1.80(2) Å) and five equatorial bonds, consisting of two short (≈ 2.28(2) Å) and three long (≈ 2.48(2) Å) $U\text{-}O_{equatorial}$ bonds. The EXAFS data for U(VI) sorbed on kaolinite under all conditions examined also showed the presence of second-neighbour Si (and/or Al) at ≈ 3.3(3) Å from U, suggesting that U(VI) forms inner-sphere complexes on the kaolinite surface (Figure 3). Samples in contact with air at $6.0 \leq pH \leq 7.0$ had predominantly monomeric uranyl species, whereas at $7.0 \leq pH \leq 7.9$, the dominant U(VI) species is multi-nuclear, suggesting that increasing pH

Figure 3. Molecular models of U(VI) sorption on kaolinite based on the EXAFS spectroscopy results of Thompson, *et al*. [58]

Possible adsorbed species include mononuclear, monodentate U(VI) complexes bonded through equatorial oxygens to the aluminol layer as well as multi-nuclear U(VI) species bonded in a bidentate fashion to the aluminol layer. Also shown are an outer-sphere U(VI)-carbonato species and an outer-sphere multi-nuclear U(VI) species, neither of which is thought to be a dominant species based on EXAFS analysis.

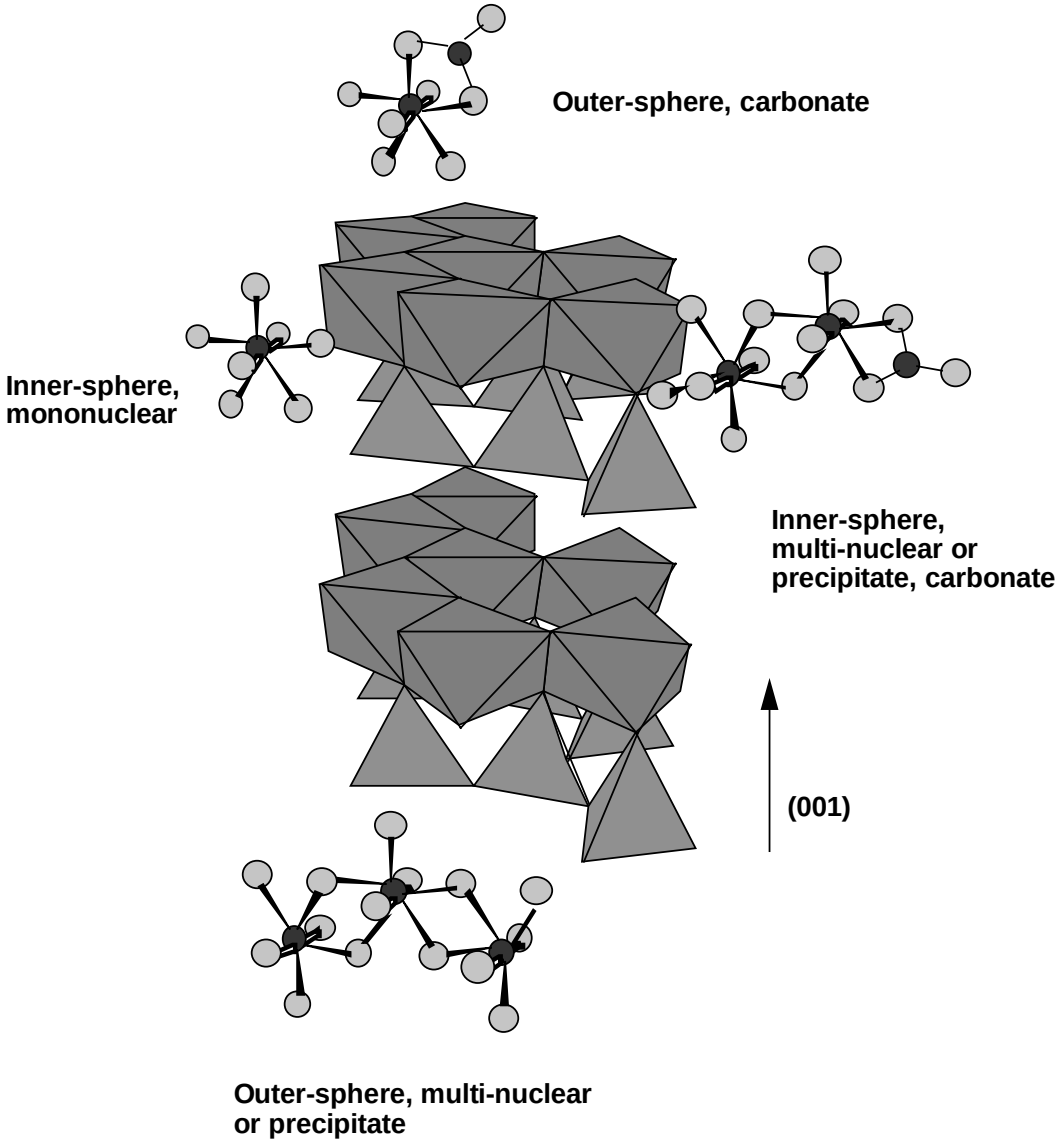

favours the formation of multinuclear U complexes. In the absence of CO_2, the results of Thompson, *et al*. [58] suggest that the kaolinite surface enhances U(VI) polymerisation, at least in the short term. These multi-nuclear surface species could be precursors to U(VI)-containing precipitates, which may form over longer time periods, or, alternatively, a surface precipitate or a U-Si/Al hydroxide co-precipitate. This finding suggests that kaolinite may be an effective sorbent for the removal of U(VI) from groundwater or ponded waste water because the formation of multi-nuclear sorption species increases kaolinite's capacity for sorbing U(VI) over that if only mononuclear U(VI) species formed. Similar experiments on hematite, followed by EXAFS and ATR-FTIR characterisation studies, indicate the presence of U(VI)-carbonato ternary surface complexes on hematite [65,71].

An interesting application of EXAFS spectroscopy to actinide transport in groundwater is the recent study by Fuller, *et al*. [72] of the interaction of $U(VI)_{aqueous}$ with an in-ground engineered barrier consisting of bone charcoal in Fry Canyon, Utah. Their hypothesis was that an insoluble uranyl phosphate would form when the U(VI)-containing groundwater interacted with apatite in the bone charcoal. Instead, the U L_{III}-EXAFS spectra of the reacted bone charcoal samples were interpreted as indicating that a significant fraction of the U(VI) was adsorbed on the surface of apatite particles. No evidence for a crystalline U-containing precipitate was found by X-ray diffraction. This example illustrates the utility of EXAFS spectroscopy in detecting adsorbed U(VI) in a complex sample.

Another recent application of micro-XAFS spectroscopy to actinides important in high level radioactive waste involves a study of the interaction of $Pu(V)_{aqueous}$ with altered tuff from the proposed Yucca Mountain, Nevada high level waste repository [9]. Among other minerals, this tuff contains clinoptilolite $[(Na,K,Ca)_2Al_3(Al,Si)_2Si_{13}O_{36}\cdot 12H_2O]$ and smectite $[(Na,Ca)Al_4(Si,Al)_8O_{20}(OH)_4\cdot 2(H_2O)]$ coated with iron and manganese oxides. Micro-XAFS mapping of the reacted tuff showed that Pu(V) is associated only with the manganese oxide coatings on smectite grains, and not with iron oxide coatings or other minerals. Unfortunately, it is not possible to infer if the Pu(V) forms a true adsorption complex on the manganese oxide from the XAFS data reported. However, this example illustrates the need to know what phase(s) a particular solution species preferentially sorbs onto in a complex mixture of phases so that laboratory studies of sorption processes of actinides and other ions make use of the appropriate model sorbents. The information from this study has very practical applications as well to understanding how $Pu(V)_{aqueous}$ might be retarded should it be released into a groundwater aquifer.

Conclusions

XAFS studies of actinides in silicate glasses and melts or sorbed on mineral surfaces have provided unique insights about their co-ordination environments not obtainable from other structural methods. When EXAFS-derived inter-atomic distances and co-ordination numbers are combined with the constraints on bonding from Pauling bond valence theory, it is possible to develop plausible molecular models of medium-range co-ordination environments around actinides (out to a radial distance of 4 Å around the absorbing atom) in these materials. The examples included in this review are illustrative of the progress made in XAFS spectroscopy on oxide materials since it was first introduced as a structural method almost 30 years ago. Over the next 30 years, it is likely that further developments in XAFS spectroscopy methods, synchrotron X-ray sources, and X-ray detectors will result in extensions of these types of studies to actinides in even more complex materials at smaller spatial scales and lower concentrations than currently possible.

Acknowledgements

We thank the organising committee for the invitation to present this paper at the Actinide-XAS-2000 Workshop in Grenoble, France. We also wish to thank Dr. David K. Shuh (Chemical Sciences Division, Lawrence Berkeley National Laboratory) for a careful review of the manuscript. Our work discussed in this review was generously supported by the US Department of Energy (DOE) and the US National Science Foundation. Our synchrotron radiation studies were carried out at the Stanford Synchrotron Radiation Laboratory (SSRL) and the Laboratoire pour l'Utilisation du Rayonnement Electromagnetique (LURE). SSRL is supported by the US DOE and the National Institutes of Health. The technical staffs of both laboratories are thanked for their help during our XAFS studies.

REFERENCES

[1] D.E. Sayers, E.A. Stern and F.W. Lytle, "New Technique for Investigating Non-crystalline Structures: Fourier Analysis of the Extended X-ray Absorption Fine Structure", *Phys. Rev. Lett*., 27, 1204-1207 (1971).

[2] J.J. Rehr, S.I. Zabinsky and R.C. Albers, "High-order Multiple Scattering Calculations of X-ray Absorption Fine Structure", *Phys. Rev. Lett*., 69, 3397-4000 (1992).

[3] A.L. Ankudinov, B. Ravel, J.J. Rehr and S.D. Conradson, "Real-space Multiple-scattering Calculation and Interpretation of X-ray Absorption Near-edge Structure", *Phys. Rev*., B 58, 7565-7576 (1998).

[4] P.A. O'Day, J.J. Rehr, S.I. Zabinsky and G.E. Brown, Jr., "Extended X-ray Absorption Fine Structure (EXAFS) Analysis of Disorder and Multiple Scattering in Complex Crystalline Solids", *J. Am. Chem. Soc*., 116, 2938-2949 (1994).

[5] J. Corbett and T. Rabedeau, "Intermediate Energy Storage Rings (2.5-4.0 GeV)", *Synchrotron Rad. News*, 12, 25-33 (1999).

[6] G.A. Waychunas and G.E. Brown, Jr., "Fluorescence Yield XANES and EXAFS Experiments: Application to Highly Dilute and Surface Samples", *Advances in X-ray Analysis*, 37, 607-617 (1994).

[7] C. Gauthier, V.A. Solé, R. Signorato, J. Goulon and E. Moguiline, "The ESRF Beamline ID26: X-ray Absorption on Ultra Dilute Sample", *J. Synchrotron Rad.*, 6, 164-166 (1999).

[8] P.M. Bertsch, D.B. Hunter, S.R. Sutton, S. Bajt and M.L. Rivers, "*In Situ* Chemical Speciation of Uranium in Soils and Sediments by Micro X-ray Absorption Spectroscopy", *Environ. Sci. Technol.*, 28, 980-984 (1994).

[9] M.C. Duff, M. Newville, D.B. Hunter, P.M. Bertsch, S.R. Sutton, I.R. Triay, D.T. Vaniman, P. Eng and M.L. Rivers, "Micro-XAS Studies with Sorbed Plutonium on Tuff", *J. Synchrotron Rad.*, 6 (3), 350-352 (1999).

[10] G.E. Brown, Jr., G. Calas, G.A. Waychunas and J. Petiau, "X-ray Absorption Spectroscopy and its Applications in Mineralogy and Geochemistry", in *Spectroscopic Methods in Mineralogy and Geology*, F. Hawthorne, ed., *Reviews in Mineralogy*, Vol. 18, pp. 431-512, Mineralogical Society of America, Washington, DC (1988).

[11] S.D. Conradson, "Application of X-ray Absorption Fine Structure Spectroscopy to Materials and Environmental Science", *Appl. Spectrosc*., 52, 252-279 (1998).

[12] G.E. Brown, Jr., A.L. Foster and J.D. Ostergren, "Mineral Surfaces and Bioavailability of Heavy Metals: A Molecular-scale Perspective", Proc. Nat. Acad. Sci. USA 96, 3388-3395 (1999).

[13] G.E. Brown, Jr., "Spectroscopic Studies of Chemisorption Reaction Mechanisms at Oxide/ Water Interfaces", in *Mineral-water Interface Geochemistry*, M.F. Hochella, Jr. and A.F. White, eds., *Reviews in Mineralogy*, Vol. 23, pp. 309-363, Mineralogical Society of America, Washington, DC (1990).

[14] G.E. Brown, Jr., V.E. Henrich, W.H. Casey, D.L. Clark, C. Eggleston, A. Felmy, D.W. Goodman, M. Grätzel, G. Maciel, M.I. McCarthy, K. Nealson, D.A. Sverjensky, M.F. Toney and J.M. Zachara, "Metal Oxide Surfaces and Their Interactions with Aqueous Solutions and Microbial Organisms", *Chem. Rev.*, 99, 77-174 (1999).

[15] G.E. Brown, Jr., F. Farges and G. Calas, "X-ray Scattering and X-ray Spectroscopy Studies of Silicate Melts", in *Structure, Dynamics, and Properties of Silicate Melts*, J.F. Stebbins, P.F. McMillan and D.B. Dingwell, eds., *Reviews in Mineralogy*, Vol. 32, pp. 317-419, Mineralogical Society of America, Washington, DC (1995).

[16] G. Calas, G.E. Brown, Jr., F. Farges, L. Galoisy, J.P. Itie and A. Polian, "Cations in Glasses Under Ambient and Non-ambient Conditions", *Nucl. Instru. Meth. Phys. Res.*, B 97, 155-161 (1995).

[17] "Synchrotron Radiation Techniques in Industrial, Chemical and Materials Science" K.L. D'Amico, L.J. Terminello and D.K. Shuh, eds., Plenum Press, New York (1996).

[18] S.E. Fendorf, "Fundamental Aspects and Applications of X-ray Absorption Spectroscopy in Clay and Soil Science", in *Synchrotron X-ray Methods in Clay Science*, Clay Minerals Society Workshop Lecture, 9, 19-67 (1999).

[19] F. Farges, M. Harfouche, P-E. Petit and G.E. Brown, Jr., "Actinides in Earth Materials: The Importance of Natural Analogues", these proceedings (2001).

[20] E.D. Crozier, J.J. Rehr and R. Ingalls, "Amorphous and Liquid Systems", in *X-ray Absorption. Principles, Applications, Techniques of EXAFS, SEXAFS and XANES*, D.C. Koningsberger and R. Prins, eds., *Chemical Analysis*, Vol. 92, pp. 373-442, John Wiley & Sons, New York (1988).

[21] F. Farges, C.W. Ponader, G. Calas and G.E. Brown, Jr., "Local Environment Around Incompatible Elements in Silicate Glass/Melt Systems. II: U(VI), U(V) and U(IV)", *Geochim. Cosmochim. Acta*, 56, 4205-4220 (1992).

[22] H.A. Thompson, G.E. Brown, Jr. and G.A. Parks, "XAFS Spectroscopic Study of Uranyl Co-ordination in Solids and Aqueous Solution", *Am. Mineral.*, 82, 483-496 (1997).

[23] F. Farges, R.C. Ewing and G.E. Brown, Jr., "The Structure of Aperiodic, Metamict, (Ca, Th)$ZrTi_2O_7$: An EXAFS Study of the Zr, Th and U sites", *J. Materials Res.*, 8, 1983-1995 (1993).

[24] F. Farges, "Structural Environment Around Th^{4+} in Silicate Glasses: Implications for the Geochemistry of Incompatible Me^{4+} Elements", *Geochim. Cosmochim. Acta*, 55, 3303-3319 (1991).

[25] F. Farges and G. Calas, "Structural Analysis of Radiation Damage in Zircon and Thorite: An X-ray Absorption Study", *Amer. Mineral.*, 76, 60-73 (1991).

[26] W.E. Jackson, G.A. Waychunas, G.E. Brown, Jr., J. Mustre de Leon, S.D. Conradson, J-M. Combes, "*In Situ* High-temperature X-ray Absorption Study of Ferrous Iron in Orthosilicate Crystals and Liquids", in *X-ray Absorption Fine Structure*, S.S. Hasnain, ed., pp. 298-301, Ellis Horwood Ltd., Chichester, UK (1991).

[27] W.E. Jackson, G.E. Brown, Jr., G.A. Waychunas, J. Mustre de Leon, S.D. Conradson and J-M. Combes, " High-temperature XAS Study of Fe_2SiO_4: Evidence for Reduced Co-ordination of Ferrous Iron in the Liquid", *Science*, 262, 229-233 (1993).

[28] F. Farges and G.E. Brown, Jr., "An Empirical Model for the Anharmonic Analysis of High-temperature XAFS Spectra of Oxide Compounds with Applications to the Co-ordination Environment of Ni in NiO, γ-Ni_2SiO_4 and Ni-bearing Na-disilicate Glass and Melt", *Chem. Geol.*, 128, 93-106 (1996).

[29] M. Winterer, Proceedings of the 9th International Conference on X-ray Absorption Fine Structure (XAFS IX, Grenoble), *J. Phys IV France*, 7, 243 (1997).

[30] J. Mustre de Leon, S.D. Conradson, A.R. Bishop, I.D. Raistric, I. Batistic, W.E. Jackson, G.E. Brown, Jr. and G.A. Waychunas, "XAFS Analysis in the Anharmonic Limit: Applications to Hi-T_c Superconductors and Ferrosilicates", in *XAFS VI, Sixth International Conference on X-ray Absorption Fine Structure*, S.S. Hasnain, ed., pp. 54-57, Ellis Horwood Ltd. Publishers, Chichester, UK (1991).

[31] Z. Wu and F. Farges, "Anharmonicity Around Th in Crystalline Oxide-type Compounds. An *In Situ*, High-temperature XAFS Spectroscopy Study", *Physica*, B 266, 282-289 (1999).

[32] N.E. Bibler, J.P. Bibler, M.K. Andrews and C.M. Jantzen, "Initial Demonstration of the Vitrification of High-level Nuclear Waste Sludge Containing an Organic Cs-loaded Ion-exchange Resin", *Mat. Res. Soc. Symp. Proc.*, Vol. 294, 81-86 (1993).

[33] J.F. Stebbins, "Dynamics and Structure of Silicate and Oxide Melts: Nuclear Magnetic Resonance Studies", in *Structure, Dynamics, and Properties of Silicate Melts*, J.F. Stebbins, P.F. McMillan and D.B. Dingwell, eds., *Reviews in Mineralogy*, Vol. 32, pp. 191-246, Mineralogical Society of America, Washington, DC (1995).

[34] N. Binstead, G.N. Greaves and C.M.B. Henderson, "An EXAFS Study of Glassy and Crystalline Phases of Compositions $CaAl_2Si_2O_8$ (Anorthite) and $CaMgSi_2O_6$ (Diopside)", *Contrib. Min. Petrol.*, 89, 103-109 (1985).

[35] D.A. McKeown, G.A. Waychunas and G.E. Brown, Jr., "EXAFS and XANES Study of the Local Co-ordination Environment of Sodium in a Series of Silica-rich Glasses and Selected Minerals within the Sodium Aluminosilicate System", *J. Non-Crystal. Solids*, 74, 325-348 (1985).

[36] W.E. Jackson, G.E. Brown, Jr. and C.W. Ponader, "X-ray Absorption Study of the Potassium Co-ordination Environment in Glasses from the $NaAlSi_3O_8$-$KAlSi_3O_8$ Binary: Structural Implications for the Mixed-alkali Effect", *J. Non-Crystal. Solids*, 93, 311-322 (1987).

[37] M.C. Eckersley, P.H. Gaskell, A.C. Barnes and P. Chieux, "Structural Ordering in a Calcium Silicate Glass", *Nature* 335, 525-527 (1988).

[38] J-M. Combes, G.E. Brown, Jr. and G.A. Waychunas, "X-ray Absorption Study of the Local Ca Environment in Silicate Glasses", in *XAFS VI, Sixth Internat. Conf. on X-ray Absorption Fine Structure*, S.S. Hasnain, ed., Ellis Horwood Ltd, Publishers, pp. 312-314 (1991).

[39] T. Allard, P. Ildefonse, K. Beaucaire and G. Calas, "Structural Chemistry of Uranium Associated with Si, Al, Fe Gels in a Granitic Uranium Mine", *Chem. Geol.*, 158, 81-103 (1999).

[40] F. Farges, G. Fiquet, J-P. Itie and D. Andrault, "A New Device for XAFS Data Collection up to 2 000 K (or 3 700 K Under Vacuum)", *Nucl. Instr. Meth. Phys.*, 101, 493-498 (1995).

[41] F. Farges and G.E. Brown, Jr., "Co-ordination of Actinides in Silicate Melts", *J. de Physique IV*, Colloque C2, 1009-1010 (1997).

[42] L. Pauling, "The Principles Determining the Structure of Complex Ionic Crystals", *J. Amer. Chem. Soc.*, 51, 1010-1026 (1929).

[43] N.E. Brese and M. O'Keeffe, "Bond-valence Parameters in Solids", *Acta Crystallogr.*, B47, 192-197 (1991).

[44] F. Farges, "Ordre local autour d'éléments fortements chargés dans des silicates amorphes: métamictes, vitreux et fondus" (*Structural Environments Around Highly-charged Cations in Aperiodic Oxide Structures: Radiation-damaged Minerals, Glasses and Melts*), Habilitation a diriger les recherches, Université Marne-la-Vallée (*in French w/abstracts in English*) (1994).

[45] R.D. Shannon and C.T. Prewitt, "Effective Ionic Radii in Oxides and Fluorides", *Acta Crystallogr.*, B25, 925-945 (1969).

[46] R.M. Hazen and L.W. Finger, "Comparative Crystal Chemistry", Wiley-Interscience, New York (1982).

[47] F. Farges, C.W. Ponader and G.E. Brown, Jr., "Structural Environments of Incompatible Elements in Silicate Glass/Melt Systems: I. Zr at Trace Levels", *Geochim. Cosmochim. Acta*, 55, 1563-1574 (1991).

[48] I.D. Brown, "Recent Developments in the Bond Valence Model of Inorganic Bonding", *Phys. Chem. Minerals*, 15, 30 (1987).

[49] J.R. Bargar, S.N. Towle, G.E. Brown, Jr. and G.A. Parks, "Structure, Composition and Reactivity of Pb(II) and Co(II) Sorption Products and Surface Functional Groups on Single-crystal α-Al_2O_3", *J. Colloid Interface Sci.*, 85, 473-493 (1997).

[50] S. Rossano, F. Farges, A. Ramos, J-M. Delaye and G.E. Brown, Jr., "Bond Valence Models in Silicate Glasses and Melts", Proc. First International Symposium on Non-crystalline Solids (in press) (2001).

[51] J.R. Bargar, G.E. Brown, Jr. and G.A. Parks, "Surface Complexation of Pb(II) at Oxide-water Interfaces: I. XAFS and Bond-valence Determination of Mononuclear and Polynuclear Pb(II) Sorption Products on Aluminum Oxides", *Geochim. Cosmochim. Acta*, 61, 2617-2637 (1997).

[52] I.D. Brown and R.D. Shannon, “Empirical Bond Strength-bond Length Curves for Oxides”, *Acta Crystallogr.*, A29, 266-282 (1973).

[53] I.D. Brown and D. Altermatt, “Bond-valence Parameters Obtained from a Systematic Analysis of the Inorganic Crystal Structure Database”, *Acta Crystallogr.*, B41, 244-247 (1985).

[54] G.E. Brown, Jr., G.V. Gibbs and P.H. Ribbe, “The Nature and Variation in Length of the Si-O and Al-O Bond in Framework Silicates”, *Amer. Mineral.*, 54, 1044-1061 (1969).

[55] D.A. McKeown, G.A. Waychunas and G.E. Brown, Jr., “EXAFS Study of the Co-ordination Environment of Aluminum in a Series of Silica-rich Glasses and Selected Minerals Within the Sodium Aluminosilicate System”, *J. Non-Crystal. Solids*, 74, 349-371 (1985).

[56] I.D. Brown, “Chemical and Steric Constraints in Inorganic Solids”, *Acta Crystallogr.*, B 48, 553-572 (1992).

[57] B.H.W.S. deJong and G.E. Brown, Jr., “Polymerization of Silicate and Aluminate Tetrahedra in Glasses, Melts and Aqueous Solutions: I. Electronic Structures of $H_6Si_2O_7$, $H_6Al_2O_7^{1-}$ and $H_6Al_2O_7^{2-}$, *Geochim. Cosmochim. Acta*, 44, 491-511 (1980).

[58] H.A. Thompson, G.A. Parks and G.E. Brown, Jr., “Structure and Composition of Uranium(VI) Sorption Complexes at the Kaolinite-water Interface”, in *Adsorption of Metals by Geomedia, Variables, Mechanisms and Model Applications*, E.A. Jenne, ed., pp. 349-370, Academic Press, New York (1998).

[59] A.J. Dent, J.D.F. Ramsay and S.W. Swanton, “An EXAFS Study of Uranyl Ions in Solutions and Sorbed onto Silica and Montmorillonite Clay Colloids”, *J. Colloid Interface Sci.*, 150, 45-60 (1992).

[60] C.J. Chisholm-Brause, S.D. Conradson, C.T. Buscher, P.G. Eller and D.E. Morris, “Speciation of Uranyl Sorbed at Multiple Binding Sites on Montmorillonite”, *Geochim. Cosmochim. Acta*, 58, 3625-3631 (1994).

[61] E.R. Sylwester, E.A. Hudson and P.G. Allen, “Surface Interactions of Actinide Ions with Geologic Materials Studied by XAFS”, *Mat. Res. Soc. Symp. Proc.*, 590, 9-16 (2000).

[62] E.R. Sylwester, E.A. Hudson and P.G. Allen, “The Structure of Uranium (VI) Sorption Complexes on Silica, Alumina and Montmorillonite”, *Geochim. Cosmochim. Acta*, 64, 2431-2438 (2000).

[63] E.A. Hudson, L.J. Terminello, B.E. Vianni, M. Denecke, T. Reich, P.G. Allen, J.J. Bucher, D.K. Shuh and N.M. Edelstein, “The Structure of Uranium(VI) Sorption Complexes on Vermiculite and Hydrobiotite”, *Clays and Clay Minerals*, 47, 439-457 (1999).

[64] T. Reich, H. Moll, T. Arnold, M.A. Denecke, C. Hennig, G. Geipel, G. Bernhard, H. Nitsche, P.G. Allen, J.J. Bucher, N.M. Edelstein and D.K. Shuh, “An EXAFS Study of Uranium(VI) Sorption onto Silica Gel and Ferrihydrite”, *J. Electron Spectrosc. Relat. Phenom.*, 96, 237-243 (1998).

[65] J.R. Bargar, R. Reitmeyer and J.A. Davis, “Spectroscopic Confirmation of Uranium(VI)-carbonato Adsorption Complexes on Hematite”, *Environ. Sci. Technol.*, 33, 2481-2484 (1999).

[66] A. Manceau, L. Charlet, M.C. Boisset, B. Didier and L. Spadini, "Sorption and Speciation of Heavy Metals on Hydrous Fe and Mn Oxides: From Microscopic to Macroscopic", *Appl. Clay Sci.*, 7, 201-223 (1992).

[67] T.D. Waite, J.A. Davis, T.E. Payne, G.A. Waychunas and N. Xu, "Uranium(VI) Adsorption to Ferrihydrite: Application of a Surface Complexation Model", *Geochim. Cosmochim. Acta*, 58, 5465-5478 (1994).

[68] P. Zhao, P.G. Allen, E.R. Sylwester and B.E. Viani, "The Sorption of Uranium(VI) and Neptunium(V) onto Hydrothermally Altered Concrete", *Radiochim. Acta*., 88, 729-736 (2000).

[69] E. Östhols, A. Manceau, F. Farges and L. Charlet, "Adsorption of Th on Amorphous Silica: An EXAFS Study", *J. Colloid Interface Sci.*, 194, 10-21 (1997).

[70] J-M. Combes, C.J. Chisholm-Brause, G.E. Brown, Jr., G.A. Parks, S.D. Conradson, P.G. Eller, I. Triay and A. Meier, "EXAFS Spectroscopic Study of Neptunium(V) Sorbed at the α-FeOOH/ Water Interface", *Environ. Sci. Technol.*, 26, 376-382 (1992).

[71] J.R. Bargar, R. Reitmeyer, J.J. Lenhart and J.A. Davis, "Characterization of U(VI)-carbonato Ternary Complexes on Hematite: EXAFS and Electrophoretic Mobility Measurements", *Geochim. Cosmochim. Acta*, 64, 2737-2749 (2000).

[72] C.C. Fuller, J.R. Bargar, J.A. Davis and M.J. Piana, "Mechanisms of Uranium Interactions with Apatite: Implications for Ground-water Remediation", *Environ. Sci. Technol.* (in review) (2001).

SOLVENT PHASE CHARACTERISATION OF LANTHANIDE(III) AND AMERICIUM(III) COMPLEXES WITH MALONAMIDE (TEMA) AND TERPYRIDINE LIGANDS BY EXAFS: COMPARISON WITH SINGLE CRYSTALS

C. Den Auwer,[1] **M. Grigoriev,**[2] **C. Madic,**[3] **M.T. Presson,**[1] **M. Nierlich,**[4] **P. Thuery,**[4] **F. David,**[5] **S. Hubert,**[5] **M.G.B. Drew,**[6] **M.J. Hudson,**[6] **P.B. Iveson,**[6] **M.L. Russell**[6]
[1]CEA/Marcoule, DCC/DRRV/SEMP, BP 17171, F-30207 Bagnols-sur-Cèze, France
[2]Institute of Physical Chemistry, Moscow, Russia
[3]CEA/Saclay, DCC
[4]CEA/Saclay, DSM/DRECAM/SCM, Gif-sur-Yvette, France
[5]Institut de Physique Nucléaire, Orsay, France
[6]Reading University, Reading, UK

Abstract

In order to develop molecules that will be good candidates for the extractive separation of the various elements contained within nuclear fuels, 4f and 5f molecular chemistry has been the subject of numerous studies. Thus, to better understand the ligand to cation interaction and to fine tune the theoretical models, precise knowledge about the cation co-ordination sphere must be obtained. More precisely, both structural and electronic data must be acquired in order to define the role of the cation frontier orbitals within the complex. To do so, various structural probes must be used, from vibrational and nuclear techniques to X-ray spectroscopies. In the field of actinide solvent extraction, the species of interest are in the solvent phase and both solid state diffraction methods and solvent phase X-ray absorption spectroscopy have become of primary importance lately.

A number of Ln(III) and Am(III) complexes of the type $M(NO_3)_3L_{1,2}$ (where M is either Ln^{3+} or Am^{3+} and L is either the 2,2',6',2''-terpyridine (Tpy) or the N,N,N',N' tetraethylmalonamide (TEMA) ligand) have been crystallographically characterised in the solid state. In order to obtain structural information in the solvent phase, EXAFS L_{III} edge measurements have been performed on the cation (DCI ring at the LURE facility). The overall contraction (-0.05 Å) of the cation co-ordination sphere from Nd^{3+} to Lu^{3+} reflects the decrease in the lanthanide ionic radii. With the TEMA ligand, this steric constraint generates the elongation of one nitrate bond, leading to one formally monodendate nitrate for the late Ln ions. Comparison is made with the Tpy ligand.

In the case of Am^{3+} cation, comparison with isostructural Nd^{3+} shows that similar co-ordination spheres are obtained, either with the TEMA or the Tpy ligands.

Introduction

To better understand the role of the 4f and 5f orbitals in the bonding modes in lanthanide or actinide organocomplexes, it is essential to describe the electronic and geometric structures of the latter. We are working on the experimental and theoretical characterisation of actinide cations in order to fine tune the design of new ligands that would be good candidates for the minor actinide(III)/ lanthanide(III) (An(III)/Ln(III)) separation. Fundamental data on lanthanide ions in the solvent phases have been the subject of wide interest in the literature. Ionic versus covalent relative character across the lanthanide series, inner or outer sphere complexation mechanisms in various solvent phases or structural characterisation of the Ln polyhedra are some of the problems to be addressed.

X-ray absorption spectroscopy (XAS) applied to actinide species has been greatly developed over the past decade and has been shown to be a very powerful technique to probe the lanthanide and actinide co-ordination sphere [1].

In this paper we present a summary of our current investigation of two series of lanthanide and americium complexes in solution with oxygen or nitrogen donor ligands: Ln(III) or Am(III)/$3NO_3^-$/ 2*TEMA* (in ethanol) and Ln(III)/$3NO_3^-$ (in pyridine) (Ln = lanthanide ions, Am(III) = trivalent americium and *TEMA* = N,N',N,N' tetraethylmalonamide). Details about these results can be found in the references [2].

Experimental

Absorption L_{III} edge spectra were recorded at both the LURE facility (Orsay, France) and the Daresbury facility (Daresbury, UK). A double crystal monochromator (Si 111 and Si 311) was used for data collection. Data extraction was carried out using a polynomial function and Fourier transformation was done in k^3CHI(k) (2.5-10.7 $Å^{-1}$) using a Kaiser window. FEFF7 calculated phases and amplitudes were used.

Details concerning data collection, data extraction and data fitting are provided in the references [2].

Results and discussion

Malonamide (TEMA) complexes of Ln(III) and Am(III) in the presence of nitrate counter-ion

The solid-state structure of $Nd(NO_3)_3$*TEMA*$_2$ is consistent with the expected stoichiometry of complexes of *TEMA* with the Nd^{3+} ion and shows the bidendate behaviour of the malonamide ligands [Figure 1(a)] [2(a)]. The Nd-O distances for the O atoms of the nitrate ions located on each side of the plane defined by the *TEMA* molecules are systematically larger than those for the ions crossing the plane, indicating a stress between the *TEMA* molecules and two nitrate ions in the co-ordination sphere of the Nd^{3+} ion. The increase in such stress for the complex with the smaller ion (Yb^{3+}) results in the change in co-ordination number and the occurrence of one monodendate nitrate ion [Figure 1(b)].

For the XAS spectra related to the solvent phase, all EXAFS adjustments have been carried out assuming as fitting initial conditions that six oxygen atoms are coming from the three nitrate groups and four oxygen atoms are coming from the two *TEMA* ligands, giving a non-fitted number of 10 oxygen neighbours. Even if this assumption does not account for likely co-ordinated water molecules coming from the hydration water molecules of the solid Ln(III) nitrates, it does satisfactorily account for the overall complex structure. The expected decrease of the averaged Ln-O bond length <Ln-O> for

Figure 1

(a) Molecular structure of $Nd(NO_3)_3(TEMA)_2$; displacement ellipsoids are represented with 10% probability [2(a)].

(b) Molecular structure of $Yb(NO_3)_3(TEMA)_2$; displacement ellipsoids are represented with 10% probability [2(a)].

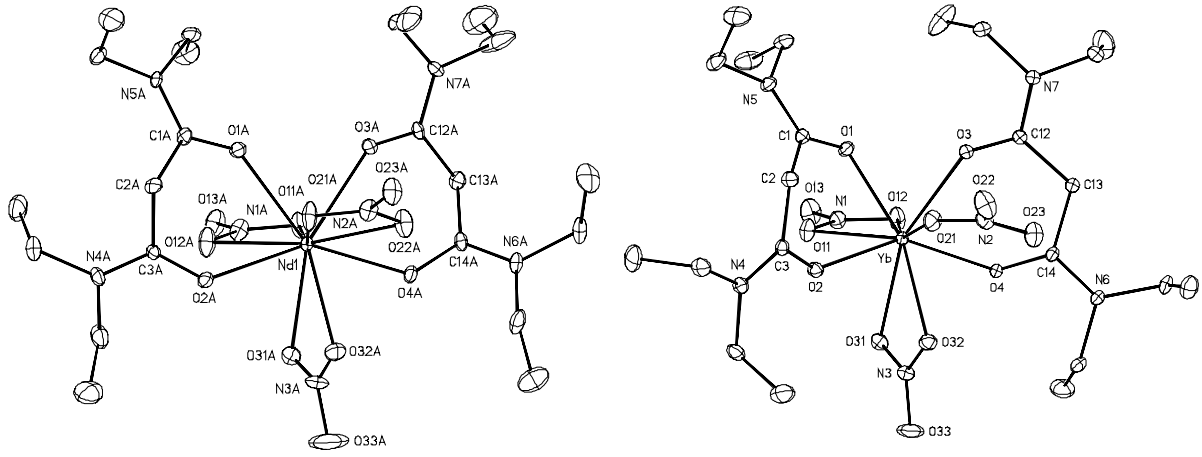

Ln = Nd, Eu, Ho, Yb, Lu given by the EXAFS measurements is in agreement with the reduction of the Ln^{3+} ionic radius r_{Ln}^{3+} when Z_{Ln} increases from Nd to Lu: <Ln-O> = 2.53 Å to 2.40 Å and r_{Ln}^{3+} = 1.107 Å (CN = 8) to 0.979 Å (CN = 8) Å, when Z_{Ln} = 60 to 71, respectively [3] (Figure 2). Surprisingly, for the Yb and Lu cations, one of the oxygen atoms of one nitrate is moved away from the lanthanide first co-ordination sphere (to about 2.8 Å). This result compares to the solid-state structure of $Yb(NO_3)_3(TEMA)_2$, which is made up of one monodendate and two bidendate nitrates. However, in this solid-state structure, the two non-bonded oxygen atoms of the monodendate nitrate are located at 3.54 and 4.38 Å from Yb.

Figure 2. M-O bond lengths in $M(NO_3)_3(TEMA)_2$ solvent phase complexes (M = Nd, Eu, Ho, Yb and Lu)

(◆,O,□,●,Δ,X represent the six oxygen atoms of the three nitrates;
▲ represents the averaged four oxygen atoms of the two TEMA ligands [2]

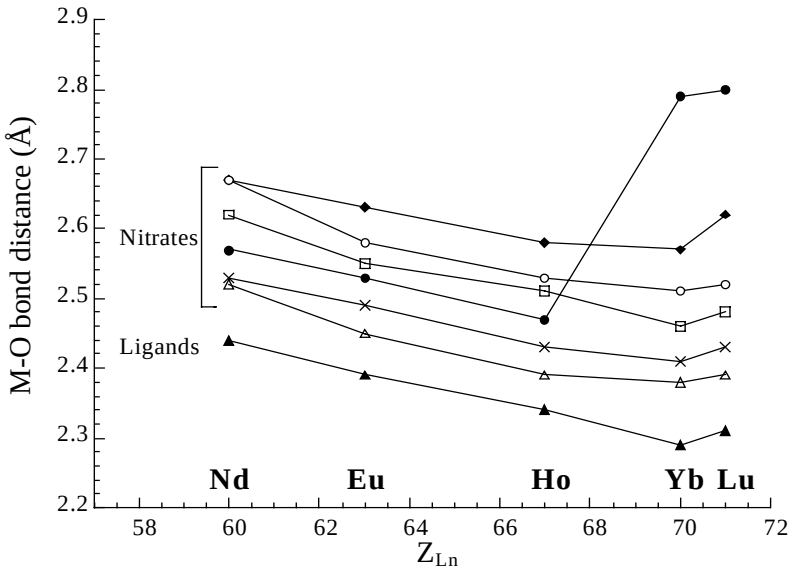

The value of 2.83 Å given by EXAFS is therefore low for a non-bonded oxygen of a monodendate nitrate and can only be explained by a strong tilt of the NO_3^- entity away from the cation. In that sense, the lanthanide polyhedron may be viewed here as a 9+1 co-ordination mode instead of a 10 co-ordination mode for the Nd to Ho species.

A comparison was made in the solvent phase with the americium(III) complex. The americium(III) cation is often compared to that of Nd(III), as both ions are isostructural ($r_{Nd(III)}$ = 1.109 Å, $r_{Am(III)}$ = 1.09 Å, CN = 8) and have the same stable oxidation state (III). The EXAFS spectrum at the americium L_{III} edge has been fitted using the same structural assumptions as for $Nd(NO_3)_3(TEMA)_2$ and the averaged Am-O distances have been found to be 0.02 Å shorter than the average Nd-O distances. This confirms that the two cations form comparable complexes with O-bearing ligands with similar polyhedra in identical experimental conditions.

Terpyridine (Tpy) complexes of Ln(III)

The solid-state structure of $[Nd(NO_3)_3TpyH_2O]\cdot 3Py$ [4] is a good structural model to study the lanthanide nitrate co-ordination sphere in pyridine (noted *Py*) since the *Tpy* ligand might be considered as an assembly of three pyridine molecules.

There is already in the literature a number of X-ray structural data for the lanthanide complexes with *Tpy* including those for nitrate-containing complexes with one to one Ln:*Tpy* molar ratio [5]. This complex is ten-co-ordinated (Figure 3) and contains a terdendate *Tpy* ligand, three bidendate nitrate anions and a co-ordination water molecule. The shortest distance in the Nd ion co-ordination polyhedron is that of Nd-O(H_2O), which is 2.396(2) Å. The Nd-N distances are from 2.553(2) to 2.5952(14) Å, the Nd-O distances for three bidendate nitrate groups are from 2.5045(14) to 2.5467(14) Å (five distances) and the sixth distance (for the O(52) atom) is 2.648(2) Å. The co-ordination polyhedron of the Nd(III) ion can be described as a distorted sphenocorona.

Figure 3. Molecular structure of $[Nd(NO_3)_3TpyH_2O]\cdot 3Py$

Displacement ellipsoids are represented with 10% probability [4]

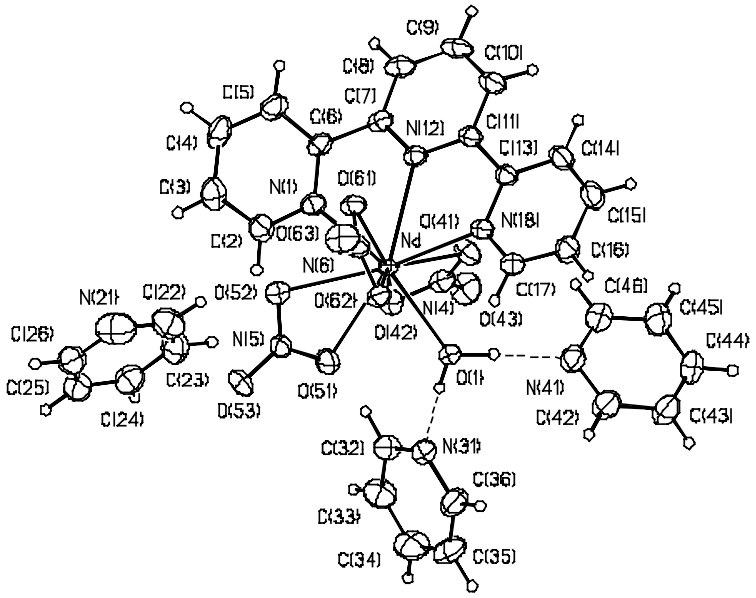

The Fourier transformed (FT) EXAFS data of the $Ln^{3+}/3NO_3^-$ complexes in pyridine are presented in Figure 4(a). As a starting assumption, the general formula of these complexes can be viewed as $Ln(NO_3)_nPy_m(H_2O)_p$. Peak A accounts for the first lanthanide neighbours that are composed of *n* nitrate ligands ($0 < n \leq 3$), *m* pyridine molecules bound to the Ln(III) ion via their nitrogen atom ($m \geq 0$) and *p* water molecules ($p \geq 0$) that originate from the hydration water molecules of the solid Ln(III) nitrates used to prepare the solutions in *Py*. The decrease of Peak A distance to the absorbing atom agrees with the lanthanidic contraction as shown above for the $Ln/3\,NO_3^-/2TEMA$ complexes. In the second sphere, Peak B intensity decreases from Nd to Lu and Peak C intensity increases from Nd to Lu. To date, the origin of this behaviour is still not clear. However, the symmetry of the nitrate ligands may account for the second co-ordination sphere modification upon reduction of the cation ionic size since Peak C has been attributed to a multiple scattering resonance of the nitrate ions.

In Figure 4(b), a comparison is made between $Ln^{3+}/3NO_3^-$ systems in pyridine and $Ln^{3+}/3Cl^-$ systems in aqueous HCl solutions. In the latter, the chloride anions have been shown to be non-complexing [6] and the lanthanide cations are totally solvated by water molecules. Throughout the lanthanide series, the averaged Ln-O(N) distances are larger for $Ln^{3+}/3NO_3^-$ systems than for $Ln^{3+}/3Cl^-$ systems; this is attributed to the steric effect of the nitrate groups that form inner-sphere complexes in pyridine versus the water molecules in aqueous medium.

Figure 4

(a) FT of the lanthanide L_{III} edge in the $Ln(NO)_3Py_n(H_2O)_p$ complexes in pyridine. From top to bottom: Pr, Nd, Sm, Eu, Gd, Tb, Dy, Ho, Er, Tm, Yb, Lu.

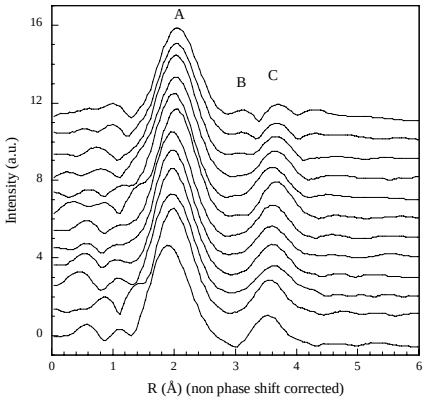

(b) Averaged Ln-O,N distances of the two series: $Ln(NO)_3Py_n(H_2O)_p$ in pyridine and $LnCl_3$ in 1.0 M HCl aqueous solutions.

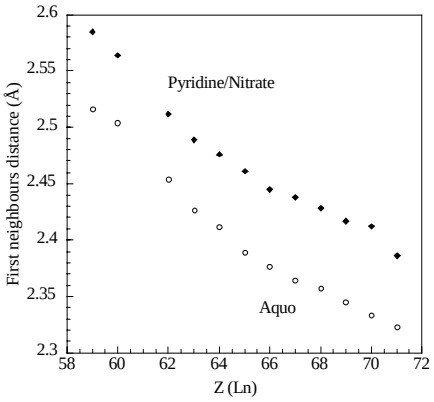

Conclusion

These preliminary results show the complexity of the structure of the lanthanide co-ordination sphere that depends on the counterion/solvent system. On the other hand, similar americium experiments are to be carried out for comparison with that of Nd.

In summary, EXAFS was found a very valuable tool for the understanding of the co-ordination modes of Ln(III) and Am(III) ions when involved in aqueous or non-aqueous solutions in interactions with O or N-bearing ligands. In such systems, solid-state model structures are indispensable to quantify the solvent phase structural evolutions.

This experimental technique will certainly have a bright future in studies in the field of nuclear hydrometallurgy.

REFERENCES

[1] See for instance as an overview the Proceedings of the XAS-Actinide 1998 Conference, Grenoble, NEA/OECD publications (1999).

[2] (a) C. Den Auwer, M.C. Charbonnel, M.G.B. Drew, M. Grigoriev, M.J. Hudson, P.B. Iveson, C. Madic, M. Nierlich, M.T. Presson, R. Revel, M.L. Russel and P. Thuéry, *Inorg. Chem.*, 39, 1487 (2000).

(b) C. Den Auwer, M.C. Charbonnel, M.T. Presson, C. Berthon, *Inorg. Chem.*, submitted.

[3] (a) F. David, *J. Less Comm. Met.*, 121, 27 (1986).

(b) F. David and B. Fourest, *New. J. Chem.*, 21, 167 (1997).

[4] C. Den Auwer, M. Grigoriev, M.C. Charbonnel and M.T. Presson, to be published.

[5] (a) M. Fréchette and C. Bensimon, *Inorg. Chem.*, *34*, 3520-3527 (1995).

(b) M.G.B. Drew, M.J. Hudson, M.L. Russel, J-O. Liljenzin, M. Skålberg, L. Spjuth and C. Madic, *J. Chem. Soc., Dalton Trans.*, 2973-2980 (1998).

(c) S.A. Cotton and P.R. Raithby, *Inorg. Chem. Commun.*, *2*, 86-88 (1999).

(d) P.C. Leverd, M.C. Charbonnel, J-P. Dognon, M. Lange and M. Nierlich, *Acta Cryst.*, *C55*, 368-370 (1999).

(e) M.G.B. Drew, M.J. Hudson, P.B. Iveson, C. Madic and M.L. Russel, *J. Chem. Soc., Dalton Trans.*, 2433-2440 (1999).

[6] T. Yaita, H. Narita, S. Suzuki, S. Tachimori, H. Motohashi and H. Shiwaku, *J. Radioanal. Nucl. Chem.*, 239, 371 (1999).

XAFS SPECTROSCOPY OF ACTINIDES IN THE SOLID STATE

Patrick G. Allen
Glenn T. Seaborg Institute for Transactinium Science, LLNL
Livermore, CA 94551

Abstract

Due to their complex electronic structure, actinides in solid-state systems display a number of unusual physical phenomena that are normally not observed in aqueous systems. Under appropriate conditions, X-ray absorption fine-structure spectroscopy (XAFS) is a sensitive probe, and can be used to study some of these effects. This paper will present recent results on: 1) anomalous background absorption effects in actinide oxides and metallic systems, 2) influence of electronic effects in XANES spectra and 3) lattice distortions observed in the temperature-dependent EXAFS spectra of alpha uranium.

Anomalous background absorption effects are observed at the L_{III} absorption edges of actinides in oxides (AnO_2 where An=Th, U, Np and Pu) and metallic systems (U and Pu). These effects manifest themselves and appear as difficult to remove "low-R" features in the EXAFS Fourier transforms. Numerous theories have been proposed to explain similar features in other non-actinide systems, most of which are referred to as atomic XAFS (AXAFS) or multi-electron excitations (MEE). Independent of a fundamental assignment, techniques for their removal as well as trends in these oxide and metallic systems will be discussed.

Actinide L_{III} XANES spectra are, in principle, assigned to a $2p_{3/2} \rightarrow 6d$ transitions. In the electronic model, edge positions and white line intensities may be described in terms of effective charge densities and *d*-orbital occupancy at the valence level. However, features and trends in the XANES spectra of actinide metals and oxides indicate that the 5*f* electrons also have an important role. This is likely due to the proximity in energy of the 6*d* and 5*f* energy levels coupled with a breakdown in the dipole selection rules that results from relativistic effects dominating over spin-orbit coupling schemes. Effects are seen in U and Pu metal XANES spectra which may be attributed to 5*f* de-localisation relative to more localised behaviour observed in the oxide systems.

In the vicinity of 40 K, alpha uranium undergoes a subtle phase transformation which has been known and studied for many decades. The phase transformation, ascribed to a charge density wave phenomenon, is depicted by a lattice shift of specified U atoms within the orthorhombic lattice. U L_{III}-edge data were collected on this system as a function of temperature. The ability of EXAFS to discern lattice shifts of this nature in solid-state systems will be discussed.

WHAT INFORMATION CAN BE OBTAINED FROM XANES SPECTRA ABOUT THE LOCAL ATOMIC AND ELECTRONIC STRUCTURES OF TRANSITION METAL OXIDES?

Rostislav Vedrinskii, Victor Kraizman, Alexander Novakovich, Igor Maznichenko, Alexander Sakun, Alan Makoev
Rostov State University, Rostov on Don, Russia

Abstract

Tc K-XANES calculated within one-electron full multiple scattering method for compounds with tetrahedral and octahedral co-ordinations of Tc atom are shown to be in good agreement with the experiment. Mechanisms which cause the pre-edge structure in transition metal K-absorption spectra in oxides are considered. It is shown that the pre-edge structure enables to obtain information about local atomic order and about occupation of d conduction bands in the crystal. The dependence of the energy of the main rise in Tc K-absorption spectra on interatomic distances, co-ordination numbers, and type of ligands are studied.

Introduction

X-ray absorption spectroscopy (XAS) is widely used for studies of local electronic and atomic structure of condensed matter. XAS can provide valuable information for crystalline solids as well as for amorphous materials and liquids, including dilute samples. Using hard X-rays one can perform *in situ* measurements at storage ring facilities. This possibility is extremely useful for studies of radioactive and hazardous materials.

X-ray absorption fine structure is separated naturally into two parts: EXAFS and XANES. The mechanisms responsible for the EXAFS formation are rather simple and as a result the direct methods were developed many years ago, enabling to obtain information on interatomic distances, co-ordination numbers, atomic numbers of the atoms near the absorbing one, and amplitudes of atomic vibrations. On the contrary, the mechanisms responsible for XANES formation are complicated and thus no direct method for XANES processing similar to that for EXAFS has yet been elaborated. Nevertheless there are some features in XANES which are used for the analysis of electronic structure and local atomic order around the absorbing atoms. We describe below the mechanisms of formation of such features in K-absorption spectra of transition metals (TM) in oxides and illustrate them using the Tc oxide spectra as examples.

The main rise of TM K-absorption cross-section in oxides occurs at about 10-20 eV above the conduction band (CB) bottom. The difficulty is that the local partial density of metal *p* states is small below the main rise since the low-energy CBs are constructed mainly by metal *d*-atomic orbitals (AO) with small admixture of oxygen O *2p*. Therefore the electron transitions from the TM K-level to the states originated from the *d* CBs cause low intensity features in spectra, which are usually called the pre-edge fine structure (PEFS). The $1s \rightarrow nd$ transitions are dipole forbidden for the free atoms but *1s* electron excitations to *d* CBs can become dipole allowed in condensed matter due to an admixture of TM *p* states to the *d* ones. Since the degree of such an admixture and respectively the intensities of the PEFS peaks are very sensitive to the local atomic structure about the absorbing atom, PEFS can provide valuable information on this structure.

Three mechanisms are responsible for the PEFS formation [1]. The first is caused by excitations of the TM *1s* electrons to the lowest unoccupied CBs of a crystal which are formed mainly by TM d AOs. The TM *1s* electron transitions to these CBs are caused by the hybridisation of the diffuse *p*-symmetry orbitals of the absorbing TM atom with *d* AOs of the TM atoms close to the absorbing one and O *2p* AOs. The energies of such MOs are weakly affected by the potential of X-ray core hole and the peaks in PEFS caused by this mechanism provide a sufficiently precise energy reference of the empty conduction bands arising from the corresponding MOs. This mechanism causes noticeable peaks in the PEFS only if neighbouring TMO_n polyhedrons share one or more oxygen atoms with the polyhedron containing the absorbing TM atom. The intensities of these peaks are determined by the type of octahedron conjunction in the crystal lattice. For example, in the perovskite structure crystals, such as $PbTiO_3$, the PEFS peaks caused by transitions to the t_{2g} MOs of the near-by TiO_6 octahedrons are not observed at all or they are very weak, whereas transitions to the e_g MOs take place. On the other hand transitions to the both e_g and t_{2g} MOs of the near-by TiO_6 octahedrons take place in the case of rutile crystal.

The second mechanism is the well-known quadrupole transition mechanism, which allows direct transitions of the TM *1s* electrons to the e_g and t_{2g} MOs of the TMO_n polyhedron containing the absorbing TM atom. Despite their weak intensities the peaks caused by this mechanism can be unambiguously identified in the experimental spectra of the single crystal sample due to the specific dependence of their intensities on the direction and polarisation of incident photons. Using this

dependence measured for single crystals it is possible to determine which *d* orbitals are empty and which are occupied. The studies carried out for the NiO single crystal [2] have shown that all the t_{2g} MOs are occupied whereas there are empty e_g MOs. The *d* MOs of the TMO_n polyhedron containing the absorbing TM atom are highly localised within its atomic sphere and, therefore, these MOs are strongly shifted down by the K-hole potential. The values of such shifts are about 3-4 eV.

The third mechanism causes the dipole transitions to the same MOs as the second. Such transitions are forbidden if absorbing atoms are disposed in the centrally symmetric positions but they can occur for the lack of inverse symmetry about the absorbing atoms, for example in the case of tetrahedral co-ordination of TM atoms. In the case of octahedral co-ordination of TM atoms, the inverse symmetry can be broken by static distortions or thermal vibrations. As a result e_g and t_{2g} MOs of the octahedron containing absorbing TM atom become weakly hybridised with *p* orbitals of this atom.

The difference of the energy position of the main edge in K spectra in different compounds, so-called chemical shift, is often associated with the variation of the K-level energy caused by changing the TM atom charge in a compound [3]. As a matter of fact this shift can also be caused by other reasons such as change of interatomic spacing, co-ordination number, atomic number of nearby atoms, and so on. The analysis of possible cases is carried out in the present paper.

For XANES calculations a traditional full multiple scattering method is used. It is described briefly in the next section. The multiple scattering method is the one-electron method, which seems to be unsuitable for calculating the spectra of TM atoms in paramagnetic state. Nevertheless it appears that using spin-dependent one-electron Xα potential, one is able to calculate XANES in K-absorption spectra for magnetically ordered systems in good agreement with the experiment [4]. Spin-dependent potential calculated using the local spin-density prescription of von Barth and Hedin along with the Hedin-Lundqvist self-energy was employed for Fe K-edge XMCD [5].

Method for calculations

Using a one-electron approximation and including dipole and quadrupole terms of the photon-electron interaction operator one can express the X-ray absorption cross-section (XACS) for an atom in a polyatomic system through the photoelectron Green's function (GF) $G(\boldsymbol{r},\boldsymbol{r}',\varepsilon)$ using the equation:

$$\sigma_i^0(\omega) = -8\pi\left(\frac{e^2}{\hbar c}\right)\hbar\omega\left[\begin{array}{l}\mathrm{Im}\int \varphi_i^*(\boldsymbol{r})\boldsymbol{e}\boldsymbol{r}G(\boldsymbol{r},\boldsymbol{r}',\varepsilon)\boldsymbol{e}\boldsymbol{r}'\varphi_i(\boldsymbol{r}')d^3rd^3r' \\ +\left(\frac{\omega}{2c}\right)^2 \mathrm{Im}\int \varphi_i^*(\boldsymbol{r})\boldsymbol{e}\boldsymbol{r}\cdot\boldsymbol{k}\boldsymbol{r}G(\boldsymbol{r},\boldsymbol{r}',\varepsilon)\boldsymbol{e}\boldsymbol{r}'\cdot\boldsymbol{k}\boldsymbol{r}'\varphi_i(\boldsymbol{r}')d^3rd^3r'\end{array}\right] \quad (1)$$

where $\sigma_i^0(\omega)$ is the cross-section of the photoionisation of the atomic core level *i* in the isolated atomic sphere number 0 by the linear polarised X-ray wave with the frequency ω, $\boldsymbol{e}$ is the electric field vector (polarisation vector) of the X-ray wave, $\boldsymbol{k}$ is its wave vector, $\varphi_i(\boldsymbol{r})$ is the wave function of the atomic level *i*, and ε is the photoelectron energy determined relatively to the *muffin-tin* (MT) zero (E_{MT}) of the crystal potential.

In order to calculate the GF in the continuum the full multiple scattering method [6-8] which employs MT approximation for the crystal potential is the most suitable. This method is based on the equation which connects the GF $G(\boldsymbol{r},\boldsymbol{r}',\varepsilon)$ in the co-ordinate representation with the GF matrix $G_{LL'}^{nn'}$ in

the so-called “orbital momentum-number of the atom” representation. We present this equation for the special case when both vectors $\boldsymbol{r}, \boldsymbol{r}'$ are inside the same atomic sphere number 0:

$$G(\boldsymbol{r},\boldsymbol{r}',\varepsilon) = G_0(\boldsymbol{r},\boldsymbol{r}',\varepsilon) + f\sum_{L,L'} e^{i(\delta_l+\delta_{l'})} R_l(\varepsilon,r) Y_L(\hat{r}) G^{00}_{LL'} R_{l'}(\varepsilon,r') Y_{L'}(\hat{r}') \tag{2}$$

where $G_0(\boldsymbol{r}, \boldsymbol{r}', \varepsilon)$ is the GF for the isolated atomic sphere, $Y_L(\hat{r})$ is the real spherical harmonic $L = (l,m)$, $\hat{r}$ is a unit vector directed along the vector $\boldsymbol{r}$, δ_l is the partial scattering phase shift for the electron wave with the orbital moment l scattered by the 0-th atomic sphere, f is a coefficient $\left(f = \left(2m/\hbar^2\right)^{3/2}\sqrt{\varepsilon}\right)$, $R_l(\varepsilon,r)$ is a regular solution of the radial Schrödinger equation for the electron with the orbital moment l and the energy ε in the atomic sphere number 0. The solution $R_l(\varepsilon,r)$ is normalised on the surface of the atomic sphere by the following boundary condition:

$$R_l(\varepsilon,r_0) = j_l(kr_0)\cos\delta_l - n_l(kr_0)\sin\delta_l \tag{3}$$

where r_0 is the radius of the atomic sphere 0, k is the electron wave number, and j_l and n_l are the spherical Bessel and Neuman functions.

Substituting Eq. (2) into Eq. (1) the XACS can easily be expressed through the GF matrix $G^{00}_{LL'}$. For instance, the expression for the K-XACS obtained within the dipole approximation is the following:

$$\sigma^0_K(\omega) = \left[8\pi\hbar\omega\left(\frac{e^2}{\hbar c}\right)\right]\left(\frac{2m}{\hbar^2}\right)^{3/2}\sqrt{\varepsilon}\left|\int\varphi_{1s}(r) r^3 R_1(\varepsilon,r)\,dr\right|^2 \cdot \sum_{i,j=1}^{3} e_i e_j \, Im \sum_{m,m'=-1}^{1}\left(i\delta_{mm'} - G^{00}_{mm'} e^{2i\delta_1}\right) S_{mi} S_{m'j} \tag{4}$$

where $S_{mi} = \int Y_{1m}(\hat{r})\hat{r}_i Y_{00}(\hat{r})\,d^2\hat{r}$.

For calculating the GF matrix $G^{n0}_{LL'}$ the following system of linear algebraic equations should be solved [6,7]:

$$G^{n0}_{LL'} = g^{n0}_{LL'} + \sum_{n',L''} g^{nn'}_{LL''} t^{n'}_{l''} G^{n'0}_{L''L'} \tag{5}$$

where t^n_l is the partial scattering t-matrix for the n-th atom in the crystal and the electron orbital moment l, $g^{nn'}_{LL''}$ is the coefficient in the bicentral expansion for the free electron GF.

The core hole influence on the absorbing atom potential breaks the translational symmetry of the crystal potential and the system of Eq. (5) can be solved in this case if one employs the cluster approximation for the crystal and, besides, restricts the number of the orbital moments included in the summation in Eq. (5). The correct choice of the representative cluster is the important point of the full multiple scattering method [1]. To include the finite lifetime of the electron-hole pair appearing at the final stage of the photoionisation process we have smeared the spectra taking into account that the photoelectron lifetime in the medium rapidly decreases with the increase of the photoelectron energy ε.

The cluster potential construction

In the present paper as in the previous one [1] we approve a semi-empirical non-self-consistent approach to the cluster potential construction assuming that the most important point for the XANES calculations is keeping the correct values of the relative energies of the atomic valence levels and/or atomic scattering resonances for different atoms in the crystal. The potential inside an atomic sphere is considered to be a sum of a free atom self-consistent potential and a constant value (potential shift) simulating both the Maudelung potential and the change of the potential caused by redistribution of the electron density inside the atomic sphere. To estimate the potential shifts one can compare the energies of the atomic levels with those determined by the self-consistent band calculations or with some experimental data. The potential outside the cluster is considered to be equal to the average interstitial potential (MT-zero). This means that we ignore the reflection of the electron waves from the atoms being outside the cluster chosen.

The electron density inside each atomic sphere is considered to be equal to that of the corresponding free atom obtained with the usual Herman-Skillman procedure [9] using the exchange parameter α taken according to the Schwarz prescription [10] ($\alpha \approx 0.75$). At the same time the potentials used for the *t*-matrix calculations for the vacant electron states in the continuum are determined using $\alpha \approx 0.5$-0.6 which is slightly decreased in comparison with that of Schwarz. Schwarz has chosen the α value in order to fit the occupied state energies to those of Hartree-Fock, consequently the X_α potential for the occupied electron states really includes two terms: the first one simulates the exchange potential and the second cancels the electron self-interaction. Of course, the second term should be excluded for calculating the vacant electron state wave functions in the continuum. To do this in a simple way we propose to decrease the α value.

The electron configurations for all the atoms in the cluster excluding the absorbing one are chosen to coincide with those for the neutral free atoms in the ground state. The configuration of the absorbing atom has been chosen to include extra atomic screening of the core hole. In the case of the metals or covalence crystals the complete extra atomic screening leads to the increase of the valence shell occupation by one electron (Z+1 model) [11]. In the case of ionic-covalent crystals the screening charge should be slightly less than the whole electron charge. It is worth noting that self-consistent cluster calculations systematically overestimate the screening charge in such crystals. It is clearly observed in calculations of Ti K XANES in $PbTiO_3$ [8], where the energy of the pre-edge structure and its shape are not in accordance with the experiment. Such calculations do not allow carrying out the analysis of the pre-edge structure. Thus, we consider the screening charge as an adjustment parameter [1,12,13]. It was shown that the best agreement with the experimental K-XANES in the case of the *d* metal oxides is reached if one increases the *d*-shell occupation of the ionised TM atom by 0.8 electron. Such a result seems to be quite reasonable. This model of the core-hole potential is called the model of incomplete extra atomic screening. Of course, it should be understood that this model can not be justified rigorously. We use it for the simple simulation of the complicated dynamic processes which occur during X-ray absorption. Nevertheless our studies have shown that the model proposed enables us to calculate the TM K-XANES for various TM oxides in good agreement with the experiment [1,12,13].

Some additional complications occur for the compounds containing TM atoms in a paramagnetic state. These complications are caused by interaction of photoelectron with the unfilled *d* shell of an absorbing atom and necessitate taking into account Pauli's principle with the one-electron calculation method. We assume in the present paper that electron-electron interaction leads only to some additional smearing of the pre-edge structure. We will explain how to include Pauli's principle using as an example the Tc K-spectrum of TcO_2.

Comparison of calculations with experimental spectra for Tc K-edge

Tc K-edge XANES in compounds with tetrahedral co-ordination: p-d-f mixture

The accuracy of the multiple scattering method based on MT approximation for the cluster potential for calculating Tc absorption spectra is not evident beforehand, especially in the pre-edge region, due to the large radius of *4d*-wave function of Tc atom. Therefore calculations of the spectra with unambiguous interpretation of pre-edge singularities are good tests for validity of the proposed approach. A common feature of all the K-edge XANES of *3d* or *4d* TM atoms in tetrahedral environment is a noticeable peak in the pre-edge region. The origin of this peak is absolutely clear. The lowest unoccupied molecular orbitals (LUMO) of TMO_4 tetrahedron constructed from metal *3d* (*4d*) states and ligand *p* states have a great admixture of metal *p* states because *x*, *y*, *z* states and *xy*, *yz*, *xz* states are transformed within the same irreducible representation of T_d group. Therefore transitions of *1s* electron to these LUMO are allowed by dipole selection rules and intensities of such transitions are great.

Spectra chosen for the analysis are Tc K-XANES of a liquid sample 1.3 mMol/L $NaTcO_4$(aq), and of a crystal $KTcO_4$ [14]. EXAFS analysis shows that the Tc atom in the solution is surrounded by four oxygen atoms at a distance of 1.72±0.01 Å [14]. The XANES for this compound is calculated employing the five-atomic cluster TcO_4 with oxygen atoms disposed in apexes of regular tetrahedron and Tc-O separation equals 1.72 Å. The crystal lattice of $KTcO_4$ is constructed by tetrahedrons TcO_4 with Tc-O separation 1.71 Å. Different tetrahedrons have no common oxygen atoms. Tc K-XANES for $KTcO_4$ is calculated employing the 55-atomic cluster $(TcO_4)K_{10}(TcO_4)_8$. Scattering phase shifts with $l \geq 3$ for Tc, with $l \geq 2$ for K, and with $l \geq 1$ for O atoms are included. The model of the cluster potential described above is employed. Comparison of the calculated and experimental spectra is presented in Figure 1. The intensities of experimental spectra are normalised in order to provide the same absorption step as calculated spectra. The energy of Peak A in the experimental spectra is adjusted to that of the calculated ones. Calculated spectra are convoluted with Lorenz function. Its full width equals 7 eV in the region of the pre-edge peak. One can see that the energy splitting between Peaks A and C and the intensity of Peak A relative to the atomic background absorption in both cases are excellently reproduced in calculations.

To understand the origin of Peaks B and C we calculated the spectrum of TcO_4 in the same cluster assuming that f-partial scattering phase shift at Tc atom equals zero and comparing the result with the previous calculations. This comparison is presented in Figure 2 along with the f-partial scattering phase shift (spectra in Figure 2 are not smeared for clarity.) The behaviour of the f-scattering phase shift testifies to the existence of f resonance at an energy of about 40 eV above MT-zero level. It is evident that inclusion of the f-scattering phase shift causes the appearance of additional features with the complicated shape in K-spectrum at an energy close to that of f-resonance. Thus one observes in Tc K-spectra in tetrahedral co-ordination the effect caused by mixture of Tc *p* states with the both Tc *d* and *f* states. We call this phenomenon *p-d-f* mixture. Peaks B and C are pronounced better in the spectra of a crystal than in those of a complex because the f resonance influences on these spectra not only via *p-f* mixture at the absorbing atom but also via sharp changing of scattering characteristics of neighbouring TcO_4 tetrahedrons.

Tc K-edge XANES in TcO_2

TcO_2 crystal has a rutile-like crystal structure. In this structure each Tc atom is surrounded by six oxygen atoms, which form slightly distorted octahedrons. Therefore the *p-d* mixture will weakly influences the Tc K-spectra. On the contrary, since in rutile structure nearby TMO_6 octahedrons share

Figure 1. Tc K-XANES in TcO_4 complex (1.3 mMol/L $NaTcO_4$(aq)) (left panel) and in $KTcO_4$ crystal (right panel)

Experiment [14]: open circles, calculations: solid line. Calculated absorption cross-sections are given in Mb, experimental spectra in arbitrary units. Energy reference of experimental spectra is chosen to fit the position of Peak A.

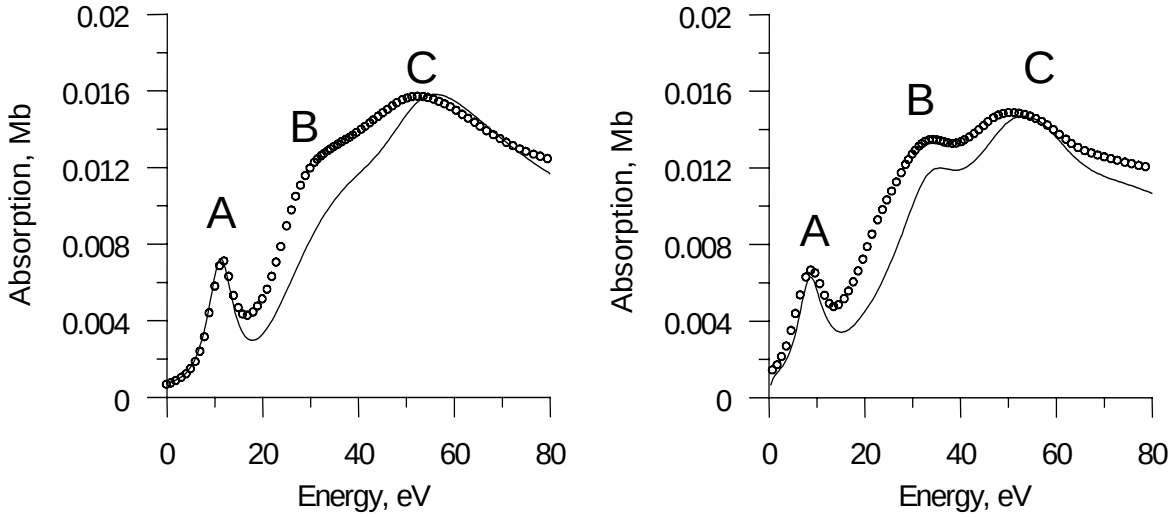

Figure 2. The influence of Tc f-scattering resonance on Tc K-spectrum in TcO_4 complex

δ_f-f partial scattering phase shift: dashed-dotted line; unsmeared Tc K-spectrum: solid line; the same spectrum calculated assuming $\delta_f = 0$: dashed line

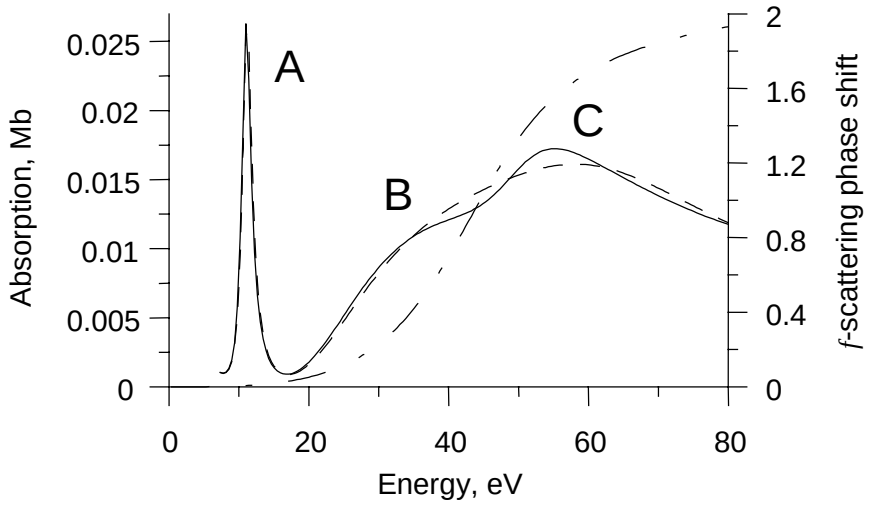

common apexes and edges, the transitions to the neighbouring octahedrons have to take place. The Tc K-absorption spectrum is calculated for 55-atomic cluster which contains 11 complete TcO_6 octahedrons: the central one containing absorbing Tc atom, and all the octahedrons which share at least one oxygen atom with the former. The Tc atom in TcO_2 crystal has three *4d* electrons which fill MOs with t_{2g} symmetry. We assume for simplicity that spin moments of all Tc atoms in the crystal have the same direction. The spectrum calculated for the case of unpolarised radiation and only dipole transitions being taken into account is presented in Figure 3. Unsmeared spectrum consists of a great

Figure 3. Unsmeared Tc K-spectrum in TcO_2 crystal; enlarged pre-edge structure is shown in inset

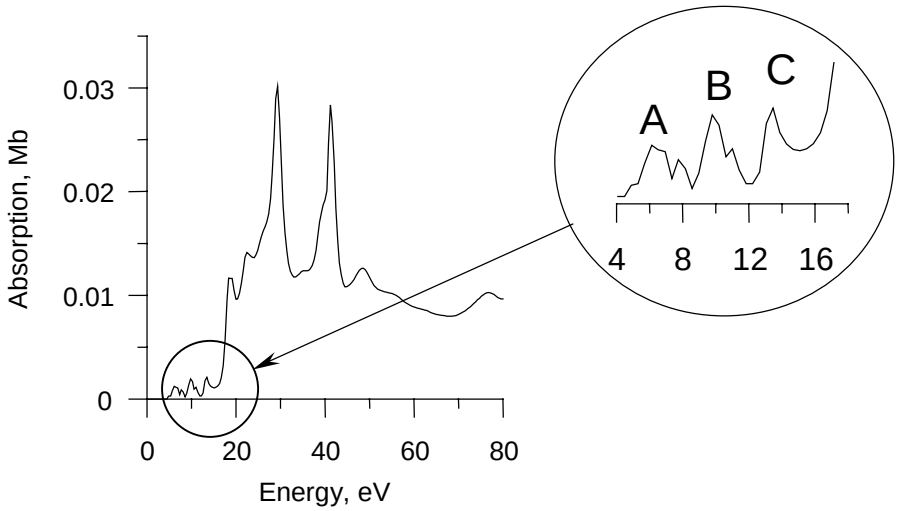

number of narrow peaks. Such structure is typical for rutile-like crystals. The pre-edge is shown enlarged in the inset. Peak A is caused by the excitations of the Tc K-electron to the t_{2g} MOs of the neighbouring octahedrons, whereas Peak B is caused by the excitations to the e_g ones. To prove this statement we have changed slightly the potential shift for neighbouring Tc atoms. Energies of Peaks A and B change together with the potential shifts. At the same time, changing the potential shift for the absorbing Tc atom or for O atoms practically does not affect the energies of Peaks A and B. Unfortunately, we could not find a simple interpretation for Peak C. The GF multiple scattering one-electron method yields transitions to both empty and filled final state. Since only three of six t_{2g} MOs are empty one has to include Peak A into the resulting spectrum with a weight equalling 0.5. The comparison of the smeared calculated spectrum with the experimental one [14] is presented in Figure 4. The great width of K-level for Tc atom along with instrumental resolution leads to the transformation of the distinct Peaks A, B and C into weak though visible features at the beginning of the main rise of the spectra.

Figure 4. Tc K-XANES in TcO_2 crystal

Experiment [14]: open circles, calculations: solid line. Calculated absorption cross-sections are given in Mb, experimental spectra in arbitrary units. Energy reference of experimental spectra is chosen to fit the main rise position.

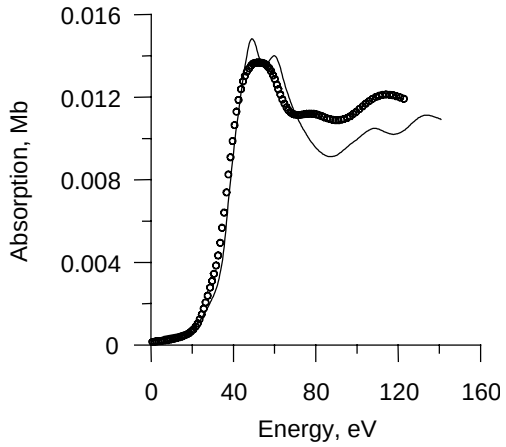

Dependence of Tc K-edge main rise on the nearest environment

The energy of the main rise of the K-absorption spectra of the identical TM atoms in different compounds may significantly differ from each other. This shift, often called a chemical shift of the K-edge, is often employed for determination of the oxidation state of TM atoms in compounds [3]. Meanwhile the shift is determined not only by the change of the binding energy of K-level but also by the change of spacing, co-ordination numbers, atomic numbers of the atoms near the absorbing atom, etc. In order to study the influence of short-range atomic order on the energy of the main rise we have carried out model calculations of the K spectra for the clusters TcL_n where L = O or Cl; n = 4, 6, 8, 12. The clusters used are regular polyhedrons with n apexes and Tc-L distances equal to 1.98, 2.35 and 2.165 Å. The first distance is characteristic for Tc-O bond length in TcO_2 whereas the second for Tc-Cl in $(NH_4)_2TcCl_6$ [15]. We should like to emphasise that the potential inside Tc atomic spheres and in the interatomic region remains unchanged in all the clusters, thus only the influence of interatomic distances, co-ordination numbers and kinds of ligand atoms has been studied. As usual, the energy of the inflection point at the main rise was considered as the edge position. The results of the calculations are presented in Figure 5. One can conclude that all the factors mentioned above significantly change K-edge energy. The results obtained explain the K-edge shift for spectra of TcO_2 and $(NH_4)_2TcCl_6$ where Tc atoms have the same valence. As follows from Figure 5, this shift equals about 4 eV which is in reasonable agreement with the experiment [15]. It seems that the well-known correlation between TM atom oxidation state and chemical shift of the K-absorption edge is mainly caused not by the change of the TM atom electric charge but by the change of the distance between these atoms and nearby anions.

Figure 5. The dependence of the main rise position in the Tc K-spectrum of TcL_n cluster. L = O, Cl; *n* = 4, 6, 8, 12.

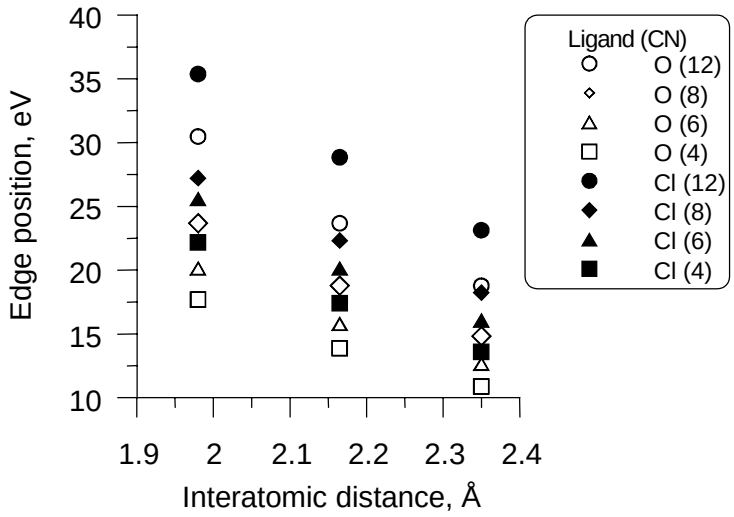

Conclusion

The analysis of the PEFS in TM K-spectra in oxides enables to obtain direct information about the symmetry of TM co-ordination polyhedron, small displacements of TM atom from the centre of the TMO_6 octahedron, type of linkage of TMO_n polyhedrons in the crystal lattice. The experimental studies of the chemical shift of TM K edge together with the theoretical calculations of the main rise shape enable to determine the oxidation state of TM atoms in different compounds.

Acknowledgement

These studies were supported by RFBR grant 00-02-17683.

REFERENCES

[1] R.V. Vedrinskii, V.L. Kraizman, A.A. Novakovich, Ph.V. Demekhin, *et al*., *J. Phys.: Condens. Matter*, 10, 9561 (1998).

[2] D. Heumann, G. Dräger, S. Bocharov, *J. de Physique IV France*, 7, C2-481 (1997).

[3] I. Almahamid, J. Bryan, J. Bucher, A. Burrell, *et al*., *Inorganic Chem*., 34, 193 (1995)

[4] R.V. Vedrinskii, V.L. Kraizman, A.A. Novakovich, Sh.M. Elyafi, *et al*., to be published.

[5] A.L. Ankudinov, J.J. *Rehr. Phys. Rev*., B 56, R1718 (1997).

[6] R.V. Vedrinskii, A.A. Novakovich, *Fis. Metall. Metallovedenie*., 39, 7 (1975).

[7] C.A. Ashley, S. Doniach, *Phys. Rev*., B 11, 1279 (1975).

[8] A.L. Ankudinov, B. Ravel, J.J. Rehr, S.D. Conradson, *Phys. Rev*., B 58, 7565 (1998).

[9] F. Herman, S. Skillman, "Atomic Structure Calculation", (Englewood Cliffs, NJ: Prentice-Hall, 1963).

[10] K. Schwartz, *Phys. Rev*., B 5, 2466 (1972).

[11] A. Bianconi, M. Dell'Arriccia, A. Gargano, C.R. Natoli, in *EXAFS and Near Edge Structure*, A. Bianconi, L. Incoccia and S. Stipcich, eds. (Springer-Verlag, Berlin, 1983), p. 57.

[12] B. Poumellec, V. Kraizman, Y. Aifa, R. Cortes, *et al*., *Phys. Rev*., B 58, 6133 (1998).

[13] B. Ravel, E.A. Stern, R. Vedrinskii, V. Kraizman, *Ferroelectrics*, 206-207, 407 (1998).

[14] T. Reich, H. Funke, C. Hennig, A. Roßberg, *et al*., to be published.

[15] P.G. Allen, G.S. Siemering, D.K. Shuh, J.J. Bucher, *et al*., *Radiochim. Acta*, 76, 77 (1997).

THE REDOX SPECIATION OF NEPTUNIUM IN ACIDIC AND ALKALINE SOLUTIONS

L. Soderholm,[1] M.R. Antonio,[1] C.W. Williams,[1] J.C. Sullivan,[1] S.R. Wasserman,[2] J-P. Blaudeau[3]
[1]Chemistry, [2]XFD Divisions, Argonne National Laboratory, Argonne IL 60439 USA
[3]Ohio Supercomputer Centre, ASC-HP, 2435 West 5th St.B76, WPAFB,OH 45433 USA

Abstract

Newly developed *in situ* capabilities at the Advanced Photon Source have been used to obtain X-ray absorption spectroscopy (XAS) data from Np in aqueous solutions. L-edge XAS data have been obtained from acidic solutions in which Np was electrochemically stabilised in the (III) to (VI) states. A purpose-built electrochemical cell [1] housed in appropriate safety containment allows the acquisition of XAS data while the solution is maintained under controlled applied potentials. This electrochemical cell has been used in a proof-of-concept experiment designed to demonstrate the use of X-ray absorption near-edge structural (XANES) data for the determination of thermodynamic formal potentials. XANES data were obtained at a series of applied potentials from a 1 M perchloric acid solution containing 5 mm Np. The relative concentrations of Np redox species as a function of applied potential were extracted from the data using principal component (factor) analyses. The formal potentials determined for the Np(VI)/Np(V) and Np(IV)/Np(III) couples agree with those previously published. Extended X-ray absorption fine structure (EXAFS) data were obtained from the same solution, held at potentials chosen to optimise the concentration of a single Np redox species [2]. These data have been used to verify the co-ordination environment of Np ions as a function of oxidation state. Density functional theory (DFT), simple geometric modelling and results from the EXAFS data analysis are in agreement for the co-ordination environment of Np(III).

In a related set of experiments, L-edge XAS data of Np(V), Np(VI) and Np(VII) were obtained from a basic solution. The Np oxidation state was varied by sparging the solution with ozone. Data were collected as the sample was sparged and also after the sparging gas was turned off. Np optical data were obtained in the same XAS cell and confirm the oxidation of Np(VI) to heptavalent Np. The concentration of Np(VII) was determined using trivalent Cr as a quantitative reductant. The Np(VII) co-ordination environment determined from both the XANES and the EXAFS data analyses are consistent with a previously reported NMR data interpretation [3]. DFT calculations on the co-ordination environment of Np(VII) support the experimental results.

Acknowledgements

This work is supported by the US DOE, Basic Energy Sciences, Chemical Sciences, under contract No. W-31-109-ENG-38. JPB acknowledges support from the Ohio Supercomputer Centre.

REFERENCES

[1] L. Soderholm, M.R. Antonio, C.W. Williams, S.R. Wasserman, *Anal. Chem*., 71, 4622-4628 (1999).

[2] M.R. Antonio, L. Soderholm, C.W. Williams, J-P. Blaudeau and B.E. Bursten (submitted).

[3] E.H. Appelman, A.G. Kostka and J.C. Sullivan, *Inorg. Chem*., 27, 2002-2005 (1988).

QUANTUM CHEMICAL CALCULATIONS ON STRUCTURES OF ACTINIDE COMPLEXES

Satoru Tsushima,* Tobias Reich
Institut für Radiochemie
Forschungszentrum Rossendorf
Germany

Abstract

The results of our recent theoretical calculations on the structures and the hydration numbers of actinide complexes are discussed together with EXAFS data. The hydration number determined from the calculated Gibbs free energy (inclusive of the solvation energy) was found to be different from the hydration number determined from the electronic energy at 0 K, 0 atm. The roles of entropy and solvation energy were found to be important with regard to the stability of the actinide complexes. The structures of the aqueous uranyl complexes obtained by EXAFS measurements were compared with the structures obtained by "gas phase" quantum chemical calculations. The importance of including the secondary co-ordination shell and counter-ions is discussed in this paper.

* On leave of absence from the Department of Quantum Engineering and Systems Science, The University of Tokyo, Japan.

Introduction

Quantum chemical *ab initio* calculations are capable of predicting various properties of molecules, including the structures, vibrational frequencies, formation energy and so on. Calculated properties are quite useful to gain further insight into actinide co-ordination chemistry. In order to do this, however, it is crucial to comprehend the correspondence between the calculated properties and those obtained by experiments. The purpose of the present work is to perform *ab initio* calculations of the actinide (uranium) complexes, determine their structures and co-ordination numbers, and to discuss the validity of the theoretical method for studying actinide complexation. This paper mainly consists of three parts. First, the co-ordination number of the uranyl ion, second the structure of the uranyl dimeric complex and third the structure of the uranyl carbonate complex.

Calculations

The GAUSSIAN 98 package of programs [1] was used for the calculations, which are based on density functional theory (DFT). The B3LYP hybrid density functional method (Becke's three-parameter hybrid functional using the LYP correlation functional [2,3]) was used since this method is known to reproduce accurate geometries and thermochemistries for uranium (VI) complexes [4,5]. Spin-orbit effects were not included since they are less important for the closed shell system that is considered here.

The calculations employed Hay's effective core potential (ECP) and corresponding basis set (without g function) for the uranium atom. The uranium core comprises the electrons in all shells up to and including the $4f^{14}$ and $5d^{10}$ shells leaving the outer $6s^2$ $6p^6$ and the outer six valence electrons (5f, 6d, 7s, 7p) treated explicitly using a [3s 3p 2d 2f] contracted Gaussian basis. The 6-31G* basis set was used for oxygen, and the 6-31G basis was used for hydrogen [6] during the optimisation calculations. The 6-31++G* basis set was used for oxygen and the 6-31++G** basis was used for hydrogen [7] for the energy calculations. The geometries were not restricted to symmetry constraints and were fully optimised.

Zero point energy correction and thermal corrections (vibrational, rotational and translational) were made to the electronic energy:

$$E = Eelec + ZPE + Evib + Erot + Etrans$$

Gibbs free energy G was calculated from:

$$H = E + RT$$

$$G = H - TS$$

where R is the gas constant, T is the temperature, H is the enthalpy and S is the entropy. The entropy was calculated from the temperature-dependent partition function.

The solvation energy was calculated using the Polarised Continuum Model (PCM) method developed by Tomasi and co-workers [8]. Scaling factor 1.2 was used for the definition of the solvent accessible surface of all elements except hydrogen. Thus, the radius of each atomic sphere was determined by multiplying the van der Waals radius by the scaling factor. Since the pressure parameter p = 1 atm used by the GAUSSIAN 98 program corresponds to the hypothetical ideal gas

phase pressure, the pressure parameter p = 1 354 atm was used to reproduce the entropy effect of concentration on Gibbs energy in aqueous solution [9]. It is calculated from $p = \rho_W RT$ and ρ_W = 997 kg/m^3, which corresponds to the experimental density of liquid water at room temperature.

Hydration number of uranyl ion

According to previous theoretical studies [10,11], the hydration number of the UO_2^{2+} ion is 5. Therefore in the present paper, the clusters of $UO_2(H_2O)_5^{2+}$ and $UO_2(H_2O)_6^{2+}$ were investigated. Three different structures were compared for each cluster.

For $UO_2(H_2O)_5^{2+}$, the three different structures being examined are:

1) Five water molecules are in the first solvation shell around the UO_2^{2+} ion [$UO_2^{2+}\cdot 5H_2O$, Figure 1(a)].

2) Five water molecules bond to the UO_2^{2+} ion but there are four water molecules in the first solvation shell and one water molecule in the second solvation shell [$UO_2^{2+}\cdot 4H_2O\cdot H_2O$**, Figure 1(b)].

3) Four water molecules are in the first solvation shell around the UO_2^{2+} ion and one water molecule bonds to the first shell water molecule through hydrogen bonding [$UO_2^{2+}\cdot 4H_2O\cdot H_2O$*, Figure 1(c)].

For $UO_2(H_2O)_6^{2+}$, the three different structures being examined are:

1) Six water molecules are in the first solvation shell around the UO_2^{2+} ion ($UO_2^{2+}\cdot 6H_2O$).

2) Six water molecules bond to UO_2^{2+} ion, but there are five water molecules in the first solvation shell and one water molecule in the second solvation shell ($UO_2^{2+}\cdot 5H_2O\cdot H_2O$**).

3) Five water molecules are in the first solvation shell around the UO_2^{2+} ion and one water molecule bonds to the first shell water molecule by hydrogen bonding ($UO_2^{2+}\cdot 5H_2O\cdot H_2O$*).

Table 1 shows the Gibbs free energies and the binding energies of the different clusters in the aqueous system. The binding energy of $UO_2(H_2O)_n^{2+}$ clusters in aqueous solution was determined as:

$$\Delta E_{UO_2^{2+}\cdot nH_2O} = E_{UO_2^{2+}\cdot nH_2O} - \left(E_{UO_2^{2+}} + nE_{H_2O}\right)$$

where $E_{UO_2^{2+}}$ is the energy of the UO_2^{2+} ion and E_{H_2O} is the energy of the water molecule, which were calculated using the same basis sets. All energies are the Gibbs free energy after adjustment for the concentration in the liquid (p = 1 354 atm) and include the PCM solvation energy. It argues that among the structures of $UO_2^{2+}\cdot 5H_2O$, $UO_2^{2+}\cdot 4H_2O\cdot H_2O$** and $UO_2^{2+}\cdot 4H_2O\cdot H_2O$*, the structure of $UO_2^{2+}\cdot 5H_2O$ has the lowest binding energy. Its binding energy in liquid phase is 11.7 kcal/mol lower than $UO_2^{2+}\cdot 4H_2O\cdot H_2O$** and 3.4 kcal/mol lower than $UO_2^{2+}\cdot 4H_2O\cdot H_2O$*. It indicates that among these three structures, the structure with five water molecules in the first solvation shell is more stable than that with four water molecules in the first co-ordination shell. On the other hand, among the structures

of $UO_2^{2+}\cdot 6H_2O$, $UO_2^{2+}\cdot 5H_2O\cdot H_2O$** and $UO_2^{2+}\cdot 5H_2O\cdot H_2O$*, the structure of $UO_2^{2+}\cdot 5H_2O\cdot H_2O$* has the lowest binding energy; in liquid phase the binding energy is 7.5 kcal/mol and 21.5 kcal/mol lower than $UO_2^{2+}\cdot 5H_2O\cdot H_2O$** and $UO_2^{2+}\cdot 6H_2O$ respectively. The structure of $UO_2^{2+}\cdot 5H_2O\cdot H_2O$** is the lowest in energy. It illustrates that the structure with five water molecules in the first solvation shell is more stable than that with six water molecules in the first solvation shell. In addition, the structure where the second shell water molecule connects to the first shell water molecule by hydrogen bonding is more stable than that of the second shell water molecule which directly bonds to the UO_2^{2+} ion. This demonstrates that five water molecules in the first shell can form the most stable complex with UO_2^{2+}, the co-ordination number of water molecules around the UO_2^{2+} ion in the first solvation shell being 5.

There is one point that must be emphasised here. All the above-mentioned binding energies are those in liquid phase. From Table 1 it is clear that the binding energies of $UO_2(H_2O)_n^{2+}$ based on "gas phase calculation" are overestimated, and that the hydration number 4 is designated the most stable. That means that the solvation energy and the entropic contribution to the free energy account for a large portion. Since pentavalent uranyl ion has large solvation energy, a small change in the ion cavity might result in significant change in solvation energy. If the hydration energy and entropy effect are not included into the energy, results for the binding energy will be wrong, and thus the co-ordination number will also be wrong.

Dimeric uranyl hydroxide complex $(UO_2)_2(OH)_2^{2+}$

Solid-state structures of the uranyl hydroxide dimer indicate that two uranyl groups are connected via a double OH bridge for the uranyl dinuclear complex, $(UO_2)_2(OH)_2^{2+}$. The initial structure of our calculation is thus based on this principle (Figure 2). At several levels of theory, we have optimised the structure of $(UO_2)_2(OH)_2(H_2O)_6^{2+}$. Generally, the choice of the basis set is very important for reliable calculations. Computation time, however, is proportional to some power of the number of the basis functions. Therefore, it is always very important to find a compromise between the accuracy and the computation time. Schreckenbach, *et al*. [4] argues that the use of the 6-31+G* basis set is a reasonable choice for the calculation of the uranyl hydroxide monomer. We had obtained a different finding during the calculations of the uranyl hydroxide dimer. By adding a set of diffuse functions to the oxygen basis (6-31G* $\rightarrow$ 6-31+G* $\rightarrow$ 6-31++G*), we observed a small change in the uranyl axial bond, but considerable lengthening of the U-O_{OH} bond by up to 0.04 Å. The effect on the U-U bond length is also significant. The U-U bond length increased from 4.06 Å to 4.09 Å (6-31G* $\rightarrow$ 6-31+G*), and then decreased to 4.04 Å (6-31++G*). The addition of a polarisation function to the hydrogen (using 6-31++G**) had only a small influence on the result, leading to a contraction of U-Oax bond lengths by 0.006 Å, and a lengthening of the U-O_{OH} bonds by 0.02 Å. Thus, we consider that the calculation of uranyl hydroxide complex should be carried out at least at the 6-31++G* level of theory.

Our calculation suggested a "bent" O=U=O structure for the uranyl dimer, having an O=U=O angle of 169-171 degrees. The *ab initio* ECP calculation at the Hartree Fock level by Wadt [12] gave the correct *cis* bent and *trans* linear structures for ThO_2 and UO_2^{2+}, respectively. ThO_2 ($6d^05f^0$) is *cis*, bent (122 degrees) because it allows π-donation from the two oxygens to two independent 6d orbitals, with a single 6d orbital shared. UO_2^{2+} ($6d^05f^0$) is *trans*, linear because of the participation of its 5f orbitals. This calculation, however, does not exclude the possibility that the UO_2^{2+} ion may show deviations from the 180° angle. Theoretical calculations of the bare UO_2^{2+} ion at the BP86 and the MP4(SDQ) levels by Ismail, *et al*. [13] gave bent uranyl ion, the bending of 2° and 98°, respectively.

A significant bending of the uranyl at MP4(SDQ) level of theory indicates failure of the perturbation theory. It was concluded that the multi-configurational aspect of the wave function invalidates the MP2 and MP4 approaches. On the other hand, the B3LYP method gave reliable results.

There is a general agreement that the uranium 6d orbitals are involved in π bonding in the O=U=O moiety. Clark, *et al*. [14] argue that the OH^- ligand is a strong π donor in uranyl hydroxide, which results in the competition of the 6d e_g orbitals between oxo and hydroxo ligands. In fact, Dai, *et al*. [15] reported a red shift of the U(VI) charge transfer (CT) band (~410 nm) upon dimeric complexation. It indicates an electron transfer to the uranyl moiety from the equatorial plane. Having two π-donating oxygens in the equatorial "*ortho*" positions, $(UO_2)_2(OH)_2(H_2O)_6^{2+}$ would have a significant asymmetry in the π orbital structure around the uranyl moiety, which probably favours the bending of the O=U=O against the OH^- ligand. A Raman spectroscopic study by Fujii, *et al*. [16] indicated that the polarisability of the U-Oax bond in $(UO_2)_2(OH)_2^{2+}$ is 10-50% higher than that of UO_2^{2+}, suggesting a "bent" $(UO_2)_2(OH)_2^{2+}$.

The present study has shown that the uranyl hydroxide dimeric complex has a "bent" O=U=O angle. It is thus not appropriate to constrict to linear O=An=O angle during the quantum chemical calculations of actinyl complexes. It is not surprising that other ligands might contribute to the formation of more bent O=U=O. Studying the O=An=O angle may provide further insight into the axial and equatorial bondings of the actinyl complexes.

Uranyl carbonate complex

The structure optimisation of $UO_2(H_2O)_5^{2+}$ and $UO_2(CO_3)_3^{4-}$ complexes were carried out using 6-31G*, 6-31++G, and 6-31++G* basis sets for H,C and O. The calculated U-Oax and U-Oeq bond lengths are given in Table 2 along with EXAFS measurement data. The EXAFS data show that U-Oax bond length of uranyl hydrate and uranyl tricarbonate does not greatly deviate. The calculated U-Oax for $UO_2(H_2O)_5^{2+}$ and $UO_2(CO_3)_3^{4-}$ is ,however, as different as ~0.08 Å. Obviously, the theoretical calculation seriously overestimates the U-Oax bond length of the $UO_2(CO_3)_3^{4-}$ complex.

The carbonate ion, CO_3^{2-}, has a resonance structure, and the carbon atom in the centre is connected with three equivalent oxygen atoms. Each oxygen atom has an effective charge of -2/3. We have carried out the optimisation calculation of the carbonate ion CO_3^{2-} at 6-31G, 6-31G*, 6-31G**, 6-31++G and 6-31++G* level of theories. At all levels of theory, we obtained only positive vibrational frequency. If the diffuse function is not added in the basis function, the effective charge of oxygen is too negative (-0.80 at the 6-31G level, -0.81 at the 6-31G* and 6-31G** levels). But the addition of diffuse function gave the oxygen effective charge close to -2/3 (-0.68 at the 6-31++G level, -0.63 at the 6-31++G* level). Thus, the diffuse function is mandatory in the calculation of the carbonate ion and carbonate complexes.

In the calculation of uranyl tricarbonate, however, we did not observe a significant impact of the addition of the diffuse function into the basis functions. It slightly changed the U-Oax bond length (~0.01 Å) but had more impact on U-Oeq bond length (~0.04 Å). This is probably because the interaction between the uranyl and the ligand is mainly electrostatic, and changes of equatorial ligand have no apparent influence on the axial bonding. It thus seems curious that the carbonate complexation significantly lengthened the U-Oax bond distance compared to the hydrate.

We have further studied this point by looking into HOMO and LUMO energies and their major orbital characters of the uranyl tricarbonate complex. According to Schreckenbach [4] and Hirata [17], the equatorial oxygen p orbitals are the main contributors of the HOMO and the nearly lying occupied MOs in uranyl hydrate, hydroxide and uranyl nitrate complexes. The LUMO and the near lying unoccupied MOs mainly consist of U 5f AOs. These facts suggest that uranyl hydrate and its complex have similar orbital character for the HOMO and LUMO and the near lying MOs. However, at the 6-31++G* level, orbitals near HOMO and LUMO of uranyl tricarbonate consist of an admixture of various Aos, suggesting the failure of the calculation. It is often pointed out that the calculation of highly negatively charged ion tends to fail.

We have carried out the structure optimisation of Liebigite, $Ca_2UO_2(CO_3)_3^0$. Because two calcium atoms cancel the negative charge of the carbonate ligand, the calculation for Liebigite does not have the problem with the charge. The calculated structure at the 6-31++G level of theory is given in Table 3. By adding two calcium atoms, the two U-Oax bond distances shortened by 0.05 Å compared to $UO_2(CO_3)_3^{4-}$. But the EXAFS measurements give 1.80 Å for the $UO_2(CO_3)_3^{4-}$ and 1.81 Å for $Ca_2UO_2(CO_3)_3^0$, suggesting that the U-Oax bond length is almost equal in these two species. Thus, we consider that the presence of the positively charged atom has solved the problem with the negative charge of the carbonate complex. In fact, the calculated structure of Liebigite does not deviate too much from the structure obtained by experiments. The addition of 10 hydration waters ($Ca_2UO_2(CO_3)_3^0 \cdot 10H_2O$, Figure 3) engendered a more reasonable accord with the experiment (Table 3).

In conclusion, we can say that the calculation of the uranyl tricarbonate tends to fail because it is a highly negatively charged ion, and the electrons do not fill the right orbitals. The addition of a cation to the system will solve the problem with the charge, and the calculated structure agrees reasonably with the experiments. Because the distal oxygen in uranyl tricarbonate has a high negative effective charge, it is probably mandatory to include polarisation, charge transfer and hydrogen bonding between the distal oxygen and the waters in the second co-ordination shell. Further studies including the second co-ordination shell seem worthwhile.

Acknowledgement

S. Tsushima was supported by a contract with Forschungszentrum Rossendorf (FZR) as a Guest Scientist at the Rossendorf Beamline at the European Synchrotron Radiation Facility (ESRF). The authors greatly appreciated the use of the SGI supercomputer ORIGIN 2000 at Technische Universität Dresden. We are grateful to Dr. Manfred Kunicke, FZR, for his technical support during the calculations and graduate student Tianxiao Yang, The University of Tokyo, for her assistance during the work.

REFERENCES

[1] M.J. Frisch, *et al*., Gaussian 98 User's Reference (2nd ed.), Gaussian, Inc., Pittsburgh, PA, (1998).

[2] A.D. Becke, *J. Chem. Phys*. 98, 5648 (1993).

[3] C. Lee, W. Yang, R.G. Parr, *Phys. Rev. B*, 37, 785 (1988).

[4] G. Schreckenbach, P.J. Hay, R.L. Martin, *Inorg. Chem*., 37, 4442 (1998).

[5] G. Schreckenbach, P.J. Hay, R.L. Martin, *J. Comput. Chem*., 20, 70 (1999).

[6] P.C. Hariharan and J.A. Pople, *Theor. Chim. Acta*, 28, 213 (1973).

[7] W.J. Hehre, R. Ditchfield and J.A. Pople, *J. Chem. Phys*., 56, 2257 (1972).

[8] S. Miertus, E. Scrocco and J. Tomasi, *Chem. Phys*., 55, 117 (1981).

[9] R. Martin, P. Jeffrey Hay and L.R. Part, *J. Phys. Chem. A*, 102, 3565 (1998).

[10] S. Tsushima, A. Suzuki, *J. Mol. Struct*. (THEOCHEM), 529, 21 (2000).

[11] S. Spencer, L. Gagliardi, N.C. Handy, A.G. Ioannou, C.K. Skylaris, A. Willetts, A.M. Simper, *J. Phys. Chem. A*, 103, 1831 (1999).

[12] W.R. Wadt, *J. Am. Chem. Soc*., 103, 6053 (1981).

[13] N. Ismail, J-L. Heully, T. Saue, J-P. Daudey, C.J. Marsden, *Chem. Phys. Lett.*, 300, 296 (1999).

[14] D.L. Clark, S.D. Conradson, R.J. Donohoe, D.W. Keogh, D.E. Morris, P.D. Palmer, R.D. Rogers, C.D. Tait, *Inorg. Chem.*, 38, 1456 (1999).

[15] S. Dai, M.C. Burleigh, J.M. Simonson, R.E. Mesmer, Z.L. Xue, *Radiochim. Acta*, 81, 195 (1998).

[16] T. Fujii, K. Fujiwara, H. Yamana, H. Moriyama, *J. Alloys Compds*., in press.

[17] M. Hirata, R. Sekine, J. Onoe, H. Nakamatsu, T. Mukoyama, K. Takeuchi, S. Tachimori, *J. Alloys Compds*., 128, 271-273, (1998).

Table 1. The binding energy of $UO_2^{2+}(H_2O)_n$ clusters (kcal/mol)

Complex	Gas phase 0 K, 0 atm	Aqueous phase 298 K, 1 atm
$UO_2^{2+}\cdot 5H_2O$	-353.1	-58.3
$UO_2^{2+}\cdot 4H_2O\cdot H_2O$*	-341.5	-46.6
$UO_2^{2+}\cdot 4H_2O\cdot H_2O$**	-353.5	-54.9
$UO_2^{2+}\cdot 6H_2O$	-349.9	-34.8
$UO_2^{2+}\cdot 5H_2O\cdot H_2O$*	-364.5	-48.9
$UO_2^{2+}\cdot 5H_2O\cdot H_2O$**	-374.1	-56.3

* Second shell water bounds to uranium.
** Second shell water is hydrogen bonded to first shell.

Table 2. The structures of $UO_2(H_2O)_5^{2+}$ and $UO_2(CO_3)_3^{4-}$ obtained by theoretical calculations and EXAFS measurements (length in Å)

Complex	Method	U-Oax	U-Oeq
$UO_2(H_2O)_5^{2+}$	B3LYP/6-31G*	1.757	2.512
	B3LYP/6-31++G	1.776	2.502
	B3LYP/6-31++G*	1.751	2.532
	EXAFS	1.77	2.42
$UO_2(CO_3)_3^{4-}$	B3LYP/6-31G*	1.838	2.564
	B3LYP/6-31++G	1.844	2.604
	B3LYP/6-31++G*	1.824	2.592
	EXAFS	1.80	2.43

Table 3. The structures of Liebigite obtained by EXAFS and by theoretical calculations (length in Å)

Method	Complex	U-Oax	U-Oeq	U-C	U-Ca	U-Odis
EXAFS	Liebigite	1.81	2.44	2.90	3.94	4.22
Calculation	$Ca_2UO_2(CO_3)_3^0$	1.79	2.36 2.55 2.84	2.97 2.97 3.37	3.83	
	$Ca_2UO_2(CO_3)_3^0\cdot 10H_2O$	1.80	2.40 2.60 2.72	2.96 2.96 3.25	3.99	4.13 4.13 4.62

Figure 1. Optimised structures of $UO_2^{2+}(H_2O)_5^{2+}$

(a) $UO_2^{2+}\cdot 5H_2O$ (b) $UO_2^{2+}\cdot 4H_2O\cdot H_2O$** (c) $UO_2^{2+}\cdot 4H_2O\cdot H_2O$*

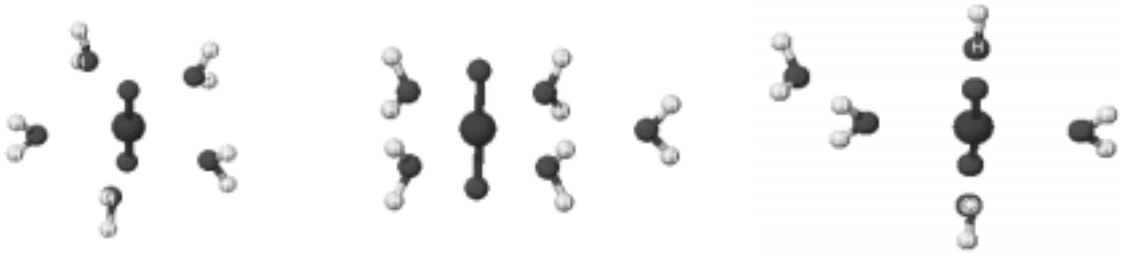

Figure 2. The structure of the dimeric uranyl hydroxide complex $(UO_2)_2(OH)_2^{2+}$

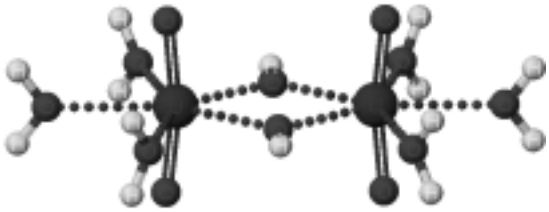

Figure 3. The structure of $Ca_2UO_2(CO_3)_3^0\cdot 10H_2O$

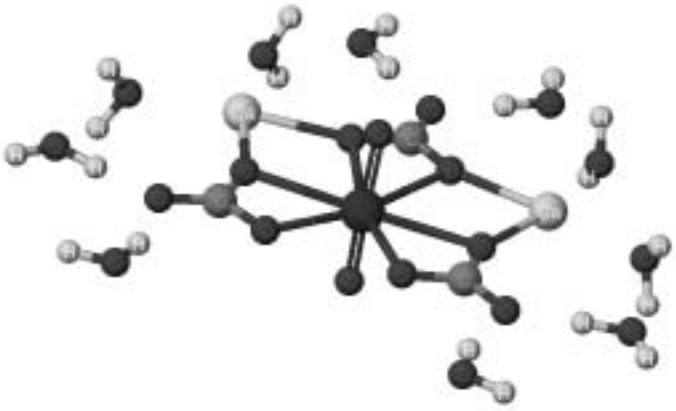

ACTINIDES IN EARTH MATERIALS: THE IMPORTANCE OF NATURAL ANALOGUES

François Farges,[1,2] **Messaoud Harfouche,**[1] **Pierre-Emmanuel Petit**[3] **and Gordon E. Brown, Jr.**[2,4]
[1]Laboratoire des Géomatériaux, Université de Marne-la-Vallée
F-77454 Marne-la-Vallée Cedex 2 (France)
[2]Surface & Aqueous Geochemistry Group
Department of Geological & Environmental Sciences
Stanford University, Stanford, CA 94305-2115, USA
[3]European Synchrotron Radiation Facility
F-38041 Grenoble Cedex
[4]Stanford Synchrotron Radiation Laboratory
2575 Sand Hill Road, MS 99
Menlo Park, CA 94025, USA

Abstract

Predictions of the stability of waste forms designed for long-term storage of actinides require an accurate knowledge of the long-term properties of these actinides in their host matrix. One useful approach to address this issue involves comparison of structural and thermodynamic information derived from short time-scale experiments on synthetic samples with similar information from natural samples, including natural glasses and metamict minerals. These natural analogues of synthetic waste forms, although significantly different in structure, properties and composition from the synthetic samples, offer a number of examples of earth materials that have received large doses of radioactivity (mainly α events) over very long time periods (10^6-10^9 years). In this paper, we present a review of the co-ordination chemistry of actinides in natural deep-seated earth systems and their analogues (mostly glasses, melts and radiation-damaged minerals). Special emphasis is given to data analysis methods that are important in determining accurate XAFS-derived interatomic distances and co-ordination numbers for actinides in these complex materials, including anharmonicity, multi-electronic transitions, deconvolution procedures, and *ab initio* calculations of near-edge structure. The effects of anharmonicity and multi-electronic transitions are best studied using high-energy resolution spectrometers on third-generation synchrotron sources. Application of these methods to selected natural minerals (crystalline and radiation-damaged) is presented, together with a comprehensive list of unusual mineral structures that are known to incorporate relatively large amounts of actinides over long periods of geologic time in a stable manner.

Introduction

In earth materials such as primary minerals, melts, hydrothermal assemblages, surficial fluids and minerals as well as soils, natural actinides (Th and U) are relatively scarce. Their normalised natural abundances in the earth's crust are relatively low (6 and 1.8 ppm for Th and U, respectively, in crustal rocks) but are higher than those of silver or mercury [1,2]. However, natural actinides are thought to be more concentrated within the deep earth, and are believed to be a significant source of the earth's internal heat because of their nuclear reactions [3].

Despite this low abundance, natural actinides are among the most important ions in geochemistry. This is because of their radioactive decay (^{232}Th, ^{235}U and ^{238}U decay into ^{208}Pb, ^{207}Pb and ^{206}Pb, respectively [4]) which provides a means of dating geological processes [5]. It is also because of their unusual geochemical properties. For instance, Th and U are "incompatible" in melts, which means that they prefer to concentrate in the melt phase during the crystallisation of magmas [6]. Also, the presence of several oxidation states of uranium [U(IV), U(V) and U(VI)] makes this element behave quite differently as a function of oxygen fugacity. For example, uranium is relatively less soluble in melts and aqueous fluids when tetravalent, but it is generally highly soluble when hexavalent.

Because of the importance of U for understanding the earth's internal processes, as well as the packaging, reprocessing and environmental remediation of high-level nuclear waste, a knowledge of its oxidation states and co-ordination environments in earth materials is needed. Although it occurs only in the 4+ oxidation state in earth materials, a similar statement can be made about a knowledge of the co-ordination environment of Th in earth materials. For instance, this type of structural information can be used as an experimental validation of molecular dynamics modelling of actinide-bearing melts and solutions, as well as the extent of radiation damage in ceramics [7]. However, because of their relatively low concentrations in most earth materials, little structural information for actinides in such materials is available. In addition, few methods are sensitive to thorium, which is essentially spectroscopically inactive. X-ray absorption fine structure (XAFS) methods (at the M- and L-edges) are by far the most powerful tools available for obtaining speciation information for thorium at low concentrations. In contrast, uranium can be studied using a variety of spectroscopic methods such a UV-vis-NIR and laser-induced fluorescence spectroscopies and imaging. However, these methods are indirect and highly sensitive to the presence of other cations (especially 3d transition elements such as Fe, which are often present in earth materials).

The use of synchrotron sources can overcome these limitations by providing quantitative, element-specific information on oxidation states and co-ordination environments for elements like Th and U (even in chemically and structurally complex materials such as crystals, finely divided minerals, molten silicates, soils or aqueous solutions [8]). Also, third-generation synchrotron sources provide higher resolution spectra with higher signal-to-noise ratios. As a result, the understanding of structural sites occupied by actinides and their oxidation states in natural systems has benefited from significant recent developments in XAFS spectroscopy methods, which we describe in this paper.

Oxidation states of uranium in geological systems

Three oxidation states are known for uranium in earth materials: U(IV), U(V) and U(VI). No metallic uranium or U(III) has been found in geological systems or in moon rocks [1], because these redox states require extremely low oxygen fugacities. The relative amounts of these oxidation states depend on oxygen fugacity (fO_2), mineral or melt composition, and, in part, on other redox couples such as Fe(II)/Fe(III) or possibly Cr(III)/Cr(VI).

In deep-seated geologic ("igneous") systems, U occurs as both U(IV) and U(V), although it is most often concentrated in U(IV)-bearing minerals such as uraninite/pitchblende UO_{2+x} (with $0 < x < 0.6$), coffinite $USiO_4$ or as inclusions of these phases in rock-forming minerals such as biotite. Tetravalent U also occurs as a minor component of accessory minerals including zircon, titanite, various (Ca, Th) oxides such as zirkelite/zirconolite, and other complex oxides of the euxenite-pyrochlore families for the most common ones (see Table 1). Tetravalent uranium is also probably the dominant oxidation state of U in the earth's mantle minerals, although some direct characterisation of these phases would be required to verify this suggestion [9]. Under more oxidising conditions, Calas [10] found that U(V) is an important oxidation state of uranium in silicate melts. Farges, *et al*. [6] determined the dominant environment of U in synthetic glasses of geological interest – a distorted six-co-ordinated environment, having a XANES L_{III}-edge position similar to that for U(VI) compounds. U(V) is rarely found in minerals, occurring in minor amounts with the more common U(IV) in some radiation-damaged ("metamict") zircons.

Under oxidising conditions, U(VI) is the stable oxidation state in which this element is most likely transported in hydrothermal (supercritical) and aqueous systems. Complexes with chlorine or carbonates [11] are suspected to transport uranium and thorium in such systems, but no direct evidence for such complexation has yet been reported. In silicate glasses and melts, U(VI) is usually found as uranyl-bearing moeities (with $U\text{-}O_{axial}$ near 1.77 Å and $U\text{-}O_{equatorial}$ near 2.25 and 2.5 Å [6]). Finally, highly damaged and weathered minerals such as zircon ("cyrtolite" variety: hydrated $ZrSiO_4$), thorite and pyrochlore show considerable amounts of U(VI). Preliminary work suggests that weathering, not radiation damage, is the cause of the tetravalent oxidation of uranium in these minerals [12].

Actinides and anharmonicity

XAFS studies of melts *in situ* (at high temperature) require an accurate understanding of the way Th-O and U-O bonds behave with increasing temperature. Such a study was conducted using the heating loop technique on a dispersive EXAFS spectrometer at LURE [13]. Several oxide and silicate compounds of Th and U were investigated between room temperature and 2 000 K [14]. Fourier transforms of the EXAFS spectra of Th in a sodium disilicate glass/melt as a function of temperature (20 to 1 474°C) are shown in Figure 1(a). The use of anharmonic theories are required to achieve accurate bond distances and co-ordination numbers from EXAFS data taken at high temperature [15]. Results of the modelling show that the anharmonic variations in the EXAFS spectra due to temperature cannot be properly modelled using cumulant expansions. In contrast, the use of an analytical function [16] resulted in excellent EXAFS-derived distances and co-ordination numbers [14]. Figure 1(b) shows the results of harmonic versus anharmonic modelling (using the analytical function of Winterer [16] for Th-O pair correlations in a Th-containing sodium disilicate melt/glass as a function of temperature. In the case of crystalline ThO_2, the EXAFS-derived linear thermal expansion coefficient ($10(2) \times 10^{-6}$ K^{-1}) is in excellent agreement with the experimental one (9×10^{-6} K^{-1}) derived by X-ray diffraction studies. In the case of uranium, similar studies are in progress and already show that, in the case of uranyl-bearing compounds, the axial U-O bond vibrates much less with temperature than the longer equatorial U-O bonds. Therefore, at high temperature, it is often difficult to extract robust structural information from U-EXAFS spectra. However, theoretical studies of U L_{III}-XANES spectra provide a more robust way of obtaining accurate information on the co-ordination environment of U at high temperature.

XANES studies of actinides: theoretical calculations and deconvolution procedures

The newest versions of the FEFF code 8.2 [17,18] make possible relatively accurate calculations of the XANES spectral region for most elements. As outlined by Ankudinov, *et al*. [18], the use of a partially non-local potential, i.e. Dirac-Fock for core, Hedin-Lundqvist for valence electrons and a constant imaginary part (the "*EXCHANGE 5*" option) provides fairly good results, although some improvements are still required [19]. In the case of α-uranotile, in which uranium is present as the uranyl moiety [20], it is possible to reproduce relatively accurately the experimental XANES spectra [Figure 2(a)]. This theoretical simulation includes the contributions arising from axial and equatorial oxygens, in excellent agreement with polarised XANES experiments on other uranyl-bearing structures [21].

The introduction of core-hole deconvolution procedures (either instrumental, multi-excitation and/or core-hole lifetime-related [22-26] provides new insights about XANES theoretical calculations and EXAFS data reduction. For instance, L-edges of actinides have a relatively large core-hole lifetime (~10 eV) [27], making it necessary to perform such procedures cautiously (i.e. with a noise level below 10^{-4}). The results (see Figure 2(a) for an example of instrumental deconvolution) are promising, however, because of the availability of high-flux spectrometers, such as beam line ID26 (ESRF, Grenoble, France), together with low-noise Si photodiode detectors [28], which makes the study of dilute natural samples feasible. These new convolution procedures will be important for materials having several redox states of uranium or for tracing selected spectral features, such as those due to multiple-scattering and partially hidden pre-edges. In addition, the excellent signal-to-noise ratio achieved on third-generation synchrotron sources as compared to older sources reveals the presence of multi-excitation transitions that were not detectable on first-generation sources (compare Figure 2(b) with [29]). In Th-bearing radiation-damaged natural zircons, for example, a probable multi-electronic feature is likely to occur in any L_{III} EXAFS spectrum of Th, near k = 10 $Å^{-1}$. In this case core-hole lifetime deconvolution procedures are required to detect these features. In these samples, another suspicious feature was found near k = 5.5 $Å^{-1}$, but its multi-electronic excitation origin is not clear as the feature is part of a wide EXAFS oscillation arising from Th-O pairs. If these contributions were ignored, it is likely that the medium-range structure (≤ 6 Å) around Th in any sample would be misinterpreted, as these features interfere with the high-frequency EXAFS signals arising from next-nearest neighbours. A similar type of analysis must be performed for the L_{III}-edge XANES and EXAFS spectra of U as well as for artificial actinides.

Actinides in silicate glasses and melts

XAFS studies of thorium and uranium in glass/melt systems of geochemical interest [6,29,30] suggest that only uranyl-bearing moieties form "complexes" in glasses and melts. Tetravalent actinides were found to adopt a different co-ordination environment in simple silicate glasses, including both six-co-ordinated environments and mixtures of six- and eight-co-ordinated environments [29]. More recent studies suggested that similar environments also exist in the melt to 1 450°C [31]. Therefore, the location of uranium and thorium in glasses gives a good approximation of the sites of these actinides in high temperature melts. No clear evidence for halogen complexation of U(IV), U(V) and U(VI) [6] or of Th [29] has been found, although such complexes are often invoked to help explain the transport properties of actinides in melts. In all U(VI)-containing glasses, there is a great deal of evidence from XANES and EXAFS spectroscopy as well as from optical absorption spectroscopy that U is present as uranyl groups with two short axial bonds [$d(U\text{-}O_{axial}) \approx 1.77\text{-}1.85$ Å] and four or five longer equatorial bonds to oxygen [$d(U\text{-}O_{equatorial}) \approx 2.18\text{-}2.25$ Å]. These results are consistent with the local structures of U(VI) in borosilicate glasses used in radioactive waste storage. All of these studies

demonstrate the stability of the uranyl group geometry in silicate, aluminosilicate and borosilicate glasses and melts of various compositions and different average structure. They also indicate that melt structure exerts little influence on the local environment around U(VI).

Bond valence models for actinides in oxide glasses and melts

Bond valence theory has been used to model the local structure around Th and U in silicate glasses [6,29] and melts [31]. These empirical models are based on the application of Pauling's second rule [32,33], see also Ref. [8] for a more detailed discussion of Pauling bond valence constraints on medium-range structure in silicate glasses and melts. The application of these empirical models is particularly useful for constraining the medium-range structure (out to 3-4 Å radial distance) around actinides in glasses and melts because of the lack of robust pair potentials for actinides required for accurate molecular dynamics modelling or for reverse Monte Carlo studies of neutron/X-ray scattering experiments.

The calculated models suggest that, because of their high charge and low co-ordination, tetravalent actinides are not likely to bond directly to a bridging oxygen (BO) in the glass network at the observed Th/U-O distances (2.3-2.4 Å range) without significantly lengthening of some individual Si-O bonds beyond their maximum observed value, and disrupting the tetrahedral network. A more plausible structural configuration corresponds to the linkage of Th/U(IV) to several non-bridging oxygens (NBOs). These oxygens are most likely around Th/U(IV) because they require one Si(IV) and one alkali to charge balance Th/U(IV). The presence of some NBOs around Th corresponds to an environment characteristic of a weak network modifier following the definition of Nelson, *et al*. [34].

The structural and chemical roles of the two types of oxygen ligands of uranyl groups can also be understood by considering the variation of U-O bond strength with bond length [35]. If we consider the EXAFS-derived U(VI)-O_{axial} distances, this relationship shows that the bond strengths of U(VI)-O_{axial} bonds range from 2.2 to 1.96 vu for the observed U(VI)-O_{axial} distances (1.77 to 1.85 Å). These bond strength values are very close to those required for "charge balance" at the axial oxygens in the Pauling sense (i.e. the sum of bond strengths to each oxygen is close to 2.0 vu [32]), suggesting that these oxygens are not bonded to other cations in the glasses studied. This idea provides a rationale for the common observation that uranyl axial oxygen ligands do not participate in other chemical bonds in crystalline uranyl-compounds. Thus these axial oxygens are not expected to interact with the glassy network. As a consequence, the U(VI)-O_{axial} distance is longer than 1.7 Å in all uranyl-containing compounds. The non-bonded character of the axial oxygens helps explain the stability of uranyl groups with low distortion in silicate melts. In contrast, the U(VI)-$O_{equatorial}$ bonds have lower bond strengths (≈ 0.60-0.65 vu). Recent molecular dynamics calculations for glasses and melts [36] have suggested that most ions follows Pauling's second rule to an accuracy level of ±2-13%.

Actinides in minerals

Accessory minerals like zircon, titanite, apatite, pyrochlore and many others (Table 1) can be studied using XAFS methods to provide useful information about the location of trace/minor amounts of actinides. Recent results suggest that substitution of actinides for smaller ions in minerals often requires substantial expansion of the original local structure of their host mineral to accommodate their larger size [12]. This local expansion effect may extend as far as 4 Å and is close to that measured in the isostructural actinide-rich equivalent (e.g. $ThSiO_4$ for Th in $ZrSiO_4$). Therefore, such replacements are the cause of a number of Å-scale defects in the structure. Molecular dynamics calculations of U in crystalline zircon confirm these preliminary results [7].

Actinides in radiation-damaged crystals

In nature, one can find minerals that were exposed to intense radiation damage (over 10^{16} α/mg of sample). These samples, which may have only moderate actinide contents, suffered only low levels of α-decay damage but were exposed to this decay for millions of years and sometimes billions of years [4]. These minerals usually retain their crystallographic faces but their internal structure is destroyed by alpha recoil, produced by the decay of actinides ("metamict"). Table 1 lists the principal metamict minerals, which are mostly oxides and include some silicates. Among these metamict minerals, zircon is the most common. The periodic to aperiodic displacive phase transition of minerals due to α-particle recoil is of special interest in both mineralogy and in materials science. Radiation-induced defects in complex ceramics are an important consideration in evaluating the long-term behaviour of individual phases that may occur in proposed crystalline, high-level nuclear waste forms [37,38,39].

Using XAFS spectroscopy, it is possible to measure the oxidation state of uranium in natural metamict minerals that have suffered major radiation damage and to evaluate the effects of the relatively highly ionising decay of natural radioactivity. In the case of natural pyrochlores [40] and the thorite/ thorogummite series [41], U was found to be oxidised, in contrast to zirconolite or zircon, which show no U oxidation [41,42]. This important conclusion, as well as other findings, enhances the choice of zirconolite and zircon as potential hosts for high-activity nuclear wastes (Pu and Am among others). However, the effect of long-term radiation damage in minerals is extremely variable. In zircon, bond valence models suggest the formation of Zr-rich domains (and concomitant Si-rich domains) in highly metamict zircons [43], which was confirmed recently using ^{29}Si NMR spectroscopy [44] and molecular dynamics calculations [7]. Such major structural reorganisation of the tetrahedral framework cannot occur in oxides, such as zirconolite.

Similar studies must be extended to Cr or Ce, which are structural analogues of Pu and Am, and can be oxidised. Additional studies are required to better understand the location of these actinides in such structures after they have received high radiation doses. These phases are known to auto-heal their defects and to be more resistant to weathering and structural reorganisation than minerals/structure types like zircon or pyrochlore.

Conclusions

Despite the limited number of studies involving actinides in deep-seated geological systems by XAFS methods, third-generation synchrotron sources and optimised computer tools (software and hardware) should dramatically improve the contributions of earth and environmental scientists to the already large database on actinides in natural materials and ceramic waste forms. More importantly, earth materials offer a diversity of structures and concepts that are interesting to investigate in order to determine if these natural analogues are suited for high-level waste containment and also to test computer methods with a combination of appropriate experimental methods such as X-ray absorption fine structure spectroscopy.

Acknowledgements

We thank the organising committee for the invitation to present this paper at the Actinide-XAS-2000 Workshop in Grenoble, France. We also wish to thank Dr. David K. Shuh (Chemical Sciences Division, Lawrence Berkeley National Laboratory) and an anonymous reviewer for a careful review of the manuscript. Our work discussed in this review was supported by the French GDR *Nomade*, the Institut Universitaire de France, the US Department of Energy (DOE) and the National Science Foundation (NSF). Our synchrotron radiation studies were carried out at the Stanford Synchrotron Radiation Laboratory (SSRL) and the European Synchrotron Radiation Facility (Grenoble, France). SSRL is supported by the US DOE and the National Institutes of Health. The technical staffs of these synchrotron laboratories are thanked for their help during our XAFS studies, particularly due to A. Solè and J. Goulon (ESRF), as well as J.R. Bargar (SSRL). Fruitful discussions with R.C. Ewing (University of Michigan, Ann Arbor) and sample donations from three national mineral collections in Paris (Muséum National d'Histoire Naturelle, École Nationale Supérieure des Mines and the Sorbonne collection at Université de Paris 6eme) are also gratefully acknowledged.

REFERENCES

[1] F. Bea, in *Encyclopedia of Geochemistry*, C.P. Marshall and R.W. Fairbridge, eds., pp. 645-648, Kluwer Academic Publishers (Dordrecht, The Netherlands, 1999).

[2] S. Krishnaswami, in *Encyclopedia of Geochemistry*, C.P. Marshall and R.W. Fairbridge, eds., pp. 630-635, Kluwer Academic Publishers (Dordrecht, The Netherlands, 1999).

[3] J.L. Vigneresse and M. Cuney, in *Terrestrial Heat Flow and the Lithosphere Structure*, V. Cermak and L. Rybach, eds., pp. 86-110 (Springer-Verlag, New York, 1991).

[4] R.C. Ewing, in *Uranium: Mineralogy, Geochemistry and the Environment*, P.C. Burns and R. Finch, eds., *Reviews in Mineralogy and Geochemistry*, Vol. 38, Mineralogical Society of America, Washington, D.C. (1999).

[5] G. Faure, *Principles of Isotope Geology*, 2nd edition, New York, John Wiley & Sons. 589 pp. (1986).

[6] F. Farges, C.W. Ponader, G. Calas and G.E. Brown, Jr., *Geochim. Cosmochim. Acta*, 56, 4205-4220 (1992).

[7] J-P. Crocombette and D. Ghaleb, *J. Nuclear Mat.*, 257, 282-286 (1998).

[8] G.E. Brown, Jr., J.R. Bargar, F. Farges and H.T. Berbeco, these proceedings (2001).

[9] E. Knittle, *Geodynamics Series*, 28, 119-130, American Geophysical Union, Washington, D.C. (1998).

[10] G. Calas, *Geochim. Cosmochim. Acta*, 43, 1521-1531 (1979) (in French).

[11] H. Keppler and P.J. Wyllie, *Nature*, 348, 531-533 (1990).

[12] M. Harfouche, F. Farges and P-E. Petit, "Structural Characterization of Natural Actinides (Th and U) in Ceramics and Analogues: XANES and EXAFS Studies on Natural Zircons", European Union of Geosciences (EUG XI), J1-2671 (in press).

[13] F. Farges, J-P. Itié, G. Fiquet and D. Andrault, *Nucl. Instrum. Meth. in Phys. Res. B*, 101, 493-498 (1995).

[14] Z. Wu and F. Farges, *Physica B*, 266, 282-289 (1999).

[15] G.E. Brown, Jr., F. Farges and G. Calas, in *Structure, Dynamics, and Properties of Silicate Melts*, J.F. Stebbins, D.B. Dingwell and P.F. McMillan, eds., pp. 317-410, *Reviews in Mineralogy*, Vol. 32, The Mineralogical Society of America, Washington, DC (1995).

[16] M. Winterer, Proceedings of the 9th International Conference on X-ray Absorption Fine Structure (XAFS IX, Grenoble), J. Phys IV France, 7, 243 (1997).

[17] J.J. Rehr, Z.I. Zabinsky and R.C. Albers, *Phys. Rev. Lett.*, 69, 3397-4000 (1992).

[18] A.L. Ankudinov, B. Ravel, J.J. Rehr and S.D. Conradson, *Phys. Rev. B* 58, 7565-7576 (1998).

[19] H.A. Thompson, G.E. Brown, Jr. and G.A. Parks, *Am. Mineral.*, 82, 483-496 (1997).

[20] F.V. Stohl and D.K. Smith, *Am. Mineral.*, 66, 610-625 (1981).

[21] D.H. Templeton and L.K. Templeton, *Acta Crystallogr.*, A38, 62-67 (1982).

[22] P.W. Loeffen and R.F. Pettifer, *Phys. Rev. B (Condensed Matter)*, 54, 14877-80 (1996).

[23] A. Filipponi, *J. Phys. B*, 33, 2835-2841 (2000).

[24] K.V. Klementev, "Deconvolution Problems in X-ray Absorption Fine Structure", *submitted* (see http://www.crosswinds.net/~klmn/viper.html) (2001).

[25] V. Gotte, J. Goulon, Ch. Goulon-Ginet, A. Rogalev, C.R. Natoli, K. Perié, J-M. Barbe and R. Guilard, *J. Phys. Chem. B*, 104, 1927-1938 (2000).

[26] F. Farges, G.E. Brown, Jr., P-E. Petit and M. Munoz, *Geochim. Cosmochim. Acta* (in press).

[27] F.C. Brown, in *Synchrotron Radiation Research*, H. Winick and S. Doniach, eds., pp. 61-100, (Plenum Press, New York, 1980).

[28] C. Gauthier, V.A. Solé, R. Signorato, J. Goulon and E. Moguiline, *J. Synchrotron Rad.*, 6, 164-166 (1999).

[29] F. Farges, *Geochim. Cosmochim. Acta*, 55, 3303-3319 (1991).

[30] L.L. Davis, H. Li, D. Caulder and J. Crum, *Geol. Soc. Am., 1999 Annual Meeting, Abstracts with Programs*, 31, p. 134 (1999).

[31] F. Farges and G.E. Brown, Jr., *J. Physique IV*, 7 (C2), 1009-1010 (1997).

[32] L. Pauling, *J. Am. Chem. Soc.*, 51, 1010-1026 (1929).

[33] I.D. Brown and D. Altermatt, *Acta Crystallogr., B* 41, 244-247 (1985).

[34] C. Nelson, T. Furukawa and W.B. White, *Mat. Res. Soc. Bull.* 18, 959-966 (1983).

[35] N.E. Brese and M. O'Keefe, *Acta Crystallogr. B*, 47, 192-197 (1991).

[36] F. Farges, S. Rossano and J-M. Delaye, "EXAFS, Bond-valence and Molecular Dynamics: The Case of KTS2 Glass/Melt, 4th European Conference in Mineralogy and Spectroscopy (in press).

[37] W. Lutze and R.C. Ewing, in *Radioactive Waste Forms for the Future*, W. Lutze and R.C. Ewing, eds., pp. 700-740 (Elsevier, Amsterdam, 1988).

[38] W.J. Weber, *J. Mat. Res.*, 5, 2687 (1991).

[39] R.C. Ewing, W.J. Weber and F.W. Clinard, Jr., *Prog. in Nuclear Energy*, 29, 63-127 (1995).

[40] G.R. Lumpkin and R.C. Ewing, *Phys. Chem. Minerals*, 16, 2-20 (1988).

[41] F. Farges and G. Calas, *Am. Mineral.*, 76, 60-73 (1991).

[42] F. Farges, R.C. Ewing and G.E. Brown, Jr., *J. Mat. Res.*, 8, 1983-1995 (1993).

[43] F. Farges, *Phys. Chem. Minerals*, 20, 504-514 (1994).

[44] I. Farnan, *Phase Transitions*, 69, 47-60 (1999).

Table 1. Main metamict minerals in nature

(a) Oxides

• Group of pyrochlore, zirkelite/zirconolite series

Zirconolite	$(Ca,Fe,REE,Zr,Th)(Zr,Nb,Ti,Ta,Fe)Ti_2O_7$
Polymignite	$(Ca,Fe,REE,Zr,Th)(Zr,Nb,Ti,Ta,Fe)Ti_2O_7$
Zirkelite	$(Ca,Th,Ce)Zr(Ti,Nb)_2O_7$

• Group of crichtonite

Davidite-(Ce)	$(Ce,La)(Y,U)(Ti,Fe)_{20}O_{38}$
Davidite-(La)	$(La,Ce,Ca)(Y,U)(Ti,Fe)_{20}O_{38}$

• Group of pyrochlore, betafite series, with Ti > (Nb,Ta)

Betafite	$(Ca,Na,U)_2(Ti,Nb,Ta)_2O_6(OH)$
Stibiobetafite	$(Sb,Ca)_2(Ti,Nb,Ta)_2(O,OH)_7$
Yttrobetafite-(Y)	$(Y,U,Ce)_2(Ti,Nb,Ta)_2O_6(OH)$
Plumbobetafite	$(Pb,U,Ca)(Ti,Nb)_2O_6(OH,F)$

• Group of pyrochlore, pyrochlore series, with Nb > Ti

Pyrochlore	$(Na,Ca)_2Nb_2O_6(OH,F)$
Calciobetafite	$Ca_2(Ti,Nb)_2(O,OH)_7$
Kalipyrochlore	$(K,Sr)_{2-x}Nb_2O_6(O,OH)\cdot n(H_2O)$
Strontiopyrochlore	$Sr_2Nb_2(O,OH)_7$
Bariopyrochlore	$Ba,Sr)_2(Nb,Ti)_2(O,OH)_7$
Yttropyrochlore-(Y)	$(Y,Na,Ca,U)_{1-2}(Nb,Ta,Ti)_2(O,OH)_7$
Ceriopyrochlore-(Ce)	$(Ce,Ca,Y)_2(Nb,Ta)_2O_6(OH,F)$
Plumbopyrochlore	$(Pb,Y,U,Ca)_{2-x}Nb_2O_6(OH)$
Uranpyrochlore	$(U,Ca,Ca)_2(Nb,Ta)_2O_6(OH,F)$

• Group of pyrochlore, microlite series, with Ta > Nb

Microlite	$(Na,Ca)_2Ta_2O_6(O,OH,F)$
Stannomicrolite	$(Sn,Fe)(Ta,Nb,Sn)_2(O,OH)_7$
Stibiomicrolite	$(Sb,Ca,Na)_2(Ta,Nb)_2(O,OH)_7$
Bariomicrolite	$Ba_2(Ta,Nb)_2(O,OH)_7$
Plumbomicrolite	$(Pb,Ca,U)_2Ta_2O_6(OH)$
Natrobistantite	$(Na,Cs)Bi(Ta,Nb,Sb)_4O_{12}$
Bismutomicrolite	$(Bi,Ca)(Ta,Nb)_2O_6(OH)$
Uranmicrolite	$(U,Ca)_2(Ta,Nb)_2O_6(OH)$

• Columbite series

Magnocolumbite	$(Mg,Fe,Mn)(Nb,Ta)_2O_6$
Manganocolumbite	$(Mn,Fe)(Nb,Ta)_2O_6$
Ferrocolumbite	$FeNb_2O_6$
Manganotantalite	$MnTa_2O_6$
Ferrotantalite	$FeTa_2O_6$

• Polycrase-(Y)-loranskite series

Polycrase-(Y)	$(Y,Ca,Ce,U,Th)(Ti,Nb,Ta)_2O_6$
Uranopolycrase	$(U,Y)(Ti,Nb,Ta)_2O_6$
Yttrocrasite-(Y)	$(Y,Th,Ca,U)(Ti,Fe)_2(O,OH)_6$
Fersmite	$(Ca,Ce,Na)(Nb,Ta,Ti)_2(O,OH,F)_6$
Euxenite-(Y)	$(Y,Ca,Ce)(Nb,Ta,Ti)_2O_6$
Samarskite-(Y)	$(Y,Fe,U)(Nb,Ta)_5O_4$
Ishikawaite	$(U,Fe,Y,Ca)(Nb,Ta)O_4$ (?)
Yttrocolumbite-(Y)	$(Y,U,Fe)(Nb,Ta)O_4$
Yttrotantalite-(Y)	$(Y,U,Fe)(Ta,Nb)O_4$
Loranskite-(Y)	$(Y,Ce,Ca)ZrTaO_6$ (?)

• Aeschynite series

Aeschynite-(Y)	$(Y,Ca,Fe)(Ti,Nb)_2(O,OH)_6$
Aeschynite-(Ce)	$(Ce,Ca,Fe)(Ti,Nb)_2(O,OH)_6$
Aeschynite-(Nd)	$(Nd,Ce)(Ti,Nb)_2(O,OH)_6$
Vigezzite	$(Ca,Ce)(Nb,Ta,Ti)_2O_6$
Niobo-aeschynite-(Ce)	$(Ce,Ca)(Nb,Ti)_2(O,OH)_6$
Niobo-aeschynite-(Nd)	$(Nd,Ce)(Nb,Ti)_2(O,OH)_6$
Rynersonite	$Ca(Ta,Nb)_2O_6$
Tantalaeschynite-(Y)	$(Y,Ce,Ca)(Ta,Ti,Nb)_2O_6$

• Thorutite-orthobrannerite series

Thorutite	$(Th,U,Ca)Ti_2(O,OH)_6$
Brannerite	$(U,Ca,Ce)(Ti,Fe)_2O_6$
Orthobrannerite	$U_2Ti_4O_{12}(OH)_2$

• Petscheckite-liandratite series

Petscheckite	UFe (Nb,Ta)2O8
Liandratite	U(Nb,Ta)2O8

(b) Oxides (cont'd)

• Serie fergusonite-(Y)-formanite-(Y)

Fergusonite β-(Y)	$YNbO_4$
Fergusonite β-(Ce)	$(Ce,La,Nd)NbO_4$
Fergusonite β-(Nd)	$(Nd,Ce)NbO_4$
Fergusonite-(Y)	$YNbO_4$
Fergusonite-(Ce)	$(Ce,Nd,La)NbO_4\cdot 0.3(H_2O)$
Fergusonite-(Nd)	$(Nd,Ce)(Nb,Ti)O_4$
Formanite-(Y)	$YTaO_4$

• Series baddeleyite-uraninite

Tazheranite	$CaTiZr_2O_8$
Calzirtite	$CaZr_3TiO_9$
Cerianite-(Ce)	$(Ce,Th)O_2$

• Non-classified oxides

Zirconolite-2M	$CaZrTi_2O_7$
Zirconolite-3T	$CaZrTi_2O_7$
IMA98.059	$(Bi,U,Ca,Pb)_{1+x}(Nb,Ta)_2O_6(OH)\cdot n(H_2O)$

(c) Phosphates (weakly metamict)

• Xenotime-(Y)-Wakefieldite-(Ce) series

Xenotime-(Y)	YPO_4

• Group of monazite

Monazite-(La)	$(La,Ce,Nd)PO_4$
Monazite-(Ce)	$(Ce,La,Nd,Th)PO_4$
Monazite-(Nd)	$(Nd,Ce,La,Pr,Sm,Gd)(P,Si)O_4$
Cheralite-(Ce)	$(Ce,Ca,Th)(P,Si)O_4$
Brabantite	$CaTh(PO4)_2$

• Group of rhabdophane

Rhabdophane-(Ce)	$(Ce,La)PO_4\cdot(H_2O)$
Rhabdophane-(La)	$(La,Ce)PO_4\cdot(H_2O)$
Rhabdophane-(Nd)	$(Nd,Ce,La)PO_4\cdot(H_2O)$
Brockite	$(Ca,Th,Ce)(PO_4)\cdot(H_2O)$
Tristramite	$(Ca,U,Fe)(PO_4,SO_4)\cdot 2(H_2O)$
Grayite	$(Th,Pb,Ca)PO_4\cdot(H_2O)$
Ningyoite	$(U,Ca,Ce)_2(PO_4)_2\cdot 1\text{-}2(H_2O)$

(d) Silicates

• Nesosilicates

zircon	$ZrSiO_4$
coffinite	$USiO_4\text{-}U(SiO_4)_{1-x}(OH)_{4x}$
thorite	$ThSiO_4$
huttonite	$ThSiO_4$
thorogummite	$Th(SiO4)_{1-x}(OH)_{4x}$
hafnon	$HfSiO_4$
Umbozerite	$Na_3Sr_4ThSi_8(O,OH)_{24}$

• Nesosubsilicates

Titanite	$CaTiSiO_5$
Gadolinite-(Y)	$Y_2FeBe_2Si_2O_{10}$
Gadolinite-(Ce)	$(Ce,La,Nd,Y)_2FeBe_2Si_2O_{10}$
Melanocerite-(Ce)	$(Ce,Th,Ca)_5(Si,B)_3O_{12}(OH,F)\cdot n(H_2O)$

• Sorosilicates

Yttrialite-(Y)	$(Y,Th)_2Si_2O_7$
Ekanite	$ThCa_2Si_8O_{20}$
Iraqite-(La)	$K(La,Ce,Th)_2(Ca,Na)_4(Si,Al)_{16}O_{40}$
Tritomite-(Y)	$(Y,Ca,La,Fe)_5Si,B,Al)_3(O,OH,F)_{13}$
Tritomite-(Ce)	$(Ce,La,Ca,Y,Th)_5(Si,B)_3(O,OH,F)_{13}$
Karnasurtite-(Ce)	$(Ce,La,Th)(Ti,Nb)(Al,Fe)(Si,P)_2O_7(OH)_4\cdot 3(H_2O)$
Tranquillityite	$Fe_8(Zr,Y)_2Ti_3Si_3O_{24}$
Chevkinite-(Ce)	$(Ce,La,Ca,Na,Th)_4(Fe,Mg_2((Ti,Fe)_3Si_4O_{22}$
Karnasurtite-(Ce)	$(Ce,La,Th)(Ti,Nb)(Al,Fe)(Si,P)_2O_7(OH)_4\cdot 3(H_2O)$
Allanite-(Y)	$(Y,Ce,Ca)_2(Al,Fe)_3(SiO4)_3(OH)$
Allanite-(La)	$Ca(La,Ce)(Fe,Mn)(Al,Fe)_2(SiO_4)(Si_2O_7)O(OH)$
Allanite-(Ce)	$(Ce,Ca,Y)_2(Al,Fe)_3(SiO4)_3(OH)$
Vesuvianite	$Ca_{10}Mg_2Al_4(SiO_4)_5(Si_2O_7)_2(OH)_4$
Steenstrupine-(Ce)	$Na_{14}Ce_6Mn_2Fe_2(Zr,Th)(Si_6O_{18})2(PO_4)_7\cdot 3(H_2O)$
Thorosteenstrupine	$(Ca,Th,Mn)_3Si4O_{11}F\cdot 6(H_2O)$

Figure 1. Comparison of (a) Fourier transforms for Th in a sodium disilicate glass/melt as a function of temperature and (b) average Th-O distances calculated using both harmonic and anharmonic EXAFS models (modified after [14])

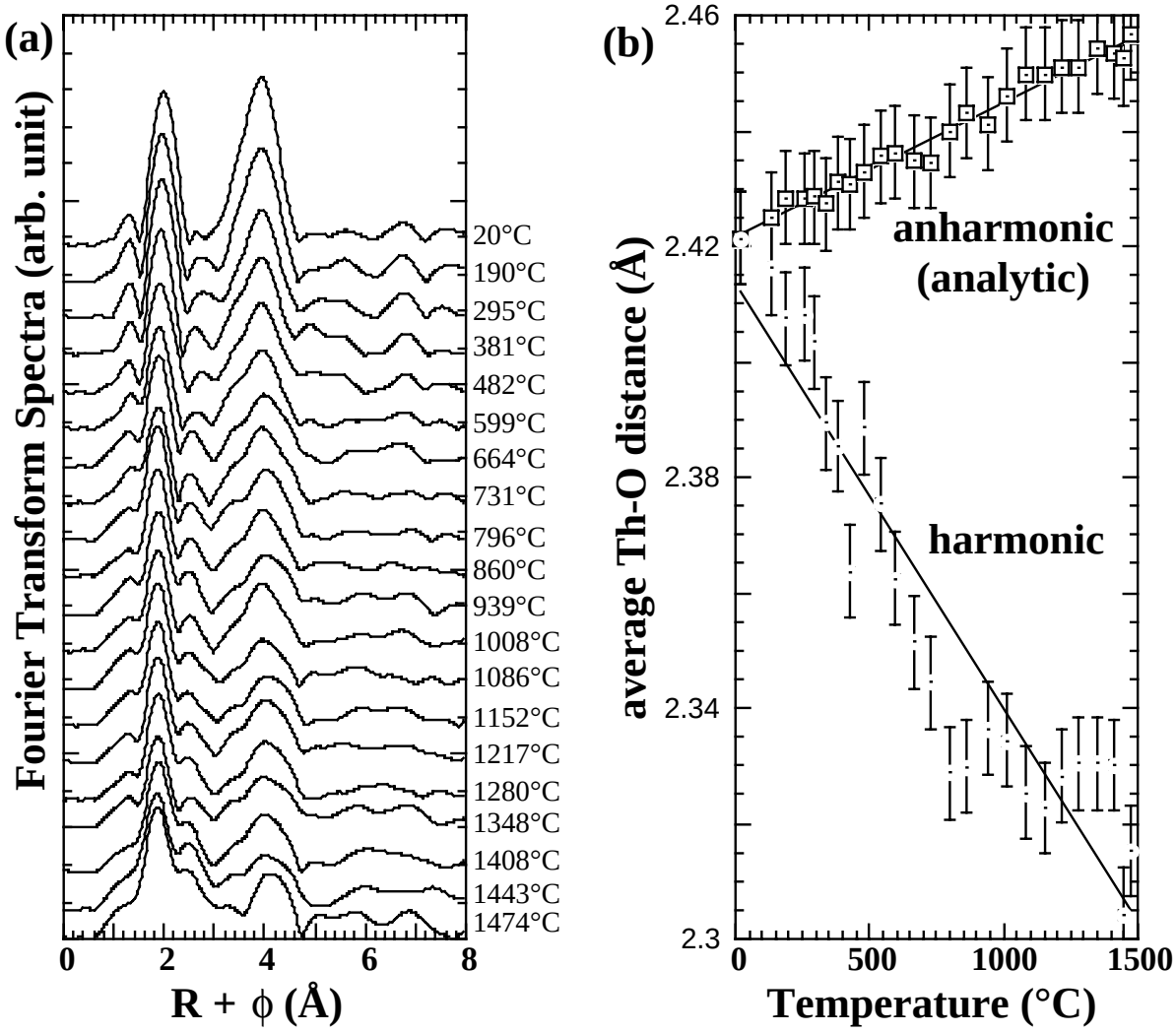

Figure 2

(a) Experimental (top curve) and calculated U-L_{III} XANES spectra (2^{nd}, 3^{rd} and 4^{th} from top) using FEFF 8.2 for α-uranotile, considering different cluster sizes: uranyl moiety (up to 3 Å from the central U, also showing the individual axial and equatorial contributions) and its medium-range environment including next-nearest neighbours (up to 4, and 6 Å, respectively). The more distant atoms (Si, U, Ca, O and H) do not contribute significantly to the measured spectrum. The normalised experimental spectrum was collected on undulator beam line ID26 at ESRF, and its instrumental deconvolution (i.e. related to monochromator broadening: bottom curve) was calculated using the VIPER code [24]. The instrumentally deconvoluted spectrum is consistent with ab initio XANES calculations.

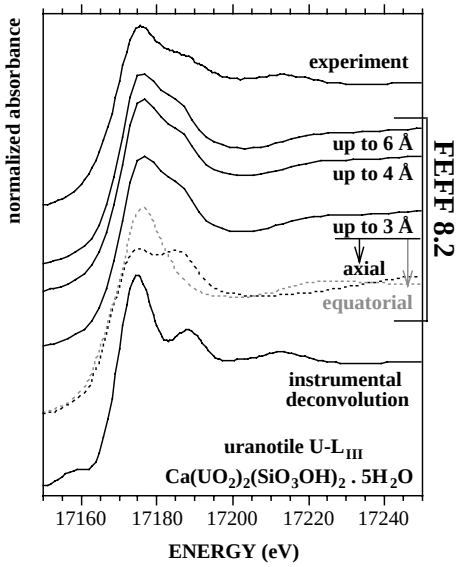

(b) normalised k^3-weighted EXAFS spectra at the L_{III}-edge of Th (100-2 000 ppm Th) in various Th-bearing zircons from different localities in Madagascar (Betafo, Ampagabe) and Japan (Naëgy): radiation damaged ("metamict": top four spectra) or annealed (at 1 200°C for four hours: bottom two spectra). Spectra were collected on undulator beam line ID26 at ESRF. The thick grey arrows indicate a probable multi-electronic excitation transition near k = 10 Å^{-1}, which is best detected using a multi-electronic excitation deconvolution procedure in the VIPER code [24]. Another possible multi-electronic excitation feature may occur near k = 5.5 Å^{-1} (light black arrow). Neglecting these multi-electronic excitation features can lead to incorrect structural information in EXAFS data analysis, particularly for next-nearest neighbour contributions.

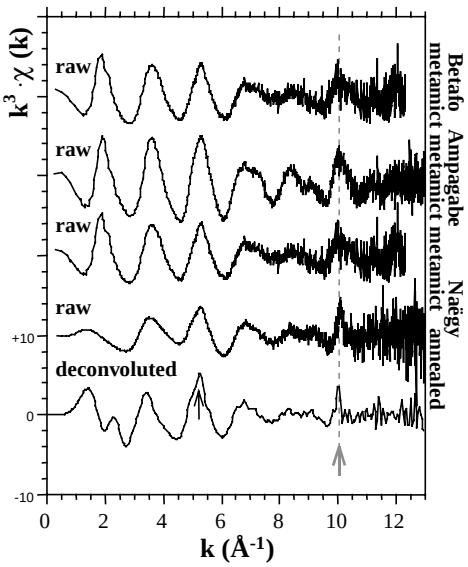

LOCAL STRUCTURE OF Th COMPLEXES ON MONTMORILLONITE CLAY MINERAL DETERMINED BY EXTENDED X-RAY ABSORPTION FINE STRUCTURE (EXAFS) SPECTROSCOPY

R. Dähn,[1] A.M. Scheidegger,[1] A. Manceau,[2] B. Baeyens[1] and M.H. Bradbury[1]
[1]Waste Management Laboratory, Paul Scherrer Institute
CH-5232 Villigen, Switzerland
[2]Environmental Geochemistry Group, LGIT-IRIGM, University of Grenoble
BP53, F-38041 Grenoble Cedex 9, France

Abstract

The research at the Waste Management Laboratory, PSI, concentrates on the understanding of safety relevant mechanisms and processes that govern the release of radionuclides from waste matrices, and their transport through engineered barrier systems and the surrounding geosphere. For this reason, detailed sorption studies of radionuclides in clay and cement systems are conducted. The studies are combined with extended X-ray absorption fine structure (EXAFS) spectroscopy measurements in order to understand the sorption mechanisms at an atomic level.

In this manuscript, a case study of Th(IV) uptake on montmorillonite is presented. EXAFS samples were prepared by incubating a montmorillonite suspension with Th for seven days at pH = 5 ($Th_{initial}$: 4.3×10^{-5} to 4×10^{-4} M). The resulting Th loadings on the clay varied between 14 and 166 μmol/g. L_{III}-Th EXAFS spectra of Th-treated montmorillonite were measured at the Rossendorf Beamline at the European Synchrotron Radiation Facility. Data analysis revealed the presence of two O shells at 2.27 Å and 2.45 Å in all samples. The spectra at low Th uptake suggest the presence of Si/Al and Th backscattering atoms at distances of 3.85 Å and 3.77 Å respectively. The presence of a Th-Si/Al backscattering pair suggests that Th is bound to Si tetrahedra by a double corner-sharing manner. At higher Th uptake, however, the spectrum shows a strong similarity with the spectrum of amorphous $Th(OH)_4$ and suggests that Th is predominately present as a newly formed $Th(OH)_4$-like phase.

Introduction

Sorption on mineral surfaces strongly affects the fate and mobility of contaminants in the geosphere. Therefore, an atomic-level understanding of sorption mechanisms of contaminants on mineral surface is of fundamental importance for maintaining environmental quality and assessing the long-term stability of waste repositories. On clay minerals several uptake mechanisms of divalent metal ions such as Ni(II), Co(II) and Zn(II) have been proposed: sorption on edge sites, sorption on interlayer sites (Figure 1) and the formation of lamellar nucleation phases such as neoformed layer silicates and mixed-layered double hydroxides [1-4].

Figure 1. Sorption modes on dioctahedral aluminous clays (V = vacancy) [5]

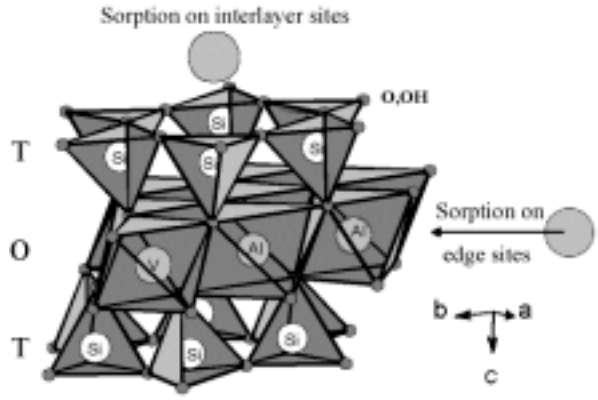

In this study EXAFS was used to investigate the uptake process of Th(IV) on montmorillonite. Th has long been recognised as an important tracer element in natural waters, soils and sediments because of its accurately known source terms, long half-life and single redox state [6]. Thorium is, therefore, a suitable analogue for other tetravalent actinides. Furthermore, Th is of major concern in nuclear waste management and an important contaminant in fly ashes from lignite power plants [7]. Th has been added to synthetic silicate glasses in order to study the structural environment of Th as a function of melt composition and polymerisation [8]. Long-term spontaneous radiation will make crystalline compounds (e.g. $ZrSiO_4$) become aperiodic and also oxide glasses to nucleate [9,10]. Dioctahedral aluminous clays are used as a backfill material in the Swiss concept for a high-level radioactive waste repository and, therefore, metal sorption on montmorillonite has been investigated in our laboratory in great detail [11].

Materials and methods

The montmorillonite STx-1 used in this study ($Si_4Al_{1.67}(Fe^{2+},Mg)_{0.33}O_{10}(OH)_2(Me_{0.33},H_2O)$, where Me refers to a metal cation in the interlayer space between sheets) was purchased from the Source Clay Minerals Repository Project of the Clay Minerals Society.

The EXAFS samples were prepared by adding 11-100 ml of a Th stock solution ($1\cdot10^{-3}$ M ($Th(NO_3)_4{\cdot}5H_2O$), pH 3.0, 0.001 M HNO_3) to 50 ml of a conditioned and purified montmorillonite suspension (ionic strength of 0.1 M ($NaClO_4$) to block cation exchange processes). The suspension was then filled with a 0.1 M $NaClO_4$ solution to 250 ml resulting in a solid to liquid ratio of 2.4 g/L and an initial Th concentration of $4.3\cdot10^{-5}$ – $4.0\cdot10^{-4}$ M. The pH was adjusted and kept constant (pH = 5) and the samples were shaken end-over-end. The preparations were performed in a glove box under N_2 atmosphere (CO_2 and O_2 < 5 ppm). The reaction conditions were within the solubility limit

of $Th(OH)_4$ [12,13,14]. After seven days of reaction time the suspensions were centrifuged and the wet pastes were filled into Plexiglas holders. The supernatant solutions were analysed by ICP-MS in order to determine the Th uptake on the Th/montmorillonite sorption system. Th L_{III}-edge EXAFS spectra were recorded at the Rossendorf Beamline (ROBL) at the ESRF [15] using a Si(111) crystal monochromator and Pt-coated mirrors. All sorption samples were measured at RT in fluorescence mode using a four-element Ge solid-state detector.

Data reduction was carried out by using the WinXAS 97 1.3 software package [16]. Radial structure functions (RSFs) were obtained by Fourier transforming k^3-weighted $\chi(k)$ functions between 2.9 to 10 $Å^{-1}$ using a Bessel window function with a smoothing parameter of 4. Amplitude and phase shift functions were calculated with FEFF 8.0 [17] using the structure of thorite (α-$ThSiO_4$) [18] as reference. Since the inner potential corrections (ΔE_0) in the Th sorption samples varied between 5.5-6.5 eV, the parameter was fixed to 6 eV in order to reduce the number of free-fit parameters. Furthermore, the amplitude reduction factor (S_0^2) was set to 1.0.

The theoretical Th-O, Th-Si and Th-Th phase and amplitude functions calculated with FEFF 8.0 were tested by fitting the EXAFS spectrum of a synthetic thorite compound provided by Farges [8]. The results gave an average co-ordination number and bond distance of 8.5 ± 1.7 O atoms at 2.39 Å (σ^2 = 0.005 $Å^2$), of 5.3 ± 1.1 Th atoms at 3.9 Å (σ^2 = 0.005 $Å^2$) and of 3.9 ± 0.8 Si atoms at 3.92 Å (σ^2 = 0.005 $Å^2$). The structural parameters for thorite as determined by X-ray diffraction (XRD) are four equatorial O at 2.36 Å, four axial O at 2.47 Å, four Si at 3.9 Å and four Th at 3.9 Å [18]. The differences between EXAFS and XRD structural data are within the uncertainty of EXAFS parameters, that is ~20% for co-ordination numbers and ~0.02 Å for interatomic distances.

Results

Figure 2 shows the background subtracted, normalised and k^3-weighted EXAFS spectra of montmorillonite treated with Th (sorbed Th concentrations of 14, 40 and 166 μmol/g). The corresponding RSFs are shown in Figure 3. For the lowest Th concentration the first peak is split into two and the amplitude is reduced, and the second peak is shifted to higher distance with higher Th concentration.

Figure 2. k^3-weighted Th L_{III}-edge EXAFS spectra for Th sorbed on montmorillonite (pH = 5)

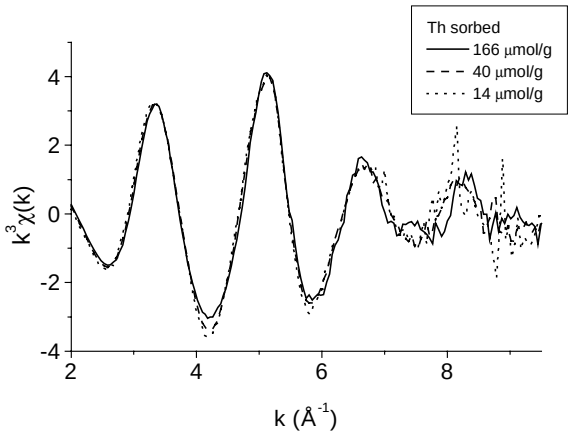

Figure 3. RSFs of k^3-weighted Th L_{III}-edge EXAFS spectra for Th sorbed on montmorillonite (pH = 5)

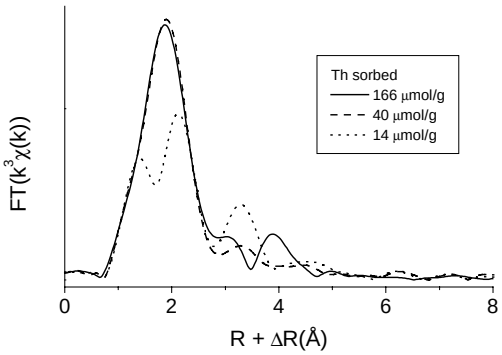

The simulation of the Fourier filtered χ_O functions obtained by back transforming first RSF peaks (ΔR = 1-2.5 Å) indicated that two nearest O distances are present in all Th sorption samples. To constrain fit parameters, the Debye-Waller (DW) factor of the second oxygen shell was fixed to σ^2 = 0.005 Å^2, as in the thorite reference. Furthermore, the DW of the first oxygen shell was set to σ^2 = 0.002 Å^2 in order to obtain a total co-ordination number of 10 for the two O shells. For steric and crystallographic reasons the total number of oxygen atoms in the first and second shell should not exceed 10. EXAFS structural parameters for the two nearest O shells are listed in Table 1. The shorter shell consists of 2.6-3.0 O atoms at 2.27-2.28 Å and the longer of 6.6-7.1 O atoms at 2.45-2.46 Å.

Table 1. EXAFS structural parameters for two nearest O shells of Th sorbed on montmorillonite (ph = 5)

Sample	Th-O[1]			Th-O[2]				
	N	R [Å]	$\sigma^{2\,f}$ [Å^2]	N	R [Å]	$\sigma^{2\,f}$ [Å^2]	$\Delta E_0{}^f$ [eV]	%Res
166 μmol/g	2.6	2.27	0.002	6.6	2.45	0.005	6	15.7
40 μmol/g	2.6	2.27	0.002	6.9	2.45	0.005	6	16.5
14 μmol/g	3.0	2.28	0.002	7.1	2.46	0.005	6	6.6

N, R, σ^2, ΔE_0 are the co-ordination numbers, interatomic distances, Debye-Waller factors and inner potential corrections.
f: Fixed during the fit procedure.
The deviation between the fitted and the experimental spectra is given by the relative residual in per cent, %Res.

The k^3-weighted Fourier back-transformed spectra of second RSF peaks (ΔR = 2.9-4.2 Å for the highest concentrated sample and ΔR = 2.9-3.7 Å for the two others) are shown in Figure 4. The structural results obtained by data analysis using Th and Si as backscatter atoms are shown in Table 2. Accordingly, the second peak consists of 1.5-1.7 Si at ~3.85 Å and ~0.7 Th at 3.77 Å (14 and 40 μmol/g). The σ^2 terms were set to 0.005 Å^2 as in the thorite reference. The spectrum of the most concentrated Th sample (166 μmol/g) clearly differs from the spectra of the two less concentrated samples (14 and 40 μmol/g), indicating differences in the Th co-ordination environment. For example, there is a beat pattern near 6.5 Å^{-1} in the most concentrated Th sample which indicates the presence of at least two cationic subshells containing heavy atoms such as Th.

At high Th concentration (166 μmol/g) neither a Th-Th and Th-Si, nor a Th-Th_1 and Th-Th_2 two-shell model provided a good fit to the experimental spectrum. Nevertheless, it is possible to propose an uptake mechanism for Th in this sample. In Figure 5 the EXAFS spectra of thorite [8] and amorphous $Th(OH)_4$ are compared to the 166 μmol/g Th sample. The likeness of the sorption sample

Figure 4. k^3-weighted EXAFS functions obtained by Fourier back-transforming second RSF peaks in Figure 3 (ΔR = 2.9-4.2 Å for 166 μmol/g, ΔR = 2.9-3.7 Å for 14 and 40 μmol/g)

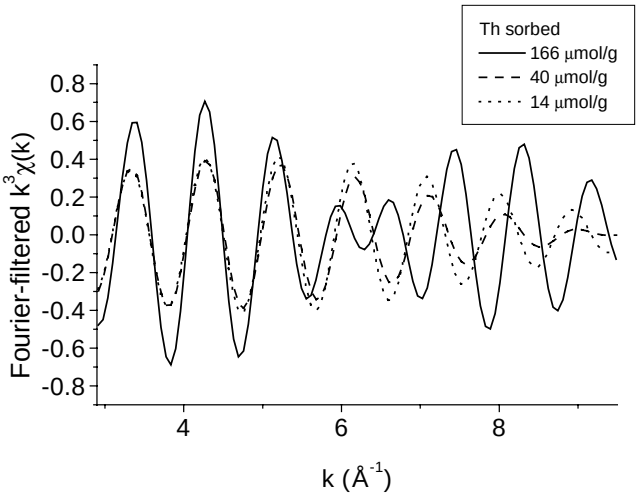

Table 2. EXAFS structural parameters for the nearest Th and Si shells and Th sorbed on montmorillonite (ph = 5)

Sample	Th-Si			Th-Th				
	N	R [Å]	$\sigma^{2\,f}$ [Å^2]	N	R [Å]	$\sigma^{2\,f}$ [Å^2]	$\Delta E_0{}^f$ [eV]	%Res
166 μmol/g	A reasonable fit could not be achieved							
40 μmol/g	1.5	3.84	0.005	0.7	3.76	0.005	6	29.7
14 μmol/g	1.7	3.85	0.005	0.7	3.77	0.005	6	25.0

f: Fixed during the fit procedure.

Figure 5. Comparison of k^3-weighted XAFS functions of reference compounds and the highest concentrated Th sample

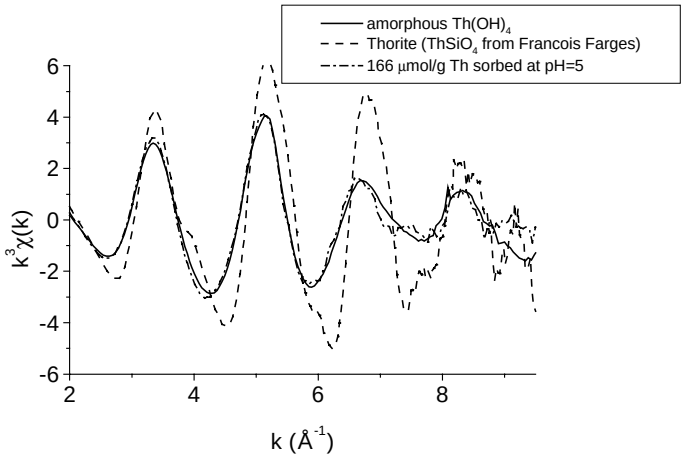

and the Th amorphous precipitate is striking, and suggests the formation of a similar precipitate at high Th concentration. Again it was not possible to fit $Th(OH)_4$ data with just one or two Th-Th backscattering pairs. The reason lies probably in the fact that the second peak of the $Th(OH)_4$ compound is too disordered to be fitted with a two-Th shell harmonic model [19].

Discussion

The results obtained in this study for the two most diluted samples compare well with those reported by Östhols, *et al*. [19] for the sorption of Th on amorphous silica: 1.7-2.7 O at 2.27-2.34 Å vs. 2.6-3.0 O at 2.27-2.28 Å (this study), 4.4-5.4 O at 2.53-2.56 Å vs. 6.9-7.1 O at 2.45-2.46 Å (this study) and 1.3-2.7 Si at 3.79-3.89 Å vs. 1.5-1.7 Si at 3.84-3.85 Å (this study). While the co-ordination numbers and interatomic distances for the first O and the Si shell match well, the second Th-O distance in the Th/montmorillonite system is significantly shorter. The distance of the second shell is characteristic for Th-H_2O bonds (2.44-2.45 Å) [20] and therefore does not modify the structural interpretation. EXAFS structural parameters for Th-sorbed silica were interpreted by Östhols, *et al*. [19] as the formation of a double corner-sharing Th surface complex. Based on the similarity of structural parameters in the two systems, it can be hypothesised that Th is bound to Si tetrahedra in a similar manner.

In conclusion, this study reveals the presence of two Th-O co-ordination spheres for the uptake of Th on montmorillonite at pH = 5. At low Th concentration (14 and 40 μmol/g), Th is bound to about two Si tetrahedra by a double-corner sharing mechanism as in Th sorbed silica. At high Th concentrations (166 μmol/g), Th precipitated as a $Th(OH)_4$-like amorphous thorium hydroxide.

Based on the data obtained in this study two structural mechanisms can be inferred for the samples with low Th concentration: The formation of a Th surface complex at the montmorillonite surface or the precipitation/neoformation of a Th-silicate. The neoformation of mixed (i.e. sorbate + sorbent metals) precipitates has recently been demonstrated in the case of Ni uptake on clay minerals [1,4,21] and Co on quartz [22].

Acknowledgements

The authors thank the staff of the Rossendorf Beamline at the ESRF for their support during the XAFS measurements, and the European Synchrotron Radiation Facility (ESRF) at Grenoble, France, for the provision of beam time. François Farges is thanked for providing the thorite spectrum. Partial financial support was provided by the National Co-operative for the Disposal of Radioactive Waste (Nagra), Wettingen (Switzerland).

REFERENCES

[1] A.M. Scheidegger, G.M. Lamble and D.L. Sparks, *J. Colloid Interface Sci*., 186, 118-128 (1997).

[2] M. Schlegel, A. Manceau, D. Chateigner and L. Charlet, *J. Colloid Interface Sci*., 215, 140-158 (1999).

[3] M.L. Schlegel, A. Manceau and L. Charlet, *J. Colloid Interface Sci*., 220, 392-405 (1999).

[4] A.C. Scheinost and D.L. Sparks, *J. Colloid Interface Sci*., 223, 1-12 (2000).

[5] S.I. Tsipursky and V.A. Drits, *Clay Minerals*, 19 (2), 177-193 (1984).

[6] P.H. Santschi and B.D. Honeymann, *Radiat. Phys. Chem*., 34 (2), 213-240 (1989).

[7] N. Savanonda, E. Prongpunyasakul and S. Ratanakorn, New York, Gordon and Breach (1985).

[8] F. Farges, *Geochim. Cosmochim. Acta*, 55, 3303-3319 (1991).

[9] G.R. Lumpkin, R.C. Ewing, B.C. Chakoumakos, R.B. Greegor, F.W. Lytle, E.M. Foltyn, F.W.J. Clinard, L.A. Boatner, M.M. Abraham, *Journal of Materials Research*, 1 (4), 564-576 (1986).

[10] R.C. Ewing, B.C. Chakoumakos, G.R. Lumpkin and T. Murakami, *Nuclear Instruments and Methods in Physics Research*, 32 (1-4), 487-497 (1987).

[11] B. Baeyens and M.H. Bradbury, *J. Contam. Hydrol*., 27, 199-222 (1997).

[12] J.L. Ryan and D. Rai, *Inorg. Chem*., 26, 4140-4142 (1987).

[13] E. Östhols, J. Bruno, I. Grenthe, *Geochim. Cosmochim Acta*, 58 (2), 613-623 (1994).

[14] V. Neck and J.I. Kim, *Radiochim. Acta*, in review (2000).

[15] W. Matz, N. Schell, G. Bernhard, F. Prokert, T. Reich, J. Claussner, W. Oehme, R. Schlenk, S. Dienel, H. Funke, F. Eichhorn, M. Betzl, D. Prohl, U. Strauch, G. Huttig, H. Krug, W. Neumann, V. Brendler, P. Reichel, M. Denecke and H. Nitsche, *Journal of Synchrotron Radiation*, 6, 1076-1085 (1999).

[16] T. Ressler, *Journal of Synchrotron Radiation*, 5 (2), 118-122 (1998).

[17] J.J. Rehr, J. Mustre de Leon, S. Zabinsky and R.C. Albers, *Journal of the American Chemical Society*, 113 (14), 5135-5140 (1991).

[18] M. Taylor and R.C. Ewing, *Acta Cryst*., B 34, 1074-1079 (1978).

[19] E. Östhols, A. Manceau, F. Farges and L. Charlet, *J. Colloid Interface Sci*., 194, 10-21 (1997).

[20] H. Moll, M.A. Denecke, J. Jalilehvand, M. Sandström and I. Grenthe, *Inorganic Chemistry*, 38 (8), 1795-1799 (1999).

[21] R. Dähn, A. Scheidegger, A. Manceau, M. Schlegel, B. Baeyens, M.H. Bradbury, *Journal of Synchrotron Radiation*, in review (2000).

[22] A. Manceau, M. Schlegel, K.L. Nagy and L. Charlet, *J. Colloid Interface Sci*., 220, 181-197 (1999).

SORPTION OF URANYL SPECIES ON ZIRCON AND ZIRCONIA

C. Lomenech,[1] R. Drot,[1] J-J. Ehrhardt,[2] J. Mielczarski[3] and E. Simoni[1]
[1]Institut de Physique Nucléaire, Orsay, France
[2]Laboratoire de Chimie Physique pour l'Environnement, Villers-lès-Nancy, France
[3]Laboratoire Environnement et Minéralurgie, Vandœuvre-lès-Nancy, France

Abstract

The safety of a long-term storage of radioactive waste in deep geological repositories would be strongly affected by the migration properties of radionuclides through the different barriers to the surface of the earth. Since the main process involved in the retention of radioactive ions is their sorption at the water/ mineral interface, a quantitative description of the sorption reactions is needed.

Macroscopic data have for a long time been the only source of information used to propose a modelling of sorption equilibria, although they bring no direct information on the nature of the sorbed species; a microscopic structural investigation of the surface complexes is difficult indeed, because of the small amount of matter sorbed. Thus, in this study, parallel to the macroscopic measurements, different complementary spectroscopic techniques have been used in order to determine the nature of the surface species. As the final purpose of such a study is the simulation of the experimental retention data, the precise structural identification of the sorption equilibria will then be very useful to constrain the data simulation code.

In this work, we present the results of both macroscopic and microscopic studies of the sorption of uranyl species on zircon and zirconia. The first part of our macroscopic approach was the surface characterisation of the non-sorbed materials by the determination of the specific areas, of the pH of the isoelectric points, and of the sorption site numbers, while the second part aimed at obtaining the sorption isotherms (percentage of sorption versus pH), which was performed using alpha spectrometry, for different uranyl concentrations, media ($NaClO_4$ or KNO_3) and ionic strengths.

The spectroscopic identification of the different surface complexes and sorption sites has been carried out using four different spectroscopies. Whereas time-resolved laser spectrofluorimetry gave a direct answer concerning the number of surface species (only for a few samples, because of the weak signals obtained), X-ray electron spectroscopy enabled us to show differences in the bonding energies between uranyl species sorbed either on zircon or on zirconia, or for the same sorbent for different pH or in different media (nitrate or perchlorate), this last point being confirmed by diffuse reflectance infrared spectroscopy. EXAFS measurements were then performed on well-characterised samples, on zircon and zirconia at different pH and in different media, for either dry or *in situ* samples. The results clearly show that the sorbed species are inner sphere complexes, and they seem to indicate strong similarities between our dry samples and the *in situ* experiments, which confirms the validity of other spectroscopic measurements. Moreover, differences between samples prepared at different pH were observed, which could possibly be explained by the formation of a surface precipitate.

SESSION II

Application of Synchrotron Radiation Techniques and Complementary Techniques

Chairs: P.G. Allen, J.I. Kim, C. Madic, T. Fanghänel, G.H. Lander, N.M. Edelstein

ACTINIDE SCIENCE WITH SOFT X-RAY SYNCHROTRON RADIATION

David K. Shuh
Actinide Chemistry Group, The Glenn T. Seaborg Center
Lawrence Berkeley National Laboratory (LBNL)
MS 70A-1150, 1 Cyclotron Road, Berkeley, CA 94720, USA

Abstract

Several workshops, some dating back more than fifteen years, recognised both the potential scientific impact and opportunities that would be made available by the capability to investigate actinide materials in the vacuum ultraviolet (VUV)/soft X-ray region of the synchrotron radiation (SR) spectrum. This spectral region revolutionised the approach to surface materials chemistry and physics nearly two decades ago. The actinide science community was unable to capitalise on these SR methodologies for the study of actinide materials until recently because of radiological safety concerns. The Advanced Light Source (ALS) at LBNL is a third-generation light source providing state-of-the-art performance in the VUV/soft X-ray region. Along with corresponding improvements in detector and vacuum technology, the ALS has rendered experiments with small amounts of actinide materials possible. In particular, it has been the emergence and development of microspectroscopic techniques that have enabled investigations of actinide materials at the ALS.

The primary methods for the experimental investigation of actinide materials in the VUV/soft X-ray region are the complementary photoelectron spectroscopies, near-edge X-ray absorption fine structure (NEXAFS) and X-ray emission spectroscopy (XES) techniques. Resonant photo-emission is capable of resolving the 5f electron contributions to actinide bonding and can be used to characterise the electronic structure of actinide materials. This technique is clearly a most important methodology afforded by the tunable SR source. Core level and valence band photoelectron spectroscopies are valuable for the characterisation of the electronic properties of actinide materials, as well as for general analytical purposes. High-resolution core-level photo-emission and resonant photo-emission measurements from the α (monoclinic) and δ (FCC) allotropic phases of plutonium metal have been collected on beam line 7.0 at the ALS and the spectra show pronounced differences between the phases. The Pu $4f_{7/2}$ core level spectra obtained from both phases have sharp metallic features indicative of core hole shielding by de-localised electrons. However, the screening is enhanced in the α-Pu spectrum and suggests a larger degree of de-localisation than in δ-Pu. The results from the resonant valence band photo-emission measurements show greater spectral enhancement from the δ-Pu than the α-Pu, which is also consistent with a greater degree of localisation in δ-Pu.

One specific consequence of third-generation VUV/soft X-ray SR source development is the renaissance of XES techniques. XES is an atom specific probe, complementary to both photo-emission and absorption, that is especially amenable to studies of buried, disordered and bulk materials systems. Thus, XES is well suited for characterising the electronic properties of actinide materials since complications with surface contamination and sample preparation can be avoided. Results from XES

studies can be interpreted within existing theoretical frameworks. The results from XES investigations of the uranium oxides materials will be presented. A significant amount of information about actinide materials chemistry and physics can be obtained from a comprehensive multi-technique approach in the VUV/soft X-ray energy region that will lead to an improved understanding of the unique properties of these materials.

Acknowledgements

This work is supported by the Director, US Department of Energy, Office of Science, Office of Basic Energy Sciences, Chemical Sciences Division and Materials Sciences Divisions at LBNL and the ALS under contract No. DE-AC03-76SF00098.

RECENT ACHIEVEMENTS IN MULTI-KEV X-RAY MICROSCOPY

J. Susini, R. Barrett, M. Salomé and B. Kaulich
European Synchrotron Radiation Facility
BP 220, F-38043 Grenoble Cedex, France

Abstract

X-ray microscopy (XRM) techniques are emerging as powerful and complementary tools for sub-micron investigations. Soft XRM traditionally offers the possibility to form direct images of thick hydrated biological material in near-native environments, at a spatial resolution well beyond that achievable with visible light microscopy. Natural contrast is available in the soft X-ray region, in the so-called "water-window", due to the presence of absorption edges of the major constituents (C,N,O). Recent advances in manufacturing techniques have enlarged the accessible energy range of micro-focusing optics and offer new applications in a broad range of disciplines. XRM in the 1-20 keV energy range is better suited to map trace elements in fluorescence yield, 3-D tomographic imaging and in micro-diffraction. After a brief introduction to the principles and methods, the main attributes of X-ray microscopy will be presented. This presentation will be biased towards sub-micron microscopy developed at the ESRF in the 2-10 keV energy. Strengths and weaknesses of X-ray microscopy and spectromicroscopy techniques will be discussed and illustrated by examples in biology, materials sciences and geology.

For a complete review on X-ray microscopy see the following:

- "X-Ray Microscopy", G. Schmahl and D. Rudolf, eds., Springer, Berlin (1984).
- "X-Ray Microscopy II", D. Sayre, M. Howells, J. Kirz, and H. Rarback, eds., Springer, Berlin (1988).
- "X-Ray Microscopy III", A.G. Michette, G.R. Morrison, C.J. Buckley, eds., Springer, Berlin, (1992).
- "X-Ray Microscopy IV", V.V. Aristov and A.I. Erko, eds., Bogorod-skii Pechatnik, Moscow, (1994).
- "X-Ray Microscopy and Spectroscopy", J. Thieme, *et al*., eds., Springer, Berlin (1998).

More specific applications are developed in the followings references:

- J. Kirz, C. Jacobsen and M. Howells, *Quat. Rev. Biophys*., 28, 33 (1995).
- G. Schneider, *Ultramicroscopy*, 75, 85 (1998).

- G. Schneider, T. Schliebe and H. Aschoff, *J. Vac. Sci. Technol*., B 13, 2809 (1995).
- S. Spector, C. Jacobsen and D. Tennant, *J. Vac. Sci. Technol*., B 15, 2872 (1997).
- D. Weiss, M. Peuker and G. Schneider, *Appl. Phys. Lett*., 72, 1805 (1998).
- B. Kaulich, *et al*., *Appl. Phys. Lett*., 75, 4061 (1999).
- W. Yun, *et al., Rev. Sci. Instrum*., 70 (9), 3537 (1999).
- E. Di Fabrizio, F. Romanato, M. Gentili, S. Cabrini, B. Kaulich, J. Susini and R. Barrett, *Nature*, 401, 895 (1999).
- J. Kirz and H. Rarback, *Rev. Sci. Instrum*., 56 (9), 1 (1985).
- G. Schmahl, D. Rudolph, P. Gutmann and O. Christ, *Quat. Rev. Biophys*., 13, 293 (1980).
- H. Ade, X. Zhang, S. Cameron, C. Costello, J. Kirz and W. Williams, *Science*, 258, 872 (1992).
- C. Buckley, N. Khaleque, S.J. Bellamy, M. Robins, X. Zhang, in Ref.[1], II-47 (1998).
- P. Dhez, P. Chevallier, T.B. Lucatorto and C. Tarrio, *Rev. Sci. Instrum*., 70 (4), 1907 (1999).

EXAFS INVESTIGATION OF U(VI) INTERACTION WITH BACTERIA

C. Hennig, P.J. Panak,* T. Reich, J. Raff, S. Selenska-Pobell,
A. Roßberg, H. Funke, M.L. Merroun, G. Bernhard
Forschungszentrum Rossendorf e.V., Institute of Radiochemistry
P.O. Box 510119, D-01314 Dresden, Germany

Abstract

Bacteria in soil, sediment and water have a significant influence on the transport of radionuclides and other heavy metals in nature. Certain bacterial strains can selectively accumulate various metal ions from aqueous systems [1] and are, therefore, important for the regulation of environmental pollution and remediation. Because of the high resistance of their spores to extreme conditions, bacilli are found in a large variety of natural habitats. Recently, it was demonstrated that two *Bacillus* strains, *B. cereus* JG-A30 and *B. sphaericus* JG-A12, recovered from a uranium mining waste site in Germany, are able to accumulate selectively a large variety of heavy metals from the drain waters of the waste site [2]. In particular, it was shown that these strains accumulate large amounts of uranium.

Uranium(VI) complex formation at vegetative cells and spores of *Bacillus cereus* and *Bacillus sphaericus* was studied using uranium L_{II}-edge and L_{III}-edge extended X-ray absorption fine structure (EXAFS) spectroscopy. A comparison of the measured equatorial U-O distances and other EXAFS structural parameters of uranyl complexes formed at the *Bacillus* strains with those of the uranyl structure family indicates that the uranium is predominantly bound as uranyl phosphate [3].

* Current address: Lawrence Berkeley National Laboratory, MS 70A-1150, Berkeley, CA 94720, USA.

REFERENCES

[1] S. Selenska-Pobell, P. Panak, V. Miteva, I. Boudakov, G. Bernhard, H. Nitsche, "Selective Accumulation of Heavy Metals by Three Indigenous *Bacillus* Strains, *B. cereus*, *B. megaterium* and *B. sphaericus*, from Drain Waters of a Uranium Waste Pile", *FEMS Microbiol. Ecol*., 29, 59-67 (1999).

[2] P.J. Panak, J. Raff, S. Selenska-Pobell, G. Geipel, G. Bernhard, H. Nitsche, "Complex Formation of U(VI) with *Bacillus*-isolates from a Uranium Mining Waste Pile", *Radiochim. Acta*, in press.

[3] C. Hennig, P.J. Panak, T. Reich, A. Roßberg, J. Raff, S. Selenska-Pobell, W. Matz, J.J. Bucher, G. Bernhard, H. Nitsche, "EXAFS Investigation of Uranium(VI) Complexes Formed at *Bacillus cereus* and *Bacillus sphaericus* Surfaces", *Radiochim. Acta*, submitted.

SPECIATION OF THE ACTINIDE HUMATE COMPLEXATION BY XAFS

Melissa A. Denecke,* Kathy Dardenne, Christian M. Marquardt, Jörg Rothe
Forschungszentrum Karlsruhe, Institut für Nukleare Entsorgung
P.O. Box 3640, D-76021 Karlsruhe, Germany
*melissa@ine.fzk.de

Mark P. Jensen
Argonne National Laboratory, Chemistry Division
9600 S. Cass Avenue, Argonne, IL 60439, USA

Abstract

EXAFS results from Hf(IV) and Th(IV) humates identify carboxylate groups as the primary humic acid (HA) binding sites for cations. EXAFS structural parameters obtained for Np(V) humate at pH = 7 show the same trend as those previously observed for U(VI) humates. Furthermore, the only measurable difference between the Np co-ordination in Np(V) humate at pH = 7 compared to pH = 9 is the presence of a Np-Np interaction near 3.84 Å. No changes in the first Np-O co-ordination sphere, which would be evidence for co-ordination of a OH ligand in a hydrolysed Np mixed colloid complex $(NpO_2(OH)HA)_{colloid}$, is observed. STXM images of HA colloids at pH = 4.4 show globular and rod-like agglomerates with diffuse contours. These diffuse contours disappear in images of mixtures of organic humic acid and inorganic clay colloids. In the mixtures, aggregates with distinct, fractal-like shapes are observed; no separate aggregation of HA occurs. The carbon *1s* NEXAFS spectrum of HA shows distinct peaks associated with $1s \rightarrow \pi^*$ transitions of C=C and C=O bonds.

Introduction

Establishing the role that humic colloid mediated actinide transport plays in immobilisation and mobilisation processes in the environment is prerequisite to the successful development of performance assessment modelling codes. To this end, actinide-humic colloid interactions must be understood. The most important characteristic endowing humic substances (HS) potential as an avenue for colloid-mediated radionuclide transport is their strong complexing ability for cations. Various experimental approaches are and have been implemented to speciate actinide cations in the presence of HS. In this paper, the primary interaction of humic acid (HA) with Np(V), Th(IV) and Hf(IV), as a tetravalent actinide homologue, are determined by comparing structural parameters of the metal cation co-ordination in their humate complexes with either previous results or with a reference system. Structural, metrical parameters are extracted from the L3 edge extended X-ray absorption fine structure (EXAFS) spectra. The effect of increasing the pH from 7 to 9 on the structure of the actinide co-ordination sphere for the Np(V) humate is also studied. The colloidal, macromolecular HS structure and changes affected by the presence of mineral colloids are determinant in the ability of humic colloids to mediate actinide transport. For this reason, the tertiary structure of HA colloids alone and in association with mineral colloids are determined from their scanning transmission X-ray microscopic (STXM) images. The C *1s* edge near-edge X-ray absorption fine structure (NEXAFS) of HA is compared to that of carboxylated latex spheres in order to identify absorption features in the spectrum. Despite the advantages of approximately a tenfold higher resolution over light microscopy, the possibility of measuring in solution that other microcroscopies do not offer and the supplemental spectroscopic, chemical information that STXM offers, only few reports of its application to studies of natural organic material have appeared in the literature [1-3].

EXAFS investigation on the interaction of Hf(IV) and Th(IV) with HA and Bio-Rex70

EXAFS investigations of U(VI) sorbed onto HA showed the structural parameters for the U(VI) co-ordination to be invariant of HA type, preparation conditions and cation loadings [4]. This suggests that the same HA functional groups are responsible for binding U(VI). According to IR results and the pH applied for sample preparation, these functional groups are carboxylate groups. Noteworthy is that a U(VI)-HA prepared using a synthetic HA also exhibited the same co-ordination, despite having a much higher phenolic OH:carboxylate group ratio than the other HA investigated [4,5]. This indicates that the HA phenolic OH groups play a subordinate role compared to carboxylate groups in complexing U(VI).

In order to test the hypothesis that HA carboxylate groups are generally responsible for binding metal cations, co-ordination numbers (N), bond distances (R) and Debye-Waller factors (σ^2) of Hf(IV) and Th(IV) sorbed onto HA are determined from their metal L3 EXAFS spectra. These are compared to those found for Hf(IV) and Th(IV) sorbed onto Bio-Rex70, a cation exchange resin having solely carboxylate groups [6]. If the HA carboxylate groups are responsible for complexing the metal cations, while HA phenolic OH groups are unimportant, then the structural parameters for Hf(IV) and Th(IV) sorbed onto HA should be the same as those exhibited by these metal cations sorbed onto Bio-Rex70.

All sorption samples are prepared from 250±1 mg either purified HA (Aldrich) or protonated Bio-Rex70 (Bio-Rad) suspended in approximately 35 mL 0.1 M $HClO_4$. Following adjustment of pH to ~2 with NaOH, 5 mL of a 0.1 M $HClO_4$ solution containing 29.5 mM Hf(IV) or 26.2 mM Th(IV) are added and the pH readjusted to ~1.6. The resulting volume of the reaction solution is near 50 mL. The solution is stirred for 66-68 h, at constant pH 1.63±0.05, under ambient conditions. The sample is isolated by centrifugation, washing once with 50 mL Milli-Q water. The quantity Hf(IV) or Th(IV) sorbed is determined as the difference between the initial and supernatant concentrations. The Hf(IV)

loading onto HA and Bio-Rex70 is 86 mg/g and 15 mg/g, respectively. With a proton exchange capacity (PEC) of 5.43 mEq/g for Aldrich HA [7] and 10.2 mEq/g for Bio-Rex70 and assuming charge neutralisation, these loadings are equivalent to 35% PEC and 3% PEC. The corresponding Th(IV) loadings are 128 mg/g HA and 41 mg/g Bio-Rex70, which is equivalent to 41% PEC and 7% PEC, respectively.

For EXAFS measurements, a portion of each sample was placed in wet paste form into a capped 400 μL polyethylene (PE) centrifuge tube. The rest of the sample was air-dried, dispersed in PE powder and pressed as 1.3 cm diameter pellets. In addition to the sorption samples, polycrystalline tetrakis-acetylacetonate hafnium(IV), $Hf(acac)_4$ and bis(tetraethylammonium) hexanitrato-thorium(IV), $[(C_2H_5)_4N]_2Th(NO_3)_6$, are also studied as pressed PE pellets.

EXAFS spectra were recorded on the Hf and Th L3 edges, at room temperature, in transmission mode, at the Hamburger Synchrotronstrahlungslabor (HASYLAB) on beam line A1. A Si(311) double-crystal monochromator, detuned 50% of the maximum incident flux, was used. Hafnium L3 edge spectra were calibrated against the first inflection point in the K edge of a Zn foil defined as 9 660.8 eV. L3 edge spectra of the Th samples were calibrated in a similar manner using the K edge of a Y foil defined as 17 038.0 eV.

The L3 electron ionisation energy, E_0, for all Hf samples was defined as 9 565.0 eV; E_0 was defined as 16 315 eV for Th samples. Averaged spectra of two or more scans for each sample were analysed using the suite of programs EXAFSPAK [8]. Theoretical oxygen backscattering amplitude and metal-oxygen phase-shift functions applied during fits to the data are calculated using FEFF7 [9] for a 29 atom cluster using either atomic positions for $Hf(acac)_4$ [10] or those for $[NH_4]_2Th(NO_3)_6$ [11]. The error associated with the bond length determination with the EXAFS method for these samples, as well as for the Np humates reported in the next section, is ±0.02 Å; the error for co-ordination number is ±20% [12].

The k^3-weighted Hf and Th L3 edge spectra and their corresponding Fourier transforms (FT) are shown in Figure 1. Visual inspection of the spectra reveals that the EXAFS pattern for all Hf(IV) sorption samples is nearly the same in HA and Bio-Rex70 samples, but different from that of the polycrystalline reference compound. The same is true for the Th(IV) samples.

The back-transformed first peak in the FT of each spectrum was fit to the EXAFS equation using oxygen atoms as backscatterers. Fit results are listed in Table 1. The excellent agreement between N and R from EXAFS fits and XRD results for the two polycrystalline compounds substantiates the "correctness" of theoretical phase and amplitude functions used. For both Hf(IV)-HA and Hf(IV)-Bio-Rex70, in wet paste and air-dried forms, approximately 6-7 oxygen atoms at R = 2.14 Å are found. Both Th(IV)-HA and Th(IV)-Bio-Rex70 exhibit 9-10 oxygen atoms at 2.43 Å.

Because similar structural parameters for metal cation sorption onto both HA and Bio-Rex70 are found, it is assumed that the same type of complexation occurs in both systems. Because Bio-Rex70 only has carboxylate groups capable of cation binding, having the same complexation implicates carboxylate groups responsible for cation binding in HA. If a significant number of HA functional groups other than carboxylate groups were involved, e.g. phenolic OH groups, then interatomic distances would be different and an EXAFS pattern unlike that of their Bio-Rex70 counterparts would be expected. For example, there is a difference greater than 0.18 Å between U-O distances associated with co-ordinated phenol and co-ordinated carboxylate for the salicylate complex reported in [13].

Figure 1. k^3-weighted Hf (top) and Th (bottom) L3 edge EXAFS (left) and their corresponding Fourier transforms (right) for the Hf(IV) and Th(IV) sorption samples (H stands for HA, B for Bio-Rex70 and P for wet paste sample), $Hf(acac)_4$ and $[(C_2H_5)_4N]_2Th(NO_3)_6$

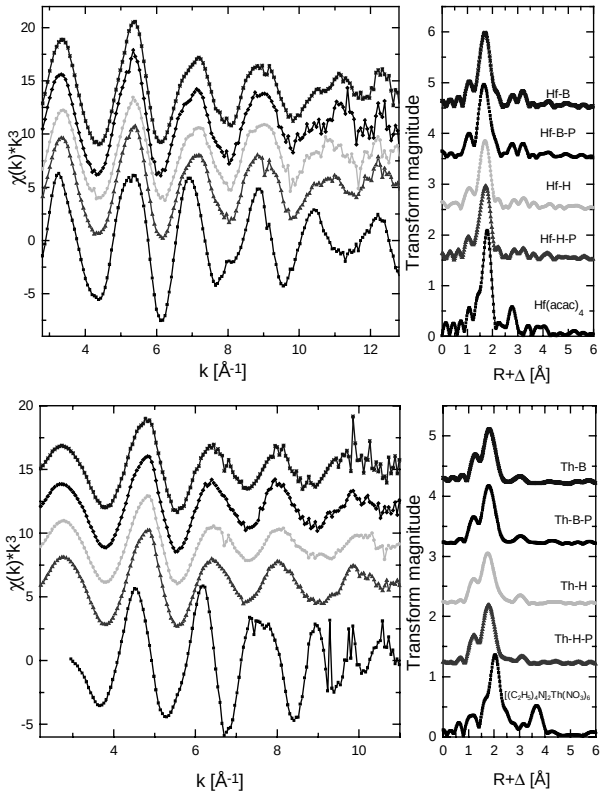

Table 1. Fit results to Fourier-filtered first oxygen shell Hf (top) and Th (bottom) L3 edge EXAFS. ΔE_0 was held constant at 8 eV for the Hf sorption samples and at 1 eV for the Th sorption samples.

Sample	**Hf-HA**	**Hf-HA paste**	**Hf-Bio-Rex70**	**Hf-Bio-Rex70 paste**	**$Hf(acac)_4$**
N	5.8	6.7	7.3	7.4	8.1 (8)*
R [Å]	2.13	2.14	2.14	2.15	2.18 (2.199)*
σ^2 [Å^2]	0.007	0.007	0.009	0.009	0.006
Sample	**Th-HA**	**Th-H paste**	**Th-Bio-Rex70**	**Th-Bio-Rex70 paste**	**$[(C_2H_5)_4N]_2Th(NO_3)_6$**
N	9.9	10.1	9.4	9.4	12.1 (12)*
R [Å]	2.43	2.43	2.44	2.44	2.57 (2.565)*
σ^2 [Å^2]	0.015	0.013	0.013	0.012	0.007

* Values in parentheses are those calculated from the XRD crystal structure determination by for $Hf(acac)_4$ [10] and for $[(C_2H_5)_4N]_2Th(NO_3)_6$ [11].

Results from IR and XPS investigations of the same samples corroborate these conclusions. Observed changes in IR spectra of the HA before and after treatment with Hf(IV) involve bands associated with vibrations of carboxylate groups. XPS measurements in vacuum are considered feasible because EXAFS results are essentially the same for wet paste and dried samples. The XPS results show that *4f*-binding energies for Hf(IV) or Th(IV) sorbed onto HA are identical to that for the corresponding Bio-Rex70 sample. In addition, the $4f_{7/2}$ and $4f_{5/2}$ lines for both HA and Bio-Rex70 sorption samples can be fit with single curves, pointing to a single type of interaction. This information confirms that Hf(IV) and Th(IV) are sorbed primarily onto HA carboxylate groups; other HA functional groups play, at most, a secondary role in metal cation sorption.

Np L3 edge EXAFS studies on Np(V) complexed with HA

Previous investigations using optical spectroscopy on NpO_2^+ humates show changes in Np speciation in samples at pH = 7 compared to samples at pH = 9 [14]. This is associated with a near four-fold increase in the loading capacity (LC) of the HA. The increase is larger than the linear increase in LC with pH observed for other cations [15]. At pH = 9 for Np(V) concentrations used in [14], NpO_2^+ is known to be partially hydrolysed and spectroscopic results are interpreted as a formation of a mixed hydrolysed NpO_2^+ hydroxo-humate colloid complex, $(NpO_2(OH)HA)_{colloid}$. Thus, EXAFS investigations are performed on the Np L3 absorption edge of aqueous solutions of Np(V) and HA at pH = 7 and 9 in order to elucidate Np(V)-HA structural changes associated with the observed speciation change going from pH = 7 to 9.

The samples are made from 2 mL of two HA (purified Aldrich) stock solutions, both with concentrations near 10 g HA/L but different pH (~7 and 9), and 60 µL 36 mM Np(V) stock solution in 1 M $HClO_4$. Samples are prepared in a N_2-purged box. The pH is readjusted following addition of the Np(V) by adding 20 µL 1 M NaOH and then 40 µL or 60 µL 0.2 M NaOH to obtain a pH of 6.99 or 9.04, respectively. Based on published values for the HA PEC (5.43 mEq/L [7]), log β (3.58 [14]), and loading capacity (13% at pH = 7 and 43% at pH = 9 [14]), the amount of Np(V) and HA in the samples provides 25 and 93 times more complexed Np(V)-HA than free Np(V) in solution at pH = 7 and pH = 9, respectively. The optical absorption spectra of the Np(V)-HA solutions show an absorption maximum at 990 nm for the pH = 7 sample and 992 nm for the pH = 9 sample; no absorption peak for free Np(V) aquo species at 980 nm is observed. Aliquots of these solutions are placed in 5 mm × 10 mm Plexiglas cuvettes for the EXAFS measurements. The solutions are contained within the cuvette by a plastic plug insert, which is sealed with two layers of epoxy, having absorbent sandwiched between them, and covering with another plastic stopper. The cuvettes are mounted in the Argonne Actinide Facility multiple sample changer [16] so that a 10 mm path is directed towards the incident beam.

XAFS measurements are performed at the Advanced Photon Source (APS), BESSRC beam line 12BM, using a Si(111) double-crystal monochromator. The 12BM beam line is equipped with a collimating and focusing mirror. The beam spot used is 0.5 mm^2. The incident beam is free of higher harmonic reflections, as is shown by the absence of the corresponding inelastic scattering peaks recorded with an energy dispersive detector. The spectra are calibrated by defining the first inflection point of the first derivative XANES spectrum of a Zr foil as 17 998 eV, which is recorded at the beginning of the XAFS measurements and again at the end. The energy shift between both measurements is less than the smallest step size in the spectra recorded, 0.5 eV. Spectra are collected in both transmission mode and fluorescence mode. Data reduction and analysis is performed using the WinXAS program [17]. The single scattering backscattering amplitude and phase-shift functions used in the analysis are calculated with the theoretical EXAFS modelling code FEFF8 [18]. E_0 is defined as 17 613 eV for both spectra.

The k^3-weighted Np L3 edge transmission EXAFS spectra of both Np(V) humate samples is depicted in Figure 2. There is little difference between the oscillatory pattern exhibited by the two samples. The Fourier filtered nearest-neighbour oxygen co-ordination shells for the pH = 7 sample fluorescence spectrum is fit to the EXAFS equation using a model with two oxygen co-ordination shells. The structural metrical parameters for the oxygen atoms belonging to the trans-dioxo neptunyl moiety are $N_{ax} = 2$ (held constant during the fit procedure), $R_{ax} = 1.83$ Å and $\sigma^2_{ax} = 0.001$ Å^2. Parameters for the equatorial oxygen atoms are $N_{eq} = 5.3$, $R_{eq} = 2.47$ Å and $\sigma^2_{eq} = 0.006$ Å^2. ΔE_0 is set as a global parameter for both shells and 13.8 eV is obtained in the fit. The ΔR value calculated from the beat-node [19] located at k = 7.38 Å^{-1} in the oscillatory pattern of the Fourier filtered data yields $\Delta R_{(beat\text{-}node)} = 0.639$ Å. This is in agreement with the difference between R_{ax} and R_{eq} obtained in the fit: $\Delta R_{(fit)} = 0.64$ Å. The Np(V) humate average equatorial oxygen bond length is somewhat shorter than that observed for the Np(V) aquo species: 2.47 Å versus 2.50 Å [20], respectively. This slight shortening of the average equatorial bond lengths is similar to the trend observed for U(VI). A decrease from 2.42 Å in the U(VI) aquo species [21] to $R_{eq} = 2.38$ Å following U(VI) complexation to humic acid [4] is observed.

Figure 2. Right: k^3-weighted Np L3 edge EXAFS for Np(V):HA at pH = 7 and pH = 9 (above) and their difference spectrum (below). Left: the corresponding FT of the EXAFS at right. FT range = 3.6-14.3 Å, using a Bessel window.

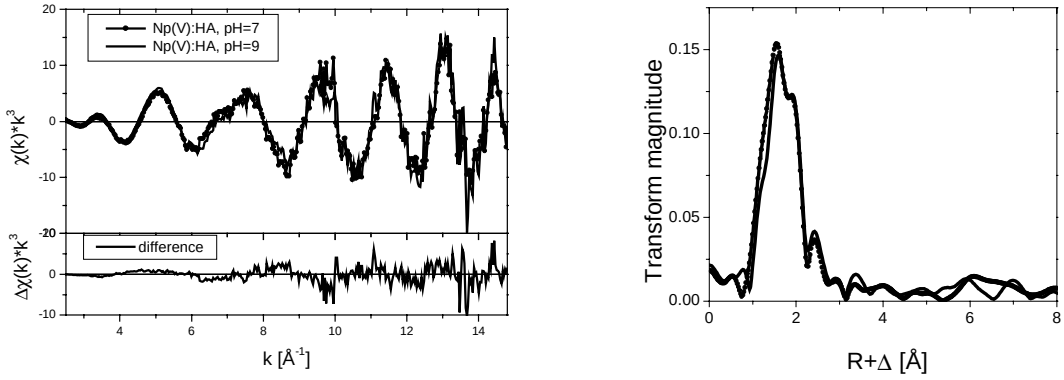

Because the two spectra are very similar, their difference spectrum is calculated in order to ascertain any change in structure between the Np(V) humate sample at pH = 7 and pH = 9. The difference spectrum shown in Figure 2 is not simply a residual but exhibits an oscillatory pattern, indicative of an associated backscattering co-ordination shell. The Fourier transform of the difference spectrum shows a peak intensity near 3.7 Å. This peak is isolated by backtransforming it to k-space. The filtered oscillation is then fit to the EXAFS equation. The phase and amplitude of this oscillation can be modelled using a Np-Np interaction. The result is shown in Figure 3. The structural parameters for this Np-Np interaction are $N_{Np} = 0.96$, $R_{Np} = 3.84$ Å, and $\sigma^2_{Np} = 0.0024$ Å^2. Attempts to model this peak with other nearest neighbour distances feasibly present at distances ~4 Å, such as a distal oxygen belonging to a co-ordinating carbonate ligand, are unsuccessful.

The EXAFS results do not explicitly substantiate the formation of a hydrolysed mixed colloid complex $(NpO_2(OH)HA)_{colloid}$ from changes in the Np-O co-ordination that might indicate co-ordination of a OH ligand. The structural difference between the Np(V) humate species at pH = 7 and pH = 9 is the presence of a single Np-Np interaction at 3.84 Å. The amount of uncomplexed Np(V) in solution for these experiments is very low, so that the Np-Np interaction is not a solution hydrolysis species. The observed anomalous increase in the LC going from pH = 7 to 9 [14,15] may be due to interaction of polynuclear species with the humate.

Figure 3. k^3-weighted filtered EXAFS oscillations extracted from the difference spectrum shown in Figure 2 and the theoretical EXAFS for the Np-Np interaction obtained as fit result

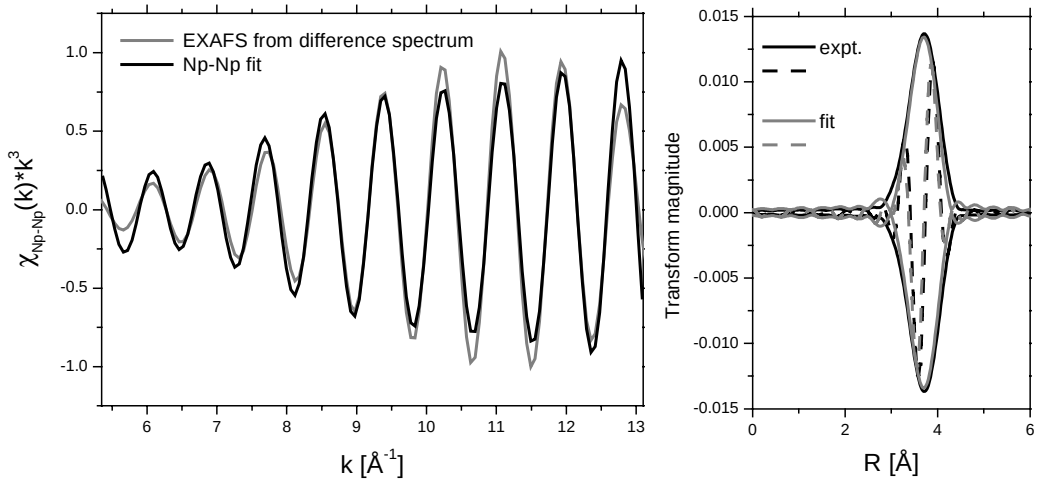

Soft X-ray spectromicroscopy of aquatic HA and clay colloid mixtures

In situ STXM images of aqueous suspensions of mixed mineral-organic colloids are recorded as a function of colloid type. The aim of these experiments is to establish, under defined conditions, whether truly mixed agglomerates form, whether the colloids cluster separately or whether an organic coating on the mineral colloid surfaces occurs. The exact nature of this interaction will effect the colloid's sorption behaviour for actinide ions. Images of aqueous suspensions of HA (0.2 mg/mL, I = 0.1 M NaCl, pH = 4) of mixtures of montmorillonite and HA (0.1 mg HA/mL, 0.21 mg clay/mL, pH = 5.8), as well as montmorillonite mixed with polystyrene (PS) latex particles (0.23 mg PS/mL, 0.21 mg clay/mL, pH = 6.8), which have been chemically modified to have a carboxylated surface, are presented. By comparing micrograph images recorded at photon energies above and below the C *1s* X-ray absorption edge, the organic components can be differentiated from inorganic components. Comparison of the HA C *1s*-NEXAFS spectra, extracted from image stacks recorded while incrementally increasing the photon energy, to that recorded for the reference latex colloids is also made.

Purified Aldrich HA, surfactant-free carboxyl polystyrene latex particles (400±8 nm diameter according to TEM, surface charge content 11.7 μEq/g, Interfacial Dynamics) and the calcium montmorillonite Ibeco, size fractioned by sedimentation [22] (Bentonit Technologie) are the materials used. The polystyrene latex with carboxylated surfaces is chosen as a reference sample because it is a suitable size standard and because the carboxylated surface should chemically mimic HA.

Aqueous colloid suspensions are sandwiched as a few μm thick film, held between Si_3N_4 membranes of 100 nm thickness by capillary forces, using a wet cell assembly to maintain the samples in a hydrated state for several hours [23]. The presence of persisting hydrated conditions in the wet cell throughout the time span of recording image stacks is confirmed by the observation of an edge of the water film after final images are recorded.

STXM investigations are performed at the National Synchrotron Light Source X1A end station, operated by the State University of New York at Stony Brook [24]. A Fresnel zone plate of 160 μm diameter and 45 nm outer ring segment width is used to focus the soft X-rays. The energy of the spherical grating monochromator is calibrated relative to the C *1s*-threshold resonance of CO_2 at

290.74 eV [25]. The C *1s*-NEXAFS spectra are obtained from 62 image stacks recorded between about 275 eV and 310 eV. The energy range is divided into three regions: 275-283 eV in 1 eV steps, 283-290 eV in 0.2 eV steps and 290-309 eV in 1 eV steps. A linear pre-edge background was subtracted from the resulting spectra, followed by normalisation (μ*d = 1) at 300 eV. For a review of the image stack data analysis, see [26].

A STXM image of a large HA agglomerate is shown in Figure 4. The HA macromolecular agglomerates observed in the micrographs exhibit only diffuse contours at dimensions in the μm range. Both globular (spherical-to-elliptical) as well as filament-type particle aggregates were observed. The absorption contrast in the images recorded above and below the C *1s* edge show that these diffuse contoured areas are zones of high carbon concentration and are therefore HA. The HA C *1s*-NEXAFS spectrum extracted from a 1 μm × 4 μm area of high absorption at 290 eV is shown in Figure 5.

Figure 4. STXM image (290 eV) of hydrated HA aggregates at pH = 4

Magnification = 2 800 ×

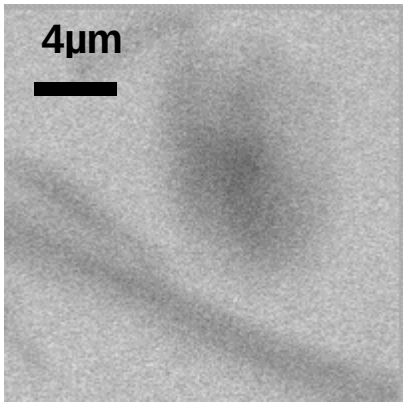

Figure 5. Normalised C *1s*-NEXAFS of carboxylated polystyrene microspheres (top), HA (bottom)

Absorption transitions marked A and B correspond to a 1s→π (C=C) and a 1s→π* (C=O) transition, respectively*

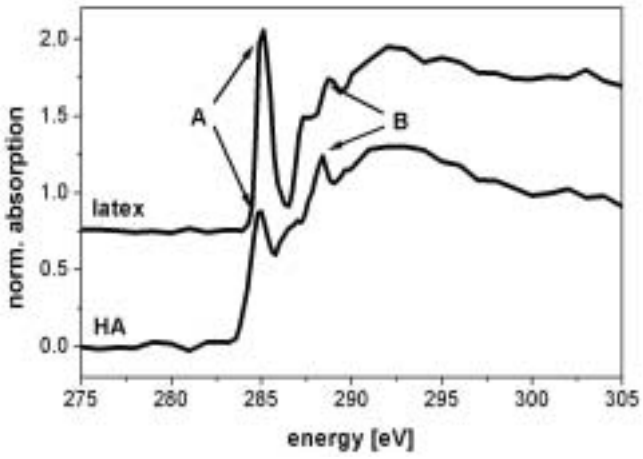

Images at 20×20 µm^2 of montmorillonite + PS suspension are shown in Figure 6 recorded below and above the C K edge. The left image appears to be brighter due to carbon deposits on optical elements such as mirrors and gratings. Clay mineral particles are visible in the left image as dark and diffuse patches due to their unspecific absorption at 281.8 eV. The polystyrene latex microspheres are clearly enhanced in the right image due to their strong C *1s* absorption at 290.7 eV. Comparison of both images shows that the latex spheres tend to cluster near or around clay mineral particles. However, there is no evidence that the presence of the latex spheres influences the structure or the arrangement of the mineral particles. The C *1s*-NEXAFS spectrum extracted from a near 1.5 µm^2 area of clustered PS spheres in an image stack are shown in Figure 5.

Figure 6. STXM images of a montmorillonite + PS suspension measured below (left, 281.8 eV) and above (right, 290.7 eV) the C *1s* edge

Magnification = 2 700 ×

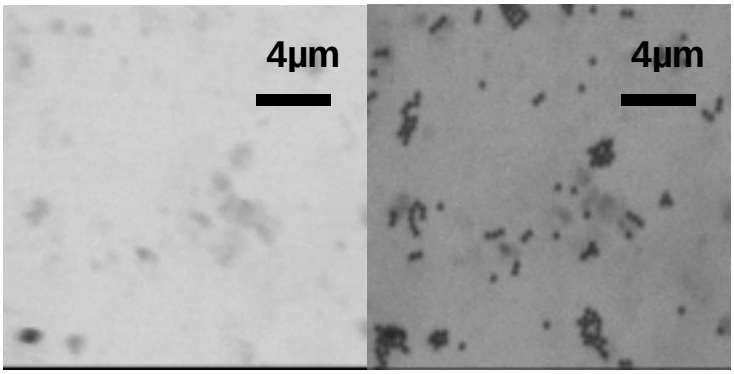

Clustering of HA on or near montmorillonite also occurs in the mixed HA + clay suspensions (Figure 7). However, in this case the diffuse-contoured HA morphology is not observed. STXM images show a specific form of aggregation of the clay particles induced by the presence of HA. Fractal-like structures of colloid aggregates are detected with HA having remarkably sharp contours. This corroborates previous X-ray microscopy results reported by Myneni, *et al*. [2], that the presence of minerals dramatically alters the humic substance macromolecular structure in aqueous solutions.

Figure 7. STXM images of montmorillonite + HA recorded at 275.5 eV (left) and 285.2 eV (right)

Magnification = 1 600 × (top), 300 × (bottom)

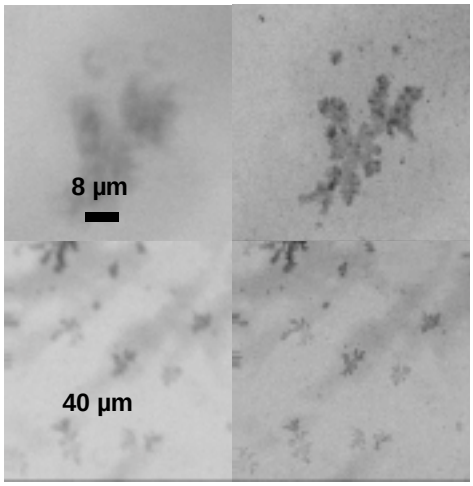

The general similar affinity of both the carboxylated PS particles and the HA colloids for the clay in the organic/inorganic mixed suspensions suggests a similar interaction in both systems. Because the PS surface carboxyl groups are presumed responsible for their affinity for the clay colloids, it is likely that HA carboxyl groups are also responsible for the HA affinity for the clay particles. The different aggregate morphologies for the two mixed colloid suspensions results from the rigidity of the PS microspheres, whereas HA has a dynamic macromolecular conformation allowing it to unfold and spread onto the clay surface.

Conclusions

The EXAFS investigation of the interaction of Hf(IV) and Th(IV) with HA and Bio-Rex70 supports the hypothesis that these metal cations are sorbed primarily onto HA carboxylate functional groups. Similar results are reported for the complexation of U(VI) with HA [4]. This may allow significant simplification of models used to predict radionuclide migration via HA-mediated transport in the hydro and geosphere. Comparison of EXAFS results from Np(V)-HA at pH = 7 with the Np(V) aquo species shows the cation-humate interaction to be similar to that previously reported for the actinyl U(VI) interaction with HA [4]. Polynuclear Np(V) sorption onto HA at pH = 9 is likely the cause for the observed anomalous LC increase at higher pH values for this cation [14,15]. Results from STXM images of mixed organic-inorganic colloids may explain previously reported observations that the presence of HA is found to mask the complexation behaviour of mineral colloids for actinide cations [27,28]. The aggregation of clay and HA, which appear to coat the clay surface, would expectedly exhibit a different sorption behaviour than that for the colloids separately. Furthermore, if conditions are such that the agglomeration/coating is great, then modelling of the actinide cation interaction with the agglomerates in solution may, in some cases, simplify to ascertaining the number of potential complexing surface groups available. By following variations in the HA C *1s*-NEXAFS features upon complexation of actinide cations to HA alone and in mixed colloid systems, it may be possible to identify functional groups responsible for the complexation.

Acknowledgements

HASYLAB, the BESSRC CAT at APS and Professor Dr. C. Jacobsen (NSLS) are gratefully acknowledged for beam time allotment. The Ibeco montmorillonite was kindly provided by Dr. A. Bauer. Use of the infrastructures of the Actinide Facility for synchrotron research in the Chemistry division of Argonne National Laboratory (ANL) is also acknowledged with gratitude. A portion of the work at ANL was supported by the US Department of Energy, Basic Energy Sciences, under contract No. W-31-109-ENG-38.

REFERENCES

[1] J. Rothe, M.A. Denecke, K. Dardenne, *J. Colloid Interface Sci*., 231, 91-97 (2000).

[2] S.C.B. Myneni, J.T. Brown, G.A. Martinez, W. Meyer-Ilse, *Science*, 286, 1335 (1999).

[3] J. Thieme, J. Niemeyer, *Progr. Colloid Polym. Sci*., 111, 193 (1998).

[4] M.A. Denecke, S. Pompe, T. Reich, H. Moll, M. Bubner, K.H. Heise, R. Nicolai, H. Nitsche, *Radiochim. Acta*, 79, 151-159 (1997).

[5] S. Pompe, M. Bubner, M.A. Denecke, T. Reich, A. Brachmann, G. Geipel, K.H. Heise, H. Nitsche, *Radiochim. Acta*, 74, 135-140 (1996).

[6] M.A. Denecke, D. Bublitz, J.I. Kim, H. Moll, I. Farkes, *J. Synchrotron Rad*., 6, 394-396 (1999).

[7] J.I. Kim, G. Buckau, G.H. Li, H. Duschner, N. Psarros, *Fresenius J. Anal. Chem*., 338, 245-252 (1990).

[8] G.N. George, I.J. Pickering, "EXAFSPAK: A Suite of Computer Programs for Analysis of X-ray Absorption Spectra", Stanford Synchrotron Radiation Laboratory, Stanford, CA, USA (1995).

[9] S.I. Zabinsky, J.J. Rehr, A. Ankudinov, R.C. Albers, M.J. Eller, *Phys. Rev*., B52, 2995-3009 (1995).

[10] J.V. Silverton, J.L. Hoard, *Inorg. Chem*., 2, 243-249 (1963).

[11] M.R. Spirlet, J. Rebizant, C. Apostolidis, B. Kanellakopulos, E. Dornberger, *Acta Cryst*., C48, 1161-1164 (1992).

[12] "X-ray Absorption: Principles, Applications, Techniques of EXAFS, SEXAFS and XANES", D.C. Koningsberger, R. Prins, eds., John Wiley & Sons, New York (1988).

[13] L.R. Nassimbeni, A.L. Rodgers, J.M. Haigh, *Inorg. Chim. Acta*, 20, 149 (1976).

[14] C. Marquardt, J.I. Kim, *Radiochim. Acta*, 80, 129-137 (1998).

[15] "Effects of Humic Substances on the Migration of Radionuclides: Complexation and Transport of Actinides" (Final Report), EUR Report, G. Buckau, ed., in print.

[16] On the internet page http://chemistry.anl.gov/heavy-element/actinide/multiple.html, the cell is described.

[17] T. Ressler, *J. Physique IV*, 7, C2-269 (1997).

[18] A.L. Ankudinov, B. Ravel, J.J. Rehr and S.D. Conradson, *Phys. Rev*., B58 (12), 7565-7576 (1998).

[19] G. Martens, P. Rabe, N. Schwenter, A. Werner, *Phys. Rev. Lett*., 29, 1411-1414 (1977).

[20] P.G. Allen, J.J. Bucher, D.K. Shuh, N.M. Edelstein, T. Reich, *Inorg. Chem*., 36, 4676-4683 (1997).

[21] H.A. Thompson, G.E. Brown, G.A. Parks, *Amer. Mineral*., 82, 483-496 (1997).

[22] A. Bauer, G. Berger, *Applied Geochemistry*, 13, 905-916 (1998). A. Bauer, B. Velde, *Clay Miner*., 34, 259-276 (1999).

[23] U. Neuhäusler, S. Abend, C. Jacobsen, G. Lagaly, *Colloid Polym. Sci*., 277, 719 (1999).

[24] C. Jacobsen, S. Williams, E. Anderson, M.T. Browne, C.J. Buckley, D. Kern, J. Kirz, M. Rivers, X. Zhang, *Opt. Commun*., 86, 351 (1991).

[25] A.P. Hitchcock, D.C. Mancini, *J. Electron Spectroscopy*, 67, 1 (1994).

[26] Stack software manual in http://xray1.physics.sunysb.edu/~jacobsen/stack/ stack.html.

[27] T. Zuyi, C. Taiwei, D. Jinzhou, D. Xiong Xin, G. Yingjie, *Applied Geochemistry*, 15, 133 (2000).

[28] Th. Rabung, “Einfluss von Huminstoffen auf die Europium(III)-Sorption an Hämatit”, Doctoral Thesis, Universität Saarbrücken (1998).

EXAFS STUDY OF U(VI) COMPOUNDS: A NEW APPROACH TO DATA ANALYSIS

Yu.A. Babanov,[1,2] **T.Ye. Zayarnaya**[1]
[1]Institute of Metal Physics
GSP-170, Ekaterinburg, 620219, Russia
[2]Udmurt State University, Izhevsk, Russia
Babanov@imp.uran.ru

T. Reich, H. Funke
Forschungszentrum Rossendorf e.V., Institute of Radiochemistry
P.O. Box 510119, D-01314
Dresden, Germany

Abstract

The regularisation method is applied to determine three partial pair correlation functions (PCFs) from one EXAFS spectrum. The mathematical procedure is discussed and applied to the EXAFS analysis of $UO_2(HAsO_4) \times 4H_2O$.

The measurements were performed at the Rossendorf Beamline (ROBL) at the ESRF in Grenoble. The As K edge and the U L3–edge absorption spectra were recorded in transmission mode at temperatures of 41 K and 15 K, respectively. From the U L3-edge EXAFS spectrum, we obtain the PCFs of the pairs U-U, U-As and U-O and determine the structural parameters for the first and the second co-ordination shells of each pair. The PCFs of the pairs As-U, As-As and As-O are obtained from the As K-edge EXAFS spectrum.

Introduction

The extended X-ray absorption fine structure (EXAFS) technique is a very powerful tool for the structure determination in a wide range of materials [1]. In general, for simple systems, the Fourier transformation methods, ratio-cumulant method and non-linear least-square fitting are used.

The Fourier transformation method is a non-inverse procedure for the integral equation describing EXAFS data. Firstly, the kernel of this equation is not a simple sin-function but a more complex function. Secondly, the integration in k space is limited at both sides: at high k the limit is given by the decreasing amplitude of oscillations with increasing k, at low k the single-scattering approximation, which is only taken into account in the integral EXAFS equation, is not valid. Formally, the integral EXAFS equation after the Fourier transformation reduces to an equivalent equation in r space, which is necessary to solve. Least-square fitting is a very unstable method. There exists an infinite amount of solutions for one set of experimental data.

The regularisation method of the numerical solution of the Fredholm integral equation of the first kind has been shown to be an attractive method to solve ill-posed problems [2]. Nearly two decades ago, it was suggested to apply this method to EXAFS data analysis [3,4]. Up to now, this technique has only been applied to experimental data of one-component and binary systems.

In this paper we use the regularisation method to study multi-component systems. We determine three pair correlation functions (PCFs) using only one experimental spectrum.

Regularisation algorithm for determining the partial pair correlation functions

If the system consists of n elements, then $N = n(n + 1)/2$ partial pair correlation functions $g_{ij}(r)$ are needed to describe the atomic structure, where $g_{ij}(r)$ is the density of the probability to find a pair of atoms i and j at an interatomic distance r.

The EXAFS integral equation in single-scattering approximation is written as [3]:

$$k\chi_i(k) = 4\pi\rho_0 \sum_{j=1}^{n} c_j \int_0^{\infty} f_j(k,r) e^{-\frac{2r}{\lambda_i(k)}} \sin\left(2kr + \psi_{ij}(k,r)\right) g_{ij}(r) dr \qquad (1)$$

where $\chi_i(k)$ is the normalised oscillating part of the X-ray absorption spectrum, ρ_0 is the atomic density of the compound, c_j is the concentration of atoms j, $f_j(k,r)$ is the backscattering amplitude of the neighbouring atom j, $\psi_{ij}(k,r) = (2\delta_i(k) + \varphi_j(k,r) + \pi)$ is the total phase shift, $\delta_i(k)$ is the phase shift on the central atom i, $\varphi_j(k,r)$ is the phase shift on the neighbouring atom j and $\lambda_i(k)$ is the mean free path of the photoelectron. The functions $f_j(k,r)$, $\psi_{ij}(k,r)$ and $\lambda_i(k)$ are obtained from curved wave approximation calculations with the program FEFF-8 for the crystalline reference sample [5]. We consider the experimental data for the U L3-edge and the As K-edge absorption spectra of $UO_2(HAsO_4) \times 4H_2O$ compound (i = U, As) and neglect the contributions of U-H, As-H pairs (j = U, As, O).

We take into account that the solution:

$$g_{ij}(r) = 0 \text{ at } r \le a_j \qquad (2)$$
$$g_{ij}(r) = 1 \text{ at } r \le b_j$$

where $a_j = r_i + r_j$ is the sum of neighbouring atoms radii and $b_j >> a_j$, and rewrite the integral EXAFS Eq. (1) in a symbolic form:

$$u_i = \sum_{j=1}^{n} A_{ij}\ g_{ij} \tag{3}$$

Here:

$$u_i(k) = \frac{k\chi_i(k)}{f_0(k)} - t_i(k) \tag{4}$$

and:

$$t_i(k) = 4\pi\rho_0 \sum_{j=1}^{n} c_j \int_b^{\infty} \frac{f_j(k,r)}{f_0(k)} \exp\left(-\frac{2r}{\lambda_i(k)}\right) \sin\left(2kr + \psi_{ij}(k,r)\right) dr \tag{5}$$

$$f_0(k) = \sum_{j=1}^{n} c_j\, f_j(k,b_j) \tag{6}$$

$f_0(k)$ is the average backscattering amplitude on the neighbouring atoms j.

The integral operator A_{ij} is defined as:

$$A_{ij}\, g_{ij} = 4\pi\rho_0 c_j \int_{a_j}^{b_j} \frac{f_j(k,r)}{f_0(k)} \exp\left(-\frac{2r}{\lambda_i(k)}\right) \sin\left(2kr + \psi_{ij}(k,r)\right) g_{ij}(r)\, dr \tag{7}$$

After discrete approximation of the integral operator, the matrix A_{ij} is ill conditioned and has an infinite number of solutions. The proposed algorithm allows to narrow the class of possible solutions and to take into account *a priori* physical information about the solution:

1. The solution $\sum_j g_{ij}(r)$ must be such that when it is acted upon by the matrix of the integral operators A_{ij}, the residual norm should not exceed the error in the experimental data δ_i. This requirement is the main criterion to choose the approximate solution by the least-squares method.

$$\left\| \left(A_{ij}\, g_{ij} - u_i\right) \right\|_{L_2[c_i,d_i]} = \left\{ \int_{c_i}^{d_i} \sum_{j=1}^{n} \left| A_{ij}\, g_{ij} - u_i \right|^2 dk \right\}^{\frac{1}{2}} \quad \leq \quad \delta_i \tag{8}$$

   where c_i, d_i are the boundaries of experimental data set in k-space.

2. The solution $\sum_j g_{ij}(r)$ and its first derivative should be smooth.

3. The solution $\sum_j g_{ij}(r)$ should be positive at any r.

Let us single out three steps in the construction of regularisation algorithm.

Regularisation

As a regular approximate solution, we take the vector $\sum_j g_{ij}$, which minimises in space L_2 the Tikhonov functional:

$$\min M[g_{ij}] = \min\left\{ \left\| \sum_{j=1}^{n} (A_{ij} g_{ij} - u_i) \right\|^2 + \sum_{j=1}^{n} \left(\alpha_j \|g_{ij}\|^2 + \beta_j \left\| \frac{d}{dr} g_{ij} \right\|^2 \right) \right\}, \; g_{ij}(r) \in L_2[a_j, b_j] \tag{9}$$

The first term of Eq. (9) is the first physical requirement stated as Eq. (8). The presence of terms with small positive regularisation parameters α_j, β_j in the functional renders the problem stable and assures that the function $\sum_j g_{ij}$ and its first derivative are smooth.

Discrete approximation

To solve Eq. (9) numerically, the equation should be rewritten in discrete form. Approximating the space L_2 by the discrete space l_2 and prescribing in space l_2 the functions $g_{ij}(r)$, $u_i(k)$ as vectors and prescribing the integral operators $A_{ij}(k,r)$ as matrix, we receive the discrete analogue of Eq. (9). Using the fulfilment of the extremum condition (min M = 0), i.e. one finds a first variation derivative of the functional M with respect to the PCF g and sets it equal to zero, we obtain the system of linear algebraic equations:

$$\sum_{k=1}^{n} \left(A_{ij}^{*} A_{ik} + B_j \delta_{kj} \delta_{ij} \right) g_{jk} = A_{ij}^{*} u_i \qquad (j = 1,2,\ldots n) \tag{10}$$

Here B_j is the regularisation matrix:

$$B_j = \begin{vmatrix} \alpha_j + 2\beta_j & -\beta_j & 0 & \ldots & 0 \\ -\beta_j & \alpha_j + 2\beta_j & -\beta_j & \ldots & 0 \\ 0 & -\beta_j & \alpha_j + 2\beta_j & \ldots & 0 \\ \ldots & \ldots & \ldots & \ldots & \ldots \\ 0 & 0 & 0 & \ldots & \alpha_j + 2\beta_j \end{vmatrix} \tag{11}$$

In case of $UO_2(HAsO_4) \times 4H_2O$ compound for the U L3-edge let us rewrite Eq. (10): n = 3 and U, As, O correspond to 1,2,3, respectively, i.e. i = 1, j = 1,2,3.

$$\left\{\begin{vmatrix} A_{11}^{*}A_{11} & A_{11}^{*}A_{12} & A_{11}^{*}A_{13} \\ A_{12}^{*}A_{11} & A_{12}^{*}A_{12} & A_{12}^{*}A_{13} \\ A_{13}^{*}A_{11} & A_{13}^{*}A_{12} & A_{13}^{*}A_{13} \end{vmatrix} + \|B\|\right\} \times \begin{vmatrix} g_{11} \\ g_{12} \\ g_{13} \end{vmatrix} = \begin{vmatrix} A_{11}^{*}u_1 \\ A_{12}^{*}u_1 \\ A_{13}^{*}u_1 \end{vmatrix} \tag{12}$$

or in symbolic form:

$$(A^{*}A+B)g = A^{*}u \tag{13}$$

The eigenvalues of the regularised matrix ($A^*A + B$) are positive. In this case it is possible to use the well-known linear algebra methods to obtain a solution for Eq. (13). The inversion of the regularised matrix results in the so-called Tikhonov solution:

$$g_0 = (A^{*}A+B)^{-1}A^{*}u \tag{14}$$

Since the matrix ($A^*A + B$) is close to A^*A, it is obvious that for the exact Eq. (1) the Tikhonov solution is an approximate solution, which is stable and unique. It will serve as the starting solution for the following iteration procedure.

Iterational refinement

Let us consider the equation:

$$(A^{*}A+B)g_m = A^{*}u + Bg_m \tag{15}$$

which is equivalent to the exact Eq. (1). The number of the iteration is m. Assuming that the magnitudes of the elements of the regularisation matrix B are small compared with the elements of A, in a first approximation step the term Bg_m on the right side of Eq. (15) will be neglected. So, the Eq. (15) reduces to (13) with the known solution g_0.

The next steps to obtain more precise solutions g_m of Eq. (15) are:

$$g_m = (A^{*}A + B)^{-1}(A^{*}u + Bg_{m-1}) \qquad m = 1,2,\ldots, \tag{16}$$

In our case, we obtain the solutions g_m as a sum of peaks with lateral oscillations (see examples in Figures 3 and 4). During the iteration process we consider that two first peaks of the previous solution $g_{m-1}(r)$ can be described and replaced by the Gaussian functions. After substitution $g_{m-1}(r)$ in a new form to the right part of Eq. (16) we solve this equation and obtain a new solution $g_m(r)$. This assumption is valid if we know that our sample has a crystalline form. Thus, *a priori* physical information is introduced in the algorithm to obtain a reliable solution.

The iteration procedure is stopped when we compare the residual norm of each iteration solution $\|g_m\|$ with the previous one $\|g_{m-1}\|$ and obtain the minimum of this difference.

Here the norm of solution in discrete form g_m^p is:

$$\|g_m\| = \sqrt{\sum_p |g_m^p|^2} \tag{17}$$

The following main characteristics of the peak for the functions $g_{m-1}(r)$ have been selected: interatomic distances, the nearest neighbours co-ordination numbers and Debye-Waller (DW) factors. We estimated these values according to the Gauss functions describing the peaks of the solution.

Experimental

To be able to evaluate the results of our method, we chose a well-defined reference compound, $UO_2(HAsO_4) \times 4H_2O$ for the EXAFS analysis. The room temperature structure of this compound was determined by powder neutron diffraction using $UO_2(DAsO_4) \times 4D_2O$ [5]. Synthetic crystalline $UO_2(HAsO_4) \times 4H_2O$ was ground, mixed with an inert material and pressed into 13 mm diameter pellets. For the As K-edge and the U L3-edge measurements, the inert material was boron nitride and Teflon, respectively. The As K-edge and the U L3-edge EXAFS spectra were collected in transmission mode at sample temperatures of 41 K and 15 K, respectively, using a closed-cycle He cryostat. The measurements were performed at the Rossendorf Beamline (ROBL) at the European Synchrotron Radiation Facility (ESRF) using a Si(111) double-crystal monochromator in fixed-exit mode [6]. Harmonic suppression better than 8×10^{-4} was achieved by two Pt coated mirrors with a cut-off energy of 35 keV. In addition, the background absorption in the As K-edge spectrum was determined by measuring the absorption spectrum without any sample in the cryostat. For the U L3-edge spectrum, a Teflon pellet was used to measure the background absorption. The photon energy was calibrated using the L3-edge and K-edge energies of Au and Y foils at 11 919 eV and 17 038 eV, respectively.

The theoretical parameters, $f_j(k,r)$, $\delta_i(k)$, $\varphi_j(k,r)$ and $\lambda_i(k)$ were calculated with the software FEFF-8 [7] using the structural parameters of $UO_2(DAsO_4) \times 4D_2O$. For the U L3-edge the size of the cluster containing 717 atoms was 12.0 Å. For the As K edge the size of the cluster containing 699 atoms was 11.6 Å. The program FEFF-8 was also used to calculate the normalised oscillating parts $\chi_U(k)$ and$\chi_{As}(k)$ in single-scattering (SS) and multi-scattering (MS) approximations. For the MS calculation, all scattering paths with up to four legs were considered.

To compare the solution of the ill-posed problem, we calculated the partial PCFs, using the atomic co-ordinates obtained by ATOMS (subroutine of the FEFF-8 package) for the known structure of $UO_2(DAsO_4) \times 4D_2O$. The DW factor was arbitrarily set to $\sigma^2 = 0.003$ Å^2 for all elements.

For the transformation of the photon energy, E, into k, we used the following dispersion law: $E = ak^2 + bk + c$. The parameters a, b and c were determined by a least-square fit of the energy of several extrema in the EXAFS region of the experimental spectrum in E space to the corresponding k values of the theoretical $\chi_i(k)$. For the U L3-edge (As K edge) the obtained parameters are a = 3.82 (3.66), b = -0.16 (2.90), and c = 17 179 (11 856). This procedure ensures that the ionisation potential for the experimental $\chi_i(k)$ is the same as that calculated by FEFF-8.

Results and discussion

Figure 1 compares the theoretical normalised oscillating $\chi_U(k)$ calculated in SS approximation with that obtained in MS approximation. Although the two curves show some differences at low k values, the contribution of MS effects is rather small and should be negligible at least for the first uranium neighbours. As can be seen from Figure 2, the theoretical $\chi_U(k)$ in MS approximation reproduces the main features of the experimental data well. This confirms the correctness of our conversion from photon energy into k space. Small deviations between the two spectra are mainly due to differences in the DW factors.

The partial PCFs for the pairs U-U, U-As and U-O were obtained from the experimental $\chi_U(k)$ and are compared to the corresponding model functions in Figure 3. As one can see, the positions of the first two peaks of each pair agree well with the expected positions. However, there is a distinct shift for the U-U_2 peak in r space toward larger values. The differences in peak heights are due to the assumed DW factors for the model function.

The comparison of the experimental and the model partial PCFs As-U, As-As and As-O are given in Figure 4. Except for the second shell of the As-As pair, the experimental peak positions coincide with those of the model functions. The As-As_2 peak has a lower r-value than the true position.

For the known crystal structure, it is possible to calculate the MS contributions and eliminate them from the experimental data. By subtracting the MS contribution shown in Figure 1 from the experimental data shown in Figure 2, we obtained new "experimental" data that should contain only SS contributions. In Tables 1-3, we refer to the modified (original) experimental data as Tikhonov SS method (Tikhonov MS method). As one can see from the interatomic distances given in Table 1, after correction for MS effects we obtain good agreement with neutron data [7] not only for the first shell but also for all second shells in all partial PCFs. The co-ordination numbers and DW factors given in Tables 2 and 3 were obtained by fitting a Gaussian line shape to the peaks of the first shell in the partial PCFs. The co-ordination numbers agree well with the expected values. For the U-O PCFs, the co-ordination number of the second shell is also in good agreement with the crystal structure. For the shells U-As and As-U the obtained structural parameters agree with each other and are independent from the central atom (see Tables 1-3).

In conclusion, a new special iterative algorithm was proposed to solve the integral EXAFS Eq. (1), which is an inverse, ill-posed problem. The procedure was applied to the analysis of As K-edge and U L3-edge EXAFS spectra of the ternary system $UO_2(HAsO_4) \times 4H_2O$, for which the crystal structure is known. Three partial PCFs could be determined for each EXAFS spectrum. For the first shells, the interatomic distances and co-ordination numbers agree with the expected values. However, MS effects can cause peaks of the second shell to be shifted relative to the true value. The main advantage of this method compared to other methods for EXAFS analysis is that the presence of a certain co-ordination shell and its interatomic distance can be detected without any structural model. This method has great potential, especially for the EXAFS analysis of systems with closely spaced co-ordination shells of the same or different type of atoms.

Acknowledgements

We thank M. Rutsch for the synthesis of $UO_2(HAsO_4) \times 4H_2O$ and C. Hennig and A. Rossberg for their assistance during the EXAFS measurements at BM20 at the ESRF.

REFERENCES

[1] D.E. Sayers, E.A. Stern, F.W. Lytle, *Phys.Rev.Lett.*, 27, 1204 (1971).

[2] A.N. Tikhonov, V.Ya. Arsenin, “Solution of Ill-posed Problems”, John Wiley and Sons, Inc., New York (1981).

[3] Yu.A. Babanov, V.V. Vasin, A.L. Ageev, N.V. Ershov, *Phys. Stat. Sol. (b)*, 105, 747 (1981).

[4] N.V. Ershov, A.L. Ageev, V.V. Vasin, Yu.A. Babanov, *Phys. Stat. Sol. (b)*, 108, 103 (1981).

[5] A.N. Fitch, L. Bernard, A.T. Howe, A.F. Wright, B.E.F. Fender, *Acta Cryst.*, C39, 159 (1983).

[6] W. Matz, N. Schell, G. Bernhard, F. Prokert, T. Reich, J. Claussner, W. Oehme, R. Schlenk, S. Dienel, H. Funke, F. Eichhorn, M. Betzl, D. Proehl, U. Strauch, G. Huttig, H. Krug, W. Neumann, V. Brendler, P. Reichel, M.A. Denecke, H. Nitsche, *J. Synchrotron Rad.*, 6, 1067 (1999).

[7] A.L. Ankudinov, B. Ravel, J.J. Rehr, S.D. Condradson, *Phys. Rev. B*, 58, 7565 (1998).

Figure 1. Theoretical U L3-edge $\chi(k)$ of $UO_2(HAsO_4) \times 4H_2O$ calculated in single -scattering (SS) approximation (solid line) and multi-scattering (MS) approximation (dashed line). The difference between MS and SS approximations is shown as dotted line.

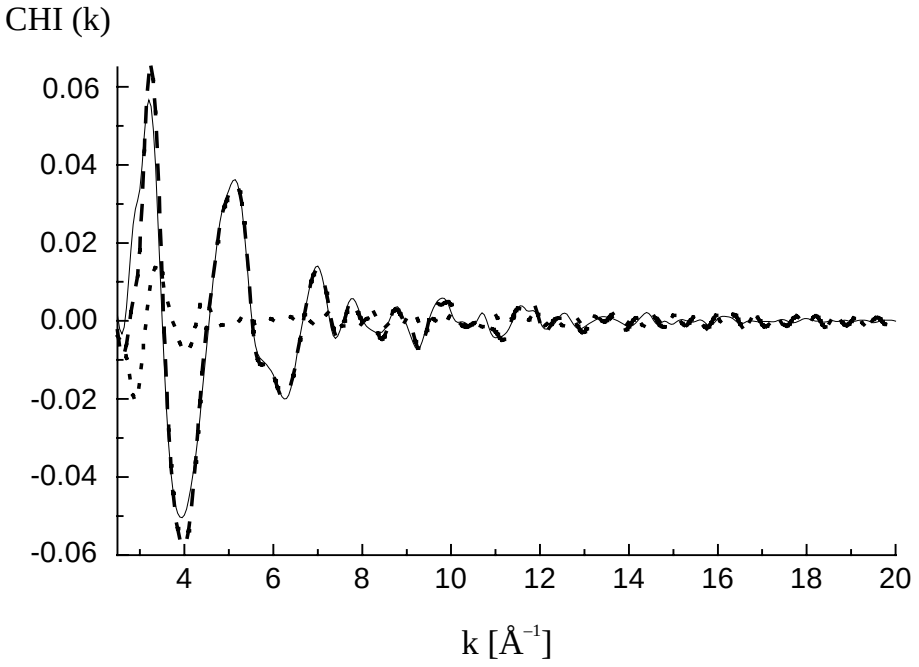

Figure 2. Experimental (solid line) and theoretical U L3-edge $\chi(k)$ (dashed line) of $UO_2(HAsO_4) \times 4H_2O$. The theoretical $\chi(k)$ was calculated in MS approximation.

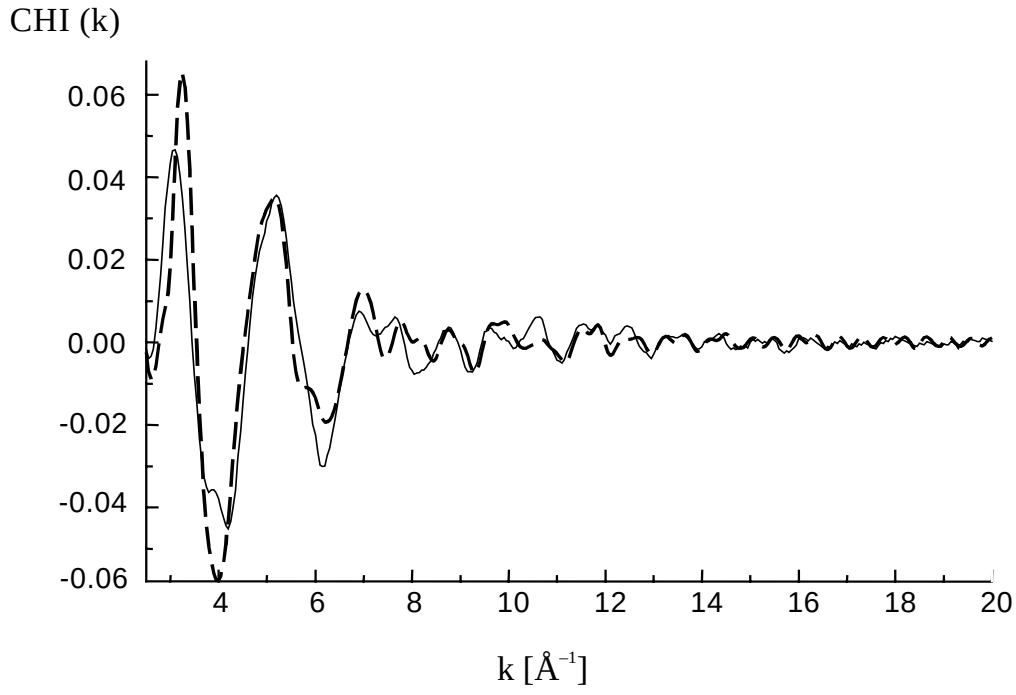

Figure 3. Comparison of experimental partial pair correlation functions (dashed line) and corresponding model functions (solid line) for $UO_2(HAsO_4) \times 4H_2O$. The experimental curve was obtained from U L3-edge $\chi(k)$.

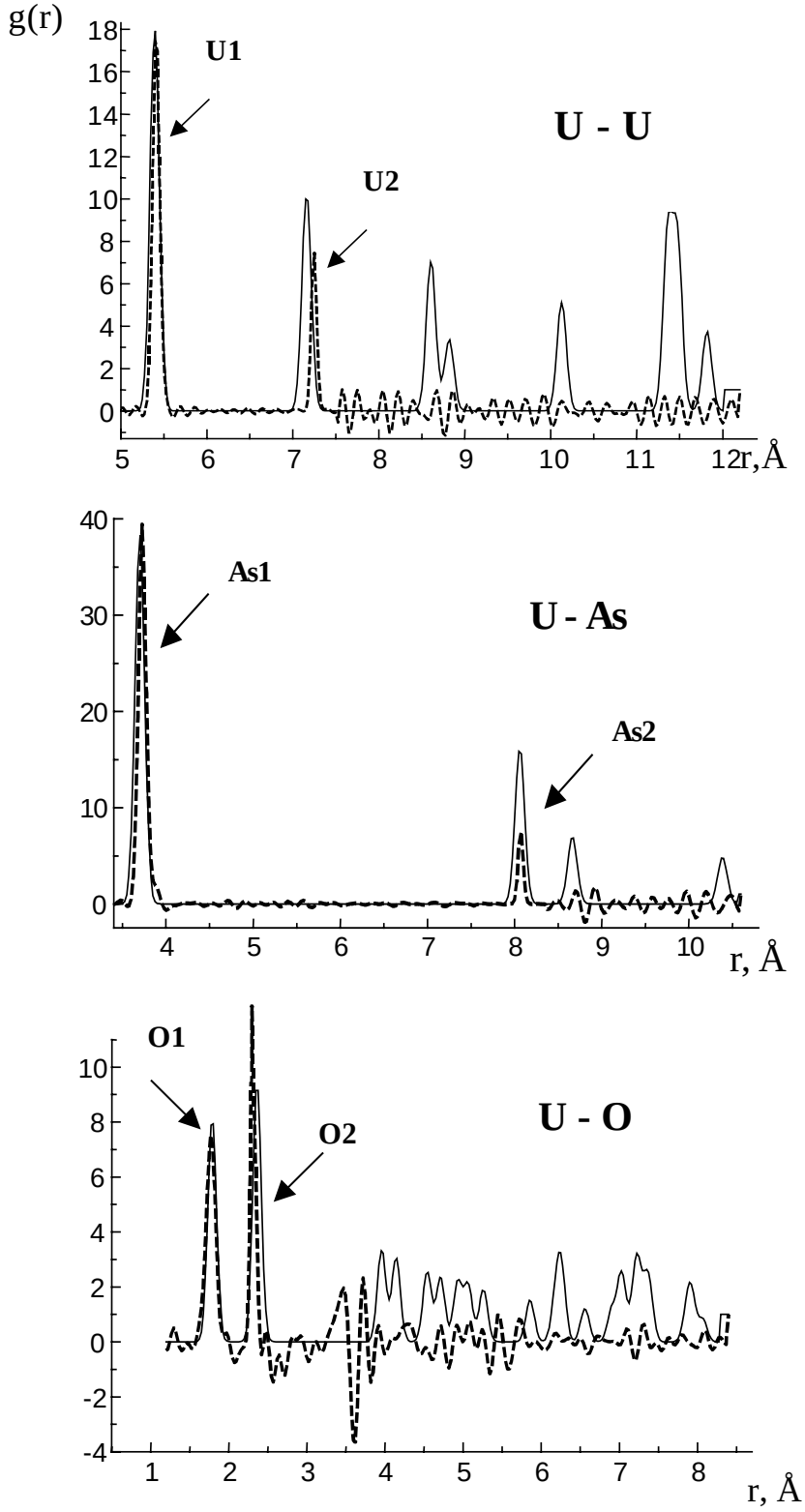

Figure 4. Comparison of experimental partial pair correlation functions (dashed line) and corresponding model functions (solid line) for $UO_2(HAsO_4) \times 4H_2O$. The experimental curve was obtained from As K-edge $\chi(k)$.

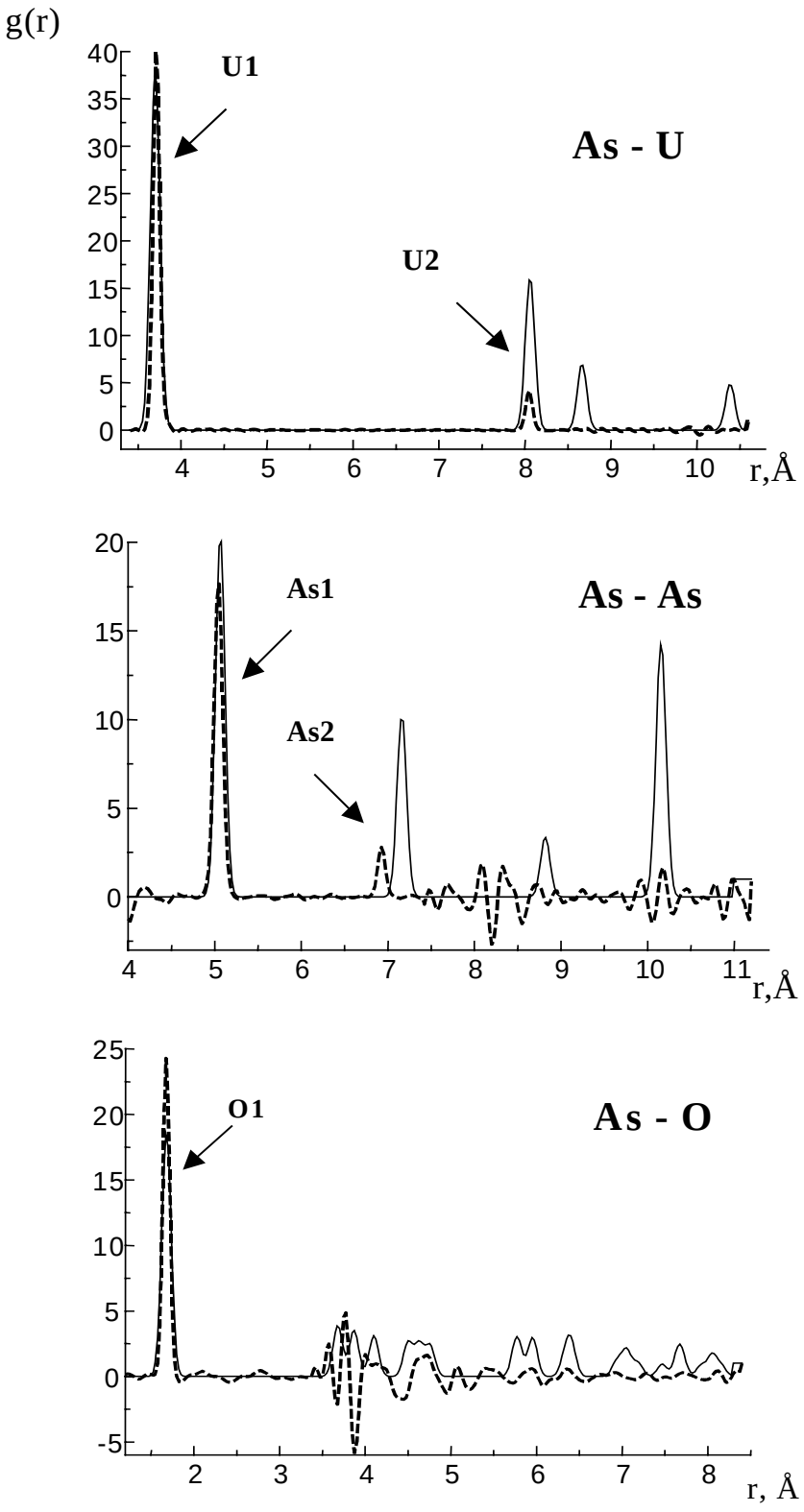

Table 1. Interatomic distances in Å for $UO_2(HAsO_4) \times 4H_2O$ (15 K)

Shell	Tikhonov SS method	Tikhonov MS method	Neutron diffraction
$U\text{-}U_1$	5.42	5.42	5.39
$U\text{-}U_2$	7.16	7.01	7.16
$U\text{-}As_1$	3.73	3.73	3.70
$U\text{-}As_2$	8.08	8.07	8.06
$U\text{-}O_1$	1.77	1.78	1.78-1.79
$U\text{-}O_2$	2.33	2.32	2.30
$As\text{-}U_1$	3.68	3.71	3.70
$As\text{-}U_2$	8.06	8.04	8.06
$As\text{-}As_1$	5.07	5.04	5.06
$As\text{-}As_2$	7.17	6.94	7.16
$As\text{-}O_1$	1.68	1.68	1.68
$As\text{-}O_2$	3.76	3.77	3.68-3.88

Table 2. Co-ordination numbers for $UO_2(HAsO_4) \times 4H_2O$ (15 K)

Shell	Tikhonov SS method	Tikhonov MS method	Neutron diffraction
$U\text{-}U_1$	4.2	4.3	4.0
$U\text{-}As_1$	4.0	3.8	4.0
$U\text{-}O_1$	2.1	2.0	2.0
$U\text{-}O_2$	4.0	3.8	4.0
$As\text{-}U_1$	4.0	3.9	4.0
$As\text{-}As_1$	4.3	4.1	4.0
$As\text{-}O_1$	3.8	3.9	4.0

Table 2. Debye-Waller factors in $Å^2$ for $UO_2(HAsO_4) \times 4H_2O$ (15 K)

Shell	Tikhonov SS method	Tikhonov MS method
$U\text{-}U_1$	0.003	0.004
$U\text{-}As_1$	0.002	0.002
$U\text{-}O_1$	0.004	0.004
$U\text{-}O_2$	0.002	0.002
$As\text{-}U_1$	0.001	0.002
$As\text{-}As_1$	0.002	0.004
$As\text{-}O_1$	0.002	0.002

EVOLUTION OF THE ELECTRONIC AND STRUCTURAL PROPERTIES OF $AnFe(CN)_6 \cdot xH_2O$ (An = Th, U, Np, Pu, Am) COMPOUNDS: AN X-RAY ABSORPTION SPECTROSCOPY STUDY

Isabelle Bonhoure,[1,6] **Christophe Den Auwer,**[1,6] **Christophe Cartier dit Moulin,**[2,6] **Philippe Moisy,**[1] **Jean-Claude Berthet,**[3] **S. Conradson**[5] **and Charles Madic**[4]

[1]CEA Marcoule, DCC/DRRV/SEMP, F-30207 Bagnols-sur-Cèze, France

[2]Laboratoire de Chimie Inorganique et Matériaux Moléculaires, ESA CNRS 7071, Université Pierre et Marie Curie, 4, Place Jussieu, F-75252 Paris Cedex 05, France

[3]CEA Saclay, DSM/DRECAM/SCM, F-91190 Gif-sur-Yvette, France

[4]CEA Saclay, DCC, F-91190 Gif-sur-Yvette, France

[5]Los Alamos National Laboratory

[6]LURE, Centre Universitaire Paris-Sud, Bât. 209 D, BP 34, F-91898 Orsay Cedex, France

Abstract

It is well known that new three-dimensional molecular structures can be obtained through the use of well-characterised building blocks. Such methods have been widely used to obtain pre-organised three-dimensional entities. Among possible building blocks, the hexacyano metallate ions $[M(CN)_6]^{n-}$ are often used to form polymeric inorganic networks such as Prussian Blue $Fe_4[Fe(CN)_6]_3 \cdot 15H_2O$. Recently, the possibility to form $An[M(CN)_6]$ solids has been evidenced [1].

The structural study of $An[M(CN)_6]$ complexes is of great interest, all the more because of their possible applications in nuclear fuel reprocessing. As microcrystalline materials were obtained, X-ray powder diffraction (XPD), infrared (IR) and X-ray absorption (XAS) spectroscopies were of particular help to probe the An and Fe environments. We investigated the long-range order using XRPD. The IR vibration bands of the cyano groups probe the chemical bonds of the carbon and nitrogen atoms in these new materials. XAS provides both information about the electronic structure via X-ray absorption near edge spectroscopy (XANES) and about the local structure around the metals via extended X-ray absorption fine structures spectroscopy (EXAFS). Moreover, the evolution of the properties of these new complexes along the actinide series is an indirect probe of the actinide bonding [2].

REFERENCES

[1] a. Y.M. Kulyako, T.I. Trofimov, D.A. Malikov, I.A. Lebedev and B.F. Myasoedov. *Radiochem.*, 35(4), 399 (1993).

b. Y.M. Kulyako, T.I. Trofimov, D.A. Malikov, I.A. Lebedev and B.F. Myasoedov. *Radiochem.*, 35(5), 549 (1993).

c. Y.M. Kulyako, D.A. Malikov, T.I. Trofimov and B.F. Myasoedov, *Mendeleev Commun.*, 173 (1996).

[2] I. Bonhoure, C. Den Auwer, C. Cartier dit Moulin, P. Moisy, J-C. Berthet and C. Madic, accepted for publication in *Can. J. Chem.* CHEM 00-006-OR.

SR-BASED X-RAY MICROBEAM TECHNIQUES UTILISED FOR SOLID-STATE SPECIATION OF U IN FUEL PARTICLES

B. Salbu,[1] **K. Janssens,**[2] **O.C. Lind,**[1] **A. Simionovici,**[3]
T. Krekling,[1] **M. Drakopoulos,**[3] **I. Snigireva,**[3] **A. Snigirev**[3]
[1]Department of Chemistry and Biotechnology, Agricultural University of Norway, Aas, Norway
[2]Department of Chemistry, University of Antwerp, Antwerp, Belgium
[3]European Synchrotron Radiation Facility, Grenoble, France

Abstract

To assess the impact of radioactive particle contamination of different ecosystems, information on particle characteristics such as structure and oxidation states of matrix elements influencing weathering and mobilisation of associated radionuclides is essential. In the present work, gamma measurements have been combined with different solid-state speciation techniques, i.e. scanning electron microscopy (SEM) and different synchrotron radiation (SR) based X-ray microbeam techniques to characterise the structures and oxidation states of uranium in fuel (UO_2) particles released from the Chernobyl reactor [1]. During the initial explosion mechanical destruction of fuel occurred and released fuel particles were characterised as inert U, probably reduced U, with low weathering rates. Particles released during the subsequent reactor core fire contained oxidised U and the weathering rates were high. Thus, SR based μ-XAS tomography and μ-XANES proved to be highly useful techniques for characterising radioactive particles and the results obtained are essential for the impact assessments of particle-associated radionuclides.

Introduction

Following nuclear events such as nuclear weapons tests, nuclear accidents and effluent discharges from nuclear installations, a major fraction of refractory radionuclides released to the environment is associated with radioactive particles [2-7]. With time, particle weathering occurs and mobilised radionuclides are subjected to biological uptake and ecosystem transfer. Information on source-dependent and release-related particle characteristics and weathering rates is therefore essential to assess long-term impacts for areas contaminated by radioactive particles. During the Chernobyl accident about 6-8 tonnes of uranium fuel were released [2] and fuel particles were identified up to 2 000 km from the site (e.g. Norway). During the initial explosion mechanical destruction of fuel occurred and fuel particles were deposited to the west of the reactor. During the subsequent reactor core fire, however, fuel particles deposited to the north. Thus, the particles deposited after the Chernobyl accident originated from the same reactor core, but were released under different temperature, pressure and oxic/anoxic conditions which should be expected to influence the structure and oxidation states.

Experimental methods and instrumentation

Sample preparation

Radioactive particles were separated from soil and dust samples collected to the west and north of the Chernobyl reactor in the period 1990-1994. The isolation of individual particles from soil and dust samples is a tedious time-consuming task and the work includes:

- Autoradiography and γ-spectrometry to identify hot spots.
- Isolation of individual particles using light microscopy.
- Mounting of individual particles on stubs, tape or capillary.
- Screening with scanning electron microscopy (SEM) interfaced with an X-ray microanalyser (XRMA).

Using SEM with XRMA, the information obtained on surface structures and elemental distributions in individual particles techniques [8] is essential for further detailed studies using SR-based X-ray microbeam. Furthermore, XRF screening of particles using a second-generation synchrotron radiation source (e.g. HASYLAB, Germany) has proven useful, as subsurface hot spot areas of elements of interest can be identified prior to the application of X-ray microbeam techniques (i.e. μ-XAS tomography, μ-XRD and μ-XANES).

Micro-tomography and micro-imaging

To obtain information on the 3-D distribution of elements in individual particles, μ-XAS tomography was performed at ESRF, beamline ID22**.** Each individual particle was mounted on a glass capillary (Figure 1), which was placed on a micro-tomography stage with 8 degrees of freedom for alignment and rotation. The sample was rotated around a horizontal axis to obtain the highest resolution in the plane of reconstruction. During rotation, images were recorded at 17 keV with a high resolution, cooled CCD-based X-ray detector with a resolution of 0.6 μm [9]. Monochromator tuning allows also the formation of images as a function of incident photon energy to perform XANES imaging (2-D oxidation state mapping) and X-ray absorption near-edge tomography (XANET) [9].

Figure 1. Particle glued on glass capillary

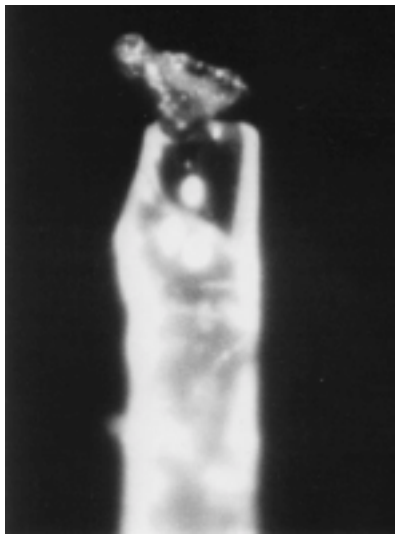

μ-XAS, μ-XRF, μ-XRD and μ-XANES

To obtain information on the composition, crystallographic structure and oxidation states of elements contained in a particle on a submicrometer scale, μ-XAS, μ-XRF, μ-XRD and μ-XANES were combined using hard X-ray microbeams at ID22. X-ray radiation from the undulator (source size 35 μm vertically and 700 μm horizontally) passed through a Si monochromator providing an X-ray beam at selected fundamental energy. The fixed exit double crystal monochromator allowed tuning of the energy over absorption edges, while keeping the beam position on the sample. The monochromatic X-ray beam was focused by a Fresnel Zone Plate to a spot of about 1.5 μm vertically and 5 μm horizontally on a sample at 0.7 m distance. The absolute flux at the beamspot on the sample was 10^9 photons/s at 17 keV. U-particles mounted on carbon tape or on capillaries were placed on the sample stage having three translations and one rotation axis. Long working distance optical microscope and a high resolution X-ray CCD camera were used to position the sample in the focused X-ray beam. To calibrate the results obtained, standards well-defined with respect to crystallographic structures and oxidation states were applied (U_{met}, UO_2, U_3O_8 and $UO_2Ac_2{\cdot}2H_2O$). The absorption spectra (μ XAS, μ XANES) were recorded with pindiodes, while the fluorescence (μ-XRF) spectra were recorded using a Si(Li) energy dispersive detector having an area of 12 mm^2 mounted at 90º to the incident beam and 15 mm from the samples.

In micro-diffraction (μ-XRD) the particles and standards were exposed for 3-10 minutes at different energies between 17 keV and 25 keV. Debye-Scherrer rings were recorded at 200 mm distance from the sample using a Fujitsu image plate (A4 format, resolution of 100×100 μm). The plate was optically scanned with a Molecular Dynamics scanner and processed to yield information on the diameter of the Debye-Scherrer rings. The penetration depth in particles was about 50 μm. Micro-diffraction (μ-XRD) allowed local crystallographic structures to be determined, demonstrating that UO_2 fuel was transformed during the release scenarios.

The μ-XANES spectra of particles and standards were obtained by scanning the X-ray energy over the U L_{III} absorption edge, while measuring the incident and transmitted beam intensity (I_0, I) with pindiodes. By determining the inflection point energy as a function of photon energy for the

standards, a correlation between the inflection point energy and oxidation state was obtained [1]. By performing a μ-XANES line scan, i.e. positioning the X-ray microbeam at various locations along a line through the particle and determining the first inflection point of the local XANES profile, the distribution of the U oxidation state across the particles was attained. The distribution of oxidation states of U within the particles was determined from a series of absorption images covering the particle. In each pixel the oxidation state was determined from the location of the first inflection point.

Results and discussion

Using μ-XAS tomography, information on the 3-D distribution of U in a fuel particle released during fire in the Chernobyl reactor [Figure 2(a)] was obtained. In addition, tomographic reconstruction and computerised slicing of the 3-D image [Figure 2(b)] demonstrated that U was inhomogeneously distributed within the particles. The porosity of the particles was attributed partly to channels and cavities produced during reactor operation by the formation of volatile radionuclides and partly to the fact that U had been oxidised during the release.

Figure 2

(a) μ-XAS tomography of an oxidised fuel particle released during the fire in the Chernobyl reactor.

(b) Computerised slicing of the 3-D image of the oxidised fuel particle.

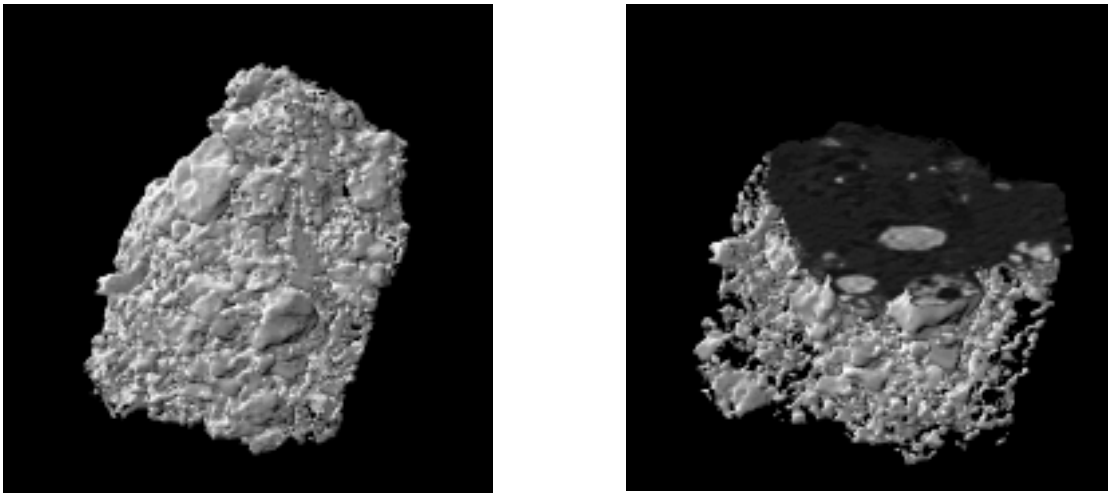

The μ-XRD results demonstrated that U in the UO_2 fuel particles released during the reactor fire (north of the reactor) was oxidised to U_3O_8 and U_2O_5. These findings were further supported by the μ-XANES images, showing a shift in the inflection point energy corresponding to that of the oxidised standards. The 2-D μ-XANES imaging (Figure 3) also demonstrated that the particles released during the fire were characterised by UO_2 cores surrounded by oxidised U (U_2O_5/U_3O_8 layers).

In contrast, the μ-XRD results demonstrated that U in crystalline fuel particles released during the explosion (west of the reactor) probably was reduced, as no sign UO_2 and oxidised forms could be observed. These findings were also supported by the μ-XANES images, showing a shift in the inflection point energy corresponding to oxidation states lower than 4 (UO_2). Thus, the different release conditions influenced the characteristics of fuel particles, originally present as UO_2, emitted from the reactor core.

Figure 3. μ-XANES imaging of a particle collected to the north of the Chernobyl reactor, released during the reactor fire. The particle has a UO_2 core surrounded by an oxidised U_2O_5/U_3O_8 surface layers.

Conclusions

Particle characteristics such as crystallographic structures and oxidation states influence the weathering and mobilisation of radionuclides associated with radioactive particles. As demonstrated in the present work, the crystallographic structures and oxidation states of uranium in fuel particles released from the Chernobyl reactor depended on the release conditions. Particles released during the initial explosion under high-temperature and high-pressure conditions contained reduced U, while particles released during the subsequent fire, lower temperature and aerobic conditions contained oxidised U. Thus, differences in crystallographic structures and oxidation states of uranium in fuel particles explain the observed differences in weathering kinetics, mobility and soil-to-vegetation transfer coefficients of radionuclides associated with particles located west and north of the Chernobyl reactor [10]. The present work also demonstrated that the combination of SR-based X-ray microscopic techniques provides essential solid-state speciation information, i.e. spatial elemental distributions, crystallographic structures and oxidation states influencing the weathering and mobilisation of particle-associated radionuclides, of importance for impact assessments of particle contaminated ecosystems and should be utilised within radioecology.

REFERENCES

[1] B. Salbu, K. Janssens, T. Krekling, A. Simionovici, M. Drakopoulos, C. Raven, I. Snigireva, A. Snigirev, O.C. Lind, D.H. Oughton, F. Adams and V.A. Kashparov, "μ-XAS Tomography and μ-XANES for Characterisation of Fuel Particles", ESRF Highlights 1999, European Synchrotron Research Facility, Grenoble, France (2000).

[2] N.V. Victorova and E.K. Garger, "Biological Monitoring of the Deposition and Transport of Radioactive Aerosol Particles in the Chernobyl NEP Zone of Influence", Proc. CEC seminar on Comparative Assessment of the Environmental Impact of Radionuclides Released During Three Major Nuclear Accidents", Kyshtym, Windscale, Chernobyl, EUR 13574, 223-236 (1990).

[3] M. Cooper, P. Burns, B. Tracy, M. Wilks and G. Williams, "Characterisation of Plutonium Contamination at the Former Nuclear Weapons Testing Range at Maralinga in South Australia", *J. Radioanal. Nucl. Chem*., 177, 161-184 (1994).

[4] P.R. Danesi, *et al*., Proceedings of the 7th Int. Conf. on Low-level Measurements of Actinides and Long-lived Radionuclides in Biological and Environmental Samples, University of Utah, Salt Lake City, September 1998.

[5] L. Devell, M. Tovedal, U. Bergström, A. Applegren, J. Chussler and L. Andersson, "Initial Observations of Fallout from the Reactor Accident of Chernobyl", *Nature*, 321, 817 (1986).

[6] B. Salbu, T. Krekling, D.H. Oughton, G. Östby, V.A. Kashparov, T.L. Brand and J.P. Day, "Hot Particles in Accidental Releases from Chernobyl and Windscale Nuclear Installations", *Analyst*, 119, 125-130 (1994).

[7] B. Salbu, "Actinides Associated with Particles", *J. Environ. Radioact. Booklets*, in press.

[8] B. Salbu, T. Krekling and D.H. Oughton, "Characterisation of Radioactive Particles in the Environment', *Analyst*., 123, p. 843-849 (1998).

[9] A. Koch, C. Raven, P. Spanne and A. Snigirev, "X-ray Imaging with Submicrometer Resolution Employing Transparent Luminescent Screens", *J. Opt. Soc. Am. (A)*, 15, 1940-1951 (1998).

[10] V.A. Kashparov, D.H. Oughton, V.P. Protsak, S.I. Zvarisch and S.E. Levchuk, "Kinetics of Fuel Particle Weathering and ^{90}Sr Mobility in the Chernobyl 30 km Exclusion Zone", *Health Physics*, 76, 251-259 (1999).

SYNCHROTRON X-RAY MICROPROBE: COMBINED TECHNIQUES FOR THE ANALYSIS OF ENVIRONMENTAL PARTICLES

M. Drakopoulos
ESRF, France

Abstract

The high brightness of synchrotron radiation sources of the third generation and the development of optical elements for X-rays make it possible to create micro-beams of micrometer size and smaller with high intensity. These beams can be used to reveal spatially resolved information about structural and chemical properties of particles. The accessible energy range of above 10 keV allows to excite fluorescence of most elements and as well to obtain crystallographic information.

In fluorescence mode very low concentrations of less then 0.1 ppm can be routinely detected. The trace elements analysis on micro-particles makes possible to follow environmental problems with very high sensitivity and without destructive sample treatment. The local resolution allows tracking the interplay between the active component and the host matrix.

Via micro-diffraction we access structural information, which may answer questions about the chemical state, about links between the matrix structure and the absorbed components and about the mineralogical phases the particles consist of. Both methods are complementary and can be performed simultaneously. In combination with micro-imaging methods such as micro-tomography we can obtain a good understanding about the properties of micro-particles.

SIMS AND NUCLEAR TRACK METHODS FOR THE CHARACTERISATION OF ACTINIDE-CONTAINING PARTICLES IN ENVIRONMENTAL SAMPLES

M. Betti, N. Erdmann, G. Tamborini, P. Carbol
European Commission, Joint Research Centre, Institute for Transuranium Elements
P.O. Box 2340, 76125 Karlsruhe, Germany

Abstract

The effectiveness of alpha and fission nuclear track analyses for the localisation of particles containing actinides in samples from different origins is discussed. Information from the latter is combined with results from secondary ion mass spectrometry (SIMS) and scanning electron microscopy (SEM) to obtain chemical and isotopic characterisation, as well as to determine the samples' morphologies.

Introduction

A variety of systems and processes may introduce radioactivity in the environment. Human activities involving nuclear weapons and nuclear fuel cycle can lead to a significant formation and potential release of radioactivity. Technology may also release pre-existing natural radionuclides which would otherwise remain trapped in the earth's crust. A general distinction can be made between gases, aerosol and particulate materials.

Particles exhibiting a very high activity are usually called "hot particles" or "radioactive particles". They may be produced in atmospheric nuclear weapon tests or nuclear reactor accidents and can be formed by two processes: disintegration of the nuclear fuel mass or condensation of evaporated products. These radioactive particles can be transferred to soil and water directly or via vegetation and movement through other biota.

The chemical and isotopic characterisations of these particles, as well as their morphological structure, are of fundamental importance for determining their diffusion mechanisms. In this presentation the methods based on nuclear tracks combined with SIMS and SEM measurements for the characterisation of these particles are discussed.

Nuclear track methods

In order to facilitate the localisation of the interesting particles, screening techniques are used. In our laboratory the use of nuclear track detection techniques for the localisation of actinide-containing particles in swipe and soil samples has been exploited. Procedures for α autoradiography and fission track detection have been developed and applied to various environmental samples of different origins. An example of α tracks created from hot spots in the analysis of a humus layer from the Chernobyl region is shown in Figure 1. It can be seen that several particles can be identified. As for their chemical and isotopic characterisation they must be measured by other techniques. The first test is performed by SEM/EDX for the chemical composition of the particles then their isotopic composition is measured by SIMS. Assuming a detection probability of α particles in the film of 100% [1] and a geometric detection efficiency of 40%, the total α activity in these spots, containing *c.a.* 600 tracks yields 0.48 mBq. From this result and those from SEM/EDX and SIMS these α spots could stem from a small fragment of Chernobyl reactor fuel. The α activity is due to low-enriched uranium as well as plutonium and americium.

The fission track method has been exploited mainly for the screening of samples after recovering of particles from swipe samples. In Figure 2 the image of the tracks obtained for one particle is illustrated.

The same particle was investigated by SEM analysis using the back-scattered mode of the microscope. The EDX spectrum showed clearly that the particle consisted of uranium. Further, by SIMS it was possible to measure the isotopic composition of this particle and correlate that with its size and number of fission tracks developed, by the use of standard particles obtained from reference materials with well-known isotopic composition [4].

In Figure 3 the SEM image (a) and the EDX spectrum (b) are shown. Figure 4 gives the image obtained by SIMS. As can be seen, both techniques can provide information relevant to the particle dimension.

Figure 1. α tracks of a hot spot from the analysis of the humus layer. The exposure time was 46 days. The total number of α tracks is approximately 600, which corresponds to an activity level of ≈ 0.5 mBq.

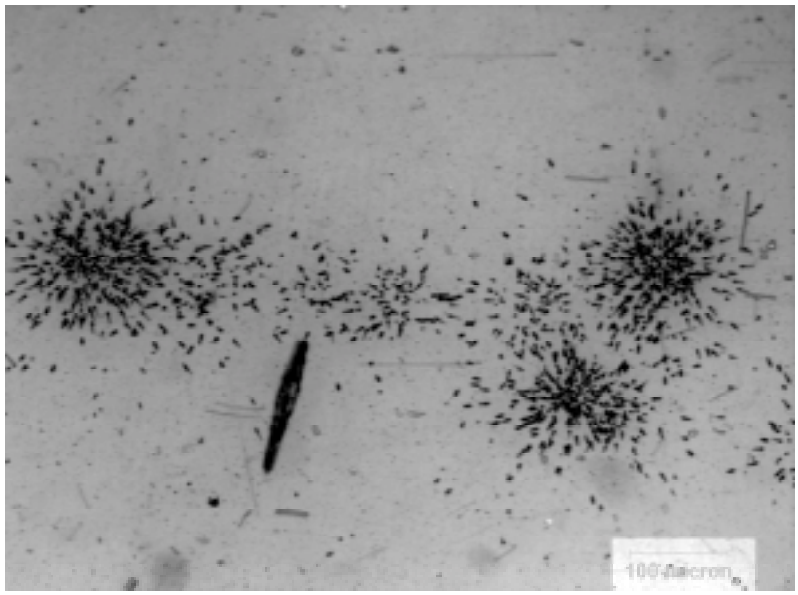

Figure 2. Fission track image of a particle from a swipe sample

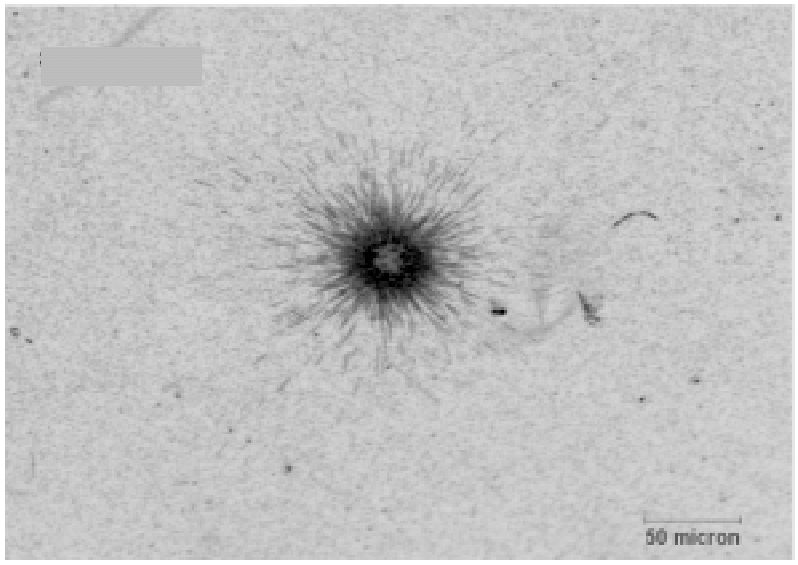

Figure 3. (a) SEM image of a uranium-containing particle from a swipe sample, located by FT analysis (see Figure 2). (b) EDX spectrum of the particle shown in (a).

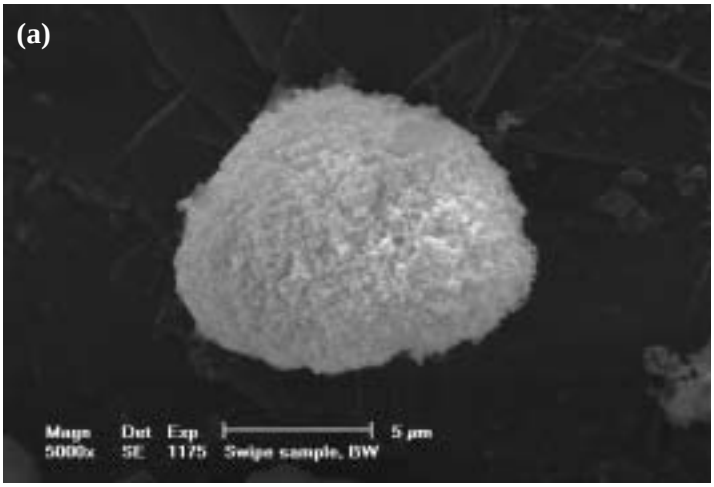

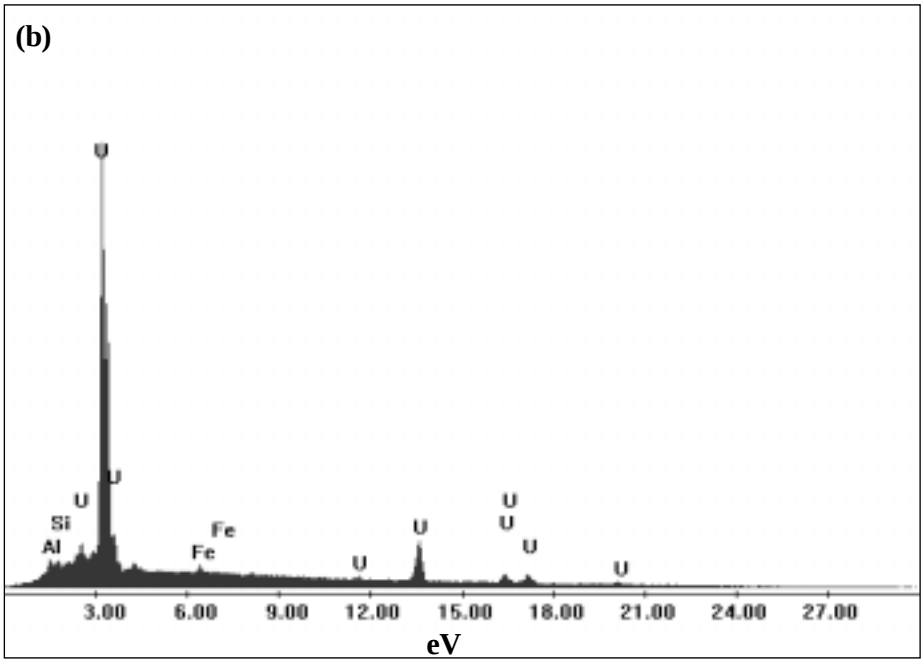

Figure 4. Secondary ion image of a uranium particle from a swipe sample, located by fission track detection and analysed by SEM and SIMS

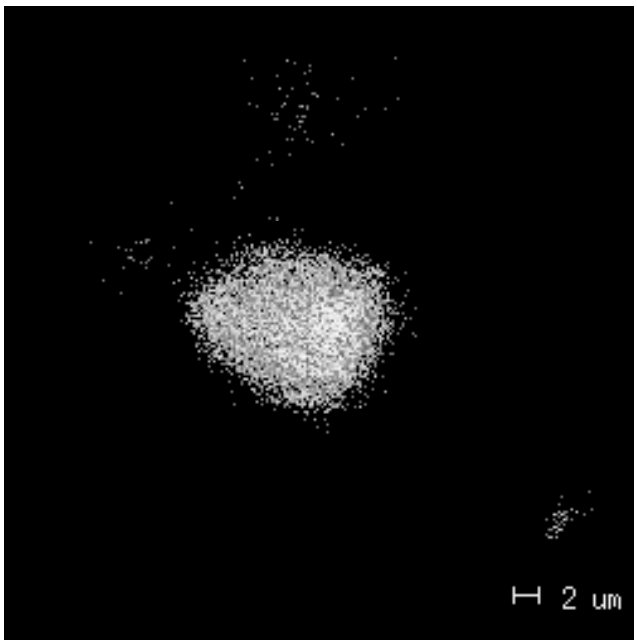

SIMS applications

Secondary ion mass spectrometry is used to verify the isotopic composition of particles [2,3] and their chemical composition. A typical application has been demonstrated on control particles consisting of uranium oxide produced in our laboratory [4].

Four batches of uranium oxide particles of 1 μm size having a different enrichment in ^{235}U were obtained. In Table 1 [4] the results obtained by SIMS for the isotopic characterisation of the produced particles are reported. It can be seen that for the measurement of the ratio $^{235}U/^{238}U$ an accuracy of better than 0.5% was obtained with a typical precision of 1%. As for the minor isotopes (^{234}U and ^{236}U with respect to ^{238}U), an accuracy of a few per cent was achieved.

The technique has also been exploited for the characterisation of plutonium particles. In Figure 5 the SIMS images obtained for the two different Pu particles are shown [5].

From the SIMS measurements the dimensions of the particles can also be obtained and compared with those from SEM. Clearly, only SEM can provide the particle structure. On the other hand, SIMS provides the unique information on the isotopic composition of the particles.

Conclusions

The combination of nuclear track methods with SIMS allows different radioactive and actinide-containing particles to be localised and to be characterised as for their chemical content and isotopic composition. SEM is used to obtain complementary information on the morphology of particles.

Further research with other techniques in order to obtain information on the speciation is ongoing.

Table 1. SIMS isotopic ratios obtained for uranium oxide particles from four different certified standard reference uranium materials: CRM U005, U010, U030 and U100

The certified and measured values for the 234/238, 235/238 and 236/238 U ratios together with % bias and % rsd are given. The 236/238 U ratio was corrected for the contribution of $^{235}UH^{+}$ using the signal on mass 239 ($^{238}UH^{+}$), except for U005.

		U005	U010	U030	U100
$^{234}U/^{238}U$	Certified value	2.19 E-5	5.46 E-5	1.96 E-4	7.54 E-4
	Measured value	(2.62 ± 0.95) E-5	(5.85 ± 0.57) E-5	(1.96 ± 0.07) E-4	(7.54 ± 0.12) E-4
	Precision (rsd%)	36.4	9.7	3.8	1.5
	Accuracy (bias%)	19.41	6.92	-0.23	0.13
$^{235}U/^{238}U$	Certified value	4.92 E-3	1.01 E-2	3.15 E-2	1.14 E-1
	Measured value	(4.90 ± 0.05) E-3	(1.02 ± 0.01) E-2	(3.15 ± 0.01) E-2	(1.14 ± 0.01) E-1
	Precision (rsd%)	1.1	1.0	0.3	0.8
	Accuracy (bias%)	-0.39	0.15	0.13	0.06
$^{236}U/^{238}U$	Certified value	4.68 E-5	6.87 E-5	2.10 E-4	4.23 E-4
	Measured value	(4.34 ± 0.32) E-5	(6.49 ± 0.51) E-5	(2.17 ± 0.20) E-4	(4.25 ± 0.27) E-4
	Precision (rsd%)	22.0	7.9	9.1	6.2
	Accuracy (bias%)	-7.3	-5.53	3.09	0.62

Figure 5. SIMS images for ^{239}Pu and ^{240}Pu in a platelet of PuO_2 (a) and in a fibrous rod (b)

In the SIMS images, the white colour indicates the maximum concentration of the isotope that is normally in the middle of the particles.

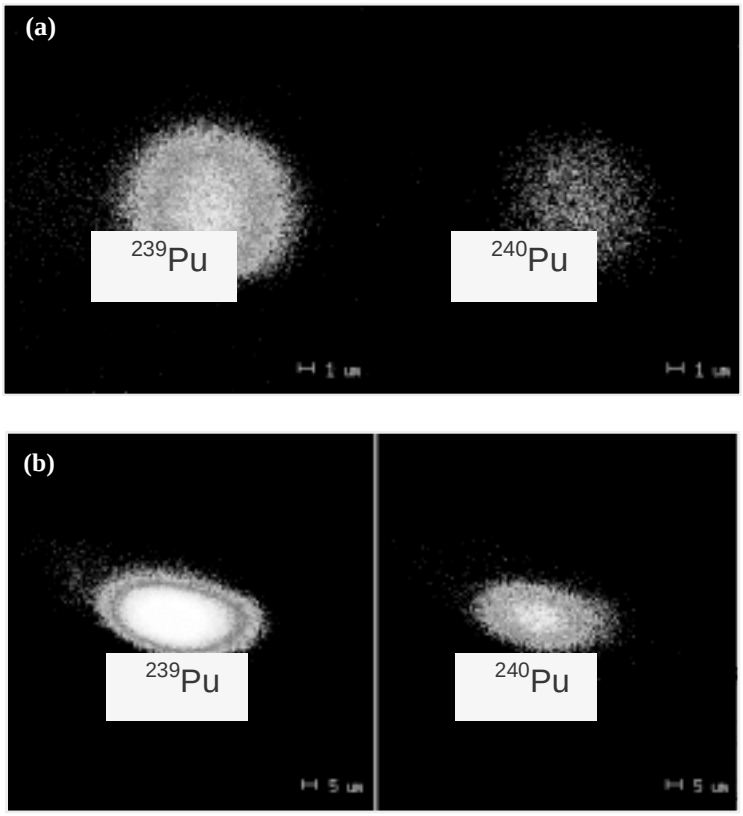

Acknowledgements

The authors are very grateful to the colleagues of the SEM laboratory (Dr. Ian Ray, Dr. T. Wiss and Mr. H. Thiele).

REFERENCES

[1] S.A. Durrani and R.K. Bull, "Solid-state Nuclear Track Detection: Principles, Methods and Applications", Pergamon Press, 71 (1987).

[2] L. Koch, I.L.F. Ray, M. Betti, A. Schubert, "Nuclear Forensics – The Investigation of Smuggled Nuclear Materials", ITU Annual Report, 26 (1998).

[3] G. Tamborini and M. Betti, "Application of Secondary Ion Mass Spectrometry for the Characterisation of Microparticles", *Mikrochimica Acta*, 132, 411 (2000).

[4] N. Erdmann, M. Betti, O. Stetzer, G. Tamborini, J.V. Kratz, N. Trautmann, J. van Geel, "Production of Monodisperse Uranium Oxide Particles and Their Characterization by Scanning Electron Microscopy and Secondary Ion Mass Spectrometry", *Spectrochimica Acta Part B*, 55, 1565-1575 (2000).

[5] M. Betti, G. Tamborini, L. Koch, "Use of Secondary Ion Mass Spectrometry in Nuclear Forensic Analysis for the Characterization of Plutonium and Highly Enriched Uranium Particles", *Analytical Chemistry*, 71, 2616 (1999).

HETEROGENEITY AND PHASE SEPARATION IN CRYSTALLINE SOLIDS MOSTLY CONTAINING PLUTONIUM

Steven D. Conradson, Francisco Espinosa-Faller, Phillip Villella
Materials Science and Technology Division, Los Alamos National Laboratory
Los Alamos, NM 87545, USA

Abstract

Within the last ten years, the once-contentious idea of local structural distortions as an intrinsic aspect of the arrangement of the atoms in crystalline materials and the complementarity of conventional diffraction methods and local structure techniques such as XAFS and PDF analysis have become standard tools in the structure determination box. However, we must now ask whether these advances go far enough or must our conceptual basis of crystal structure become even more radical if we are to accurately depict precisely how a crystal is assembled from its constituent atoms. Synchrotron X-ray measurements – both XAFS and X-ray PDF – on many different systems, but especially ones containing plutonium, show evidence for off-lattice atoms that exceed simple displacements or distortions. What we observe in these systems is most consistent with the formation of actual, relatively well-ordered alternative arrangements of the atoms that can involve up to one-quarter to one-third of the material but that do not diffract. One origin of this heterogeneity or phase separation will be composition fluctuations in non-stoichiometric materials. If a dopant is randomly distributed, the local fluctuations in its concentration will naturally tend towards a size just at or below the diffraction limit. A rearrangement of the atoms in these domains of different composition into a different structure will result in the observed effects. Furthermore, this local behaviour offers an explanation for correlated electronic and atomic effects in many of these materials, corroborating the idea of heterogeneity.

X-RAY MAGNETO-OPTICS IN LANTHANIDES AND PERSPECTIVES FOR STUDYING ACTINIDES

K. Starke, F. Heigl, A. Vollmer, G. Kaindl
Institut für Experimentalphysik, Freie Universität Berlin
Arnimallee 14, D-14195 Berlin-Dahlem, Germany

Abstract

Magneto-optical methods in the visible light regime generally lack element specificity, which has become a considerable shortcoming in research on advanced hetero-magnetic systems for storage technology. Here we review the recent discovery of magneto-optics in lanthanide materials [1] through which it has become feasible to study the element-specific magnetisation of lanthanides in hetero-magnetic compounds. To this end we employ circularly polarised soft X-rays in the energy regime of 100 eV, tuned to individual electric dipole $4d \rightarrow 4f$ transitions of lanthanide elements. We describe the experimental set-up and measurements of the element-specific magnetisation reversal of lanthanide films and nm-sized islands. In contrast to magneto-optics in the visible light regime, the temperature dependent X-ray magneto-optical signals from core-level transitions are not influenced by the thermal lattice expansion. Possible extensions of X-ray magneto-optics to higher photon energies and perspectives for studying magnetically ordered actinide systems are briefly discussed.

Introduction

Magneto-optical (MO) effects [2] are well known as the principle of how magnetic "bits" are read from an MO disk, where left and right-hand circularly polarised light is reflected with different intensity depending on the local disk magnetisation. In the visible-light regime MO effects are generally quite small. Yet refined optical methods yield sufficient contrast to not only distinguish between regions (bits) of opposite magnetisation, but even to observe details of magnetic domains in optical microscopes [3]. All MO techniques are ideally suited to study the magnetisation reversal process in external magnetic fields (hysteresis), which is impossible with many other techniques like, e.g. electron microscopes involving slow cascade electrons that are strongly affected by the Lorentz force.

Besides all merits, conventional MO techniques in the visible-light regime lack element specificity, simply because optical transitions in the visible take place between valence-electron band states which are spread over many lattice sites. Lacking element specificity has become a severe limitation in analysing modern materials for information storage [2,4] and small permanent magnets with nanometer dimensions [5]. Such advanced systems are composed of several magnetic elements to compromise technical requirements. In particular, lanthanide elements (mostly Tb) are used to reach a larger perpendicular magnetic anisotropy than usually obtained in 3d transition metal systems [6], or to achieve very large coercitive fields, e.g. in spring magnets [5].

Element-specific magnetic information can reliably be obtained by techniques which involve core level transitions, e.g. by magnetic circular dichroism in X-ray absorption (XA) [7,8]. In the soft X-ray range which is most relevant for magnetism studies, absorption signals are commonly detected by electron-yield methods [9], so that in general no large external magnetic fields can be employed. Hence no element-specific hysteresis loop (reaching typical coercitve fields in the kOe range) has ever been recorded via electron yield. There are alternative XA detection modes which do not employ electrons; yet they are either limited to special samples suspended on transparent foils [8], or they suffer from saturation effects for all but highly diluted samples (fluorescence yield) [10]. Thus, in order to probe magnetisation reversal in external fields in an element-resolved way, it appears natural to employ X-rays to reach core-levels and also to use light reflection as in conventional magneto-optics. Furthermore, the high X-ray penetration depth in low-Z elements, such as Be, allows one to use low-Z materials for sample protection, or as containment (e.g. Be cans) of radioactive materials [11].

Apart from their technological relevance in soft and hard magnetic films [5,6], lanthanide elements constitute a unique case in soft X-ray optics: the $4d \rightarrow 4f$ electric dipole transitions, so-called Giant resonances, are among the strongest in the periodic table [12]. They give rise to a high absorptivity and reflectivity, corresponding to an exceptionally short X-ray absorption length of $l \approx 1$ nm [13]. It is much shorter than the wavelength at which the lanthanide $4d \rightarrow 4f$ transition occurs ($\lambda \approx 8$ nm) representing the case $\lambda >> l$. This is quite different from $2p \rightarrow 3d$ transitions in Fe-like transition metals studied earlier [14,15], where attenuation lengths are much longer than the wavelength, $\lambda << l$, leading to complicated interferences for samples which are structured on the nanometer scale [15].

Experimental

The soft X-ray reflectivity experiments at the 4d-4f excitation thresholds of Gd and Tb (photon energy range: 130 eV-170 eV) have been performed in an ultra-high vacuum chamber (UHV, low 10^{-11} mbar range) using circularly polarised X-rays form the UE56 undulator beam line [16] at the synchrotron radiation source BESSY 2 at Berlin, Germany. As samples we prepared 1 nm-10 nm thin lanthanide metal films by *in vacuo* metal-vapour deposition onto a W(110) single-crystal substrate [17].

Figure 1 shows the W(110) coin-shaped single crystal mounted on a L-He flow cryostat (top centre) which allows a wide sample temperature range (between 20 K and 2 200 K). Magnetic fields up to 0.2 Tesla are applied through a (rotatable) horseshoe electromagnet. The reflected light intensity is measured using a standard Si photodiode; both photodiode and sample can be rotated about the same vertical axis, serving as a low-precision θ-2θ goneometer. The overall sample magnetisation was controlled *in situ* by standard (not element specific) magneto-optical Kerr effect (MOKE) using visible light.

Figure 1. Photograph of the wide temperature range W(110) sample holder (centre), placed inside a horseshoe electromagnet (fields up to 0.2 Tesla). Lower left: back side of a rotatable Si photodiode for in vacuum soft X-ray reflectivity.

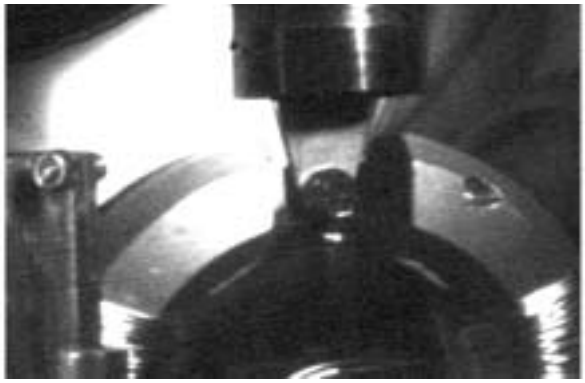

Results and discussion

As a first example we present absorption and reflectivity spectra of an in-plane magnetised 8-nm thick Gd metal film. Figure 2(a) (bottom) shows two Gd 4d $\rightarrow$ 4f absorption spectra, with the film magnetised either parallel (dotted) or anti-parallel (solid curve) to the projected direction of a beam of circularly polarised (CP) light. All spectral ranges change upon magnetisation reversal: the broad absorption maximum near $h\nu$ = 149 eV apparently shifts by some 1 eV, while energy and intensity of the much weaker pre-edge absorption lines change strongly [13]. The associated pair of X-reflectivity spectra in Figure 2(b) (above) is recorded from the same film in specular geometry; all spectra were recorded at θ = 18° grazing light incidence (see inset) and at T = 25 K sample temperature. For both magnetisation directions, there is a pronounced maximum of 20 times higher reflected intensity than at the minimum near 136 eV; the reflectivity maxima (solid and dotted curves) are located ~1.5 eV above the corresponding Giant absorption peaks [Figure 2(a)]. In the pre-edge range, only dispersive-like structures appear in reflectivity, with the points of steepest slope coinciding with the associated absorption peaks; this is nicely reflected by the almost isolated, lowest energy line magnified in Figure 2(c).

The shape of the reflectivity spectral features is well understood within elementary dispersion theory which formally describes the interaction of light with metals by introduction of a complex refractive index $\tilde{n} = (1 - \delta) - i\,k$ [18]. While for normally incident light both the absorptive part k and the dispersive part δ (deviation of the real part of $\tilde{n}$ from unity) contribute equally to the reflected intensity, the dispersive part clearly dominates at grazing incidence as is described by the Fresnel formulae [18,19]. Owing to the particularly short attenuation length l near the lanthanide 4d $\rightarrow$ 4f Giant absorption maxima, the difference in reflected light intensity upon magnetisation reversal is

Figure 2

(a) Gd 4d-4f absorption spectra obtained via electron yield from an 8 nm thick film with remanent in-plane magnetisation parallel (dotted curve) and anti-parallel (solid curve) to the (surface projected) incidence direction of a circularly polarised X-ray beam [inset of (b)].
(b) Associated spectra of specularly reflected light intensity.
(c) The lowest energy pre-edge structure at 139.2 eV in reflection (top) and absorption (below) [1].

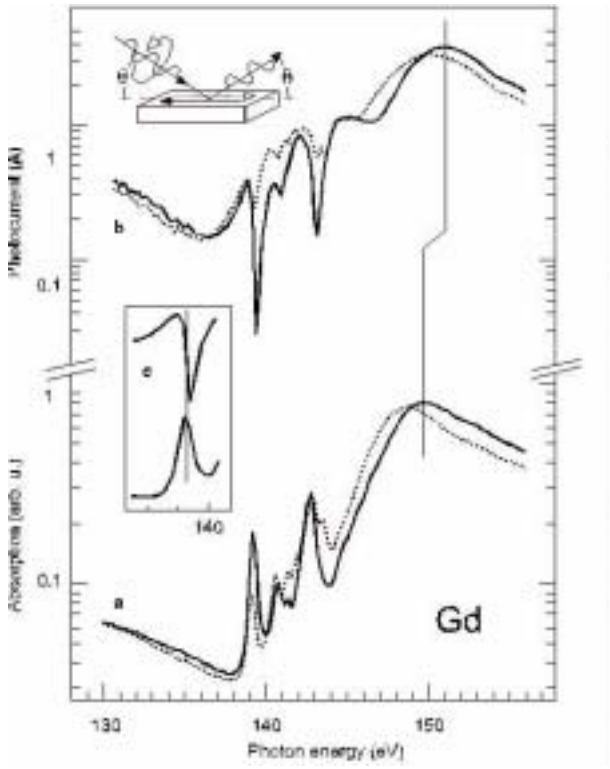

approximately proportional to the magnetisation, as long as the thickness *d* of the layer containing the absorbing element clearly exceeds *l*. This is quite different from previously investigated transition metals [15] involving 2p → 3d transitions (~20 nm attenuation length) where strong interference between individual magnetic layers has been observed in structures of a few nanometer size.

Unlike MO spectra in the visible-light regime involving valence-band transitions [2], 4d → 4f transition energies change significantly in going across the lanthanide series so that even neighbours in the periodic table such as, e.g. Gd and Tb can easily be distinguished. In Figure 3 we compare difference reflectivity spectra, obtained for opposite magnetisations of Gd and of an in-plane magnetised Tb film. The MO signal from Tb peaks near the Tb Giant absorption at hν = 157 eV, i.e. at several eV above the range of a substantial MO signal from Gd.

The energy separation between elemental MO signals at the lanthanide 4d-4f threshold allows one to record element-specific hysteresis loops from hetero-magnetic systems. As a first demonstration we fabricated a $Gd_{1-x}Tb_x$/Gd nanostructure, prepared by annealing of a 0.3 nm Tb layer deposited on top of a ~3 nm thick Gd film on W(110) at 1 070 K; at such a high temperature, the metastable film is expected to break up into large three-dimensional islands [20]. Figures 4(a) and 4(b) present hysteresis loops recorded at two different photon energies, 147 eV and 153 eV. By inspection of Figure 3, we identify 147 eV with the maximum of the Gd spectrum and with a node in the Tb spectrum (energy 1); the 147 eV hysteresis loop in Figure 4(a) thus reflects the magnetisation reversal of the Gd atoms only.

Figure 3

(a) Difference spectrum obtained from the Gd 4d → 4f reflectivity spectra in Figure 2(b).
(b) 4d → 4f difference spectrum of reflected intensity from an 8 nm thick Tb metal film (T = 25 K). Photon energies 1 and 2 are used to record hysteresis loops (Figure 4) [1].

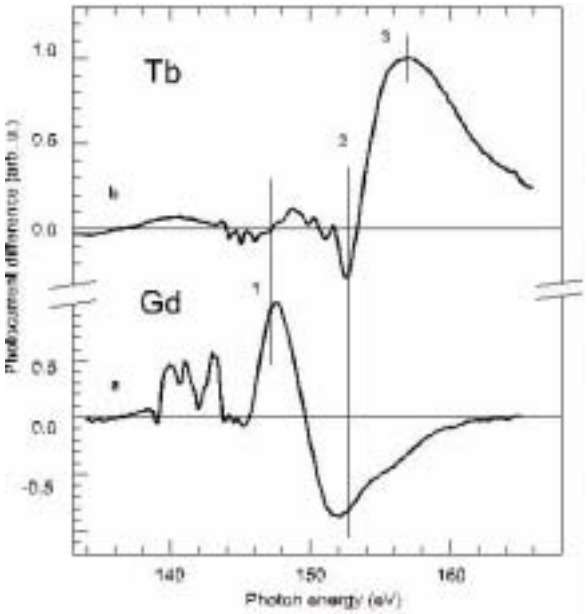

The loop shows two magnetically different Gd species, a magnetically soft one with low coercivity (80 A/cm) and another one in which magnetisation reverses at a five times higher external field (400 A/cm). The overshoot clearly reveals that Gd moments in these two phases are oriented parallel to each other for increasing fields between the two coercivities, but anti-parallel to each other in high external fields – a quite surprising behaviour at first glance. The 153 eV hysteresis [Figure 4(b)] comprises MO signals of both elements (see point 2 in Figure 3). Like the 147 eV loop, it indicates that the magnetisation reverses in two steps, yet there is no overshoot. Assuming the absence of interference effects as was discussed above, we obtain the shape of the magnetisation-reversal curve of Tb simply by subtracting the 147 eV loop (Gd) from the one at 153 eV (superposition of Tb and Gd), with the result given in Figure 4(c).

From the element-specific Gd hysteresis [Figure 4(a)] and the difference loop in Figure 4(c), which we identify with the magnetisation reversal of Tb atoms, we conclude: (1) It is the presence of Tb which gives rise to the magnetically harder Gd phase. (2) The orientation of Gd 4f-moments (at high fields anti-parallel to the external field) is due to an anti-ferromagnetic coupling of Gd and Tb moments in the magnetically hard Gd phase. The hard phase is tentatively assigned to a $Gd_{1-x}Tb_x$ alloy, in which the larger Tb 4f moment (9 μ_B) dominates over the Gd 4f moment (7 μ_B) and points along high external fields, see dashed arrows in Figure 4(b). Note that the low-coercivity Gd, which we identify with the metallic (not alloyed) phase, is not magnetically coupled to the hard magnetic phase; this observation is consistent with the expected separated-island structure of the film.

Another principal difficulty of visible-light MO spectroscopy concerns thermal changes of non-magnetic origin: valence-band energies slightly change with the thermally expanding lattice, which affects the optical constants and thus the reflected intensity of visible light. This complication impedes in many cases a magneto-optical measurement of magnetisation-versus-temperature curves, $M(T)$. By contrast, lanthanide 4d → 4f transitions only involve core levels which do not take part in

Figure 4

(a) Hysteresis loops of a $Gd_{1-x}Tb_x$/Gd nanostructure at different photon energies. At 147 eV, changes in the reflected light intensity are solely due to Gd. The loop reveals two magnetically different Gd phases, a low-coercivity one (Gd metal) and a magnetically harder phase ($Gd_{1-x}Tb_x$ alloy). The associated magnetic orientations are indicated by big and small solid arrows, respectively.

(b) The 153 eV loop reflects magnetisation changes of both elements. The Tb magnetisation is indicated by dashed arrows at different stages of the magnetisation reversal process.

(c) The difference of the loops in (b) and (a) is interpreted as the shape of the Tb hysteresis [1].

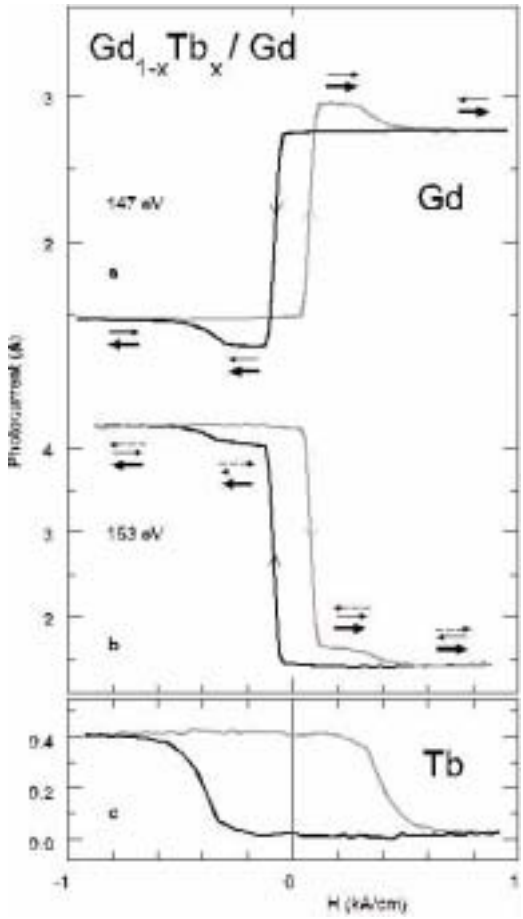

chemical bonding, and we may anticipate that 4d → 4f transition intensity changes reveal only changes in the 4f magnetisation. Figure 5(a) demonstrates that this is indeed the case. A Tb film was cooled, from above room temperature where it is paramagnetic to ~20 K, in the presence of an external magnetic field of 1 kA/cm applied along the film plane, while recording the specular intensity at 157 eV (compare with Figure 3). Above the ordering temperature (Neel temperature T_N) of 220 K, which is reduced as compared to the bulk value (232 K) owing to the small sample thickness (8 nm), the reflected intensity remains constant and it is independent of the field direction. Below T_N it steeply rises (drops) when the field is parallel (anti-parallel) to the projected light propagation direction. As is well known from previous analyses of bulk samples [21], we find that a helical magnetic phase exists within a few Kelvin below the ordering temperature; it has been suppressed by the external field (1 kA/cm). The difference in reflected intensity [Figure 5(b)] amounts to several μA of photocurrent which is easily measured with high accuracy. Such accurate $M(T)$ data provide access to fundamental magnetic quantities such as, e.g. the critical exponent of the magnetisation β, defined through

Figure 5

(a) Temperature-dependent reflectivity curves of an 8 nm thick Tb film, cooled down in external magnetic fields of opposite directions (dotted and solid curves). The constant reflectivity in the paramagnetic temperature regime demonstrates that 4d → 4f core-level transitions are not affected by non-magnetic thermal effects.

(b) Magnetisation curve M(T), which is the difference of the two curves in (a).

(c) Double logarithmic plot of the Tb film magnetisation as a function of the reduced temperature $t = (1 - T/T_C)$. The critical exponent $\beta = 0.31 \pm 0.02$ is determined by a least-squares fit analysis in the range $1 \cdot 10^{-2} < t < 8 \cdot 10^{-2}$ [1].

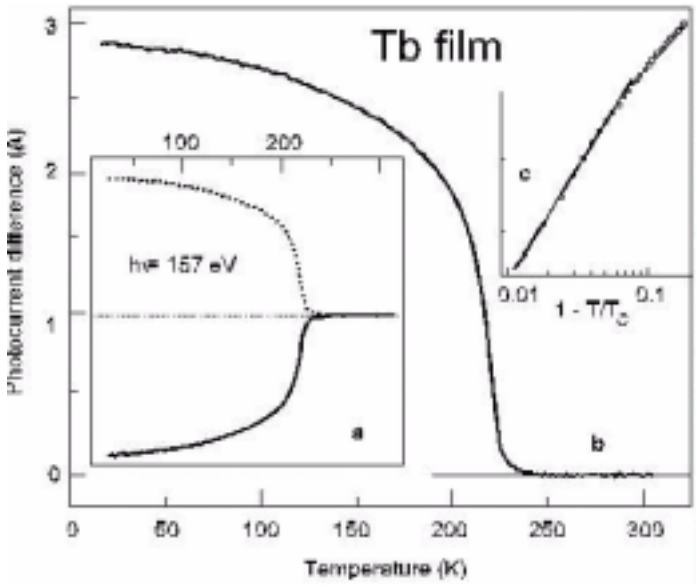

$M(T)/M(0) = (1 - T/T_C)^{\beta}$. For comparison we measured the Tb film magnetisation also by standard MOKE using visible light (λ = 633 nm). As expected, both methods yield the same $M(T)$ behaviour of the Tb magnetisation; however the visible-light MOKE data show a substantial temperature variation of non-magnetic origin which we attribute to thermal lattice expansion [22].

A closer inspection of the critical regime just below the ordering temperature in Figure 5(c) yields a critical exponent $\beta = 0.31 \pm 0.02$. It agrees with the theoretically expected value for a three-dimensional Ising system, indicating the presence of a substantial considerable magnetic anisotropy in the Tb metal film; the latter is likely to be induced by the bcc W(110) substrate of uniaxial symmetry.

Summary and perspectives

The discovery of large and easy-to-measure magneto-optical signals in the soft X-ray regime opens several new avenues in magnetism research. *(1)* Intense X-ray beams from third-generation synchrotron radiation sources can be focused down to a few 10 nm spot size by Fresnel zone plates, utilised in several X-ray microscopes world-wide. So far a magnetic resolution of ~60 nm has been obtained using transparent samples suspended on organic foils [23]. MO signals in reflectivity from lanthanides at the 4d → 4f threshold will now allow element-specific microscopy studies on technically relevant non-transparent metal or semiconductor substrates, e.g. on the currently most relevant question concerning the switching behaviour of heteromagnetic nanoscale systems [4,5]. *(2)* The XMOKE method can be extended into the hard X-ray regime, employing CP light excitation at lanthanide 3d → 4f thresholds [24] and at 3d → 5f thresholds of actinide systems ($M_{4,5}$ edges).

A remarkable 3d $\rightarrow$ 5f resonance enhancement of the magnetic X-ray scattering cross-section by 10^7, as compared to off-resonance scattering, has been observed at the M_4 edge of uranium compounds [25]. It has been applied to a first X-ray scattering study of magnetic structures near the surface of UO_2 [11]. Although pronounced resonance enhancements should also be expected at the shallower actinide nd $\rightarrow$ 5f thresholds [26], measurements at $M_{4,5}$ edges might be most convenient since low-Z containment materials become transparent at higher photon energies (U M_5: 3.55 keV)

Acknowledgements

The authors are indebted to the staff of BESSY II for their co-operation in the preparation and performance of the experiments at the U56/1-PGM. This work was supported by the BMBF, project 05-SC8 KEB-6 and the DFG, Sfb290/TP A06.

REFERENCES

[1] K. Starke, F. Heigl, A. Vollmer, M. Weiss, G. Reichardt, G. Kaindl, *Phys. Rev. Lett*., submitted April 2000.

[2] S. Sugano and N. Kojima, *Magneto-Optics* (Springer, Berlin, Heidelberg, 2000); D.S. Bloomberg and G.A.N. Connell in *Magnetic Recording Handbook: Technology and Applications*, C.D. Mee, E.D. Daniel, eds., (McGraw-Hill, New York, 1990).

[3] A. Hubert and R. Schäfer, *Magnetic Domains* (Springer, Berlin, Heidelberg, 1998).

[4] G.A. Prince, *Science*, 282, 1660 (1998).

[5] J.S. Jiang, *et al*., *J. Appl. Phys.*, 83, 6238 (1998); S.A. Majetich, Y. Jin, *Science*, 284, 470 (1999).

[6] D. Weller and W. Reim, *Appl. Phys. A*, 49, 599 (1989); Y. Takeno, K. Kaneko, Y. Shimada, *J. Magn. Soc. Jpn.*, 19, S229 (1994).

[7] G. Schütz, *et al*., *Phys. Rev. Lett.*, 58, 737 (1987).

[8] C.T. Chen, *et al*., *Phys. Rev. Lett.*, 75, 152 (1995).

[9] J. Stöhr and R. Nakajima, *IBM J. Res. Develop.*, 42, 73 (1998).

[10] L. Tröger, *et al*., *Phys. Rev. B*, 46, 3283 (1992); C.T. Chen, *et al*., *ibid.*, 48, 642 (1993).

[11] G.M. Watson, D. Gibbs, G.H. Lander, B.D. Gaulin, L.E. Berman, Hj. Matzke, W. Ellis, *Phys. Rev. Lett.*, 77, 751 (1996); *Phys. Rev. B*, 61, 8966 (2000).

[12] B.L. Henke, E.M. Gullikson, J.C. Davis, *Atomic Data and Nucl. Data Tables*, 54, 180 (1993).

[13] K. Starke, *et al*., *Phys. Rev. B*, 55, 2672 (1997); *Eur. Phys. J. B*, 12, 171 (1999).

[14] H.A. Dürr, *et al*., *Science*, 284, 2166 (1999).

[15] C-C. Kao, *et al*., *Phys. Rev. B*, 50, 9599 (1994); Y.U. Idzerda, V. Chakarian, J.W. Freeland, *Phys. Rev. Lett.*, 82, 1562 (1999).

[16] K.J.S. Sawheney, *et al*., *Nucl. Instr. Met. A*, 390, 395 (1997).

[17] K. Starke, *Magnetic Dichroism in Core-level Photoemission* (Springer, Berlin, Heidelberg, 2000), Sect. 3.

[18] M. Born and E. Wolf, *Priciples of Optics* (Pergamon, London, 1959).

[19] A semiquantitative description of the reflected light intensity in both, the pre-edge and the Giant resonance range is given in Ref. [1].

[20] E.D. Tober, *et al*., *Phys. Rev. B*, 53, 5444 (1996).

[21] J. Jensen and A.R. Mackintosh, *Rare Earth Magnetism Structures and Excitations* (Clarendon, Oxford, 1991), Sect. 5.7.

[22] F. Heigl, G. Kaindl, K. Starke (unpublished).

[23] P. Fischer, *et al*., *Z. Phys. B*, 101, 313 (1996).

[24] Z. Hu, *et al*., *Phys. Rev. B*, 59, 9737 (1999).

[25] E.D. Isaacs, D.B. McWhan, C. Peters, G.E. Ice, D.P. Siddons, J.B. Hastings, C. Vettier, O. Vogt, *Phys. Rev. Lett.*, 62, 1671 (1989).

[26] G. Kalkowski, G. Kaindl, W.D. Brewer, W. Krone, *Phys. Rev. B*, 35, 2667 (1987).

THE PRESSURE BEHAVIOUR OF ACTINIDES VIA SYNCHROTRON RADIATION

R.G. Haire,[1] **S. Heathman,**[2] **T. Le Bihan**[3] **and A. Lindbaum**[4]
[1]Oak Ridge National Laboratory, Oak Ridge, TN 37831-6375 USA
[2]Institute for Transuranium Elements, Karlsruhe, German
[3]European Synchrotron Radiation Facility, Grenoble, France
[4]Institute for Experimental Physics, Vienna University of Technology, Austria

Abstract

Various aspects of performing high-pressure studies with radioactive f-elements using synchrotrons as sources of X-rays are discussed. For ultra-high pressures, intense well-focused beams of 10 to 30 microns in diameter and a single wavelength of 0.3 to 0.7 Å are desired for angle dispersive diffraction measurements. Special considerations are necessary for the studies of transuranium elements under pressure at synchrotron facilities. Normally, with these actinides the pressure cells are prepared off-site and shipped to the synchrotron for study. Approved containment techniques must be provided to assure there is not a potential for the release of sample material. The goal of these high-pressure studies is to explore the fundamental science occurring as pressure is applied to the actinide samples. One of the primary effects of pressure is to reduce interatomic distances, and the goal is to ascertain the changes in bonding and electronic nature of the system that result as atoms and electronic orbitals are forced closer together. Concepts of the science being pursued with these f-elements are outlined. A brief discussion of the behaviour of americium metal under pressure performed recently at the ESRF is provided as an example of the high-pressure research being performed with synchrotron radiation. Also discussed here is the important role synchrotrons play and the techniques/procedures employed in high-pressure studies with actinides.

Introduction

Electromagnetic radiation has long been employed for characterising materials, and third-generation synchrotrons offer unparalleled opportunities in this regard. In the area of X-ray diffraction, a classical tool for structural determinations, synchrotrons offer not only a very intense X-ray source but also provide beams of superior dimensions and stability that can be readily customised. These are the characteristics that have greatly expanded the ability to perform ultra-high pressure research, and have attracted researchers wishing to investigate actinides under pressure at synchrotron facilities.

There has been increased interest in the effects of pressure on f-elements and compounds, especially as pressures in the megabar region are now easily attainable. An important issue in these studies is to determine how the decreasing interatomic distances, brought about by applying pressure, can effect the electronic nature and/or bonding in these materials. Specifically, for the f elements, the question is whether such changes effect the normally non-bonding (localised) f electrons themselves and incorporated them in some manner into the bonding of the materials. The 5f electrons of the actinide elements, which are all radioactive to varying degrees, are particularly intriguing in this regard.

Whereas it is accepted that the actinide elements from protactinium through plutonium have f electrons involved in their bonding at normal pressure, in contrast the transplutonium elements are considered to be more lanthanide-like and do not. Thus, one goal for investigating transplutonium metals is to determine if pressure can bring about delocalisation of their f electrons and thereby alter the nature of the bonding in the materials.

The spatial extent of the 5f electrons is greater than that of the 4f electrons, and close in energy to the 6d, 7p and 7s electrons. Altering certain parameters, such as pressure, may then change the total energy of the system. An especially interesting element in this regard is americium (element 95), the near neighbour of plutonium (element 94). At room temperature and pressure, plutonium is accepted as having overlapping orbitals, which involve its 5f electrons (hybridised band structure), while americium has localised 5f electrons (e.g. 5f electrons in a narrow region). The question becomes whether pressure can reverse this sudden change in 5f electron behaviour that is observed in this region of the actinide series. That is, can pressure cause the 5f electrons of americium to participate in the bonding? There is also interest in the behaviour of different actinide compounds and alloys under pressure. These latter materials present an additional complexity in that more than one kind of atom is involved.

Structural information in high-pressure studies is basically obtained in the classical manner using X-rays, except that a diamond anvil cell (DAC) is employed for applying pressure on the sample. The DAC imposes some restrictions in the diffraction studies, but the nature and flexibility of the synchrotron radiation makes it the preferred choice for pressure work, especially at the higher pressures. There are several obvious advantages to using synchrotron radiation for pressure studies, but for pressures of one or more megabars, the small (10-30 micron diameter) X-ray beams of high intensity are very significant, in some instances even being a necessity.

This work will cover different aspects, both positive and negative, of performing high-pressure studies with radioactive f elements at synchrotron facilities. The important role synchrotrons play in studies with actinides, together with the needs and responsibilities of scientists performing such investigations will also be addressed. Some of the science being pursued with actinides will be outlined and demonstrated by a brief discussion of selected studies, which includes the investigation of americium metal under pressure recently performed at the ESRF (Grenoble, France).

Experimental aspects

Materials

The actinide elements are all electropositive metals and display variable reactivity toward water and air. They are prepared by various techniques [1-3], depending on their particular physicochemistry and availability. In experiments with the limited quantities of the element and with isotopes having short half-lives, the preparation of the metals becomes an integrated part of the high-pressure studies. Reactivity of the metal is a concern, especially considering the small amounts of the sample employed in the high-pressure study. In most cases, sample loading of the DAC must be performed in inert atmosphere glove boxes to protect the sample from moisture and air, as well as to provide containment for the radioactive materials. Thought must also be given to the pressure-transmitting medium being used, to assure that it will not bring about sample degradation, especially with a lengthy transportation period. Generally, silicon oil and liquefied gases (Ar, He, N_2, etc.) are acceptable, whereas alcohol (e.g. mixtures of methanol and ethanol) can react with some actinide metals, especially those with higher radiation fields that decompose the alcohol to more reactive products.

Diamond anvil cell

There are a number of diamond anvil cell (DAC) designs and it is not the purpose here to compare them. Nor is there an attempt to discuss the preparation of loading/unloading techniques employed. Rather, the discussion is aimed at operations necessary to allow radioactive samples in a DAC to be studied at a synchrotron.

In this work we employed three cell designs:

- Cornell design [4].
- Syassen-Holzapfel design [5].
- Megabar design [6].

The first design is best suited for pressure of a megabar or more, whereas the second design is limited to pressures of ~ 60 GPa. The DAC by necessity (for alignment, installation of parts, etc.) has several openings to the diamond anvil area. These openings must be “sealed” when using radioactive samples at a synchrotron. The diamonds and gasket provide the first level of containment. In addition, other containment must also be provided. For the latter perspective, some cell designs are more adaptable than others. We have found that the Cornell DAC design lends itself nicely for such containment. A photograph of two views of the Cornell cells is shown in Figure 1.

This DAC is essentially a precision-bored, block of stainless steel that contains a fixed diamond anvil and is fitted with a movable piston containing a matching diamond anvil. The piston is associated with the large nut on the right side of the left-hand cell in Figure 1. The accesses through the block are sealed with oval aluminium plugs (threaded hole in centre) and a second Allen screw in each corner. A brass piece fitted with a 6 mm diameter beryllium window is screwed and sealed into the movable piston (visible only as a nut on the left cell), and rests just before the base of the diamond. The X-ray beam enters the piston opening and then passes through a beryllium window. After passing through this window, the movable diamond, the sample and the fixed diamond, the X-rays exit pass through the end slit.

Figure 1. Two Cornell-type diamond anvil cells with special containment pieces for studying radioactive samples (a beryllium window inside of the housing of the movable piston is not shown)

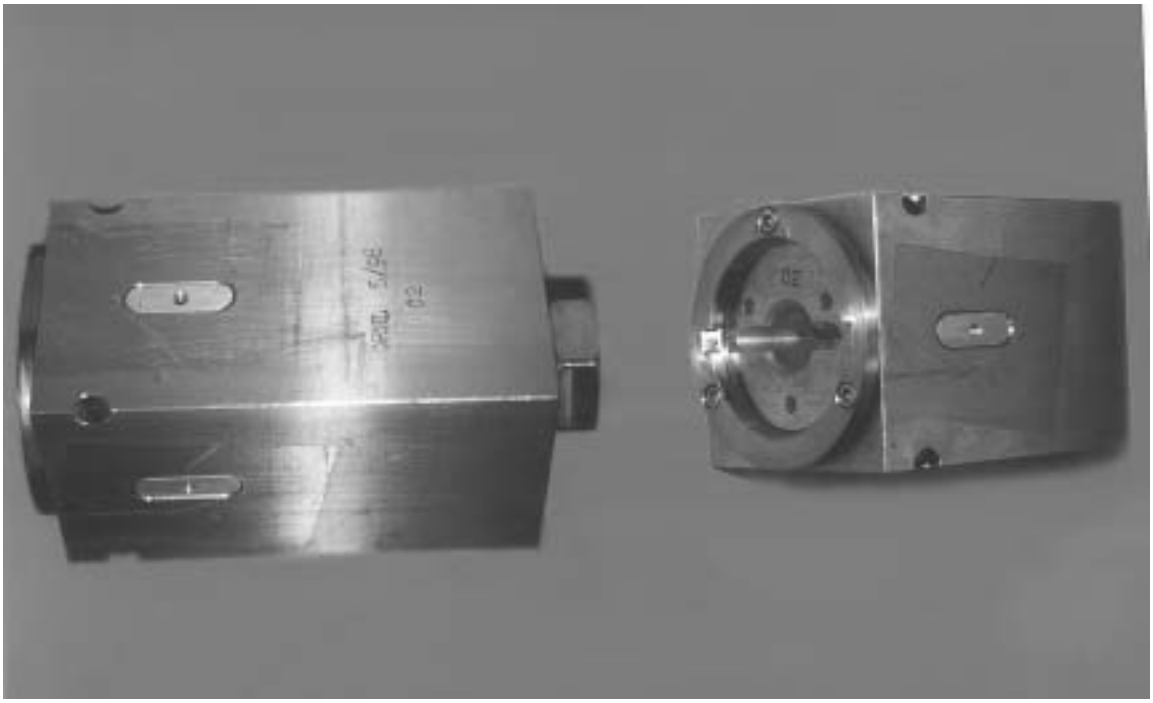

The exit slit is visible in the right hand cell (Figure 1) and provides limited two-theta angle of some twenty degrees. The exit slit is fitted with a large brass ring which has a high strength plastic (Melinex®, a polyester film by Dupont) sealed to it. The ring is held on the DAC by three screws. The plastic window was chosen both for its strength and its ability to transmit the ruby's fluorescence, when the latter is used for pressure determination. Either ruby fluorescence or the equation-of-state for platinum were the techniques used for the pressure determination. Using a plastic film over an aluminium frame also provided additional containment for the cell.

Containment for the other two cell designs was similar in principal, through both were more difficult given the different cell constructions. Containment for these two cell designs is not discussed here, but a similar approach was used for the other cells.

Special techniques have been developed for loading/unloading the DAC at ORNL. Experience has shown these cells can be loaded with radioactive samples, used in the studies and then unloaded without contaminating the DAC, except for the gasket and diamond surfaces. It has been found that the diamonds can easily be de-contaminated and re-used in other studies.

DAC and synchrotron radiation

High-pressure studies with a DAC can employ either energy dispersive or angle dispersive techniques. Both techniques have advantages and disadvantages but overall we have preferred the angle dispersive technique for studies with synchrotron radiation. This approach provides excellent resolution, most flexible operational conditions, and given the high intensity of the radiation, does not suffer with regard to the collection time for the diffraction data. Angle dispersive studies with a DAC do have some special requirements, and these vary with the properties of the specific cells being used.

A few comments relative to the study of f-elements in a DAC at synchrotrons are provided here. With the angle dispersive technique, X-rays of a wavelength shorter than ~0.7 Å (e.g. 0.7-0.3 Å) are used to maximise the diffraction data that can be collected. A wavelength of 0.7 Å is sufficient to pass through the two diamonds and the sample. Shorter wavelengths allow "compressed" diffraction data to be collected to favour higher angles. Altering the sample to detector distances and/or rotating the cell relative to the beam are other approaches that can be undertaken at advanced facilities. These techniques help overcome the limitation of having relatively small diffraction angles provided by the DAC (~20-25 degrees 2 Θ). Finally, the rapid image plates and readout used at the ESRF facility are very important, and allow complete diffraction patterns to be obtained with the synchrotron radiation in less than a minute.

The superiority of synchrotron radiation for high-pressure studies with actinides is in the machine's ability to provide intense, well-focused and stable X-ray beams with of 10-30 microns in diameter. As the desired pressure region for the studies increases, there is a need for smaller diamond anvils, small gasket openings and smaller sample sizes. In many cases, diamond anvils with 70-100 micron surfaces and having a gasket with 30-60 microns in diameter opening are used; only a few micrograms of actinide sample are employed. These conditions require the small, intense X-ray beams provided by synchrotrons in order to perform a complete study of the material at very high pressures in the allotted experimental time.

Specifically, the experimental procedure often uses micro-focused beams of nominally 25×25 μm (two bent mirrors in conjunction with a 30 μm pinhole filter) in many of the studies. Under these conditions, a 15-second exposure is sufficient (2/3 fill machine mode, at 200 mA) to yield excellent diffraction images. The images are captured with a Fastscan image detector [7] and can be viewed in 15-60 seconds. This allows a large number of diffraction images to be collected in a short time.

Presently, facilities are not available at synchrotrons for loading and preparing DAC with radioactive samples, although facilities exist for preparing certain types of samples at the synchrotron. For high-pressure studies, it is required that the DAC samples be loaded, prepared for study at a synchrotron site and then transported to that site by official carriers. This transportation is costly, time consuming and the process is not forgiving if the sample is unsatisfactory upon arrival.

This transportation process also limits the number of samples and increases the inability to successfully study a particular sample. The DAC is an expensive sample device and only a limited number are normally available at one time. Transportation itself limits the number of cells that can be transported at one time. Thus, the experimenter must choose between having different samples or having one or two materials with back-up samples. The total number of samples often falls into a range of one to six in these high-pressure synchrotron studies with actinides.

f-elements under pressure

Over the past few decades there have been several studies of the lanthanides and actinides under pressure. Given recent advancements in high-pressure work and the use of synchrotrons, higher pressures have been attained and new concepts concerning behaviour under pressure have been formed. The reader is referred to reviews [8-11] on high-pressure studies with f-elements and recent work on Ce metal [12]. There is strong evidence that the 4f electrons in the lanthanide series delocalise under pressure and that these metals adopt low-symmetry structure types known for the Pa-Pu metals, which normally have itinerant f electrons. The pressure for this delocalisation process increases as one moves across the lanthanide series (as the f electrons are "pulled in" by the greater nuclear charge);

it has not been reported for members of the second half of this series. The greater spatial extension of the 5f electrons in the actinides, as compared to the 4f electrons in the lanthanides, is expected to permit the delocalisation process in the former to occur at lower pressures.

The physicochemical properties of the actinide metals at normal pressure vary considerably across the series. This is largely due to the changing role of the 5f electrons. It is accepted that the 5f electrons in the protactinium through plutonium metals are involved in bonding at normal temperature and pressure, and these metals display quite different properties than the lanthanide or transplutonium metals. The 5f electrons of the transplutonium metals are localised and their behaviour is more like that of the lanthanide metals. In this regard, americium metal is in a pivotal position in the series and its behaviour under pressure is especially interesting. The determination of whether pressure can bring about this delocalisation is an important aspect of DAC studies with transuranium elements.

The concept of identical homologues between the lanthanide and the actinide metals is seriously limited, especially in terms of their pressure behaviour, although some comparisons/relationships are valid and useful. In these pressure studies using X-ray diffraction, the approach is to monitor the structure of the metals as a function of pressure and extract the bonding behaviour from established structure-bonding relationships. These structure-bonding relationships have both an experimental and theoretical basis. The goal is to use both theory and experiment to understand the pressure behaviour and to promote the convergence of experimental and theoretical views of the metals under pressure.

There are at least two different processes envisioned for the 5f electrons when the metals are subjected to pressure. One effect is for the 5f electrons to combine/overlap with other electron orbitals to form a hybrid-type of bonding band (as exists with the Pa-Pu metals at normal pressure). In essence, the 5f electrons become delocalised and become involved in bonding, either totally or partially. In this situation, it would be expected that lower symmetry structures would form, perhaps similar or identical to the structures exhibited by the protactinium through plutonium metals.

The second process is for the pressure to cause promotion of the f-electron to another state (e.g. f $\rightarrow$ d) and then this new state would become involved in bonding. This does not seem to have been observed experimentally in pressure studies to date. A potential example would be to apply pressure on divalent einsteinium metal ([Rn core] $5f^{11}$ $7s^2$) and force it to become trivalent einsteinium metal ([Rn core] $5f^{10}$ spd). Simple calculations indicate this could occur at relatively lower pressures.

The primary structural effects of pressure are: dynamic compression, structural transformations and volume collapses. In many of the structural transformations involving high symmetry, common metal structures, s-d interactions are the driving force, as the relative energies of these orbitals change with pressure. Transformation from a high to lower symmetry structure can suggest potential incorporation of f-electron character. A sudden volume collapse is indicative of the onset of f-electron involvement.

The above discussion provides a snapshot of what investigations of actinide metals under pressure are pursuing in high-pressure studies at synchrotrons. The studies require the application of established structure-bonding concepts and relationships. Other complimentary analysis under pressure would of course be useful/informative, and some have been done at lower pressures. However, the situation is that these other analytic probes (magnetism, resistivity, etc.) are far more limited in the pressures that can be obtained. The DAC probably provides the highest pressure that can be experimentally obtained in static measurements. The types of changes being pursued very likely require these high pressures.

In the subsequent section, important aspects of americium's behaviour under pressure, determined in recent studies at the ESRF [13], will be discussed. Studies of americium under pressure have been reported previously at lower pressures using conventional X-ray radiation sources. The recent work on americium [13] differs significantly in the structures observed in the mid- to high-pressure regions, and these new findings were made possible through the use of synchrotron radiation.

Recent studies on americium metal

Americium metal was studied recently at the ESRF high-pressure diffraction facility (ID30) and the initial findings reported [13]. These studies greatly extended the pressure range examined previously, from 60 GPa to the reported limit of 100 GPa. In addition, the high quality (resolution) and extensive diffraction data acquired at the ESRF resolved previous disagreements about the high-pressure behaviour of americium. These new data have allowed a new understanding of the behaviour of americium under pressure. These data are shown in graphical form in Figure 2 as a plot of relative volume (volume at pressure/volume at normal pressure) versus pressure. The insert in the figure displays the atomic volume of the different actinide metals versus the atomic number, showing the sharp increase in volume in going from plutonium to americium. This increase reflects the change from having delocalised electrons in plutonium (smaller than expected atomic volume) to having localised f electrons found in americium. If the localised f electrons in americium suddenly became delocalised (e.g. by applying pressure), a sharp reduction in its atomic value would be expected (e.g. the volume for americium in the insert would drop down toward the volume shown for plutonium). Conversely, if f-electron involvement could be removed in α plutonium (generation of localised f electrons), its volume should increase towards that of americium. This can be partially accomplished by heating or alloying of plutonium with small amounts of other metals.

Figure 2. Relative volume versus pressure curve for americium metal

Inset shows the atomic volume of the actinides as a function of element

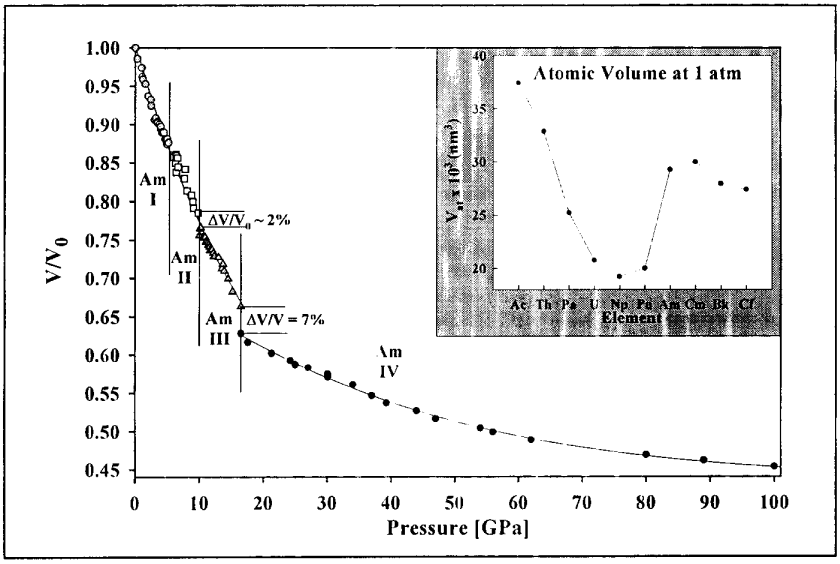

Figure 2 displays that four phases were observed for americium metal under pressure in a recent study [13] at the ESRF. Previous researchers have reported data and interpretations about the behaviour of americium metal under pressure below 60 GPa [14-21]. The main differences in Figure 2 from earlier work are found in the two phases labelled Am(III) and Am(IV). Differences included both the

structural assignments and the transition pressures for these two phases. In addition, a second, small volume collapse was observed for the first time at the transition between the Am(II) and Am(III) forms (Figure 2).

The structures observed for the four forms were: Am(I) – dhcp (P63/mmc); Am(II) – fcc (Fm3m); Am(III) – orthorhombic (Fddd) and Am(IV) – orthorhombic (Pnma). The Am(IV) form is similar to the α uranium type structure (Cmcm) [13], while the Am(III) structure is isostructural with an elevated temperature form of plutonium metal (γ plutonium). Both the Am(III) and the Am(IV) structures are believed to involve f-electron character, as do α plutonium and α uranium. A detailed discussion and experimental information can be found in the paper [13]. The results of the pressure study on americium metal can be looked at as a form of "modern structural alchemy". Under pressure americium (II) adopts first the structure of γ plutonium and then a structure with a "slightly altered" arrangement of the atoms than found in α uranium (loosely speaking, a slightly altered form of α uranium). The structures are displayed graphically in Figure 3, where the arrangement of the americium atoms in each form and the transformation processes between structures can be visualised.

Figure 3. A form of modern alchemy

Under high pressure, americium [Am(II)] first adopts the structure of γ plutonium [Am(III)] and then a structure that is "slightly altered" from that of α uranium [Am(IV)]

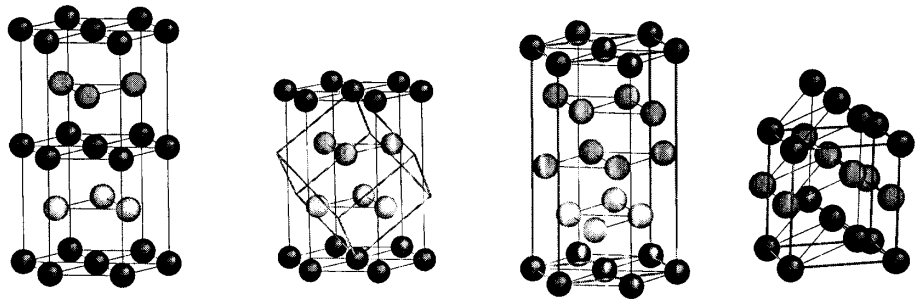

The ability to resolve the behaviour of americium under pressure was the result of the high quality of the diffraction data obtained at the ESRF synchrotron facility. The quality of these data was confirmed in Rietveld analyses of the data at different pressures, and Bragg-R factors of 5-8% were obtained for the derived structures. The results of the refinements for some data sets for the face centred orthorhombic Am(III) and primitive, orthorhombic Am(IV) structures are shown in Figure 4. The space group for the Am(III) structure is Fddd and that for the Am(IV) structure is Pnma. The latter space group has a lower symmetry than the Cmcm space group for α uranium, which itself is a complex structure.

Summarising comments

The attributes of synchrotron radiation have permitted and hopefully will continue to advance the high-pressure science of the actinides. Obtaining high-quality diffraction data is crucial to ascertain the proper structural behaviour from which electronic and bonding nature of the material is extracted. Synchrotron radiation is very important when ultra-high pressures are sought, as it can provide the characteristics and the very critical beam conditions that are required for these particular DAC investigations. The flexibility and variability of the beams from modern synchrotrons are additional benefits.

Figure 4. Rietveld fits for the Am(III) and Am(IV) structures at 10.9 and 17.6 GPa

Shown are experimental (dark lines) and calculated (grey lines) diffraction patterns, reflection tick marks and difference profiles (bottom line) [13]

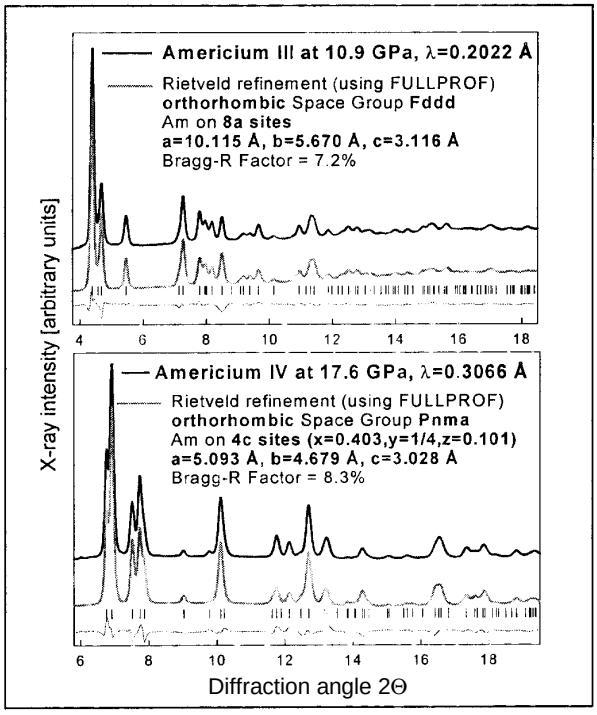

Drawbacks to high-pressure studies with actinides at synchrotrons are the lack of on-site facilities for loading/unloading the DAC. These are not likely to be available, especially in the near term, given the requirements for handling DACs, as well as more extensive work needed with radioactive materials in DACs. In the absence of such facilities, it is necessary to transport the DACs pre-loaded with sample and contained. This can be expensive, difficult and time-consuming, and the transport of radioactive materials is not likely to become easier in the future. This situation is made even less attractive by the fact that researchers are likely to have only a limited number of DACs for transportation at any one time. This reduces the number of samples that can be available for study during a particular allotment of beam time. In many instances, a choice must be made between having a back-up sample or another sample material for study.

The potential for new advancing actinide science is good for these high-pressure studies. In condensed matter studies, the large reductions in interatomic distances attainable with pressure are much greater than increases in such distances acquired by temperatures for conditions attainable in the laboratory. Hence, important changes can be induced in the bonding and physicochemical changes in actinide metals and compounds by applying pressure.

The recent studies of americium metal using synchrotron radiation provides an example of the type of new information that can be obtained with modern techniques. Properly identifying the Am(III) and Am(IV) pressure phases in recent studies at the ESRF allowed new insights to be obtained into the behaviour of 5f electrons both under pressure and at normal pressure. Observing a partial delocalisation of americium's 5f electrons in the Am(III) phase to form a γ plutonium type structure followed by a second delocalisation step is perhaps the first example of the occurrence of a multi-step delocalisation process in actinide metals which normally have localised 5f electrons.

Overall, such high-pressure studies, which reach out to new pressure limits, require synchrotron radiation to obtain the quality data that are needed. Synchrotron radiation offers a new potential for establishing important structural and electronic behaviour of actinides. Such studies are important not only for advancing actinide science, but also for providing new information for evaluating theoretical concepts/calculations. Hopefully, these studies will promote the convergence of experimental findings and theoretical views regarding the behaviour of 5f electrons under pressure.

Acknowledgements

This work is supported by the Division of Chemical Sciences, Geosciences and Biosciences, Office of Basic Energy Sciences, US Department of Energy, under contract DE-ACO5-00OR22725 with Oak Ridge National Laboratory, managed/operated by UT-Battelle, LLC, and also sponsored by the European Commission. The beam time allocated at the ID30 beam line at the ESRF for performing the americium experiments is also acknowledged, as is the Health Physics coverage and co-operation provided by P. Berkvens and P. Colomp at the ESRF.

REFERENCES

[1] R.G. Haire, in *Actinides in Perspective*, N.M. Edelstein, ed., Pergamon Press (New York, 1982), pp. 309-342.

[2] R.G. Haire, *J. Less-common Metals*, 121, 379-398 (1986).

[3] J.C. Spirlet and O. Vogt, in *Handbook on the Physics and Chemistry of the Actinides*, A.J. Freeman and G.H. Lander, eds., North-Holland (Amsterdam, 1984), p. 79 and references therein.

[4] Design of Prof. Ruoff, Cornell University, NY.

[5] Design of K. Syassen and W.B. Holzapfel.

[6] Mao-Bell Megabar Cell, Geophysical Laboratory, Washington D.C.

[7] M. Thoms, S. Bauchau, D. Häusermann, M. Kunz, T. Le Bihan, M. Mezouar, D. Strawbridge, *Nuclear Instruments and Methods in Physics Research*, A 413, 175 (1998).

[8] U. Benedict and W.B. Holzapfel, in *Handbook on the Physics and Chemistry of Rare Earths*, K. Gschneider, Jr., L. Eyring, G.H. Lander, G.R. Choppin, eds., Elsevier Science (Netherlands, 1993), Vol. 17, Chap. 113, pp. 245-300 and references therein.

[9] R.G. Haire, in *Resources, Science Technology and Applications*, R. Bautista, N. Jackson, eds., TMS (Pennsylvania, 1991), pp. 449-462 and references therein.

[10] U. Benedict, in *Handbook on the Physics and Chemistry of the Actinides*, A.J. Freeman and G.H. Lander, eds., Elsevier Science (Netherlands, 1987), Chapter 3, pp. 227-269 and references therein.

[11] K.A. Gschneider, Jr. and F.W. Calderwood, in *Handbook on the Physics and Chemistry of the Rare Earths*, K.A. Gschneider, Jr. and L. Eyring, eds., North-Holland (Amsterdam, 1986), Vol. 8, Chapter 54, pp. 156-160 and references therein.

[12] M.I. McMahon and R.J. Nelmes, *Phys. Rev. Lett*., 78, 3883 (1997).

[13] S. Heathman, R.G. Haire, T. Le Bihan, A. Lindbaum, K. Litfin, Y. Méresse and H. Libotte, *Phys. Rev. Lett*., 85, No. 14, 2961-2964 (2000).

[14] J. Akella, Q. Johnson, W. Thayer and R.N. Schock, *J. Less-common Metals*, 68, 95 (1979).

[15] J. Akella, Q. Johnson and R.N. Schock, *J. Geophys. Res.*, B85, 7056 (1980).

[16] R.L. Reichlin, J. Akella, D. Smith and M. Schwab, LBL-12441, pp. 218-219 (1981).

[17] R.B. Roof, R.G. Haire, D. Schiferel, L.A. Schwalbe, E.M. Kmeto and J.L. Smith, *Science*, 207, 1353 (1980).

[18] R.B. Roof, *J. Applied Cryst*., 14, 447 (1981).

[19] R.B. Roof, *Z. Zristallographie*, B15, 307 (1982).

[20] U. Benedict, J.P. Itíe, C. Dufour, S. Dabos and J.C. Spirlet, in *Americium and Curium Chemistry and Technology*, N.M. Edelstein, J.D. Navratil and W.W. Schultz, eds., Reidel, Dordrecht (Boston, 1985), pp. 221-224.

[21] U. Benedict, J.P. Itíe, C. Dufour, S. Dabos and J.C. Spirlet, *Physica B*, 139/140, 284 (1986).

THIN FILMS OF ACTINIDES: MODEL SYSTEMS IN FUNDAMENTAL AND APPLIED RESEARCH

T. Gouder,[1] L. Havela,[1,2] F. Wastin[1] and J. Rebizant[1]
[1]European Commission, Joint Research Centre, Institute for Transuranium Elements
Post Box 2340, D-76175 Karlsruhe, Germany
[2]Department of Electronic Structures, Charles University
Ke Karlovu 5, CZ-121 16 Prague 2, Czech Republic

Abstract

The surface of actinide solids plays an important role in determining their chemical behaviour. In particular the long-term stability of waste materials strongly depends on aspects of the microstructure of surface layers such as defects, grain boundaries and local heterogeneities. We use thin films for studying these aspects both in simple model systems and in more complex real-world systems. We are interested in particular in variable electronic structure in surface layers, surface reconstruction, over-layer/substrate bonding and the electrochemical and leaching properties of the surface layers. The films are produced *in situ* by sputter deposition from small actinide targets (100 mg to 2 g), and studied by photoelectron spectroscopy (XPS and UPS), Auger electron spectroscopy (AES) and ion scattering spectroscopy (ISS). Two examples describing our approach are given below.

Thin films of Pu have been deposited on various substrates: Mg, Al and single crystalline Si(111). For low thickness (around one mono-layer) the films lose their bulk electronic structure. The 5f electrons which in the bulk are de-localised tend to localisation, i.e. they no longer participate in the chemical bonding. This phenomenon is more pronounced for Al and Si substrates, where the surface films seem to spread out because of good over-layer/substrate bonding, while for Mg thick, bulk-like clusters seem to be formed. For thicker films the 5f electrons generally become itinerant but show unexpected temperature dependence, which is attributed to the highly correlated nature of the 5f states, i.e. the closeness to the localisation threshold. Experiments are planned to probe the chemical reactivity of these films.

We investigated the evolution of the electronic structure and chemical reactivity in various U-Ga compounds: UGa_2, UGa_3 inter-metallics, and thin films of U on Ga. It was shown that the surface reactivity of the inter-metallics depends strongly on the deposition temperature. At high temperatures (573 K) a mono-layer of Ga forms at the top surface, as shown by ISS. This leads to a strong passivation of the systems. We were faced with an unusual situation in which working at high temperatures resulted in cleaner films than working at room temperature. The surface reactivity was further probed by adsorption experiments of CO.

SESSION III

Present and Future Synchrotron Facilities for Radionuclide Studies

Chair: L. Soderholm

CURRENT AND FUTURE STUDIES OF ACTINIDE MATERIALS AT THE ADVANCED LIGHT SOURCE

David K. Shuh
Actinide Chemistry Group, The Glenn T. Seaborg Center
Lawrence Berkeley National Laboratory (LBNL)
MS 70A-1150, 1 Cyclotron Road, Berkeley, CA 94720, USA

Abstract

The vacuum ultraviolet (VUV)/soft X-ray region of the synchrotron radiation (SR) spectrum has revolutionised the approach to surface materials chemistry/physics. This spectral region has long been recognised for its potential to afford investigations of fundamental actinide science and to provide an improved analytical surface characterisation capabilities for actinide materials. Previously, the actinide science community was unable to take advantage of the opportunities afforded by VUV/soft X-ray SR methodologies because of radiological safety concerns and the need to prepare pristine actinide materials compatible with experiments in ultra-high vacuum end stations. With the advent of third-generation light sources operating in the VUV/soft X-ray region, such as the Advanced Light Source (ALS) at LBNL, experiments with small amounts of actinide materials are possible. Actinide investigations at the ALS are based on a graded approach to radioactive materials safety and are conducted with the assistance of LBNL Environment, Health and Safety (EH&S) personnel during the experiments. LBNL EH&S personnel have many years of experience supporting experiments utilising radioactive materials at LBNL user-based accelerator facilities.

The SR techniques and technologies used in this energy region have continued to mature, permitting more complicated investigations and enabling new spectroscopic approaches. Of particular importance for work with actinides is the development of the micro-spectroscopy and spectro-microscopy capabilities on several beamlines at the ALS. These capabilities allow the use of small amounts of actinide material. In addition, these techniques can provide information on the spatial distribution of actinide species that complements the spectral information. Early demonstrations of the ability to safely collect data from actinide micro-samples and the active support of the ALS for such experiments has led to the investigations of actinide materials on several different ALS beamlines.

Results from current studies, pending scientific plans and future opportunities for the investigation of actinide materials at the ALS will be presented. The status and capabilities of the ALS Molecular Environmental Science (ALS-MES) Phase I Beamline, an important component for actinide research at the ALS in the near future, will also be discussed.

Acknowledgements

This work is supported by the Director, US Department of Energy, Office of Science, Office of Basic Energy Sciences, Chemical Sciences Division and Materials Sciences Divisions at LBNL under contract No. DE-AC03-76SF00098.

SYNCHROTRON STUDIES ON ACTINIDE-CONTAINING SAMPLES AT THE ADVANCED PHOTON SOURCE

L. Soderholm
Chemistry Division, Argonne National Laboratory
Argonne IL 60439

Abstract

The Advanced Photon Source (APS) is a third-generation synchrotron source located at Argonne National Laboratory in Chicago, IL USA. The APS currently provides a wide range of opportunities for synchrotron studies, including standard spectroscopy techniques as well as beam lines dedicated to micro-focusing and scattering. Of particular interest to the actinide community is the availability of high-energy (> 60 keV) photons that provide high-quality diffraction or scattering data with high resolution and that are not vitiated by absorption or extinction problems. The location of the APS on a DOE site with existing facilities for handling radioactive samples provides a unique opportunity for the experimenter wishing to perform *in situ* studies on actinide-containing samples. Access to these hot laboratory facilities and user support for experiments at the APS may be obtained through the Actinide Facility. Examples of experimental capabilities will be outlined, as will the current availability of the APS for experiments involving radioactivity.

Acknowledgements

This work (LS) is supported by the US DOE, BES-Chemical Sciences and (APS) BES-Material Sciences, under contract No. W-31-109-ENG-38.

OPPORTUNITIES FOR XAFS SPECTROSCOPY ON ACTINIDES AT THE ROSSENDORF BEAMLINE (ROBL) AT THE EUROPEAN SYNCHROTRON RADIATION FACILITY

T. Reich,[1] **G. Bernhard,**[1] **H. Funke,**[1] **C. Hennig,**[1] **N. Schell,**[2] **W. Matz**[3]
Forschungszentrum Rossendorf e.V., P.O. Box 510119, D-01314 Dresden, Germany
[1]Institute of Radiochemistry
[2]Project Group ESRF-Beamline
[3]Institute of Ion Beam Physics and Materials Research

Abstract

Since January 1999 two different experimental stations have been fully operational at the Rossendorf Beamline (ROBL): a radiochemistry laboratory for X-ray absorption spectroscopy of non-sealed radioactive samples and a materials-research station for X-ray diffraction and reflectometry. Both experimental stations have been utilised by external users on the basis of peer-reviewed proposals submitted to the ESRF or in collaboration with the Forschungszentrum Rossendorf (FZR). Since spring 2000, ROBL has become a European Large Scale Facility. This gives external research groups an additional opportunity to obtain beamtime for their experiments at ROBL, which is financially supported in part by the European Commission.

The radiochemistry end station has been designed to study radionuclides of environmental importance. The current regulations agreed upon the ESRR and the French authorities make it possible to study the following actinides at ROBL: ^{nat}Th, ^{231}Pa, ^{nat}U, ^{237}Np, ^{238}Pu, ^{239}Pu, ^{240}Pu, ^{241}Pu, ^{242}Pu, ^{241}Am, ^{243}Am, ^{244}Cm, ^{246}Cm, ^{248}Cm as well as the radionuclides ^{226}Ra, ^{208}Po, ^{209}Po and ^{99}Tc. The maximum equivalent activity of all samples present at ROBL at any given time is 185 MBq (5 mCi). The main characteristics of the optics of ROBL and its radiochemistry end station will be presented [1]. Selected XAFS results obtained on Tc, U, Np and Pu samples will illustrate the performance and the experimental opportunities available at ROBL.

REFERENCE

[1] W. Matz, N. Schell, G. Bernhard, F. Prokert, T. Reich, J. Claußner, W. Oehme, R. Schlenk, S. Dienel, H. Funks, F. Eichhorn, M. Betzl, D. Pröhl, U. Strauch, G. Hüttig, H. Krug, W. Neumann, V. Brendler, P. Reichel, M.A. Denecke, H. Nitsche, "ROBL – A CRG Beamline for Radiochemistry and Materials Research at the ESRF", *J. Synchrotron Rad*., 6, 1076 (1999).

A NEW HARD X-RAY ABSORPTION SPECTROSCOPY MOLECULAR ENVIRONMENTAL SCIENCES BEAMLINE AT SSRL

John R. Bargar,[1] **Gordon E. Brown, Jr.,**[1,2] **Ian Evans,**[1]
Thomas Rabedeau,[1] **Michael Rowen**[1] **and Joe Rogers**[1]
[1]Stanford Synchrotron Radiation Laboratory
P.O. Box 4349, Stanford, CA 94309-0210, USA
[2]Aqueous & Surface Geochemistry Group
Department of Geological & Environmental Sciences
Stanford University, Stanford, CA 94305-2115, USA

Abstract

The growth of X-ray absorption spectroscopy (XAS) as an important tool in molecular environmental sciences (MES) has generated substantial demand for beamline facilities optimised for MES XAS experiments. Chief among these is a beamline designed to accommodate the analysis and safe handling of radioactive materials such as soils contaminated with actinides. In response to this demand, the Stanford Synchrotron Radiation Laboratory (SSRL) has built a new hard X-ray beamline optimised for XAS experiments on MES samples of all types and designed for the safe handling of radioactive samples. A description of the facility concept and commissioning results to date are provided. General user operation of this facility is anticipated to begin in the summer of 2001.

Introduction: Growth of XAS and synchrotron-based molecular environmental sciences

XAS spectroscopy has grown rapidly during the past decade to become one of the essential techniques in MES. Evidence for this growth at SSRL is shown in Figure 1, which includes information on the number of MES beam time proposals submitted, the number of eight-hour shifts awarded to MES users, the number of MES publications and important milestones over the past 10 years. This increased MES activity derives from the unique chemical and local atomic structural information for cations and anions provided by XAS studies, and the ability to probe complex natural materials, solutes, amorphous solids and mixtures of phases that may be inaccessible to other techniques. Recently, XAS studies have been widely used to characterise the speciation and chemical forms of metal contaminants, including actinides and other radionuclides [1-3], in environmental samples. Similar measurements have been performed to optimise chemical separation technologies for high-level waste (HLW) [4-6], to develop stable waste forms for HLW disposal [7-9], and to study the effectiveness of *in situ* remediation technologies for contaminated groundwater such as permeable reactive barriers (PRBs) [10]. The utility of the XAS technique has led to demand for beam time by the MES community in excess of the available capacity of SSRL and other US synchrotron facilities.

Figure 1. Growth of molecular environmental science activity at SSRL over the past 10 years

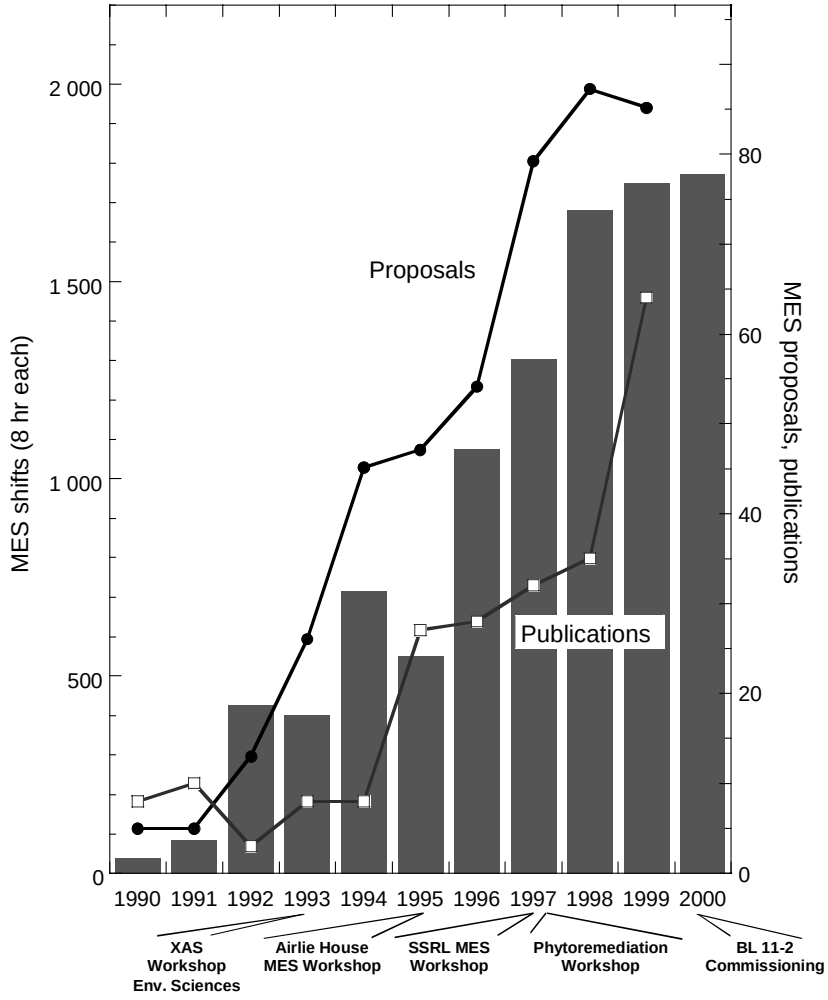

Extension of the XAS technique to demanding problems such as *in situ* characterisation of radioactive and/or nanoscale environmental materials is necessary to fully realise its role in technology and science-based policy development. Meeting these challenges has required development of beamline facilities possessing engineered controls for the safe handling of radioactive samples and optimised specifically for the needs of MES experiments. Chief among these needs are (1) high X-ray fluxes over the range 5-23 keV to provide access to transition-metal K- and heavy-metal and actinide L-edges, (2) high-resolution/high-throughput detector systems for dilute sample fluorescence measurements on chemically heterogeneous samples and (3) high spatial resolution to probe structural and chemical heterogeneities on the micron scale, which are ubiquitous in environmental materials.

Beamline 11-2 concept

Beamline 11-2 was conceived in the context of these issues and designed to provide a dedicated facility for MES XAS measurements. Key aspects of beamline 11-2 are illustrated in Figure 2 and include the following items:

Figure 2. Schematic layout of principle optical components of SSRL BL 11-2

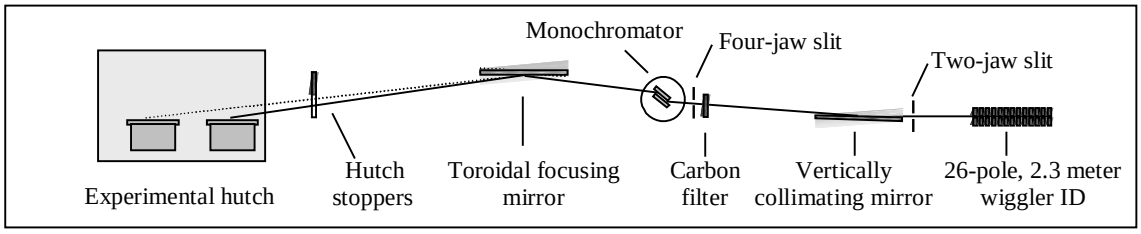

Source

The 26-pole, 2 Tesla hybrid magnet wiggler has a critical energy of 12 keV, providing continuous high flux throughout the 5-23 keV energy range. Figure 3 shows a comparison of the flux from this source on the current SPEAR2 storage ring at SSRL versus an APS undulator A insertion device. When SPEAR3 is completed in late 2003 and is operating at the design current of 500 mA, the flux curve for the BL 11-2 wiggler will be similar to that of an APS undulator A insertion device over the energy range 5-15 keV.

Monochromator

The necessity of stable beam during scanned energy (XAS) measurements drove the design of a mechanically robust, pseudo-channel cut (variable exit geometry), double-crystal monochromator. Intensive cooling, provided by a pressurised liquid nitrogen (LN) closed-loop re-circulating chiller system, is required to minimise thermal deformation of the monochromator crystals under the high power loadings produced by the beamline 11 wiggler. The monochromator chamber contains two pairs of Si(220) crystals (0° and 90° azimuthal angle orientations). These crystals were chosen because of their accessible energy range, energy resolution and user familiarity with their glitch curves. Both pairs of crystals are maintained in vacuum on a rotating turret and can be interchanged via computer control, dramatically improving the efficiency of crystal changes. Commissioning tests performed in June 2000 indicate the LN-cooled monochromator to be remarkably stable; I_0 noise attributable to the monochromator was measured to be ≤ 0.05% during scanned measurements at LN flow rates of 500 L/hr. and 2 atm pressure.

Figure 3. Beamline 11-2 calculated flux at 2 T wiggler field, SPEAR 2 (100 mA), 1.5 mrad horizontal fan and full vertical acceptance

Flux curves for an APS undulator A are shown for comparison, calculated at 7.0 GeV, 100 mA, full central cone. To facilitate a general comparison, calculations do not account for X-ray optic efficiencies or carbon and beryllium windows/ filters. (Beamline 11-2 contains 50 μm carbon and 660 μm beryllium windows.)

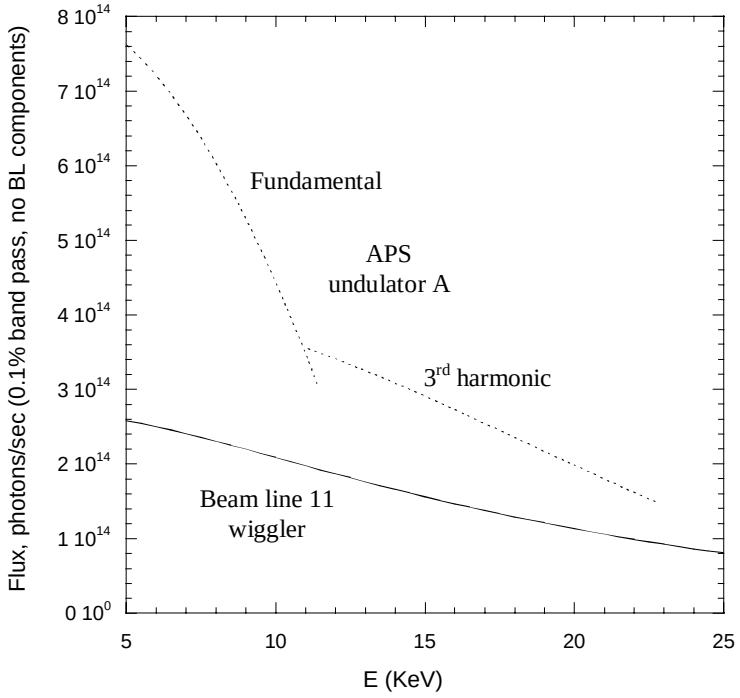

Rh-coated reflecting optics

A collimating mirror is located upstream of the monochromator to optimise monochromator energy resolution and provide high energy power filtering. Low-energy power filtering is provided by an insertable graphite filter located between the collimating mirror and the monochromator. A toroidally bent cylindrical mirror located between the monochromator and experimental hutch provides vertically and horizontally focused beam into a spot of dimensions ca 0.4×2 mm at 5 to 10 KeV, reducing to about 0.25×1 mm at 19 KeV (SPEAR2 storage ring). These beam dimensions should reduce by approximately a factor of 2 when SPEAR3 is fully operational in late 2003. Quasi-focused beam is available from 19 to 23 KeV. A mirror pitch feedback system integrated with the M1 mirror provides automatic correction of vertical beam motion at frequencies ≤ 1Hz. Table 1 lists X-ray fluxes and accessible energy ranges for operation of BL 11-2, together with focused beam size and monochromator energy resolution.

Table 1. Beamline 11-2 characteristics at 2 T wiggler field

Flux (10 KeV)	2.0×10^{13} sec^{-1}
Focused beam size (10 KeV)	0.4×2 mm
Energy resolution (10 KeV)	0.65 eV (FWHM)
Focused energy range	4.5-38 KeV
Unfocused energy range	4.5-19 KeV

Hutch instrumentation

As shown in Figure 4, two hutch tables (forward and rear, centred at 27 and 29 m from the source, respectively) are provided for experiments at beamline 11-2. Measurements on radioisotopes will be carried out on the rear table, which is optimally located for focused beam measurements in the 15 to 19 keV range. The hutch is also equipped with a high-resolution/high-throughput 30-element Ge array detector, equipped with digital signal processors under full computer control. The detector is supported by a variable-angle stand that can be positioned in horizontal side-observing and vertical down-observing attitudes. Commissioning tests conducted in June 2000 indicate that the 30-element detector performs well. Detector energy resolution at 0.25 μsec shaping time is *ca* 250 eV FWHM (Zn Kα), and high quality XAS data have been collected from dilute samples at incoming count rates up to 400 KHz. As a feasibility test, U L_{III}-edge EXAFS spectra were measured from a dilute sample (190 ppm U and *ca* 5 000 ppm Sr) collected from an aquifer remediation field site (Figure 5). Due to the low U concentration and overlap between the Sr Kα and U Lα fluorescence lines, it was previously not possible to analyse this sample beyond 6 A^{-1} at SSRL wiggler beamlines used for MES measurements. On beamline 11-2, EXAFS data were collected from this sample (using the 30 element array) up to *ca* k = 12 A^{-1}.

Figure 4. Layout of beamline 11-2 hutch area and radiological controls

Radioactive samples that require continuous monitoring will be analysed on the rear hutch table within Zone 1, which is defined by a small enclosure of approximately 0.5 m^3 volume surrounding the sample space.

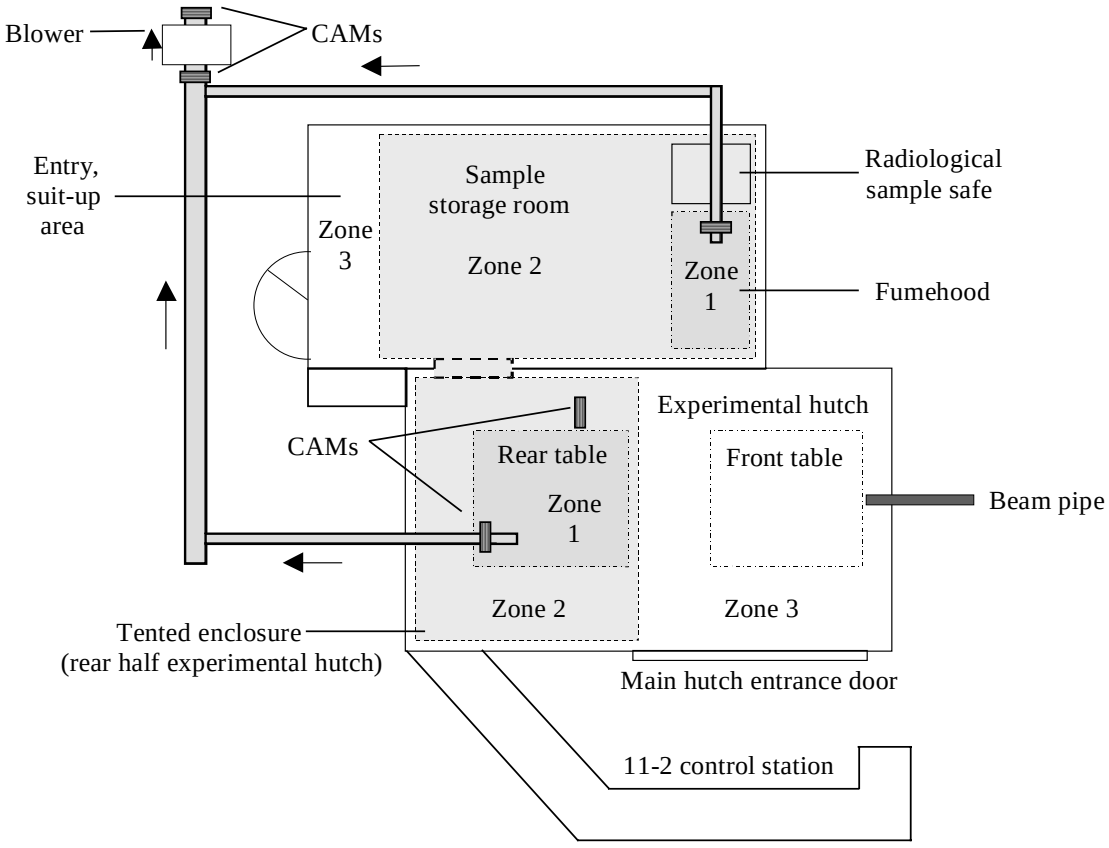

Figure 5. Comparison of background-subtracted, k^3-weighted U L_{III}-EXAFS spectra collected on SSRL wiggler BL 11-2 and wiggler BL 4-1 (10 scans each) from a field sample collected at Fry Canyon, Utah and containing 190 ppm uranium [10]

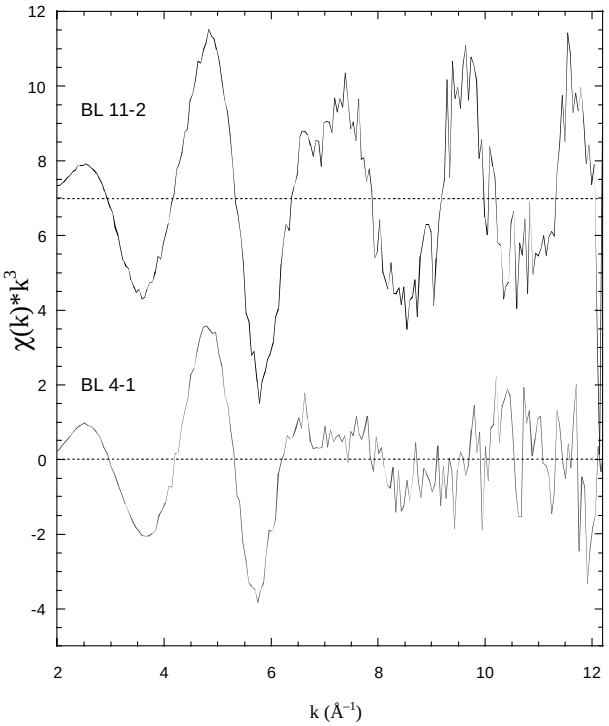

The beamline 11-2 hutch is also equipped with a spectrometer designed for grazing incidence XAS, reflectivity, and specular XSW measurements. Metal micro-capillary optics that can focus 10^{11} photons/sec into a 5 μM beam spot size using SPEAR2 are currently under design, and will be installed on the forward hutch table. Other detectors and instrumentation available include a liquid-helium cryostat modified to accommodate high X-ray power loadings, a Lytle-type fluorescence detector, transmission ionisation chambers and computer-controlled slits and sample positioners.

Radiological controls at beamline 11-2

A series of radiological controls have been implemented at beamline 11-2 to permit analysis of radioactive samples, while providing an acceptable level of safety to the SSRL community. Primary elements of the radiological controls include engineered barriers (cf. Figure 4), personal protective equipment and administrative measures. Radioactive samples are required to be contained within one to three layers of containment material, depending on isotope class and toxicity. In addition, samples undergoing analysis at beamline 11-2 will be separated from the general laboratory air space by three containment zones defined by physical enclosures, through which air flow is controlled by negative pressure gradients. Continuous air monitoring (CAM) of the ventilation system and use of high efficiency particulate air (HEPA) filters insure that an accidental release of radioactivity in the hutch can be detected in real time and radioactive material entrapped, thereby minimising the impact to other SSRL operations. Activity levels are monitored at multiple points along the ventilation system. Critical monitoring points include the entry point to the system (i.e. above the sample) and immediately upstream and downstream of the HEPA filters.

A sample inventory/storage room is located immediately adjacent to the beamline 11-2 hutch to accommodate sample unpacking/repacking, inspection, containment preparation and activity surveying in a controlled, monitored environment. Samples can be transported into the beamline 11-2 experimental hutch via a direct doorway, obviating the need to enter the communal SSRL air space with prepared samples. In addition to the alarmed CAM system, the beamline is equipped with hand-held radiation monitors, swipe counters, hand friskers and a variety of accessory probes to accommodate detection of α, β and γ radiation.

Isotope quantity limits and administrative controls

Radiological controls required for a given experiment are based primarily on the isotope to be studied, its physical form and the total isotope quantity required. Upper limits on isotope quantities have been established by SLAC, based on the US Department of Energy standards (document DOE-ST-1027-92). These limits generally exceed the isotope quantity necessary to conduct an experiment by one or more orders of magnitude. The total radiation levels allowed at SSRL at any particular time are limited to half the limit of a DOE Category 3 Non-nuclear Facility (e.g. up to 260 mCi (4.2 g) of ^{239}Pu or up to 210 mCi (300 g) of ^{237}Np). Users are urged to plan experiments based on the minimum isotope quantities required. This procedure is key to minimising the total on-site quantity of isotopes and associated risks to the SSRL community and facility. Based on such an analysis and in conjunction with the experimenter, SSRL establishes isotope quantity limits specific to the individual experiment. Forms and guidelines relevant to this process can be found on the web at http://www-ssrl.slac.stanford.edu/safety/.

Acknowledgements

We wish to acknowledge the support of the US Department of Energy, Division of Chemical Sciences for providing construction funding for beamline 11-2 at SSRL and continuing operating support for this beamline for the Molecular Environmental Science community.

REFERENCES

[1] M.C. Duff, M. Newville, D.B. Hunter, P.M. Bertsch, S.R. Sutton, I.R. Triay, D.T. Vaniman, P. Eng, M.L. Rivers, *J. Synchrotron Rad*., 6, 350-352 (1999).

[2] M.J. Piana, C.C. Fuller, J.R. Bargar, J.A. Davis, M. Kohler, in review (2001).

[3] J.R. Bargar, R. Reitmeyer, J.J. Lenhart, J.A. Davis, *Geochim. Cosmochim. Acta*, 64, 2737-2749 (2000).

[4] P.G. Allen, J.J. Bucher, D.K. Shuh, N.M. Edelstein, I.M. Craig, *Inorg. Chem.*, 39, 595-601 (2000).

[5] M.P. Jensen, L.R. Morss, J.V. Beitz, D.D. Ensor, *J. Alloys and Compounds*, 303, 137-141 (2000).

[6] D.L. Clark, S.D. Conradson, R.J. Donohoe, D.W. Keogh, *Inorg. Chem.*, 38, 1456-1466 (1999).

[7] C.H. Booth, P.G. Allen, J.J. Bucher, N.M. Edelstein, D.K. Shuh, G.K. Marasinghe, M. Karabulut, C.S. Ray, D.E. Day, *J. Mater. Res.*, 14, 2628-2639 (1999).

[8] B.D. Begg, N.J. Hess, W.J. Weber, S.D. Conradson, M.J. Schweiger, R.C. Ewing, *J. Nuclear Mater.*, 278, 212-224 (2000).

[9] N.J. Hess, W.J. Weber, S.D. Conradson, *J. Alloys and Compounds*, 271-273, 240-243 (1988).

[10] C.C. Fuller, M.J. Piana, J.R. Bargar, J.A. Davis, M. Kohler, in review (2001).

INSTRUMENTAL DEVELOPMENTS FOR XAFS ANALYSIS OF DILUTE ENVIRONMENTAL SAMPLES AT HASYLAB

E. Welter
HASYLAB at DESY, Hamburg, Germany

Abstract

In many environmental samples the detection limit of XAFS analyses is less determined by the flux of the X-ray source than by the detector concept. Two major problems restrict the detection limits on the detector side. First, the fact that a detector must initially count all photons, including those originating from the matrix, meaning that the detector might be in overflow although the number of photons from the analyte is still small. Second, the limited energy resolution of conventional energy-dispersive detectors causes overlaps between neighbouring emission lines. Both problems can be overcome by use of a secondary monochromator which filters out unwanted photons before they reach the actual detector. The design and projected abilities of a planned secondary detector for analyses in dilute (environmental) samples at HASYLAB will be described in the following.

Introduction

Over the past few years XAFS spectroscopy has turned out to be a valuable instrument for the determination of the chemical form of metals in environmental samples. The chemical form of metals, radioactive and non-radioactive, has been investigated in real environmental samples, mainly by fingerprint methods [1,2] and in synthetic environmental samples. The latter investigations aim at the exploration of the interaction of metals of interest with single important constituents of environmental samples like clay, iron and manganese minerals or different organic compounds. In either case the concentration of the analyte is normally small. That means that XAFS spectra from these samples have to be measured in diluted samples. The most often used technique to do this is to measure the spectra using the fluorescence yield technique (Fl-XAFS). The detectors used are (multiple) energy-dispersive semi-conductor detectors.

Conventional energy dispersive X-ray detectors must measure all photons coming from the sample, including the elastically scattered photons and fluorescence photons from matrix elements. This fact results in three major problems: First, the elastically scattered photons produce a background which, to make it worse, changes its value during an energy scan (see Figure 1, right). Second, the detector is in overflow although the number of the interesting photons is still small (Figure 1). Third, it is sometimes impossible to separate neighbouring emission lines (see Figure 2), because the FWHM of an emission line is between ~130 and 1 000 eV, depending on the integral count rate and the resulting necessary shaping time.

As a result of the described problems is the detection limit in many cases more strongly determined by the detector than by flux from source. A better detector should avoid the mentioned problems by excluding the background photons from the actual counting device.

Secondary monochromator

A secondary monochromator for XAFS analysis of diluted samples should fulfil two major tasks. First it must offer an energy resolution which is large enough to cut off the emission lines from neighbouring matrix elements and from the elastically scattered photons. The bandwidth on the other hand should not be smaller than the width of the interesting fluorescence peak. So typically a bandwidth of roughly 10 eV seems suited. The second task a secondary monochromator should fulfil is that it should increase the used solid angle, meaning that the analysator design has to focus the emitted photons on the detector.

Figure 1. Pb *L3* Fl-XAFS measured in a sample from the cinder disposal of a metal smelter facility

c(Zn) = 116.0 g/kg, c(Pb) = 42.5 g /kg, c(Cu) = 8.2 g/kg
Left total count rate spectra, right energy-filtered spectra

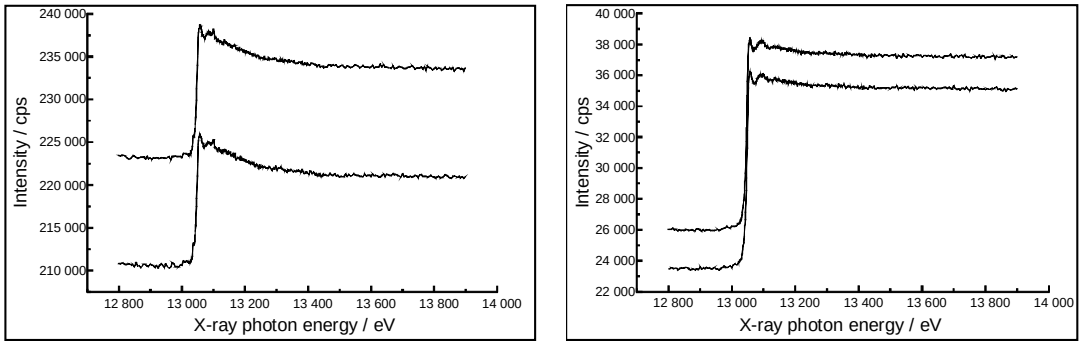

Figure 2. Fluorescence spectrum of a sample which contained small amounts of Cu and Cr in a Fe matrix, measured with a "conventional" energy dispersive detector (Ge 5 Pixel) at high count rates (200 kcps)

Note that the energy of the incident beam (elast.) is much higher than it would be during a XAFS measurement

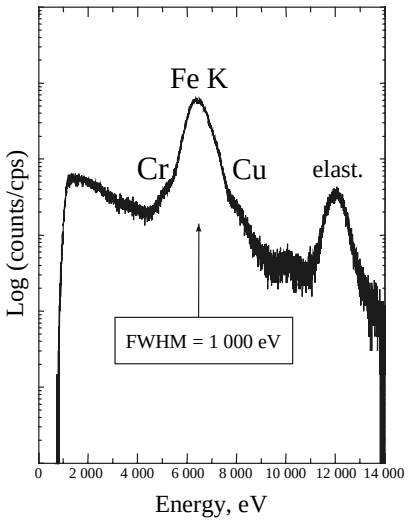

An often-used design that fulfils both tasks mentioned above is the Johann Geometry. The Johann Geometry is based on the Rowland circle, meaning that sample, analysator crystal and detector are positioned on a circle with radius R. In the Johann Geometry a bent analysator crystal with a bending radius of 2R is employed. This leads to focusing on the detector.

In contrary to the more common design with sample, analysator crystal and detector on the circumference of the Rowland circle [3], the sample will be positioned inside the circumference of the Rowland circle (see Figure 3). This enables to work with an illuminated area on the sample, thus minimising the risk of radiation damage at high flux beamlines and the need for homogenous samples [4]. In contrast, the "classical" design works with a spot source on the Rowland circle and the energy resolution depends strongly on the spot size. Both designs are currently used at synchrotron radiation sources in several different fields of science, mostly for X-ray Raman spectroscopy [5-10]. If for one reason or another spot measurements are necessary, it is possible to mount the sample on the circumference of the Rowland circle. The large flexibility of the design can only be used with a 2-D detector, therefore a CCD chip will be used as detector.

Figure 4 shows the broadness of the energy band that can be mapped on a 3 cm wide CCD detector over the Rowland radius (R_{row}). Together with the chosen crystal and the resulting Bragg angle, R_{row} determines the achievable energy resolution and limits the achievable bandwidth. However even with a Si(111) crystal working at an incident angle of roughly 20° the energy resolution is better than 1 eV/pixel (for a detector with 2 000 pixels in a row and an R_{row} of 0.5 m).

Figure 6 shows a schematic top view of the proposed detector system. Four or five crystals are mounted on a crystal changer, because it is necessary to use different crystals for different resolutions and energies. The whole secondary monochromator is installed in an elliptical-shaped steel tank to enable working under UHV conditions if necessary. The Rowland circle, which is defined by the analysator crystal and the detector, can be moved along the long axis to adjust the distance between the fixed sample and the analysator crystal. This enables measurements with different solid angles and energy resolutions. The analysator crystals used are either spherically (for large solid angle) or cylindrically (for high-energy resolution) bent.

Figure 3. Ray paths for the proposed secondary monochromator

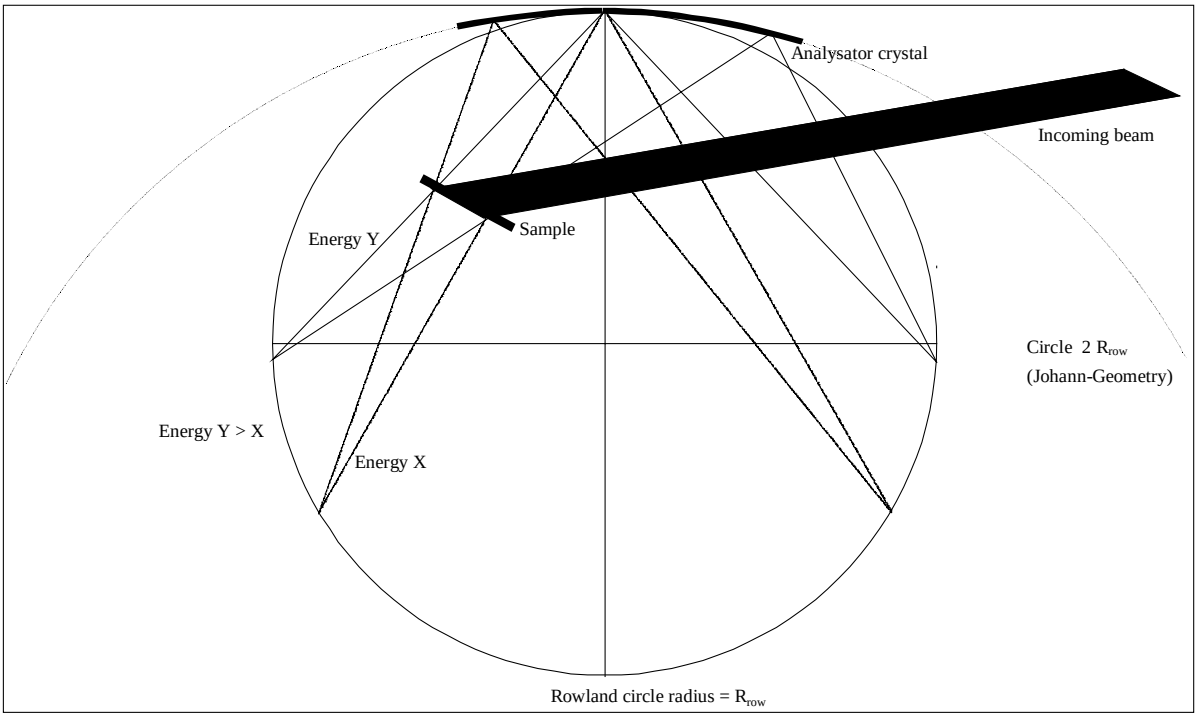

Figure 4. Energy range mapped on a 3 cm wide CCD detector vs. Rowland radius, Si(111), 6 000 eV, θ = 19.2°

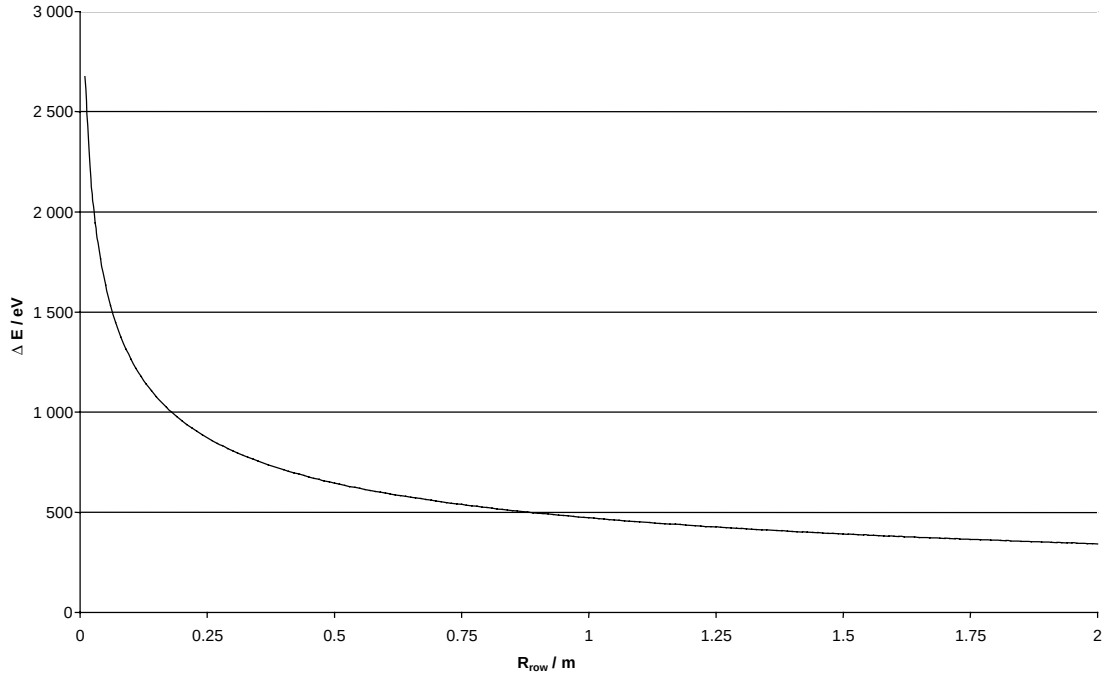

Figure 5. Energy range mapped on a 3 cm wide CCD detector vs. Rowland radius, Si(111), 6 000 eV, θ = 19.2°

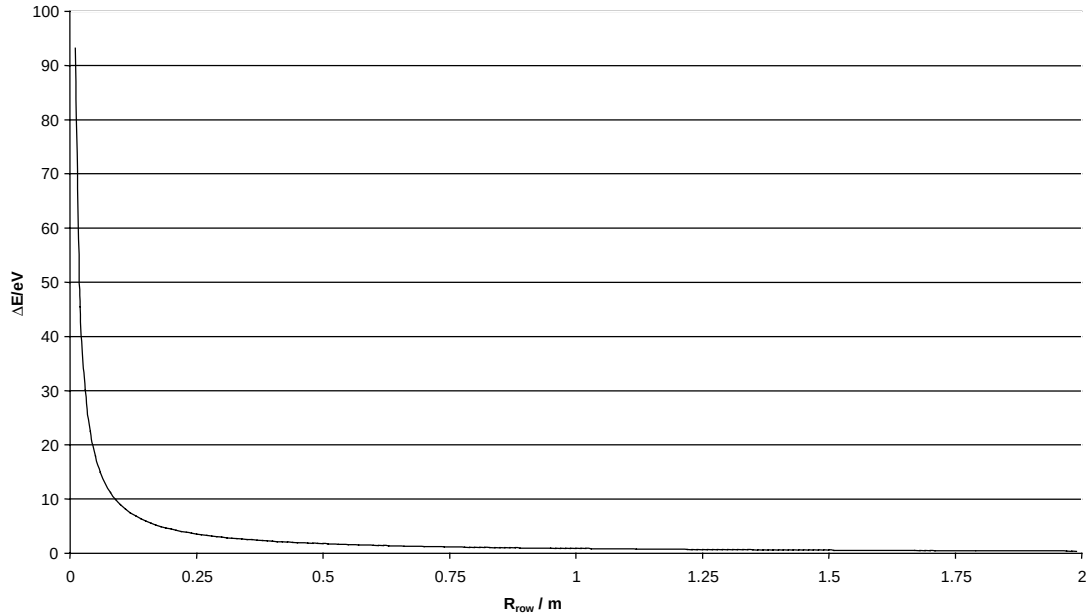

Figure 6. Top view of the principal design of the proposed second monochromator

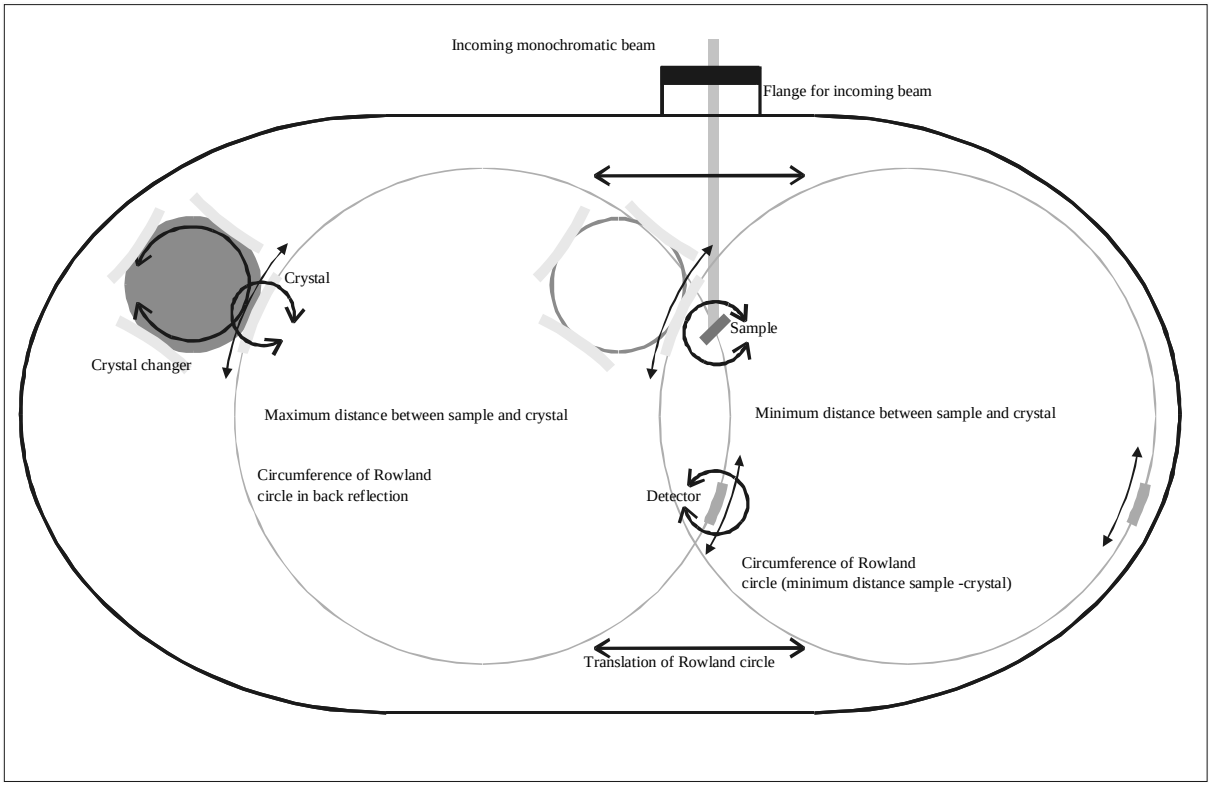

Possible use in other research fields

Due to the large flexibility of parameters such as energy resolution, band width, illuminated area, etc., the detector can be used in several other scientific fields. Examples are methods like non-resonant inelastic X-ray scattering (X-ray Raman spectroscopy) or resonant inelastic X-ray scattering (RIXS). This might offer some additional fields of work with environmental samples. X-ray Raman spectroscopy for instance enables the measurement of the K-edge “absorbance spectra” of light elements like C, N and O in the hard X-ray region. That means under ambient conditions (pressure, humidity, etc.) [10].

Conclusion

A secondary monochromator which uses a modified Johann geometry seems suited to overcome the problems which arise in the measurement of Fl-XAFS in highly diluted samples. This detector design offers, aside from the expected considerable decrease of the detection limits in speciation analysis, some potential use in different areas of physics.

REFERENCES

[1] A. Manceau, M.C. Boisset, G. Sarret, J.L. Hazemann, M. Mench, P. Cambier, R. Prost, *Environ. Sci. Technol*., 30, 1540-1552 (1996)

[2] E. Welter, W. Calmano, S. Mangold, L. Tröger, *Fresenius J. Anal. Chem*., 364: 238-244 (1999).

[3] U. Bergmann, S.P. Cramer, SPIE, Vol. 3448, 198-209 (1998).

[4] Th. Kirchner, S. Bocharow, M. Henke, G. Dräger, HASYLAB Annual Report 1998, 309-310 (1998).

[5] Y. Izumi, H. Oyanagi, H. Nagamori, *Bull. Chem. Soc. Jpn*., 73, 1-7 (2000).

[6] K. Tohji, Y. Udagawa, *Phys. Rev. B*, 36, 9410-9412 (1987).

[7] P. Pattison, H-J. Bleif, J.R. Schneider, *J. Phys. E*, 14, 95-99 (1981).

[8] X. Wang, S.P. Cramer, *J. Phys. IV France*, 7, C2-361-C2-363 (1997).

[9] J-J. Gallet, J-M. Mariot, L. Journel, C.F. Hague, J-P. Kappler, G. Schmerber, D.J. Singh, G. Krill, J. Goulon, A. Rogalev, *Phys. Rev. B*, 57, 7835-7840 (1998).

[10] N. Watanabe, H. Hayashi, Y. Udagawa, K. Takeshita, H. Kawata, *Appl. Phys. Lett*., 69, 1370 (1996).

SYNCHROTRON ENVIRONMENTAL LABORATORY (SUL) AT ANKA

Melissa A. Denecke
Forschungszentrum Karlsruhe, Institut für Nukleare Entsorgung
P.O. Box 3640, D-76021 Karlsruhe; Germany

Abstract

A research facility dedicated to environmental/geochemical research, the Synchrotron Environmental Laboratory (SUL), is planned to be installed and operated at ANKA. ANKA is the new synchrotron facility at the Research Centre Karlsruhe (FZK), Karlsruhe, Germany. ANKA is now in commissioning and planning operations for the fall of 2000.

As the Institute for Nuclear Waste Disposal (INE) at FZK conducts a vigorous synchrotron-based research programme, INE was instrumental in the original impetus for installing such a facility at ANKA. These research activities at INE concentrate on actinide speciation in nuclear waste forms, geological media and geochemical model systems. In order for INE to direct their synchrotron research activities to ANKA, equipment and licensing required for performing experiments on actinide-containing samples is required. One great advantage of performing experiments on actinide-containing samples at ANKA is that the INE radiological laboratories lie in the near vicinity of the facility. This will minimise transport hazards and costs and allow experiments to be performed on samples whose characteristics may change with time.

Experiments on radioactive samples with activities below the exemption level, according to German regulations, will be possible at ANKA at the start of operations. Licensing for work on higher levels of activity will be applied for in the future. The decades of experience in radiological work at FZK will facilitate development of procedure and equipment as prerequisites to licensing.

A consortium of synchrotron radiation-user groups with environmental research interests has specified their requirements and needs for this facility. This scientific case serves as the foundation for the SUL design and is the basis for an application for federal funding. The SUL design reflects the heterogeneity and complexity of challenges facing researchers in the environmental/geochemical sciences. X-ray absorption fine structure (XAFS) speciation methods, applications of micro-focusing for studies on heterogeneous systems and imaging techniques as well as synchrotron infrared spectroscopy are planned to be available.

BEAMLINE PROJECT TO STUDY RADIOACTIVE MATERIALS AT SOLEIL SYNCHROTRON RADIATION SOURCE

S. Lequien,[1] **M. Idir,**[2] **J-P. Duraud,**[1] **J-P. Itié**[3]**, P. Berkvens**[4]
[1]Laboratoire Pierre Süe, CEA-CNRS, CE Saclay, F-91191 Gif-sur-Yvette, France
[2]LSAI, Centre Universitaire Paris Sud, F-91898 Orsay Cedex, France
[3]LURE, CNRS-CEA-MR, Centre Universitaire Paris Sud, Bât. 209D, F-91898 Orsay Cedex, France
[4]ESRF, B.P. 220, F-38043 Grenoble Cedex, France

Abstract

In the perspective of the construction of the new French synchrotron radiation facility SOLEIL, the scientific council decided that a beamline dedicated to study radioactive materials would be erected. Based on collaboration between different scientific groups, a multi-purpose beamline has been chosen regarding the needs of each. Either XAS or diffraction experiments could be performed. Special attention will be paid to the focusing beam in order to reduce the radioactivity by studying small samples or to probe local atomic arrangements.

This presentation will report on the conceptual design of the station including ray-tracing studies and layout.

POSTER SESSION

Chairs: D.K. Shuh, T. Reich

EXAFS INVESTIGATIONS OF EARTH-ALKALINE METAL URANYL TRICARBONATO COMPLEXES

S. Amayri, T. Reich, G. Bernhard
Forschungszentrum Rossendorf e.V., Institute of Radiochemistry
P.O. Box 510119, D-01314 Dresden, Germany

Abstract

Carbonate and bicarbonate are the common anions found in significant concentrations in many natural waters, and are exceptionally strong complexation agents for actinide ions. Seepage, flooding and mining waters from the uranium mining area in the south-east of Germany (Saxony and Thuringia) contain relatively high amounts of magnesium, calcium, carbonate and sulphate ions. In these waters the pH values range from 7.0 to 8.0 and the uranium content is about 0.02 mmol/L where magnesium, calcium and carbonate concentrations are 11.6 mmol/L, 6.9 mmol/L and 3.9 mmol/L, respectively [1]. The existence of the natural complexes $Ca_2UO_2(CO_3)_{3(aq)}$ and $Mg_2UO_2(CO_3)_{3(aq)}$ were recently able to be confirmed by spectroscopic measurements [2].

We performed extended X-ray absorption fine structure (EXAFS) measurements at the uranium L_{III}-edge to study the structures of these complexes. The results obtained from these complex solutions are compared with those from the corresponding EXAFS and XRD data related to the secondary minerals of uranium, liebigite, $Ca_2[UO_2(CO_3)_3]\cdot 10H_2O$ and bayleyite, $Mg_2[UO_2(CO_3)_3]\cdot 10H_2O$ and they are in good agreement.

REFERENCES

[1] G. Bernhard, G. Geipel, V. Brendler, H. Nitsche, "Uranium Speciation in Waters of Different Uranium Mining Areas", *J. of Alloys and Compounds*, 201, 271-273 (1998).

[2] G. Bernhard, G. Geipel, V. Brendler, H. Nitsche, "Speciation of Uranium in Seepage Waters of a Mine Tailing Pile Studied by Time-resolved Laser-induced Fluorescence Spectroscopy (TRLFS)", *Radiochim. Acta*, 74, 87-91 (1996).

PHOTO-EMISSION STUDIES OF THE α AND δ PHASES OF PLUTONIUM AT THE ADVANCED LIGHT SOURCE

D.A. Arena and J.G. Tobin
Lawrence Livermore National Laboratory (LLNL)
Livermore, CA 94550, USA

J. Terry, R. Schulze, J. Lashley, J.D. Farr, and T. Zocco
Los Alamos National Laboratory (LANL)
Los Alamos, NM, USA

D.K. Shuh and E. Rotenberg
Lawrence Berkeley National Laboratory (LBNL)
Berkeley, CA 94720, USA

Abstract

Metallic plutonium has one of the most complex and intriguing structural phase diagrams on the periodic table. Of particular importance are the low symmetry, high density α (monoclinic) phase and the higher symmetry, lower density δ (fcc) phase. We have examined the α and δ allotropic phases of Pu using high resolution soft X-ray photo-emission (XPS) and resonant photo-emission spectroscopy (ResPES) conducted at the Spectro-microscopy Facility at the Advanced Light Source of LBNL and have identified several pronounced differences in the photo-emission spectra between the two phases. The core level XPS spectra of the $4f_{7/2}$ spectral line from both α and δ Pu samples exhibit a sharp metallic peak which is indicative of a core hole that is readily screened by de-localised electrons. However, the screening is enhanced in the α Pu spectrum, suggesting a larger degree of de-localisation in α Pu than in δ Pu. A similar picture emerges from the valence band ResPES measurements. In those data, the resonant enhancement of the valence band signal was more pronounced in δ Pu than in α Pu. Such an increased resonant enhancement is consistent with a greater degree of localisation in δ Pu.

The flexibility afforded by the use of synchrotron radiation as the excitation source also allows the accurate determination of the cleanliness of the Pu samples. Spectra acquired at photon energies corresponding to laboratory XPS sources show little oxidation of the samples. Spectra acquired at lower photon energies, which enhances the sensitivity to the O 1s level, indicate that non-negligible amounts of oxygen are present in samples that were thought to be clean. As a result, we are currently constructing an improved spectrometer and vacuum system which will minimise the interval between sample cleaning and data acquisition. Such a system shall allow us to systematically examine the development of oxidation on Pu and other highly reactive samples. The system is also designed to heat and cool the sample *in situ* and thus allow us to follow the changes in the electronic structure of metallic Pu as it undergoes the transformation from the α phase through the δ phase.

Acknowledgement

This work is supported by the US Department of Energy.

ELECTROCHEMISTRY AND SPECTRO-ELECTROCHEMISTRY OF UO_2^+ COMPLEXES IN AQUEOUS SOLUTION

B. Atkins, F.R. Livens, D. Collison and I. May
Department of Chemistry, The University of Manchester
Manchester M13 9PL, UK

Abstract

Uranyl ions (UO_2^{2+}) are strongly complexed by $[CO_3]^{2-}$ in aqueous solution, the tricarbonato complex being the most extensively studied. Cyclic voltammetry studies show that the U(VI)/U(V) couple is irreversible, whereas the analogous Np couple is reversible. Electrochemical and spectro-electrochemical experiments have determined the stability of the reduced U(V) species under varying conditions. The stability of the reduced species increases with increased $[CO_3]^{2-}$ concentration. EXAFS experiments have shown that both axial and equatorial U-O distances increase on reduction, however the basic geometry remains unchanged [1]. Cyclic voltammetry studies at pH 12.5 suggest that the formation of a mixed CO_3^{2-}/OH^- ligand species is increased at the reduced U(V) centre compared to U(VI). An *in situ* spectro-electrochemical cell has been designed to allow study of less stable U(V) species.

Introduction

The solution chemistry of U(V) is not as widely studied as other oxidation states because of its susceptibility to disproportionation:

$$2UO_2^+ + 4H^+ \rightarrow UO_2^{2+} + U^{4+} + 2H_2O$$

UO_2^{2+} in aqueous solution is readily complexed by $[CO_3]^{2-}$ anions, this is reflected in high stability constants [2] and electrochemically in large negative shifts in reduction potential compared to the aquated ion [3].

Methods

The main experimental tool used is cyclic voltammetry, a linear potential sweep technique. A three-electrode cell is used comprising a mercury drop working electrode, a Pt wire secondary electrode and a Ag/AgCl reference electrode. A potential is applied to a solution cell starting at an initial value E_i, the potential is swept to a switching potential, E_λ where the sweep is reversed back to E_i. The current flow is measured as a function of applied potential.

Results

Cyclic voltammograms for the UO_2^{2+}/UO_2^+ couple at (a) varying $[CO_3]^{2-}$ concentration and (b) repeated scans at pH 12.5 are shown in Figures 1 and 2 respectively and the results summarised in Tables 1 and 2. As $[CO_3]^{2-}$ concentration is increased there is a decrease in the peak separation indicating an increase in reversibility of the system which would suggest a greater stability of the $[UO_2(CO_3)_3]^{5-}$ complex. The trend in $i_{pa}/i_{pc} \rightarrow 1$ also indicates an increase in reversibility. The cathodic peak shifts a great deal more than the anodic peak which again points to an increase of stability.

Figure 1. First scan voltammograms of UO_2^{2+}/UO_2^+ in aqueous solution with varying concentration of carbonate

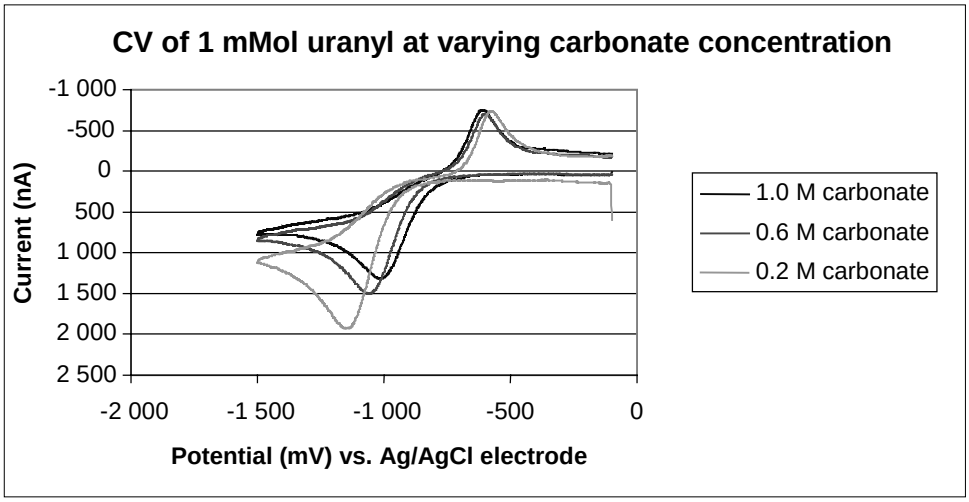

Table 1. Summary of cyclic voltammetry results for UO_2^{2+}/UO_2^{+} in aqueous solution with varying concentration of carbonate. Formal potentials are calculated at a scan rate of 50mV s^{-1} vs. Ag/AgCl electrode.

$[CO_3]^{2-}$ concentration (M)	Cathodic peak (V)	Anodic peak (V)	Formal potential (V)	i_{pa}/i_{pc}
0.2	-1.45	-0.57	-0.856	0.46
0.4	-1.095	-0.51	-0.845	0.51
0.6	-1.05	-0.60	-0.825	0.50
0.8	-1.02	-0.61	-0.815	0.57
1.0	-1.00	-0.61	-0.805	0.61

Figure 2. First and fifth scan voltammograms of UO_2^{2+}/UO_2^{+} in aqueous carbonate solution at pH 12.7

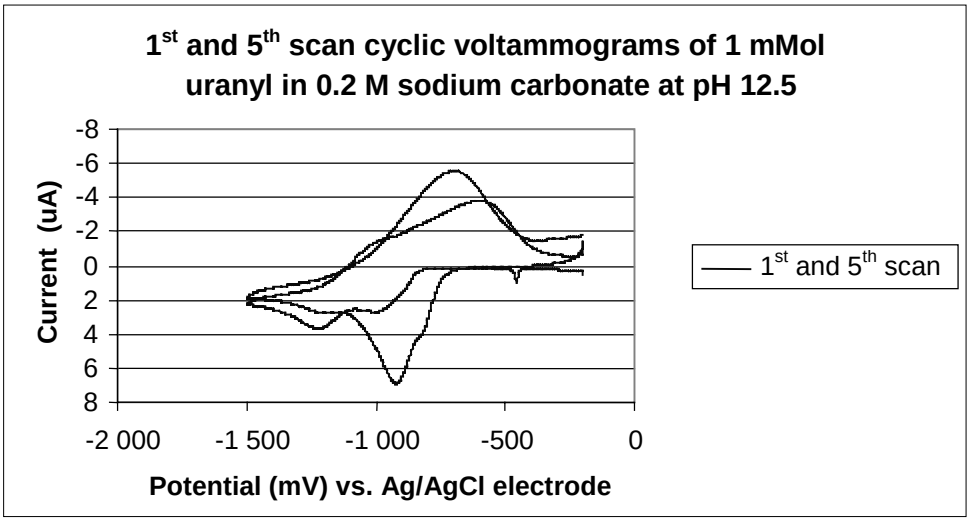

Table 2. Summary of cyclic voltammetry results for UO_2^{2+}/UO_2^{+} in aqueous solution with 0.2 M carbonate at pH 12.5. Formal potentials are calculated at a scan rate of 50mV s^{-1} vs. Ag/AgCl electrode.

Scan no.	Cathodic peak (V)	Anodic peak (V)	Formal potential (V)	i_{pa}/i_{pc}
1	-1.22	-0.58	-0.90	0.99
2	-0.92	-0.70	-0.81	0.82

Cyclic voltammetric experiments have shown that if a solution of uranyl carbonate at pH 13 is repeatedly scanned there is a gradual disappearance of the characteristic $[UO_2(CO_3)_3]^{4-}/[UO_2(CO_3)_3]^{5-}$ reduction peak and the appearance of another reduction peak at a potential about 300 mV more positive. We suggest that it is possible that there is increased ligand exchange when the uranyltricarbonato species has undergone reduction, a theory that is consistent with the decreased charge on the uranyl ion. A suggested reaction scheme is shown in the scheme:

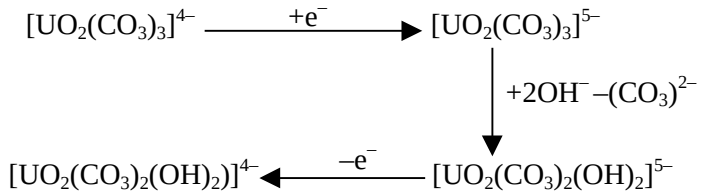

The new complex is significantly less stable than the original tricarbonato complex, as demonstrated in the large positive translation both reduction and oxidation peaks.

Conclusions

The oxidation state U(V) is stabilised to a higher degree than expected in carbonate solution and this stability of a 1 mMol solution increases dramatically with $[CO_3]^{2-}$ concentration within the range of 0.2-1.0 M. The reduced state is more susceptible to ligand exchange with OH^- groups at high pH than the oxidised state.

Future work

The limited stability of U(V) solution species requires the development of an *in situ* spectro-electrochemical cell (Figure 3) to study these short-lived species.

Figure 3. Design of *in situ* spectro-electrochemical cell optical and XAS measurements

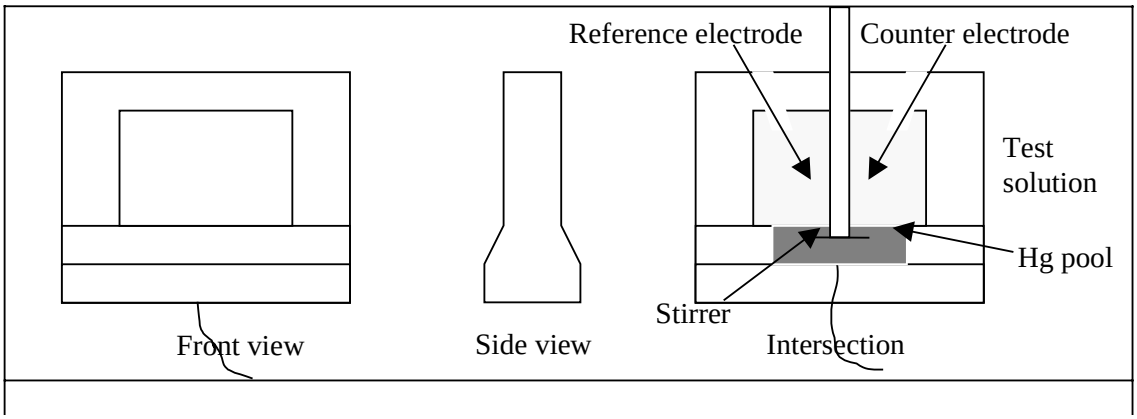

The cell has already been tested by reducing and re-oxidising methyl violegen which is reduced at a mercury pool from a colourless solution to a dark blue solution at -0.73 V vs. a Ag/AgCl electrode.

Acknowledgements

This study is jointly funded by the EPSRC and BNFL.

REFERENCES

[1] T.I. Docrat, J.F.W. Mosselmans, J.M. Charnock, M.W. Whiteley, D. Collison, F.R. Livens, C. Jones and M.J. Edmiston, *Inorg. Chem.*, 38, 1879-1882 (1999).

[2] U. Kramer-Shanabel, H. Bishoff, R.H. Xi, G. Marx, *Radiochim. Acta*, 56, 183-188 (1992).

[3] D.W. Wester, J.C. Sullivan, *J. Inorg. Nucl. Chem.*, 43, 2919-2922 (1981).

SYNCHROTRON X-RAY MICROPROBE ANALYSIS OF RADIOACTIVE TRACE ELEMENTS IN ZIRCON AND ILMENITE

N. Blagojevic, R.F. Garrett, A.P.J. Stampfl
Australian Nuclear Science and Technology Organisation
PMB 1, Menai, NSW, 2234, Australia

Z. Cai, B. Lai, D.G. Legnini and W. Rodrigues
Synchrotron Radiation Instrumentation CAT, Argonne National Laboratory
Argonne, IL, 60439, USA

Abstract

Many types of metalliferous ores contain low levels of uranium and thorium. The radioactivity associated with these elements can report to mineral concentrates, intermediates and eventually to the final product. The broad objective of this project is designed to take a strategic, industry-wide approach to the question of effective removal of radionuclide contamination from minerals and concentrates during the process phase, evaluate the impact on mining operations and report on waste disposal and health and safety issues. Although the work is still in progress we report the results from preliminary studies using zircon and ilmenite models to determine if the synchrotron X-ray microprobes are capable of quantifying U, Th and radioactive elements at micro scale with a spatial resolution of 1 μm to 2 μm.

Introduction

Mineral sands concentrates such as zircon and ilmenite contain low levels of U, Th and their radioactive decay products. In recent years there has been an increased legislative threat to lower the radioactivity levels in concentrates, as radioactivity causes considerable problems in the sale of these commodities as well as problems in the disposal of radioactive waste produced in initial processing and in subsequent industrial chemical processes such as in pigment manufacture [1]. These trends could adversely impact Australian mining operations and raise the need to fully understand the implication of changing regulations. The consequence of becoming complacent is the inability to penetrate and supply markets as the legislation becomes tougher.

The long-term goal of the study of these minerals is to develop cost-effective processes for the removal of radionuclides from minerals. Based on our current knowledge of the levels of radioactivity in mineral products and process intermediates the following categories are the most likely source of concern to industry:

- Copper concentrates, anode slimes and smelter dust.
- Titanium ores and concentrates such as ilmenite and intermediate products.
- Rare earth concentrates.
- Zircons.

Mineral industries with potential problems also include:

- Bauxite mining and aluminium production.
- Phosphate ore mining and processing, fertiliser industry and phosphoric acid producers.
- Oil and gas exploration and production, coal-fired power stations.
- Iron and steel production including scrap metal processing.

A major objective within the current project is focused on identification, location and speciation of the radioactivity in ores, minerals or processed materials. A much-studied model (zircon) and a less well-understood mineral ilmenite were chosen to evaluate capabilities of the synchrotron X-ray microprobe for this work.

The presence of low levels of radioactivity in ores and concentrates is in reality comparable to the presence of other undesirable impurities. Specific removal processes are often developed for such impurities, and the same can be undertaken for the radioactive elements. The main difference between radioactive and non-radioactive impurities is the very low mass concentration of most radionuclides, with the result that it is difficult to determine their location in mineral matrices (before and after processing). It is also difficult to predict their response to specific chemical treatments. The distribution of these trace elements must therefore be studied in order to understand the geological processes resulting in the presence of the radioactive elements as well as processes required for the removal of these elements.

The synchrotron X-ray microprobe had the potential to determine the concentration, distribution and chemical state of these trace elements. Other micro-probe techniques (electron or proton) do not have the combination of sensitivity and spatial resolution required, and do not provide chemical

information. For example, the bulk concentration of thorium in Australian ilmenite is of the order of 100 ppm, while U is much lower, in the 10-30 ppm range or less [2]. Electron and proton microprobe EDS is not sensitive enough to map elements at these concentration levels: minimum detection limits for heavy elements can be as low as 20-30 ppm but the required count times are of the order of minutes per analysis [3].

Experimental

A number of single grain samples of zircon and ilmenite were measured at the 2-ID-D microprobe beam line at SRI-CAT at the Advanced Photon Source [4], using a ~1 μm monochromatic beam at 17.2 keV. This energy was chosen to excite the U L_{III}-edge, but avoid exciting the Zr K-edge in the zircon samples, which is a significant advantage of monochromatic microprobe beam lines.

The principal beam line components of the X-ray microprobe include a high-brilliance APS X-ray undulator, a mirror, a double-crystal Si(111) monochromator for selecting the X-ray energy and a Fresnel zone plate to focus the X-ray beam on the sample. The zone plate was located 72 m from the undulator source, while the sample was placed about 21 cm from the zone plate, resulting in a beam spot of 2×0.2 μm at 17 keV. At the Fe K-edge the focus was 1×0.14 μm. An order sorting aperture is placed between the zone plate and sample so that only first order light is used and a 30 micron diameter central stop was used to eliminate the direct beam. An energy-dispersive Ge-detector (Canberra Ultra-LEGE) was used to measure fluorescence from the sample; the sample was scanned across the focused X-ray spot and spectra acquired at each point. In this way the spatial maps of different elements were acquired simultaneously.

Samples of west Australian ilmenite and zircon, sourced approximately 300 km north of Perth, were sectioned and polished so that the sample thickness was less than 10 μm. The sections were mounted on a 100 μm thick polycarbonate sheet to allow both visible light and X-ray transmission. All samples were inspected by SEM using backscatter imaging to locate appropriate areas of interest.

Results and discussion

Elemental distribution maps were measured from a number of ilmenite and zircon grains. Figure 1 shows U, Th and Pb maps from a representative zircon sample, and shows that these elements are concentrated into zoned regions, overlaying the dark bands in the SEM image. U and Th are known to mainly substitute for Zr, to form actinide orthosilicates. Non-radioactive elements which are also incorporated into the zircon structure include yttrium, probably incorporated into the crystal in a form of a solid solution, which shows an almost identical banding to U and Th in Figure 1. The presence of lead (Pb) can be attributed to the natural decay of U and Th, as well as common lead incorporated during the crystallisation process. In general, the X-ray microprobe results reflect the known mineralogy of this model system.

The fluorescence yield from uranium, thorium and lead in the zircons was calibrated using a well-known geo-chronological zircon standard SL13 [5]. The concentration range of U in Figure 1 is between 13 ppm and 33 ppm and for Th 3 ppm to 11 ppm. The lead concentration was much lower, varying between 3 ppm to 4 ppm.

Figure 1. Th, U and Pb elemental maps of a zircon grain, taken in the region indicated on the SEM image at top left

The images follow the zoned regions as shown by SEM backscatter image. The elemental concentrations within the regions for: a) Th ranged between 3 ppm and 11 ppm, b) U range was 13 ppm to 33 ppm and c) Pb was 3 ppm to 4 ppm.

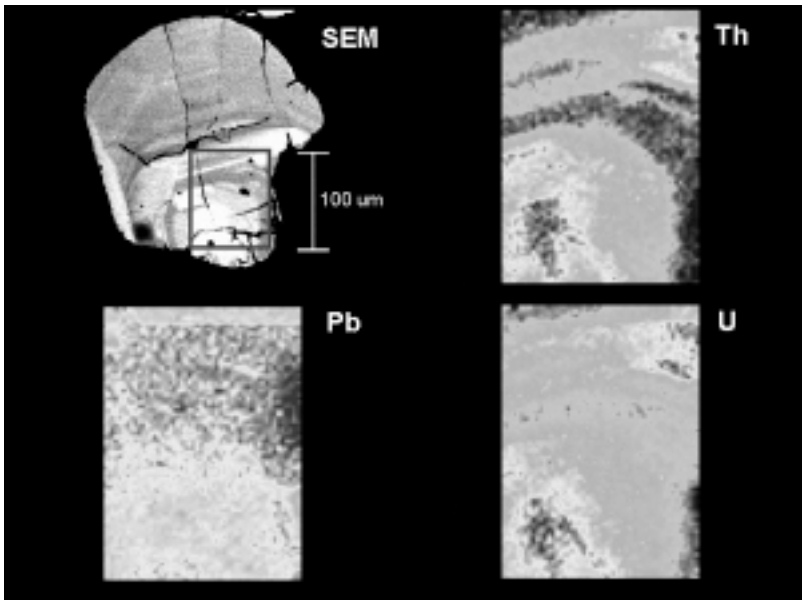

U L_{III}-edge XANES spectra were acquired in regions of high uranium concentration. Figure 2 shows a representative spectrum indicating that uranium is present as U(VI), which has important implications for possible processing techniques as mentioned in the introduction. The oxidation state of uranium will effect amenability of the uranium to leaching with U(VI) being the more susceptible to removal or extraction during the process.

Figure 2. Uranium L_{III}-edge XANES of a zircon mineral grain and standards. Results indicate that U in zircon is present primarily as U(VI).

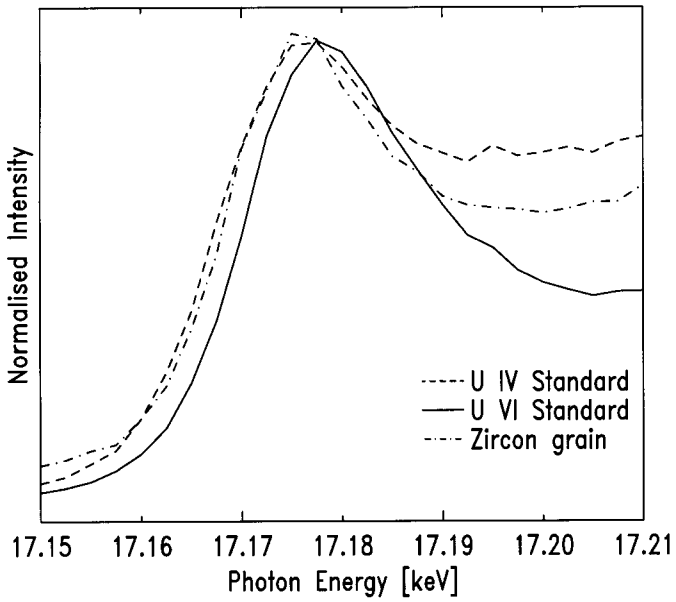

Figure 3 shows synchrotron microprobe elemental maps from a weathered ilmenite grain, again compared with an electron microscope image of the grain. Current theories to account for the elevated concentration of U and Th in these materials include accumulation during weathering as well as contamination during rock formation. The mechanism of accumulation during the weathering process has been described but is not well understood [6]. Levins infer from SEM images, bulk chemistry and alpha track imaging that the thorium content of ilmenite increases with the extent of weathering of the ore and should therefore be concentrated in weathered sections of a mineral grain. Weathered parts of ilmenite are converted to leucoxene, with a reduced iron concentration, and appear dark in backscattered SEM images, as seen around the cracks in the grain in Figure 3. The U and Th increase in concentration should then be associated with Fe(III), which is formed in the weathering and is known to be an excellent scavenger of foreign ions and colloids. The synchrotron microprobe images in Figure 3 supply direct evidence that thorium is associated with weathered areas. Weathered regions can be seen extending several microns from cracks in the ilmenite grain. These regions have much-reduced Fe concentration, and elevated Th (and Pb and U, not shown), which supports the weathering model. The Ti distribution is almost unaffected by weathering, which is expected from solubility levels. Determinations of Fe speciation from XANES are difficult from the edge position and post-edge structure, and have relied on the position of the pre-edge feature in the spectrum [7]. Fe K-edge XANES spectra are shown in Figure 4. The pre-edge peak is not evident in most of the spectra taken; nevertheless the edge position indicates that Fe in the weathered ilmenite zone has predominantly Fe(III) character thus providing direct proof that the adsorption mechanism is due to a ferric oxide present in weathered zones.

Figure 3. Ti, Fe and Th elemental maps of a weathered ilmenite grain, taken in the region indicated on the SEM image at top left

It is evident that removal of Fe by the leaching process, with no effect on the Ti contents, produces an increase in Th. Elevated Th levels are associated with the leached areas or with reduced iron content. Titanium concentration map shows uniform distribution with the exception of areas where physical cracks are confirmed by the SEM image.

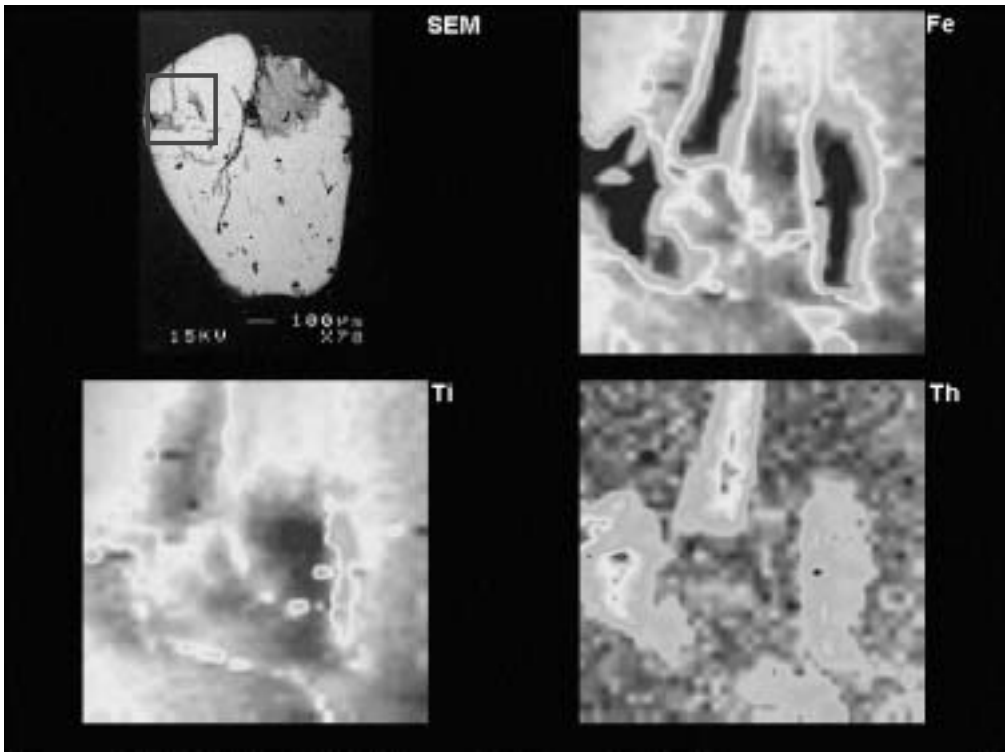

Figure 4. Fe K-edge XANES spectrum of unweathered and weathered ilmenite compared to standards of Fe(II) and Fe(III)

Iron in the unleached area is as expected present predominantly as Fe(II), while iron in the leached area is predominantly as Fe(III).

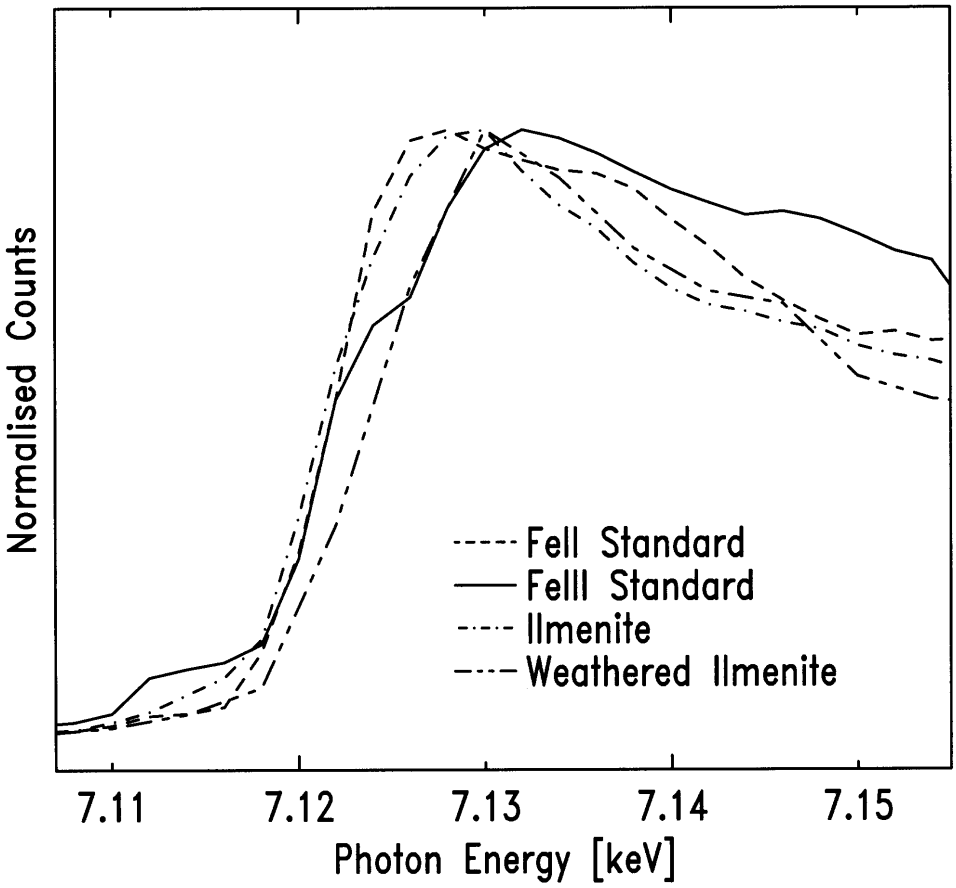

Conclusion

The results for the zircon grains studied confirm that the synchrotron X-ray microprobe has sufficient sensitivity and resolution to map the distribution and speciation of U, Th and their decay daughter products, in this case Pb, in mineral sands concentrates. The ilmenite measurements supply direct confirmation of the previously inferred weathering adsorption mechanism of U and Th in this system. Further work will focus on measuring the radioactive decay chain daughters of U and Th.

Acknowledgements

This work was supported by the Australian Synchrotron Research Program, which is funded by the Commonwealth of Australia under the Major National Research Facilities Program. Use of the Advanced Photon Source was supported by the US Department of Energy, Basic Energy Sciences, Office of Energy Research, under contract No. W-31-109-Eng-38.

REFERENCES

[1] L. Bruzzi, M. Baroni, G. Mazzotti, R. Mele and S. Righi, *J. Environ. Radioactivity*, 47, 171 (2000).

[2] D.M. Levins, R.A. Day, P.J. McGlinn and R. Stanojevic, Proc. Int. Conf. on Radiation Protection and Radioactive Waste Management in the Mining and Minerals Processing Industries, Johannesburg, South Africa, 1995.

[3] D.R. Cousens, R. Rasch and C.G. Ryan, *Micron*, 28, 231-239 (1997).

[4] W. Yun, *et al*., *Rev. Sci. Instrum*., 70, 2238 (1999).

[5] J.C. Roddick and O. van Breemen, Radiogenic Age and Isotopic Studies: Report 8; Geological Survey of Canada, Current Research (1994-F), 1-9.

[6] L. Khor, T. Parks, F.J. Lincoln and J. Graham, *Aust. J. Chem*., 49, 847-860 (1996).

[7] S. Bajt, S.R. Sutton and J.S. Delaney, *Geochim. Cosmochim. Acta*, 58, 5209 (1994).

EXAFS STUDIES OF CO-PRECIPITATION AND ADSORPTION REACTIONS OF TC

D.J. Bunker,[1] **M.J. Jones,**[1] **J.M. Charnock,**[3] **F.R. Livens,**[1] **R.A.D. Pattrick,**[2] **D. Collison**[1]
[1]Department of Chemistry, [2]Department of Earth Sciences
University of Manchester
Oxford Road, Manchester M13 9PL, UK
[3]CLRC Daresbury Laboratory
Warrington, Cheshire WA4 4AD, UK

Abstract

Adsorption and co-precipitation reactions may be a simple way of removing $[TcO_4]^-$ from aqueous solution. The effectiveness of a range of potential and adsorbents precipitants has been evaluated and some are capable of near-quantitative (>98%) removal of $[TcO_4]^-$ from solution. X-ray absorption near edge structure (XANES) has been used to determine Tc oxidation states and extended X-ray absorption fine structure spectroscopy (EXAFS) has been used to identify the local environment of Tc. The absorption edge position has been determined using $[PPh_4][TcO_4]$, TcS_2 and Tc_2S_7 as model compounds, and is diagnostic of Tc oxidation state.

Introduction

^{99}Tc is a high-yield (~6%) fission product with a half-life of 2.13×10^5 years, and it decays by the emission of β^- particles with E_{max} 300 keV. It is present in the environment as a result of nuclear weapons testing and low and intermediate-level waste disposal, and is becoming an increasingly important component of high-level wastes [2]. In the environment, Tc exists in two stable oxidation states depending on the redox conditions; Tc^{4+} in strongly reducing environments and in more oxidising conditions, Tc(VII), which forms the pertechnate anion, $[TcO_4]^-$. The pertechnate anion only interacts weakly with mineral surfaces [3], with Kd ~ 1 ml/g, making it amongst the most mobile of all radionuclides in the environment [4], whereas Tc(IV) species are expected to be strongly retained [5], with Kd ~ 1 000 ml/g. In spite of their potential for controlling Tc mobility, the mechanisms of interaction between Tc species and mineral phases, particularly reduced iron minerals, are not clearly understood. The effectiveness of a range of adsorbents and precipitants have been evaluated, including:

- *Mackinawite (tetragonal FeS)*. Environmentally, this is the first sulphide phase formed following the onset of reducing conditions. It is commonly found in anoxic horizons and is believed to play an important role in controlling metal speciation in such systems [6].

- *"Green rusts"*. These are mixed Fe(II)/Fe(III) hydroxides which contain interlayer anions such as carbonate or sulphate.

Although these compounds first appeared in the literature over 40 years ago, due to their extreme sensitivity to oxidation, there has been little work carried out with them until fairly recently.

Method

1. *Co-precipitation of Tc with mackinawite*. Experimental details are given elsewhere [1].

2. *Sorption of Tc on mackinawite*. Mackinawite was prepared using a method based on that of [7]. Aliquots of $[TcO_4]^-$ were added to centrifuge tubes containing 150 mg of mackinawite/20 ml DI water. After 24 hours, the tubes were centrifuged and supernatant decanted. The spiked mackinawite precipitate was transferred to an EXAFS cell. An inert atmosphere was maintained throughout.

3. *Sorption of Tc on green rusts*. Sulphate green rust was prepared using a method based on that of [8]. Aliquots of $[TcO_4]^-$ were added to centrifuge tubes containing approximately 150 mg of damp green rust/20 ml DI water. After 24 hours the tubes were centrifuged and the supernatant decanted. The spiked green rust precipitate was transferred to an EXAFS cell. An inert atmosphere was maintained throughout.

4. *Synthesis of model compounds*. $[PPh_4][TcO_4]$ (Tc in tetrahedral 4 co-ordination); TcO_2 (approximately octahedral); Tc_2S_7 (unknown); TcS_2 (distorted octahedral). Experimental details are given in [1] and [9] and further structural information in [9] and [10].

5. *X-ray absorption spectroscopy*. All samples were contained in Ar-filled, doubly contained cells, fabricated from Perspex to minimise bremsstrahlung production. These were heat-sealed into two Ar-filled polythene bags to provide a third and fourth level of containment.

Technetium K-edge X-ray absorption spectra were collected on Station 16.5 at the CLRC Daresbury Synchrotron Radiation Source, operating at 2 GeV with a typical beam current of 150 mA. A double-crystal Si(311) monochromator was used, detuned to 50% of maximum intensity for harmonic

rejection. Spectra for the samples were recorded in fluorescence mode, using a 30-element Ge detector. A minimum of four scans per sample were collected at ambient temperature to improve data quality. The spectral data were calibrated and background subtracted using the Daresbury Laboratory programs EXCALIB and EXBACK. The isolated EXAFS data were analysed using EXCURV98 [11] employing Rehr-Albers theory [12] and using single scattering. Additional shells were included in the fit only where the R-factor (overall goodness of fit) decreased by >5%. Analysis of the model compounds was used to test the modelled phases and amplitudes, which were derived from *ab initio* calculations.

Results and discussion

Results of the EXAFS data fitting are given in Table 1. Figures 1 and 2 show the Tc K-edge EXAFS and associated Fourier transform for FeS/$[TcO_4]^-$ sorption and green rust/$[TcO_4]^-$ sorption respectively.

- FeS/$[TcO_4]^-$ co-precipitate: The Tc-S distance is within error of the mean Tc-S distance in TcS_2, implying that during co-precipitation, Tc(VII) is reduced to Tc(IV) and forms a TcS_2-like phase [1].

- FeS/$[TcO_4]^-$ sorption: The Tc-S distances and the Tc-Tc distance are in good agreement with the TcS_2 data, indicating that during sorption, Tc(VII) is reduced to Tc(IV) and forms a TcS_2-like phase.

- Green rust/$[TcO_4]^-$ sorption: The Tc-O distance is within error of the Tc-O distance in TcO_2, indicating that during sorption, Tc(VII) is reduced to Tc(IV) and forms a TcO_2-like phase.

Conclusions

In co-precipitation/sorption with FeS and sorption on to green rust, $[TcO_4]^-$ was scavenged from solution and reduced to Tc(IV), thereby restricting its mobility. Both sorption on to and co-precipitation with FeS form a TcS_2-like phase. It is not presently possible to confirm if Tc is incorporated into the mackinawite or green rust, of if it is present as a discrete phase. Rates of reaction and mechanisms will require further study.

REFERENCES

[1] M.J. Wharton, B. Atkins, J.M. Charnock, F.R. Livens, R.A.D. Pattrick and D. Collison, "An X-ray Absorption Spectroscopy Study of the Co-precipitation of Tc and Re with Mackinawite (FeS)", *Appl. Geochem.*, 15, 347-354 (2000).

[2] R.E. Wildung, K.M. McFadden and T.R. Garland, "Technetium Sources and Behaviour in the Environment", *J. Environ. Quality*, 8, 156-161 (1979).

[3] F.B. Walton, J. Paquette, J.P.M. Ross and W.E. Lawrence, "Tc(IV) and Tc(VII) Interactions with Iron Oxyhydroxides", *Nucl. Chem. Waste Manag.*, 6, 121-126 (1986).

[4] T.R. Garland, D.A. Cataldo, K.M. McFadden, R.G. Schreckhise and R.E. Wildung, "Comparative Behaviour of ^{99}Tc, ^{129}I and ^{137}Cs in the Environment Adjacent to a Fuel Reprocessing Facility", *Health Phys.*, 44, 658-662 (1983).

[5] K.H. Lieser and C. Bauscher, "Technetium in the Hydrosphere and in the Geosphere – Chemistry of Technetium in Natural Waters and the Influence of Redox Potential on the Sorption of Technetium", *Radiochim. Acta*, 42, 205-213 (1987).

[6] A.R. Lennie, S.A.T. Redfern, P.F. Schofield and D.J. Vaughan, "Synthesis and Rietveld Crystal Structure Refinement of Mackinawite, Tetragonal FeS", *Mineral. Mag.*, 59, 677-683 (1995).

[7] A.R. Lennie and D.J. Vaughan, "Spectroscopic Studies of Iron Sulphide Formation and Phase Relations at Low Temperatures", in *Mineral Spectroscopy: A Tribute to Roger G. Burns*, M.D. Dyar, C. McCammon, M.W. Schaefer, eds., The Geochemical Society, Special Publication No. 5, pp. 117-131.

[8] A.H. Cuttler, V. Man, T.E. Cranshaw and G. Longworth, "A Mössbauer Study of Green Rust Precipitates: I. Preparations from Sulphate Solutions", *Clay Miner.*, 25, 289-301 (1990).

[9] I. Almahamid, J.C. Bryan, J.J. Bucher, A.K. Burrell, N.M. Edelstein, E.A. Hudson, N. Kaltsoyannis, W.W. Lukens, D.K. Shuh, H. Nitsche and T. Reich, "Electronic and Structural Investigations of Technetium Compounds by X-ray Absorption Spectroscopy", *Inorg. Chem.*, 34, 193-198 (1995).

[10] H.J. Lamfers, A. Meetsma, G.A. Wiegers and J.L. de Boer, "The Crystal Structure of Some Rhenium and Technetium Dichalcogenides", *J. Alloy. Compd.*, 241, 34-39 (1996).

[11] N. Binsted, Daresbury Laboratory EXCURV98 Program, CLRC Daresbury Laboratory, Warrington (1998).

[12] J.J. Rehr and R.C. Albers, "Scattering Matrix Formation of Curved Wave Multiple Scattering Theory – Application to X-ray Absorption Fine Structure", *Phys. Rev.*, B41, 8139-8149 (1990).

Table 1. Results of EXAFS data fitting

Interatomic distances in Å, Debye-Waller factors ($2\sigma^2$) in $Å^2$. R-values are a measure of overall goodness of fit. Uncertainties in co-ordination numbers are ±1 and in distances are ±0.02Å.

Sample	Shell	C.N.	Type	Distance	$2\sigma^2$	R
$[PPh_4][TcO_4]$ [1]	1	4	O	1.72	0.007	22.9
TcO_2 [9]	1	6	O	1.98	0.0076	
	2	1	Tc	2.61	0.0076	
	3	1	Tc	3.10	0.0070	
	4	4	Tc	3.64	0.0080	
	5	4	Tc	3.67	0.0080	
Tc_2S_7 [1]	1	4	S	2.39	0.012	30.9
	2	2	Tc	2.78	0.014	
TcS_2 [1]	1	3	S	2.36	0.014	30.9
	2	3	S	2.41	0.038	
	3	1	Tc	2.77	0.008	
FeS/$[TcO_4]^-$ co-precipitate [1]	1	6	S	2.42	0.020	34.7
FeS/$[TcO_4]^-$ sorption	1	3	S	2.35	0.009	33.9
	2	3	S	2.48	0.012	
	3	1	Tc	2.82	0.013	
GR/$[TcO_4]^-$ sorption	1	4	O	1.99	0.010	23.7
	2	1	Cl	2.21	0.013	
	3	1	Fe	3.08	0.014	
	4	1	Fe	3.55	0.005	

Figure 1. (a) Tc K-edge EXAFS and (b) associated Fourier transform for $FeS/[TcO_4]^-$ sorption. Solid lines are experimental data, broken lines are best fit.

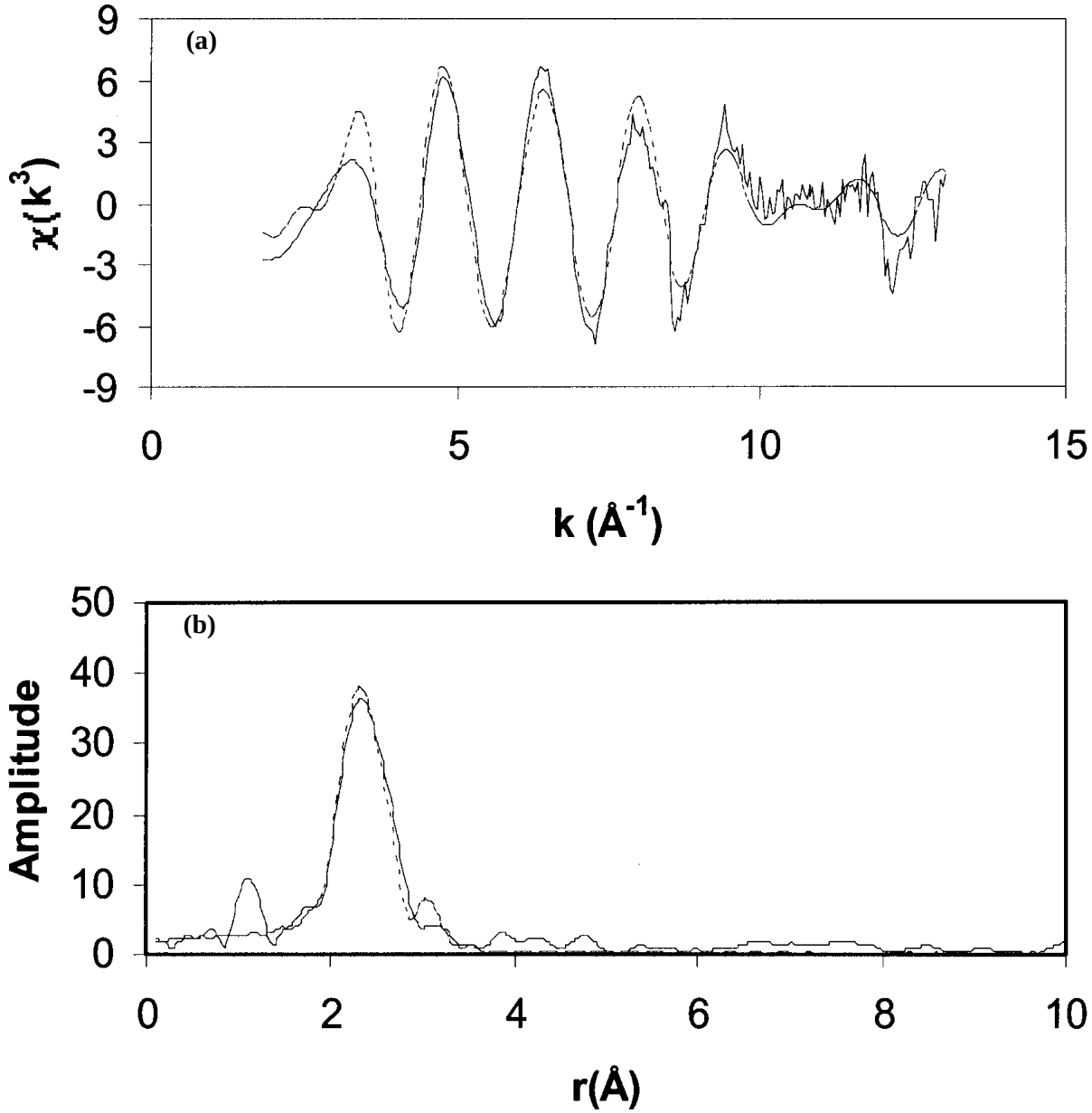

Figure 2. (a) Tc K-edge EXAFS and (b) associated Fourier transform for "green rust"/$[TcO_4]^-$ sorption. Solid lines are experimental data, broken lines are best fit.

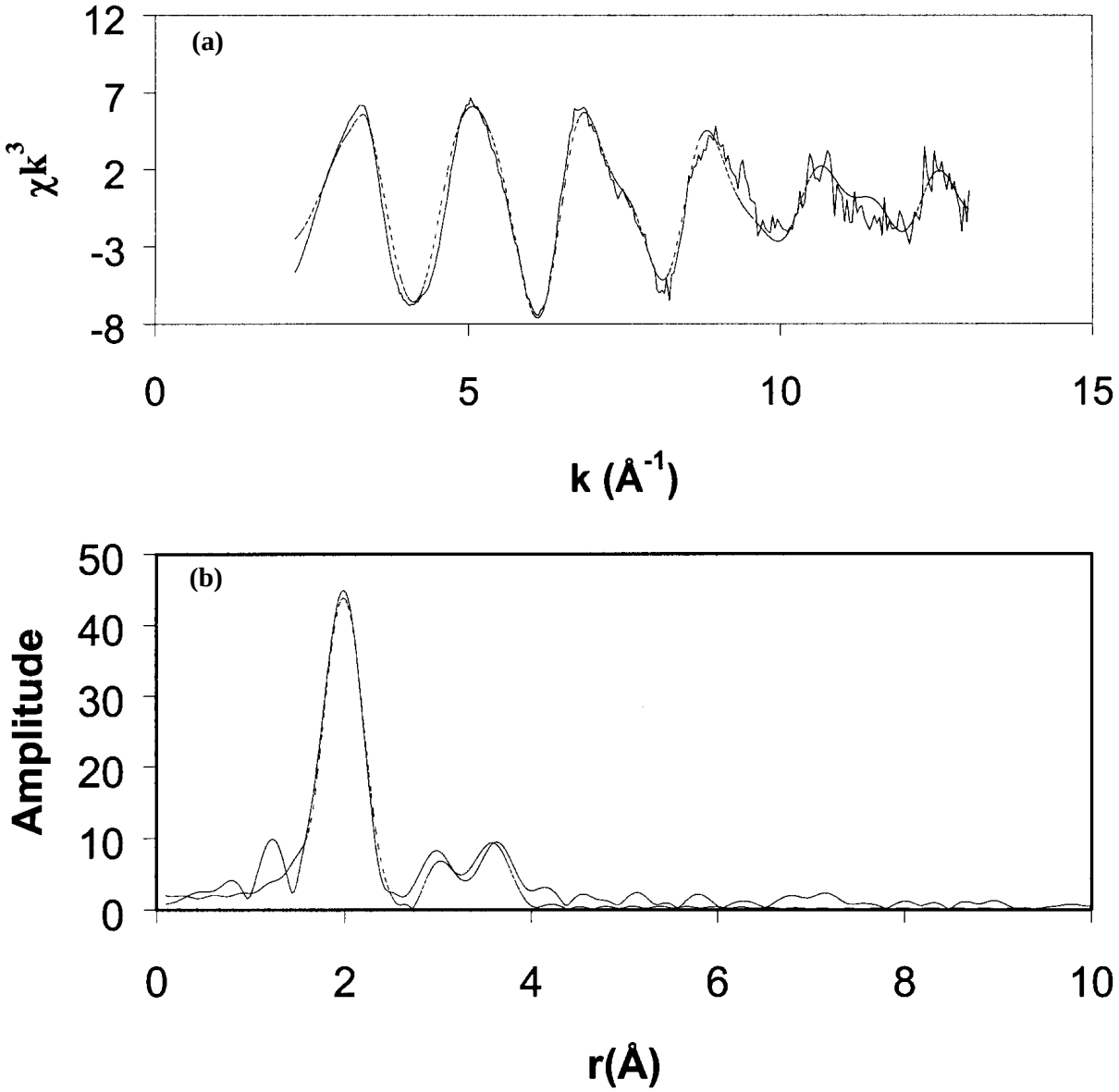

X-RAY FLUORESCENCE MICROTOMOGRAPHY WITH SYNCHROTRON RADIATION: IMAGE RECONSTRUCTION

M. Chukalina
Institute of Microelectronics Technology, RAS
Chernogolovka, Russia

A. Simionovici, A. Snigirev
European Synchrotron Radiation Facility
Grenoble, France

Abstract

The algebraic technique of an element distribution reconstruction from fluorescence projections is described. The application of the software under development to the image reconstruction is demonstrated by processing thorium sinogram from a measurement of laser-ablated resin samples at the ESRF beam line ID22.

Introduction

Modern element-sensitive X-ray systems provide unique possibilities of measurement and visualisation of the interior microstructure of objects. Tomography has many applications in engineering, materials science (the investigation of nuclear waste diffusion in storage material [1]), biology, medicine and ecology [2].

X-ray transmission tomography refers to the cross-sectional imaging of an object from attenuation data collected by illuminating the object from many different directions. Tomographic imaging deals with reconstruction of an image from its projections. In the strict sense of the word, a projection at a given angle is the integral of the image in the direction specified by that angle, as illustrated in Figure 1. The result obtained by X-ray tomography is a function that describes the linear X-ray attenuation coefficient distribution in an object under investigation. The linear attenuation coefficient is the following sum:

$$\nu = \sum_{i=1}^{N_{elem}} C^i \nu^i$$

where N_{elem} is the number of the recorded elements contained in the object, C^i is the concentration of the ith element and ν^i is the linear attenuation coefficient of the ith element. If the main objective of the investigation is to obtain the distribution of a particular element concentration then the X-ray computed tomography does not always give an unambiguous answer. Two examples which describe this situation, are given below:

1. Values ν^i and ν^j for the ith and jth elements are of the same order of magnitude.

2. Values $C^i\nu^i$ and $C^j\nu^j$ for the ith and jth elements are of the same order of magnitude.

Figure 1. Two projections of an object are shown

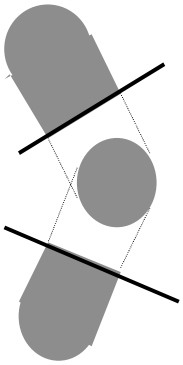

Only the X-ray fluorescence tomography as a case of emission tomography, allows to solve the problem of the element distribution quantitatively. Fluorescence-computed tomography poses more difficult problems in comparison to the X-ray transmission tomography. The reason is that two unknown distributions influence the result. The first one is the element distribution function under reconstruction and the second is the distribution of the X-ray linear attenuation coefficient. The reconstruction of both distributions would be preferable. However, the system of non-linear equations, which arises from this approach, creates essential obstacles. Effective integral approaches, which could define the values of the two unknown two-argument functions (concentration distribution and attenuation coefficient distribution) from the values of the two-argument functions, are unknown.

Iterative techniques are employed to solve this problem. A modified algebraic technique is proposed to reconstruct the element distribution from the fluorescence projections. A scheme of the experimental set-up for the projection collection is presented. The order of the principal steps in the reconstruction technique is described. The result of implementation of this technique for Th image reconstruction is demonstrated.

Reconstruction technique

Figure 2 is a schematic diagram showing the principle of a projection image registration. The scanning procedure, the beam focusing and the data collection have been detailed in our previous publications [3-5]. In this work we would like to attract the readers attention to the mathematical signal processing.

Figure 2. Schematic diagram of the experimental set-up

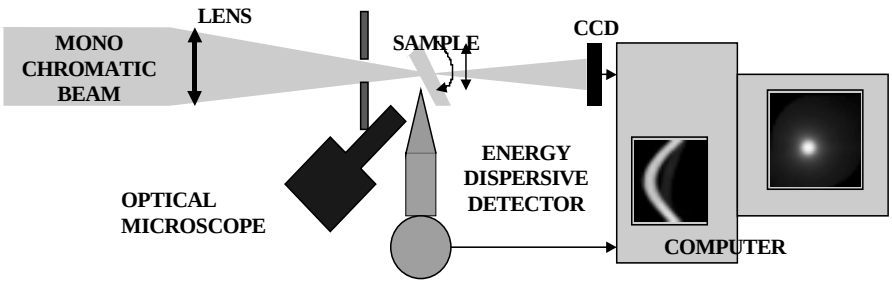

Modified algebraic reconstruction techniques, with a partial correction of each individual projection provided that the fluorescence linear attenuation coefficient along the projection line is a constant on the first step, consists of two sequential steps.

Omitting the constant multipliers, the signal equation can be written:

$$P(\eta,\theta)=\int_{L_1} C(x,y)\nu^{*}\exp\left(-\int_{0}^{l(\eta,\xi)}\nu(x,y)dp\right)\exp\left(-\int_{L_2}\left[C(x,y)\mu^{*}+(1-C(x,y))\mu^{-}\right]dq\right)d\xi \qquad (1)$$

where $C(x,y)$ is the concentration of a fluorescent element, ν^{*} is the X-ray linear attenuation coefficient of the fluorescent element, μ^{*} is the fluorescence linear attenuation coefficient of the fluorescent element and $(1-C(x,y))\mu^{-}$ is the linear attenuation coefficient of the full object without taking into account the fluorescent element.

The sample rotation is characterised by angle θ (Figure 3). The detector observation for the fixed angle is called "a projection" (Figure 4). The rotating co-ordinate system (η,ξ) is connected with the detector. The axis ξ is parallel to the incident beam. The axis η is normal to the detector face. The following relations connect these two co-ordinate systems among themselves:

$$\begin{cases}\eta = x\cos\theta + y\sin\theta\\ \xi = -x\sin\theta + y\cos\theta\end{cases}\qquad\begin{cases}x = \eta\cos\theta - \xi\sin\theta\\ y = \eta\sin\theta + \xi\cos\theta\end{cases} \qquad (2)$$

Figure 3. Connection of the two co-ordinate systems

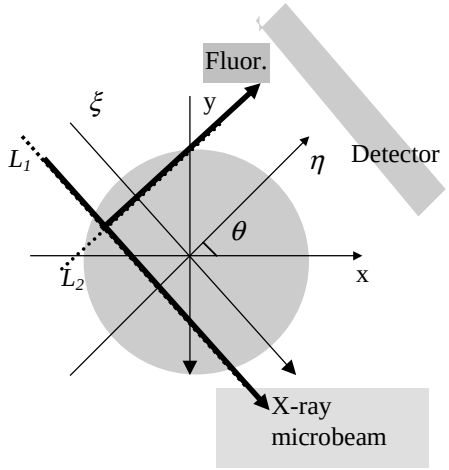

Figure 4. Scheme of the X-ray fluorescence signal formation

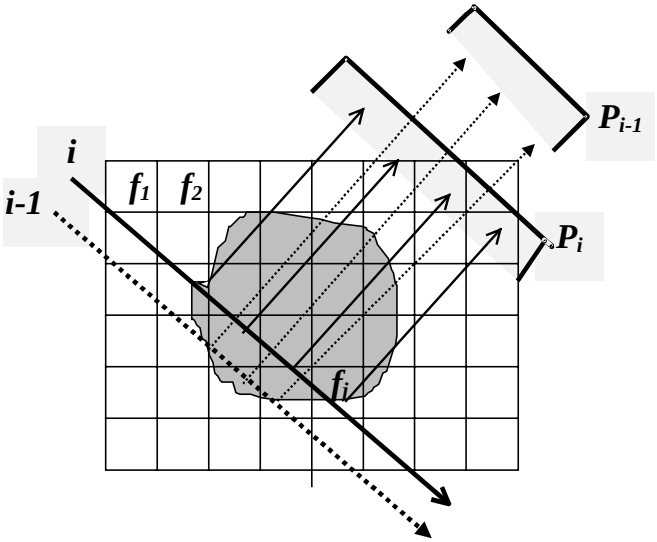

If the absorption projections are measured, the coefficient $\nu(x,y)$ distribution can result from the traditional reconstruction technique implementation. Then the Eq. (1) may be rewritten:

$$P(\eta,\theta) = \int_{L_1} f(x,y) K(\eta,\xi) \exp(-\mu L_2) d\xi$$

where $f(x,y) = C(x,y)\nu^*$, $K(\eta,\xi)$ describes the X-ray attenuation, μ is a constant for the first step of the technique and L_2 is the path length inside the sample from the point where the fluorescence is emitted to the detector. Below we will focus on $f(x,y)$.

In contrast to the integral reconstruction techniques, where the sampling is fulfilled only on the last stage for the numerical scheme completion, in algebraic techniques the sampling is performed in the beginning of the calculation. A further description is provided in the sampling mode. In this context, the reconstruction problem is reduced to the solution of a linear equation system.

The linear integral will be called a ray-sum. The image under reconstruction $f(x,y)$ for a lth element under investigation is covered by a square grid (Figure 4). Everywhere below we use the lth index only for the element under investigation. f is assumed to be constant in each square. Let N be the total number of squares (pixels). This amounts to replacing the function f by a vector whose jth component is the value of f in the jth square. Like the image, the projections will also be given a one-index representation. Let p_i be the ray-sum measured with the ith ray for an element under investigation as shown in Figure 4. The relationship between f_j and p_j may be expressed as:

$$\sum_{j=1}^{N} a_{ij} f_j = p_i, i = 1,2,...,M \tag{3}$$

where M is the total number of rays and a_{ij} describes the attenuation of the X-ray and the fluorescence attenuation. In the first step of the technique the matrix element a_{ij} is calculated by:

$$a_{ij} = b_{ij} \exp\left(-\sum_{k=1}^{j} \nu_k b_{ik} \right) \exp\left(-\mu L_{2ij}\right) \tag{4}$$

where L_{2ij} is the distance from the jth square to the analysed region edge in the detector direction for the ith measurement. Coefficient b_{ij} is equal to one pixel size if the ith ray intersects the jth square and ν_k is the linear attenuation coefficient for the kth square. This coefficient is calculated from the transmission X-ray projections.

In computed tomography, direct methods for solving Eq. (3) cannot be applied. The main reasons are the large system dimension, the poorly worded matrices, the non-square matrices over-determined as well as underdetermined, the errors of the matrix elements definition and the projection measurement errors. Iterative methods that are based on the “method of projections” as first proposed by Kaczmarz [7] are used for solving Eq. (3). To explain the computational steps involved in the method used, we rewrite Eq. (3) in the expanded form:

$$\begin{cases} a_{11} f_1 + a_{12} f_2 + ... + a_{1N} f_N = p_1 \\ a_{21} f_1 + a_{22} f_2 + ... + a_{2N} f_N = p_2 \\ \qquad\qquad ... \\ a_{M1} f_1 + a_{M2} f_2 + ... + a_{MN} f_N = p_M \end{cases} \tag{5}$$

A grid presentation with N squares gives an image with N degrees of freedom. Therefore, an image, represented by $(f_1,f_2,...,f_N)$ may be considered to be a single point in an N-dimensional space. When a unique solution to these equations exists, the intersection of all these hyperplanes is a single point giving that solution. Mathematically it can be written:

$$f_j^{(k+1)} = f_j^{(k)} + \frac{\sum_{i=1}^{M} a_{ij} \dfrac{p_i - \sum_{j=1}^{N} a_{ij} f_j^{(k)}}{\sum_{j=1}^{N} a_{ij}}}{\sum_{i=1}^{M} a_{ij}} \tag{6}$$

where k is an iteration number. For each projection value p_i, all components of f, which were involved in the formation process of p_i are corrected.

We use a prior information about the non-negativity of the desired vector values and apply the partly limited version of the method $f_j^{(k+1)} = \max\{0, f_j^{(k+1)}\}$.

We introduce the effective atomic concentration of lth element per analysed sample $C^l = \frac{I(E^l)}{\sum_{l=1}^{N_{elem}} I(E^l)} \approx \frac{n^l \sigma^l}{\sum_{l=1}^{N_{elem}} n^l \sigma^l}$ to define $f(x,y)$. Here $I(E^l)$ is a full amount of the lth element fluorescence quanta over all projections, n_l is a number of lth element atoms per analysed sample and σ^l is the lth element fluorescence cross-section. Then $f(x,y)$ for the lth element can be written $f_j = g_j^l c^l \nu_j$, where $C^l = c^l \sum_{j=1}^{N} g_j^l$, g_j^l is a 0-1 scaling factor and $c^l g_j^l$ is "an effective atomic concentration" per the jth square. Results of the implementation of the first step for the processing of the Th projections from a sample of laser-ablated resin (Figure 5) are presented in Figure 6. The scanning step is 4 microns. Pixel size is equal to the scanning step. The number of scanning steps is 51. The number of rotation angles is 79. The value of the rotation angle is 4.6°. The X-ray beam energy is 22.8 keV.

Figure 5. Set of the projections (T. Jeffries, *et al*. [5])

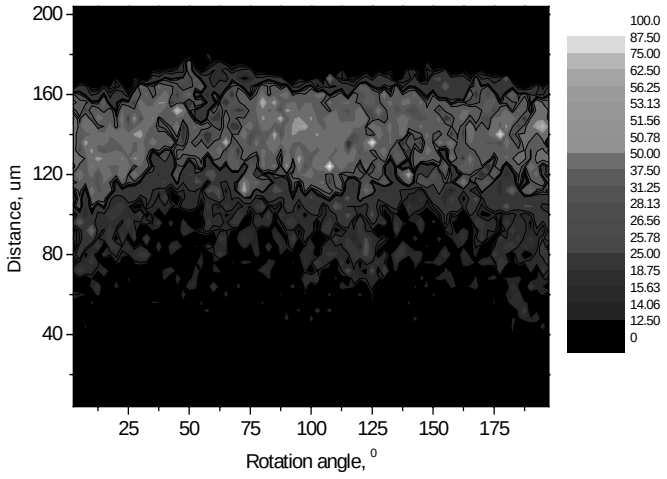

Figure 6. Reconstructed image

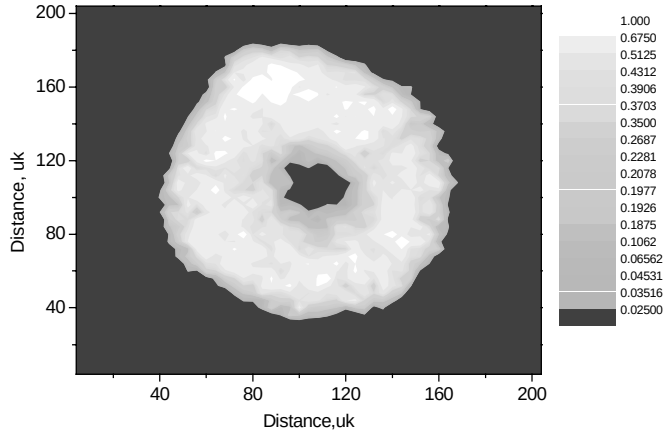

The second step of the technique includes taking account of the fluorescence attenuation. Now the following expression for the matrix element a_{ij} is used:

$$a_{ij} = b_{ij} \exp\left(-\sum_{k=1}^{j} \nu_k b_{ik} \right) \exp\left(-\sum_{n=1}^{N} d_{ijn} \sum_{l_1=1}^{Nelem} F\left(f_n^{l_1} \right) \right) \tag{7}$$

where F still takes into account the attenuation of the fluorescence by the sample similar to Eq. (4). But in contrast to it F is calculated from the elemental distribution f. The value d_{ijn} is equal to one pixel size if the fluorescence ray from the jth square intersects the nth square with the ith ray. The described iteration procedure is repeated with the new a_{ij} matrix to obtain the final reconstructed image. The results including the second step of the quantitative fluorescence correction will be discussed elsewhere [6].

REFERENCES

[1] J. Jolie, Th. Materna, B. Masschaele, W. Mondelaers, V. Honkimaki, A. Koch, Th. Tschentscher, "Uranium Sensitive Tomography Using Synchrotron Radiation above 100 keV", Book of Abstract Materials Science at Third Generation Synchrotron Radiation Facilities, 28 (1999).

[2] B. Salbu, K. Janssens, T. Krekling, A. Simionovici, M. Drakopoulos, C. Raven, I. Snigireva, A. Snigirev, O.C. Lind, D.H. Oughton, F. Adams, V. Kashparov, "Initial Release of Reduced U Particles and Subsequent Releases of Oxidised U_3O_8 Particles During the Chernobyl Reactor Accident Evidenced by Hard X-ray Microscopy Techniques", ESRF Highlights 1999, D. Cornuejols, G. Admans, eds., ESRF, Grenoble, France, to be published in *Analyst*, 24-25 (2000).

[3] A. Simionovici, M. Chukalina, M. Drakopoulos, I. Snigireva, A. Snigirev, Ch. Schroer, B. Lengeler, K. Janssens, F. Adams, "X-ray Fluorescence Microtomography: Experiment and Reconstruction", *SPIE*, 3772, 304 (1999).

[4] T. Weitkamp, M. Drakopoulos, A. Simionovici, A. Snigirev, I. Snigireva, M. Chukalina, Ch. Schroer, "X-ray Fluorescence Tomography with Synchrotron Radiation", Proceeding of Conference X-ray Optics, Nizhnii Novgorod, 22-25 February 2000, 66-72 (in Russian).

[5] B. Lengeler, C.G. Schroer, M. Richwin, J. Tummler, M. Drakopolous, A. Snigirev, I. Snigireva, "A Microscope for Hard X-rays Based on Parabolic Compound Refractive Lenses", *Appl. Phys. Lett*., Vol. 74, No. 26, 3924-3926 (1999).

[6] T. Jeffries, *et al*., to be published.

[7] S. Kaczmarz, *Bull. Acad. Poll. Sci. Lett. A*, Vol. 6-8A, 355 (1937).

XAFS INVESTIGATION OF LANTHANIDE SORPTION ONTO FERRIHYDRITE AND TRANSFORMATION PRODUCTS BY TEMPERING AT 75°C

K. Dardenne, T. Schäfer, M.A. Denecke, J. Rothe
Forschungszentrum Karlsruhe, INE
P.O. Box 3640, 76021 Karlsruhe, Germany

Abstract

The time-dependent changes of Lu speciation, initially sorbed onto hydrous ferric oxides (HFO) during tempering (75°C) and leading to stable crystalline transformation product hematite, is studied. Three-step sequential extraction ($MgCl_2$, oxalate/oxalic acid; dithionite-citrate-bicarbonate) of the solid material shows that the amount of Lu extracted with crystalline Fe-phases (Fe_D) increases with ageing time. Extended X-ray absorption fine structure (EXAFS) study reveals a shortening of the Lu-O bond distance and an increase of the asymmetry of the first shell contribution in the Fourier transform with increasing tempering time. Both EXAFS and the extraction study show that Lu(III), an actinide analogue, is likely incorporated into the Fe oxide phase during transformation.

Introduction

Amorphous or low crystalline Fe hydroxides are one of the major sorption surfaces limiting the migration of hazardous substances in nature. Due to their metastability, knowledge of changes in sorption properties (e.g. reversibility) during dissolution/re-crystallisation processes into their stable counterparts hematite and/or goethite are essential. Sorption processes of organic and inorganic pollutants on natural and synthetic Fe oxide/hydroxide systems have been studied in numerous investigations [1]. However, the incorporation/occlusion process of hazardous substances in ageing products of HFO is still matter of research.

We are investigating the interaction of HFO with trivalent actinide (An) homologues, e.g. Lu(III). Knowledge of the interaction of An(III) with mineral surfaces and their occlusion or inclusion into minerals are required for predictive transport models used in performance assessment for nuclear waste repositories. This study focuses on the time-dependent changes of Lu speciation, initially sorbed onto HFO, during the transformation to hematite at 75°C. Three-step sequential extraction ($MgCl_2$, Fe_E; oxalate/oxalic acid, Fe_O; dithionite-citrate-bicarbonate, Fe_D) of the solid material is used to determine the amount of exchangeable Lu. Metrical parameters describing the Lu co-ordination are extracted from extended X-ray absorption fine structure (EXAFS) spectra.

Experimental methods

Sample preparation

The three synthetics phases, HFO, hematite and goethite were prepared according to the method described by Schwertmann and Cornell [2]. The specific surface area determined by BET N_2 adsorption was 360 m^2/g for ferrihydrite, 29 m^2/g for hematite and 72 m^2/g for goethite. Lutetium sorption onto the synthetic phases (3.49×10^{-4} mol Lu/g HFO or goethite and 3.32×10^{-4} mol Lu/g hematite) suspensions is performed at room temperature. The suspension solution is adjusted to 8 following addition of Lu. The metal concentration range for the experiments is selected to be less than ~24% occupation of the total HFO sorption sites to inhibit surface precipitation of Lu-phases. After 24 h reaction time, transformation experiments are performed by tempering reaction vessels at 75°C in an oven for various reaction times. The pH value is kept constant during the transformation reaction at pH 8.0 ± 0.3 and controlled daily. Fe/Lu element analysis of solid extraction solutions are quantified using a Varian ELAN 6000 ICP-MS.

Extraction

A large number of selective dissolution techniques exists to determine bio-available Fe and estimate Fe present in different solid-phase forms. Most are applied to extract Fe in complex soil matrices. None of these extraction procedures, however, is absolutely phase selective and depends strongly on parameters such as mineral size and surface roughness. Selective dissolution can be used as a practical operational approach, based on the chosen specific extraction procedure (Table 1).

Extractions are performed to differentiate between “free” Fe oxide Fe_D (dissolution of hematite, goethite and ferrihydrite), “amorphous” or “active” Fe oxide Fe_O (dissolution of ferrihydrite and ferrihydrite-like, poorly crystallised iron oxides) and the exchangeable or water-soluble iron Fe_E (Table 1). No step for extracting organically bound Fe is included because the samples under investigation did not contain organic matter. The extraction steps are performed separately with untreated samples and quantification of each extraction step. The results are shown in Figure 1.

Table 1. Summary of extraction procedure used in this study

Phase	Chemical procedure	Reference
Fe_D, total "free" Fe oxides	Citrate-dithionite-bicarbonate (buffered at pH 7)	[3]
Fe_O, poorly crystalline "active" Fe oxides	NH_4-oxalate-oxalic acid (pH 3) in the dark	[4]
Fe_E, exchangeable Fe	1 M $MgCl_2$	[5]

Figure 1. Fe and Lu relative distributions in the different Fe phases, low crystalline (HFO), crystalline (hematite, goethite) and exchangeable Fe in dependence of temper time. Fe_D and Lu_D correspond to 100%, i.e. complete dissolution.

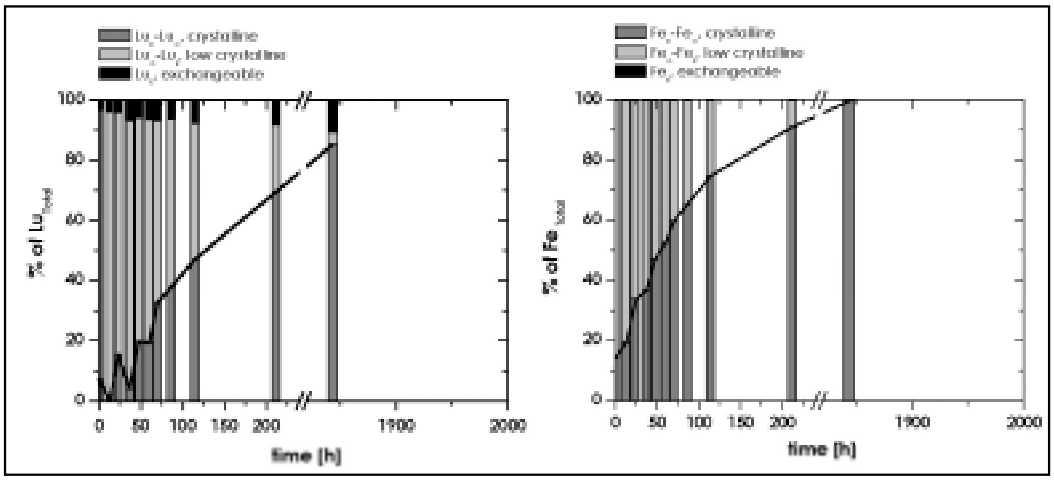

EXAFS

EXAFS spectra are collected at the Hamburger Synchrotronstrahlungslabor (HASYLAB) positron storage ring DORIS III, operating at 4.44 GeV with a maximal current of 150 mA, at beam line A1. A double-bounce monochromator with a Si(111) channel-cut crystal, equipped with a piezo-driven feedback to stabilise incident intensity, is used. The crystals are detuned to 50% in order to reject higher harmonic contamination of the beam.

Sample spectra are energy calibrated using the first inflection point in the K-edge spectrum of a zinc metal foil, defined as 9 659 eV [6], recorded simultaneously. The AUTOBK program [7] is used to extract $\chi(k)$ from the absorption spectrum. Data analysis is performed based on conventional methods [8] using the WinXAS97 software [9]. Theoretical backscattering amplitude and phase functions for modelling the experimental data are calculated with the scattering code FEFF8 [10] using single scattering Lu-O atom pairs.

A list of the EXAFS samples investigated, their Lu loadings, and experimentally measured Lu L3 edge jumps is found in Table 2. EXAFS spectra at the Lu L3 edge (9 244 eV) for four Lu(III):HFO sorption samples with varying temper times (0, 49 h, 115 h, 212 h) and three polycrystalline "reference samples" (Lu_2O_3 and Lu(III) sorbed onto hematite and goethite at pH 8) are recorded. Powdered samples (~ 50 mg) are measured dispersed in polyethylene powder (PE) and pressed into 13 mm diameter pellets.

Table 2. EXAFS samples, temper times for transformation experiments, Lu(III) loadings, Lu L3 measured edge jumps

Samples	Temper times (h)	Loading (mg Lu/g)	Measured edge jump
HFO:Lu(III)	–	58.3*	0.096
	49	58.3*	0.111
	115	57.9*	0.124
	212	57.9*	0.273
Hematite:Lu(III)	–	56.2	0.069
Goethite:Lu(III)	–	58.1	0.044
Lu_2O_3	–	879	0.84

* mg Lu/g HFO initially introduced.

Results and discussion

Figure 1 depicts the sequential extraction results. Steady changes in the $(Fe_D\text{-}Fe_O)/Fe_D$ ratio, corresponding to the relative quantity of crystalline phase, occur with HFO transformation. A variation in the solid phase composition from ~10% crystalline phase in the starting product, HFO, to 100% in the transformation products occurs. This indicates that the crystallised Fe oxide hematite has formed after ~1 840 h (~76 d). Changes in the $(Lu_D\text{-}Lu_O)/Lu_D$ ratio from these extraction results show a similar trend: 0% in HFO and 85% of the Lu is extracted from crystallised phases.

The amount of exchangeable Fe does not change during the transformation process and is constant at ~0.1% Fe_D, whereas the water-soluble amount of Lu increases from 3.4% to 10.7%.

These results indicate that Lu binding changes with HFO transformation and suggest that high Lu concentrations are incorporated into the goethite/hematite structure. To confirm these results, EXAFS investigations are performed.

Figure 2 shows the Fourier filtered first shell oxygen neighbour k^2-weighted EXAFS spectra for the Lu samples studied. Results of fits to the filtered oscillation are listed in Table 3. Comparison of results show that Lu first oxygen co-ordination shell in the transformation product differs from the sorbed species and varies with the temper time. The intensity and symmetry of this shell's Fourier transform (FT) peak decrease and the peak maximum shifts towards shorter distances as a function of temper time. The metrical parameters associated with these changes show an increase in the Debye-Waller factor and a decrease in Lu-O bond length. The Lu species initially sorbed onto HFO at $pH \geq 5.1$ has been identified in a previous EXAFS investigation as a bidentate species [11]. The species exhibits a Fe-Lu distance of 3.38 Å corresponding to bonding of Lu cations to FeO_6 polyhedra edges. No evidence of Lu precipitation is found. The transformation products differ from that observed for Lu_2O_3 and from Lu sorbed onto HFO, hematite and goethite. Similar to Lu sorbed onto HFO, the transformation products exhibit a FT peak at ~3.0 Å (without phase shift correction) attributed to a second co-ordination shell of Fe atoms. This peak shows less variation in position and intensity than the first oxygen shell. No reliable fit of the data using Lu-Lu phase and amplitude scattering functions is possible. The lack of a Lu-Lu interaction excludes the presence of sorbed polynuclear species and significant precipitation of the Lu phase. A minor fraction of poorly ordered Lu-precipitate might, however, remain undetected.

Figure 2. k^2-weighted Lu L3 transmission spectra first shell FT filtered EXAFS (left) and Fourier transforms (right) of experimental EXAFS (open circles) and theoretical contribution of the first Lu-O shell obtained from fits (lines)

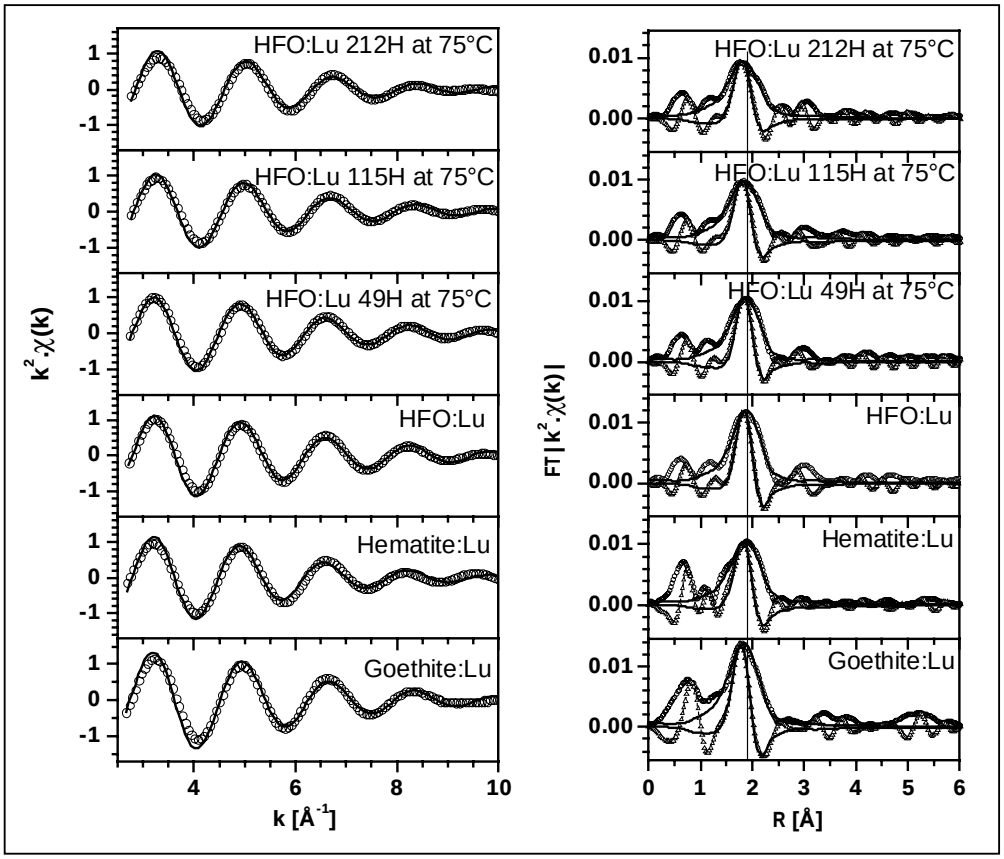

Table 3. EXAFS results from the fit of the first Fourier filtered Lu-O shell. S_0^2 = 1.

Sample	Temper time (h)	N	R [Å]	σ^2 [10^{-3} Å^2]	ΔE_0 [eV]
HFO:Lu	0	6.8	2.30	8.60	4.0
	49	6.2	2.29	9.68	4.0
	115	6.2	2.26	10.94	3.9
	212	6.8	2.25	13.03	4.0
Hematite:Lu	0	7.4	2.29	11.55	4.1
Goethite:Lu	0	8.2	2.27	10.44	2.8
Lu_2O_3	0	6.5	2.22	6.8	7.5

A major difference between EXAFS spectra of the transformation products and the reference samples of Lu sorbed onto goethite and hematite is the missing Fe co-ordination shell at ~3 Å. Because the Lu co-ordination is observed to be different than in the case of Lu sorbed onto HFO, goethite or hematite, which excludes the possibility of a Lu re-sorption onto the newly hematite phase, and because the Lu co-ordination changes during the transformation process, we conclude that Lu is incorporated into the Fe oxide during transformation of HFO, corroborating interpretation of extraction results.

Conclusion

The speciation of Lu(III) initially surface sorbed onto HFO changes during the HFO transformation into hematite. Extraction studies show that Lu is extracted with the crystalline Fe phase from the transformation products. Results of the EXAFS study show that the Lu co-ordination in the transformation product differs from that in Lu sorbed onto HFO, hematite or goethite.

Both extraction results and EXAFS investigation suggest that Lu(III) (as homologue for trivalent actinides), is incorporated into the Fe oxide phase following transformation. This result has direct implications for the solubility/mobility of actinides incorporated into Fe oxide phases forming from, for example, nuclear waste container corrosion products.

REFERENCES

[1] J.L. Jambor, J.E. Dutrizac, "Occurrence and Constitution of Natural and Synthetic Ferrihydrite, a Widespread Iron Oxyhydroxide", *Chem. Rev*., 98, 2549 (1998).

[2] U. Schwertmann and R.M. Cornell, "Iron Oxides in the Laboratory (Preparation and Characterization)", VCH Verlagsgesellschaft mbH Weinheim (1991).

[3] O.P. Mehra and M.L. Jackson, "Iron Oxide Removal from Soils and Clays by a Dithionite-citrate System Buffered with Sodium Bicarbonate", *Clays Clay Minerals*, 7, 317 (1960).

[4] U. Schwertmann, "Differenzierung der Eisenoxide des Bodens durch Extraktion mit Ammoniumoxalat-Lösung", *Z. Pflanzenernähr. Düng. Bodenkund.*, 105, 194 (1964).

[5] D.L. Sparks, *et al*. "Methods of Soils Analysis Part 3: Chemical Methods", Soil Science Society of America, Inc., Madison, Wisconsin, USA (1996).

[6] W.H. McMaster, N. Kerr Del Grande, J.H. Mallett and J.H. Hubbell, "Compilation of X-ray Cross-sections", Lawrence Livermore National Laboratory (1969).

[7] M. Newville, P. Livins, Y. Yacoby, J.J. Rehr and E.A. Stern, *Phys. Rev. B*, 47, 14126 (1993).

[8] D.E. Koningsberger and R. Prins, "X-ray Absorption : Principles, Applications, Techniques for EXAFS, SEXAFS and XANES", Wiley Interscience New York (1988).

[9] T. Ressler, "WinXAS: A New Software Package Not Only for the Analysis of Energy-dispersive XAS Data", *J. Physique IV*, 7 (C2), 269 (1997).

[10] L.A. Ankudinov, B. Ravel, J.J. Rehr and S.D. Conradson, "Real-space Multiple Scattering Calculation and Interpretation of X-ray Absorption Near-edge Structure", *Phys. Rev. B*, 58 (12), 7565 (1998).

[11] K. Dardenne, T. Schäfer, M.A. Denecke, J. Rothe and J.I. Kim, *Radiochim. Acta* (accepted).

A SPLICE PROGRAM TO CONNECT TWO DIFFERENT EXAFS SPECTRA OF THE SAME SAMPLE

Harald Funke[1], **Horst Böttger**[2], **Tobias Reich**[1], **Christoph Hennig**[1], **André Roßberg**[1]
[1]Institute of Radiochemistry
[2]Department Communication and Data Processing
Forschungszentrum Rossendorf e.V.
01314 Dresden, Postfach 510119, Germany

Abstract

A computer program is presented that is able to connect (to "splice") two EXAFS spectra of the same sample if they have an overlapping energy region. This tool will be useful in many situations when it is impossible to measure a spectrum over the desired energy range in a single scan.

Technical details of the SPLICE program are described to overcome the difficulties concerning the adjustment of different EXAFS spectra containing information about the same sample at different energies. The SPLICE program was tested at the U L_{III} edge using EXAFS spectra of a uranyl arsenate sample measured up to k of 22 $Å^{-1}$ at a temperature of 15 K.

Introduction

The radiochemical experimental station at the Rossendorf beam line has been designed, among other things, to perform EXAFS experiments using a closed cycle He-cryostat, which allows cooling of the sample down to 15 K. During the first commissioning experiments with the cryostat in autumn 1999, sometimes the technical problem of obtaining one continuous low-noise EXAFS scan over a wide k range arose. In spite of the fact that this situation was overcome, the idea of connecting two different parts of an EXAFS scan in a unique way was developed. Thus, the computer program SPLICE was written to merge two different EXAFS spectra of the same sample in an overlapping energy region. The word “splice” was chosen because of the analogy to the old sailing trade “splicing”.

The SPLICE program may be a useful tool to overcome difficulties due to insufficient time during an EXAFS experiment. Different situations may cause such time problems, e.g.:

- Any interruption or perturbation of the synchrotron beam.
- The refill times are too frequent for the experiment.
- Only the noisy part (in general the rear part of the spectrum) needs some repetitions for an amendment of the statistics of the EXAFS scan.

In this article the idea and some computational details of the Fortran program SPLICE will be described. The functionality of the SPLICE program is demonstrated by the application to a set of real EXAFS spectra.

Description of the program SPLICE

Two raw EXAFS scans of the same sample – SCAN1 and SCAN2 – are given. Both sets are recorded at different energy regions with an overlapping region of about 50 data points. Therefore, each scan is represented by the energy values E (the abscissa x) and the attached absorption values (the ordinate y), which are for transmission experiments defined by $\ln(I_0/I_1)$. Thus, we have two pairs of data vectors: SCAN1X, SCAN1Y of size n_1 and SCAN2X, SCAN2Y of size n_2. The first scan covers an energy range from below the absorption edge up to an energy E_2, which corresponds in our theoretical and real (see below) examples to wave vector ranges of k = 12...18 $Å^{-1}$. The second scan begins nearly 50 scan points (about 250 eV) below the end of SCAN1 (at energy E_1) and ends at an energy which corresponds to higher values of k.

The energy range between the beginning of SCAN2 and the end of SCAN1 forms an overlapping area (E_1,E_2). Ideally, within this area both scans should be identical. However, by reason of physical and technical conditions the following small differences of the second scan relative to the first scan will occur:

- Displacement of measured energy values of SCAN2.
- Differences of SCAN2 caused by background noise.
- Calibration difference concerning the absorption magnitude $\ln(I_0/I_1)$ of SCAN2.

The intention of the program is to find an optimal translation for SCAN2 (concerning x and y) and a re-calibration factor λ (very close to 1.0) for "splicing" both scans together to handle them like one continuous scan. To do this, the shape differences of the two scans within the overlapping area will be evaluated and SCAN2 will be translated so that the shapes will optimally correspond.

By means of the Hermite third power polynomial interpolation method with non-equal intervals, the SCAN1 data form a unique, continuous and differentiable function $F_1(x)$ over the energy interval of SCAN1, as well as SCAN2 data form the function $F_2(x)$ in the same sense. Within the overlapping area (E_1,E_2) both functions are defined and integrable (see Figure 1).

Figure 1. Schematic illustration of the task of the program SPLICE. See text for the details.

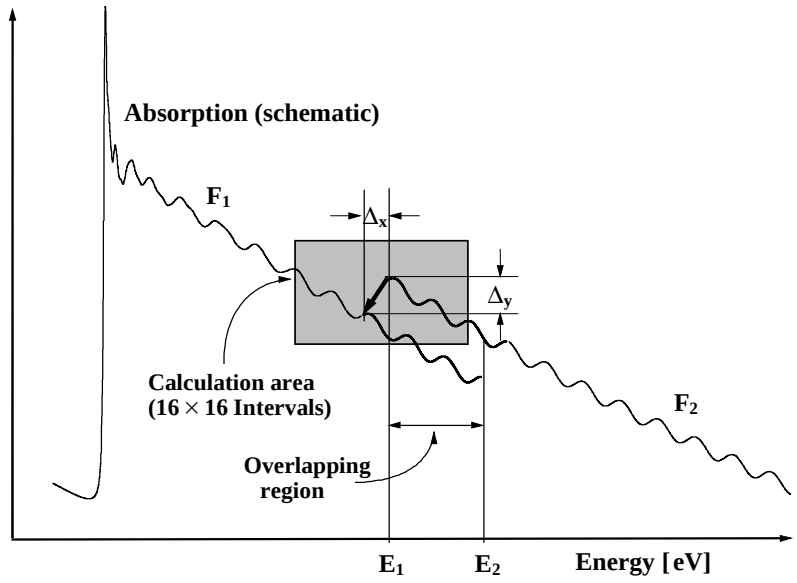

Now, the object is to find three parameters Δx, Δy and λ with the property that the area S(Δx, Δy) will achieve a minimum:

$$S(\Delta x, \Delta y) = \int_{E_1}^{E_2} \left\| F_1(x) - \left(F_2(x - \Delta x) - \Delta y\right) \cdot \lambda \right\| dx \Rightarrow \min$$

Here a dilatation parameter λ is introduced to correct some calibration differences between the two absorption functions F_1 and F_2 caused by small changes of the experimental conditions. Otherwise a unique minimum of S cannot be found. Note that the only fit parameter for the search of the minimum are Δx and Δy. Therefore, λ must be chosen so that for each Δx and Δy is valid:

$$\int_{E_1}^{E_2} \left(F_1(x) - \left(F_2(x - \Delta x) - \Delta y\right) \cdot \lambda\right) dx = 0$$

or explicitly:

$$\lambda = \int_{E_1}^{E_2} F_1(x)\,dx \Big/ \int_{E_1}^{E_2} \left(F_2(x - \Delta x) - \Delta y\right) dx$$

The initial placement of the points of SCAN2 means $\Delta x = 0$, $\Delta y = 0$ and $\lambda = 1$. To find the optimal values for the parameters, the following iteration method is carried out. First a primary fit area of suitable extent Dx, Dy (20 eV in energy and 20% of the absorption turn out to be convenient default values) is defined to vary Δx and Δy:

$$-Dx/2 < \Delta x < +Dx/2$$
$$-Dy/2 < \Delta y < +Dy/2$$

Over this small rectangle a lattice of 17×17 points is constructed. $S(\Delta x,\Delta y)$ will be calculated on each x-y-lattice point by integration described above. The values of the function S form a mesh over the lattice. These 289 values will be sorted by increasing order. Five subsets of 200, 100, 50, 20 and 10 lattice points are built, in each case that with the lowest values of S. To find the minimum of S within the lattice, for all 289 points and for the five subsets, six polynomials of second order:

$$P(x,y) = ax^2 + by^2 + cxy + dx + ey + f$$

will be fitted according to the Gaussian normal equations. For each fit, the coefficients of P are analysed: If $a > 0$ and $b > 0$, a real minimum (vertex) exists and will be calculated. From these (maximum six) vertices that with the best fitting is chosen (as a rule, this concerns the fit with 10 points). The position of this minimum within the lattice leads to the values of the parameters Δx and Δy that have been searched for. Now, for the points taking part in the best fit, the surrounding rectangle is built. If this rectangle is still too big, its extent will become the new fit area (Dx,Dy) and a new iteration step will take place. Otherwise the iteration terminates and Δx, Δy and the corresponding λ are considered to be the solution of the task. In practice four or five iteration steps are necessary.

Thus, the program generates the spliced scan that consists of two parts:

1. All points of SCAN1 with energy values below the reference point. These data will not be changed.

2. The points of SCAN2, beginning with the reference point. These data are changed according to our objective:

$$SCAN2X.out = SCAN2X + \Delta x$$
$$SCAN2Y.out = (SCAN2Y + \Delta y)\cdot\lambda$$

The output file for the spliced scan consists of three columns:

1. Index, pointing of the former position within the original scan.

2. Value of x (energy).

3. Value of y (absorption).

More detailed information to follow the optimisation process is stored in a result file. First experience shows that the results are practically does not depend on the type of chosen interpolation, integration and norm. The crucial point for the iteration procedure to find a unique minimum is the introduction of the depending calibration parameter λ.

If the iteration process cannot find a stable minimum as a result of too much noise or other defects of the spectra, the user will get a message that a splicing of the two scans is impossible.

The final range of the parameters found is usually:

$$|\Delta x| < 1 \text{ eV}$$
$$|\Delta y| < 0.005$$
$$|\lambda - 1| < 0.001$$

Test experiments

Experiments were performed to test the SPLICE program using real EXAFS spectra up to a k of 22 $Å^{-1}$ at the U L_{III} edge of a uranyl arsenate sample with the sum formula $H_2[UO_2AsO_4]_2 \cdot 8H_2O$. To reduce thermal vibrations, the sample was cooled to 15 K using a closed-cycle He cryostat. The measurements were carried out on the Rossendorf Beamline (ROBL) at the European Synchrotron Radiation Facility (ESRF). The data were analysed by standard methods using the computer program EXAFSPAK [1]. Phase and amplitude functions were calculated with the FEFF8 program [2]. Aspects of the structure and co-ordination chemistry of the EXAFS studies on uranyl arsenates and similar compounds are discussed elsewhere [3].

Three different EXAFS spectra as well as the corresponding Fourier transforms and fit results using EXAFSPAK were compared. The first two spectra consist of two different scans connected by the program SPLICE, and the third spectrum consists of one uninterrupted continuous scan.

- *Splice A*: Two absorption spectra, both scanned with an equal step in k-space of $\Delta k = 0.05$ $Å^{-1}$ are spliced at k = 15 $Å^{-1}$ to give an entire EXAFS spectrum with a length of k = 22 $Å^{-1}$.

- *Splice B*: Two absorption spectra, the first scanned with an equal step in k-space of $\Delta k = 0.05$ $Å^{-1}$ and the second with an equal step of $\Delta k = 0.02$ $Å^{-1}$ are spliced at k = 15 $Å^{-1}$ to give an entire EXAFS spectrum with a length of k = 22 $Å^{-1}$. This is a demonstration of the ability of the SPLICE program to connect two scans recorded with different steps in k-space.

- *Without splicing C*: For comparison with the spliced spectra, one entire spectrum was recorded over the whole range of k = 22 $Å^{-1}$ with an equal step of $\Delta k = 0.05$ $Å^{-1}$.

Figure 2 compares the graphs of the three test spectra. The values of the fit results and their standard deviations using the OPT module of EXAFSPAK are shown in Table 1. The present fit model was chosen in analogy to [3] to demonstrate the equality of the three spectra A, B and C. A detailed fit analysis is presented in [3].

Significant differences are not visible between the graphs of the three spectra. Table 1 shows the numerical values of the fitted data including the standard deviations. Within the standard deviation, the fit results are identical for spectra A, B and C.

Note that the normalised cross-correlation function $G(\kappa = 0)$ of any two of the three spectra are very close to one. This means that if κ is the lag size of k, the following relation is fulfilled:

$$G(\kappa) = \int A(k) \cdot C(k - \kappa) dk \Big/ \sqrt{\int A(k)^2 dk \cdot \int C(k)^2 dk}$$

with $G(\kappa) \Rightarrow 1$ for $\kappa \Rightarrow 0$.

Keeping in mind the nearly equal form of the graphs of the functions A(k) and C(k), this is the analytical expression for the fact that both functions A(k) and C(k) contain the same information.

Figure 2. Uranium L_{III}-edge k^3-weighted EXAFS spectra and corresponding Fourier transforms of the spliced spectra A and B in comparison with the spectrum C (without splicing)

Experimental data – solid lines; fit – thin solid lines

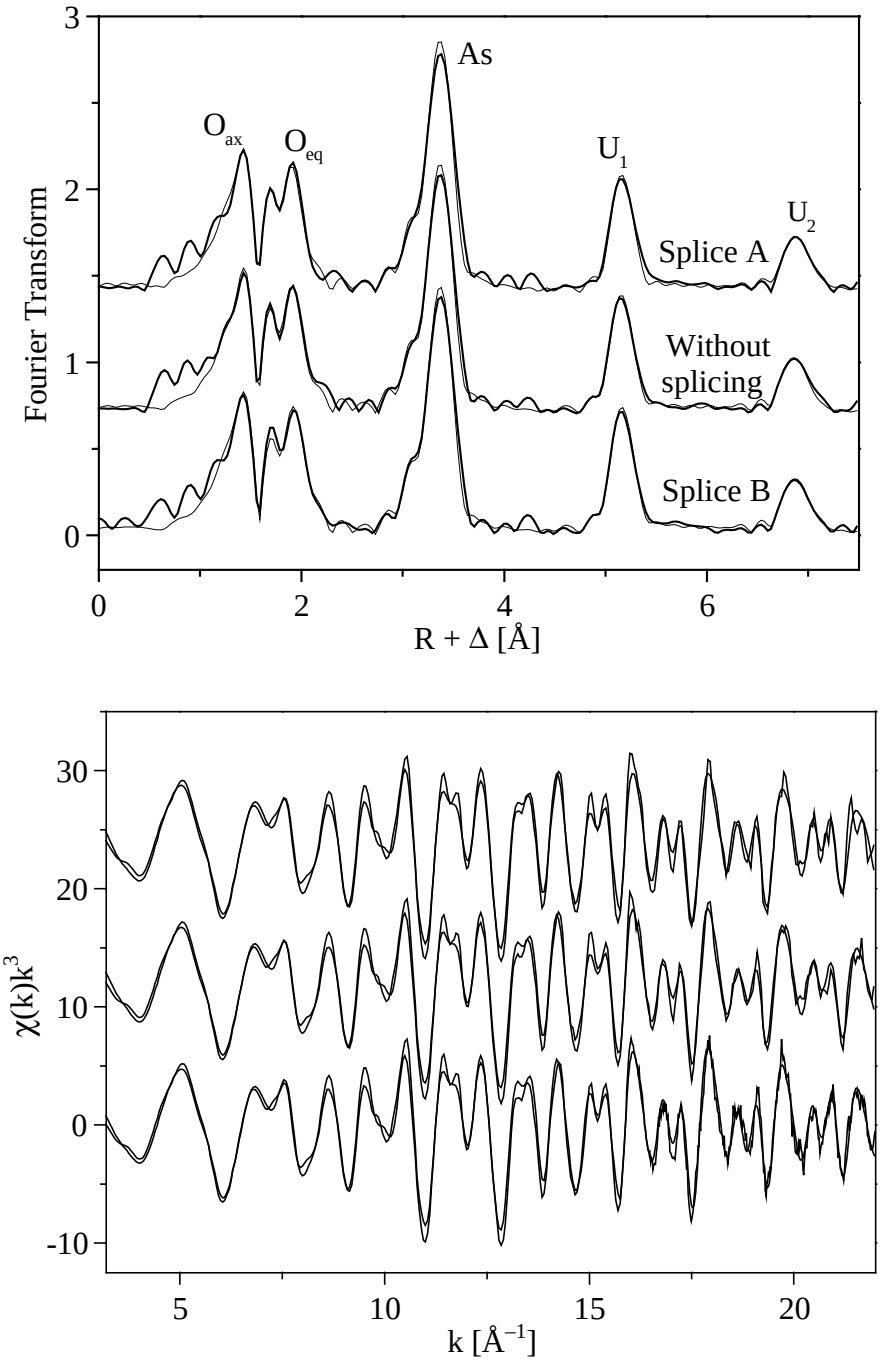

Table 1. Fitted co-ordination numbers, distances, Debye-Waller factors and ΔE_0 shifts of the three test spectra (see text) for the five relevant co-ordination shells

The multiple scattering (ms) path U-Oax-U-Oax-U (coupled to U-Oax-U) is included in the fits

Co-ord. shell	A	B	C	A	B	C
	N			R [Å]		
Oax	1.94(0.11)	2.05(0.10)	1.82(0.10)	1.789(0.003)	1.791(0.002)	1.790(0.002)
Oax(ms)	2.0	2.0	2.0	3.578	3.583	3.579
Oeq	4.65(0.26)	4.31(0.22)	4.76(0.25)	2.296(0.003)	2.306(0.002)	2.302(0.003)
As	3.99(0.17)	4.15(0.15)	3.90(0.15)	3.702(0.001)	3.700(0.001)	3.702(0.001)
U1	5.88(0.67)	5.16(0.49)	5.32(0.57)	5.402(0.003)	5.400(0.002)	5.400(0.003)
U2	4.61(1.16)	5.88(1.17)	5.92(1.32)	7.191(0.006)	7.181(0.004)	7.180(0.005)
	$\sigma^2 \cdot 10^3$ [Å^2]			ΔE_0		
Oax	1.56(0.18)	1.69(0.14)	1.29(0.16)	-10.2(1.3)	-9.8(1.1)	-10.5(1.2)
Oax(ms)	3.12	3.39	2.61	-10.2	(-9.8	-10.5
Oeq	2.29(0.21)	1.94(0.14)	2.39(0.20)	-16.4(1.0)	-14.5(0.8)	-15.2(0.9)
As	1.49(0.09)	1.62(0.07)	1.45(0.09)	-14.2(0.5)	-14.9(0.5)	-14.6(0.5)
U1	3.03(0.20)	2.61(0.14)	2.80(0.19)	-13.3(0.9)	-13.8(0.8)	-14.1(0.9)
U2	2.17(0.38)	2.58(0.30)	2.62(0.36)	-23.5(1.8)	-25.0(1.5)	-24.5(1.6)

Summary

The possibility to connect two different absorption spectra of the same sample with an overlapping energy region is demonstrated on two spliced example-spectra in comparison with the corresponding spectrum received from one continuous scan. The computer program SPLICE is presented, which has been developed to perform the desired connection procedure.

REFERENCES

[1] G.N. George and I.J. Pickering, "EXAFSPAK, A Suite of Computer Programs for Analysis of X-ray Absorption Spectra", Stanford Synchrotron Radiation Laboratory, Stanford, USA (1995).

[2] A.L. Ankudinov, B. Ravel, J.J. Rehr and S.D. Conradson, *Phys. Rev*., B58, 7565-7576 (1998).

[3] C. Hennig, T. Reich, H. Funke, A. Rossberg, M. Rutsch, G. Bernhard, "EXAFS as a Tool for Bond Length Determination in the Environment of Heavy Atoms", *J. Synchrotron Radiat*., 8, 695-697, (2001).

ANALYSIS OF ATOMIC DISTANCES IN INACCURATELY DETERMINED HEAVY-ATOM CRYSTAL STRUCTURES USING EXAFS SPECTROSCOPY

C. Hennig, T. Reich, H. Funke, A. Roßberg, M. Rutsch, G. Bernhard
Forschungszentrum Rossendorf e.V., Institute of Radiochemistry
P.F. 510119, 01314 Dresden, Germany

Abstract

X-ray diffraction techniques allow a precise analysis of crystal structures. With modern equipment, even hydrogen atoms can be determined adjacent to heavy atoms. In the presence of heavy atoms, X-ray diffraction analysis is complicated because the structure factor is mainly influenced by the heavy scatterers. The error in the determination of atomic co-ordinates increases for light atoms. Additionally, if the heavy atoms are located at special positions, the space group can remain uncertain. In such cases it is difficult to find an independent criterion for the accuracy of the bond-length determination additional to the R-value. We demonstrate that extended X-ray absorption fine structure (EXAFS) spectroscopy is a useful tool for the investigation of local bond lengths in the environment of heavy atoms. As an example, the atomic distances of meta-zeunerite, $Cu[UO_2AsO_4]_2 \cdot 8H_2O$, and trögerite, $H[UO_2AsO_4] \cdot 4H_2O$, were determined by EXAFS measurements and compared to literature data of diffraction measurements.

Introduction

Extended X-ray absorption fine structure (EXAFS) spectroscopy allows a direct determination of bond lengths in heavy-atom structures and avoids, therefore, problems in the XRD analysis caused by the coexistence of very heavy and light scatterers. But EXAFS is limited to a short range around the absorbing atom and provides only average bond length values. We chose a structure type with a high symmetry around uranium to avoid uncertainties from averaging different bond lengths in the same co-ordination shell. EXAFS was used to determine bond lengths around heavy scatterers in meta-zeunerite, $Cu[UO_2AsO_4]_2 \cdot 8H_2O$, and trögerite, $H[UO_2AsO_4] \cdot 4H_2O$.

Meta-zeunerite and trögerite belong to the structure family with the following chemical formula $A^{n+}[UO_2XO_4]_n^- \cdot mH_2O$, where $[XO_4]^{3-}$ appears as phosphate or arsenate and A is a hydrated monovalent or divalent cation. Each $[UO_2]^{2+}$ unit in this group of structures is built up by uranium with two double bonded oxygen atoms in axial direction (O_{ax}). This uranyl unit is surrounded in the equatorial plane by four oxygen atoms (O_{eq}) in a square planar arrangement. Tetrahedra of $[XO_4]^{3-}$ and tetragonal dipyramidal co-ordinated uranyl ions $[UO_2]^{2+}$ built up stable two-dimensional layers. These $[UO_2XO_4]_\infty$ layers are connected together forming a tetragonal or pseudo-tetragonal crystal morphology and a platy (001) habit. Charge neutrality of the uranyl arsenate layers is given by different interlayer cations like $[Cu(H_2O)_4]^{2+}$ in meta-zeunerite and $[H_3O]^+$ in trögerite. A detail of the uranyl arsenate layer structure $[UO_2AsO_4]_\infty$ is depicted in Figure 1. Table 1 gives lattice parameters and some bond distances within the $[UO_2XO_4]$ layer of the crystal structures with X = As, which are known up to now. Uranium and the axial oxygen atoms are positioned in the tetragonal space group at the four-fold symmetry axes. The positions of the surrounding O_{eq} and As atoms are symmetry equivalent. At low temperature, the crystal symmetry of $D[UO_2AsO_4] \cdot 4D_2O$ changes from the tetragonal space group P4/ncc at 305 K to triclinic space group $P\bar{1}$ at 4 K. However, the change in the lattice constants is small. A distance comparison within this group of crystal structures shows that the deviations in distances between uranium and surrounding heavy scatterers like arsenic and uranium are smaller than the deviations in distances between uranium and oxygen.

Figure 1. Detail of the uranyl arsenate layer $[UO_2AsO_4]_\infty$ in meta-zeunerite and trögerite. Distances are given for meta-zeunerite determined by EXAFS measurements.

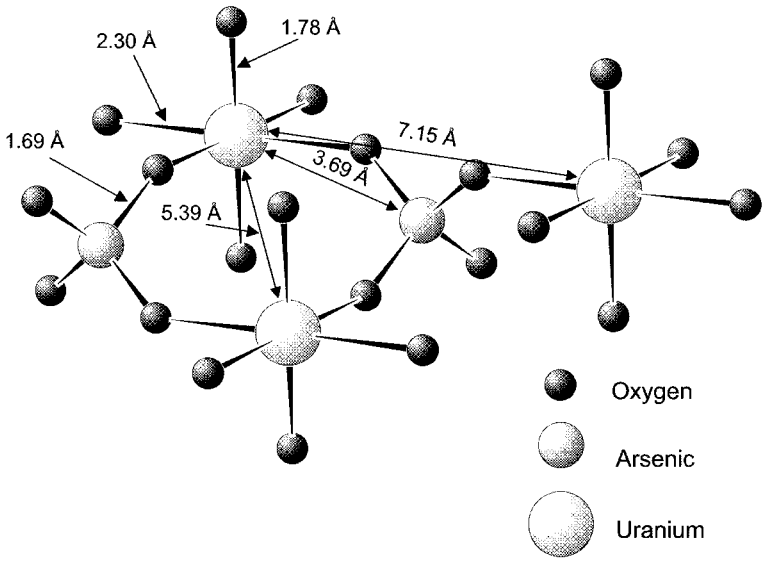

Table 1. Comparison of characteristic distances in the surrounding of uranium in the crystal structures of the type $A^{n+}[UO_2AsO_4]^-_n \cdot mH_2O$. Lattice constants and distances are given in Å.

Formula	Ref.	S.G.	a	c	U-O_{ax1}	U-O_{ax2}	U-O_{eq}	U-As	U-U
$Cu[UO_2AsO_4]_2 \cdot 8H_2O$	[1]	P 4_2/nmc	7.105	17.704	1.78	1.94	2.17	3.68	5.38
$K[UO_2AsO_4] \cdot 3H_2O$	[2]	P4/nnc	7.176	18.126	1.70	1.81	2.35	3.71	5.41
$KH_3O[UO_2AsO_4]_2 \cdot 6H_2O$	[2]	P4/nnc	7.171	18.048	1.70	1.77	2.33	3.71	5.41
$NH_4[UO_2AsO_4] \cdot 3H_2O$	[2]	P4/nnc	7.189	18.191	1.73	1.85	2.38	3.71	5.41
$Li[UO_2AsO_4] \cdot 4D_2O$	[3]	P4/n	7.0969	9.1903	1.76	1.82	2.31	3.68	5.37
$D[UO_2AsO_4] \cdot 4D_2O$*	[4]	P4/nnc	7.1615	17.6390	1.78	1.80	2.30	3.70	5.39
$D[UO_2AsO_4] \cdot 4D_2O$**	[5]	$P\bar{1}$	a = 7.1644 Å, b = 7.1124 Å, c = 17.5537 Å						
			α = 90.187°, β = 89.947°, γ = 90.003°						
				U(1)	1.78	1.80	2.25	3.66	5.30
							2.31	3.68	5.31
							2.35	3.68	5.46
							2.39	3.74	5.47
				U(2)	1.78	1.80	2.19	3.67	5.34
							2.25	3.70	5.35
							2.32	3.70	5.46
							2.36	3.73	5.47
			Average values:		1.78	1.80	2.30	3.70	5.39

*T = 305 K, ** T = 4 K

Experimental

A natural meta-zeunerite mineral, $Cu[UO_2AsO_4]_2 \cdot 8H_2O$, from Wheal Basset, Cornwall/England and a synthetic compound of $H[UO_2AsO_4] \cdot 4H_2O$ were used for EXAFS measurements. The samples were ground, mixed with boron nitride and pressed as 1.3 cm diameter pellets.

EXAFS measurements were carried out on the Rossendorf Beamline (ROBL) at the European Synchrotron Radiation Facility (ESRF) under dedicated ring conditions (6.0 GeV, 100-200 mA). The monochromator equipped with a water-cooled Si(111) double-crystal system was used in fixed-exit measuring mode. Higher harmonics were rejected by two Pt-coated mirrors [6]. Energy steps were calculated to give equidistant steps in *k*-space of 0.05 $Å^{-1}$. Uranium L_{III}-edge and arsenic K-edge EXAFS were collected in transmission geometry using argon-filled ionisation chambers. First inflection points at the Zr K-edge at 17 995.9 eV and at the Au L_{III}-edge at 11 919.7 eV of corresponding metal foils were used for energy calibration, respectively. The measurements were performed at room temperature. In addition, samples were measured at low temperature using a closed-cycle He cryostat to reduce thermal vibrations. EXAFS data were extracted from the raw absorption spectra by standard methods using the computer program EXAFSPAK [7]. Backscattering phase and amplitude functions were calculated using the FEFF8 code including self-consistent potential calculations [8]. The amplitude reduction factor, S_0^2, was held constant at 1.0 in the FEFF8 calculation and during the fit procedures. Phase and amplitude functions for the scattering pairs were calculated using clusters with a radius of 8.5 Å build-up by atomic co-ordinates of $D[UO_2AsO_4] \cdot 4D_2O$ [5] and own crystal structure data from X-ray diffraction measurements on $Cu[UO_2AsO_4]_2 \cdot 8H_2O$ [9].

Results and discussion

Uranium k^3-weighted EXAFS spectra of meta-zeunerite, $Cu[UO_2AsO_4]_2 \cdot 8H_2O$, and trögerite, $H[UO_2AsO_4] \cdot 4H_2O$ at T = 298 K and T = 15 K are shown in Figure 2.

Figure 2. U L_{III}-edge k^3-weighted EXAFS spectra (left) and the corresponding Fourier transforms (right) for $Cu[UO_2AsO_4]_2 \cdot 8H_2O$ at T = 298 K (a), $Cu[UO_2AsO_4]_2 \cdot 8H_2O$ at T = 15 K (b), $H[UO_2AsO_4] \cdot 4H_2O$ at T = 15K (c)

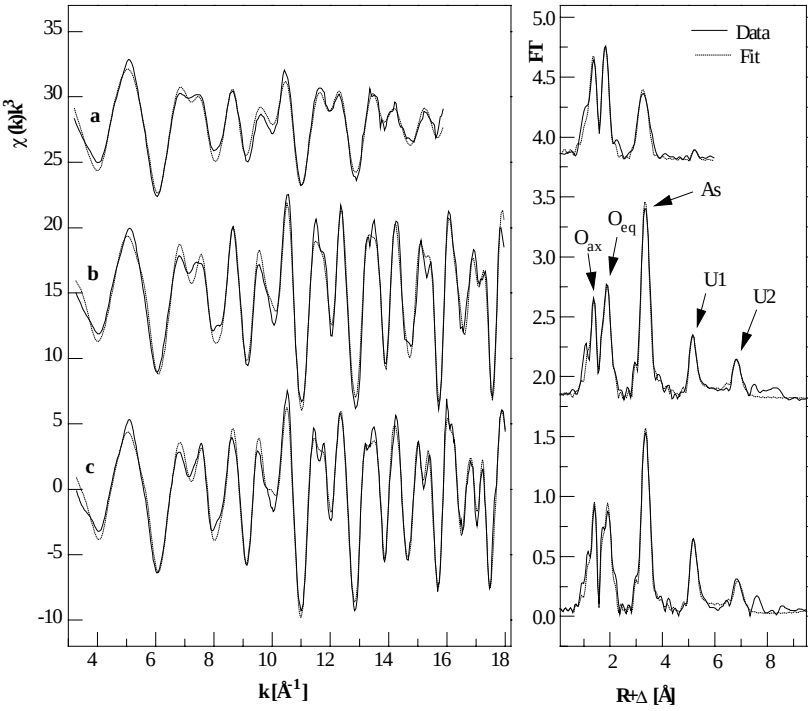

The first shell in both compounds represents the axial oxygen atoms, O_{ax}, at a distance of 1.77-1.78 Å and a co-ordination number of 1.6 (Table 2). The second shell corresponds to the bond distance of four symmetry-equivalent equatorial atoms (O_{eq}) with a bond length of 2.29-2.30 Å and a determined co-ordination number between 4.3 and 4.6. Deviations between expected co-ordination numbers (N_{Oax} = 2, N_{Oeq} = 4) and measured values arise from polarisation effects originating from the preferred orientation of the uranyl arsenate layers in the sample [10]. The arsenic scattering contribution gives a significant third Fourier transform peak with a calculated distance of 3.69-3.70 Å. At T = 298 K the U-U scattering contribution generates only a weak peak. To analyse higher shells, low temperature measurements were performed. At a temperature of 15 K, the scattering contributions of uranium appear in a U-U1 distance of 5.39 Å and a U-U2 distance of 7.15 Å for $Cu[UO_2AsO_4]_2 \cdot 8H_2O$. Within the error limits, EXAFS measurements on $H[UO_2AsO_4] \cdot 4H_2O$ at 15 K show the same distances except for the U-U2 shell. The distance values are calculated using Fourier filter procedures and used as start parameters for the fit of the entire spectrum. Multiple scattering (MS) effects were analysed using the FEFF8 program package. Because of their weak amplitude ratio, the $U\text{-}O_{ax1}\text{-}U\text{-}O_{ax2}\text{-}U$ MS contributions could be neglected. The energy shifts ΔE, used as a free parameter for low temperature measurements, differ widely from one another. A subtraction of the theoretical $U\text{-}U2\text{-}O_{eq}\text{-}U$ and $U\text{-}O_{eq}\text{-}U2\text{-}O_{eq}\text{-}U$ MS contributions from the experimental spectra reduces the energy shift of the U-U2 shell by 4 eV without

Table 2. U L_{III}-edge EXAFS structural parameters for $Cu[UO_2AsO_4]_2 \cdot 8H_2O$ (1) and $H[UO_2AsO_4] \cdot 4H_2O$ (2) at T = 298 K and T = 15 K

Sample	Shell	R [Å][a]	N[b]	σ^2 [Å^2]	ΔE [eV]
1	U-O_{ax}	1.77	1.6(1)	0.0021	0.1
298 K	U-O_{eq}	2.29	4.5(1)	0.0035	
	U-As	3.70	2.7(2)	0.0039	
1	U-O_{ax}	1.78	1.6(1)	0.0028	5.5
15 K	U-O_{eq}	2.30	4.3(2)	0.0021	2.1
	U-As	3.69	3.5(2)	0.0012	0.2
	U-U1	5.39	3.7(6)	0.0027	-1.4
	U-U2	7.15	3.1(9)	0.0012	-10.8
2	U-O_{ax}	1.78	1.6(1)	0.0016	6.2
15 K	U-O_{eq}	2.30	4.6(1)	0.0020	2.4
	U-As	3.70	4.1(2)	0.0015	0.7
	U-U1	5.40	5.4(5)	0.0029	1.7
	U-U2	7.21	6.3(2)	0.0023	-9.1

[a] Errors in distances R are ± 0.02 Å.
[b] Errors in co-ordination numbers N are ± 25% with standard deviations in ( ), σ^2 Debye-Waller factor.

significantly changing the distance determined. The atomic distance U-U2 corresponds to the **a** lattice constant. The crystal structure of $[UO_2DAsO_4] \cdot 4D_2O$ shows a phase transition between temperatures of 305 K and 4 K [5], but the calculated average atomic distances are only weakly influenced. For $Cu_2[UO_2AsO_4]_2 \cdot 8H_2O$, a similar phase transition is expected. At 298 K the space group of the crystal structure is also P4/ncc [9].

EXAFS measurements with As as the absorbing atom are shown for meta-zeunerite at 298 K and 15 K in Figure 3. Calculated values are given in Table 3. The arsenate tetrahedra is characterised by the As-O_{eq} distance of 1.68-1.69 Å with a calculated co-ordination number of 5.1 at room temperature and 3.7 at 15 K. The As-U1 distance is determined to 3.68-3.69 Å with co-ordination number of 2.8 at room temperature and 4.2 at 15 K. At low temperature, the fit procedure gives for the As-As shell a distance of 5.02 Å and for the As-U2 shell a distance of 8.01 Å. Within the error limits, the measurements on $H[UO_2AsO_4] \cdot 4H_2O$ at 43 K show the same distances. Similar to the U L_{III}-edge, the energy shift ΔE differs, in particular for the distant shells. FEFF8 simulation showed that MS contributions are negligible for the As K-edge.

Both the EXAFS measurements at the uranium L_{III}-edge and the measurements at the arsenic K-edge give only distances within the uranyl arsenate layer, but no structural information concerning the interlayer cation arrangement.

In Table 4, atomic distances determined by EXAFS measurements are compared to X-ray diffraction data from the literature. The EXAFS data on the $H[UO_2AsO_4] \cdot 4H_2O$ sample show a good agreement with the neutron diffraction literature data. The measurements on $D[UO_2AsO_4] \cdot 4D_2O$, described in the literature, were taken with neutron diffraction on a powder sample at room temperature [4] and at 4 K [5] and analysed using Rietveld refinement procedures. For $Cu[UO_2AsO_4]_2 \cdot 8H_2O$, the observed atomic distances between heavy and light scatterers deviate approximately 0.1-0.2 Å from the literature data of single crystal X-ray diffraction measurements [1]. However, the atomic distances

Figure 3. As K-edge k^3-weighted EXAFS spectra (left) and the corresponding Fourier transform (right) for $Cu[UO_2AsO_4]_2 \cdot 8H_2O$ at T = 298 K (a), $Cu[UO_2AsO_4]_2 \cdot 8H_2O$ at T = 15 K (b), $H[UO_2AsO_4] \cdot 4H_2O$ at T = 43 K (c)

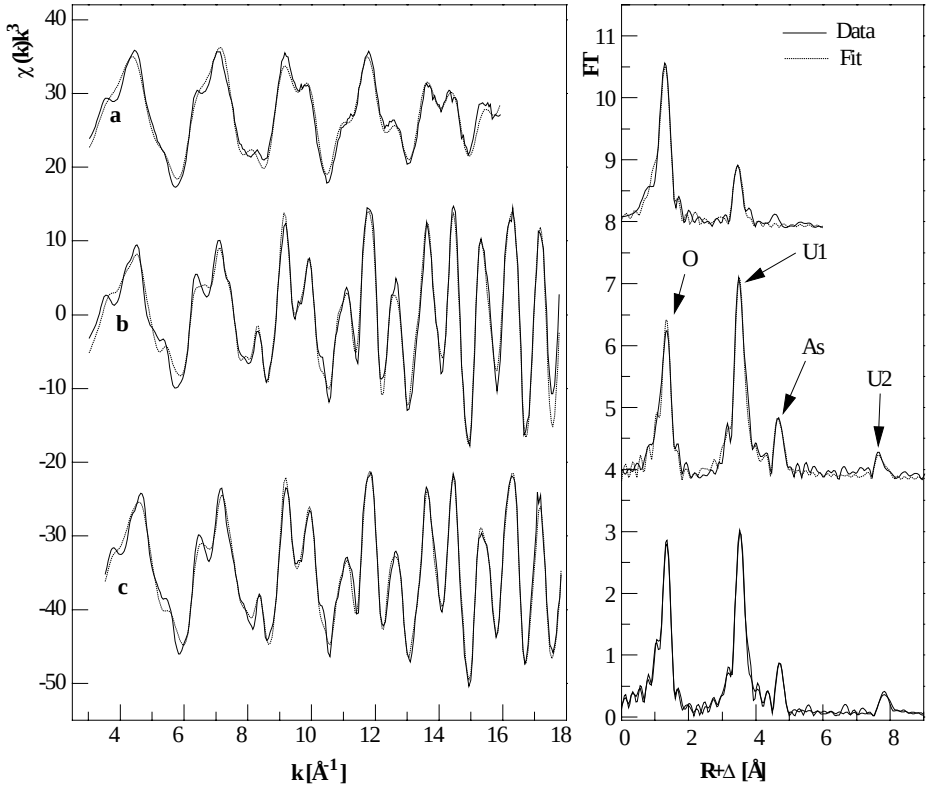

Table 3. As K-edge EXAFS structural parameters for $Cu[UO_2AsO_4]_2 \cdot 8H_2O$ (1) at T = 298 K and T = 15 K and $H[UO_2AsO_4] \cdot 4H_2O$ (2) at T = 43 K

Sample	Shell	R [Å] [a]	N [b]	σ^2 [Å^2]	ΔE [eV]
1	As-O_{eq}	1.68	5.1(1)	0.0025	-7.2
298 K	As-U1	3.68	2.8(13)	0.0042	
1	As-O_{eq}	1.69	3.7(1)	0.0014	-1.7
15 K	As-U1	3.69	4.2(2)	0.0016	-7.1
	As-As	5.02	3.1(5)	0.0013	-9.7
	As-U2	8.01	6.5(9)	0.0030[c]	-13.9
2	As-O_{eq}	1.69	4.1(1)	0.0018	0.6
43 K	As-U1	3.70	3.9(2)	0.0018	-3.9
	As-As	5.06	4.9(6)	0.0036	-0.8
	As-U2	8.04	8.3(8)	0.0035[c]	-9.5

[a] Errors in distances R are ± 0.02 Å.
[b] Errors in co-ordination numbers N are ± 25% with standard deviations in ( ).
[c] Fixed, σ^2 Debye-Waller factor.

Table 4. Comparison of the atomic distances from EXAFS measurements with diffraction data from literature. Distances are given in Å.

Shell	$Cu[UO_2AsO_4]_2 \cdot 8H_2O$		$X[UO_2AsO_4] \cdot 4X_2O$	
	EXAFS	XRD [1]	EXAFS	ND [4,5]
U-O_{ax}	1.78	1.94, 1.78	1.78	1.78, 1.80
U-O_{eq}	2.30	2.17	2.30	2.30
U-As	3.69	3.68	3.70	3.70
U-U1	5.39*	5.38	5.40*	5.39
U-U2	7.15*	7.10	7.21*	7.16
As-O_{eq}	1.68	1.77	1.69**	1.68
As-As	5.02*	5.02	5.06**	5.06
As-U2	8.01*	8.00	8.04**	8.04

XRD = X-ray diffraction.
ND = Neutron diffraction.
X = H for the EXAFS measurements
X = D in the literature [4,5].
*T = 15 K, **T = 43 K

between heavy scatterers agree well with the EXAFS data. As sometimes observed in heavy atom structures, the position of the heavy scatterers are correctly determined, but the positions of the light atoms are incorrect. However, EXAFS measurements are restricted to atomic distance determinations in the form of radial distribution functions. This is connected with a loss of the bonding angle information. For this reason and taking into account that Hanic [1] could use only intensities from Weißenberg photographs for his structure analysis, the crystal structure of meta-zeunerite was completely redetermined using single crystal diffraction measurements [9]. These measurements confirmed the structural parameters given by the EXAFS measurements. The difficulty for this single crystal structure analysis seems to be caused by stacking faults of the $[UO_2XO_4]_\infty$ layers in the **c** lattice direction.

Conclusion

The atomic distances between heavy and light atoms in meta-zeunerite show differences of approximately 0.1 Å in comparison to X-ray diffraction literature data [1], whereas the EXAFS measurements and the neutron diffraction literature data of trögerite [4,5] are in good agreement. A revision of the $Cu[UO_2AsO_4]_2 \cdot 8H_2O$ crystal structure shows an agreement in the error limits of 0.02 Å between atomic distances determined by EXAFS and X-ray diffraction measurements [9]. The presented investigation demonstrates that a bond-length determination independent from crystal quality, knowledge of symmetry and lattice parameters can be helpful as a criterion of the accuracy of distances between heavy and light atoms. EXAFS spectroscopy has proven to be a useful tool for determining local bond lengths in the environment of heavy atoms. The comparison between $H[UO_2AsO_4] \cdot 4H_2O$ and $Cu[UO_2AsO_4]_2 \cdot 8H_2O$ points out that no significant structural differences appear in the uranyl arsenate layers.

REFERENCES

[1] F. Hanic, "The Crystal Structure of Meta-zeunerite $Cu(UO_2)_2(AsO_4)_2 \cdot 8H_2O$", *Czech. J. Phys. B*, 10, 169-181 (1960).

[2] M. Ross, H.T. Evans, Jr., "Studies of the Torbernite Minerals (I): The Crystal Structure of Abernathyite and the Structurally Related Compounds $NH_4UO_2AsO_4 \cdot 3H_2O$ and $KH_3O(UO_2AsO_4)_2 \cdot 6H_2O$", *Am. Mineral.*, 49, 1578-1602 (1964).

[3] A.N. Fitch, B.E.F. Fender, A.F. Wright, "The Structure of Deuterated Lithium Arsenate Tetrahydrate $LiUO_2AsO_4 \cdot 4D_2O$ by Powder Neutron Diffraction", *Acta Cryst. B*, 38, 1108-1112 (1982).

[4] A.N. Fitch, L. Bernard, A.T. Howe, A.F. Wright, B.E.F. Fender, "The Room Temperature Structure of $DUO_2AsO_4 \cdot 4D_2O$", *Acta Cryst. C*, 39, 159-162 (1983).

[5] A.N. Fitch, L. Bernard, A.T. Howe, A.F. Wright, B.E.F. Fender, "The Structure of $UO_2DAsO_4 \cdot 4D_2O$ at 4 K by Powder Neutron Diffraction", *Acta Cryst. B*, 39, 2546-2554 (1982).

[6] W. Matz, N. Schell, G. Bernhard, F. Prokert, T. Reich, J. Claußner, W. Oehme, R. Schlenk, S. Dienel, H. Funke, F. Eichhorn, M. Betzl, D. Pröhl, U. Strauch, G. Hüttig, H. Krug, W. Neumann, V. Brendler, P. Reichel, M.A. Denecke, H. Nitsche, "ROBL – A CRG Beamline for Radiochemistry and Materials Research at the ESRF", *J. Synchrotron Radiat*., 6, 1076-1085 (1999).

[7] G.N. George, I.J. Pickering, "EXAFSPAK, A Suite of Computer Programs for Analysis of X-ray Absorption Spectra", Stanford Synchrotron Radiation Laboratory, Stanford, CA, USA (1995)

[8] A.L. Ankudinov, B. Ravel, J.J. Rehr, S.D. Conradson, "Real-space Multiple-scattering Calculation and Interpretation of X-ray Absorption Near-edge Structure", *Phys. Rev. B*, 58 7565-7576 (1998).

[9] C. Hennig, G. Reck, T. Reich, A. Rossberg, W. Kraus, J. Sieler, in preparation.

[10] C. Hennig, G. Nolze, "Characterisation of the Preferred Orientation in EXAFS Samples Using Bragg-Brentano X-ray Diffraction", Proceedings of the Workshop on Speciation, Techniques and Facilities for Radioactive Materials at Synchrotron Light Sources, 4-6 Oct. 1998, Grenoble, France, NEA/OECD Paris, 235-343 (1999).

EXAFS ANALYSES OF TECHNETIUM(I) TRICARBONYL COMPLEXES – LIGAND EXCHANGE STUDIES

J-U. Künstler, S. Seifert, T. Reich,* H. Funke,* B. Johannsen
Forschungszentrum Rossendorf
Institut für Bioanorganische und Radiopharmazeutische Chemie
*Institut für Radiochemie
P.O. Box 510119, D-01314 Dresden, Germany

Abstract

Tc(I) thioether tricarbonyl complexes were prepared and characterised by chromatographic and spectrometric methods. The complexes undergo various ligand exchange reactions in aqueous solutions. In Tc(I) dithioether tricarbonyl complexes of the formula $[Tc(CO)_3Cl(S\text{-}S)]$ (S-S = bidentate dithioether ligand) chlorine is substituted by water in aqueous solution. Moreover, we found that Tc(I) tricarbonyl complexes containing a bidentate dithioether ligand, $[Tc(CO)_3Cl(S\text{-}S)]$, as well as a tridentate carboxylato dithioether ligand, $[Tc(CO)_3Cl(S\text{-}S\text{-}O)]$, react with histidine and form the complex $[Tc(CO)_3His]$. EXAFS measurements were performed to estimate structural parameters of the dissolved Tc(I) tricarbonyl complexes and their substitution products with water and histidine.

Introduction

Nowadays, nearly 80% of all radiopharmaceuticals used in routine nuclear medicine imaging procedures are ^{99m}Tc labelled compounds. Moreover ^{186}Re or ^{188}Re labelled pharmaceuticals are being developed for radiotherapy. Due to the extremely small concentration of the radionuclide present in the radiopharmaceutical preparation (10^{-6}-10^{-9} M), XAS studies as well as chemical investigations employ the long-lived isotope ^{99}Tc (K-edge at 21.044 keV) or Re (L_{III}-edge at 10.535 keV) as surrogates.

Intensive investigations in the Tc and Re carbonyl chemistry made available an organometallic M(I) aqua ion, $[M(CO)_3\ (H_2O)_3]^+$, as precursor for the preparation of complexes containing the small $[M(CO)_3]^+$ moiety. Tc(I) and Re(I) tricarbonyl complexes represent a new promising approach to low valent, non-polar and inert compounds [1,2]. Complexes with N-donor or S-donor chelating ligands co-ordinated to the M(I) tricarbonyl moiety with high stability in aqueous solution may serve for the design of radiopharmaceuticals.

The aim of this work was to investigate the stability of model Tc(I) thioether tricarbonyl complexes in aqueous solution, their reactivity against histidine and to estimate structural parameters of the dissolved compounds.

Experimental

We prepared the complexes $[Tc(CO)_3ClL^1]$, Tc1, $[Tc(CO)_3(H_2O)L^1]^+$, Tc1a, $[Tc(CO)_3L^2]$, Tc2, and as reference $[Tc(CO)_3His]$, Tc3, both at ^{99}Tc and ^{99m}Tc levels using 3,6-dithiaoctane, L^1 and 1-carboxy-3,6-dithiaheptane, L^2, as prototypical bidentate thioethers without and with an additional donor atom in the chelating unit. We applied EXAFS measurements, chromatography (UV and γ-ray detection), electrophoresis and mass spectroscopy to investigate the behaviour of these complexes. For studying a possible substitution of the thioether ligands in complexes Tc1 and Tc2 by histidine, an excess of the challenge ligand was given to the complex solutions and the reaction was controlled by HPLC and capillary electrophoresis. The resulting complexes were named Tc1b and Tc2b.

EXAFS measurements of the ^{99}Tc compounds were performed, using the Rossendorf Beamline (ROBL) facility at the European Synchrotron Radiation Facility (ESRF) in Grenoble, France [3]. All complexes were measured in aqueous solution. The solution of the complexes ($c \approx 2 \times 10^{-2}$ M) were filled into polypropylene vials (sample thickness ≈ 1 cm) and shrink-wrapped in a PE containment. The EXAFS spectra were measured in transmission mode at room temperature using the Si(111) double-crystal monochromator in fixed-exit mode detuned ~50% of the maximum incident flux. Two or three spectra for each sample were averaged. The spectra were recorded up to k = 16 Å^{-1} (for Tc1b up to k = 14 Å^{-1} due to technical reasons) in steps of 0.05 Å^{-1} with gradually increasing counting time per data point from 2 to 20 s. The energy of the first inflection point was defined as 21 044 eV corresponding to the Tc K-edge energy. The ionisation energy for the Tc K electron was arbitrarily set to 21 065 eV. The EXAFS spectra were evaluated using the program package EXAFSPAK; single and multiple effective scattering amplitude and wave phase-shift functions were generated with the theoretical EXAFS modelling code FEFF6 [4,5]. For the fits, constraints between parameters of different scattering paths were set. For all paths the shift in threshold energy, ΔE_0, was forced to be the same [for ΔE_0 were obtained: -13.1 ± 1.3 (Tc1a), -11.5 ± 2.0 (Tc1b), -11.5 ± 2.6 (Tc2a), -11.2 ± 2.1 (Tc2b), -11.1 ± 1.6 (Tc3)]. All other variables were freely floated, if not stated otherwise in the table with the results. The amplitude reduction factor was held constant at 0.9 for all fits.

Results and discussion

From no carrier added studies of Tc(I) thioether tricarbonyl complexes of the general formula $[Tc(CO)_3Cl(S\text{-}S)]$ (S-S = bidentate dithioether ligand) it is known that chlorine is likely substituted in aqueous solution by water. The resulting cationic complex $[Tc(CO)_3(H_2O)(S\text{-}S)]^+$ can be reversibly converted into the neutral species by adding an excess of sodium chloride (Figure 1). Here EXAFS spectroscopy was successfully applied to investigate the co-ordination spheres of the complexes Tc1 and Tc1a and to confirm the exchange of chlorine against water [6].

Figure 1. Reversible transformation of the complex Tc1 in aqueous solution

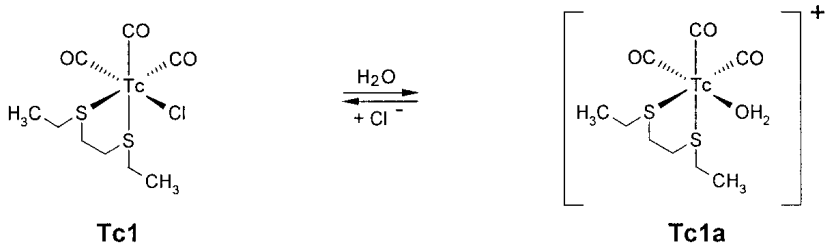

Tc1 Tc1a

We found that the complexes Tc1 and Tc2 react with histidine to the products Tc1b and Tc2b in aqueous solution which are identically with the reference Tc3 (Figure 2). HPLC experiments confirm a complete conversion of Tc1 or Tc2 into the Tc(I) histidine tricarbonyl complex. Capillary electrophoresis studies confirm the neutrality of all three complexes.

Figure 2. Reaction of Tc(I) thioether tricarbonyl complexes with histidine

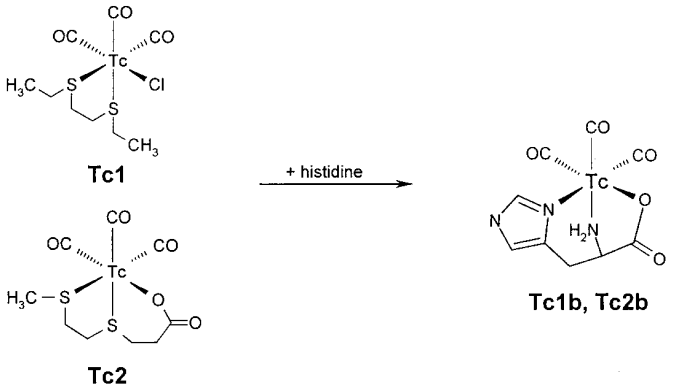

We applied EXAFS spectroscopy to determine structural parameters of the dissolved ^{99}Tc complexes and to prove the substitution of the thioether ligands by histidine.

EXAFS analyses

Calculating of wave phase-shift and effective scattering amplitude functions

Imidazole co-ordination occurs in many metalloproteins and so several publications deal with its investigation using XAFS analysis. In special cases, the multiple scattering approach including atoms of the imidazole ring can give proof of the imidazole co-ordination and provide the basis for determining the number of imidazole ligands [7].

Recently, the structure of [Re(CO)$_3$His], obtained by single crystal X-ray diffraction analysis was published [8]. For this complex, single and multiple effective scattering amplitude and wave phase-shift functions were generated as well as the importance of the scattering path, defined as the integral over the full energy range of $|\chi(k)| * dk$, was calculated using FEFF6. For the multiple scattering including the atoms of imidazole, the most important paths are Re-N$^{\pi}$-N$^{\tau}$-Re, Re-N$^{\pi}$-N$^{\tau}$-N$^{\pi}$-Re, Re-N$^{\pi}$-C^{5}-Re and Re-N$^{\pi}$-C^{5}-N$^{\pi}$-Re (see Figure 3); scattering length: 4.35 Å, 4.38 Å, 4.39 Å and 4.41 Å; scattering angles: Re-N$^{\pi}$-N$^{\tau}$: 159.2°, Re-N$^{\pi}$-C^{5}: 164.6°. However these multiple scattering paths have a distinct lower importance in comparison e.g. with those paths including the CO ligands and they overlap with other multiple scattering paths. They cause a peak system in the Fourier transform of the EXAFS data in the range around 4R + Δ[Å], but show peaks which stand out only less against the background (Figure 4). Therefore the proof of the co-ordination of one imidazole ring is not possible for the investigated type of complexes. Consequently, for the evaluation of the EXAFS spectra effective scattering amplitude and wave phase-shift functions were generated using simple atom clusters represented in Table 1 which include only the important scattering atoms and reduce the number of scattering paths by degeneration of scattering paths owing to an idealised geometry.

Figure 3. Representation of [Re(CO)$_3$His] showing the atom labelling scheme

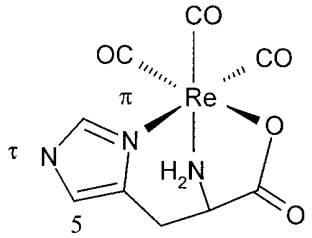

Figure 4. Tc K-edge k^3-weighted EXAFS spectra and the corresponding Fourier transforms

(Solid line: experimental data, dotted line: fit)

Tc1: [Tc(CO)$_3$ClL^1], Tc1b: Tc1 after the reaction with histidine
Tc2: [Tc(CO)$_3$L^2], Tc2b: Tc2 after the reaction with histidine
Tc3: [Tc(CO)^{3}His]

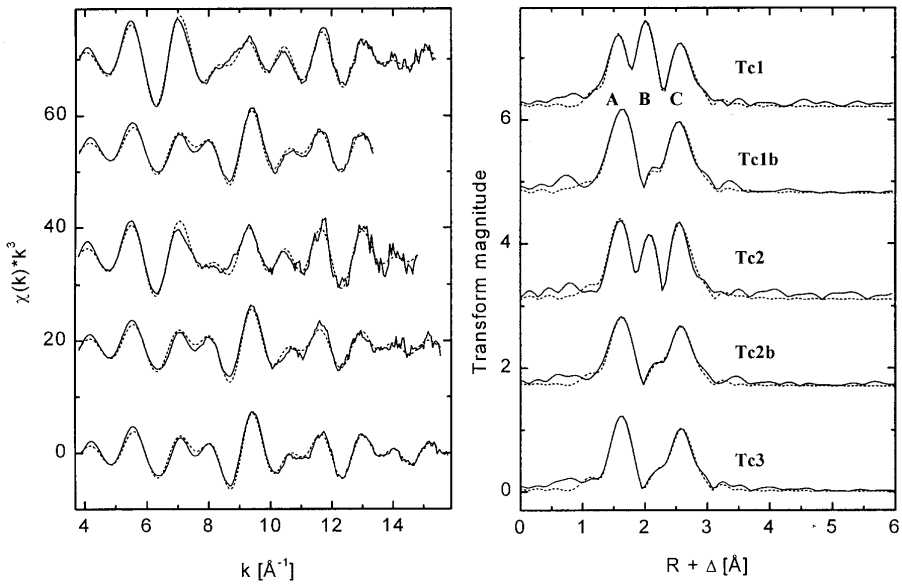

Table 1. Atom clusters used to calculate wave phase-shift and effective scattering amplitude functions

Atom	Cartesian co-ordinates [Å]		
	x	y	z
Tc	0.0	0.0	0.0
C	0.0	-1.9	0.0
C	-1.9	0.0	0.0
C	0.0	0.0	-1.9
O	0.0	-3.1	0.0
O	-3.1	0.0	0.0
O	0.0	0.0	-3.1
X1	0.0	x1	0.0
X2	x2	0.0	0.0
X3	0.0	0.0	X3

$[Tc(CO)_3His]$, Tc3, Tc1b, Tc2b: X1 = X2 = N, X3 = O, x1 = x2 = x3 = 2.2
$[Tc(CO)_3ClL^1]$, Tc1: X1 = X2 = S, X3 = Cl, xl = x2 =x3 = 2.5
$[Tc(CO)_3L^2]$, Tc2: X1 = X2 = S, x1 = x2 = 2.5, X3 = O, x3 = 2.2

Interpretation of the EXAFS spectra

To obtain a satisfactory interpretation of the EXAFS spectra and the corresponding Fourier transforms the following single-scattering paths had to be included in the fit to the experimental EXAFS data: Tc-S/Cl (N = 3) for Tc1; Tc-S (N = 2) and Tc-O (N = l) for Tc2; Tc-N/O (N = 3) for Tc3, Tc1b and Tc2b; Tc-C (N = 3) for all samples. Given in parentheses are the co-ordination numbers N derived from the structural model (Table 1). Effective scattering amplitude and wave phase-shift functions for the Tc-S, Tc-Cl or the Tc-N, Tc-O scattering paths are nearly identically since the functions depend only weakly on scatterer identity and S, Cl or N and O are neighbouring elements in the periodic table. Hence, fitting to the experimental EXAFS data including amplitude and phase-shift functions either for the Tc-S (Tc-N) or the Tc-Cl (Tc-O) paths does not affect the estimated structural parameters. To model the oxygen atom of carbonyl groups (N = 3), the equivalent multiple-scattering paths Tc-C-O-Tc and Tc-O-C-Tc (3 legs, degeneracy of 2), the non-degenerated path Tc-C-O-C-Tc (4 legs) and the single-scattering path Tc-O were taken into account (Table 2). All other possible scattering paths did not lead to a significant improvement of the fit results.

The Fourier transforms of the experimental EXAFS data of Tc1 and Tc2 show three well resolved peaks and two clearly resolved peaks for Tc1b, Tc2b and Tc3. Peak A represents mainly the C co-ordination shell but also the co-ordination of the N and O atoms (Tc1b, Tc2, Tc2b, Tc3), Peak B the S and Cl atoms (Tc1) or the S and partly the O atom (Tc2) and Peak C the O co-ordination shell of CO. The co-ordination of an O atom from the carboxylic group (Tc2) in comparison with the co-ordination of a Cl atom (Tc1) causes a decrease in magnitude of Peak B of the Fourier transform because oxygen is a weak back-scatterer compared to chlorine.

The estimated atomic distances in Tcl and Tc2 are almost the same as those found by single crystal X-ray diffraction analyses of similar Re carbonyl complexes containing dithioether ligands, which we recently published [2]. The estimated co-ordination numbers agree with the expected values.

Table 2. Structural parameters obtained by the Tc K-edge k^3-weighted EXAFS spectra of Tc1, Tc1b, Tc2, Tc2b and Tc3

R: atomic distance, N: co-ordination number, σ^2: Debye-Waller factor

	Path	Tc-S or Tc-S/Cl	Tc-O or Tc-N/O	Tc-C	Tc-CO (2, 3 and 4 legs, respectively)
Tc1	R [Å]	2.49 ± 0.02		1.92 ± 0.02	3.07 ± 0.02 [1)]
	N	3.9 ± 0.9		3.4 ± 0.6[1)]	6.8 ± 1.1 [1,a)] 3.4 ± 0.6 [1,b)]
	σ^2 [10^{-3} Å^2]	5.0 ± 0.9		2.3 ± 0.8	3.7 ± 0.6 [1)]
Tc1b	R [Å]		2.21 ± 0.02	1.90 ± 0.02	3.07 ± 0.02 [1)]
	N		3.0 ± 1.2	3.0 ± 1.0 [1)]	6.1 ± 2.0 [1,a)] 3.0 ± 1.0 [1,b)]
	σ^2 [10^{-3} Å^2]		2.6 ± 2.7	1.6 ± 1.7	2.9 ± 1.1 [1)]
Tc2	R [Å]	2.50 ± 0.02	2.21 ± 0.02	1.92 ± 0.02	3.07 ± 0.02 [1)]
	N	2.1 ± 0.6 [1)]	1.0 ± 0.3 [1)]	3.0 [2)]	6.0 [2,a)] 3.0 [2,b)]
	σ^2 [10^{-3} Å^2]	3.3 ± 1.7	1.1 ± 3.1	1.0 ± 0.7	2.7 ± 0.7 [1)]
Tc2b	R [Å]		2.20 ± 0.02	1.91 ± 0.02	3.07 ± 0.02 [1)]
	N		3.0 ± 1.1	3.4 ± 0.9 [1)]	6.9 ± 1.8 [1,a)] 3.4 ± 0.9 [1,b)]
	σ^2 [10^{-3} Å^2]		2.7 ± 2.1	2.6 ± 1.3	3.7 ± 0.9 [1)]
Tc3	R [Å]		2.20 ± 0.02	1.91 ± 0.02	3.06 ± 0.02 [1)]
	N		3.2 ± 0.8	3.1 ± 0.6 [1)]	6.3 ± 1.1 [1,a)] 3.1 ± 0.6 [1,b)]
	σ^2 [10^{-3} Å^2]		3.0 ± 1.5	1.5 ± 0.8	3.0 ± 0.6 [1)]

[1)] In each line, identically marked parameters were forced to have constant ratios during the fits.
[2)] These parameters were held constant.
[a)] Path Tc-CO (3 legs).
[b)] Path Tc-CO (2 legs) and path Tc-CO (4 legs).

The substitution of the chlorine ligand of Tc1 by water results in the complex Tc1a. EXAFS analysis of Tc1a shows the same atomic distances for the S/Cl, C and CO co-ordination shells as Tc1 and additionally, an O co-ordination shell at the distance of 2.19 ± 0.02 Å and a co-ordination number of 1.2 ± 0.3, which proves the substitution of chlorine by water [6].

The EXAFS spectra, their Fourier transforms and the fit results of Tc1b and Tc2b are almost identical to the results of EXAFS analysis of reference Tc3. This fact proves the substitution of bidentate dithioether and tridentate carboxylato dithioether ligands by histidine, which co-ordinates in a tridentate manner. The obtained atomic distances are in agreement with those found for the Re congener by single crystal X-ray diffraction analysis [8].

Conclusion

EXAFS analyses were successfully used to determine structural parameters of Tc(I) tricarbonyl complexes. In connection with chromatographic, electrophoretic and mass spectrometric methods, it was found that Tc(I) tricarbonyl complexes containing a bidentate thioether ligand are able to react with water by exchange of chlorine whereas complexes containing a tridentate dithioether ligand with an additional carboxylic group are stable in aqueous solution. Both types of complexes undergo ligand exchange reactions with N-containing ligands like histidine under formation of the corresponding Tc(I) histidine tricarbonyl complex. It is likely that similar reactions lead to the strong protein binding of Tc(I) thioether tricarbonyl complexes *in vivo.*

Acknowledgements

We acknowledge the European Synchrotron Radiation Facility for provision of synchrotron radiation facilities and we would like to thank Christoph Hennig and Andre Roßberg for assistance during the EXAFS measurements at BM20.

REFERENCES

[1] R. Alberto, R. Schibli, R. Waibel, U. Abram, A.P. Schubiger, *Coordination Chem. Rev.*, 190-192, 901 (1999).

[2] H-J. Pietzsch, A. Gupta, M. Reisgys, A. Drews, S. Seifert, R. Syhre, H. Spies, R. Alberto, U. Abram, P.A. Schubiger, B. Johannsen, *Bioconj. Chem.*, 11, 414 (2000).

[3] W. Matz, N. Schell, G. Bernhard, F. Prokert, T. Reich, J. Claußner, W. Oehme, R. Schlenk, S. Dienel, H. Funke, F. Eichhorn, M. Betzl, D. Pröhl, U. Strauch, G. Hüttig, H. Krug, W. Neumann, V. Brendler, P. Reichel, M.A. Denecke, H. Nitsche, *J. Synchrotron Radiat.*, 6, 1076 (1999).

[4] G.N. George, I.J. Pickering, "EXAFSPAK: A Suite of Computer Programs for Analysis of X-ray Absorption Spectra", Stanford Synchrotron Radiation Laboratory, Stanford, CA, USA (1995).

[5] S.I. Zabinsky, J.J. Rehr, A. Ankudinov, R.C. Albers, M.J. Eller, *Phys. Rev. B*, 52, 2995 (1995).

[6] S. Seifert, J-U. Künstler, A. Gupta, H. Funke, T. Reich, C. Hennig, A. Roßberg, H-J. Pietzsch, R. Alberto, B. Johannsen, *Radiochim. Acta*, 88, 239 (2000).

[7] R.W. Strange, N.J. Blackburn, P.F. Knowles, S.S. Hasnain, *J. Am. Chem. Soc.*, 109, 7157 (1987).

[8] R. Schibli, R. La Bella, R. Alberto, E. Garcia-Garayoa, K. Ortner, U. Abram, P.A. Schubiger, *Bioconj. Chem.*,11, 345 (2000).

HEAVY-METAL SPECIATION OF CONTAMINATED SOILS BY SEQUENTIAL EXTRACTION AND X-RAY ABSORPTION FINE STRUCTURE SPECTROSCOPY (XAFS)

Stefan Mangold, Wolfgang Calmano
TU Hamburg-Harburg, Germany

Abstract

The sequential extraction procedure of Förstner and Salomons [1,2] of two highly lead-contaminated soil samples was investigated by XAFS using a two-step evaluation method. Data reduction was done to obtain comparable spectra and linear combinations of reference spectra were used to approximate the spectra of samples and to evaluate the amounts of the main reference compounds.

Introduction

The potential risk of heavy metals in the environment is determined by their toxicity, their total concentration and their chemical form. While the toxicity of metals is already known and methods for the measurement of total concentration of metals are widely used, the speciation of heavy metals in complex matrices is still a work in progress.

Metal speciation in natural environments is, therefore, often evaluated by indirect methods like sequential extractions. These extractions are used to subdivide the heavy metal content of environmental samples into several operational defined groups of more or less soluble species. They are simple to perform and inexpensive, but the solvents are not selective for one species and there is strong evidence for alteration of the composition of the sample during the first step(s) [3,4], leaving the following steps strongly influenced.

In contrast to organo-metallic compounds with short organic groups most other heavy metal species in natural environments, such as inorganic compounds and metals sorbed to matrix components, can not be separated from the soil matrix. Therefore the characterisation of heavy metals in natural systems requires a species and element specific instrumental method such as XAFS spectroscopy.

Experimental

Sample preparation

In our first studies of extractions we investigated the sequential extraction scheme of Förstner and Salomons [1,2] on two highly lead-contaminated soil samples (89 g/kg, 150 g/kg). The general outline of this sequential extraction is presented in Table 1. The soil samples, which were taken near a battery factory in Hanover, Germany, were air-dried and ground in a ball mill. Six subsamples of 2 g were used for the sequential extraction and after each step the solid remnants of one subsample were air-dried and ground. All samples were mixed with polyethylene (PE) as a binding agent and pressed in a KBr-press.

Table 1. Sequential extraction of Förstner and Salomons [1,2]

Step	Extractant	Group
1	NH_4Ac (c_{NH_4OAc} = 1 mol/L), 10 mL, 2 h	Easily exchangeable
2	NaAc (c_{NaAc} = 1 mol/L) + HAc, pH = 5, 10 mL, 5 h	Carbonate bound
3	$NH_2OH{\cdot}HCl$ ($C_{NH_2OH{\cdot}HCl}$ = 0.1 mol/L) + HCl, pH = 2, 50 mL, 12 h	Easily reducible
4	$(NH_4)_2C_2O_4$($c_{(NH_4)_2C_2O_4}$ = 0.1 mol/L) + ($c_{H_2C_2O_4}$= 0.1 mol/L +HNO_3, pH = 3, 50 mL, 24 h	Moderately reducible
5	H_2O_2 (30 %), pH = 5, 15 mL, 80°C, 2 h + solution from step 1, 12 h	Oxidisable
6	HNO_3 (68 %), 120°C, 2 h	Residual fraction

Insoluble inorganic lead compounds, lead sorbed to montmorillonite, iron and manganese oxides and lead complexed by humic acids are used as reference compounds. While the inorganic compounds were of p.a. grade and were used as delivered, the adsorbed and complexed species were obtained by shaking the respective substances with $PbAc_2$ solutions of different concentrations for 24 h at pH 5. For 48 hours the solutions were shaken at pH 5, 6 or 7. The yielded concentrations of sorbed or complexed lead was between 0.1% and >10%.

XAFS measurements

The XAFS spectra were measured at HASYLAB at DESY (Hamburg, Germany) at experimental stations A1 and X1. All spectra were measured at room temperature, using an elemental metal foil as standard for energy calibration. The spectra of the Pb L3-edge were recorded between 12 800 eV and 13 900 eV and the step size in the edge-region was 1 eV. While the spectra at the beam line X1 were measured in transmission mode, on experimental station A1 the signals of a five-element germanium detector were also recorded.

Spectrum evaluation procedure

The method used for the analysis of the soil sample can be separated into two steps, the data reduction and the evaluation of amounts of the compounds in the sample [5]. The data reduction, which is shown in Table 2, is adopted to obtain comparable spectra. While the pre-evaluation is only necessary for fluorescence spectra, the main data reduction has to be performed for each spectrum. When the concentration of lead in the sample was small, several spectra were added to obtain better data. In case of fluorescence spectra this summation is weighted with count rates of the Ge5-detector.

Table 2. Steps and procedures of the data reduction

Step	Procedures
Pre-evaluation (only for fluorescence spectra)	Deadtime correction of each pixel
	Weighted average of all pixel
	Correction of the self-absorption
Main data reduction	Background removal • Pre-edge: polynomial • Post-edge: polynomial/cubic-spline
	Energy calibration • Multi-point energy calibration
	Normalisation • Edge → 100%
Refining	Weighted sum of several spectra
	Deglitching/smoothing

The evaluation of amounts of the compounds in the sample was performed by a least square fitting between 13 000 eV and 13 200 eV using linear combinations of the large set of reference compounds described above. It was attempted to reduce the range of possible reference compounds due to SEM/EDX-spectra and historical information. The utilisation of the Levenberg-Marquardt algorithm makes it possible to evaluate linear combinations of all reference compounds spectra, but local minima can not be avoided. Therefore the results of the first method were verified by an algorithm that uses a mixture of “brute force” calculation and minimisation. While the data evaluation and the fitting with the Levenberg-Marquart algorithm were implemented in IgorPro (Wavemetrics [6]), the second fitting algorithm was written in C++. The program calculates the estimated error (standard deviation) for each of the coefficients in the fits. The standard deviation of the coefficients was 0.5-4% for inorganic compounds and 3-8% for the other compounds.

While the differences between the three inorganic reference compounds, which are shown in Figure 1, are obvious, there is only a small but significant difference between the reference compounds shown in Figure 2.

Figure 1. Reference spectra of $PbCO_3$, $PbSO_4$ and PbO

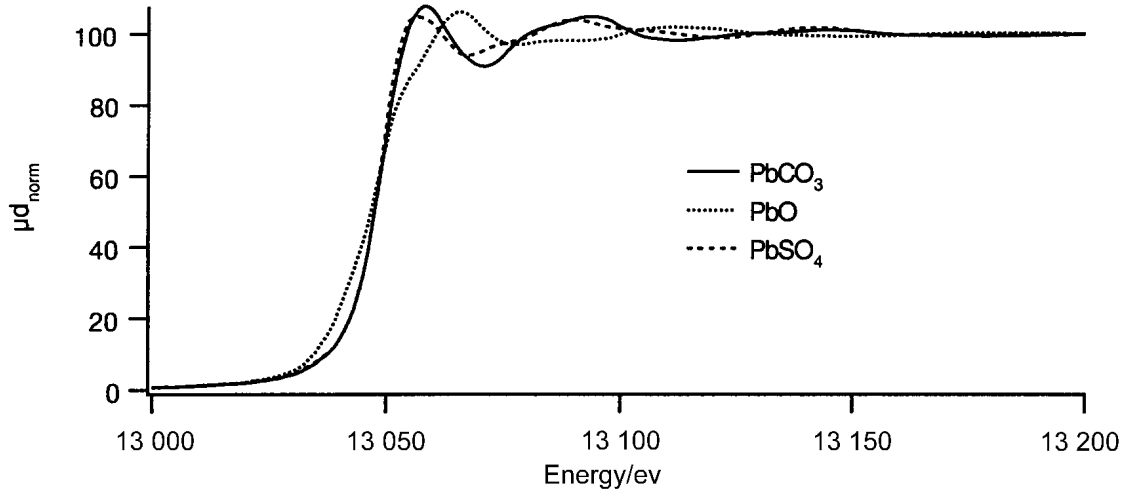

Figure 2. Reference spectra of lead sorbed to montmorillonite (c_{Pb} = 3.4%) and lead complexed by humic acid (c_{Pb} = 2.1%)

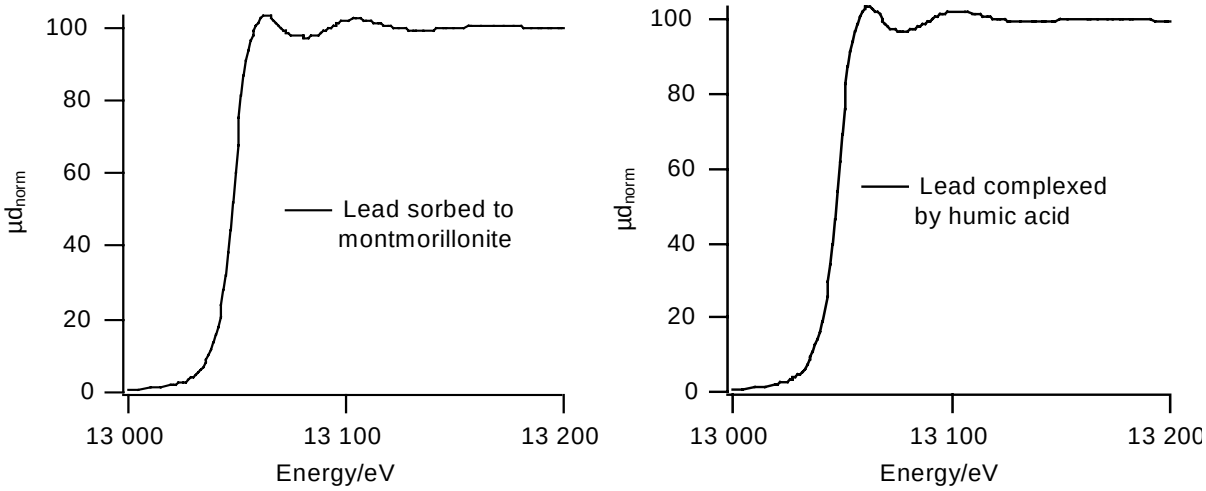

Table 3. Minimisation method

No.	Method	Advantage & disadvantage
1	• Using linear combinations of all reference compounds • Levenberg-Marquardt algorithm	• Fast • Perhaps local minimum
2	• Using all combinations of linear combinations of five reference compounds • Mixture between “brute force” calculation and minimisation	• Local minimum should be avoided • Slow

Results and discussion

Figure 3 shows extraction results of soil sample 1 whose lead content is 150 g/kg. Significant is the occurrence of $PbAc_2$ (first and second step), $PbCl_2$ (third step), PbOx (fourth step) and lead sorbed to clay minerals (third-fifth step). These compounds can also be seen in the extraction results (Figure 4) of soil sample 2.

Figure 3. Sequential extraction after Förstner and Salomons of soil sample 1

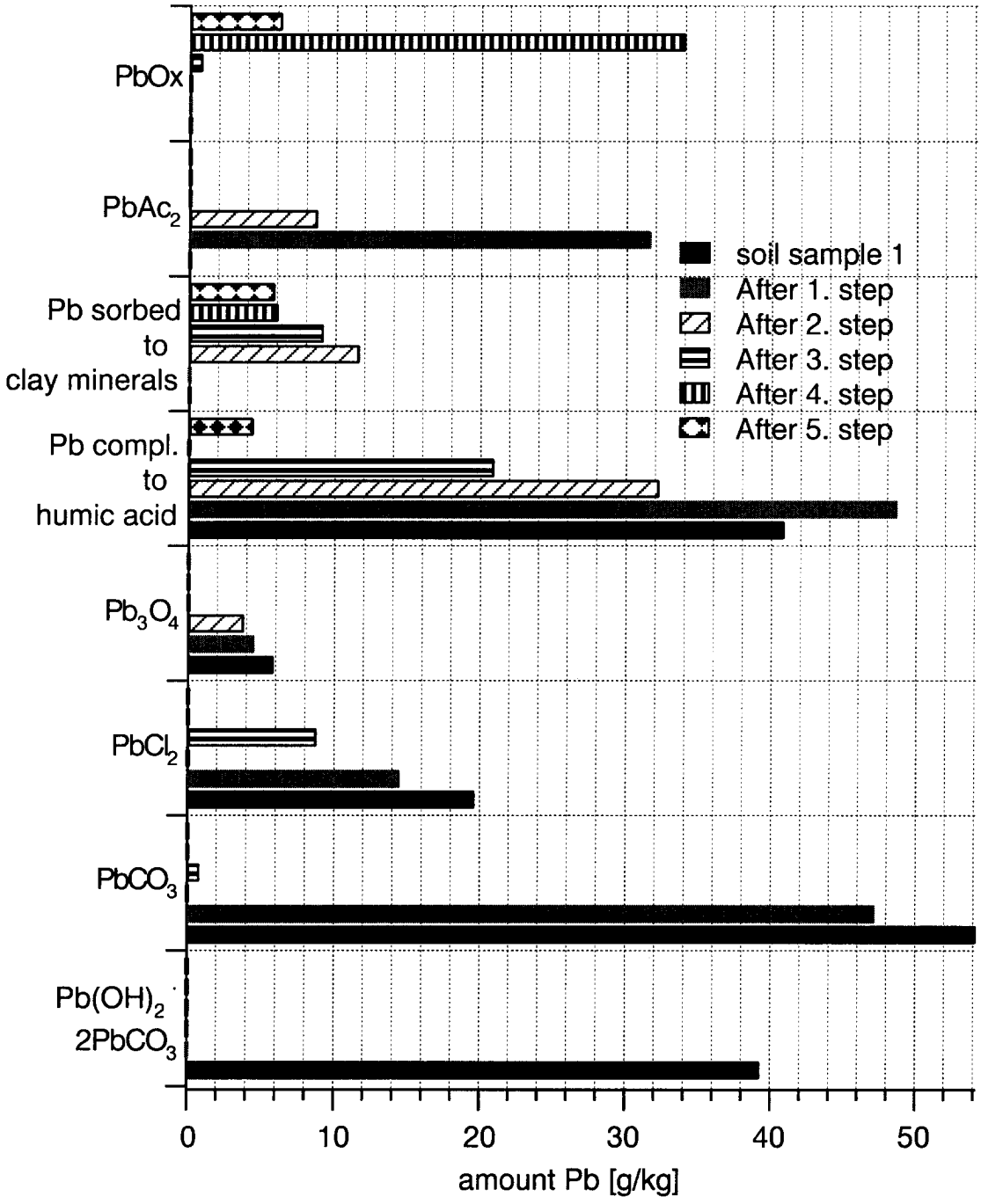

But one of the most impressive results is the dissolution of the sparingly soluble compound $PbSO_4$. Theoretical calculations with PHREEQC and experiments show that the dissolution of $PbSO_4$ occurs due to complexation of the NH_4Ac or NaAc solution ($c_{NaAc} = c_{NH4Ac} = 1$ mol/L).

Figure 4. Sequential extraction after Förstner and Salomons of soil sample 2

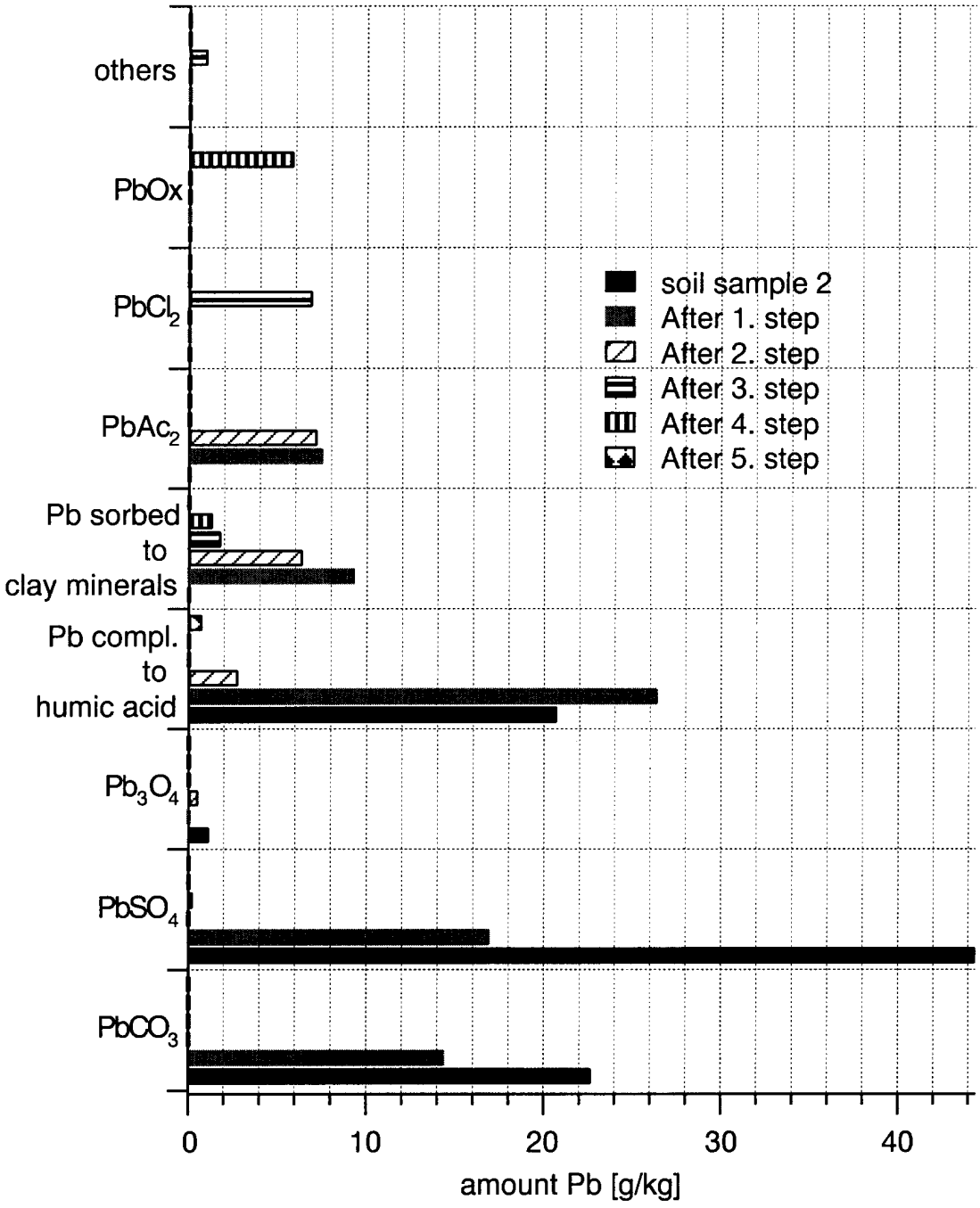

The above results can be summarised in the following four categories:

- Precipitation of readily soluble compounds due to reactions with the extractants (Pb-acetate, $PbCl_2$).
- Precipitation of insoluble compounds due to reactions with the extractants (Pb-oxalate).
- Re-adsorption to clay minerals.
- Dissolution of sparingly soluble compounds due to complexation by the extractants ($PbSO_4$).

Perspectives

XAFS is an instrumental method which enables speciation analysis in solid samples. Our results show that it is possible to investigate sequential extractions with XAFS used as a fingerprint method, but until now several drawbacks have existed. The major drawbacks are the high detection limit (2 000 ppm for lead-contaminated soil sample) and the difficult data reduction. Therefore the major aspects of our current research are the optimisation of the data reduction and improvements in the detector system.

Acknowledgements

The authors wish to thank the HASYLAB at DESY (Hamburg, Germany) for the beam time to perform the XAFS measurements and especially Dr. L. Tröger, K. Attenkofer and E. Welter (HASYLAB at DESY) for their support.

REFERENCES

[1] W. Salomons, U. Förstner, “Metals in the Hydrocycle”, Springer Berlin, 1984.

[2] W. Salomons, U. Förstner, “Trace Metal Analysis on Polluted Sediments, Part II: Evaluation of Environmental Impact”, *Environ. Tech. Lett*., 1, 506-518 (1980).

[3] W. Calmano, Schwermetalle in kontaminierten Feststoffen, Verlag TÜV Rheinland, Köln, 1989.

[4] R. Rubio, G. Rauret, “Validation of Methods for Heavy Metal Speciation in Soil and Sediments”, *J. Radioanal. Nucl. Chem*., 208, 529-540 (1996).

[5] S. Mangold, Entwicklung von Auswerteverfahren zur Schwermetall-Speziesanalyse an Böden unter Anwendung von XAFS, Diplomarbeit, Universität-Marburg 1998.

[6] See http://www.wavemetrics.com.

EXAFS INVESTIGATION OF URANIUM(VI) COMPLEXES FORMED AT *ACIDITHIOBACILLUS FERROOXIDANS* TYPES

Mohamed Merroun, Tobias Reich, Christoph Hennig and Sonja Selenska-Pobell
Institute of Radiochemistry, Forschungszentrum Rossendorf
PO Box 510119, D-01314 Dresden, Germany

Abstract

Mining activities have brought excessive amounts of uranium into the environment. In uranium deposits a number of acidophilic chemolithoautotrophic bacteria have been identified which are able to oxidise sulphide minerals, elemental sulphur, ferrous iron and also (in the presence of uranium mineral) U(IV). In particular, the interaction of one representative of the group *Acidithiobacillus ferrooxidans* (new designation of *Thiobacillus ferrooxidans*) with uranium has been investigated.

Uranium(VI) complex formations at the surfaces of *Acidithiobacillus ferrooxidans* were studied using uranium L_{III}–edge extended X-ray absorption fine structure (EXAFS) spectroscopy. In all samples uranium is co-ordinated by two axial oxygen atoms (O_{ax}) at a distance of 1.77-1.78 Å. The average distance between uranium and the equatorial oxygen atoms (O_{eq}) is 2.35 Å. The co-ordination number for O_{eq} is 5-6. In comparison to the uranium crystal structure data, the U-O_{eq} distance indicates a co-ordination number of the equatorial oxygen of 5.

Within the experimental error, there are no differences in the U-O bond distances between samples from the three types of *A. ferrooxidans* investigated. The fit to the EXAFS data of samples measured as wet pastes gave the same results as for dried samples. No significant structural differences were observed for the uranium complexes formed by the eco-types of *A. ferrooxidans.* However, the EXAFS spectra do indicate a formation of uranium complexes which are different from those formed by *Bacilli* [1] where the bond length of 2.28 Å indicates a co-ordination number of 4 for the equatorial oxygen atoms.

REFERENCE

[1] C. Hennig, *et al.*, "EXAFS Investigation of Uranium(VI) Complexes Formed at *Bacillus cereus* and *Bacillus sphaericus* Surfaces", *Radiochim. Acta* (submitted).

XAS STUDY OF ACID ROCK DRAINAGE SAMPLES FROM AN ABANDONED Zn-Pb-Ag MINE AT FREIBERG, GERMANY

H. Moll,* H. Zänker, W. Richter, V. Brendler, T. Reich, C. Hennig, A. Roßberg, H. Funke
Forschungszentrum Rossendorf e.V., Institute of Radiochemistry
P.O. Box 51 01 19, D-01314 Dresden, Germany
*moll@fz-rossendorf.de

A. Kluge
TU Bergakademie Freiberg, Institute of Mineralogy
Brennhausgasse 14, D-09596 Freiberg, Germany

Abstract

In the aqueous environment of abandoned ore mines, iron sulphide ore crystals play a key role in the sulphide oxidation and water mineralisation process occurring there. Highly mineralised, red-coloured solutions are formed by weathering of ore particles which causes acid rock drainage (ARD). Major cationic components (>1 g/l) of the ARD solution under study were Zn, Fe, Mg, Al and Mn. Important minor components were toxic heavy metals, e.g. As, Cu, Pb and Cd. This XAS investigation deals with the *in situ* characterisation of the near-order surrounding of As in ARD solutions containing colloidal particles as well as with the determination of the particle mineralogy. The atomic surrounding of Fe and As in ARD samples is compared to those found in model compounds. The presented study is an example for the broad applicability of X-ray absorption spectroscopy (XAS) techniques to environmental research.

Introduction

In a previous study [1] we demonstrated that the elements Fe, As and Pb showed a pronounced colloidal behaviour in the ARD sample (pH = 2.7, 0.41 M sulphate) taken from the "Himmelfahrt Fundgrube" at Freiberg. Fifteen per cent (15%) of the Fe, 50% of the As and 80% of the Pb occur as particles of a size of <5 nm. Very little is known about the speciation of heavy and toxic metals and about the mineralogy of the colloidal particles of such ARD solutions. XAS is the method of choice to explore the short-range order of "amorphous" colloids by providing structural information about the first atomic shells surrounding the chosen X-ray absorbing metal (e.g. Fe and As). A big advantage is that colloidal particles can be studied *in situ* in their original aqueous environment. A problem arises because colloidal suspensions often contain mixtures of particles and truly dissolved species from the same element between which XAS cannot differentiate. Therefore, we investigated different filtrates: (a) raw sample, (b) 5 μm filtrate, (c) solution of strongly enriched colloidal particles and (d) solution strongly depleted of colloidal particles. Our goal was to characterise the colloidal particles' mineralogy by comparing the Fe K-edge EXAFS data of the ARD solutions and filtrates with that from a precipitate found in the ARD sample after 10 months and with those from various model compounds (schwertmannite, jarosite, goethite, scorodite and bukowskyite). Secondly we tried to determine the type of bonding of toxic contaminants, e.g. arsenic, onto the colloids.

Experimental

Sample information

Table 1. Chemical analysis of the ARD samples

Sample	Fe [M]	As [M]	[As]/[Fe]
Raw sample	0.080	$5.2 \cdot 10^{-3}$	0.065
5 μm filtrate	0.070	$4.8 \cdot 10^{-3}$	0.068
1 kD retentate	0.368	0.080	0.217
1 kD filtrate	0.054	$1.4 \cdot 10^{-3}$	0.026
	Fe [mg/g]	**As [mg/g]**	
Precipitate	324	68	0.210

The ARD solutions were transferred into polyethylene cuvettes of 3 mm diameter to measure Fe K-edge XAS spectra. The path length was 10 mm for As K-edge experiments. The XRD analysis of the precipitate clearly shows that jarosite, $(H_3O)Fe_3(SO_4)_2(OH)_6$, is the major component. We cannot exclude trace amounts of poor crystalline phases like schwertmannite. The scorodite, $FeAsO_4 \cdot 2H_2O$, and bukowskyite, $Fe_2AsO_4SO_4OH \cdot 7H_2O$, were from Dr. F. Krantz Rheinisches Mineralien-Kontor. Schwertmannite, $Fe_8O_8(OH)_6SO_4$, was prepared as described in [2]. Jarosite, $(H_3O,K)Fe_3(SO_4)_2(OH)_6$, was precipitated from an acidic Fe(II) sulphate solution containing *Thiobacillus ferrooxidans* cells. The goethite sample, α-FeOOH, was synthesised according to [3]. All model substances and the precipitate were analysed using XRD and/or REM/EDX [1]. The particle size, 2 to 5 μm, of the precipitate was estimated from REM images. Appropriate amounts of the solid samples were mixed with Teflon and then pressing to give pellets with a diameter of 13 mm.

XAFS measurements

XAFS data were recorded at the Rossendorf Beamline (ROBL) at the ESRF in Grenoble. Transmission and/or fluorescence spectra were measured at room temperature using a water-cooled Si(111) double-crystal monochromator of fixed-exit type (E = 5-35 keV). For details concerning the ROBL see [4]. For energy calibration of the sample spectra, the spectrum from a Fe or Pt foil was recorded simultaneously. The energy of the first inflection point in the spectrum of the Fe and Pt foil was defined as 7 112 and 11 564 eV, respectively. The ionisation energy of the Fe and As K electron, E_0, was defined as 7 132 and 11 825 eV, respectively. The data were treated using the EXAFSPAK software developed by George and Pickering at SSRL. Theoretical backscattering phase and amplitude functions, $\delta(k)$ and $F(k)$, used in data analysis were calculated using the theoretical EXAFS modelling code, FEFF6 [5].

Results and discussion

Figure 1 shows the Fe K-edge EXAFS spectra of the model compounds and the corresponding Fourier transforms (FTs). The determined structural parameters are summarised in Table 2. The atomic surrounding of Fe in the model compounds jarosite, goethite and scorodite is in fair agreement with XRD data [6-8]. To our knowledge there are no EXAFS structure parameter for bukowskyite published up to now. The Fe-O octahedra in goethite and schwertmannite are connected about two edges at $R_{Fe\text{-}Fe1} \approx 3.02$ Å, and two edges plus four corners at $R_{Fe\text{-}Fe2} \approx 3.39$ Å [3]. The later results in a shoulder measured at 3.37 Å. In contrast to these samples a longer Fe-Fe distance of 3.66 Å was measured in the jarosite sample indicating that the $Fe(O)_6$ are linked corner-shared [6].

Figure 1. Experimental iron K-edge EXAFS spectra and corresponding Fourier transforms of model compounds (schwertmannite, jarosite, goethite, scorodite and bukowskyite) and ARD samples

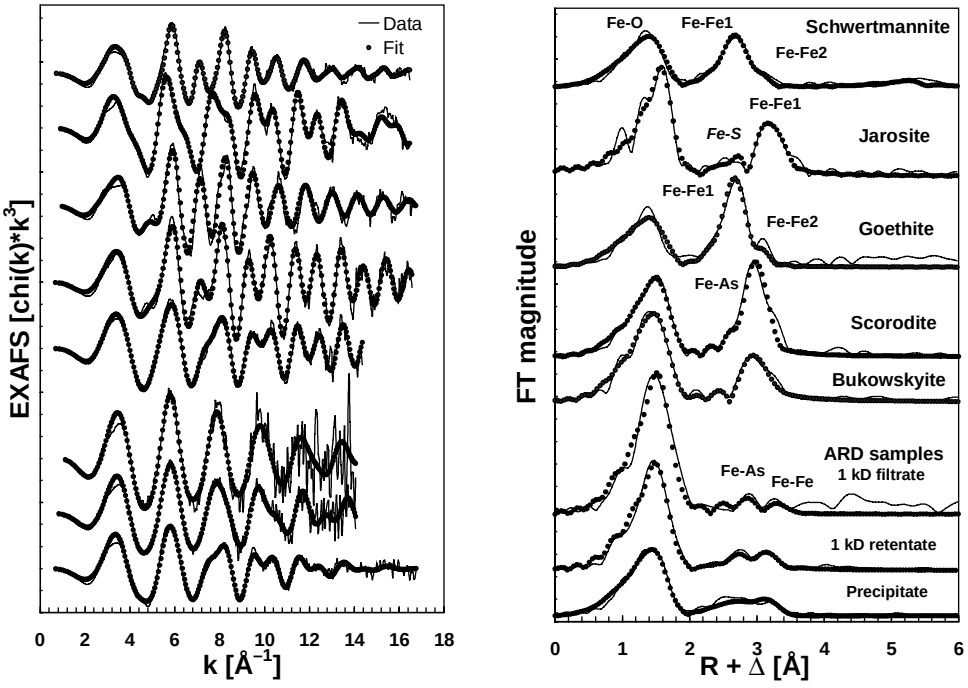

Table 2. Summary of the EXAFS structural parameters. XRD values are in parentheses.

Sample	Fe K-edge				As K-edge			
	Shell	N	R [Å]	σ^2 [Å^{-2}]	Shell	N	R [Å]	σ^2 [Å^{-2}]
Schwertmannite	Fe-O	4.9	1.96	0.0105				
$Fe_8O_8(OH)_6SO_4$	Fe-Fe1	1.3	3.03	0.0046				
	Fe-Fe2	1.9	3.37	0.0091				
Jarosite	Fe-O	4.0 (6)	1.99 (2.01)	0.0037				
$(H_3O, K)Fe_3(SO_4)_2(OH)_6$	Fe-S	0.6 (2)	3.23 (3.23)	0.0010				
	Fe-Fe1	1.5 (4)	3.66 (3.66)	0.0025				
Goethite	Fe-O	5.0 (6)	1.97 (2.02)	0.0114				
α-FeOOH	Fe-Fe1	2.0 (2)	3.02 (3.02)	0.0042				
	Fe-Fe2	6.5 (6)	3.37 (3.40)	0.0164				
Scorodite (mineral)	Fe-O	4.5 (6)	1.97 (2.00)	0.0053	As-O	5.0 (4)	1.68 (1.68)	0.0027
$FeAsO_4•2H_2O$	Fe-As	2.2 (4)	3.36 (3.35)	0.0030	As-Fe	3.7 (4)	3.34 (3.33)	0.0048
Bukowskyite (mineral)	Fe-O	5.4	1.98	0.0073	As-O	5.2	1.68	0.0025
$Fe_2AsO_4SO_4OH•7H_2O$	Fe-As	0.5	3.34	0.0010	As-Fe	3.2	3.33	0.0042
ARD solution raw sample					As-O	4.3	1.69	0.0013
					As-Fe	2.2	3.28	0.0047
ARD solution					As-O	4.5	1.69	0.0017
(5 µm filtrate)					As-Fe	2.2	3.27	0.0046
ARD solution	Fe-O	6.0	2.00	0.0052	As-O	4.4	1.68	0.0011
(1 kD filtrate)	Fe-As	2.0	3.43	0.0122	As-Fe	1.9	3.26	0.0032
	(Fe-Fe	0.4	3.65	0.0025)				
ARD solution	Fe-O	5.1	1.98	0.0060	As-O	4.7	1.69	0.0021
(1 kD retentate)	Fe-As	0.3	3.29	0.0011	As-Fe	2.5	3.29	0.0067
	Fe-Fe	1.5	3.55	0.0118				
ARD solution, precipitate	Fe-O	5.3	1.97	0.0053	As-O	5.0	1.68	0.0022
	Fe-As	2.9	3.32	0.0104	As-Fe	4.5	3.28	0.0110
	Fe-Fe	2.2	3.62	0.0101				
0.066 M As solution					As-O	5.2	1.68	0.0025

ΔE_0 = -27 eV for Fe K-edge EXAFS data. ΔE_0 = -14 eV for As-O shells and -22 eV for As-Fe shells.

The Fe K-edge EXAFS data of the ARD samples are different. In comparison with the As K-edge data (see Table 2 and Figure 3) we could identify the second shell as As. One might hypothesise that at least for the 1 kD filtrate the EXAFS spectrum might primarily be caused by the dissolved complexes $FeHAsO_4^+$ and $FeH_2AsO_4^{2+}$ [9]. This ,however, is not really supported by our results: The arsenic is surrounded by more than one Fe atom in this filtrate (Figure 1 and Table 2), and the behaviour of the scattered light intensity after the 1 kD filtration indicates that particles also play a major role in the 1 kD filtrate [1]. The EXAFS data of the freshly formed colloids (1 kD sample) might indicate that an amorphous Fe phase dominates the colloidal matrix. On the other hand, the EXAFS oscillation of the precipitate shows the presence of a more crystalline Fe phase. The data of the 5 µm filtrate might indicate an intermediate between these two stages. The Fe-Fe distance of ≈3.60 Å suggests a closer relationship between the ARD samples and the jarosite. By considering the REM/EDX analysis of particle agglomerates on the Nucleopore filter [1] and the EXAFS results, we assume that the colloidal particles might be an intermediate in the precipitate formation process having a mineralogy similar to that of the precipitate. The XRD and REM/EDX analysis of the precipitate gives rise to the assumption that amorphous Fe phases could also be present. To obtain more information on this subject, we tried to describe the EXAFS spectra of the precipitate by linear combinations of the EXAFS oscillations of the model compounds. It showed that this amorphous phase should be schwertmannite.

The relevant toxic contaminants of the colloidal particles in the ARD solution are arsenic and lead. According to our EQ3/6 calculations, the arsenic should exist in the form of scorodite. Scorodite, however, seems to be stable only at pH values of ≤ 2 [9] which is below the pH of our ARD solution.

Figure 2 depicts a selection of X-ray absorption spectra measured at the As K-edge. The intensive white line and the As K-edge energies of 11 875.0 eV indicate the +5 oxidation state of As in all ARD samples. Two features at the end of the XANES range (~70 and ~90 eV above the white line) were detected. They could be associated with ordered second neighbour correlations. These features are most pronounced in crystalline compounds (e.g. scorodite) with an high-ordered second neighbour distance of As-Fe at 3.34 Å. These maxima are moving to larger energies when the second neighbour distance is decreasing, e.g. in the ARD samples As-Fe of 3.28 Å. In the arsenate solution there are no pronounced maxima detectable. As can be seen in Figure 3, the FTs of the ARD fractions are quite different from those of the pure arsenate solution. On the other hand, the results in Figure 3 and Table 2 are similar for all the ARD fractions. Taking the EXAFS results alone one might draw the conclusion that arsenate interacts with the solid iron hydroxy sulphates in a similar way in all fractions. The pronounced As-Fe contribution at 3.28 Å (see Figure 3) measured in the ARD raw sample and the different filtrates shows that arsenate is bonded to the colloids (iron hydroxy sulphate) in a similar manner to that of arsenate onto ferrihydrite by a inner-sphere surface complexation [10,11]. Foster, *et al*. reported similar results for an oxidising tailing in California [12]. The authors found As(V) adsorbed/co-precipitated on Fe(III) oxyhydroxides. The picture is different for the precipitate. Taking the relatively large arsenic content found in the precipitate into consideration (see Table 1), a surface complexation of arsenate is not very likely. The larger co-ordination number of 4.5 compared to approximately 2 for the other ARD samples is a further argument against a surface complexation process. A better explanation here is a epitaxial growth of a scorodite phase within/on the iron hydroxy sulphate. Relaxation processes of the As-Fe bond occurring in such small scorodite zones could explain the untypical As-Fe distance of 3.28 Å.

Figure 2. X-ray absorption spectra of selected model compounds and ARD samples

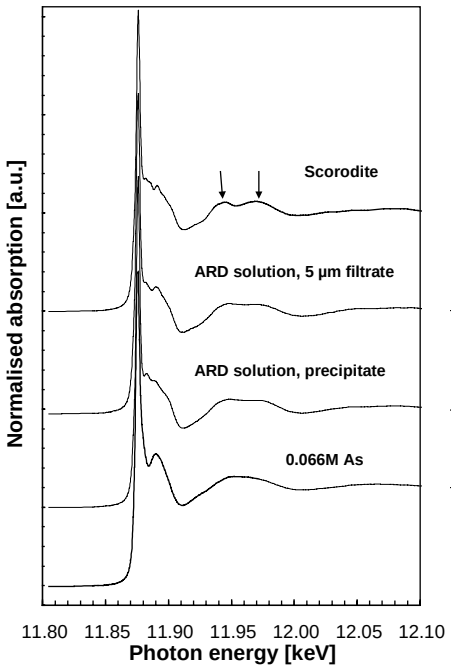

Figure 3. EXAFS results at the arsenic K-edge. Experimental EXAFS oscillations and corresponding Fourier transforms of the model compounds and the ARD fractions

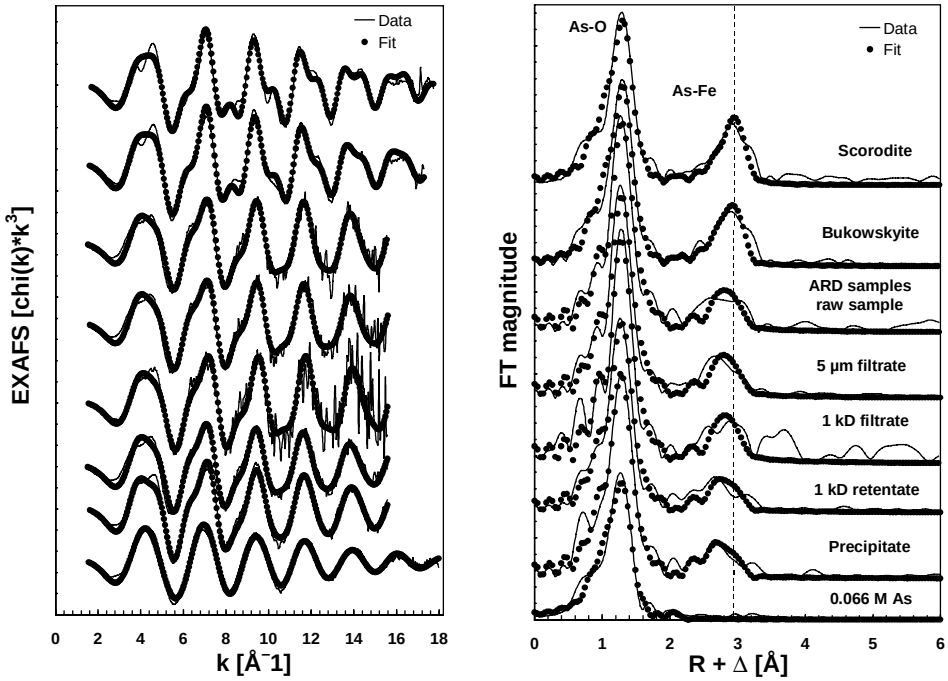

Acknowledgements

We thank A. Scholz and E. Christalle for the XRD and REM/EDX investigations, W. Wiesener and her group for the ICP-MS and AAS analyses, G. Hüttig and C. Fröhlich for assistance in the chemical laboratory work. The authors thank T. Arnold for providing us with the schwertmannite sample. Gratefully acknowledged is the help of K. Flemming, J. Raff and M. Merroun in supplying us with the jarosite. This paper represents publication No. 130 of the Priority Program 546 “Geochemical processes with long-term effects in anthropogenically-affected seepage and groundwater”. Financial support was provided by Deutsche Forschungsgemeinschaft (contract ZA238/1-3).

REFERENCES

[1] H. Zänker, H. Moll, W. Richter, V. Brendler, T. Reich, A. Kluge, G. Hüttig, "The Colloid Chemistry of Acid Rock Drainage Solution from an Abandoned Zn-Pb-Ag Mine", in preparation (2000).

[2] T. Arnold, G. Bernhard, H. Nitsche, Forschungszentrum Rossendorf, Institute of Radiochemistry, Annual Report 1999, FZR-247, p. 17.

[3] R.M. Cornell, U. Schwertmann, "The Iron Oxides", VCH Weinheim, 1996, p. 489.

[4] W. Matz, N. Schell, G. Bernhard, F. Prokert, T., Reich, J. Claußner, W. Oehme, R. Schlenk, S. Dienel, H. Funke, F. Eichhorn, M. Betzl, D. Pröhl, U. Strauch, G. Hüttig, H. Krug, W. Neumann, V. Brendler, P. Reichel, M.A. Denecke and H. Nitsche, *J. Synchrotron Rad*., 6, 1076-1085 (1999).

[5] J.J. Rehr, R.C. Albers, S.I. Zabinsky, *Phys. Rev. Lett*., 69, 3397 (1992).

[6] S. Menchetti, C. Sabelli, *Neues Jahrbuch f. Mineralogie*, 1976, 406-417.

[7] J.L. Hazemann, J.F. Berar, A. Manceau, *Materials Science Forum*, 79, 821-826 (1991).

[8] F.C. Hawthorne, *Acta Cryst*., B 32, 2891-2892 (1976).

[9] R.G. Robins, *Am. Mineral*., 72, 842-844 (1987).

[10] G.A. Waychunas, B.A. Rea, C.C. Fuller, J.A. Davies, *Geochim. Cosmochim. Acta*, 57, 2251-2269 (1993).

[11] C.C. Fuller, J.A. Davies, G.A. Waychunas, *Geochim. Cosmochim. Acta*, 57, 2271-2282 (1993).

[12] A.L. Foster, G.E. Brown, Jr., T.N. Tingle, G.A. Parks, *Am. Mineral*., 83, 553-568 (1998).

STRUCTURAL ASPECTS OF THE NEW QUASI-2-D HEAVY FERMION MATERIALS $CeIrIn_5$ AND $CeRhIn_5$

E.G. Moshopoulou,[1,2] **Z. Fisk,**[2,3] **J.L. Sarrao,**[2] **J.D. Thompson**[2]
[1]National Center for Scientific Research "Demokritos", Institute of Materials Science
15310 Agia Paraskevi (Athens), Greece
[2]Los Alamos National Laboratory, Los Alamos, New Mexico 87545, USA
[3]National High Magnetic Field Laboratory, Florida State University, Tallahassee, FL 32306, USA

Abstract

The title compounds are new heavy fermion materials. They adopt a quasi two-dimensional crystal structure and exhibit unusual (for a heavy fermion system) low temperature properties. Although the study of their physical and structural behaviour at low temperatures and/or high pressures is still in progress, we present here some results concerning their average crystal structure, and we discuss very briefly their similarities and differences with the compounds $CeIn_3$ and $UTGa_5$ (T: Co, Ni, Ir, Pd, Cu, Ru).

Introduction

The linear homologous series $M_mT_nT'_{3m+2n}$ (M: rare earth, Y or U; T: transition metal and T´: Ga or In) was discovered by Grin, *et al*. more than twenty years ago [1]. Since then several members of the series have been prepared [1-10] but very few studies have been reported about their physical and structural behaviour.

The $M_mT_nT'_{3m+2n}$ compounds exist as well-defined phases whose structures consist of periodic intergrowths of segments of two simple parent structures: $AuCu_3$-type cuboctahedra [MT'_3], and $PtHg_2$-type rectangular parallelepipeds [TT'_2]. All known $M_mT_nT'_{3m+2n}$ compounds adopt tetragonal structure (space group P4/*mmm*) and are formed by *n* [TT'_2]-type and *m* [MT'_3]-type layers alternatively stacked along the c axis.

Among the various members of the series $M_mT_nT'_{3m+2n}$, the materials U-T-Ga (T: Co, Ni, Ir, Pd, Cu, Ru) attracted considerable attention [7-10] as strong candidates for heavy fermion behaviour. However, no such behaviour has been observed.

Recently several new members of the series $M_mT_nT'_{3m+2n}$ have been discovered at Los Alamos National Laboratory: $CeRhIn_5$, $CeIrIn_5$, Ce_2RhIn_8 and Ce_2IrIn_8. All compounds exhibit unusual fermion behaviour and quasi-two-dimensional crystal structure [11,12]. Their parent structure is the well-known cubic heavy fermion material $CeIn_3$. This paper reports briefly the structural characterisation of $CeRhIn_5$ and $CeIrIn_5$ at ambient conditions. A more detailed article will be published in the Journal of Solid State Chemistry.

Diffraction results

Single crystals of the title-compounds have been grown by the flux technique out of In flux.

Despite their relatively simple chemical formula, the determination of the accurate crystal structure of $CeIrIn_5$ and $CeRhIn_5$ presents two principal difficulties: first, both materials have very high absorption coefficients for either X-ray or neutron radiation; and second, some of their atoms do not have sufficient differences in either their neutron or X-ray scattering factors. Our approach to overcome these difficulties was to combine electron, neutron and X-ray diffraction. Electron diffraction has been used to check for weak effects such as diffuse scattering or superstructure which, due to the problems just mentioned, would hardly be observed by X-rays or neutrons. Such effects might occur in our samples for the following reason: $CeRhIn_5$ and $CeIrIn_5$ contain $PtHg_2$-type "cubes", "$RhIn_2$" and "$IrIn_2$" respectively. In this type of structural unit (and consequently in the structural series containing it) there is some doubt about the extent of ordering of the constituent atoms [13-15].

The electron diffraction experiments demonstrated that no diffuse streaks between the Bragg spots or extra reflections violating the space group *P*4/*mmm* exist. The diffraction spots do not appear elongated or split, indicating the absence of any disoriented adjacent domains in the crystallites.

The accurate structural parameters of $CeRhIn_5$ and $CeIrIn_5$ were determined by refinements of single crystal X-ray and neutron diffraction data respectively. The results of the refinements are listed in Tables 1 and 2. The cell constants, the main interatomic distances and angles are given in Table 3 and compared with the corresponding ones of the parent compound $CeIn_3$.

Table 1. Atomic co-ordinates and thermal factors for $CeIrIn_5$

Atom	*x*	*y*	*z*	U_{11} (Å^2)	U_{22} (Å^2)	U_{33} (Å^2)
Ce	0	0	0	0.00452(63)	0.00452(63)	0.00622(82)
Ir	0	0	0.5	0.00315(36)	0.00315(36)	0.00539(46)
In1	0.5	0.5	0	0.00748(80)	0.00748(80)	0.0159(12)
In2	0	0.5	0.30524(18)	0.01606(75)	0.00478(62)	0.00755(59)

Table 2. Atomic co-ordinates and thermal factors for $CeRhIn_5$

Atom	*x*	*y*	*z*	U_{11} (Å^2)	U_{22} (Å^2)	U_{33} (Å^2)
Ce	0	0	0	0.009(2)	0.009(2)	0.005(2)
Rh	0	0	0.5	0.002(1)	0.002(1)	0.010(2))
In1	0.5	0.5	0	0.014(2)	0.014(2)	0.011(2)
In2	0	0.5	0.3059(2)	0.018(2)	0.008(1)	0.007(2)

Table 3. Select interatomic distances (Å) and angles for $CeIrIn_5$, $CeRhIn_5$ and $CeIn_3$. The cell constant for $CeIn_3$ was taken from Ref. [16].

$CeIrIn_5$ (P4/*mmm*)		**$CeRhIn_5$ (P4/*mmm*)**		**$CeIn_3$ (P*m*3*m*)**	
Unit cell constants (Å)		Unit cell constants (Å)		Unit cell constants (Å)	
a	4.674(1)	*a*	4.656(2)	*a*	4.689(2)
c	7.501(5)	*c*	7.542(1)		
[$CeIn_3$] cuboctahedra		*[$CeIn_3$] cuboctahedra*		*$CeIn_3$ cuboctahedra*	
Interatomic distances (Å)		Interatomic distances (Å)		Interatomic distances (Å)	
Ce-In1 × 4	3.3050(7)	Ce-In1 × 4	3.2923(14)	Ce-In × 12	3.3156(6)
Ce-In2 × 8	3.2717(11)	Ce-In2 × 8	3.2775(7)		
Angles (°)		Angles (°)		Angles (°)	
In1-Ce-In1	90(0)	In1-Ce-In1	90(0)	In-Ce-In	90(0)
In1-Ce-In2	59.662(11)	In1-Ce-In2	59.851(7)	In-Ce-In	60(0)
In1-Ce-In2	120.338(11)	In1-Ce-In2	120.149(7)	In-Ce-In	120(0)
In2-Ce-In2	91.17(4)	In2-Ce-In2	90.517(26)	In-Ce-In	90(0)
In2-Ce-In2	60.675(23)	In2-Ce-In2	60.298(15)	In-Ce-In	60(0)
In2-Ce-In2	88.83(4)	In2-Ce-In2	89.483(26)	In-Ce-In	90(0)
[$IrIn_2$] parallelepipeds		*[$RhIn_2$] parallelepipeds*			
Interatomic distances (Å)		Interatomic distances (Å)			
Ir-In2 × 8	2.7560(7)	Rh-In2 × 8	2.7500(9)		
Angles (°)		Angles (°)			
In2-Ir-In2	73.682(17)	In2-Rh-In2	73.539(11)		
In2-Ir-In2	64.02(4)	In2-Rh-In2	64.325(23)		

Discussion

The basic structural units (co-ordination polyhedra) of the structure of $CeRhIn_5$ and $CeIrIn_5$ are $[CeIn_3]$ cuboctahedra and $[RhIn_2]$ or $[IrIn_2]$ rectangular parallelepipeds. Comparison of the main interatomic distances of $CeIrIn_5$, $CeRhIn_5$ and $CeIn_3$ (Table 3) reveals that in $CeIrIn_5$ and $CeRhIn_5$, the $[CeIn_3]$ cuboctahedra are significantly distorted compared with the cubic heavy fermion compound $CeIn_3$. The quasi two-dimensional nature of the crystal structure $CeIrIn_5$ and $CeRhIn_5$ is illustrated in Figure 1. This structure can be described as an alternate stacking in the [001] direction of monolayers of distorted face-sharing cuboctahedra $[CeIn_3]$, and monolayers of edge-sharing rectangular parallelepipeds $[IrIn_2]$ or $[RhIn_2]$. Because of this ordered intergrowth 2-D structure, the physical properties of $CeRhIn_5$ and $CeIrIn_5$ can be directly compared with the corresponding ones of their parent compound, the 3-D heavy fermion $CeIn_3$. Indeed such comparison allowed us to understand at least qualitatively the high pressure/low temperature behaviour of $CeRhIn_5$ [16].

Figure 1. The quasi-2-D crystal structure of $CeRhIn_5$ and $CeIrIn_5$ viewed along [100]. Ce atoms are at the centre of the distorted cuboctahedra $[CeIn_3]$.

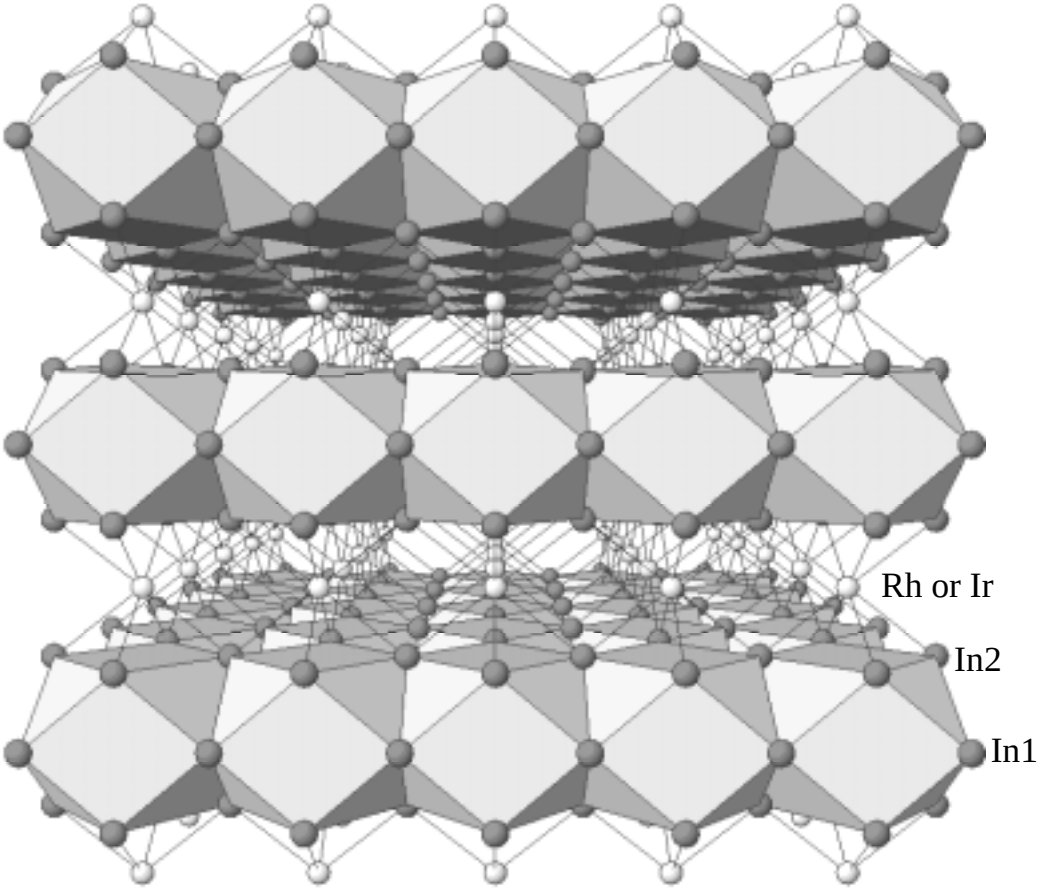

This comparison between the corresponding interatomic distances of the three compounds is reliable despite the fact that their crystal structure was determined by different techniques (powder X-ray diffraction for $CeIn_3$, single crystal neutron diffraction for $CeIrIn_5$ and single crystal X-ray diffraction for $CeRhIn_5$). Indeed, it is well-established [17] today that for simple inorganic compounds

there is very good agreement between the positional parameters deduced by different diffraction methods. In opposite, no satisfactory comparison can be made between the thermal factors. Thermal diffuse scattering and anharmonic atomic motions can seriously affect the thermal factors; these effects could not be corrected during the data reduction because not only the experimental conditions but also the elastic constants of the materials have to be known. However, both $CeRhIn_5$ and $CeIrIn_5$ exhibit large U_{11} for In2. U_{11} represents the thermal vibration of In2 along the c axis. A large thermal factor is usually due to static or dynamic disorder. Static disorder can be excluded because no superlattice reflections were found by electron diffraction. Consequently In2 exhibits rather important dynamic disorder. However, low temperature diffraction data are necessary in order to deduce accurate atomic displacement parameters and make a precise comparison among them.

We also investigate these materials by other techniques in both local and average scales and we extend our work to other compounds of the series $M_mT_nT'_{3m+2n}$ based on either Ce or U in order to obtain a deeper understand of this fascinating and relatively unexplored series.

REFERENCES

[1] Y.N. Grin, Y.P. Yarmolyuk and E.I. Giadyshevskii, *Sov. Phys. Crystallogr.*, 24 (2), 137 (1979).

[2] R.V. Lapunova, Y.N. Gryn and Y.P. Yarmolyuk, *Dop. Ak. Nauk Ukr. RSR Ser. B Transl.*, 8, 43 (1984).

[3] Y.N. Grin, P. Rogl and K. Hiebl, in "Actinides '85, Abstracts", p. 114. Aix-en-Provence, 1985.

[4] Y.N. Grin, P. Rogl and K. Hiebl, *J. Less-Common Metals*, 121, 497 (1986).

[5] Y.N. Grin, P. Rogl, L.G. Akselrud, V.K. Pecharskii and Y.P. Yarmolyuk, *Russ. Metall.*, 4, 206 (1988).

[6] Y.M. Kalychak, V.I. Zaremba, V.M. Baranyak, V.A. Bruskov and P.Y. Zavalii, *Russ. Metall.*, 1, 213 (1989).

[7] V. Sechovsky, L. Havela, G. Schaudy, G. Hilscher, N. Pillmayr, P. Rogl and P. Fischer, *J. Magn. Magn. Mat*., 104-107, 11 (1992).

[8] S. Noguchi and K. Okuda, *J. Magn. Magn. Mat.*, 104-107, 57 (1992).

[9] S. Noguchi and K. Okuda, *Physica B*, 188, 749 (1993).

[10] M. Schonert, S. Corsepius, E.W. Scheidt and G.R. Stewart, *J. Alloy. Compd.*, 224, 108 (1995).

[11] H. Hegger, C. Petrovic, E.G. Moshopoulou, M.F. Hundley, J.L. Sarrao, Z. Fisk, J.D. Thompson, *Phys. Rev. Lett.*, 84, 4986 (2000).

[12] C. Petrovic, *et al*., upublished data.

[13] E. Bauer, H. Nowotny and A. Stempfl, *Monatshefte Fuer Chemie*, 84, 693 (1953).

[14] "Atlas of Crystal Structure Types for Intermetallic Phases", Vol. 2, J.L.C. Daams, P. Villars, and J.H.N. van Vucht, eds., pp. 3541-3543, ASM International, Materials Park, Ohio, 1991.

[15] B.G. Hyde and Sten Andersson, in "Inorganic Crystal Structures", pp. 189-190, Wiley, New York, 1989.

[16] Jon Lawrence, *Phys. Rev. B*, 20, 3770 (1979).

[17] P. Coppens, J. Dam, S. Harkema, D. Feil, R. Feld, M.S. Lehmann, R. Goddard, C. Krüger, E. Hellner, H. Johansen, F.K. Larsen, T.F. Koetzle, T.F. McMullan, E.N. Maslen, E.D. Stevens, *Acta Crystallogr. Sect. A*, 40, 184 (1984); B.B. Iversen, F.K. Larsen, B.N. Figgis, P.A. Reynolds and A.J. Schultz, *Acta Crystallogr. Sect. B*, 52, 923 (1996), and references therein.

NEPTUNIUM(V) COMPLEXATION BY VARIOUS HUMIC ACIDS IN SOLUTION STUDIED BY EXAFS AND NIR SPECTROSCOPY

S. Pompe,* K. Schmeide, T. Reich, C. Hennig, H. Funke,
A. Roßberg, G. Geipel, V. Brendler, K.H. Heise, G. Bernhard
Forschungszentrum Rossendorf e.V., Institute of Radiochemistry
P.O. Box 510119, D-01314 Dresden, Germany
*s.pompe@fz-rossendorf.de

Abstract

The structure of Np(V) humic acid (HA) complexes at pH 7 was studied by EXAFS. For the first time, the influence of phenolic OH groups on the complexation of HA and Np(V) in the neutral pH range was investigated using a modified natural HA with blocked phenolic OH groups and Bio-Rex70, a cation exchange resin having carboxyl groups as proton exchanging sites. Near-infrared (NIR) spectroscopic measurements verified the formation of Np(V) humates under the applied conditions. Co-ordination numbers and bond distances were determined for the axial and equatorial co-ordination shells of neptunium. These were compared to structural parameters of Np(V) hydrates and carboxylates.

Introduction

Humic acids (HA) influence the migration of actinides in the environment due to their solubility in natural waters and their ability to complex metal ions. Thus, detailed knowledge about the interaction between HA and actinides is important in order to assess the mobility of actinides in natural aquifer systems.

The complexation of humic substances with neptunium in the pentavalent oxidation state has already been studied by different authors [e.g. 1-5]. Various methods were used to determine complex stability constants. However, not much is known about the structure of these complexes. Such information can help to validate the assumed complexation process and to enhance complexation models used for the predictive modelling of the migration behaviour of actinides in the environment.

In the present study we determined structural parameters for Np(V) humate complexes of a natural and a synthetic HA by EXAFS. Near-infrared (NIR) absorption spectroscopy was applied to verify the formation of the Np(V) humate complexes. In order to improve knowledge about the contribution of different functional groups to the interaction between HA and metal ions, we continued our investigations regarding the influence of phenolic OH groups on the complexation behaviour of HA [6]. Applying a chemically modified HA with blocked phenolic OH groups, we investigated the influence of phenolic OH groups on the local structure of Np(V) in Np(V) humate complexes in the neutral pH range. For comparison, we studied the interaction of Np(V) with Bio-Rex70. This is a cation exchange resin which has, in contrast to HA, only carboxyl groups as complexing sites. The obtained results were compared to structural parameters of Np(V) carboxylates and hydrates given in the literature.

Experimental

Samples

Np(V) complexes were prepared from commercially available natural HA from Aldrich (Germany) which was previously purified (AHA, charge A2/98), chemically modified HA Aldrich with blocked phenolic OH groups (AHA-PB) [6], synthetic HA-type M42 (charge M81), which shows a carboxyl group content comparable to natural HA [7], and Bio-Rex70 from Bio-Rad (Germany). Table 1 shows the functional group content of the HA and of Bio-Rex70.

Table 1. Functional group content of the investigated HA and of Bio-Rex70

	COOH [meq/g]	Phenolic OH groups [meq/g]	Phenolic OH/COOH	PEC[a] [meq/g]
AHA	4.49 ± 0.14	3.1 ± 0.1	0.69	4.60 ± 0.08
AHA-PB	3.25 ± 0.05	1.1 ± 0.4	0.34	3.58 ± 0.23
M42	4.10 ± 0.10	2.3 ± 0.4 [b]	0.56	3.90 ± 0.18
Bio-Rex70	10	–	–	10

[a] PEC: Proton exchange capacity.
[b] Acidic OH groups.

All samples were prepared under nitrogen atmosphere using carbonate-free solutions. Np(V) humates were made by adding aliquots of a Np(V) stock solution (5.2×10^{-2} M, 0.1 M HNO_3, ^{237}Np) to HA solutions, that were prepared by degassing the HA in aqueous suspension and subsequent dissolving with NaOH. The ionic strength of the Np(V) humate solutions was set to 0.1 M with 1 M $NaClO_4$. Np(V)-Bio-Rex70 sorbate was synthesised by contacting pre-equilibrated Bio-Rex70

(pH 7) with aliquots of the Np(V) stock solution in 0.1 M $NaClO_4$. The pH values of all samples were adjusted to pH 7.0 by adding NaOH and $HClO_4$. For EXAFS measurements 2 mL of each Np(V) humate solution were filled into polyethylene vials. The Np(V)-Bio-Rex70 sorbate was isolated by centrifugation and measured in the form of a wet paste that was filled into a special sample holder for pastes. All samples were sealed in double polyethylene bags. The Np(V) concentration of the samples was determined by γ-spectroscopy. The compositions of the investigated samples are summarised in Table 2.

Table 2. EXAFS sample composition

Sample	HA [g/L]	Np [mmol/L]	pH	I_{NaClO4} [mol/L]	NpO_2^+-loading [% PEC]
Np(V)-AHA	8.1	0.90	7.0	0.1	2.4
Np(V)-AHA-PB	10.8	0.88	7.0	0.1	2.3
Np(V)-M42	9.9	0.89	7.0	0.1	2.3
	NpO_2^+-loading [mg Np/g Bio-Rex70]				
Np(V)-Bio-Rex70	121.3				5.1

NIR measurements

NIR absorption spectra of the Np(V) humate solutions were recorded with the UV-Vis-NIR spectrophotometer CARY-5G (Varian). For comparison, the absorption spectrum of a 5.2×10^{-4} M Np(V) solution (0.1 M HNO_3) was measured. It was not necessary to adjust the pH of this solution to pH 7.0. Calculations of the Np(V) species distribution (5×10^{-3} M NpO_2^+, I: 0.1 M $NaClO_4$) have shown that Np(V) occurs in the form of the free NpO_2^+ ion up to pH 7.

EXAFS measurements

Neptunium L_{III}-edge EXAFS spectra were recorded in fluorescence mode [Np(V) humates] as well as in transmission mode [Np(V)-Bio-Rex70] at the Rossendorf Beamline (ROBL) at the ESRF in Grenoble. The Si(111) double-crystal monochromator was used in the fixed-exit mode. Fluorescence spectra were collected with a four-pixel germanium fluorescence detector. The energy scale of the spectra was calibrated using the first inflection point of the absorption spectrum of an yttrium foil (17 038 eV). The threshold energy for the Np L_{III}-edge, E_0, was defined as 17 630 eV. For data analysis the transmission spectra were averaged and baseline corrected. The fluorescence spectra were dead-time corrected, statistically weighted and averaged. Data analysis was performed using the suite of programs EXAFSPAK [8] applying standard techniques [9]. Theoretical scattering amplitudes and phases were calculated for a hypothetical cluster of $NpO_2(H_2O)_4^+$ with the scattering code FEFF6 [10].

Results

NIR spectroscopy

Figure 1 shows the NIR absorption spectra of the investigated Np(V) humate solutions in comparison to the absorption spectrum of a 5.2×10^{-4} M Np(V) solution (0.1 M HNO_3).

Figure 1. Absorption spectrum of a 5.2×10^{-4} M Np(V) solution (0.1 M HNO_3) in comparison to the absorption spectra of the investigated Np(V) humate solutions at pH 7.0

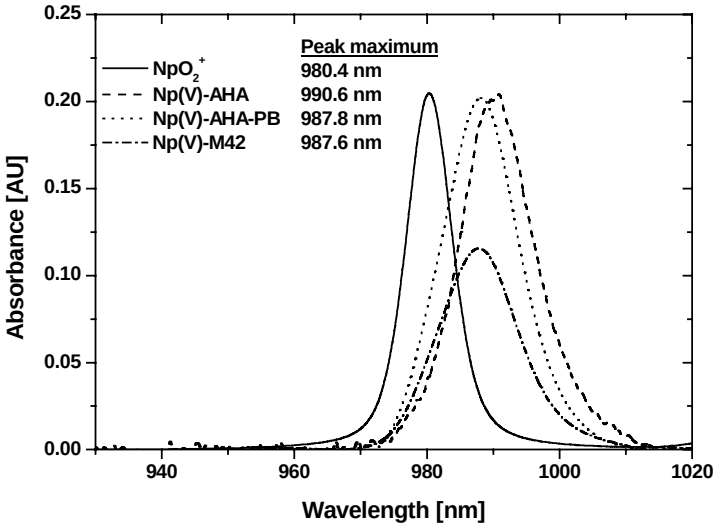

Comparing the absorption spectra, it becomes obvious that the absorption peak maxima of the Np(V) humate solutions are significantly shifted to higher wavelengths than the peak maximum of the free NpO_2^+ ion. This indicates the Np(V) humate complex formation for all HA under the applied experimental conditions. In all samples more than 90% of the total Np(V) occurs in the form of the Np(V) humate complex. These results are in agreement with spectroscopic data for the complexation of Np(V) with HA of Marquardt and Kim [5], who determined absorption peak maxima of 980.4 nm and 990 nm for the aqueous NpO_2^+ ion and its humate complex, respectively. No indications for the reduction of Np(V) to Np(IV) by humic acids were observed.

EXAFS results

The Np L_{III}-edge k^3-weighted EXAFS oscillations for all Np(V) samples and their Fourier transforms (FT) are shown in Figure 2. The FT are not corrected for EXAFS phase-shifts causing peaks to appear at shorter distances (R + Δ) relative to the true distance R. The EXAFS oscillations of all samples are comparable. Two co-ordination shells are evident in the FT in Figure 2. The FT of all samples are dominated by a peak at approximately 1.3 Å. This peak corresponds to the axial oxygen atoms of the neptunyl unit (NpO_2^+). The next shoulder at about 2.0 Å represents oxygen atoms co-ordinated to neptunium in the equatorial plane. The weak peak at about 3.2 Å results from multiple scattering along the neptunyl unit.

The EXAFS oscillations were fitted to the EXAFS equation [9] in the k-range between 2.9 and 8.7 $Å^{-1}$ using a structural model involving the axial and equatorial neptunium co-ordination shells with oxygen as backscatterer (O_{ax}, O_{eq}). In addition, a four-legged multiple scattering path along the neptunyl unit ($Np \rightarrow O_{ax1} \rightarrow Np \rightarrow O_{ax2} \rightarrow Np$) was included in the fit. The axial co-ordination number was held constant at 2 during the fits. The calculated structural parameters are compiled in Table 3 in comparison to literature data for Np(V) hydrates in 0.1 M HNO_3 [11] and 3 M Cl^- medium [12].

Figure 2. Np L_{III}-edge k^3-weighted EXAFS spectra and their corresponding Fourier transforms

Solid lines: experimental data, dashed lines: fit results, MS: multiple scattering along the neptunyl unit

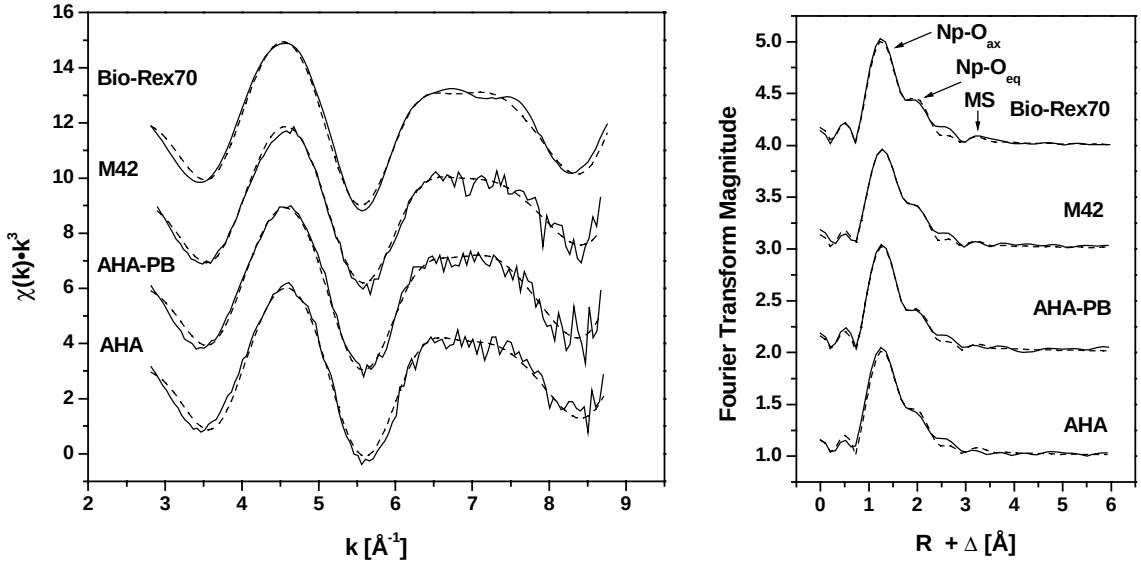

Table 3. EXAFS structural parameters of Np(V) humates in comparison to Np(V)-Bio-Rex70 sorbate and to Np(V) hydrates [11,12]

N: co-ordination number, R: bond distance, ax: axial, eq: equatorial,
σ^2: EXAFS-Debye-Waller factor, ΔE_0: shift in threshold energy

Sample	Np-O_{ax}			Np-O_{eq}			ΔE_0	Ref.
	N	R [Å]	σ^2 [Å^2]	N	R [Å]	σ^2 [Å^2]	[eV]	
Np(V)-AHA	2	1.84±0.01	0.0035	2.9±0.7	2.48±0.01	0.0047	-7.8	This work
Np(V)-AHA-PB	2	1.85±0.01	0.0034	2.8±0.8	2.49±0.01	0.0054	-8.0	This work
Np(V)-M42	2	1.84±0.01	0.0048	3.3±0.9	2.48±0.01	0.0078	-8.8	This work
Np(V)-Bio-Rex70	2	1.85±0.01	0.0034	2.9±0.5	2.50±0.01	0.0046	-8.2	This work
$NpO_2(H_2O)_x^+$	1.9±0.2	1.822±0.003	0.0023	3.6±0.6	2.488±0.009	0.006	-8.5	[11]
$NpO_2(H_2O)_x^+$	2	1.85±0.009	0.0018	5.0±1.0	2.50±0.02	0.007	-6.7	[12]

95% confidence limits are given for N and R as estimated by EXAFSPAK.

All Np(V) humates show comparable axial Np-O bond lengths that are comparable to the axial Np-O bond lengths of Np(V)-Bio-Rex70. In addition, the equatorial co-ordination numbers of the Np(V) humates are similar to those determined for Np(V)-Bio-Rex70 sorbate. Independent of the HA origin and of the HA functional group content the equatorial Np-O bond lengths of the Np(V) humates are comparable with each other and also with those of Np(V)-Bio-Rex70 sorbate. Furthermore, they are comparable with the equatorial Np-O bond lengths of $NpO_2(H_2O)_x^+$ [11,12]. This means that the complexation of Np(V) by HA, which was confirmed by NIR spectroscopy, induces no shortening of the equatorial Np-O bond lengths. Within the experimental error the structural data of Np(V) humates and $NpO_2(H_2O)_x^+$ are similar. Nevertheless, differences in the EXAFS oscillations of Np(V) humates and hydrates [11,12] between 6 and 8 Å^{-1} indicate structural differences due to the HA complexation.

Due to the fact that the Np(V) humates of modified Aldrich HA with blocked phenolic OH groups (AHA-PB) and unmodified Aldrich HA (AHA) show comparable structural parameters it can be concluded that the blocking of phenolic OH groups has no influence on the local structure of neptunium in the studied Np(V) humates. Since Bio-Rex70 solely shows carboxyl groups as proton exchanging sites, similar co-ordination numbers and bond lengths of Np(V) humates and of Np(V)-Bio-Rex70 sorbate indicate that carboxyl groups dominate the interaction between Np(V) and HA. However, a contribution of phenolic OH groups to the interaction between HA and Np(V) cannot completely be excluded by the EXAFS results, because the obtained parameters represent average values over all interactions between HA and Np(V). Furthermore, there is the possibility that phenolic OH groups interacting with Np(V) show equatorial bond lengths similar to those of carboxylate groups. For instance, for a U(VI) pyrogallol (1,2,3-trihydroxybenzene) complex an equatorial U-O bond length of 2.40 Å was obtained [13]. Similar bond distances were also found for uranyl humates with modified HA, where carboxyl groups dominate the interaction [14].

The comparison of the results for Np(V) humates with structural parameters of Np(V) carboxylates given in the literature show that the equatorial Np-O bond lengths of the Np(V) humates are comparable with those of monodentate co-ordinated carboxylate groups of Np(V) carboxylates. Monodentate co-ordinated carboxylate groups in the Np(V) malonate complex $(NpO_2)_2C_3H_2O_4 \cdot 4\ H_2O$ show a Np-O bond length of 2.50 Å [15]. However, due to the fact that the equatorial Np-O bond lengths of the Np(V) humates are also comparable with the Np-O bond distances of Np(V) hydrates, a differentiation between water molecules and monodentate co-ordinated carboxylate groups is not possible with the obtained EXAFS results. A predominate bidentate co-ordination of humic acid carboxylate groups around the neptunyl unit can be excluded. For the Np(V) formate complex, $(NH_4)NpO_2(OOCH)_2$, equatorial Np-O bond distances of 2.60 ± 0.04 Å were described for bidentate carboxylate groups [16]. In addition, the comparison of the obtained equatorial Np-O bond lengths with those of bidentate co-ordinated carbonate ligands in the solid $K_3NpO_2(CO_3)_2$ complex (R = 2.55 Å) [17] points to a not primarily bidentate co-ordination of humic acid carboxylate groups around the neptunyl unit.

Conclusions

Structural parameters for different Np(V) humates at pH 7, whose formation has been confirmed by NIR spectroscopy, were determined by EXAFS. For the first time, the influence of phenolic OH groups on the Np(V) complexation by HA in the neutral pH range was studied using a modified HA with blocked phenolic OH groups and Bio-Rex70, a cation resin having only carboxyl groups. Independent of their origin and functionality, all HA show comparable structural parameters that also agree with those obtained for Bio-Rex70. This indicates that the interaction between Np(V) and HA in the neutral pH range is dominated by carboxyl groups. However, up to now a contribution of phenolic OH groups to the interaction process cannot fully be excluded. The obtained equatorial Np-O bond lengths for Np(V) humates are comparable with equatorial Np-O bond lengths of Np(V) hydrates as well as with Np-O bond lengths of monodentate co-ordinated carboxylate groups in Np(V) carboxylates. Thus, a differentiation between both is still not possible. A predominantly bidentate co-ordination of humic acid carboxylate groups can be excluded.

Acknowledgements

This work was supported by Bundesministerium für Wirtschaft und Technologie under contract number 02E9299. We thank G. Grambole for her help during sample characterisation. EXAFS measurements were performed at BM20 at the European Synchrotron Radiation Facility in Grenoble.

REFERENCES

[1] J.I. Kim, T. Sekine, "Complexation of Neptunium(V) with Humic Acid", *Radiochim. Acta*, 55, 187 (1991).

[2] L. Rao, G.R. Choppin, "Thermodynamic Study of the Complexation of Neptunium(V) with Humic Acids", *Radiochim. Acta*, 69, 87 (1995).

[3] C. Marquardt, N. Trautmann, "Complexation of Neptunium(V) with Humic Acids at Very Low Metal Concentrations", *Radiochim. Acta*, 73, 119 (1996).

[4] C. Marquardt, J.I. Kim, "Complexation of Np(V) with Fulvic Acid", *Radiochim. Acta*, 81, 143 (1998).

[5] C. Marquardt, J.I. Kim, "Complexation of Np(V) with Humic Acid: Intercomparison of Results from Different Laboratories", *Radiochim. Acta*, 80, 129 (1998).

[6] S. Pompe, K. Schmeide, M. Bubner, G. Geipel, K.H. Heise, G. Bernhard, H. Nitsche, "Investigation of Humic Acid Complexation Behavior with Uranyl Ions Using Modified Synthetic and Natural Humic Acids", *Radiochim. Acta*, 88, 553 (2000).

[7] S. Pompe, A. Brachmann, M. Bubner, G. Geipel, K.H. Heise, G. Bernhard, H. Nitsche, "Determination and Comparison of Uranyl Complexation Constants with Natural and Synthetic Humic Acids", *Radiochim. Acta*, 82, 89 (1998).

[8] G.N. George, I.J. Pickering, "EXAFSPAK: A Suite of Computer Programs for Analysis of X-ray Absorption Spectra", Stanford Synchrotron Radiation Laboratory, Stanford, CA, USA, 1995.

[9] "X-ray Absorption: Principles, Applications, Techniques of EXAFS, SEXAFS and XANES", D.C. Koningsberger, R. Prins, eds., John Wiley & Sons, New York, 1988.

[10] J.J. Rehr, R.C. Albers, S.I. Zabinsky, "High-order Multiple-scattering Calculations of X-ray Absorption Fine Structure", *Phys. Rev. Lett*., 69, 3397 (1992).

[11] T. Reich, G. Bernhard, G. Geipel, H. Funke, C. Hennig, A. Roßberg, W. Matz, N. Schell, H. Nitsche, "The Rossendorf Beam Line ROBL – A Dedicated Experimental Station for XAFS Measurements of Actinides", *Radiochim. Acta*, 88, 633 (2000).

[12] P.G. Allen, J.J. Bucher, D.K. Shuh, N.M. Edelstein, T. Reich, "Investigation of Aquo and Chloro Complexes of UO_2^{2+}, NpO_2^+, Np^{4+} and Pu^{3+} by X-ray Absorption Fine Structure Spectroscopy", *Inorg. Chem.*, 36, 4676 (1997).

[13] A. Roßberg, L. Baraniak, T. Reich, C. Hennig, G. Bernhard, H. Nitsche, "EXAFS Structural Analysis of Aqueous Uranium(VI) Complexes with Lignin Degradation Products", *Radiochim. Acta*, 88, 593 (2000).

[14] S. Pompe, K. Schmeide, M. Bubner, T. Reich, A. Roßberg, C. Hennig, H. Funke, K.H. Heise, G. Bernhard, "The Influence of Phenolic Hydroxyl Groups on the Complexation Behavior of Humic Substances with Uranyl(VI) Ions: III. EXAFS Investigations of Solid UO_2^{2+} Complexes with Modified and Unmodified Humic Acids", Report FZR-285, Rossendorf, 2000, p. 31.

[15] M.S. Grigoriev, I.A. Charushnikova, N.N. Krot, A.I. Yanovskii, Yu.T. Struchkov, "Crystal and Molecular Structure of Neptunyl Malonate Tetrahydrate $(NpO_2)_2C_3H_2O_4 \cdot 4H_2O$", *Radiokhimiya*, 4, 24 (1993).

[16] M.S. Grigoriev, I.A. Charushnikova, N.N. Krot, A.I. Yanovskii, Yu.T. Struchkov, "Crystal Structure of the Neptunyl Formate Complex $(NH_4)NpO_2(OOCH)_2$", *J. Neorgan. Chim.*, 39, 1328 (1994).

[17] Yu.F. Volkov, G.I. Visyashcheva, S.V. Tomilin, I.I. Kapshukov, A.G. Rykov, "Study of the Carbonate Compounds of Pentavalent Actinides with Alkali Metal Cations", *Radiokhimiya*, 23, 248 (1981).

THE APPLICATION OF ITERATIVE TRANSFORMATION FACTOR ANALYSIS TO RESOLVE MULTI-COMPONENT EXAFS SPECTRA OF URANIUM(VI) COMPLEXES WITH ACETIC ACID AS A FUNCTION OF PH

A. Roßberg, T. Reich
Forschungszentrum Rossendorf e.V., Institut für Radiochemie
P.O. Box 510119, D-01314 Dresden, Germany

Abstract

Synchrotron-based EXAFS spectroscopy is a powerful technique to obtain structural information on radionuclide complexes in solution. Depending on the chemical conditions of the samples several radionuclide species can coexist in the solution as is often the case for environmentally related samples. All radionuclide species, which may have different near-neighbour environments, contribute to the measured EXAFS signal. In order to isolate the EXAFS spectra of the individual species (pure spectral components), it is necessary, in a first step, to measure a series of samples where their composition is changed by variation of one physico-chemical parameter (e.g. pH, concentration, etc.). For the spectral decomposition it is necessary that the EXAFS signal change as a function of the chosen physico-chemical parameter. In a second step, the series of EXAFS spectra is analysed with Eigenanalysis and Iterative Transformation Factor Analysis (ITFA) [1]. As a result of the ITFA one obtains: a) for each sample the relative concentration of the structural distinguishable species and b) their corresponding pure spectral components. From the information obtained in a), one can construct a speciation diagram. The pure spectral components contain the structural information of the individual species, which can be extracted by conventional EXAFS analysis.

To evaluate our ITFA algorithm for EXAFS analysis of mixtures, we prepared a series of eight solution samples of 0.05 M uranium(VI) and 1 M acetate (Ac) in the pH range of 0.1 to 4.5. From thermodynamic constants it is known that under these conditions up to four species can occur: uranyl hydrate, and the 1:1, 1:2 and 1:3 complexes of uranyl acetate [2]. The uranium L_{III}-edge EXAFS spectra were measured at room temperature in transmission mode at the Rossendorf Beamline (ROBL) at the ESRF. The average bond length between uranium and the equatorial oxygen atoms (O_{eq}) increases from 2.40 to 2.46 Å with increasing pH. This increase of the U-O_{eq} bond length is attributed to the exchange of water molecules (2.40 Å) by bidentate co-ordinated acetate ligands (2.46 Å) as a function of pH. The ITFA of the eight uranium L_{III}-edge EXAFS spectra yielded two pure spectral components corresponding to the species $UO_2(H_2O)_5^{2+}$ and $UO_2(Ac)_3^-$. The EXAFS spectra of the 1:1 and 1:2 complexes contain these two pure spectral components. Therefore, the ITFA yielded only two spectral components for four chemical species. The uranium(VI) speciation as a function of pH calculated from ITFA agrees with the speciation based on the known complexation constants.

Our results show that the ITFA is a powerful mathematical tool to determine the pure spectral components and their relative concentrations in a series of EXAFS spectra. This is important for the structural analysis of multi-component samples using EXAFS spectroscopy.

Acknowledgements

We thank C. Hennig and H. Funke for their help with the EXAFS measurements. We thank H. Neubert for preparation of the samples.

REFERENCES

[1] M. Fernandez-Garcia, C. Marquez Alvarez, G.L. Haller, *J. Phys. Chem*., 99, 12565 (1995).

[2] S. Ahrland, *Acta Chem. Scand*., 5, 199 (1951).

INTERACTION OF NEPTUNIUM(IV) WITH HUMIC SUBSTANCES STUDIED BY XAFS SPECTROSCOPY

K. Schmeide,* S. Pompe, T. Reich, C. Hennig, H. Funke, A. Roßberg, G. Geipel, V. Brendler, K.H. Heise, G. Bernhard
Forschungszentrum Rossendorf e.V., Institute of Radiochemistry
P.O. Box 510 119, D-01314 Dresden, Germany
*k.schmeide@fz-rossendorf.de

Abstract

The complexation of neptunium(IV) with various natural and synthetic humic and fulvic acids at pH 1 was studied using X-ray absorption fine structure (XAFS) spectroscopy to observe the local structure around the neptunium ion. The results were compared to the interaction of neptunium(IV) with Bio-Rex70, a cation exchange resin having solely carboxylic groups. For both neptunium humate complexes and neptunium Bio-Rex70 complexes, 11 oxygen atoms were found at a mean distance of 2.36 Å. This verified that the carboxylic groups of humic substances are responsible for binding neptunium(IV) in the acidic pH range. The humic acid carboxylate groups are predominantly monodentately co-ordinated to neptunium(IV) ions.

Introduction

Humic substances are able to influence the speciation and thus the mobility of radionuclides in natural aquatic systems due to their high complexing ability. Therefore, risk assessments related to the radionuclide migration under environmentally relevant conditions require basic knowledge of the interaction of humic substances with metal ions. It is known that under reducing conditions and in the presence of enhanced levels of organics, neptunium occurs in the tetravalent oxidation state [Np(IV)] and is often complexed to humic substances [1]. The reduction of Np(V) to Np(IV) by chemical interaction of the NpO_2^+ ion with humic substances in the neutral pH range was shown by Zeh, *et al.* [2]. Structural parameters have been determined for the aqueous Np^{4+} ion in hydrochloric and sulphuric medium by Allen, *et al.* [3] and by Reich, *et al.* [4], respectively, using XAFS spectroscopy. However, data related to the interaction of tetravalent neptunium with humic substances are scarce. Recently, stability constants determined at pH 1 and 1.5 were reported [5]. However, there is no information on the structure of neptunium humate complexes formed in anoxic waters.

In the present paper, we studied the interaction of Np(IV) with various natural and synthetic humic substances at pH 1 by XAFS spectroscopy. XAFS spectroscopy, which includes the X-ray absorption near-edge structure (XANES) and the extended X-ray absorption fine structure (EXAFS), is a powerful technique that can be applied to determine the oxidation state and the local chemical environment of an absorbing atom [6]. The structural parameters obtained for Np(IV) humate complexes are compared with those determined for the interaction between Np(IV) and Bio-Rex70. Bio-Rex70 is a cation exchange resin that has in contrast to humic substances no phenolic OH groups, but exclusively carboxylic groups as functional groups capable of binding metal ions. Thus, it was chosen as reference substance to study the nature of metal complexation sites in humic substances. The structural parameters of Np(IV) humate complexes are further compared with structural parameters of Np(IV) hydrates and carboxylates given in the literature.

Experimental

Sorbents

Two natural humic substances were applied: Kranichsee fulvic acid (KFA) that was isolated from surface water of the mountain bog *Kleiner Kranichsee* (Saxony, Germany) [7] and the commercial Aldrich humic acid (AHA, charge A2/98 from Aldrich, Germany) which was purified before use [8]. The synthetic product was the humic acid type M42 (charge M81) [9]. Bio-Rex70 (Bio-Rad, Germany), was used as reference substance. The functional group contents of the sorbents are compiled in Table 1.

Table 1. Functionality of humic substances and Bio-Rex70 and Np loading of Np(IV) samples

Run	Sorbent	Functionality			Sample	Np loading	
		COOH [meq/g]	Phenolic OH [meq/g]	PEC[a] [meq/g]		[mg Np/g sorbent]	[% PEC][c]
1	KFA	6.05 ± 0.31	4.8 ± 0.7	5.60 ± 0.12	Np(IV)-KFA	21.3	6.4
	AHA	4.49 ± 0.14	3.1 ± 0.1	4.60 ± 0.08	Np(IV)-AHA	32.7	12.0
	M42	4.10 ± 0.10	2.3 ± 0.4 [b]	3.90 ± 0.18	Np(IV)-M42	18.0	7.8
	Bio-Rex70	10	–	10	Np(IV)-Bio-Rex70	4.2	0.7
2	AHA	4.49 ± 0.14	3.1 ± 0.1	4.60 ± 0.08	Np(IV)-AHA	41.1	15.1
	Bio-Rex70	10	–	10	Np(IV)-Bio-Rex70	9.3	1.6

[a] Proton exchange capacity.
[b] Acidic OH groups.
[c] Calculated on the assumption that one Np ion occupies four proton exchanging sites of the sorbents.

Sample preparation

Np(IV) stock solutions were prepared by electrochemical reduction of a Np(V) solution ($5.2 \cdot 10^{-2}$ M Np in 0.1 M HNO_3; isotope: ^{237}Np) to Np(III) followed by air oxidation to Np(IV). For electrolysis, a conventional H-formed electrolysis cell with a diaphragm between anode and cathode was used. As anolyte, 1 M H_2SO_4 and 2 M $HClO_4$ were used for first and second experimental runs, respectively. The concentrations of the resulting Np(IV) stock solutions used for the experimental runs 1 and 2 were $3.6 \cdot 10^{-2}$ M Np in 1 M $HClO_4$ and $1.7 \cdot 10^{-2}$ M Np in 1 M $HClO_4$, respectively. The tetravalent oxidation state of Np was verified by NIR absorption spectroscopy (Mod. CARY-5G, Varian) using the absorption band at 960 nm.

Np(IV) complexes were prepared in a glove box under N_2 atmosphere by adding aliquots of the Np(IV) stock solutions to humic acid and Bio-Rex70 suspensions in 0.1 M $HClO_4$. Previously, Bio-Rex70 was equilibrated at pH 1 in 0.1 M $HClO_4$ and the aqueous humic acid suspensions were degassed. The sample suspensions were stirred at constant pH 1.01 ± 0.05 for 48 h. The reaction products were then isolated by centrifugation and subsequently washed with 0.1 M $HClO_4$ to remove uncomplexed Np ions and Np hydrolysis products. The Np loading of the humic substances and of Bio-Rex70 is given in Table 1. The formation of Np(IV) complexes and their stability was confirmed for KFA by NIR absorption spectroscopy. The absorption band at 960 nm, characteristic for the free Np(IV) ion, shifts to about 970 nm due to the formation of Np(IV) fulvate.

For XAFS spectroscopy, the wet pastes of the humic acid (AHA, M42) and Bio-Rex70 samples were placed in Teflon sample holders for pastes that were sealed with Capton tape, whereas the Np(IV)-KFA precipitate (about 1.5 mL) was filled in a polyethylene (PE) vial together with 0.5 mL of the supernatant. All sample holders were double-sealed in PE bags for safety purposes. The Np content, determined by γ-spectroscopy, was between 1 and 3 mg Np per sample.

XAFS measurements and data analysis

XAFS measurements were carried out at the Rossendorf Beamline (ROBL) at the European Synchrotron Radiation Facility in Grenoble, France. Np L_{III}-edge X-ray absorption spectra were collected in transmission mode at room temperature using a Si(111) water-cooled double-crystal monochromator in fixed-exit mode. Four to six XAFS scans were collected from each sample and averaged. The energy scale of the spectra was calibrated using the energy of the first inflection point of the absorption spectrum of an yttrium foil (17 038 eV). The Np L_{III} ionisation threshold, E_0, was defined as 17 630 eV.

The XANES and EXAFS data were extracted from the raw absorption spectra by standard procedures [6] using the suite of programs EXAFSPAK [10]. The scattering code FEFF6 [11] was used to calculate theoretical scattering amplitudes and phase-shift functions for a hypothetical cluster of $Np(H_2O)_8^{4+}$. The EXAFS oscillations were fitted to the EXAFS equation using a one-shell fit with oxygen atoms as backscatterers in the *k*-range between 3.2 and 7.7 $Å^{-1}$. The shift in the threshold energy, ΔE_0, was allowed to vary during initial fitting. During the final fit, the average value calculated for all samples (ΔE_0 = -11.1 eV) was held constant.

Results and discussion

XANES

Representative of all Np(IV) samples, the normalised Np L_{III}-edge XANES spectrum of Np(IV)-AHA is shown in comparison to that of Np(V)-AHA in Figure 1.

Figure 1. Normalised Np L_{III}-edge XANES spectra of Np(IV)-AHA and Np(V)-AHA

Data for Np(V)-AHA are taken from [12]

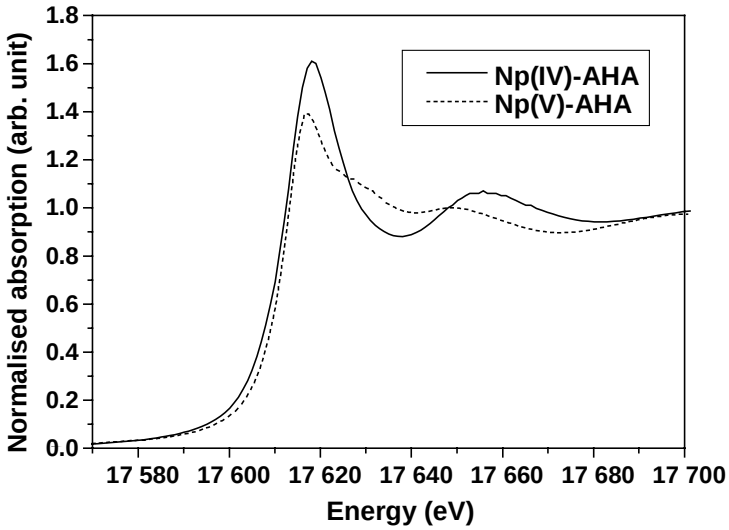

The XANES spectrum of Np(IV)-AHA shows the characteristic near-edge features of tetravalent Np compounds [3,4,13]. First, the "white line" peak in the Np(IV) spectrum is more intense than in the Np(V) spectrum which shows an additional shoulder on the high-energy side of the peak. Second, the edge energy of the Np(IV) sample, determined as the inflection point of the edge, is shifted to slightly lower energy. However, this second feature is less suitable to distinguish between the tetravalent and pentavalent oxidation state of actinides due to the combination of structural and electronic changes as was shown for plutonium by Conradson, *et al.* [14]. Identical spectral features were obtained for the Np(IV) complexes of KFA, M42 and Bio-Rex70. This confirms the stability of the tetravalent oxidation state of Np in all complexes studied within the time of our experiment.

EXAFS

In Figure 2, the Np L_{III}-edge k^3-weighted EXAFS spectra of the Np(IV) complexes with humic substances and Bio-Rex70 and the corresponding Fourier transforms are shown for experimental run 1.

Both the EXAFS oscillations and the Fourier transforms of all Np(IV) complexes are similar. The Fourier transforms indicate a single co-ordination shell (Np-O). The structural parameters of the Np(IV) samples are summarised in Table 2. Data are given both for experimental run 1 and 2.

Within the experimental error, identical structural parameters are determined for all investigated Np(IV) humates. Independent of the type of the humic substances and of their proportion of functional groups (cf. Table 1), the Np(IV) ion is surrounded by about 11 oxygen atoms at a distance of 2.36 Å.

Figure 2. Raw Np L_{III}-edge k^3-weighted EXAFS spectra (a) and corresponding Fourier transforms (b) of Np(IV) complexes with KFA, AHA, M42 and Bio-Rex70

Solid lines – experimental data; dashed lines – theoretical fit of the data

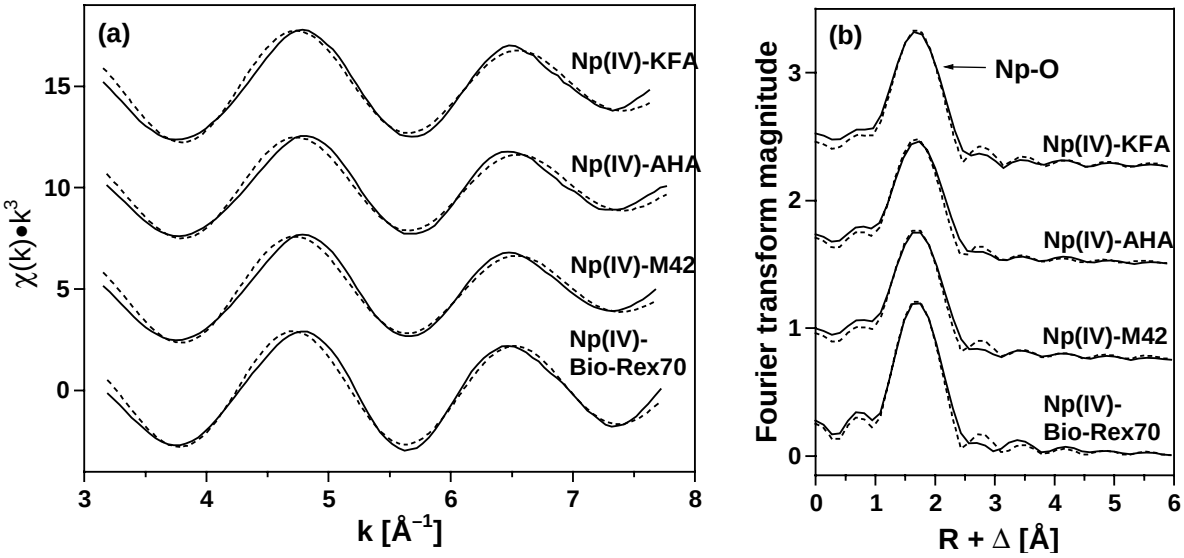

Table 2. EXAFS structural parameters of Np(IV) complexes with humic substances and Bio-Rex70 in comparison to those of Np(IV) in hydrochloric and sulphuric medium

Run	Sample	Shell	N	R [Å]	σ^2 [Å^2]	Ref.
1	Np(IV)-KFA	Np-O	11.3 ± 1.7	2.36 ± 0.01	0.0162	This work
	Np(IV)-AHA	Np-O	10.1 ± 1.7	2.36 ± 0.01	0.0159	This work
	Np(IV)-M42	Np-O	11.0 ± 1.7	2.36 ± 0.01	0.0166	This work
	Np(IV)-Bio-Rex70	Np-O	10.2 ± 1.3	2.37 ± 0.01	0.0127	This work
2	Np(IV)-AHA	Np-O	11.6 ± 2.2	2.35 ± 0.01	0.0178	This work
	Np(IV)-Bio-Rex70	Np-O	10.9 ± 1.8	2.36 ± 0.01	0.0154	This work
	Np(IV) in 1 M HCl	Np-O	11.2 ± 1.1	2.40 ± 0.012	0.0075	[3]
	Np(IV) in 2 M H_2SO_4	Np-O Np-S	11 ± 1 2.2 ± 0.9	2.39 ± 0.01 3.07 ± 0.02	0.0118 0.0070	[4]

N: co-ordination number, R: bond distance, σ^2: Debye-Waller factor.
The 95% confidence limits are given for N and R as estimated by EXAFSPAK.

The structural parameters obtained for Np(IV) humate complexes agree well with those determined for Np(IV)-Bio-Rex70 complexes. Since Bio-Rex70 has no phenolic OH groups but exclusively carboxylic groups as functional groups capable of binding metal ions, it can be concluded that in the humate complexes the carboxylic groups are predominantly responsible for the binding of Np ions at pH 1. This result was expected, since at pH 1 the phenolic OH groups are fully protonated.

Since 1 M H_2SO_4 was used as anolyte during the preparation of the Np(IV) stock solution applied in experimental run 1, it was assumed that this stock solution could possibly contain a sulphate impurity. However, the structural parameters determined in experimental run 1 and 2 are identical (cf. Table 2). Thus, first assumptions that the small Fourier transform peak occurring at about 2.7 Å could be caused by a Np-S shell, as was observed for Np(IV) in 2 M H_2SO_4 by Reich, *et al*. [4], can be excluded.

The co-ordination number, $N_{Np\text{-}O}$ = 11, determined for the humate complexes, agrees well with the values reported for the hydrated Np(IV) ion in hydrochloric [3] or sulphuric [4] medium, meaning that, due to complexation of Np(IV) ions by humic substances, some of the water molecules previously attached to Np ions are replaced by carboxylate groups. Simultaneously, the humate complexation leads to a shortening of the Np-O bond length by about 0.04 Å. This is a significant shortening since 0.04 Å exceeds the statistical fit error given in Table 2 and the conservative error estimate of ±0.02 Å for the absolute bond distance value. A similar shortening of the bond length was observed for U(VI) humate complexes ($R_{U\text{-}Oeq}$ = 2.37-2.39 Å) [15] compared to $UO_2(H_2O)_5^{2+}$ ($R_{U\text{-}Oeq}$ = 2.41 Å) [3] and can be interpreted as further evidence of actinide humate complex formation. The difference in the lengths of the Np-O bonds, formed by carboxylate groups and water molecules, is too small to be distinguishable by XAFS spectroscopy. Thus, the Np-O bond length determined for humate complexes represents an average value over all interactions between Np ions and humic acid functional groups and water molecules, respectively. This is evident in the large Debye-Waller factors. Since it was also not possible to detect carbon atoms of the binding humic acid carboxylate groups, it is not possible to determine separate co-ordination numbers for carboxylate groups and water molecules co-ordinated to Np by EXAFS analysis.

To identify the binding mode (monodentate, bidentate or bridging) of the humic acid carboxylate groups to Np(IV) ions, the bond distances of Np(IV) humate complexes are compared to those reported for Np(IV) carboxylates of known crystal structure. For bridging and chelate forming carboxylate groups in Np(IV) oxalate [16], $Np(C_2O_4)_2 \cdot 6H_2O$, distances of 2.39 Å and 2.51 Å were determined using XRD. For bidentate binding carboxylate groups in Np(IV) formate [17], $Np(HCOO)_4$, a distance of 2.50 Å was calculated from XRD results. Compared to these data, the Np-O bond distance determined for the Np(IV) humates (R = 2.36 Å) is smaller. From this we conclude that the humic acid carboxylate groups are predominantly monodentately bound to Np(IV) ions. This should be verified by future studies with additional Np(IV) model substances.

Summary

For Np(IV) humates structural parameters were determined using EXAFS analysis. The tetravalent oxidation state of Np and its stability in the humate complexes was verified by XANES and NIR absorption spectroscopy. The Np(IV) ion is surrounded by 11 oxygen atoms at a mean distance of 2.36 Å. The carboxylate groups of the humic substances, responsible for binding Np(IV) ions under the experimental conditions applied in this work, are predominantly monodentately co-ordinated to Np(IV) ions.

Acknowledgements

The XAFS measurements were carried out at BM20 at the European Synchrotron Radiation Facility in Grenoble. We thank the Bundesministerium für Wirtschaft und Technologie for financial support (contract no. 02 E 9299). We also thank G. Grambole for γ-spectroscopic measurements.

REFERENCES

[1] G.R. Choppin, P.J. Wong, "The Chemistry of Actinide Behavior in Marine Systems", *Aquatic Geochemistry*, 4, 77 (1998).

[2] P. Zeh, J.I. Kim, C.M. Marquardt, R. Artinger, "The Reduction of Np(V) in Groundwater Rich in Humic Substances", *Radiochim. Acta*, 87, 23 (1999).

[3] P.G. Allen, J.J. Bucher, D.K. Shuh, N.M. Edelstein, T. Reich, "Investigation of Aquo and Chloro Complexes of UO_2^{2+}, NpO_2^{+}, Np^{4+}, and Pu^{3+} by X-ray Absorption Fine Structure Spectroscopy", *Inorg. Chem.*, 36, 4676 (1997).

[4] T. Reich, G. Bernhard, G. Geipel, H. Funke, C. Hennig, A. Roßberg, W. Matz, N. Schell, H. Nitsche, "The Rossendorf Beam Line ROBL – A Dedicated Experimental Station for XAFS Measurements of Actinides", *Radiochim. Acta*, 88, 633 (2000).

[5] C.M. Marquardt, V. Pirlet, J.I. Kim, "Initial Studies on the Complexation of Tetravalent Neptunium with Fulvic Acid", in *FZKA 6524*, G. Buckau, ed., Karlsruhe, 2000, pp. 45-70.

[6] "X-ray Absorption: Principles, Applications, Techniques of EXAFS, SEXAFS and XANES", D.C. Koningsberger, R. Prins, eds., John Wiley & Sons, New York, 1988.

[7] K. Schmeide, H. Zänker, K.H. Heise, H. Nitsche, "Isolation and Characterization of Aquatic Humic Substances from the Bog *Kleiner Kranichsee*", in *FZKA 6124*, G. Buckau, ed., Karlsruhe, 1998, pp. 161-195.

[8] J.I. Kim, G. Buckau, "Characterization of Reference and Site Specific Humic Acids", RCM-Report 02188, TU München, Institute of Radiochemistry, München, 1988.

[9] S. Pompe, A. Brachmann, M. Bubner, G. Geipel, K.H. Heise, G. Bernhard, H. Nitsche, "Determination and Comparison of Uranyl Complexation Constants with Natural and Model Humic Acids", *Radiochim. Acta*, 82, 89 (1998).

[10] G.N. George, I.J. Pickering, "EXAFSPAK: A Suite of Computer Programs for Analysis of X-ray Absorption Spectra", Stanford Synchrotron Radiation Laboratory, Stanford, CA, USA, 1995.

[11] J.J. Rehr, R.C. Albers, S.I. Zabinsky, "High-order Multiple-scattering Calculations of X-ray Absorption Fine Structure", *Phys. Rev. Lett.*, 69, 3397 (1992).

[12] S. Pompe, K. Schmeide, T. Reich, C. Hennig, H. Funke, A. Roßberg, G. Geipel, V. Brendler, K.H. Heise, G. Bernhard, "Neptunium(V) Complexation by Various Humic Acids in Solution Studied by EXAFS and NIR Spectroscopy", these proceedings.

[13] S. Bertram, G. Kaindl, J. Jové, M. Pagès, J. Gal, “Electronic Structure of Actinide Compounds from L_{III}-edge X-ray Absorption”, *Phys. Rev. Lett.*, 63, 2680 (1989).

[14] S.D. Conradson, I.A. Mahamid, D.L. Clark, N.J. Hess, E.A. Hudson, M.P. Neu, P.D. Palmer, W.H. Runde, C.D. Tait, “Oxidation State Determination of Plutonium Aquo Ions Using X-ray Absorption Spectroscopy”, *Polyhedron*, 17, 599 (1998).

[15] M.A. Denecke, S. Pompe, T. Reich, H. Moll, M. Bubner, K.H. Heise, R. Nicolai, H. Nitsche, “Measurements of the Structural Parameters for the Interaction of Uranium(VI) with Natural and Synthetic Humic Acids using EXAFS”, *Radiochim. Acta*, 79, 151 (1997).

[16] M.S. Grigor’ev, I.A. Charushnikova, N.N. Krot, A.I. Yanovskii, Yu.T. Struchkov, “Crystal Structure of Neptunium(IV) Oxalate Hexahydrate $Np(C_2O_4)_2 \cdot 6H_2O$”, *Radiokhimiya*, 39, 419 (1997).

[17] J. Hauck, “The Crystal Structure of $Me(HCOO)_4$, Me = Th, Pa, U, Np”, *Inorg. Nucl. Chem. Lett.*, 12, 617 (1976).

RESONANT MAGNETIC X-RAY SCATTERING FROM *IN SITU* GROWN HOLMIUM-METAL FILMS

C. Schüßler-Langeheine,[1] E. Weschke,[1] R. Meier,[1] A.Yu. Grigoriev,[1] H. Ott,[1] Chandan Mazumdar,[1] D.V. Vyalikh,[1] C. Sutter,[2] D. Abernathy,[2] G. Grübel,[2] G. Kaindl[1]

[1]Institut für Experimentalphysik, Freie Universität Berlin
Arnimallee 14, D-14195 Berlin-Dahlem, Germany

[2]European Synchrotron Radiation Facility
B.P. 220, F-38043 Grenoble Cedex, France

Abstract

Resonant magnetic X-ray scattering (RMXS) experiments at the Ho-L_3 and M_5 thresholds have been performed on thin holmium-metal films grown *in situ* in ultra-high vacuum on W(110). The experimental set-up for these experiments as well as results for the magnetic structure of these films will be described. The magnetic structure stays bulk-like down to a thickness of 14 monolayers.

Introduction

Ultra-thin metal films are currently the subject of intense studies, not only because of their technological relevance but also because their properties are interesting from a fundamental point of view. The electronic structure of thin films can be different from that of bulk samples because the translational symmetry is lifted in one direction leading, e.g. to standing electron waves, which reveal details of the potential in the material [1]. Also, the magnetic properties of thin films can be altered relative to the bulk, e.g. due to shape anisotropy [2], strain [3] and finite-size effects [4]. Thin-film samples are either grown *ex situ*, usually by molecular-beam epitaxy (MBE), and transferred to the measuring chamber or grown *in situ* in the measuring chamber itself. One advantage of the latter procedure is that no protective cap layers are needed to prevent the samples from oxidation during transfer. Furthermore, samples grown *in situ* can be probed by surface-sensitive techniques, like photoelectron spectroscopy (PES) or scanning tunnelling microscopy (STM), giving access to the electronic structure and surface morphology.

A well-suited technique for the study of structural and magnetic properties of thin films is X-ray scattering, probing the electron distribution [5] as well as the spin and angular momentum distribution [6]. The probing depth for hard X-rays is of the order of a few μm, well adapted to the dimensions of thin films. Furthermore, the resonant enhancement of the scattering cross-section at the absorption thresholds can be used to perform element-selective measurements [6-8]. One of the prototype materials for resonant magnetic X-ray scattering (RMXS) is Ho metal [7-9] because the open 4*f* shell in Ho carries the strongest magnetic moment among all elements, and Ho is anti-ferromagnetic over a wide temperature range with the magnetic scattering signal well separated from that of charge scattering. The Ho L_3 resonance at 8 074 eV corresponds to a photon wavelength of 1.54 Å, well suited for structural studies. The helical anti-ferromagnetic structure in Ho consists of ferromagnetically ordered moments in the basal planes of the *hcp* lattice with each plane rotated by a certain angle with respect to the neighbouring plane, thus forming a helix along the crystallographic *c* axis [10]. In this contribution, we report on resonant magnetic X-ray scattering experiments performed on epitaxial Ho-metal films grown *in situ* on W(110) at the Ho L_3 threshold in the hard and the M_5 threshold in the soft X-ray range, where films of thickness of only a few monolayers (ML) can be studied.

Experimental

For the experiments, two different UHV diffractometer set-ups were designed adapted to the hard and soft X-ray regions, respectively. For hard X-rays, a vacuum chamber made from a modified commercial CF100 double-cross was built, small enough to fit onto common diffractometers. For the incoming and outgoing photons, two UHV-compatible Be windows of about 0.5 mm thickness were used. The chamber was pumped by a turbomolecular pump backed by an oil-free turbo/diaphragm pump combination. Together with a Ce sublimation pump and with the closed-cycle He refrigerator for sample cooling in operation, vacuum in the 5×10^{-11} mbar range was readily achieved. For film preparation, the chamber was equipped with a quartz-microbalance thickness monitor and a quadrupole mass spectrometer for residual-gas analysis. The chamber could be mounted in different orientations allowing both horizontal and vertical scattering geometries. The weight of the whole set-up was about 70 kg, but the load on the diffractometer could be further reduced by a counterbalance. The set-up was successfully installed at the ID10A (Troïka 1) beam line of the ESRF, where the hard X-ray data shown in this contribution were recorded, at the HASYLAB W1.1 beam line, and also on a laboratory diffractometer. Since for the soft X-ray range around the lanthanide $M_{4,5}$ thresholds no suitable window material is available, a second set-up was built, where the sample and the detector could be moved inside an UHV chamber that was directly attached to the beam line. Since the limitations concerning size and weight of the set-up do not apply here, a conventional, fully-equipped vacuum

chamber could be used in this case. A silicon-diode detector behind an adjustable rectangular slit was mounted on an arm, which could be rotated in vacuum. The sample was mounted on a second rotational feedthrough with the rotational axes of sample and detector aligned. The necessary mechanical precision was readily achieved in UHV, since at the larger wavelengths in the soft X-ray region, the requirements concerning angular resolution are more relaxed and the diffraction features move to comparably larger angles. The angular resolution was of the order of 0.1°. The soft X-ray data presented here were recorded at the U49/1-SGM beam line of BESSY II.

Both experimental set-ups were equipped with the same sample holder, W(110) substrate crystal, and with identical home-built evaporators. The substrate crystal was held in a Ta frame attached via a sapphire plate to a closed-cycle refrigerator. The sample could be heated by a filament situated at the back side of the substrate crystal either irradiatively or by electron bombardment. This design allowed to cover a temperature range of the sample from 30 K up to ~2 000 K, which is needed to desorb a film from the substrate surface. The temperature was determined by a carefully calibrated $W_{0.95}Re_{0.05}$/ $W_{0.74}/Re_{0.26}$ thermocouple attached in a small hole in the substrate crystal with the thermocouple wires led without interruption to a commercial temperature controller.

Ho metal was evaporated from an evaporation cell that consisted of a doubly-shielded Ta crucible and that was heated by electron bombardment. During evaporation, the pressure rose to about 5×10^{-10} mbar. The growth and annealing process could be monitored *in situ* via the X-ray reflectivity [11,12] as shown in Figure 1 for the case of a 77-Å thick Ho film.

Figure 1. Ho film preparation

The upper curve shows the X-ray reflectivity during the process, the lower curve represents the corresponding sample temperature; see text for details

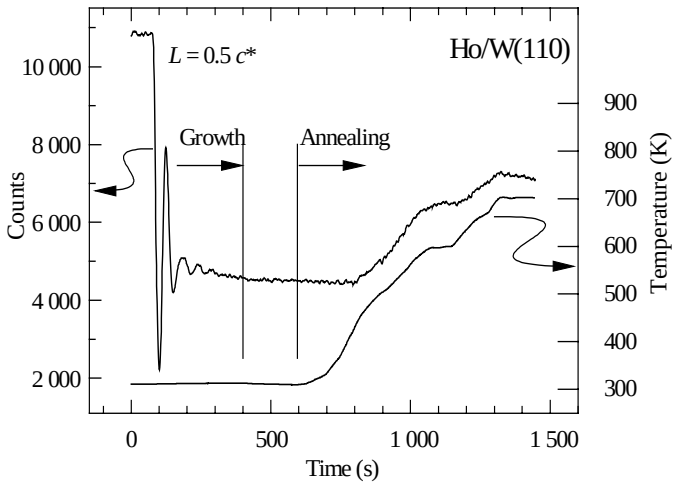

The data were taken in specular geometry at a photon energy of 8 074 eV, with the length of the scattering vector, L, given in units of the Ho reciprocal lattice vector, c^*. In this notation, $L = 2c^*$ corresponds to the Bragg condition for the close-packed planes. The upper curve displays the X-ray reflectivity as a function of time and the lower curve the temperature. The film was grown with the substrate kept at room temperature; the high reflectivity in the beginning stems from the clean W substrate. After the shutter of the evaporator was opened, the reflectivity dropped and damped growth oscillations were observed. For the case of heteroepitaxial growth, one oscillation corresponds to $2c^*/L$ double layers (because in an *hcp*-lattice c refers to the double-layer spacing) [11], i.e. four layers per oscillation in the present case. The damping of the oscillations is caused by an increasing

roughness of the film. Upon annealing, the reflectivity increases indicating a smoothening of the film. At about 710 K, the reflectivity starts to decrease, which is a signature of a re-entrant roughening, probably caused by a breaking of the film and islands formation, as observed for Gd/W(110) at about the same temperature [13]. Because in most cases multiple-scattering is not important for X-rays, the analysis of X-ray scattering data can often be performed within a simple kinematic theory. For the case of growth oscillations of Ho and Yb metal on W(110), details in the shape of the curves could be analysed taking relaxations of the interface layers during the growth of the first film layers into account [12]. Hence, beyond the obvious advantage of monitoring film thickness and annealing processes, *in situ* X-ray scattering allows access to the growth dynamics of the film. Lanthanide metal films grown in this way in UHV are characterised by a mosaic width of the order of 0.04°, i.e. they represent high-quality samples for magnetic structure studies.

Results

RMXS data from a 113-ML Ho film at various temperatures are shown in Figure 2. The charge contribution was suppressed by polarisation analysis using a graphite(006) analyser crystal [9]. The curves are still dominated by the charge-scattering Bragg peak at $L = 2c^*$ leaking through the analyser. The Bragg peak has the broad Laue shape with side oscillations because of the small number of scattering planes [5]. At low temperatures, two satellites caused by the magnetic superstructure are visible on both sides of the Bragg peak, offset by the magnetic modulation wave vector, τ. At 41 K, $\tau = 0.2\ c^*$, which corresponds to a bulk-like ten-layer magnetic period. Like in the bulk, τ is temperature dependent and the decreasing intensity of the satellite upon heating reflects the decaying magnetic order. A detailed analysis of the temperature dependence of τ and the satellite intensity reveals a high similarity to published bulk data, e.g. from Ref. [10] (see [14]). From the width of the magnetic satellite one can conclude that the whole film contributes coherently to the magnetic structure over the whole temperature range (see inset of Figure 2).

Figure 2. RMXS data from a 113-ML Ho/W(110) film at various temperatures

The data are taken at the Ho L_3 resonance with applied polarisation analysis in the $\sigma\pi$ channel. The inset shows the number of lattice planes contributing to the helical structure, N, as determined from the width of the (002-τ) satellite.

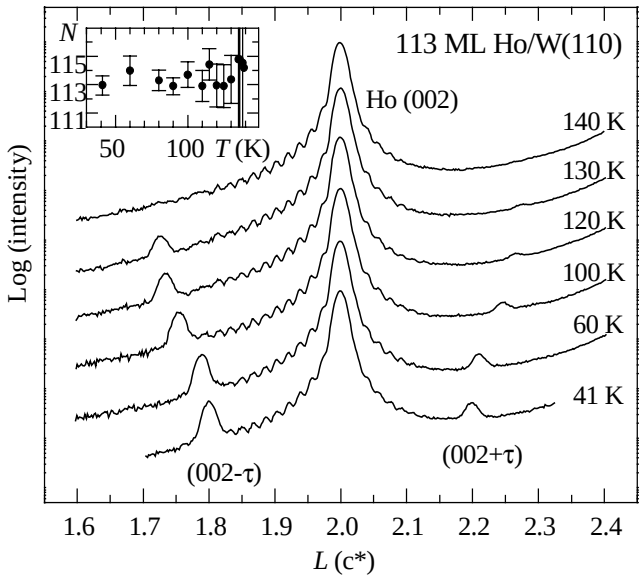

Since an Ho film of 113-ML thickness still behaves bulk-like, it is interesting to look at thinner films. Data from the thinnest film investigated so far using hard X-rays are shown in Figure 3. In the upper panel, the magnetic scattering signal (solid symbols) is plotted together with the charge scattering background (open symbols), which has been recorded with the polarisation analyser turned by 90° ($\sigma\sigma$-channel) [9] normalised to the same Bragg-peak height for both scans. The difference between the two curves, which represents the magnetic contribution, is shown in the lower panel on a linear scale. The magnetic satellite is clearly visible, and the magnetic modulation wave vector is the same as in the bulk. A detailed analysis of the temperature dependence, however, is not possible because of the strong charge-scattering background at the position of the satellite. The signal-to-background ratio will get even worse for thinner films because the satellite intensity is proportional to the squared number of layers whereas the increasing width of the charge-scattering Bragg peak leads to an essentially thickness-independent background height at the satellite position.

Figure 3. Upper panel: RXMS from a 33-ML Ho film in the charge-scattering ($\sigma\sigma$, open symbols) and in the magnetic-scattering ($\sigma\pi$, filled symbols) channel. Lower panel: The difference between the two upper curves on a linear scale.

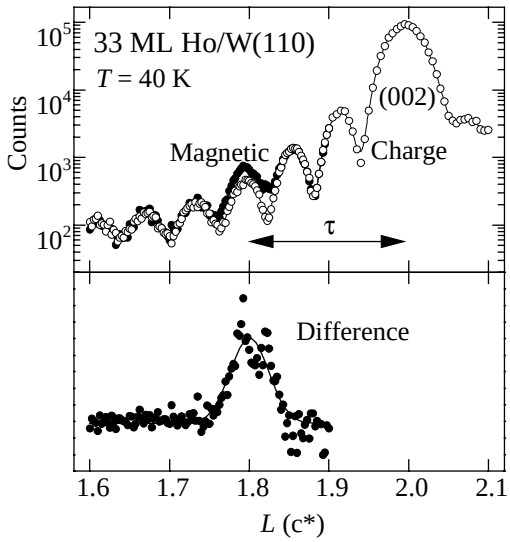

The situation is more favourable in the soft X-ray region. At the Ho M_5 threshold, where dipole excitations involve the shallow 4*f* states, which carry the magnetic moments, the resonant enhancement of the magnetic scattering cross-section is about 6 orders of magnitude [8,15] and thus much higher than the 50-fold enhancement at the L_3 threshold [7]. Even though the photon wavelength of about 9.2 Å at this energy is too large to allow a study of the crystal structure, it is well suited for the more extended magnetic structure of Ho metal. The (000+τ) magnetic satellite can be readily observed. Data taken from a 14-ML thick Ho metal film at the M_5 resonance are presented in Figure 4. The upper panel shows the reflectivity recorded at 40 K in the helical phase and at 180 K, well above the Néel temperature, respectively. The high-temperature data show pronounced oscillations which are caused by the interference between X-rays scattered at the film surface and the film-substrate interface [16]. At low temperatures, additional intensity appears, which represents the magnetic contribution. The corresponding difference is plotted in the lower panel. The magnetic satellite is again clearly visible having the same Laue shape as the Bragg peak. Even though the main maximum cannot be seen in all detail because of total reflection and footprint effects, its position is fully determined by the well-resolved side maxima (Laue oscillations). The value obtained for the satellite position (arrow in Figure 4) is $\tau = (0.2 \pm 0.04)c^*$, which is again the bulk value.

Figure 4. Reflectivity from a 14-ML thick Ho film measured at the M_5 resonance

Upper panel: Data recorded above (open symbols) and below (filled symbols) the Néel temperature. The difference, plotted in the lower panel, is the magnetic contribution, i.e. the (000+ τ) satellite (arrow) with two of the magnetic Laue oscillations visible.

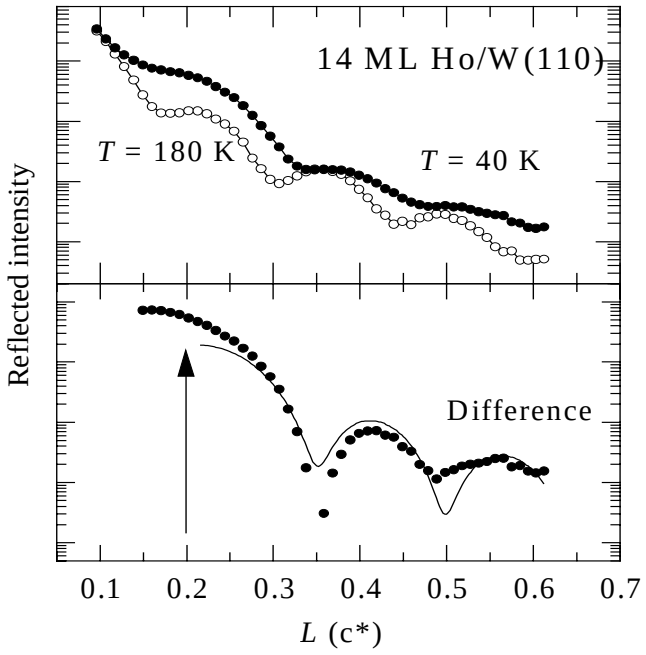

Discussion

Ho-metal films grown on W(110) exhibit a bulk-like magnetic structure down to thicknesses of at least 14 ML. This is quite surprising because the interaction responsible for the anti-ferromagnetic coupling is of long-range character. In a mean-field calculation for a 15-ML slab of Ho metal by Bohr, *et al*., the outermost three layers on each side of the slab are predicted to be ferromagnetically ordered due to their reduced number of neighbours [17]. Such a behaviour, which would lead to a substantial broadening of the magnetic satellite, is not observed in our data. Our method, however, is not sensitive to a ferromagnetic contribution caused by a canting of the moments out of the basal planes by a certain angle, like in the ferromagnetic low-temperature phase of bulk Ho metal.

Interesting results concerning the influence of cap layers and the kind of substrate material on the sample can be inferred from a comparison of the present results for on uncovered 14-ML film with those for a ≈16-ML Ho film sandwiched between two Y layers studied by neutron scattering by Leiner, *et al*. [18]. In contrast to our results, the authors of the neutron-scattering study find the helix period distinctly shorter than in the bulk with the coherence length of the helix almost twice as long as the thickness of the Ho film, probably due to the fact that the helix is continued in the polarisable Y metal layers.

Whereas the investigation of ultra-thin films is not feasible in the hard X-ray region due to the high charge-scattering background, it is quite possible at the M_5 resonance because of the strong resonant enhancement of the magnetic-scattering cross-section at this threshold. Soft X-ray scattering experiments are not only restricted to lanthanide metals. Strong magnetic scattering signals have been observed at the Fe-L_3 [19] and the uranium $M_{4,5}$ thresholds [20,21]. For actinide systems, the

wavelengths at the $M_{4,5}$ resonances are short enough to reach charge-scattering peaks and thus to correlate structural and magnetic properties. The *in situ* preparation method is not only restricted to metal films but has also been successfully applied for the preparation of, e.g. graphite-intercallation compound [22] and alloy films [23].

Summary

The anti-ferromagnetic structure of Ho-metal films grown *in situ* on W(110) has been investigated by resonant magnetic X-ray scattering at the L_3 and M_5 resonances. The much stronger resonant enhancement in the latter case allows to investigate films down to a thickness of only a few monolayers. Films in the thickness range from 14 to 113 ML show a bulk-like magnetic structure, in contrast to theoretical predictions, at least for the thinnest film studied here. From a comparison with the results of a recent neutron-scattering study of a 16-ML thick Ho film sandwiched between Y layers, the strong influence of cap layers and/or of the kind of the substrate materials can be inferred.

Acknowledgements

The authors are indebted to the staff of BESSY II for their co-operation in the preparation and performance of the experiments at the U49/1-SGM. This work was supported by the BMBF, project 05 SF8 KEC8, the DFG, Sfb290/TP A06, and the European Union (EFRE). C.M. acknowledges support from the Alexander von Humboldt foundation.

REFERENCES

[1] J.J. Paggel, T. Miller, T-C. Chiang, *Science*, 283, 1709 (1999).

[2] A. Pang, A. Berger, H. Hopster, *Phys. Rev. B*, 50, 6457 (1994).

[3] M. Hong, R.M. Fleming, J. Kwo, L.F. Schneemeyer, J.V. Waszcak, J.P. Mannaerts, C.F. Majkrzak, D. Gibbs, J. Bohr, *J. Appl. Phys*., 61, 4052 (1987).

[4] M. Farle, K. Baberschke, U. Stetter, A. Aspelmeyer, F. Gerhardter, *Phys. Rev. B*, 47, 11571 (1993).

[5] B.E. Warren, "X-ray Diffraction", Addison-Wesley Publishing Company, Reading (1969).

[6] M. Blume, *J. Appl. Phys*., 57, 3615 (1985).

[7] D. Gibbs, D.R. Harshman, E.D. Isaacs, D.B. McWhan, D. Mills C. Vettier, *Phys. Rev. Lett*., 61, 1241 (1988).

[8] J.P. Hannon, G.T. Trammell, M. Blume, D. Gibbs, *Phys. Rev. Lett*., 61, 1245 (1988).

[9] D. Gibbs, M. Blume, D.R. Harshman, D.B. McWhan, *Rev. Sci. Instrum*., 60, 2990 (1994).

[10] G. Helgesen, J.P. Hill, T.R. Thurston, D. Gibbs, J. Kwo, M. Hong, *Phys. Rev. B.*, 50, 2990 (1994).

[11] E. Weschke, C. Schüßler-Langeheine, R. Meier, G. Kaindl, C. Sutter, D. Abernathy, G. Grübel, *Phys. Rev. Lett*., 79, 3954 (1997).

[12] E. Weschke, C. Schüßler-Langeheine, R. Meier, G. Kaindl, C. Sutter, G. Grübel in *Advances in Solid State Physics*, B. Kramer, ed., p. 541, Vieweg Braunschweig (1999).

[13] A. Aspelmeier, F. Gerhardter, K. Baberschke, *J. Magn. Magn. Mater*., 132, 22 (1994).

[14] C. Schüßler-Langeheine, E. Weschke, A.Yu. Grigoriev, H. Ott, R. Meier, D.V. Vyalikh, C. Mazumdar, C. Sutter, D. Abernathy, G. Grübel, G. Kaindl, *J. Electron. Spectrosc. Relat. Phenom*. (in print 2000).

[15] E. Weschke, A.Yu Grigoriev, C. Schüßler-Langeheine, R. Meier, G. Kaindl, in preparation.

[16] L.G. Parratt, *Phys. Rev*., 95, 359 (1954).

[17] J. Bohr, D. Gibbs, J.D. Axe, D.E. Moncton, K.L. D'Amico, D.F. Majkrzak, J. Kwo, M. Hong, C.L. Chien, J. Jensen, *Physica B*, 159, 93 (1989).

[18] V. Leiner, D. Labergerie, R. Siebrecht, C. Sutter, H. Zabel, *Physica B*, 283, 167 (2000).

[19] H.A. Dürr, E. Dudzik, S.S. Dhesi, J.B. Goedkoop, G. van der Laan, M. Belakhovsky, C. Mocuta, A. Marty, Y. Samson, *Science*, 284, 2166 (1999).

[20] E.D. Isaacs, D.B. McWhan, C. Peters, G.E. Ice, D.P. Siddons, J.B. Hastings, C. Vettier, O. Vogt, *Phys. Rev. Lett*., 62, 1671 (1989).

[21] G.M. Watson, D. Gibbs, G.H. Lander, B.D. Gaulin, L.E. Berman, Hj. Matzke, W. Ellis, *Phys. Rev. B*, 61, 8966 (2000).

[22] S. Danzenbächer, S.L. Molodtsov, J. Boysen, Th. Gantz, C. Laubschat, A.M. Shikin, S.A. Gorovikov, M. Richter, *Physica B*, 259-261, 1153 (1999).

[23] W. Schneider, S.L. Molodtsov, M. Richter, Th. Gantz, P. Engelmann, C. Laubschat, *Phys. Rev. B*, 57, 14930 (1998).

TECHNETIUM SPECIATION IN RADIOACTIVE WASTES GENERATED IN PYROCHEMICAL REPROCESSING

M. Simonoff,[1] **K. Guerman,**[1,2] **T. Reich,**[3] **C. Hennig,**[3]
R. Ortega,[1] **C. Sergeant,**[1] **G. Deves,**[1] **M-H. Vesvres**[1]
[1]UMR 5084/CNRS – Université Bordeaux – 1, Le Haut Vigneau, Gradignan, France
[2]Institute of Physical Chemistry, R.A.S., 31 Leninsky pr, 117915 Moscow, RF
[3]Forschungszentrum Rossendorf, Institute of Radiochemistry, Dresden, Germany

Abstract

Pyrometallurgy of uranium and plutonium in chloride and fluoride molten salts is now intensively studied while little attention is given to the long-lived fission product technetium, which is one of the most hazardous nuclear wastes. Regarding the study of the speciation of technetium-99 in the course of pyrochemical reprocessing of spent nuclear fuel, now considered the most probable alternative approach to reprocessing of spent MOX and high burn-up nuclear fuel, EXAFS measurements were performed at the Rossendorf Beamline (ROBL) on the samples simulating radioactive wastes generated by pyrochemical reprocessing, prepared at UMR5084. During pyrometallurgical spent fuel reprocessing, technetium can remain in the fused salt or enter (depending on the applied temperatures, reagents and oxidative or reducing potentials) either the sedimented phase, contaminating Pu-enriched phase or the electrodeposited U phase. The Tc phase could not be detected by means of X-ray diffraction either in the sediment or in the deposit. The Tc phase is finely dispersed and X-ray amorphous. There are some data showing that technetium in such matrix forms not only a hexagonal but also a metastable cubic lattice with higher chemical reactivity. Therefore, it is very important to develop methods of analyses like EXAFS that allow to determine the Tc speciation in such samples. Our results show that under conditions when chlorine or oxygen could be formed or injected into the melt, Tc can also form several oxides, oxychlorides and chlorides of different but rather high volatility, turning on an important polluting risk linked to gas-off. The available EXAF spectra of technetium species are fragmentary and do not present the whole of the species possible under pyrometallurgy conditions. Some recent studies gave indications on the presence of unknown Tc chloride complexes. It was of high importance to carry out synthetic work to supply a large set of technetium compounds in the closed containers which met the security and quality demands, radioactivity level, special requirements on sample size, thickness and sample homogeneity for EXAFS measurements. Based on this set of reference samples, which include technetium metal, different techentium halogenides, oxohalogenides, oxides and pyrometallurgically-formed sediments, Tc chemical forms responsible for Tc accumulation in fused salts, deposits or gas-off depending on if the applied reprocessing conditions are studied by means of XANES and EXAFS. The EXAFS data obtained for technetium hexahalides are in good agreement with literature. For lower oxidation states of technetium including oxides, chlorides and metal state, further EXAFS study both of reference compounds and of simulated radioactive wastes is necessary.

THE STUDY OF IONIC COMPOSITION OF THE "HOT PARTICLES" CONTAINING U, Cs AND Sr ON THE BASIS OF PARAMETERS OF THE XPS SPECTRA FROM THE OUTER U5f AND THE INNER U4f, Cs3d, 4d, Sr3d ELECTRONS

Yu.A. Teterin,[1] V.I. Nefedov,[2] A.S. Nikitin,[1] C. Ronneau,[3] J. Vanbegin,[3] J. Cara,[3] A.P. Dementiev,[1] I.O. Utkin,[1] A.Yu. Teterin,[1] K.E. Ivanov,[1] V.G. Yarzhemsky[2]

[1]Russian Research Centre "Kurchatov Institute"
Moscow, Russia
[2]Kurnakov Institute of General and Inorganic Chemistry of RAS
Moscow, Russia
[3]University Catholique de Louvan
Louvain-la-Neuve, Belgium

Abstract

Elemental and ionic quantitative analysis of reactor fuel (UO_2) containing 0.1 wt.% of Cs and 0.5 wt.% of Sr relative to U was carried out using X-ray photoelectron spectroscopy (XPS). The "hot" particles formed during the heating of the fuel at 2 300°C and extra-heated at 900°C in air and argon atmosphere, condensed on aluminium substrates, were analysed. U and Cs were shown to sublime primarily in the first 20 seconds of heating. In the next 360 seconds U, Cs and Sr sublimed. Thus, the "hot" particles collected during the first 20 seconds and then extra-heated at 900°C in air flux were found to contain 68% of U and 32% of Cs, while those collected during the next 360 seconds and extra-heated at 900°C in air flux contained 51% of U, 13% of Cs and 36% of Sr. Formation of uranyl compounds such as UO_2CO_3, Cs_2UO_4, $Cs_4UO_2(CO_3)_3$, $CsUO_2(OH)_3$, $SrUO_4$, Sr_3UO_6, $SrUO_2CO_3(OH)_2$ in the "hot" particles was suggested.

Introduction

Contamination of environment with "hot" particles containing ^{234}U, ^{235}U, ^{238}U, ^{137}Cs, ^{90}Sr, $^{238\text{-}241}Pu$, ^{241}Am and other radionuclides is known to be one of the worst NPP accident consequences. For the liquidation of such consequences, it is necessary to obtain information on the physical and chemical states of radionuclides in the "hot" particles. That is why the study of the formation of "hot" particles under laboratory conditions is important [1,2]. X-ray photoelectron spectroscopy (XPS) proved to be the most suitable method for determination of elemental and ionic composition of the "hot" particles, the functional groups around the metal ions in them and the structure of their local environment [3,4]. In the present work, the simulation of the processes during a NPP accident was performed. XPS study of the "hot" particles formed due to the heating of the reactor fuel at 2 300°C condensed on aluminium foil during different stages of emission was carried out.

Experimental

The laboratory generator for preparation of the "hot" microparticles from fuel UO_2, containing Sr and Cs was made of a modified graphite oven [1]. The fuel was heated in the graphite oven at 2 300°C in argon atmosphere. The microparticles formed during heating in the oven were moved with argon flow to the quartz oven and heated again at 900°C in argon or air atmosphere. After formation, the "hot" particles were collected in the cascade seven-stage collector (impactor) at the exit of the quartz oven. The sublimation of the fuel and formation of the "hot" particles lasted for 380 seconds, and 10-15 seconds at 900°C in argon or air atmosphere. The fuel tablets were prepared as follows. Water solutions of $Sr(NO_3)_2$, $CsNO_3$ and $UO_2(NO_3)_2 \times 6H_2O$ were mixed and the solution was put into the quartz oven. The water was vaporised at 120°C in the H_2 flow. The temperature was then increased in order to decompose nitrates and was maintained at 600°C to complete the transition of U(VI) ions into U(IV). As a result, the fuel powders (UO_{2+x}) containing 0.1 wt.% of Cs and 0.5 wt.% of Sr relative to U were obtained. These powders were pressed at 5.1 tonne/m^2 as 1 or 2 mm thick tablets of 5 mm diameter. In the present work the XPS study of the initial fuel and the "hot" particles formed due to the heating of the model fuel at 2 300°C within the first 20 and the next 360 seconds and kept at 900°C for 10-15 seconds in air or argon atmosphere was performed for the following samples:

- *Sample I-1*. Initial fuel containing 0.1 wt.% of Cs and 0.5 wt.% of Sr relative to U (98.5 at.% of U, 0.2 at.% of Cs and 1.3 at.% of Sr).

- *Sample I-2*. Sample I-1, whose surface was cleaned with Ar^+ for 20 seconds.

- *Samples II-1 and III-1*. "Hot" particles formed within the first 20 seconds of heating of different fuel tablets and kept in air atmosphere at 900°C for10-15 seconds.

- *Samples II-2 and III-2*. Samples II-1 and III-1 whose surface was cleaned with Ar^+ for 5 and 20 seconds, respectively.

- *Samples IV-1 and V-1*. "Hot" particles formed within the next 360 seconds of heating of the fuel tablets right after formation of Samples II-1 and III-1, respectively, and kept in air atmosphere at 900°C for 10-15 seconds.

- *Samples IV-2 and V-2*. Samples IV-1 and V-1 whose surfaces were cleaned with Ar^+ for 20 seconds.

- *Samples VI and VII-1*. "Hot" particles formed within the first 20 seconds of heating of different fuel tablets and kept in argon atmosphere at 900°C for 10-15 seconds.

- *Samples VII-2, VII-3, VII-4, VII-5*. Sample VII-1 whose surface was cleaned with Ar^+ for 20, 60, 120 and 180 seconds respectively.

- Sample VIII. "Hot" particles formed within the next 360 seconds of heating of the fuel tablet right after formation of Sample VII-1 and kept in argon atmosphere at 900°C for 10-15 seconds.

XPS spectra of the studied compounds were taken with a HP-5950A spectrometer using monochromatised Al $K_{\alpha 1,2}$ ($h\nu$ = 1 486.6 eV) X-rays and with a MK II VG Scientific spectrometer under ~1.3×10^{-7} Pa at room temperature. Overall resolution measured as the $Au4f_{7/2}$ electron line full width half maximum (FWHM) was 0.8 eV (HP 5950A) and 1.2 eV (MK II VG Scientific). Electron binding energies are given relative to the E_b of the C1s electrons from adventitious hydrocarbons at the sample surface defined as 285.0 eV. On the gold substrate E_b(C1s) = 284.7 eV, E_b(Au4f) = 83.8 eV. The measurement errors of line positions and widths were ±0.1 eV, whereas relative line intensity errors were about 10%. The samples were studied as ultra-dispersed powders that were ground in an agate mortar to form thick powder layers pressed into indium on titanium substrates (Samples I, IX-XII), or as "hot" particles collected on aluminium foil (Samples II–VIII). An argonion gun (U = 8 KV, I = 8 μA) was used to clean sample surfaces. Quantitative elemental and ionic analysis was done using the following equation: $n_i/n_j = (S_i/S_j)(k_j/k_i)$ where n_i/n_j is the relative concentration of the studied atoms, S_i/S_j is the relative electron line intensity (area) of the corresponding atomic shells and k_j/k_i is the experimental relative sensitivity coefficient. In this work sensitivity coefficients relative to carbon were 1.00 (C1s), 2.8 (O1s), 7.8 (Cs4d), 18.2 ($Cs3d_{5/2}$), 5.9 ($Sr3d_{5/2}$), 3.7 ($Sr3p_{3/2}$) and 18.4 ($U4f_{7/2}$).

Results and discussion

The technique of determination of physical and chemical states of radionuclides in the environment is based on both traditional spectral parameters (binding energies of inner electrons and line intensities) and fine spectral structure parameters of the inner and outer (valence) levels (intensity of the An5f electrons, inner valence molecular orbitals (IVMO) binding energies, multiplet splitting of the inner electron lines, parameters of the fine spectral structure due to the dynamic effects and the relative position of shake-up satellites [3,4]). Such spectral data allow information on the physical and chemical states of radionuclides in the samples to be obtained [5].

XPS spectral region of the low binding energy electrons

The structure of the low energy XPS spectral region showed that the studied samples contained uranium both in the form of UO_x, ($2 \le x \le 3$) and in the form of uranyl compounds such as UO_2CO_3, $SrUO_4$, Sr_3UO_6, $SrUO_2CO_3(OH)_2$, Cs_2UO_4, $CsUO_2(OH)_3$ and $Cs_4UO_2(CO_3)_3$. The low binding energy spectrum exhibits the U5f, Cs5p and Sr4p lines, as well as the structures due to the outer and inner valence molecular orbitals (OVMO, IVMO). On the basis of the dependence of the U5f relative intensity on the oxygen coefficient [3,12] the uranium ionic composition can be determined. It can be determined based on the approximation that UO_x contains U(IV), U(V) and U(VI) ions. The term U(V) means some spectral state observed as an extra component in the $U4f_{7/2,5/2}$ spectra located between the $U4f_{7/2,5/2}$ lines of U(IV) and U(VI) ions [3,12]. For instance, the U5f electron line relative intensity

found as the ratio of the U5f to $U4f_{7/2}$ areas for the "hot" particles (Sample VIII) was found to be 0.014. On the basis of the experimental dependence [3,12], a complex oxide with the general formula $UO_{2.29}$ contained 2% of U(IV), 69% of U(V) and 29% of U(VI) was found to form on the surface. Although such approximation is not precise because the samples contained caesium and strontium besides uranium, it was still possible to estimate the oxygen coefficient x. In the present work the results were considered in the approximation that the samples contained only U(IV) and U(VI) ions. In this case half of U(V) ions must be attributed to U(IV) and the other half to U(VI), since a U(V) ion contains only one U5f electron. Using such an approximation, the formal decomposition of the U4f line was calculated. This was the result for Sample VIII – 40% of U(IV) and 60% of U(VI), which agreed with the data obtained on the basis of the U5f spectral parameters (Table 1). Unfortunately, reliable spectra of the low binding energy electrons were measured only from Samples II-1, II-2, VII-1 and VIII. For the rest of the samples uranium ionic composition was determined solely on the basis of the U4f spectral parameters. So the accuracy of the ionic composition determination for Samples III-1, III-2, IV-2 and V-1 was much less than for other samples (Table 1).

Such analysis of the uranium ionic composition for the samples containing caesium and strontium is well based since the line of the U5f electrons does not overlap with the Cs6s and the Sr5s line from caesium and strontium oxide, hydroxide or carbonate and the U5f relative photoemission cross-section per shell (0.784) is higher than that for the Cs6s (0.0059) and the Sr5s (0.0026) shells [7]. Therefore, taking into account that the U5f electron binding energy is 1.9 eV (Sample II-2), those of the Sr5s electrons are 3.3 eV (SrO) and 5.4 eV ($SrCO_3$) [11] and the Cs6s line lies in the same spectral region. Even at comparable concentrations of U, Cs and Sr, the U5f line must be much more intense than the Sr5s and Cs 6s lines.

It should be noted that presence of different uranium oxides in the studied sample complicates the IVMO spectral structure in the binding energy range 15-50 eV (Figure 1). On the basis of the IVMO structure parameters for uranyl compounds, interatomic distances in axial and equatorial direction can be determined [3-6]. Unfortunately, in the case of the "hot" particles the IVMO spectral structure due to the U6p electrons overlaps with the Cs5p and the Sr4p lines (see Figure 1). Indeed, the $Cs5p_{3/2}$ binding energy is 12.9 eV (Cs), the $Sr4p_{3/2}$ binding energy is 18.2 eV (Sr), 18.6 eV (SrO) and 19.5 eV ($SrCO_3$) [11], the $U6p_{3/2}$ binding energy is 18.6 eV(UO_2), 15.7 and 19.4 eV (γ-UO_3) [3], photoemission cross-sections per a shell are: 0.278 ($Cs5p_{3/2}$), 0.504 ($Sr4p_{3/2}$) and 0.094 ($U6p_{3/2}$) [7]. This complicated the interpretation of such structure for the studied samples.

XPS spectra of the U4f electrons

The most intense line in uranium spectra is U4f. This spectrum consists of a spin-orbit doublet with the splitting ΔE_{SO} = 10.8 eV [3,4]. Shake-up satellites are observed in this spectrum on the higher binding energy side. The structures of such satellites are different for different uranium oxides. Thus, in the U4f spectrum from $UO_{2.06}$, the most intense (~15%) shake-up satellite is located at 7.0 eV from the basic line, while that in the spectrum of γ-UO_3 is at 3.8 eV from the basic line (Table 1, [3,4]). The basic U4f lines of the studied samples are complicated and can be decomposed into lines corresponding to U(IV), U(V), U(VI). However, this requires analysis of the core and VMO spectral fine structure. Unfortunately, for complex oxides this is very difficult in practice. Therefore, in this work the U4f spectrum was assumed to consist of the lines corresponding to U(IV) and U(VI) ions. On the basis of the areas of these lines, the percent ionic composition was calculated (Table 1). In this approximation, the U4f spectrum from the "hot" particles containing uranium, caesium and strontium was decomposed into two spectra – one of UO_2 and the other of γ-UO_3. For example, the surface of Sample VII-1 was found to consist of 38 at.% of U(IV) and 62 at.% of U(VI) (Figure 2, Table 1).

Table 1. Binding energies (eV), ionic and elemental compositions (at.%) of I-VIII

No. of sample	E_b U4f$_{7/2}$, eV	Oxidation state U(N)	Ionic composition U(N) at.%	E_bSr3d$_{5/2}$ eV	Oxidation state Sr(N)	Ionic composition Sr(N) at.%	E_bCs4d$_{5/2}$ eV	E_bCs3d$_{5/2}$ eV	Elemental composition, at.%
I-1	380.3 382.6 386.7	U(IV) U(VI) Sat.	80 20	132.6 133.7	SrO $SrCO_3$	33 67	–	–	98(U) >0.5(Cs) ~2(Sr)
I-2	380.4 382.6 386.9	U(IV) U(VI) Sat.	93 7	132.8 133.8	SrO $SrCO_3$	61 39	–	–	98(U) >0.5(Cs) ~2(Sr)
II-1	380.6 381.7 386.0 387.8	U(IV) U(VI) Sat. 1 Sat. 2	25 75	–	SrO $SrCO_3$	–	75.2	724.3	68(U) 32(Cs) >0.5(Sr)
II-2	380.3 381.5	U(IV) U(VI)	48 52	–	SrO $SrCO_3$	–	75.3	724.3	67(U) 33(Cs) >0.5(Sr)
III-1	380.5 381.7 386.2	U(IV) U(VI) Sat.	~20 ~80	–	SrO $SrCO_3$	–	75.4	724.5	58(U) 42(Cs) >0.5(Sr)
III-2	380.4 381.5	U(IV) U(VI)	~85 ~15	–	SrO $SrCO_3$	–	75.2	724.3	70(U) 30(Cs) >0.5(Sr)
IV-1	380.7 381.7 385.4 387.5	U(IV) U(VI) Sat. 1 Sat. 2	70 30	132.3 133.4	SrO $SrCO_3$	47 53	75.2	724.3	51(U) 13(Cs) 36(Sr)
IV-2	380.6 381.8	U(IV) U(VI)	~80 ~20	132.4 133.6	SrO $SrCO_3$	35 65	75.4	724.5	52(U) 12(Cs) 36(Sr)
V-1	380.6 381.9 385.8	U(IV) U(VI) Sat.	~25 ~75	132.4 133.7	SrO $SrCO_3$	30 70	75.4	724.5	61(U) 9(Cs) 30(Sr)
V-2	380.4 381.8	U(IV) U(VI)	52 48	132.4 133.7	SrO $SrCO_3$	60 40	75.2	724.3	62(U) 8(Cs) 30(Sr)
VI	380.7 381.6 386.6	U(IV) U(VI) Sat.	70 30	–	SrO $SrCO_3$	–	75.4	724.5	78(U) 22(Cs) >0.5(Sr)
VII-1	380.3 381.5	U(IV) U(VI)	38 62	–	SrO $SrCO_3$	–	-	724.6	68(U) 32(Cs) >0.5(Sr)
VII-2	380.4 381.9 386.9	U(IV) U(VI) Sat.	79 21	–	SrO $SrCO_3$	–	75.3	724.4	88(U) 12(Cs) >0.5(Sr)
VII-3	379.4 380.7 382.4 387.4	U(III) U(IV) U(VI) Sat.	10 76 14	–	SrO $SrCO_3$	–	75.3	724.3	88(U) 12(Cs) >0.5(Sr)
VII-4	379.3 380.8 382.4 387.4	U(III) U(IV) U(VI) Sat.	19 72 9	–	SrO $SrCO_3$	–	75.3	724.4	94(U) 6(Cs) >0.5(Sr)
VII-5	379.2 380.9 382.4 387.8	U(III) U(IV) U(VI) Sat.	18 73 9	–	SrO $SrCO_3$	–	–	724.5	97(U) 3(Cs) >0.5(Sr)
VIII	380.8 382.0	U(IV) U(VI)	40 60	132.4 133.7	SrO $SrCO_3$	42 58	75.3	724.4	62(U) 21(Cs) 17(Sr)
IX $UO_{2.06}$ [3]	380.9 387.9	U(IV) Sat.	84 16						100(U)
X γ-UO_3 [3]	382.4 386.2	U(VI) Sat.	85 15						100(U)
XI SrO [11]				132.4	SrO				100(Sr)
XII $SrCO_3$ [11]				133.4	$SrCO_3$				100(Sr)

Figure 1. XPS spectrum of the low binding energy electrons from the "hot" particles (Sample VIII) collected with the MK II VG Scientific Spectrometer

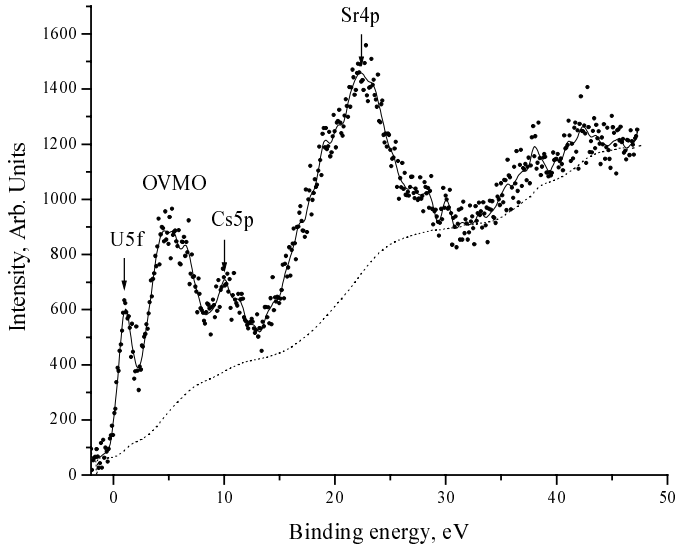

Figure 2. XPS spectrum of the U4f electrons from the "hot" particles (Sample VII-1). Spectrometer MK II VG Scientific.

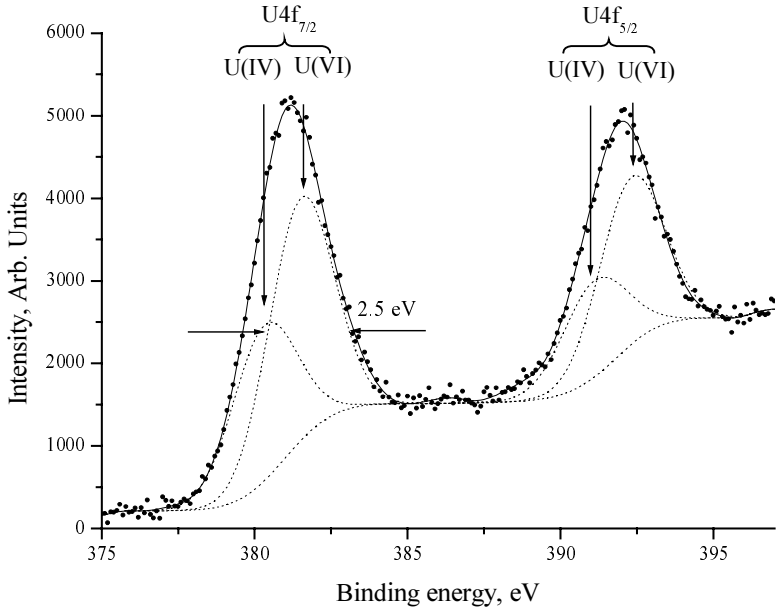

It is known [8] that going from γ-UO_3 to, for example, $CaUO_2O_2$, the U4f binding energy decreases from 382.4 eV to 381.6 eV. Going from the nuclear fuel (Sample I) to the "hot" particles (Samples II-VIII), the decrease of the U4f (U(VI) ion) binding energy to 381.8 eV (Table 1) was observed. Apparently, uranyl gets included in the anionic part of compounds like $Cs^{1+}[(UO_2^{2+})O^{2-}(OH^-)]^{1-}$ or $Cs_2^{1+}[(UO_2^{2+})(CO_3^{2-})\ (OH^-)_2]^{2-}$, $Sr^{2+}[(UO_2^{2+})(O^{2-})_2]^{2-}$ or $Sr^{2+}[(UO_2^{2+})CO_3^{2-}(OH^-)_2]^{2-}$. As a result, extra electronic density on uranium ions causes a significant (0.8 eV) decrease of the binding energy. This

phenomenon was for the first time was studied in Ref. [9]. High concentrations of Sr and Cs also make the formation of such uranyl compounds possible. After 5-20 second Ar^+ cleaning of the surface of the studied samples (fuel and the "hot" particles), the concentration ratio U(IV)/U(VI) increased significantly (Table 1). After longer cleaning (60 seconds and more) an extra component at E_b = <379.3> (Samples VII-3, VII-4, VII-5) appeared in the U4f spectra. Taking into account an empirical rule [10] that when the oxidation state changes by 1, the corresponding binding energy must change by ~1 eV, this extra component was attributed to uranium ions formally referred to as ~U(III). However, during the ion cleaning complex structures attributed to oxygen-insufficient U(IV) forms to unequal sample charging could arise. That could cause the U4f line of the U(IV) ion to widen. This widening and possible presence of oxygen-insufficient structures in this work was described by introducing a new spectral component formally referred to as U(III). Dependence of the U(III), U(IV) and U(VI) concentrations on the surface of the "hot" particles (Sample VII) upon Ar^+ cleaning time was built (Figure 3). This dependence shows that significant changes in the ionic compositions of U took place only in the first 60 seconds of Ar^+ cleaning. After 60 seconds these concentrations remained practically constant. This must be explained by establishment of phase equilibrium on the surface.

Figure 3. Dependence of the relative concentration $n_i = N_i/N_U$ of uranium ions of different oxidation states on the surface of the "hot" particles (Sample VIII) on the Ar^+ cleaning time t

N_i – concentration of U ions of oxidation state I, N_U – concentration of U atoms
○ – U(VI) ions, ● – U(III) ions, ■ – U(IV) ions, □ – U atoms

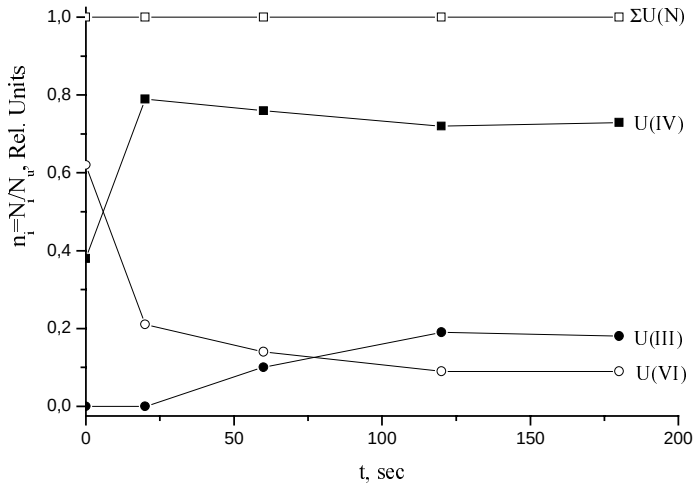

XPS spectra of caesium

Caesium participates actively in chemical reactions in the environment and forms oxides, hydroxides, carbonates etc. This complicates the spectral identification of the reaction products. The XPS spectra of Cs, as well as those of all alkaline metals, exhibit a slight chemical shift while Cs has only oxidation state Cs(I). This further complicates the spectral identification of the reaction products [10].

The most intense Cs lines in XPS spectra from the studied materials (Samples II-VIII) were the Cs3d ($E_b(Cs3d_{5/2})$ = <724.4> eV) and the Cs4d ($E_b(Cs4d_{5/2})$ = <75.3> eV) (Table 1, Figure 4). For the studied samples these lines were always observed as single (Figure 4). The $Cs3d_{3/2}$ line overlaps with the $U4d_{5/2}$ line. Therefore, the narrowest $Cs4d_{5/2,3/2}$ lines as well as the $Cs3d_{5/2}$ one were used in

Figure 4. XPS spectrum of the Cs4d electrons from the "hot" particles (Sample III-1). Obtained with the MK II VG Scientific Spectrometer.

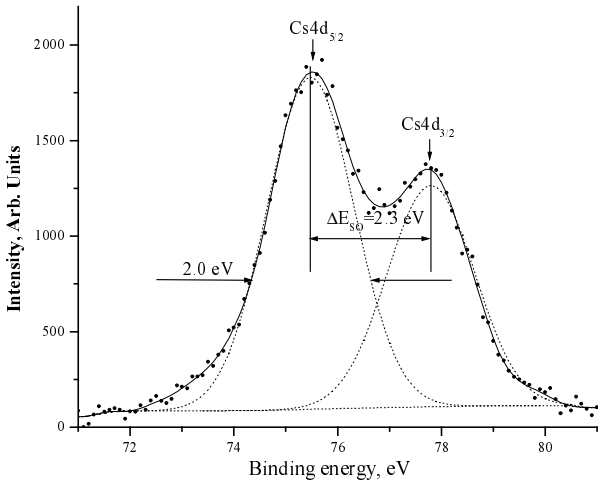

determination of the elemental composition of the studied samples. In particular, the relative concentration of Cs ions was noticed to decrease after Ar^+ cleaning, and the longer the cleaning, the less Cs relative concentration on the surface. This effect was especially noticeable during Ar^+ cleaning of Sample VII (Figure 5). Apparently it can be explained by weak binding of Cs^+ ions in the studied compounds.

Figure 5. Dependence of the relative concentration $n_i = N_i/N_U$ of atoms of observed elements on the surface of the "hot" particles (Sample VII) on the Ar^+ cleaning time t

N_i – concentration of element I, N_U – concentration of U atoms
▲ – $(CO_3)^{2-}$ groups, ● – Cs atoms, ■ – U atoms, ○ – O atoms, □ – C atoms

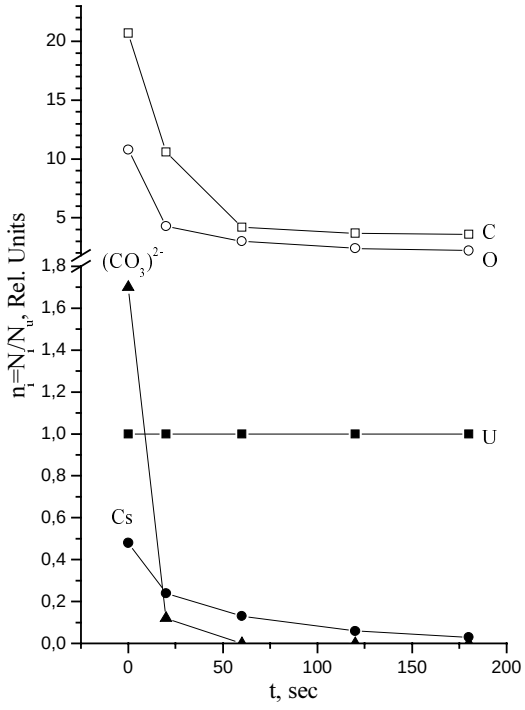

XPS spectra of strontium

The valence electronic configuration of strontium is $4s^2 4p^6 5s^2$. Strontium effectively reacts with the environment and forms oxides, hydroxides and carbonates, which complicates the spectral identification of its reaction products. However, the XPS study of strontium, strontium oxide and carbonate was done in Ref. [11]. It was shown that the surface of metallic strontium could contain oxide, hydroxide and carbonate: Sr (18.2, 131.9 and 267.7 eV), SrO (18.6, 132.4 and 268.1 eV) and $SrCO_3$ (19.5, 133.4, 269.0 eV and 289.5 eV for the C1s of CO_3^{2-} group), where the binding energies of the Sr4p, $Sr3d_{5/2}$ $Sr3p_{3/2}$ electrons are given in parentheses, respectively.

In the XPS spectra of the studied compounds (Samples I-VI), the most intense were the Sr3p and Sr3d lines. For the studied samples the $Sr3d_{5/2,3/2}$ lines (spin-orbit splitting ΔE_{so} = 1.8 eV [11]) were observed structured (Figure 6). It indicated the presence of Sr ions with different oxidation states. In the region of the Sr3p line, the lines of the C1s electrons from both surface contamination hydrocarbons and carbonate groups were observed. Since the Sr3d lines were found to be the narrowest, they were used for the quantitative ionic analysis. For example, the Sr3d spectrum of the "hot" particles (Sample VIII, Figure 6) after heating, besides a doublet attributed to strontium oxide ($E_bSr3d_{5/2}$ = 132.6 eV), exhibited an extra doublet which was attributed to strontium carbonate ($E_bSr3d_{5/2}$ = 133.3 eV). Thus, the surface concentrations of Sr(II) from oxide and carbonate were 40 at.% and 60 at.% respectively. These data agreed with previous XPS data on strontium oxide and carbonate [11].

Figure 6. XPS spectrum of the Sr3d electrons from the "hot" particles (Sample VIII). Collected from the MK II VG Scientific Spectrometer.

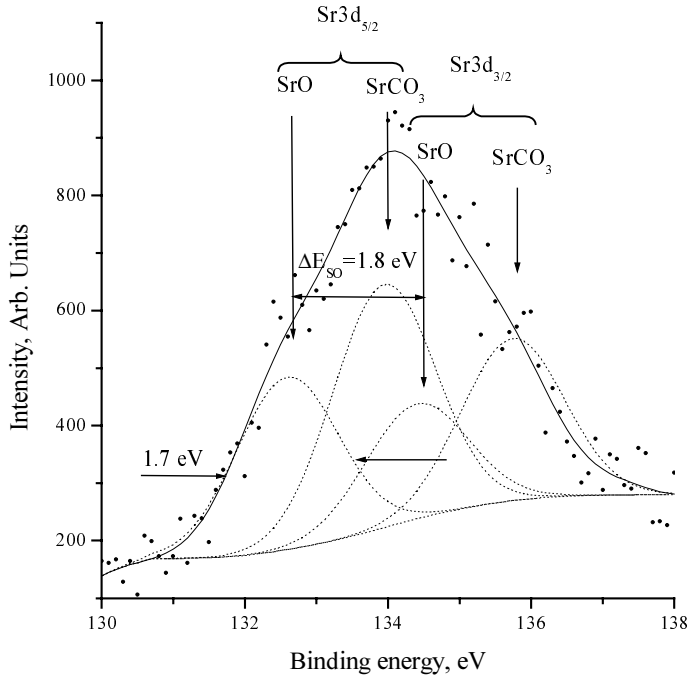

It should be noted that the Sr3d and Sr3p lines were observed as intense only for the reactor fuel (Sample I) and the "hot" particles collected within the next 360 seconds (Samples IV, V and VIII), while for the rest of the samples these lines were observed only as traces (Table 1). This indicates that within the first 20 seconds of heating Sr did not sublime. This agreed with chemical analysis data.

XPS spectra of the C1s electrons

For all the studied samples (I-VIII) intense C1s structured and broadened lines were observed. For the reactor fuel (Sample I) the number of carbon atoms was ~1.5 times greater than the number of uranium ions, while for the "hot" particles (Samples II–VIII) this number was about 10 times greater than the number of uranium ions. However, the spectra of inner and outer electrons from the studied samples were well observed. The main line (E_b = 285.0 eV) attributed to carbon surface contamination was used as a standard line for the calibration of the spectra. The area of the line at E_b = 289.0 eV was attributed to the carbon from the carbonate groups (CO_3^{2-}) and is proportional to the number of such groups on the sample surface. The number of CO_3^{2-} groups relative to the number of uranium atoms was found to be: 0.17 (Sample I), 1.47 (Sample II), 0.75 (Sample III), 0.68 (Sample IV), 0.82 (Sample V), 0.36 (Sample VI), 1.7 (Sample VII) and 1.29 (Sample VIII). These data allowed the suggestion that compounds like UO_2CO_3, $SrUO_2CO_3(OH)_2$, $Cs_4UO_2(CO_3)_3$ form on the surface of the "hot" particles. Ar^+ cleaning decreased significantly the number of carbonate (CO_3^{2-}) groups on the surface of the "hot" particles, and at $t \geq 60$ seconds these groups were not observed. This suggests that these groups are present only in the surface layers of the studied samples (Figure 5, Sample VII). The number of contamination carbon atoms on the surface (line at E_b = 285.0 eV) also decreased significantly (three times) after the Ar^+ cleaning, however, even after a 120-180 sec cleaning it remained constant (Figure 5).

XPS spectra of the O1s electrons

Spectra of the O1s electrons from the studied samples had structure. There are several possible reasons for this eventuality. First, the samples contained oxides: SrO (E_bO1s = 528.5 eV) UO_2 (E_bO1s = 530.5 eV) UO_3 (E_bO1s = 531.4 eV) and possibly hydroxides [3,10,11]. Second, adsorbed water could be present on the surface (E_b = 533.5 eV [10]) as well as some other molecules containing oxygen, for instance, CO_2. That could lead to formation of carbonates (E_bO1s = 531.5 eV [10]). The O1s spectra from the studied samples containing Sr (Samples I, IV, V, VIII) exhibited the typical lines at 528.4 eV, 530.2 eV, 531.6 eV and 533.5 eV, and the O1s spectra from the rest of the samples showed three lines at 530.2 eV, 531.7 eV and 533.5 eV. The line at 533.5 eV must be attributed to water, at 528.4 eV to strontium oxide, at 530.5 eV to UO_2, and at 531.5 eV to UO_3, metal hydroxides and carbonates. The Ar^+ cleaning caused the oxygen concentration relative to uranium to decrease. After a 120-180 sec Ar^+ cleaning, the ratio oxygen/ uranium on the surface went down to 2. That indicated formation of UO_2 on the surface (Figure 5).

In this work samples of the "hot" particles formed at similar conditions but in different experiments (Samples II and III, IV; Samples V, VI and VII respectively) were examined. Table 1 shows that the elemental compositions agreed well. It should be particularly noted that while the initial reactor fuel contained only 0.2 at.% of Cs and 1.3 at.% of Sr, the concentrations of U, Cs and Sr in the "hot" particles were comparable. Also the "hot" particles collected within the first 20 and next 360 seconds of fuel heating (Samples II and IV, III, Samples V, VII and VIII respectively) were studied. Table 1 shows that the samples collected within the first 20 seconds contained only Cs and U (that agreed with the data of chemical analysis), while those collected within the next 360 seconds contained U, Sr and Cs, and the relative concentrations of Sr in Samples IV and V were found to be higher than the relative concentrations of Cs (Table 1). Obviously, within the first 20 seconds of heating the emission of Cs was much higher than the emission of Sr, while within the next 360 seconds they were comparable. The samples of the "hot" particles were collected at different maturation conditions. Maturation of Samples II, III IV and V was done under air, while that of Samples VI, VII and VIII was in Ar atmosphere. Table 1 shows significant differences in the elemental compositions

for Samples IV, V and VIII. Thus, in Samples IV and V the relative Sr concentration was much higher (more than three times) than the Cs concentration, while in Sample VIII they were comparable. Apparently, in air atmospheres Sr forms complexes with uranyl group in aerosols preferably, while under inert atmospheres Cs and Sr both form such complexes.

Conclusions

- The technique of simulation of an NPP accident was developed. It allowed obtaining samples of reactor fuel (UO_2) containing caesium, strontium and uranium (UO_2 + 0.1% Cs + 0.5% Sr) before and after 2 300°C heating, as well as the "hot" particles of 0.2-4 μm size formed in argon or air atmosphere at different temperatures, to be collected on aluminium substrates.

- For the first time XPS spectra of valence and inner electrons from the "hot" particles were measured. This allowed determination of their quantitative elemental and ionic composition and suggestions on the nature of the formed compounds. On the basis of the intensities of the U4f, Cs3d, 4d and Sr3d spectral lines, samples of the "hot" particles collected within the first 20 seconds of heating of the initial fuel were found to contain up to 58% of U and 42% of Cs, without any appreciable Sr. The "hot" particles collected within the next 360 seconds contained up to 62% of U, 21% of Cs and 17% of Sr. This data agreed with the data from chemical analysis justify property.

- Taking into account chemical shifts of uranium, caesium and strontium inner levels, as well as the U5f and U4f fine spectral structure parameters, the first ionic quantitative analysis of the studied samples of the "hot" particles was carried out. That allowed suggestions that the samples contained oxides (UO_x, where $2 < x \leq 3$) and uranyl compounds like UO_2CO_3, $SrUO_4$, Sr_3UO_6, $SrUO_2CO_3(OH)_2$, Cs_2UO_4, $Cs_4UO_2(CO_3)_3$, $CsUO_2(OH)_3$ containing carbonate and hydroxyl groups in equatorial planes.

- The Ar^+ cleaning of the "hot" particles was found to cause significant decreasing of caesium contents relative to uranium and strontium contents. That indicated weak binding of Cs^+ ions in compounds of the studied "hot" particles. The concentration ratio [U(IV)/U(VI)] was observed to increase during such cleaning.

Acknowledgement

This work was supported by INTAS Grant Ref. No. 96-1927.

REFERENCES

[1] V. Tinant, P. Froment, J. Vanbegin, J. Cara, C. Ronneau, *Radiochim. Acta*, 79, 51-55 (1997).

[2] C. Ronneau, J. Cara, J. Vanbegin, P. Froment, "Biotechnology for Waste Management and Site Restoration", C. Ronneau and O. Bitchaeva, eds., Dordrecht/Boston/London (printed in the Netherlands): Klumer Academic Publishers, Ser. 2: Environment, 34, 51-54 (1997).

[3] Yu.A. Teterin, V.M. Kulakov, A.S. Baev, *Phys. Chem. Minerals*, 7, 151-158 (1981).

[4] Yu.A. Teterin, A.S. Baev, K.E. Ivanov, L.G. Mashirov, D.N. Suglobov, *Radiohimiya*, 39, 4 365-370 (1996) (in Russian).

[5] Yu.A. Teterin, A.S. Baev, S.A. Bogatov, *J. Electr. Spectr. Relat. Phenom*., 68, 685-694 (1994).

[6] V.I. Nefedov, Yu.A. Teterin, T. Reich, H. Nitsche, *A.N. Doklady*, 348, 5, 634-636 (1996) (in Russian).

[7] J.H. Scofield, *J. Electr. Spectr. Relat. Phenom*., 8, 129-137 (1976).

[8] A.S. Baev, Yu.A. Teterin, L.G. Mashirov, D.N. Suglobov, *Radiohimiya*, 28, 4, 460 (1986) (in Russian).

[9] V.I. Nefedov, M.N. Firsov, I.S. Shaplygin, *J. Electron Spectr. Related Phenom*., 26, 65 (1982).

[10] V.I. Nefedov, "X-ray Photoelectron Spectroscopy of Chemical Compounds", Moscow: Himiya, 1984, 255 p. (in Russian).

[11] M.I. Sosulnikov, Yu.A. Teterin, *J. Electr. Spectr. Relat. Phenom*., 59, 111-126 (1992).

[12] Yu.A. Teterin, V.M. Kulakov, A.S. Baev, A.G. Zelenkov, N.B. Nevzorov, I.V. Melnikov, V.A. Streltsov, L.G. Mashirov, D.N. Suglobov, A.N. Doklady, *SSSR*, 255, 2, 434-437 (1980) (in Russian).

INTERACTION OF UO_2^{2+} AND Fe^{3+} IONS WITH NATURAL HUMIC ACID

Yu.A. Teterin,[1] **V.I. Nefedov,**[2] **A.S. Nikitin,**[1] **A.Yu. Teterin,**[1] **K.E. Ivanov,**[1] **K.I. Maslakov,**[1]
I.O. Utkin,[1] **M. Bubner,**[3] **T. Reich,**[3] **S. Pompe,**[3] **K.H. Heise,**[3] **H. Nitsche**[3]
[1]Russian Research Centre "Kurchatov Institute"
Moscow, Russia
[2]Kurnakov Institute of General and Inorganic Chemistry of RAS
Moscow, Russia
[3]Institute of Radiochemistry "Forschungszentrum Rossendorf e.V."
Dresden, Germany

Abstract

Cation exchange in uranyl (UO_2^{2+}) and iron [Fe(III)] humates was studied. At high Fe(III) ion concentration, Fe(III) is not exchanged by uranyl ions. However, even at a high concentration of uranyl in complexes with natural humic acid, the Fe(III) ion is able to substitute uranyl. The X-ray photoelectron spectral data showed that, in contrast to uranyl, the formation of complexes with Fe(III) occurred predominantly on the surface of the natural humic acid. This fact explains why Fe(III) prevents formation of complexes with uranyl since Fe(III) hinders diffusion of uranyl to the inner of the HA particles.

Introduction

The interaction of natural humic acid (HA) with uranyl and Fe(III) ions was studied by X-ray photoelectron spectroscopy in Ref. [1]. The reaction was established to be heterogeneous, i.e. HA reacted like particles. The concentrations of UO_2^{2+} and Fe(III) were different on the surface and inside the particles. During the reaction of HA with a mixture of UO_2^{2+} and Fe(III) at pH 2.1, complexes of HA formed predominantly with Fe. The XPS data showed that the concentration of iron in the Fe(III)-HA complexes was higher on the surface than in the bulk of HA particles.

This work is a continuation of our study of the complex-formation of UO_2^{2+} and Fe(III) ions with HA. Unlike in our previous work [1], all reactions were carried out at the same pH of 1.8. This excluded the influence of acidity on the results. In addition, the exchange reactions Fe(III) $\rightarrow$ UO_2^{2+} and UO_2^{2+} $\rightarrow$ Fe(III) were studied for these humate complexes.

Experimental

The complexes were prepared using HA A2/97 (Aldrich) containing 4.0±0.11 meq/g of COOH groups and 3.4±0.5 meq/g of OH groups. The functional group content of the HA was determined radiochemically. The elemental composition of A2/97 is: C 58.7%, H 4.2%, N 0.77%, S 4.08%, Fe 0.1%, H_2O 7.95%, minerals (residual) 0.5±0.3% [2]. Samples were prepared by reaction of the HA with 0.1 M stock solutions of $UO_2(ClO_4)_2$ and $Fe(ClO_4)_3$ at pH 1.8. The aim was to prepare humates with an offer of 12 and 0.4 meq/g UO_2^{2+} and Fe(III), respectively. This corresponds to a metal-ion concentration of 300% and 10% with respect to the HA's content of carboxylic groups of 4.0 meq/g. In the exchange reaction, the concentration (meq/g) of the corresponding cation in the reaction solution was equal to the content of carboxylic groups in the HA.

In a first step, 1 g HA A2/97 was suspended in 10 ml Milli-Q water, degassed three times under vacuum, and brought into equilibrium with air pressure. To prepare Sample 1 (2), 40 (1.33) ml $Fe(ClO_4)_3$ stock solution was added to this HA suspension. To adjust the pH to 1.8, the supernatant was separated from the HA precipitate after 10 min, 10 h, 3 h and 3 h. After each pH adjustment, the supernatant was united with the precipitate. Finally, the Fe(III) humate was washed with 20 ml Mill-Q water, dialysed for 48 h and lyophilised. Samples 3 and 4 were prepared the same way at pH 1.8 by adding 60 and 2 ml 0.1 M $UO_2(ClO_4)_2$ solution, respectively, to 1 g HA, which was suspended in 10 ml water.

For the exchange reaction, 0.5 g (relative to the humic acid) of the metal humate (Samples 1-4) was suspended in 10 ml Milli-Q water, degassed three times under vacuum and equilibrated with air to normal pressure. During intensive stirring, the stock solution containing 2 meq of the antagonistic cation was added to the humate suspension. The following steps in the sample preparation, including pH adjustment, were identical to those described above. In summary, Sample 5 was produced from Sample 1 (1 $\rightarrow$ 5), Sample 6 from Sample 2 (2 $\rightarrow$ 6), Sample 7 from Sample 3 (3 $\rightarrow$ 7) and Sample 8 from Sample 4 (4 $\rightarrow$ 8).

Experimental data on the chemical compositions of the studied complexes are given in Table 1. Uranium and iron contents were determined by the inductively coupled plasma mass spectrometry (ICP-MS). The sensitivities for U and Fe were 1 and 100 ppb, respectively. The relative error was 5-10%.

Table 1. Chemical compositions of the HA complexes with uranyl and Fe(III)

N	Complex	Concentrations of elements (wt.%)					Loading of HA relative to COOH (%)		
		C	H	N	Fe	U	Fe^{3+}	UO_2^{2+}	Σ
1	A2-Fe^{3+}	50.3	3.8	0.65	9.0	–	141	–	141
2	A2-Fe^{3+}	57.0	4.0	0.78	0.95	–	13	–	13
3	A2-UO_2^{2+}	43.3	3.0	0.59	–	21.3	–	60.5	60.5
4	A2-UO_2^{2+}	55.1	3.8	0.75	–	5.0	–	11.3	11.3
5	A2-Fe^{3+}/UO_2^{2+}	46.4	3.7	0.58	7.8	5.2	133	12.3	145
6	A2-Fe^{3+}/UO_2^{2+}	45.3	3.2	0.59	0.6	19.5	10	53	63
7	A2-UO_2^{2+}/Fe^{3+}	48.5	3.4	0.65	4.6	8.1	75	20.5	95
8	A2-UO_2^{2+}/Fe^{3+}	52.8	3.6	0.68	5.8	2.0	86	4.5	90

The experimental XPS data are given in Table 2. The XPS spectra of Samples 5-8 were measured with a MK II VG Scientific spectrometer under $\sim 1.3 \times 10^{-7}$ Pa at room temperature. The overall resolution measured as full width at half maximum (FWHM) of the $Au4f_{7/2}$ electron line was 1.2 eV. Electron binding energies, E_b, are given relative to E_b of C1s electrons from adventitious hydrocarbons at the sample surface defined as 285.0 eV. On the gold substrate, E_b(C1s) equalled 284.7 eV and $E_b(Au4f_{7/2})$ was 83.8 eV. The experimental errors in the line position and FWHM were ±0.1 eV, whereas errors of relative line intensities were about 10%. The background was subtracted using the Shirley method [3] (Figures 1-4). Samples were ground in an agate mortar and studied as ultra-dispersed powders in the form of thick layers pressed into indium on aluminium substrates. The relative intensities $I(Fe2p_{3/2}/U4f_{7/2})$ were found using the formula $I(Fe2p_{3/2}/U4f_{7/2}) = S(Fe2p_{3/2})/S(U4f_{7/2})$, where $S(Fe2p_{3/2})$ is the area under the $Fe2p_{3/2}$ line and $S(U4f_{7/2})$ is the area under the $U4f_{7/2}$ line. The relative atomic concentrations of uranium and iron atoms, n_{Fe}/n_U, were calculated using the ratio $n_{Fe}/n_U = I(Fe2p_{3/2}/U4f_{7/2})k$, where k is the experimental sensitivity factor, which equalled to 2.3 [4].

Table 2. XPS data for Samples 5-8 and data of chemical analysis from Table 1

N	Relative concentrations of Fe and U from chemical analysis (at.%)		$I(Fe2p_{3/2}/U4f_{7/2})$		Relative concentrations of Fe and U from XPS data (at.%)			
					Non-ground		Ground	
	Fe	U	Non-ground	Ground	Fe	U	Fe	U
5	87	13	2.045	1.883	82	18	81	19
6	12	88	–	–	0	100	0	100
7	71	29	0.857	0.464	67	33	52	48
8	92	8	2.845	2.334	87	13	84	16

Results and discussion

Table 1 allows the following conclusions:

- At pH 1.8 and comparable excess of cations in the reaction blend (300%), the amount of uranyl groups bound to HA is noticeably less (Sample 3) than the amount of Fe(III) cations (Sample 1) bound. In an earlier study [1], it was observed that uranyl at pH 4.0 binds more than Fe(III) at pH 2.2.

- At high iron concentration, the Fe(III)-UO_2^{2+} exchange (transition $1 \rightarrow 5$) goes feebly (Table 1). The relative concentration of Fe(III) ions does not change in the bulk compared to the surface (Table 2). However, at low iron content (transition $2 \rightarrow 6$), the uranium content increases significantly while the iron content changes only slightly.

- In contrast, the$UO_2^{2+} \rightarrow$ Fe(III) exchange (transitions $3 \rightarrow 7$, $4 \rightarrow 8$) is accompanied by a significant decrease of the uranyl concentration and an increase of the iron concentration. Thus, in Samples 7 and 8 the surface content of Fe is significantly higher than in the bulk (see I($Fe2p_{3/2}$/$U4f_{7/2}$) values for non-ground (surface) and ground (bulk) samples in Table 2).

The latter two conclusions confirm previous results [1] that the formation of Fe complexes takes place predominantly at the HA surface in contrast to the formation of uranyl complexes. The presence of Fe(III) on the surface prevents the Fe(III)-UO_2^{2+} exchange. Also, it was confirmed that Fe(III) can diminish the formation of uranyl-HA complexes and prevent the migration of uranyl associated to HA in soil water.

In the present work, Samples 5-8 were studied by XPS as non-ground and ground powders. The valence band of HA lies in the binding energy range of 0-40 eV (Figure 1) due to the interaction of the C2s, 2p and O2s, 2p electrons from neighbouring atoms and the formation of the outer (OVMO) and inner (IVMO) valence molecular orbitals. The spectral structure of the low binding energy electrons at 0 eV is due to the C2p and O2p interaction and formation of OVMOs. The spectral structure around 40 eV binding energy is due to the C2s and O2s interaction and the formation of the IVMOs [1].

Figure 1. XPS spectrum of the low binding energy electrons from HA complex with UO_2^{2+} and Fe(III) (Sample 7 non-ground)

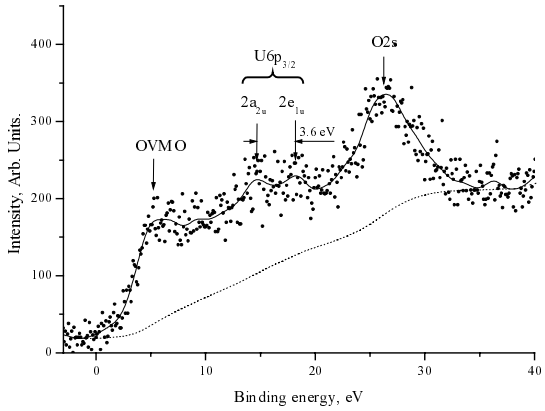

XPS spectra of the low binding energy electrons of interaction products of HA with uranyl groups compared to the corresponding spectra of pure HA exhibit additional spectral features due to the OVMO and IVMO of the uranyl compounds. Thus, more intense lines were observed in the OVMO range (0-15 eV). The absence of the U5f line at E_b = 1.9 eV [5] in this region indicates the absence of tetravalent uranium in the samples (presence of hexavalent uranium only). In the range 14-20 eV, two extra peaks (Figure 1) were observed due to IVMO orbitals like $2a_{2u}$ and $2e_{1u}$ formed by the interaction of the $U6p_{3/2}$ and O2s (L2s) orbitals, where L is ligand [for clusters like $[UO_2^{2+}O_6]^{10-}(D_{6h})$] [6]. It is known that the interatomic distances U-O in uranyl compounds in equatorial and axial directions can be determined on the basis of the energy difference between these orbitals ($2e_{1u}$ and $2a_{2u}$) and the $U4f_{7/2}$

inner level, i.e. $\Delta E_1(U4f_{7/2}\text{-}2a_{2u})$ and $\Delta E_2(U4f_{7/2}\text{-}2e_{1u})$ [6]. This is also possible using the difference $\Delta E(2e_{1u}\text{-}2a_{2u})$ [7]. Since the valence spectra from the studied samples had a low signal-to-noise ratio, it was difficult to measure ΔE_1 and ΔE_2. Therefore, we used the formula of Ref. [7] to determine the interatomic distances in axial $r_1 = (U\text{-}O)_{ax}$ and equatorial $r_2 = (U\text{-}O)_{eq}$ directions. These data gave a smaller error than the data of Ref. [6]. For the non-ground Sample 7, the measured $\Delta E(2e_{1u}\text{-}2a_{2u})$ value was 3.6 eV. The calculated interatomic distances are: $r_1 = 1.76$ Å, $r_2 = 2.36$ Å (Figure 1). These results agree with those for other uranyl-HA complexes [8].

Humic acid A2/97 contained 4.0±0.11 meq/g of COOH groups. Therefore, beside the basic C1s line at $E_b = 285.0$ eV due to surface contamination by hydrocarbons ($\text{-}CH_2\text{-}CH_2\text{-}$), the C1s spectrum was also expected to contain lines at $E_b = 287$ eV (≡ C-OH) and at $E_b = 289.4$ eV (-COO-) [4]. Indeed, the C1s spectra from the studied samples exhibited a line at $E_b = 288.8$ eV due to -COO- groups. Unfortunately, it was difficult to distinguish the peak corresponding to ≡ C-OH groups due to the limited spectrometer resolution. Also, due to the high concentration of such groups on the surface, the IVMOs corresponding to uranyl compounds in the binding energy range 0-40 eV could not be observed clearly.

XPS spectra in the range of the U4f electrons consisted of two main lines, which are split due to spin-orbit interaction ($\Delta E_{so} = 10.8$ eV), and satellite lines as a result of many-body perturbation (shake-up process) on the higher binding energy side. The position of the $U4f_{7/2}$ peak and the distance to the satellite characterises the uranium oxidation state [9]. For the studied materials, the $U4f_{7/2}$ binding energy was 382.6±0.2 eV. The shake-up satellite of 15-20% intensity was observed 2.7-3 eV from the main line at higher binding energy (Figure 2). Such an U4f structure is typical for hexavalent uranium compounds [9]. This means that the HA complexes contained uranium in the form of uranyl groups.

Figure 2. XPS spectrum of the U4f and N1s electrons from HA complex with UO_2^{2+} and Fe(III) (Sample 6 non-ground)

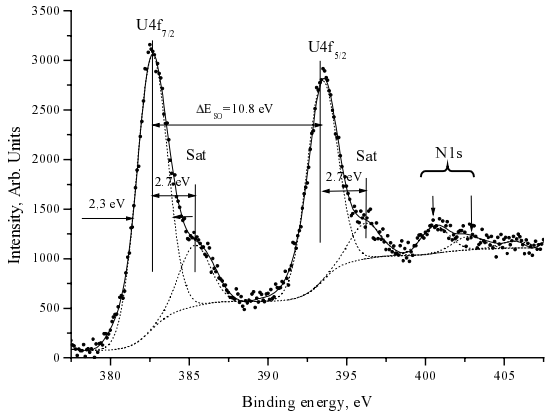

A N1s line with low intensity was observed at 400.3-400.8 eV, which indicated the presence of HNR_2^+ groups [1,8]. The observed N1s line consisted of several poorly resolved components (Figure 2), which require extra analysis. The XPS spectrum in the Fe2p region consisted of a spin-orbit doublet ($\Delta E_{so} = 13.1$ eV) and satellites due to the shake-up process at the higher binding energy side (Figure 3). These shake-up satellites were structured and intense relative to the main $Fe2p_{3/2,1/2}$ lines. This complicated the interpretation of the spectra and increased significantly the error of the $Fe2p_{3/2}$ line

Figure 3. XPS spectrum of the Fe2p electrons from HA complex with UO_2^{2+} and Fe(III) (Sample 5 non-ground)

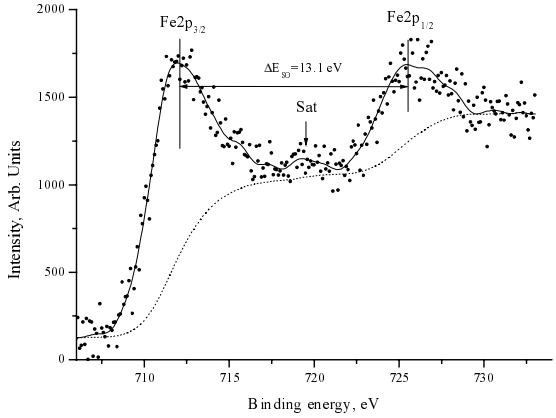

area determination. The $Fe2p_{3/2}$ binding energy for the studied samples was 712.0±0.2 eV, which indicated the presence of Fe(III) ions (Figure 3) [4]. In the spectrum from both non-ground and ground Sample 6, the $Fe2p_{3/2}$ line was not observed due to the low iron concentration. This agrees with the data of the chemical analysis (Table 2).

The S2p spectra exhibited two lines (Figure 4). The lines with binding energies of 164.4±0.2 eV and 168.1±0.2 eV are due to S2p electrons of organic sulphide and sulphate, respectively [4]. It should be noted that the Cl2p line at E_b = 208 eV was not observed in spectra of the samples studied (neither ground nor non-ground). This indicates that ClO_4^- anions were not included in the complexes, i.e. there was no physical and chemical sorption of $UO_2(ClO_4)_2$ or $Fe(ClO_4)_3$ on the HA surface and no diffusion of ClO_4^- anion into the bulk. This confirms the results of Ref. [1].

Figure 4. XPS spectrum of the S2p electrons from HA complex with UO_2^{2+} and Fe(III) (Sample 6 non-ground)

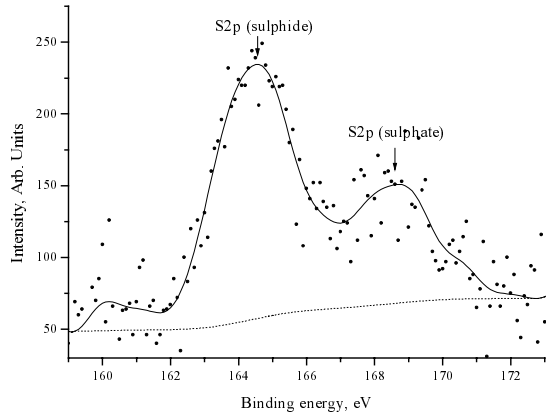

In the present work, the spectral intensities from non-ground and ground samples were compared. That allowed to draw a conclusion on the differences in concentrations on the surface and in the bulk of the HA particles. The relative intensity $I(Fe2p_{3/2}/U4f_{7/2})$ for Samples 5, 7 and 8 was established to be higher for non-ground samples than for ground ones (Table 2, Figure 5). For Sample 6 (both

Figure 5. Dependence of the relative intensities I(Fe2p$_{3/2}$/U4f$_{7/2}$) on the relative concentrations $\delta = m_{Fe}/m_U$ for Samples 5-8 (○– non-ground samples, ● – ground samples)

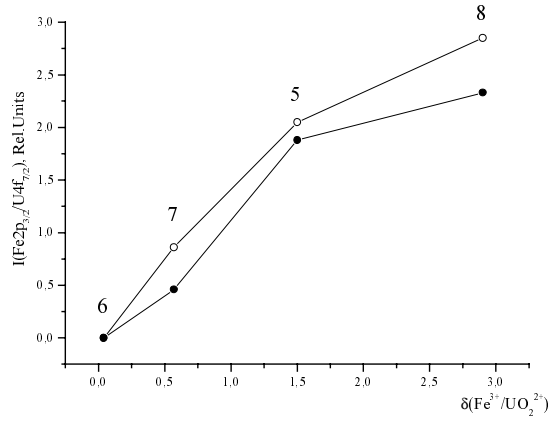

non-ground and ground), I(Fe2p$_{3/2}$/U4f$_{7/2}$) was zero due to the low iron concentration. The dependence of I(Fe2p$_{3/2}$/U4f$_{7/2}$) on the relative mass concentration, $\delta = m_{Fe}/m_U$ (Figure 5), allows to conclude that the formation of complexes with iron goes better on the surface of the HA particles, while formation of complexes with uranyl is favoured in the bulk. Table 2 gives the relative concentrations obtained using XPS for Fe and U atoms in Samples 5-8. One apparent reason for the unsatisfactory coincidence of these results with the results of the chemical analysis is the large error in determining the Fe2p$_{3/2}$ line area due to the complicated satellite structure and the high background.

Conclusions

- The ClO_4^- anion was not observed on the surface and in the bulk of the samples using X-ray photoelectron spectroscopy analysis. This indicated the absence of physical and chemical sorption of $UO_2(ClO_4)_2$ and $Fe(ClO_4)_3$ on the HA surface as well as of ClO_4^- diffusion into the bulk.

- It was established that uranium was not reduced to U(IV) but remained U(VI) in the result of the reaction of $UO_2(ClO_4)_2$ with HA.

- At pH 1.8, the complex-formation ability of HA with Fe(III) ions was higher than that with uranyl ions. Fe(III) ions were able to substitute uranyl groups in uranyl humates even at low Fe(III) concentrations in solutions.

- The formation of Fe(III) complexes with HA goes more preferably on the HA surface than that of uranyl complexes. The reaction of HA with solutions containing UO_2^{2+} and Fe(III) ions is heterogeneous. The presence of Fe(III) ions on the surface of HA particles prevents the Fe(III) $\rightarrow UO_2^{2+}$ exchange. Therefore, Fe(III) ions can diminish formation of HA complexes with uranyl and reduce migration of uranium in form of soluble humates in soil water.

- On the basis of the XPS fine structure parameters, the formation of uranyl compounds on the HA surface was confirmed. In particular, the interatomic uranium-oxygen distances in axial (R_{U-O} = 0.176 nm) and equatorial (R_{U-L} = 0.236 nm) directions, as well as the presence of functional groups (-OH^-, -COO^-) in equatorial planes, were determined.

Acknowledgement

This work was supported by the ISTC (No. 1358), RFBR.

REFERENCES

[1] Yu.A. Teterin, A.Yu. Teterin, A.M. Lebedev, A.P. Dementiev, I.O. Utkin, V.I. Nefedov, M. Bubner, T. Reich, S. Pompe, K.H. Heise, H. Nitsche, *J. Prakt. Chem*., 341, 8, 773-777 (1999).

[2] S. Pompe, K. Schmeide, M. Bubner, G. Geipel, K.H. Heise, G. Bernhard, H. Nitsche, *Radiochim. Acta*, 88, 553-558 (2000).

[3] D.A. Shirley, *Phys. Rev*., 35, 4709 (1972).

[4] V.I. Nefedov, "X-ray Photoelectron Spectroscopy of Chemical Compounds", Moscow, Himiya, 1984, 256 p. (in Russian).

[5] Yu.A. Teterin, V.M. Kulakov, A.S. Baev, N.B. Nevzorov, I.V. Melnikov, V.A. Streltsov, L.G. Mashirov, D.N. Suglobov, A.G. Zelenkov, *Physics and Chemistry of Minerals*, 7, 151-158 (1981).

[6] Yu.A. Teterin, A.S. Baev, K.E. Ivanov, L.G. Mashirov, D.N. Suglobov, *Radiohimiya*, 38, 5, 395-402 (1996) (in Russian).

[7] V.I. Nefedov, Yu.A. Teterin, T. Reich, H. Nitsche, *Doklady Akademii Nauk*, 348, 5, 634-636 (1996) (in Russian).

[8] V.I. Nefedov, Yu.A. Teterin, A.M. Lebedev, A.Yu. Teterin, A.P. Demetjev, M. Bubner, T. Reich, S. Pompe, K. Heise, H. Nitsche, *Inorg. Chim. Acta*, 273, 1-2, 234-237 (1998).

[9] Yu.A. Teterin, A.S. Baev, A.Yu. Teterin, K.E. Ivanov, L.G. Mashirov, D.N. Suglobov, *Radiohimiya*, 39, 2, 177-181 (1997) (in Russian).

X-RAY SPECTRAL STUDY OF THE Th6p,5f ELECTRON STATES IN ThO_2 AND ThF_4

Yu.A. Teterin,[1] **V.A. Terehov,**[2] **M.V. Ryzhkov,**[3] **A.Yu. Teterin,**[1]
I.O. Utkin,[1] **K.E. Ivanov,**[1] **A.S. Nikitin,**[1] **L.J. Vukchevich**[4]
[1]Russian Research Centre "Kurchatov Institute"
1, Kurchatov sq., Moscow 123182 Russia
[2]Voronezh State University
1, University sq., Voronezh 394693 Russia
[3]Institute of Solid State Chemistry
91, Pervomaiskaya st., Ekaterinburg 620219 Russia
[4]Natural Mathematics Dept. of "Veljko Vlahovich" University
Podgorica 81000 Yugoslavia

Abstract

The study of the Th6p,5f electron states in Th, ThO_2 and ThF was carried out on the basis of the X-ray photoelectron fine spectral structure parameters in the binding energy range of 0-~1 000 eV, X-ray $O_{4,5}$(Th) emission spectra of the shallow (0-~50 eV) electrons and results of theoretical calculations. As a result, despite the absence of the Th5f electrons in thorium atoms, the Th5f atomic orbitals were established to participate in the formation of molecular orbitals in thorium dioxide and tetrafluoride. In the MO LCAO approximation this allowed to suggest the possible existence of filled Th5f electronic states in thorium compounds. On the basis of the X-ray $O_{4,5}$(Th) emission spectral structure parameters the effective formation of the inner valence molecular orbitals in the studied compounds was confirmed.

Introduction

One of the most important questions in the study of the nature of the chemical bond in actinide compounds, in particular in thorium compounds, is the question about the role of the outer (OVMO) (An5f,6d,7s) and inner (IVMO) (An6s,6p) valence molecular orbital electrons. Thus, atomic Th in the ground state does not have Th5f electrons. However, as it follows from theoretical results [l], the atomic Th5f orbitals can participate in formation of molecular orbitals and filled Th5f electronic states can exist. This can be confirmed experimentally. For example, since the Th5f photoemission cross-section (Th5f) is much higher than that of the Th6d (0.0949) and Th7s (0.0216) electrons [2]. The degree of participation of Th5f electrons in MO formation can be evaluated on the basis of the XPS OVMO line intensities in Th compounds. On the other hand, the filled Th5f states can cause intense peaks in XES $O_{4,5}$(Th) spectra reflecting Th5d ← Th5f transitions, since the dipolar selection rules ($\Delta 1 = \pm 1$) are met.

Earlier, while studying the electronic structure of materials, only electrons from the low binding energy range (0-~15 eV) were suggested to participate in the chemical bonding. Although the quantum mechanics theory did not forbid electrons from deeper shells (~15-~50 eV) to participate in formation of the inner valence molecular orbitals (IVMO) [3], their participation was considered negligible compared to the electrons from the outer valence molecular orbitals (OVMO) (0-~15 eV). However, on the basis of XPS fine spectral structure parameters for various elements the strong interaction of electrons from the low-energy shells of neighbouring atoms and formation of IVMOs was shown to exist [3].

Previously X-ray $O_{4,5}$(Th) emission spectra from ThO_2 and ThF_4 were measured with low resolution [4]. This did not allow to observe their fine structure. In papers [5,6] such spectra were measured with high resolution, and the fine structure was observed. This fine structure was associated with the formation of the IVMO and OVMO. The present work examines the Th6p,5f states in ThO_2 and ThF_4 on the basis of the X-ray photoelectron and $O_{4,5}$(Th) emission spectra and theoretical calculations for these compounds.

Experimental

XPS spectra were taken using a HP-5950A spectrometer using monochromatised Al $K_{\alpha 1,2}$ ($h\nu$ = 1 486.6 eV) X-rays utilising a low energy electron flood gun for charge compensation of ~10^{-9} Torr at room temperature. Overall resolution measured as the $Au4f_{7/2}$ electron line full width of half maximum (FWHM) was better than 0.8 eV. Electron binding energies are given relative to the E_b of the C1s electrons from adventitious hydrocarbons on the sample surface defined as 285.0 eV. The measurement errors of line positions and widths were ±0.1 eV, whereas relative line intensity errors were about 10%. The sample materials were prepared by pressing powders into iridium on titanium substrates.

X-ray $O_{4,5}$(Th) emission spectra (XES) from ThO_2 and ThF_4 reflecting the Th6p and the Thnp,5f electron states were measured with a RSM-500 spectrometer ($P = 5 \times 10^{-6}$ Torr) with a resolution of 0.3 eV, with an X-ray anode operating at 3 kV (2 mA) during 60 minutes. The variation of the excitation energy allowed to vary the effective depth from 15 to 50 nm. The area of the electron beam was 5×5 mm^2. The samples were powderised in the agate mortar and the powder was pressed into the silver plate attached to the anode of the X-ray tube. The secondary photo-multiplier “VEU-1” was used to detect the spectra. CsI films with quantum yield in the analysing spectral region was used as a photocathode. Each $O_{4,5}$(Th) spectrum was collected three times. The lines of Zr (75.55 eV) and Nb (85.85 eV) were used for the calibration in the second order of reflection M_ξ.

Results and discussion

Electronic structure of Th and ThO_2

The electronic configuration of atomic thorium is $6s^26p^66d^27s^2$ and it does not contain Th5f electrons in the ground state. Energies E (eV), mean radii ⟨r⟩ (mn), and ionisation potentials I_i (eV) of these shells are given in Table 1. Corresponding data for oxygen and fluorine are given in Table 2. As follows from these data, at R_{Th-O} = 0.241 nm in ThO_2 [1] the Th6s,6p,5f,6d and the O2s,2p shells can participate actively in the chemical bonding. Mean radii ⟨r⟩ of the Th7s and the Th7p shells are too big to bring any significant positive contribution in interaction with the O2p,2s shells. Indeed, for example, the sum of the mean radii of the $Th6d_{5/2}$ and $O2p_{3/2}$ shells is $\langle r_{6d5/2} + r_{O2p3/2}\rangle$ = 0.234 nm, which is comparable with R_{Th-O} = 0.241 nm in ThO_2, while the corresponding sums for the Th7s and O2p and the $Th7p_{3/2}$ and $O2p_{3/2}$ are $\langle r_{7s} + r_{O2p3/2}\rangle$ = 0.344 nm and $\langle r_{7p3/2} + r_{O2p3/2}\rangle$ = 0.552 nm, respectively. The last values (0.344 nm and 0.552 nm) are significantly higher than the interatomic distance ThO_2 (0.241 nm). Therefore, electrons from these orbitals can hardly contribute in the binding between thorium and oxygen (fluorine) atoms. To a certain extent this also concerns the Th6d electrons. The mean radii of the Th6s,6p and Th5f shells are comparable and under certain conditions these shells can interact effectively with the O(F)2s,2p atomic shells forming molecular orbitals.

Results of these qualitative evaluations agree well with the spin-restricted approximation SCF X_α-DV calculation data of the electronic structure of a $ThO_8^{12-}(O_h)$ cluster [1] (Figure 1). As is seen from the schematic in Figure 1, the Th7s and the Th7p AOs practically do not participate in formation of the filled OVMOs (from $2t_{2g}$ to $4t_{1u}$) while the Th6s,6p and Th5f AOs do. The Th6p and O2s AOs bring the main contribution in the IVMO formation (from $1a_{1g}$ to $2t_{1u}$). Thus, the bonding $1t_{1u}$ IVMO consists of 68% of O2s + 18% of Th6p + 12% of O2p + 1.6% of Th5f, while the corresponding $2t_{1u}$ IVMO contains 55% of Th6p+27% of O2s + 16% of O2p + 1.3% of Th7p + 0.5% of Th5f. These results agree well with the data of the muffin-tin approximation SCF X_α-SW calculations for the $ThO_8^{12-}(O_h)$ cluster (Table 3).

Table 1. Number of electrons N, energy of the Th_{nlj} levels E (eV) and mean radii ⟨r⟩ (nm), of atomic Th low-energy shells in ground state

I_i – ionisation potentials found in Hartree-Fock-Dirack approximation, E_0 = -721444.57 eV – full energy*

N	Th_{nlj}	N	E	⟨r⟩	I_i
1	$7p_{3/2}$	0.0000	2.076	0.486	–
2	$7p_{1/2}$	0.0000	2.308	0.433	–
3	7s	2.0000	5.703	0.278	5.43
4	$6d_{5/2}$	1.2000	5.648	0.168	4.98
5	$6d_{3/2}$	0.8000	6.131	0.160	5.3
6	$5f_{7/2}$	0.0000	10.346	0.093	–
7	$5f_{5/2}$	0.0000	10.789	0.092	–
8	$6p_{3/2}$	4.0000	27.273	0.103	25.48
9	$6p_{1/2}$	2.0000	35.868	0.092	33.68
10	$6s_{1/2}$	2.0000	56.229	0.083	53.8
11	$5d_{5/2}$	6.0000	101.205	0.050	96.06
12	$5d_{3/2}$	4.0000	108.359	0.048	103.02

* The program (I.M. Band and M.B. Trhaskovslaya) was used.

Table 2. Number of electrons N, energy of the $O(F)_{nlj}$ levels E (eV), and mean radii ⟨r⟩ (nm), of atomic oxygen and fluorine in ground states

I_i – ionisation potentials found in Hartree-Fock-Dirack approximation, $E_0(O)$ = -2036.47 eV, $E_0(F)$ = -2707.95 eV – full energies*

N	$O(F)_{nlj}$	N	E	⟨r⟩	I_i
1	$O2p_{3/2}$	2.6667	16.751	0.066	14.58
2	$O2p_{1/2}$	1.3333	17.030	0.065	14.84
3	$O2s_{1/2}$	2.0000	34.050	0.060	31.77
4	$O1s_{1/2}$	2.0000	563.215	0.011	545.56
1	$F2p_{3/2}$	3.3333	19.829	0.057	17.10
2	$F2p_{1/2}$	1.6667	20.039	0.057	17.29
3	$F2s_{1/2}$	2.0000	42.868	0.053	40.12
4	$F1s_{1/2}$	2.0000	718.717	0.009	698.17

* The program (I.M. Band and M.B. Trhaskovslaya) was used.

Figure 1. Composition (%) and MO schematic of $ThO_8^{12-}(O_h)$ cluster [7], built by calculation results for R_{Th-O} = 0.241 nm (Xα-DVM [1])

Empty MOs shown as dashed lines. AOs and corresponding IVMOs connected with dashed lines. Energetic scale is not exact.

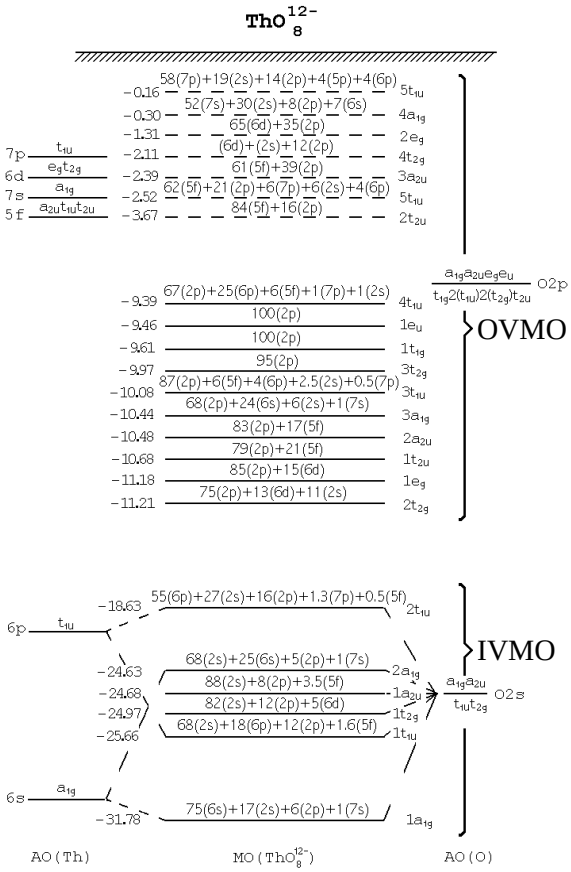

Table 3. MO energies E (eV), partial electronic contributions (%) in different regions of ThO_8^{12-} (O_h) cluster for R_{Th-O} = 0.241 nm and full partial charges Q_l^j (electr. charge units), calculated by SCF X_α-SV[a]

MO		-E	Th				O		Regions	
			s	p	d	f	S	p	II	III
OVMO	$2t_{2u}$	0.10	–	–	–	91.5	–	1.7	3.4	3.4
	$5t_{1u}$	0.54	–	0.0	–	11.8	1.1	7.8	10.3	69.0
	$4a_{1g}$	1.46	0.4	–	–	–	3.4	2.7	24.7	68.8
	$4t_{1u}$[b]	3.43	–	8.2	–	6.0	0.5	60.4	13.8	11.1
	$1e_u$	3.35	–	–	–	–	–	76.7	23.3	–
	$1t_{1g}$	3.58	–	–	–	–	–	74.7	21.3	4.0
	$3a_{1g}$	4.29	4.3	–	–	–	0.0	65.7	16.8	13.8
	$3t_{2g}$	4.08	–	–	1.9	–	0.5	66.4	19.4	11.8
	$2a_{2u}$	4.27	–	–	–	15.3	0.1	64.0	10.7	9.9
	$3t_{1u}$	4.61	–	0.7	–	2.1	0.5	57.1	30.4	9.2
	$2t_{2g}$	5.07	–	–	6.6	–	0.2	64.9	21.6	6.7
	$1t_{2u}$	5.25	–	–	–	3.3	–	60.3	29.7	6.7
	$1e_g$	5.95	–	–	3.1	–	–	51.9	37.0	8.0
IVMO	$2t_{1u}$	13.60	–	74.4	–	0.0	11.4	4.9	8.4	0.9
	$1a_{2u}$	18.22	–	–	–	0.8	86.2	0.0	10.8	2.2
	$2a_{1g}$	18.50	4.4	–	–	–	79.7	0.0	13.8	2.1
	$1t_{2g}$	18.49	–	–	1.1	–	84.2	0.0	12.6	2.1
	$1t_{1u}$	19.22	–	10.5	–	0.2	72.6	0.2	15.1	1.4
	$1a_{1g}$	27.13	91.8	–	–	–	2.6	0.6	5.0	0.0
Q_j^l [c]			2.0	5.6	0.7	1.0	1.7	3.9	13.9	4.0

[a] A program from A.P. Kovtun was used.
[b] Upper filled MO.
[c] $Q_l^j = \sum_i Q_{l_i}^j$, where i is the filled state.

Even though these results are qualitative, they really help interpreting the fine structure of XPS and other spectra. Unfortunately, at the present time any correct quantitative calculations for such complicated electronic systems as actinide compounds have not yet been done.

XPS spectral structure of the low-energy electrons from ThO_2 and ThF_4

The XPS spectra of ThO_2 and ThF_4 in the E_b range 0-~15 exhibit a poorly resolved relatively wide band (Figure 2) due to the outer valence molecular orbitals [7,8]. This structure reflects participation of the $Th6d^27s^2$ and O(F)2p shells in the chemical binding. Full widths at half maximums of these lines were found to be 3.3 eV and 3.7 eV for ThO_2 and ThF_4 respectively.

Figure 2. XPS spectra of the low-energy electrons from ThO_2 and ThF_4. MO energies for ThO_8^{12-} (O_h), cluster SCF X_α-DVM [1,7] given below the ThO_2 spectrum

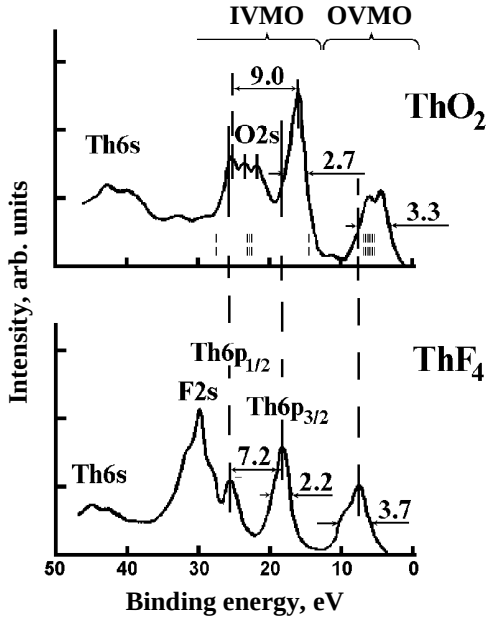

In the E_b range from ~15 eV to 50 eV the considered spectra exhibited structures due to the Th6s,6p and O(F)2s electrons. These structures differed significantly from the summary atomic spectra of thorium and oxygen (fluorine). Ionisation potentials of Th, O and F (Tables 1 and 2) are given in Table 4 for comparison with the experimental data for ThO_2 and ThF_4. For convenience of comparison of theoretical and experimental data (Tables 1 and 2) the theoretical ionisation potentials for thorium, oxygen and fluorine were reduced by 10.66 eV, 15.36 eV and 12.67 eV, such that $I_i^T(Th5d_{5/2}) = E_b^{exp}(Th5d_{5/2})$, $I_i^T(O1s) = E_b^{exp}(O1s)$ and $I_i^T(F1s) = E_b^{exp}(F1s)$. In this case one can see satisfactory agreement of theoretical and experimental results for thorium. Thus, experimental and theoretical spin-orbit splittings $\Delta E_{so}(Th6p)$ and $\Delta E_{so}(Th5d)$ are 7.9 eV and 8.20 eV and 7.1 eV and 6.96 eV respectively (Table 4). The biggest discrepancy was observed for the O2s electrons.

For low binding energies the spin-orbital splitting of inner levels is known to depend weakly on the nature of the atomic neighbourhood. However, as follows from Table 4, $\Delta E_{so}(Th6p)$ differs significantly for ThO_2 (9.0 eV) and ThF_4 (7.2 eV). For thorium oxide and tetrafluoride such difference in spin-orbital splitting cannot be explained by superposition of the Th6p line with the lines of ligands. In this case the shift of the $Th6p_{1/2}$ spin-doublet component would be inverse. Since thorium compounds do not contain uncoupled electrons (diamagnetic), the observed change in the Th6p spectrum is not due to the multiplet splitting. It is also not due to the dynamic effect because it would have been observed in both spectra. The Th6p spectral range can contain extra peaks due to shake up satellites, but they must not exceed ~15% of the basic lines [7].

Also, the extra structure in the O2s-F2s range can not be explained by the presence of ligands in different oxidation states in ThO_2 and ThF_4, because the O1s and F1s XPS line were observed single and 1.4 eV and 2.7 eV (to broad a single chem. state) wide for ThO_2 and ThF_4, respectively [7]. On the basis of the above-mentioned, Th6p electrons were suggested not to be core-like but to participate effectively in the IVMO formation [3,7,9,10].

Table 4. Th, ThO_2 and ThF_4 electron binding energies E_b (eV) from XPS data and theoretical results for Th, O and F atoms

N	$Th(O,F)_{nlj}$	Th		O	F	ThO_2	ThF_4
		Exp.	Theor.[a]	Theor.[b]			
1	Th7s		-5.23				
2	$Th6d_{5/2}$		-5.68				
3	$Th6d_{3/2}$		-5.36			5.8	8.3
4	$Th6p_{3/2}$	16.6	14.82			16.5 23.8	18.4
5	$Th6p_{1/2}$	24.5	23.02			25.5	25.6 30.8
6	Th6s	41.4	43.14			41.9	44.5
7	$Th5d_{5/2}$	85.4	85.40			86.3	88.5
8	$Th5d_{3/2}$	92.5	92.36			93.3	95.5
9	$O(F)2p_{3/2}$			-0.78	4.44		
10	$O(F)2p_{1/2}$			-0.52	4.62	5.8	8.3
11	O(F)2s			16.41	27.42	22.2	29.8
12	O(F)1s			530.2	685.5	530.2	685.5

[a] Theoretical values reduced by 10.66 eV so that $I_i^T(Th5d_{5/2}) = E_b^{exp}(Th5d_{5/2})$ for convenience.

[b] Theoretical values reduced by 15.36 eV for O and by 12.67 eV for F, so that $I_i^T(O1s) = E_b^{exp}(O1s)$ for ThO_2 and $I_i^T(F1s) = E_b^{exp}(F1s)$ for ThF_4.

The schematic of such MOs for the $ThO_8^{12-}(O_h)$ cluster built by the results of non-relativistic X_α-DV [1] calculations and the data of the present work (without taking into account the influence of the OVMOs and the $Th6p_{1/2}$,6s atomic shells) is given in Figure 3(b). Chemical shifts are not shown and the binding energies E_b (eV) are given on the right side. Figure 3(a) presents the binding energies for metallic thorium [11]. The MO schematic in the figure allows qualitative understanding of the O2s spectral structure of ThO_2 (Figure 2), where instead of a single line the two peaks corresponding to the quasi-atomic (a_{2u}, t_{2g}, a_{1g}) and inner valence ($1t_{1u}$) MOs are observed. Similar considerations can be made for the XPS spectra from ThF_4 on the basis of the MO schematic for the $ThF_8^{4-}(D_{4d})$ cluster (Figure 2). In this case the fine XPS spectral structure in the F2s binding energy range can be explained by the IVMO formation from the Th6p and F2s AOs (Figure 2). The data obtained allow to suggest [3] that, like in uranium compounds [3,9], the XPS spectral structure in the Th6p binding energy range reflected the formation of the IVMOs mostly due to the Th6p and O(F)2s electrons from the neighbouring thorium and oxygen (fluorine) atoms.

Partial atomic composition of the outer valence molecular orbitals in ThO_2 and ThF_4

As it was already noted on the basis of theoretical data, the Th5f orbitals could directly participate in formation of filled molecular orbitals. The MO LCAO approximation allows to suggest that the valence band in this case must contain Th5f states (orbital quantum number l = f). The degree of such participation can be estimated on the basis of the OVMO band relative intensity for thorium compounds.

Figure 3. Schematic of energy levels of atomic Th (a) and $ThO_8^{12-}(O_h)$ (b) cluster reflecting ThO_2 structure built by the calculation results [1]. Experimental XPS data for metallic Th [11] (a) and ThO_2 [7] (b) given to the right side.

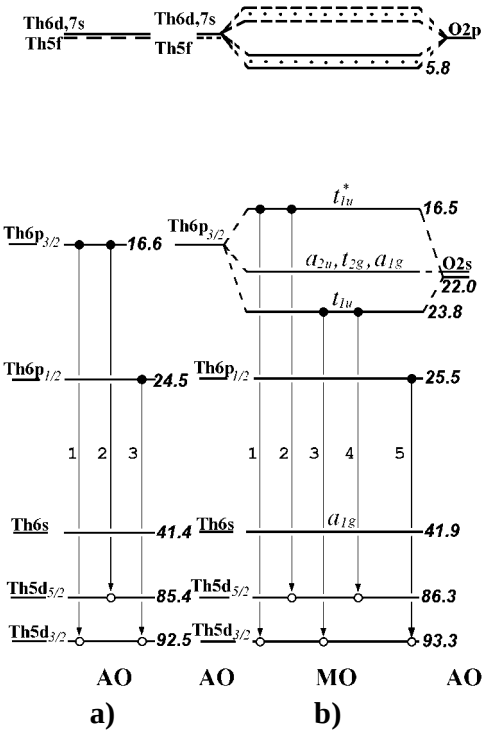

This relative intensity I_{OVMO}^{exp} is the ratio of the OVMO intensity (including the Th5f orbitals) to the IVMO intensity (including the U6p and O(F)2s orbitals). Corresponding theoretical intensities I_{OVMO}^{T} for thorium dioxide and tetrafluoride were calculated using the photoionisation cross-sections [2] as:

$$I_{OVMO}^{T} = \frac{n_{Th5f}\sigma_{Th5f}^{I} + n_{Th6d}\sigma_{Th6d}^{I} + n_{Th7s}\sigma_{Th7s}^{I} + \nu n_{L2p}\sigma_{L2p}^{I}}{n_{Th6p}\sigma_{Th6p}^{I} + \nu n_{L2s}\sigma_{L2s}^{I}} \quad (1)$$

where n_{Thnl} and σ'_{n1} are the number of electrons and corresponding photoionisation cross-section (per 1 electron), ν is the number of oxygen (fluorine) atoms ($\nu = 2$ for ThO_2 and $\nu = 4$ for ThF_4). It was suggested that $\sigma'_{Th5f} \approx \sigma'_{U5f}$. Since all the considered lines were within the 40 eV binding energy range, Eq. (1) does not contain extra corrections by different photoelectron energies.

The I_{OVMO}^{T} thus obtained can be compared with the corresponding experimental relative intensities for ThO_2 and ThF_4 (Table 5). The experimental relative intensities are given in Table 5 for electronic configurations corresponding to the filling numbers n_{Thnl} equal to 0.5, 1.5 and 2 for the Th5f, Th6d and Th7s states respectively. Despite the I_{OVMO}^{exp} measurement error can reach 20%, and the An5f and other valence electrons delocalise during the chemical bond formation (their photoionisation cross-sections decrease), some qualitative conclusions can be made. Indeed, the fact that I_{OVMO}^{exp} (0.35 for ThO_2 and 0.30 for ThF_4) are significantly higher than the corresponding I_{OVMO}^{T} (0.20 for ThO_2 and 0.23 for ThF_4),

Table 5. Theoretical (I^{T}_{OVMO}) and experimental (I^{exp}_{OVMO}) XPS OVMO relative intensities for ThO_2 and ThF_4 for different filling numbers n_{Thnl}

N	Numbers of filling n_{Thnl}			ThO_2		ThF_4	
	n_{Th5f}	n_{Th6d}	n_{Th7s}	I^{T}_{OVMO}	I^{exp}_{OVMO}	I^{T}_{OVMO}	I^{exp}_{OVMO}
1	0	2	2	0.20		0.23	
2	0.5	1.5	2	0.32	0.35	0.31	0.30
3	1	1	2	0.47		0.39	
4	2	0	2	0.75		0.55	
5	1	2	1	0.52		0.42	

can be explained by participation of the Th5f atomic orbitals in formation of the outer valence molecular orbitals. This points to the presence of filled Th5f states in the valence bands of the studied compounds. This is an important, although qualitative, experimental result agreeing with the results of calculations of ThO_2 electronic structure (Figure 1).

Another reason for the increased OVMO intensity may be the admixture of the Th6p and L(O,F)2s states to OVMO due to significant participation of the Th6p and L(O,F)2s electrons in the chemical binding. Indeed, photoemission cross-sections of such electrons are only about 3 times lower than that of the Th5f electrons. However, this suggestion requires further special investigations.

The structure of the X-ray $O_{4,5}$(Th) emission spectra from ThO_2 and ThF_4

The emission spectra reflecting the $Th5d_{5/2,3/2} \leftarrow Th6p_{3/2,1/2}$,np,5f $[O_{4,5}(Th) \leftarrow P_{2,3}, O_{VI}(Th)]$ electronic transitions were observed in the range $60 < h\nu < 85$ eV and in the short-wave region. They overlapped with the absorption spectra [4], which could distort them due to self-absorption (Figure 4). Earlier [4], the long-wave group of lines was suggested to be due to the electronic transitions between the core levels $Th5d_{5/2,3/2} \leftarrow Th6p_{3/2,1/2}$ $[O_{4,5}(Th) \leftarrow P_{2,3}(Th)]$ (Figures 3(a) and 4, Table 6). However, this could not explain the influence of the ligand neighbourhood on the spectral structure and help interpret this structure. Thus, in the present work the Th6p levels were taken into account not to be core levels and to participate in the IVMO formation [3,7,9,10].

The emission spectra studied showed poorly-resolved low-energy bands despite the spectrometer resolution being good enough to resolve the calculated lines in the range 60-76 eV (Figures 3 and 4, Table 6). This could be due to some extra transitions not shown on the schematic (Figure 3), which reflected IVMOs due to the $Th6p_{1/2}$,6s and L2s,2p electrons from thorium and ligand L atoms.

The spectrum of ThO_2 contained eight peaks in the range 63.5-78.0 eV and a small peak at 80.7 eV. Taking into account the above considerations the peaks in the first energy range could be explained by the transitions from the IVMOs, while the last one by the transitions from OVMO to the Th5d level (Figures 3 and 4, Table 6). According to the dipolar selection rule ($\Delta l = 1$ and $\Delta j = 0;1$) the holes on the Th5d level can be filled with only p or (5)f OVMO electrons. This agrees with the calculations [1,7], indicating that OVMO beside the O2p include a significant portion of the Th5f states. Such considerations can be made only under the approximation that the molecular orbitals maintain their partial atomic nature. The considered spectra allow suggestions about the possible contribution of the Th5f states in OVMOs. These data at least do not contradict the suggested participation of the Th5f AOs in formation of MOs, and the presence of filled Th5f states in the valence band, made on the basis of XPS data and theoretical calculations.

Figure 4. X-ray $O_{4,5}$(Th) emission spectra measured at 3 kV (2 mA) reflecting the Th5d ← Th6p,np transitions in ThO_2 (a) and ThF_4 (b) [5,12]

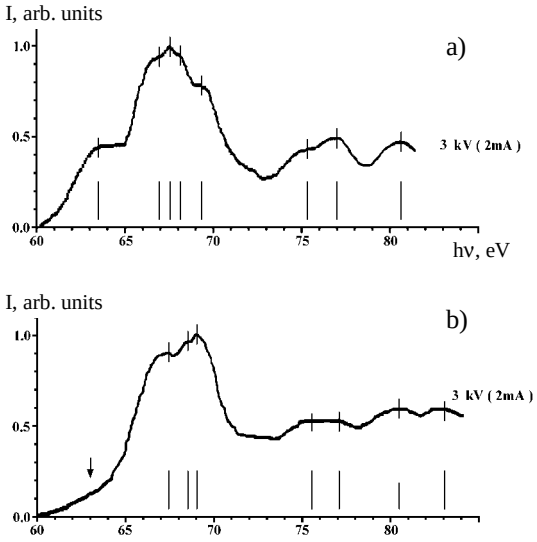

Table 6. X-ray $O_{4,5}$(Th) emission Th5d ← Th6p,np transitions in Th (eV), ThO_2 and ThF_4 on the basis of XPS and XES data

Th			ThO_2			ThF_4*	
Transition	**XPS**	**XES**	**Transition**	**XPS**	**XES**	**XPS**	**XES**
			$5d_{5/2} \leftarrow t_{1u}$	62.9	63.5 66.8	56.7	?
$5d_{3/2} \leftarrow 6p_{1/2}$	68.0	–	$5d_{3/2} \leftarrow 6p_{1/2}$	67.8	67.6 68.1	69.9	69.2 68.3
$5d_{5/2} \leftarrow 6p_{3/2}$	68.8	–	$5d_{5/2} \leftarrow t_{1u}^*$	69.8	69.5	70.1	69.2
			$5d_{3/2} \leftarrow t_{1u}$	69.5	69.5 75.4	67.7	67.2 75.5
$5d_{3/2} \leftarrow 6p_{3/2}$	75.9	–	$5d_{3/2} \leftarrow t_{1u}^*$	76.8	77.0	77.1	77.0
			$5d_{5/2} \leftarrow$ VMO	80.5	80.7	80.2	80.5 83.1
			$5d_{3/2} \leftarrow$ VMO	87.5		87.2	

* Data in approximation of $ThF_8^{4-}(O_h)$ cluster.

In the low-energy spectral region of ThF_4 60-72 eV (as well is in that of ThO_2) a poorly resolved band containing distinctive peaks at 67.2, 68.3 and 69.2 eV was observed. This band in the spectrum from ThF_4 was narrower than in that from ThO_2 mostly due to the absence of an intense low-energy shoulder at 63.5 eV and suppression of the peak at 69.2 eV. As seen from the MO schematic for ThO_2 the extra peak at 63.5 eV can be explained by effective formation of IVMO like a bonding t_{1u} [Figure 3(b)]. This shows a good qualitative agreement of the XPS and XES data on effective participation of the Th6p and O(F)2s shells in IVMO formation. Th atoms in ThF_4 have D_{4d} symmetry. Since the calculations of the $ThF_8^{4-}(D_{4d})$ cluster has not yet been performed, the interpretation of the XES spectrum from ThF_4 was done in approximation of the $ThF_8^{4-}(O_h)$ cluster (Figure 3(b), Table 6).

During the X-ray emission process in thorium compounds, the initial state with a hole in the Th5d shell transits in the final state with a hole in one of the molecular orbitals, while during the formation of the XPS spectrum the system does not have any holes in the initial state and has a hole on one of the core levels in the final state. This fact may result in significant energetic difference between the XPS and XES spectra. Therefore, the comparison of the XPS and XES spectra done in this work was approximate (Table 6). For a more precise and strict comparison special calculations should be undertaken.

The obtained data did not contradict the suggestion on the participation of the Th5f shells in formation of molecular orbitals in ThO_2 and ThF_4 resulting in the presence of the filled Th5f states. The structures of the $O_{4,5}$(Th) emission spectra from ThO_2 and ThF_4 were found to differ significantly and were interpreted only taking into account effective formation of IVMOs, in particular, due to the Th6p and •(F)2s interaction.

Conclusions

On the basis of the X-ray photoelectron (0-~1 000 eV) and X-ray $O_{4,5}$(Th) emission (0-~50 eV) spectral fine structure parameters and results of theoretical calculation of Th, ThO_2 and ThF_4 electronic structures, a study of the Th6p,5f states in ThO_2 and ThF_4 was carried out. The following conclusion were drawn:

- Despite the absence of the Th5f electrons in atomic thorium, the Th5f atomic orbitals can participate in the formation of molecular orbitals in thorium dioxide and tetrafluoride, which results in the formation of the Th5f filled states. This was suggested to be one of the main reasons of the intense X-ray photoelectron spectral bands in the spectra of the outer valence molecular orbitals in the binding energy range 0-~15 eV from ThO_2 and ThF_4 as well as the peaks at ~80 and ~87 eV (Th5d ← Th5f transitions) in the X-ray $O_{4,5}$(Th) emission spectra.

- The structure of the X-ray photoelectron spectra in the binding energy range 15-~50 eV of ThO_2 and ThF_4 reflects the inner valence molecular orbitals formed mostly from the Th6p and O(F)2s electrons. On the basis of the $O_{4,5}$(Th) emission spectral structure parameters, the evidence of effective formation of the inner valence molecular orbitals was obtained.

Acknowledgements

This work was supported by the RFBR fund and ISTC grant No. 1358.

REFERENCES

[1] V.A. Gubanov, A. Rosen, D.E. Ellis, *J. Inorg. Nucl. Chem*., 41, 975-986 (1979).

[2] J.H. Scofield, *J. Electron. Spectr. Relat. Phenom*., 8, 129-137 (1976).

[3] Yu.A. Teterin, S.G. Gagarin, *Russian Chemical Reviews*, 65, 10, 825-847 (1996).

[4] I.I. Lyahovskaya, V.M. Ipatov, T.M. Zimkina, *Journal of Structural Chemistry*, 18, 668-672 (1977) (in Russian).

[5] Yu.A. Teterin, V.A. Terekhov, A.Yu. Teterin, I.O. Utkin, A.M. Lebedev, L.J. Vukchevich, *Dokl. AN*. 358, 2, 637-640 (1998) (in Russian).

[6] Yu.A. Teterin, V.A. Terekhov., A.Yu. Teterin, K.E. Ivanov, I.O. Utkin, A.M Lebedev, L. Vukchevich, *J. Electron. Spectr. Relat. Phenom.*, 96, 229-236 (1998).

[7] Yu.A. Teterin, A.S. Baev, S.G. Gagarin, V.D. Klimov, *Radiohimiya*, 27, 1, 3-13 (1985) (in Russian).

[8] B.W. Veal, D.J. Lam, *Phys.Rev. B*., 10, 12, 4902-4908 (1974).

[9] Yu.A. Teterin, V.M. Kulakov, A.S. Baev, N.B. Nevzorov, I.V. Melnikov, V.A. Streltsov, L.G. Mashirov, D.N. Suglobov, A.G. Zelenkov, *Phys. Chem. Minerals*, 7, 151-158 (1981).

[10] Yu.A. Teterin, A.S. Baev, "Questions of Atomic Science and Technology", *Ser.: General and Nuclear Physics*, 4, 33, 53-54 (1985) (in Russian).

[11] J.C. Fuggle, A.F. Burr, L.M. Watson, D.Y. Fabian, W. Lang, *J. Phys. F. – Metal Phys*., 4, 2, 335 (1974).

[12] Yu.A. Teterin, V.A. Terekhov., A.Yu. Teterin, I.O. Utkin, A.M. Lebedev, L. Vukchevich, *J. Struct. Chem.*, 39, 6, 1 052-1 058 (1998).

X-RAY PHOTOELECTRON SPECTROSCOPY STUDY OF RUTHENIUM IONS AFTER EMISSION FROM THE NUCLEAR FUEL

Yu.A. Teterin,[1] **C. Ronneau,**[2] **R.M. Polevoi,**[1] **V.F. Shikalov,**[1]
P. Froment,[2] **J. Cara,**[2] **I.O. Utkin,**[1] **A.S. Nikitin,**[1] **K.E. Ivanov**[1]
[1]Russian Research Centre "Kurchatov Institute"
Moscow, Russia
[2]University Catholique de Louvan
Louvain-la-Neuve, Belgium

Abstract

Dependence of the volumetric radioactivity of ^{106}Ru (10^{-10} Ci/m^3) from the "hot" particles collected on the Petryanov filter in a ventilation channel of the IV unit of Chernobyl nuclear power plant (CNPP) upon the time and the ambient temperature from May to July 1987 was obtained. It was found that from 13-15 June there was a strong throw-out of the ^{106}Ru radioactivity. The mechanism of such throw-out is discussed. Under laboratory conditions the sublimation of particles containing ^{101}Ru and ^{238}U ions in the air was carried out at 1 500°C. The particles were accumulated on aluminium foil in a manifold. This allowed to study the mechanism of the formation of the "hot" particles. Quantitative elemental and ionic analysis of initial nuclear fuel, burnt-out fuel and products condensed from gas was performed with X-ray photoelectron spectroscopy.

Introduction

Radioactivity of the "hot" particles resulting from the accident at Chernobyl NPP is highly determined by the contents of isotopes, in particular ruthenium. The understanding of formation and deposition of radioactive particles after the accident is important for successful liquidation of the consequences. For the rehabilitation of the environment it is important to understand the physical and chemical states of the radionuclides. Therefore it is necessary to analyse such processes on the basis of the data obtained in laboratory simulation [1,2].

This work presents the results of analysis of the yield of "hot" ruthenium-containing particles from the IV unit of CNPP during May-July 1987. The quantitative X-ray photoelectron spectroscopy data on the ionic composition of Ru and U in the initial mixtures of ruthenium and nuclear fuel (UO_2), in products of short high-temperature heating (NPP accident simulation) and "hot" particles condensed from the environment are also given. X-ray photoelectron spectroscopy proved to be an effective method for physical and chemical analysis of radionuclides in the environment [3-6]. Therefore, this method was widely applied in researches [5-8].

Experimental

The radioactivity of the "hot" particles collected on a special fibrous filter for radioactive aerosols, the so-called Petryanov filter (10^{-10} Ci/m^3), was measured with a semiconductor γ-spectrometer. The air temperature at the IV unit of the CNPP and temperature in two points was also determined: T_1 being the temperature inside the fuel and T_2 the temperature inside the outer wall area of the reactor. From the γ-spectra, both absolute and relative contents of γ-emitting radionuclides in the collected samples were obtained. From these data it follows that by the beginning of March 1987, the main γ-activity was determined by ^{95}Zr, ^{95}Nb, ^{106}Ru, ^{134}Cs, ^{137}Cs, ^{90}Sr and ^{144}Ce. The share of ^{106}Ru in the majority of samples exceeded 40%, and in some cases was close to 100%.

The laboratory generator for preparation of "hot" particles containing ^{101}Ru and ^{238}U and tablets formed during heating of UO_2 fuel containing ruthenium is described in [1]. Emission temperature during the experiment is usually 1 000-1 500°C in the air and 1 500-2 100°C in argon. The "hot" particles formed in the graphite oven were extracted by air or argon flow. The sublimation time of particles varied from 1 to 2 minutes. In case of formation of the "hot" particles, they were transferred to the second quartz oven to be able to oxidise in air or argon. Formation of the "hot" particle phases was performed after the sublimation in the air at 1 500°C and in argon at 1 900°C. After formation the "hot" particles were collected in a cascade seven-stage manifold at the exit of the first oven after sublimation, or at the exit of the second oven after phase formation. A filter of about 0.2 microns thickness was located at the exit of the manifold [1]. The initial fuel tablet was prepared by mixing the powders of $UO_{2.06}$ and RuO_2 (5 wt.% of Ru). The mixture was carefully homogenised, and the tablets (0.2 g) of 4 mm diameter and 2 mm width were pressed at 4.7 T/sm^2.

- *Sample I*. Initial tablet with the surface cleaned for 5 sec with Ar+ ions (U = 4 kV; I = 30 μA).
- *Sample II*. Powder formed after the 2 minute heating of the initial tablet at 1 500°C in the air. The surface was cleaned by Ar+ ions for 5 sec (U = 4 kV; I = 30 μA).
- *Sample III*. "Hot" particles condensed on aluminium foil obtained after the 2 minute heating of Sample I at 1 500°C in the air. The particles were transferred in the airflow from the first oven and formed in the air at 700°C for 13 seconds.

X-ray photoelectron spectra were measured on the electrostatic spectrometer HP 5950A using monochromatised $AlK_{\alpha 1,2}$ X-rays (1 486.6 eV) under 1.3×10^{-7} Pa at room temperature. Electron binding energies E_b (eV) are given relative to E_b of C1s electrons from hydrocarbons on the sample surface accepted to be 285.0 eV. The errors in the binding energies and the line widths did not exceed 0.1 eV, and those of the relative intensities did not exceed 10%. The samples were studied as tablets (Sample I), as powder ground in an agate mortar pressed into indium on the titanium substrate (Sample II) and as "hot" particle condensed on the aluminium foil (Sample III). Quantitative elemental and ionic analysis was performed using the following equation: $n_i/n_j = (S_i/S_j)(k_j/k_i)$ where n_i/n_j is the relative concentration of the studied atoms, S_i/S_j the relative intensity (area) of the inner electron lines and k_j/k_i the experimental relative coefficient of sensitivity. In this work the following coefficients were used: 1.00 (C1s), 2.8 (O1s), 8.6 ($Ru3d_{5/2}$), 5.2 ($Ru3p_{3/2}$) and 18.4 ($U4f_{7/2}$). For decomposition of the XP spectra and peak fitting the method of the differential moments was used.

Results and discussion

Radioactivity measurements at IV unit of CNPP

In the present work the results of the measurement of volumetric activity at the IV unit of CNPP due to ^{106}Ru ($T_{1/2}$ = 1 year) and mean air temperature above the IV unit (T,°C), inside the fuel-containing masses (T_1,°C) and inside the reactor walls (T_2,°C) are presented (Figure 1). The concentration of radioactive particles in the "shelter" from April to June 1987 increased by two orders of magnitude. The share of radioactive ruthenium changed from 0.5 to 0.99. Over the same period the concentration of radioactive aerosols at IV unit of CNPP changed by about an order of magnitude. The share of ruthenium oscillates randomly about the average value of 0.2. From 15 April to 13 June 1987 the radioactivity of particles in the "shelter" varied in phase with temperature. From 16 June to 30 July the temperature changed weakly, and the radioactivity of ruthenium dropped approximately seven times. From 1 August to 1 October an in-phase course of temperature and concentration was observed again.

The results obtained here for ^{106}Ru are presented as histograms in Figure 1(a). The volumetric radioactivity of ^{106}Ru grows while the temperature of the air increases [Figure 1(b)]. In contrast to the previous data over the period 13-15 June, a sharp surge of ^{106}Ru volumetric radioactivity at a rather small increase of temperature was observed. To explain this phenomenon we supposed the following. The penetration of oxygen inside the damaged unit causes the oxidation of ruthenium to RuO_4. This oxide melts at 25°C and sublimes at 27°C [9]. Therefore the evaporated RuO_4 from the fuel heated to about 100°C [T_1, Figure 1(c)] moves toward the cooler layers both by diffusion and the airflow, afterwards condensing at this location. As the temperature grows, the upper layers dries up. As a result, the evaporation of aerosols with increased contents ^{106}Ru takes place. When the air temperature comes closer to a boiling (sublimation) temperature of RuO_4, a sharp throw-out of RuO_4 stored for winter in cold layers occurs. This gaseous oxide can partially be sorbed on "cold" dust above the damaged unit. This fact may explain the increased contents ^{106}Ru on filters. The main part of RuO_4 collected during the winter was released in the atmosphere. The further air temperature rise by 13-15 June 1987 was not accompanied by any throw-out of RuO_4. However volumetric activity of ^{106}Ru correlates with the temperature in this season. That indirectly confirms the explanation offered in the present work, that ^{106}Ru accumulates in surface layers of fuel at low temperature and is released after the temperature rises.

Unfortunately the evaluation of the total ^{106}Ru yield during the time when the air temperature was close to RuO_4 boiling temperature is impossible since there are no data about the Petryanov filter's capture effectiveness for gaseous RuO_4 and RuO_4 in "hot" particles.

Figure 1. Changes of ^{106}Ru volumetric radioactivity (10^{-10} Ci/m^3) of the "hot" particles collected on the Petryanov filter in a ventilation channel of the IV unit of CNPP, in May-July 1987 (day)

(a) A temperature variation T(℃) of free air at IV unit of CNPP in this period
(b) Temperature of fuel-containing mass T_1 (℃) and reactor wall T_2 (℃) in this period (c)

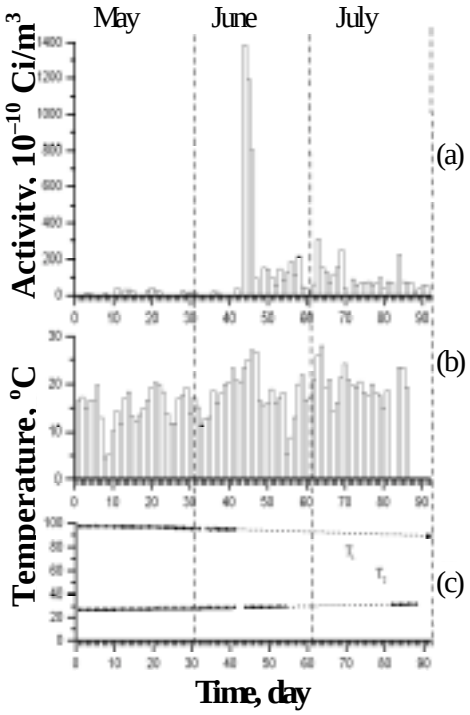

The study of ^{101}Ru emission from the fuel under the influence of temperature under laboratory conditions

The electronic configuration of ruthenium is $4d^75s^1$. It forms oxides and compounds with the formal oxidation state from I up to VIII. Oxides RuO_2, RuO_3 and RuO_4 are well known. Ru_2O_3 exists only in hydrated state $Ru_2O_3 \times nH_2O$. RuO_4 exists as yellow (or brown) chips melted at 25-25.5°C and sublimed at 27°C [9]. The most dangerous are ^{103}Ru ($T_{1/2}$ = 39.8 days) and ^{106}Ru ($T_{1/2}$ = 1 year) isotopes. Ruthenium is a refractory solid silvery metal with a melting point of T_m = 2 250°C. At 450°C it oxidises to almost non-volatile RuO_2 whose thermal dissociation starts at 930-950°C. RuO_4 forms when fine-dispersed ruthenium is heated with oxygen at 700°C or with NO_2 at 275°C [9,10].

The diversity of ruthenium oxidation states hinders the XPS identification of reaction products since only 50 Å surface can be studied. However this method allowed the study of different ruthenium oxides [10], and it was shown that on the surface both ruthenium and its oxides of different oxidation states [Ru (280 eV), RuO_2 (280.7 eV), $RuO_2 \times H_2O$ (281.4 eV), RuO_3 (282.5 eV), RuO_4 (283.3 eV), $RuOCO_3$ (the E_b values of the $Ru3d_{5/2}$-electrons are given in parentheses)] can exist. When the surface is cleaned with Ar+, a considerable change in the surface composition occurs. Despite this, RuO_2 was shown to have stable RuO_3 on its surface as well as $RuOCO_3$. The same process was observed for a single-crystal RuO_2. It should be noted [10] that at 1 000°C and higher in a gas phase RuO_3 dominates, at ~800°C, as does RuO_4. At 100°C RuO_2 is connected with H_2O and/or CO_2.

In this work the following samples were studied with X-ray photoelectron spectroscopy: initial fuel tablet (Sample I) with the impurity of ruthenium, powder (Sample II) formed after the heating of the initial tablet at 1 500°C on the air for 2 minutes and "hot" particles (Sample III) containing uranium and ruthenium oxides condensed on. RuO_{2+x} was also studied. XP spectra of electrons from different shells of uranium, ruthenium and oxygen from the studied samples are complicated (Figures 2,3). This is explained by the complex ionic structures of these elements in the studied samples. It was suggested that in the studied samples only the ions U(IV), U(VI), Ru(IV) and Ru(VI) presented. Using such an approximation the decomposition of spectral lines and discussion of the obtained results was conducted. The electron binding energies of different ions are: 380.9 eV [U(IV)], 381.9 eV [U(VI)], 280.8 eV [Ru(IV)] and 282.7 eV [Ru(VI)]. The data for ruthenium are consistent with results [10], taking into account that the $Ru3d_{5/2}$ binding energy for metallic Ru at our calibration is 280.0 eV. As it follows from the previous results, ruthenium as well as uranium does not have stable phases of individual oxides, but presents as an equilibrium composite phase containing ions of a different oxidation states.

Figure 2. X-ray photoelectron spectrum of the Ru3d-electrons from the "hot" particles (Sample III)

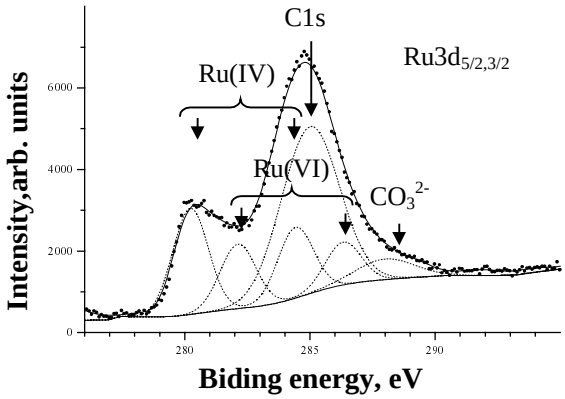

Figure 3. X-ray photoelectron spectrum of the U4f-electrons from the "hot" particles (Sample III)

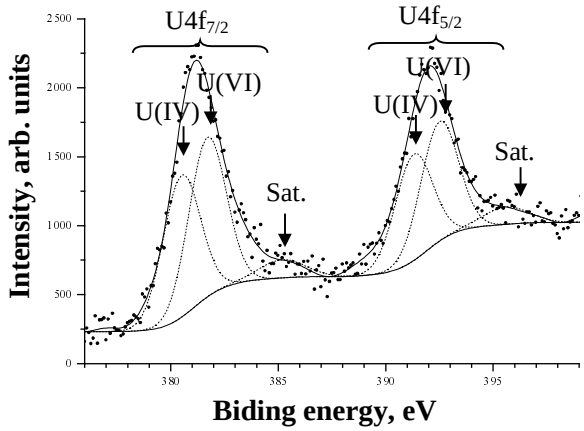

The XP spectrum of the Ru3d-electrons from RuO_{2+x} is complicated. This is explained by the fact that in this energy region the following lines are observed: 280.8 eV (Ru(IV)$3d_{5/2}$), 282.7 eV (Ru(VI)$3d_{5/2}$), 285.0 eV (C1s), 285.0 eV (Ru(VI)$3d_{3/2}$), 286.9 eV (Ru(VI)$3d_{3/2}$) and 289.0 eV [C1s(CO_3^{2-})], where C1s and C1s(CO_3^{2-}) electrons are from hydrocarbons and carbonate group respectively. The experimental intensity ratio of the $Ru3d_{5/2}$ to the $Ru3p_{3/2}$ electron lines is 1.5. The surface contains 66 at.% of Ru(IV) and 34 at.% of Ru(VI). The O1s spectrum consists of three lines at 529.3 eV (RuO_2), 530.7 eV (RuO_3) and 533.1 eV (H_2O). In the spectrum of low-energy electrons of RuO_{2+x} at 0.4 eV, a narrow line weakly participating in the chemical bonding Ru4d-electrons is observed. Its intensity is proportional to the number of such electrons and is a measure of the ruthenium oxidation state.

The spectral structure of the Ru3d-electrons from the studied samples (I-III) is in many respects comparable to the corresponding structure of the RuO_{2+x} spectrum (see, for example, Figure 2). Since Sample III is amorphous, there is a weak shake-up satellite structure in the spectrum of U4f-electrons (Figure 3). The lines of U5f (1.9 eV for UO_2 [3]) and Ru4d (0.4 eV) electrons are overlapped and observed as a wide line.

In this work it was found that the surface of the initial fuel tablet contained 11 at.% of Ru and 89 at.% of U. This fact agreed with the data of the chemical analysis (5 wt.% of Ru). The ionic composition of the surface was also determined: 78 at.% of U(IV) and 22 at.% of U(VI), 75 at.% of Ru(IV) and 25 at.% of Ru(VI). After the surface was cleaned with argon ions, the content of U(VI) ions essentially decreased, and the ionic composition of ruthenium did not change, while its contents increased slightly. Although the initial fuel tablet was in the air at a room temperature for several months, ruthenium did not diffuse to the surface.

After the fuel tablet was heated to 1 500°C in the air, all ruthenium transited in the gas phase. Diffusing to a surface under the influence of temperature and interacting with oxygen, ruthenium forms volatile oxides and escapes the surface. After this process there are no more U(VI) ions in the sample, but there are uranium ions of oxidation states less than U(IV) in oxide. In this paper they are formally referred to as U*(IV) ions, and Sample II contains 64 at.% of U*(IV), 32 at.% of U(IV) and 4 at.% of U(VI). The formation of U*(IV) ions at such heating agrees with the data for the fuel from IV unit of CNPP [5]. This is explained by the shortage of oxygen in such processes. It should be noted that the initial fuel tablet has practically the same ionic composition after the heating in the argon atmosphere. However in this case there must be an accumulation of Ru(IV) ions on the fuel surface. This is explained by the fact that in the argon atmosphere the volatile oxides of ruthenium do not form and Ru remains on the surface.

The condensed phase of aerosols and particles (Sample III) contains 20 at.% of U and 80 at.% of Ru with ionic composition: 52 at.% [U(IV)], 48 at.% [U(VI)], 62 at.% [Ru(IV)] and 38 at.% [Ru(VI)]. The cleaning of the sample surface with argon ions practically does not change the uranium/ruthenium ratio. However, the noticeable increase of the U(VI) contents and the decrease of the number of Ru(VI) ions was observed. After the bombardment with argon ions, considerable decreasing of U(VI) ions contents in the fuel samples was always observed. On the basis of this fact it is possible to conclude that the condensed phase of aerosols contains U(VI) ions. As it follows from the obtained data, the uranyl compounds with CO_3^{2-} groups in equatorial planes form on the surface of the condensed phase. However after the surface is cleaned with argon ions, the reference line at 289.0 eV attributed to carbonates in the spectrum of the C1s electrons is not observed. This can be explained by the fact that uranyl compounds with carbonate groups form only on the sample surface.

Thus it was found that as a result of strong heating of the fuel in the air, the particles condensing in the environment form. These particles contain a significant amount of ruthenium as a mixture of nuclear fuel and stable oxides RuO_2 and RuO_3, and also possibly uranyl compounds such as $Ru(UO_2)O_3$.

Acknowledgements

This work was supported by INTAS and RFBR.

REFERENCES

[1] V. Tinant, P. Froment, J. Vanbegin, J. Cara, C. Ronneau, *Radiochimica Acta*, 79, 51 (1997).

[2] C. Ronneau, J. Cara, A. Rimski-Korsakov, *J. Environ. Radioactivity*, 26, 63 (1995).

[3] Yu.A. Teterin, V.M. Kulakov, A.S. Baev, *et al*., *Phys. Chem. Minerals*, 7, 151 (1981).

[4] Yu.A. Teterin, A.S. Baev, K.E. Ivanov, L.G. Mashirov, D.N. Suglobov, *Radiokhimiya*, 38, 4, 365 (1996) (in Russian).

[5] A.S. Baev, Yu.A. Teterin, K.E. Ivanov, A.Yu. Teterin, S.A. Bogatov, *Radiokhimiya*, 39, 2, 171 (1997) (in Russian).

[6] Yu.A. Teterin, A.S. Baev, Yu.A. Teterin, K.E. Ivanov, L.G. Mashirov, D.N. Suglobov, *Radiokhimiya*, 39, 2, 177 (1997) (in Russian).

[7] V.I. Nefedov, Yu.A. Teterin, A.M. Lebedev, *et al*., *Inorganic Chimica Acta*, 273, 1-2, 234 (1998).

[8] Yu.A. Teterin, V.I. Nefedov, A.Yu. Teterin, A.M. Lebedev, A.P. Dementiev, I.O. Utkin, M. Bubner, T. Reich, S. Pompe, K.H. Heise, H. Nitsche, *Journ. Inorgan. Chem*., 44, 595 (1999) (in Russian).

[9] Gmelins Handbuch der Anorganischen Chemie Ruthenium (System Nummer 63), Verlag Chemie GMBH – Weinheim/Bergstr, 1970, 586 s.

[10] K.S. Kim, N. Winograd, *J. Catalysis*, 35, 66-72 (1974).

X-RAY ABSORPTION STUDIES OF Zn-DOPED CEMENT PHASES

Caterina Tommaseo, Michael Kersten
Geoscience Institute, Johannes Gutenberg University
D-55099 Mainz, Germany

Abstract

Cement phases are often used for the solidification/stabilisation of heavy metal-containing waste. The extended X-ray absorption fine structure (EXAFS) method helps to explain the mechanism of chemical zinc (Zn) incorporation. We demonstrate that zinc is incorporated into CSH solid solution in tetrahedral co-ordination replacing the “bridging tetrahedra” in fragments of Si_3O_9H silicate chains.

Introduction

Zinc is known to interact chemically with cement during curing, leading to retardation of the hydration but acceleration of the setting. The exact mechanism of these processes is still a matter of debate, although a considerable number of papers have been published on the characterisation of the binding states, the chemical and physical mechanisms of interaction and the leaching mechanisms. Calcium and zinc dissolved in the highly alkaline cement pore solution initially form a new calcium zincate hydrate phase ($CaZn_2(OH)_6{\cdot}2H_2O$). However, this intermediate Zn-phase vanishes in X-ray diffractograms (XRD) within a few days [1]. Zinc seems to be chemically bound into the bulk of the formed calcium silicate hydrate (CSH) phases. From macroscopic observations on exchange reactions in solution, Zn^{2+} appears to replace Ca^{2+} in octahedral position [2]. EXAFS was selected as a method to elucidate the mechanism of zinc incorporation.

CSH is basically considered a disordered solid solution of two end-members, one of which is related to 1.4 nm tobermorite and the other to that of jennite [3-5]. Relative to the ordered Si_3O_9H silicate chain structure, many or all of the bridging tetrahedra can be absent in the CSH gel phase. Richardson and Groves [6,7] present the following general formula (1) for such CSH phases:

$$\left\{ Ca_{2n}H_w\left(Si_{1-a}R_a^{[4]}\right)_{(3n-1)}O_{(9n-2)} \right\}\cdot Y^{c+}_{\frac{a}{c}(3n-1)}\cdot(OH)_{w+n(y-2)}\cdot Ca_{\frac{n}{2}y}\cdot m(H_2O) \qquad (1)$$

The part in brackets represents a “tobermorite-like core” consisting of a highly disordered layer structure comprising finite silicate chains of average length $3n - 1$. In immature CSH gels, dimer ($n = 1$) is the most abundant silicate species, while in mature cements, these are linked by “bridging” tetrahedra to form mainly pentamer ($n = 2$) and higher polymers. R stands for a cation in tetrahedral co-ordination, replacing silicon in bridging tetrahedra. Y is an interlayer (“zeolithic”) cation (additional to Ca^{2+}) of c+ valence in octahedral position, charge balancing the R substitution for Si. The parameter a follows from the constraint that there are only $n - 1$ bridging tetrahedra, i.e. $0 \le a((n - 1)/(3n - 1))$ (for pentameric chains, $n = 2$ and $a < 0.2$). The parameter y can be regarded as the amount of the “interlayer” calcium (and/or similar cation and hydroxyl ions) exceeding the tobermoritic Ca/Si ratio (thus moving towards formation of the jennite-like structure according to Taylor [5], or build-up of internally bound portlandite moieties [8]. According to Richardson and Groves [6], the parameter w is constrained by values of n and y such as if $0 \le y \le 2$ then $n(2 - y) \le w \le 2n$, or if $2 \le y \le 4$ then $0 \le w \le 2n$, and if $4 \le y \le 6$ then $0 \le w \le n(6 - y)$.

Methods

ZnO was thoroughly mixed with pure Ca_3SiO_5 (the major cement clinker mineral) at a fixed Zn:Ca molar ratio of 1:10. Subsamples of 2.5 g of this pure Al-free cement formulation were cured by mixing with water at a s/w ratio of 1:1 in glass vials under Ar for time intervals of 8 h, 1, 3, 7, 14, 28 and 100 days. At these times the reaction was immediately stopped by smashing the vials, grinding the hardened product under ethanol, subsequent rinsing with acetone over a glass filter funnel and pouring Ar through the filter cake on the funnel until dryness. The water-free samples were kept under Ar in glass vials until analysis. The XRD results showed the presence of portlandite, tricalcium silicate and calcium zincate as the only detectable crystalline phases.

EXAFS energy versus absorbance spectra at the Zn K-edge was measured at Hamburg National Laboratory (DESY) on beam line A1 in transmission mode at room temperature. EXAFS spectra were collected using a Si(111) double crystal monochromator, which provided energy resolution of 1.5 eV

at the Zn K-edge (9 659 eV) for a beam height of ca. 1 mm. Energy was calibrated using Zn metal foil at the Zn K-edge. Incident beam intensity was monitored using an ionisation chamber filled with nitrogen. EXAFS spectra were normalised in absorbance using polynom and spline functions and recalculated into k space (k represents the photoelectron momentum). The energy where k = 0 ($E_{k=0}$) was always chosen as the halfway point of the absorption step. The k^3-weighted EXAFS was Fourier transformed (FT) over the 3-14 $Å^{-1}$ range using a Kaiser window in order to minimise termination effects [9]. The modulus of the Fourier transform (FT) shows the various atomic shells contributing to EXAFS. The last step of data analysis consists of back-transforming (FT^{-1}) a selected region of the radial distribution function (RDF). The structural parameters of the various shells around zinc (their average distance to zinc, R, their average number of atoms, N and the corresponding Debye-Waller type factor, σ) are obtained through non-linear least-square fits of this FT^{-1}, using zincite, calcium zincate hydrate and calcium zinc silicate hydrate phases as experimental standards and as theoretical standards, calculated with the FEFF code [10].

Results

ZnO reacts initially to a calciumzincate phase. After 14 days, both ZnO and calciumzincate phases are no more detectable by XRD analysis. The only crystalline phases left in the respective XRD spectra (Figure 1) are portlandite and diminishing C_3S. It is impossible to get information by XRD analysis about how zinc is ultimately intercalated in the CSH phase.

Spectra fits indicate that the zinc cation is tetrahedrally co-ordinated with four oxygen atoms at a mean distance of 1.975 Å up to seven days. The Debye-Waller factor, however, showed a strong time dependence for the Zn-O and Zn-Zn co-ordination shells with decreasing zincite phase during reaction. The Debye-Waller factor rises with time up to seven days according to a $\sqrt{t}$-relationship, which indicates first-order reaction kinetics [Figures 2(a), 2(b)]. The increase of the Debye-Waller factor can be related to a decreasing zincite phase and hence an increasing dispersion of Zn-O distances towards the distorted zinc tetrahedron in the new phase. After 14 days, when both zincite and calcium zincate hydrate phase are no longer detectable by XRD, the zinc cation remains tetrahedrally co-ordinated with a slight decrease of 0.02 Å of the Zn-O distance as shown in Figure 3. The amplitude of the second peak in EXAFS spectra corresponding to the Zn-Zn absorber-backscatterer distance (3.20 Å) decreases, and finally disappears after 14 days, when both ZnO and the secondary zincate phase are no longer detectable by conventional XRD analysis. This loss of the second shell in EXAFS and the simultaneous increase of the Debye-Waller factor suggests a degradation of the short-range order and hence a dispersion of Zn into the CSH lattice [Figures 2(c), 2(d)].

In a second step, with the help of theoretical and experimental phase and amplitude functions of the crystalline Ca-Zn silicate phases, it was possible to fit the second peak corresponding to a Zn-Si distance, resulting in a mean Zn-Si distance of 3.24 Å (Figure 4). This distance agrees with the mean Zn-Si distances measured in the Ca-Zn silicate reference phase clinohedrite ($CaZnSiO_4 \cdot H_2O$), in which the zinc tetrahedron also acts as a bridging tetrahedron [11].

Discussion

The results of (i) the XRD/EXAFS analyses, (ii) the stoichiometric reasoning including the relationships between reactants and products and (iii) application of Eq. (1), are all together evidence that zinc is incorporated into CSH by solid solution in tetrahedral co-ordination acting as bridging tetrahedron, rather than in the octahedral calcium positions, as it has often been claimed.

In both 1.4 nm tobermorite and jennite, the silicon tetrahedra chains are linked at intervals of three tetrahedra. Two of them share oxygen atoms with Ca-O octahedra; the third one may be called a "bridging tetrahedron". Our hypothesis is that the latter is probably replaced by a distorted zinc tetrahedron, $ZnO_2(OH)_2^{4-}$. Formal application of Eq. (1) at a = 0.2 and c = 2 for Zn^{2+} leads to a possible pentameric tobermorite-type stoichiometry, $(Ca_4H_4ZnSi_4O_{16})Y_{0.5}\cdot 6(H_2O)$. The exchange position Y can be occupied with either ½ Ca^{2+} or ½ Zn^{2+}, respectively, or both ions at a relatively low pH. The EXAFS data, showing a slight decrease of the Zn-O distance, indicate replacement of the bridging silicate tetrahedra by distorted $ZnO_2(OH)_2^{4-}$ tetrahedra rather than any substitution of Ca^{2+} by Zn^{2+} in interlayer octahedral positions. Using Eq. (1) with n = 2, w = 4 and y = 0, a pentameric Zn-substituted tobermorite-like compound can be described by a $\{Ca_4H_4Si_4O_{14}Zn(OH)_2\}(H_20)$ formula. For a Zn-substituted jennite-like CSH compound with n = 2, y = 6 and w = 0, the following formula $\{Ca_4Si_4O_{14}Zn(OH)_8Ca_6\}(H_2O)_m$ appears to be preferable, reflecting incorporation of hydroxyl and calcium ions in the interlayer.

During the initial retardation process, surface formation of the zincate phase obviously prevents the necessary material transport for the hydration of C_3S [12]. The hydration process, however, can be accelerated again once the solid solution process reverses the zincate formation in the late period of hydration. Formation of bridging tetrahedra by incorporation of zinc then acts to increase silicate chain polymerisation and, hence, ultimately the setting process.

Acknowledgements

It is a pleasure to thank Carl A. Francis, Harvard University, for kindly providing a clinohedrite sample (HMM# 114681) from the type locality Franklin, Sussex County, NJ, USA. We gratefully acknowledge the provision of beam time at stations X1.1 and A1 at HASYLAB/DESY, the help by operators at DESY and especially the support of Larc Tröger, Klaus Attenkofer, Edmund Welther and Stefan Mangold. We would like to thank the DFG for its financial support (Ke 508/5-1).

REFERENCES

[1] W. Lieber and J. Gebauer, "Intercalation of Zinc into Calcium Silicate Hydrates", *Zement-Kalk-Gips*, 4, 161-164 (1969).

[2] S. Komarneni, E. Breval, D.M. Roy and R. Roy, "Reactions of Some Calcium Silicates with Metal Cations", *Cem. Concr. Res*. 18, 204-220 (1988).

[3] H.F.W. Taylor, "Proposed Structure for Calcium Silicate Hydrate Gel", *J. Am. Ceram. Soc.*, 69, 464-467 (1986).

[4] H.F.W. Taylor, "Tobermorite, Jennite and Cement Gel", *Z. Kristallogr*., 202, 41-50 (1992).

[5] H.F.W. Taylor, A discussion of the papers "Models for the Composition and Structure of Calcium Silicate Hydrate Gel in Hardened Tricalcium Silicate Pastes" and "The Incorporation of Minor and Trace Elements into Calcium Silicate Hydrate Gel in Hardened Cement Pastes" by I.G. Richardson and G.W. Groves, *Cem. Concr. Res*., 23, 995-998 (1993).

[6] I.G. Richardson and G.W. Groves, "The Incorporation of Minor and Trace Elements into Calcium Silicate Hydrate (C-S-H) Gel in Hardened Cement Pastes", *Cem. Concr. Res.*, 23, 131-138 (1993).

[7] I.G. Richardson and G.W. Groves, "Models for the Composition and Structure of Calcium Silicate Hydrate (C-S-H) Gel in Hardened Tricalcium Silicate Pastes", Proc. of the 10th International Congress on the Chemistry of Cement in Göteborg, Sweden (1997).

[8] K. Fuji and W. Kondo, "Estimation of Thermochemical Data for Calcium Silicate Hydrate", *Comm. Amer. Ceram. Soc.*, C220-221 (1983).

[9] D. Bonnin, D. Kaiser, C. Fretigny and J. Desbarres, "Depouillement des spectres d'absorption X sur micro-ordinateur IBM-PC", in *Structures fines d'absorption des rayons X en chimie. Vol. 3: Logiciel d'analyse de spectres d'absorption X sur IBM-PC*, H. Dexpert, A. Michalowicz and M. Verdageur, eds., ESPCI, Orsay-Garchy, pp. 1-32 (1988).

[10] J.J. Rehr, Alberts S.I. Zabinsky, *Phys. Rev. Lett.*, 69, 3397 (1992).

[11] Cl.C. Venetopoulos and P.J. Rentzeperis, "Redetermination of the Crystal Structure of Clinohedrite, $CaZnSiO_4 \cdot H_2O$", *Z. Krist.*, 144, 377-392 (1976).

[12] Yousuf, *et al*., "The Interfacial Chemistry of Solidification/Stabilization of Metals in Cement and Pozzolanic Material Systems", *Waste-Management*, 15, 137-148 (1995).

Figure 1. XRD spectras of the Zn-doped samples at different reaction times. After 14 days the reactants zincite (ZnO) and tricalcium silicate (C_3S) and the secondary calcium zincate hydrate phase (CHZ) disappear.

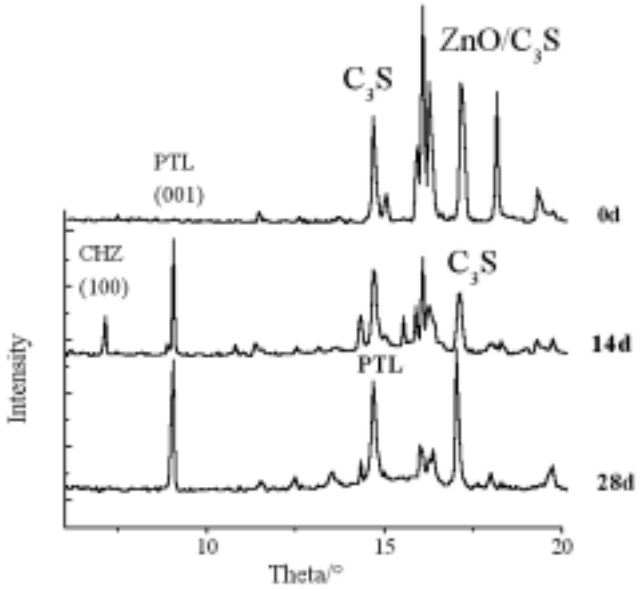

Figure 2. Debye-Waller factor (σ) of the Zn-O co-ordination shell versus reaction time at room temperature (a,b) and Debye-Waller factor (σ) of the Zn-Zn co-ordination shell versus reaction time at room temperature (c,d)

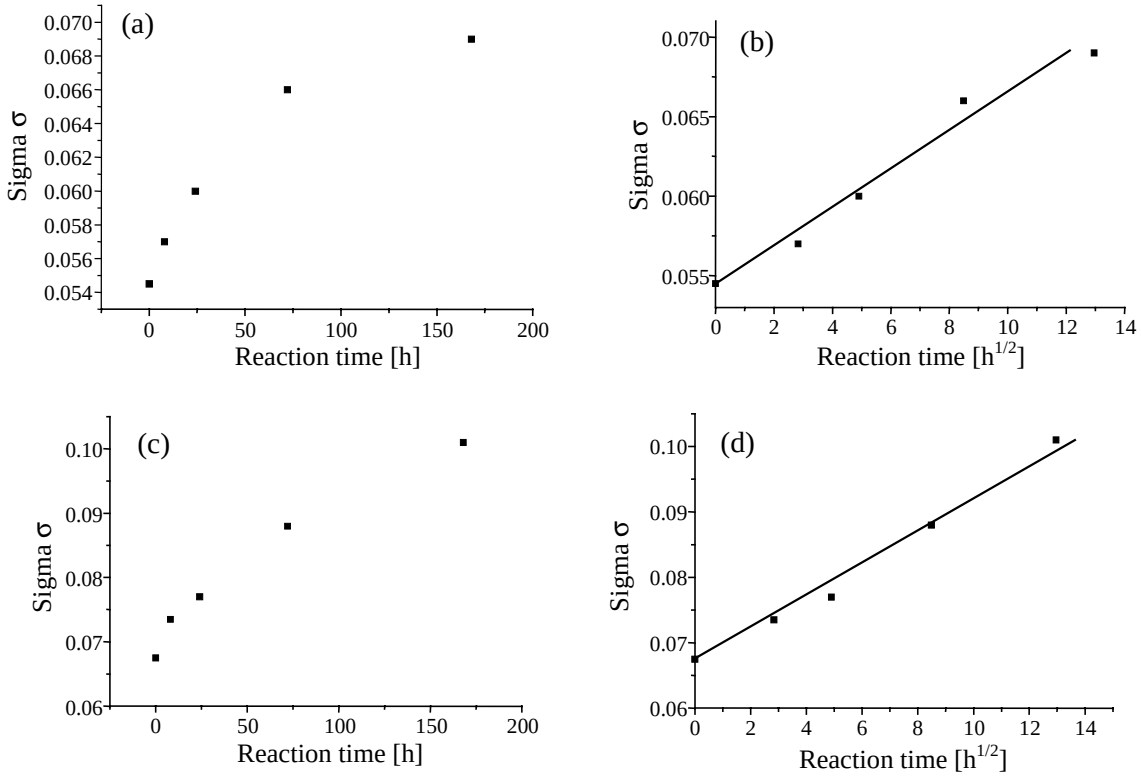

Figure 3. Radial structure functions of Zn-doped CSH samples reacted at different time intervals (0 day until 100 days), showing disappearance of the second shell (Zn-Zn absorber-backscatterer distance) with time

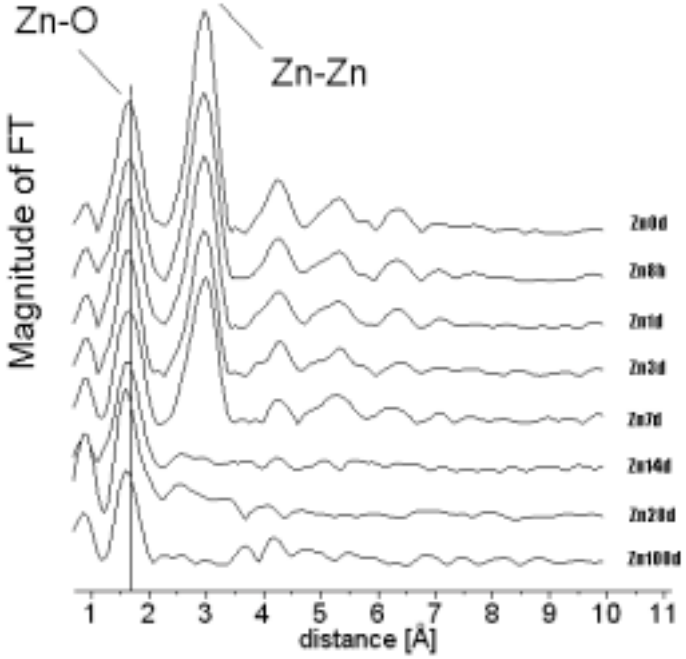

Figure 4. Fourier filtered experimental EXAFS Zn-Si contributions at Zn K-edge of the Zn-doped CSH

The solid line shows experimental data and the dotted curve represents calculated data

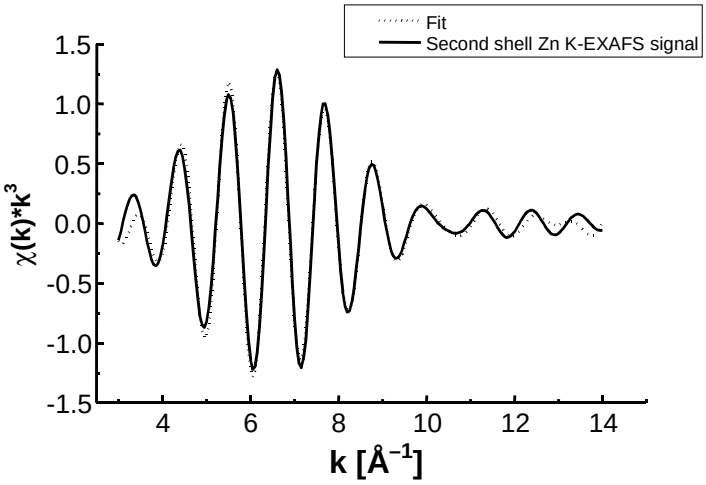

DEVELOPMENT OF ID DRIVE SYSTEM FOR THE UNDULATOR BEAMLINE OF SPRING8, AND K, L_{III} EXAFS OF LANTHANUM IN THE NITRATE SOLUTION

Tsuyoshi Yaita,[1] **Hideaki Shiwaku,**[2] **Hajime Tanida,**[3] **Yoshihiro Okamoto,**[1]
Hirokazu Narita,[1] **Shinichi Suzuki,**[1] **Shoichi Tachimori,**[1] **Haruhiko Motohashi**[4]
[1]Department of Materials Science, Japan Atomic Energy Research Institute (JAERI)
Tokai-mura Naka-gun, Ibaraki 319-1195, Japan
[2]Synchrotron Radiation Research Centre, Japan Atomic Energy Research Institute (JAERI)
1-1-1 Kouto Mikazuki-cho Sayo-gun Hyogo 679-5198, Japan
[3]Japan Synchrotron Radiation Research Institute (JASRI)
1-1-1 Kouto Mikazuki-cho Sayo-gun Hyogo 679-5198, Japan
[4]SPring8 Service, 1-1-1 Kouto Mikazuki-cho Sayo-gun Hyogo 679-5198, Japan

Abstract

The EXAFS spectra of lanthanum in aqueous nitrate solution were measured using both the K-edge and L_{III}-edge. The resolution of the spectrum obtained by the L_{III}-edge measurement was not sufficient for determination of structural parameters in detail, since the energy difference between L_{II}-edge and L_{III}-edge is very small. In contrast, K-edge XAFS was very effective for acquiring a high-resolution spectrum. In this study, we utilised a new system that synchronises the gap value of the undulator with energy scanning. This system provides a high flux X-ray, and therefore makes it possible to measure EXAFS spectrum for a trace amount of elements in a sample. The L_{III} and K-EXAFS data were acquired at the BL27B of KEK PF and the BL11XU of SPring8, respectively. In this paper, we also introduce the new system in addition to co-ordination properties of nitrate ion to lanthanum.

Introduction

The extended X-ray absorption fine structure (EXAFS) is one of the most powerful methods for speciation of elements in various samples. Furthermore, utilising the synchrotron radiation facility (SOR) makes it possible to measure EXAFS more sensitively than with a laboratory-type EXAFS apparatus. Recently, the third generation SOR such as SPring8, having undulator beamline, has been built in many countries. Using an undulator as the insertion device (ID) produces a high flux X-ray, but their harmonics peaks in the flux density with energy scanning while maintaining a constant gap value is inconvenient for EXAFS measurement. To solve this problem, we have installed a new system into the undulator beamline, the BL11XU of SPring8. This system synchronises gap value of ID with energy scanning so that we can obtain high flux and smooth curve in the plot of flux density versus energy.

Light lanthanides are the nuclides of which separations are necessary for the transmutation of the minor actinides, because the fission products include much volume of light lanthanides and the cross-sections of neutron capture of light lanthanide are relatively large. Accordingly, development of a separation method for light lanthanides is very important for the establishment of transmutation technology. Under such a background, many structural studies for lanthanides in separation system have been carried out for elucidation of their separation behaviours. Yaita, *et al*. [1] reported on the co-ordination structure of nitrate complexes for the lanthanides Nd to Lu (atomic number = 60 to 71). The co-ordination structures of light lanthanides with the nitrate ion have not been discussed by the L_{III} EXAFS measurement yet, since the small energy difference between L_{III} and L_{II} did not provide a sufficient resolution. When the K-edge is used in the EXAFS measurement of light lanthanides, however, it can provide satisfactory resolution. Furthermore, the K-edge EXAFS reduces some restrictions, including sample thickness, matrix absorption and so on. In this study, we will show the experimental results for the K-edge EXAFS of lanthanum at BL11XU of SPring8 utilised with the ID drive system, and discuss the comparisons of spectrum qualities between L_{III} and K-EXAFS and co-ordination properties of nitrate ion to lanthanum.

Sample preparation

Sample solutions were prepared by dissolution of $La(NO_3)_3nH_2O$ salt into aqueous 13 M HNO_3 solution. The metal concentrations in these samples were 0.1 mol/L. The sample solution for SPring8 (K-EXAFS) was sealed into 2 ml polyethylene tube being 1 cm thick for EXAFS measurement for transmission mode, while that for KEK PF (L_{III}-EXAFS) was sealed in 0.2 ml polyethylene bag having 1 mm Teflon spacer for EXAFS measurement for transmission mode.

EXAFS measurement

General procedure

The K-edge EXAFS of lanthanum (38.9 keV) was measured at the BL11XU of SPring8 in which an ID drive system was installed, and the L_{III}-edge EXAFS of lanthanum (5.48 keV) was measured at the BL27B of the High Energy Accelerator Research Organisation (KEK). The synchrotron radiation was monochromatised by the double crystal monochrometer of diamond (111) for the BL11XU of SPring8 and Si(111) for the BL27B of KEK. The X-ray used at the BL11XU is third order harmonics of ID. The polyethylene tube that had the thickness of about 1 cm for K-EXAFS and the polyethylene cell which included the Teflon spacer of 1 mm for L_{III}-EXAFS were used. Theoretical parameters for EXAFS fits were calculated by FEFF8.

ID drive energy scan system

The ID drive system was developed by Tanida [2]. The most suitable value of the beginning and the end of the gap are determined in advance, and the first order equation was made using these two points of the values. The most suitable gap value in each energy, calculated by using this equation, is sent to synchronise the ID with the monochrometer moving. The rocking curve is measured by the Piezo element being installed in the first crystal, and a degree of parallel of double crystal is kept in each energy by doing tuning. The EXAFS measurements utilised by the ID drive system were operated by the program written by LabVIEW (National Instruments Co.). Figure 1 shows an outline of ID drive XAFS system at the BL11XU of SPring8.

K and L_{III}-EXAFS results

Figure 2 shows the oscillations of lanthanum in 13 mol/L nitric acid solution. The *k* range of oscillation for K-EXAFS was from about 4 to 18.5 $Å^{-1}$, while the L_{III}-EXAFS ranges from 2 to 10 $Å^{-1}$. The peak due to the double electron excitation, $2p4d \rightarrow 5d^2$ [3] is observed at 6 $Å^{-1}$ of L_{III}-EXAFS, which is not negligible for the structural analysis. The radial structural functions (RSF) of lanthanum nitrate in 13 M HNO_3 obtained by K-EXAFS and L_{III}-EXAFS (Figure 3). The RSF of K-EXAFS consists of two parts, arising from the interaction with oxygen of water and oxygen and nitrogen of nitrate ion for around 2 Å, and from the multiple scattering interaction with oxygen and nitrogen of nitrate ion for 4 Å. These results agreed with the previous works regarding the lanthanide and actinide nitrate complexes [1,4,5]. The first shell consists of two interactions, and the difference in oxygen bond distance between water and nitrate ion (ΔR) was 0.14 Å from K-EXAFS result, but these interactions could not be separated in L_{III}-EXAFS. Essentially, it need the maximum value of *k* more than 12 $Å^{-1}$ ($\Delta R < \pi/2k_{max}$) to distinguish difference of these interactions. The L_{III}-EXAFS does not provide us the *k* range more than 10 $Å^{-1}$, while K-EXAFS which can give us the *k* range more than 18 $Å^{-1}$ is very useful for a structural determination of light lanthanides. The peak around 4 Å, arising from the multiple scattering of the La-N-O-N-Ln (4-leg path) and La-O-N-La (3-leg path), is a good evidence for the direct co-ordination of nitrate ion to lanthanide ion. However, it was not observed clearly in the RSF of L_{III}-EXAFS. This is due to the spectrum not being measured in the higher *k* region and double electron excitation as mentioned above. Figure 4 shows the fitting example of EXAFS of lanthanum nitrate in 13 M HNO_3, demonstrating the fit quality (R = 0.16 for R space; 0.09 for *k* space). The obtained co-ordination number, bond distance and Debye-Waller factor are summarised in Table 1. In the previous work, the two nitrate ions co-ordinated to heavier lanthanides in 13 M HNO_3 [1]. However, it was reasonable from the viewpoint of fit quality that co-ordination number of nitrate ion to lanthanum is regarded to be three (R = 0.09 for three-nitrate ion; R = 0.2 for two-nitrate ion in *k* space fitting). The bond distances of oxygen of nitrate ion for lanthanum was located at 0.14 Å longer position than those of oxygen of water.

REFERENCES

[1] T. Yaita, H. Narita, S. Suzuki, S. Tachimori, H. Motohashi, H. Shiwaku, *J. Radioanal. Nucl. Chem.*, 239(2), 371 (1999).

[2] H. Tanida, *Proceedings of Annual Meeting for Japan Synchrotron Radiation Society*, p. 73 (2000) (in Japanese).

[3] J.A. Solera, J. Garcia and M.G. Proietti, *Phys. Rev. B*, 51(5), 2678 (1995).

[4] P.G. Allen, D.K. Veirs, S.D.Conradson, C.A. Smith and S.F. Marsh, *Inorg. Chem.*, 35, 2841 (1996).

[5] H. Yokoyama, G. Johansson, *Acta Chem. Scand.*, 44, 567 (1990).

Figure 1. Outline of ID drive EXAFS system at the BL11XU of SPring8

I.C.: Ion chamber; PIN: Pin detector; Amp.: Amplifier; VF-C: V-F converter; WS: Work station; AD/DA: Interface board ; BOX: Multifunction I/O box

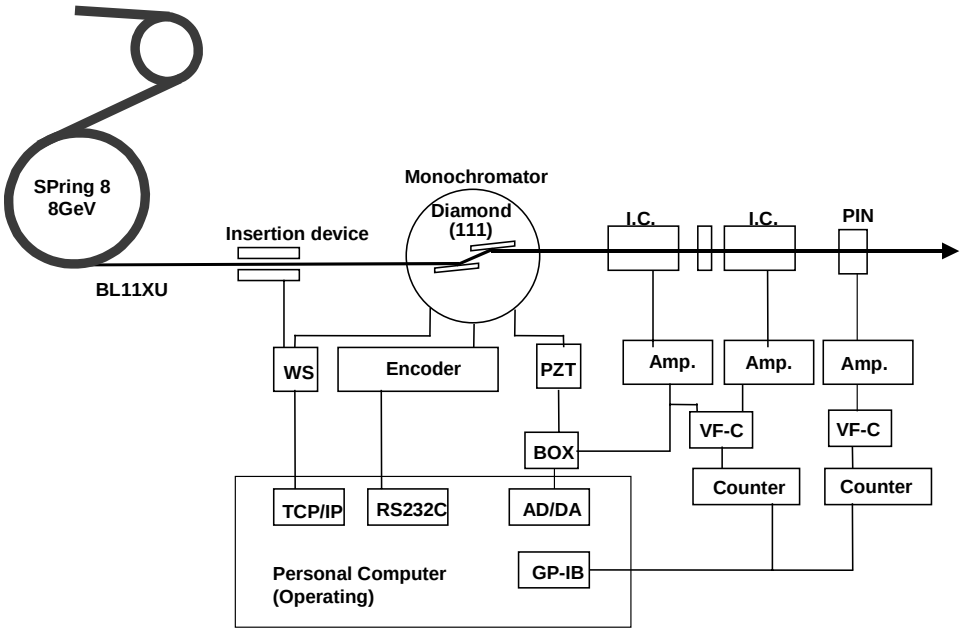

Figure 2. Comparison of oscillations from L_{III} and K-EXAFS

Sample solution was 0.1 M $La(NO_3)_3$ in 13 M HNO_3
The dotted circle means the effect of double electron excitation

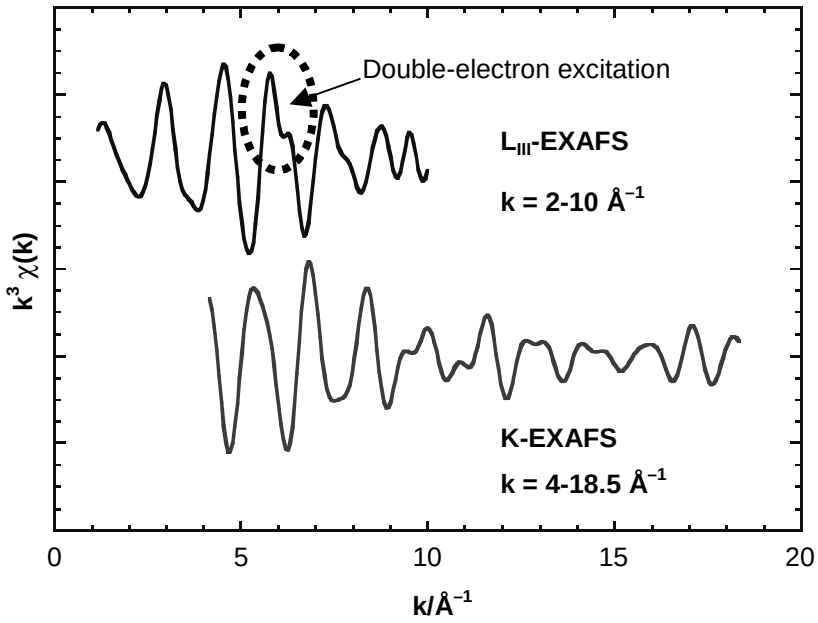

Figure 3. The radial structural functions of lanthanum nitrate in 13 M HNO_3 obtained by K and L_{III}-EXAFS

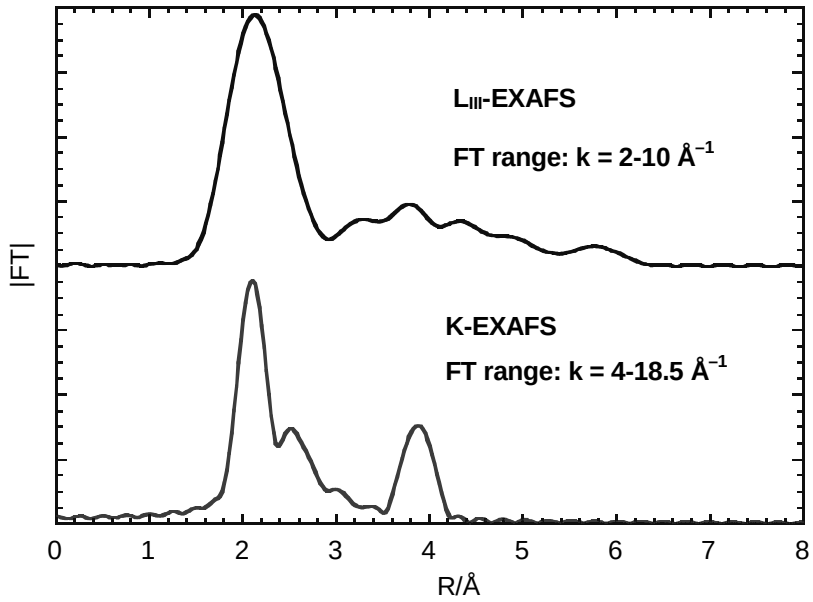

Figure 4. The K-EXAFS fitting results for the radial structural function and oscillation of cerium nitrate in 13 M HNO_3

R = 0.16 for R space, R = 0.09 for k space

$R = \left\{\Sigma\left|y_{exp}(i) - y_{theo}(i)\right| / \Sigma\left|y_{exp}(i)\right|\right\}$; *y denotes experimental data points*

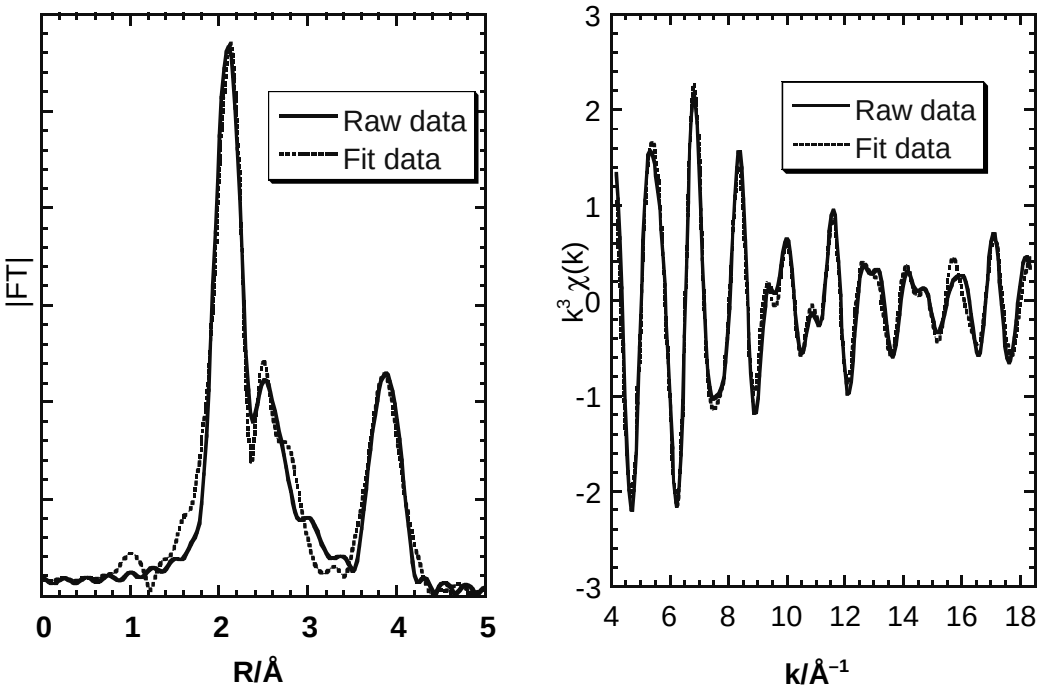

Table 1. The fitting results of EXAFS for lanthanum in 13 M HNO_3

SS: Single scattering; MS: Multiple scattering

Interaction	N*	R/Å	σ^2/Å^2
La-$\underline{O}H_2$ (SS)	3	2.57	0.002
La-$\underline{O}_2NO$ (SS)	6	2.70	0.006
La-$O_2\underline{N}O$ (SS)	3	3.11	0.005
La-$O_2\underline{N}\underline{O}$-$\underline{O}_2NO$(3-leg MS)	6	4.23	0.01
La-$O_2\underline{N}O$-$O_2\underline{N}\underline{O}$ (4-leg MS)	3	4.26	0.01

***** Fix parameter.

APPLICATION OF THE TIKHONOV REGULARISATION METHOD TO THE EXAFS ANALYSIS OF $UO_2(H_2AsO_4)_2 \times H_2O$

T.Ye. Zayarnaya
Institute of Metal Physics
GSP-170, Ekaterinburg, 620219, Russia
zayarnaya@imp.uran.ru

T. Reich, C. Hennig, H. Funke
Forschungszentrum Rossendorf e.V., Institute of Radiochemistry
P.O. Box 510119, D-01314
Dresden, Germany

Abstract

We consider the possibility of determining structural parameters from partial pair correlation functions (PCFs) for $UO_2(H_2AsO_4)_2 \times H_2O$ assuming that its crystal structure is unknown. $UO_2(HAsO_4) \times 4H_2O$ being chemically similar to $UO_2(H_2AsO_4)_2 \times H_2O$, we wanted to investigate whether the scattering characteristics calculated by FEFF-8 for the uranium hydrogen arsenate with a known crystal structure are transferable for the analysis of the uranium dihydrogen arsenate.

The Tikhonov regularisation method was applied to solve the inverse ill-posed problem of finding up to three partial PCFs from one EXAFS spectrum of $UO_2(H_2AsO_4)_2 \times H_2O$. From the U L_{III}-edge EXAFS spectrum, we determined the U-U, U-As and U-O PCFs. The As-As, As-U and As-O PCFs were received from the As K-edge EXAFS spectrum. The interatomic distances obtained for the first and in several cases also for the second co-ordination shell of all pairs are in agreement with recently published crystallographic values. This demonstrates that the Tikhonov regularisation method is a powerful tool for the structural analysis of samples for which only chemical information (oxidation state, elemental composition, type of ligands) is known.

Introduction

The EXAFS integral equation in single-scattering approximation for *n*-component system is given as [1]:

$$k\chi_i(k) = 4\pi\rho_0 \sum_{j=1}^{n} c_j \int_0^{\infty} f_j(k,r) e^{-\frac{2r}{\lambda_i(k)}} \sin\left(2kr + \psi_{ij}(k,r)\right) g_{ij}(r) dr \quad (1)$$

where $\chi_i(k)$ is the normalised oscillating part (NOP) of the X-ray absorption spectrum, ρ_0 is the atomic density of the compound, c_j is the concentration of atoms j, $f_j(k,r)$ is the backscattering amplitude of the neighbouring atom j, $\psi_{ij}(k,r) = (2\delta_i(k) + \varphi_j(k,r) - \pi)$ is the total phase shift, $\delta_i(k)$ is the phase shift on the central atom i, $\varphi_j(k,r)$ is the phase shift on the neighbouring atom j, and $\lambda_i(k)$ is the photoelectron mean free path. The physical meaning of a partial pair correlation function (PCF), $g_{ij}(r)$, is the density of probability to find a pair of atoms i and j at an interatomic distance r. The Tikhonov regularisation method [2] has been successfully applied to the inverse ill-posed problem of numerically solving the Fredholm first kind integral Eq. (1) and determining the partial PCFs $g_{ij}(r)$ [1,3].

The Tikhonov regularisation method was applied to obtain partial PCFs from the experimental As K-edge and U L_{III}-edge EXAFS spectra for a quasi three-component system with a known crystal structure, i.e. $UO_2(HAsO_4) \times 4H_2O$ [4]. The co-ordination numbers, interatomic distances and Debye-Waller (DW) factors for the first co-ordination shell could readily be determined from the U-U, U-As, U-O, As-U, As-As and As-O PCFs. For the second co-ordination shell, we obtained the bond distances. The interatomic distances and co-ordination numbers agree with the crystallographic values.

The main interest of the present investigation is to study the possibility of applying the Tikhonov regularisation method to a sample without knowing its crystal structure. In this case we can only use chemical information about it and a reference compound of known structure. Based on the chemical similarity of $UO_2(HAsO_4) \times 4H_2O$ and $UO_2(H_2AsO_4)_2 \times H_2O$ (uranium in the oxidation state +6, same elements in the near-neighbour surrounding), we propose to use scattering characteristics [$f_j(k,r)$, $\delta_i(k)$, $\varphi_j(k,r)$ and $\lambda_i(k)$] of the uranyl hydrate arsenate tetrahydrate reference for uranyl dihydrogen arsenate hydrate. As described in Ref. [4], the functions $f_j(k,r)$, $\delta_i(k)$, $\varphi_j(k,r)$ and $\lambda_i(k)$ were obtained from curved wave approximation calculations with the program FEFF-8 [5] for the reference sample $UO_2(DAsO_4) \times 4D_2O$ [6]. After solving the ill-posed problem, we determine the interatomic distances for $UO_2(H_2AsO_4)_2 \times H_2O$ from the $g_{ij}(r)$ and compare them with recently published single-crystal X-ray diffraction (XRD) data [7].

Experimental and data treatment

For EXAFS measurements, crystalline $UO_2(H_2AsO_4)_2 \times H_2O$ powder was mixed with boron nitride (BN) to obtain a homogeneous sample and pressed into 13 mm diameter pellets. The As K-edge and U L_{III}-edge EXAFS spectra were measured in transmission mode at the Rossendorf Beamline (ROBL) at the European Synchrotron Radiation Facility (ESRF) using a Si(111) double-crystal monochromator in fixed-exit mode [8]. The Au L_{III}-edge (11 919 eV) and Y K-edge (17 038 eV) energies of the corresponding metal foils were used for energy calibration. The absorption background (apparatus function) was determined by measuring the X-ray absorption spectrum of a BN pellet in the energy range of the As K-edge and U L_{III}-edge spectra.

The preliminary treatment of the obtained EXAFS spectra included the following steps:

- The apparatus function was removed from the experimental spectrum by subtraction of the spectrum without uranyl arsenate in the BN pellet from the sample spectrum [9].

- The X-ray absorption spectrum measured in transmission mode can be distorted by fluorescence radiation leaking into the gas ionisation chamber detectors. This effect was estimated and corrected for according to the procedure described in [10].

- Isolation of the X-ray absorption spectrum of the absorbing atom alone by subtraction of a pre-edge function that was fitted through the region of the data before the initial rise of the absorption edge.

- Extraction of the NOP from X-ray absorption spectrum in energy space using a spline fit followed by a transformation from energy *E*-space to *k*-space. This transition is described in detail in Ref. [4] for the As K-edge and U L_{III}-edge spectra of $UO_2(HAsO_4) \times 4H_2O$. Since the co-ordination and chemical state of As and U are very similar in both compounds, one can assume that energy dispersion law $E(k)$ of the As K and U L_{III} absorption edges are identical both for $UO_2(HAsO_4) \times 4H_2O$ and $UO_2(H_2AsO_4)_2 \times H_2O$. Before transforming energy space into *k*-space, we carefully checked that the maxima of the white lines in the As K-edge and U L_{III}-edge spectra coincided. After this check, we used the same parameters *a*, *b* and *c* in the law of dispersion given as $E = ak^2 + bk + c$ as for uranyl hydrate arsenate tetrahydrate for the uranyl dihydrogen arsenate hydrate. The U L_{III}-edge and As K-edge EXAFS spectra were analysed in the *k*-range of 2.5 to 20.0 and 3.5 to 20.0 $Å^{-1}$, respectively.

Results and discussion

The determination of the partial PCFs by solving the inverse ill-posed problem using an iterative algorithm is described in detail in Ref. [4]. The PCFs for the pairs U-U, U-As and U-O obtained from the U L_{III}-edge EXAFS spectrum of $UO_2(H_2AsO_4)_2 \times H_2O$ are shown in Figure 1 as dotted lines. In Figure 2, the corresponding As-U, As-As and As-O PCFs for the As K-edge EXAFS spectrum of $UO_2(H_2AsO_4)_2 \times H_2O$ are depicted. In order to evaluate our results, we calculated the atomic positions for cluster size of 10 Å using the XRD data given in [7] and the program ATOMS. Then we describe the partial PCFs $g_{ij}(r)$ according to Eq. (2):

$$g_{ij}(r) = 1/4\pi\rho_0 \sum_{l=1}^{l_m} \frac{N_l}{r_l^2 \sigma_l \sqrt{2\pi}} \exp\left(-\frac{(r-r_l)^2}{2\sigma_l^2}\right) \qquad (2)$$

where the sum is taken over the number of the co-ordination spheres *l*; N_l is the number of atoms *j* in the co-ordination sphere; r_l is the distance from the central atom *i* to the corresponding co-ordination sphere *l*; σ_l is the DW factor. In our calculation all DW factors were assumed to be equal to 0.003 $Å^2$. The U-U, U-As and U-O partial PCFs calculated for the U L_{III}-edge are shown in Figure 1 as solid lines. As can be seen in the figure, the positions of the first two peaks of each partial PCF given in Figure 1 coincide with the true positions. The good agreement between the interatomic distances determined with an accuracy of ±0.02 Å from the peak maxima of the partial PCFs with the crystallographic values is also indicated by the values given in Table 1. The co-ordination numbers for the pairs U-O_1 and U-O_2 equal 1.5 and 5.0, respectively. The expected values are 2 and 5.

The three partial PCFs of the pairs As-U, As-As and As-O for the As K-edge are shown in Figure 2. Except for the As-As PCF, we received the interatomic distances only for the first shell of these pairs.

The co-ordination number of As-O_1 equals 3.3, which is somewhat lower than the expected value of 4.

As one can see from Table 1, the interatomic distances obtained by the Tikhonov regularisation method agree both with the XRD values and the results of a standard EXAFS analysis [11] using the EXAFSPAK software package [12]. The difference of 0.12 Å between our results and the least-square fit for the U-U_1 shell is probably due to the influence of As atoms at this distance, which were not included in the fit [11]. Additionally, the Tikhonov analysis was able to detect the As-As_1 and As-As_2 co-ordination shells (see Table 1). In contrast to the conventional method of a least-square fit to the experimental EXAFS spectrum, the Tikhonov regularisation method does not rely on a structural model.

Differences in the crystal structure of $UO_2(HAsO_4) \times 4H_2O$ and $UO_2(H_2AsO_4)_2 \times H_2O$ become evident in the U-O_2 co-ordination shell. For $UO_2(HAsO_4) \times 4H_2O$, the average bond distance to four equatorial oxygen atoms is 2.30 Å. In $UO_2(H_2AsO_4)_2 \times H_2O$ five oxygen atoms surround the uranium in the equatorial plane with an average distance of 2.40 Å. Both the change in co-ordination number and interatomic distance are reproduced by our analysis.

In summary, our calculations show that it is indeed possible to extract structural information, i.e. interatomic distances and co-ordination numbers, from the As K-edge and U L_{III}-edge EXAFS spectra of $UO_2(H_2AsO_4)_2 \times H_2O$ without a structural model as is needed for a least-square fit. It is possible to utilise the scattering characteristics obtained for a reference compound which is similar in its chemical nature. The Tikhonov regularisation method as developed in Ref. [4] will be extremely useful for obtaining EXAFS structural parameters in complicated systems where exact structural information, e.g. from single-crystal XRD, is unavailable.

Acknowledgements

We are grateful to M. Rutsch for synthesising uranyl dihydrogen arsenate hydrate and to Yu.A. Babanov for advice and stimulating discussions. A.F. Sidorenko and A.V. Ryazhkin are thanked for providing the computer software for the preliminary data treatment. T.Ye. Zayarnaya thanks the Sächsische Staatsministerium für Wissenschaft und Kunst for financial support (grant number SMWK/4-7531.50-04-844-00/18). The EXAFS measurements were performed at BM20 at the ESRF. The assistance of A. Rossberg in the acquisition of EXAFS data is gratefully acknowledged.

REFERENCES

[1] Yu.A. Babanov, V.V. Vasin, A.L. Ageev, N.V. Ershov, *Phys. Stat. Sol. B*, 105, 747 (1981).

[2] A.N. Tikhonov, V.Ya. Arsenin, Solution of Ill-posed Problems, John Wiley and Sons, Inc., New York (1981).

[3] N.V. Ershov, A.L. Ageev, V.V. Vasin, Yu.A. Babanov, *Phys. Stat. Sol. B*, 108, 103 (1981).

[4] Yu.A. Babanov, T.Ye. Zayarnaya, T. Reich, H. Funke, these proceedings.

[5] A.L. Ankudinov, B. Ravel, J.J. Rehr, S.D. Condradson, *Phys. Rev. B*, 58, 7565 (1998).

[6] A.N. Fitch, L. Bernard, A.T. Howe, A.F. Wright, B.E.F. Fender, *Acta Cryst.*, C39, 159 (1983).

[7] T.M. Gesing, C.H. Rüscher, *Z. Anorg. Allg. Chem*., 626, 1414 (2000).

[8] W. Matz, N. Schell, G. Bernhard, F. Prokert, T. Reich, J. Claussner, W. Oehme, R. Schlenk, S. Dienel, H. Funke, F. Eichhorn, M. Betzl, D. Proehl, U. Strauch, G. Huettig, H. Krug, W. Neumann, V. Brendler, P. Reichel, M.A. Denecke, H. Nitsche, *J. Synchrotron Radiat.*, 6, 1067 (1999).

[9] A.V. Ryazhkin, T.Ye. Zayarnaya, Yu.A. Babanov, K.A. Gins, A.F. Sidorenko, *Kondensirovannie sredy i mezhpaznie granitsy*, 1, 52 (2000) (in Russian).

[10] Yu.A. Babanov, A.V. Ryazhkin, T. Miyanaga, *Nucl. Instrum. Methods A* (in press).

[11] C. Hennig, private communication.

[12] G.N. George, I.J. Pickering, "EXAFSPAK – A Suite of Computer Programs for Analysis of X-ray Absorption Spectra", Stanford Synchrotron Radiation Laboratory (1995).

Figure 1. Comparison of experimental partial pair correlation functions (dashed line) and corresponding model functions (solid line) for $UO_2(H_2AsO_4)_2 \times H_2O$. The experimental curve was obtained from U L_{III}-edge $\chi(k)$.

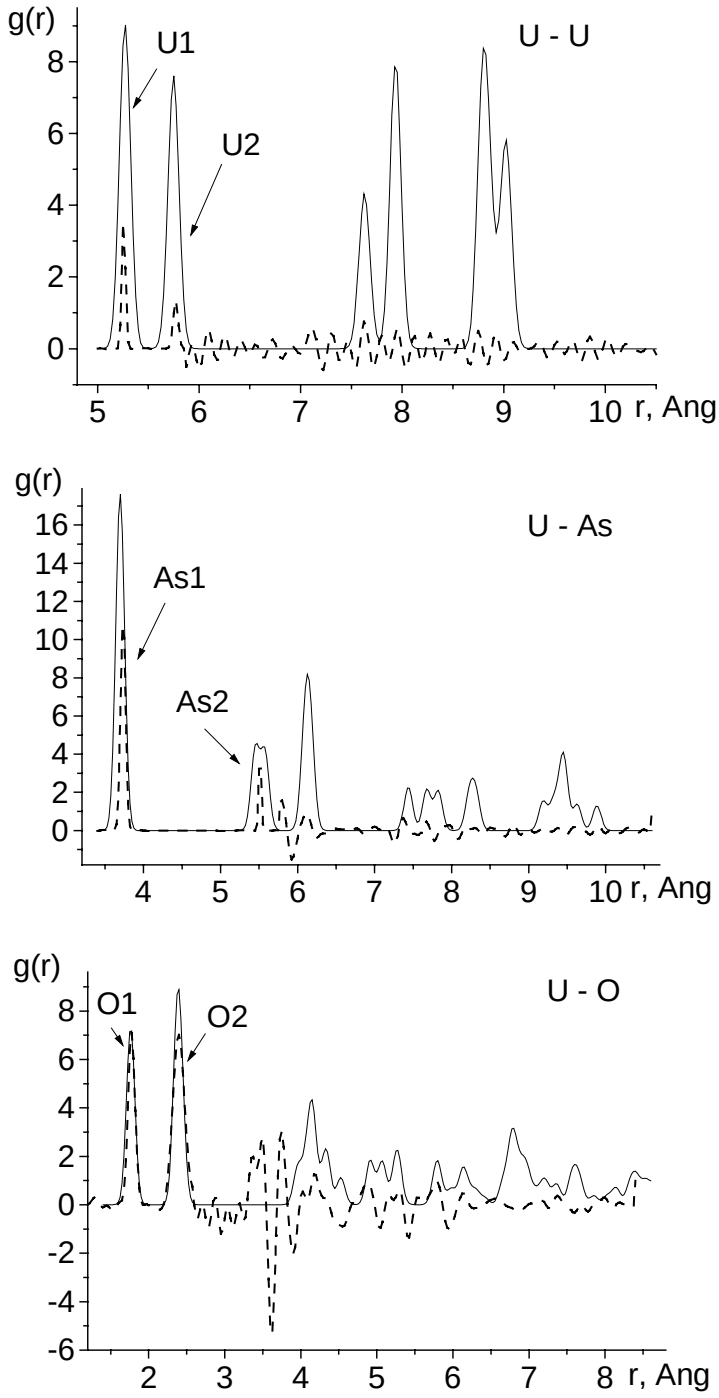

Figure 2. Comparison of experimental partial pair correlation functions (dashed line) and corresponding model functions (solid line) for $UO_2(H_2AsO_4)_2 \times H_2O$. The experimental curve was obtained from As K-edge $\chi(k)$.

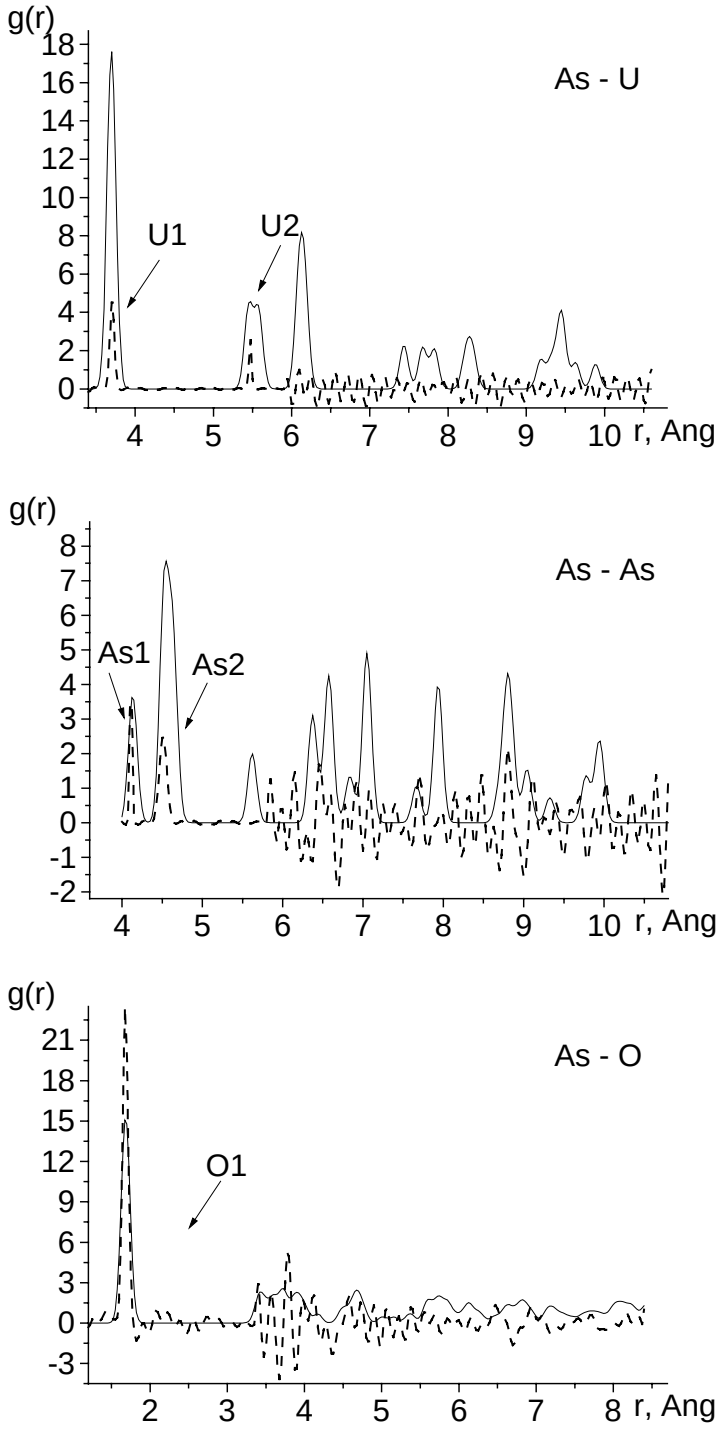

Table 1. Interatomic distances in Å for $UO_2(H_2AsO_4)_2 \times H_2O$ (15 K)

Shell	Least-square method [11]	Tikhonov method	X-ray diffraction [7]
$U\text{-}U_1$	5.38	5.26	5.27
$U\text{-}U_2$	5.73	5.77	5.75
$U\text{-}As_1$	3.70	3.73	3.70
$U\text{-}O_1$	1.79	1.76	1.76
$U\text{-}O_2$	2.35	2.39	2.39
$As\text{-}U_1$	3.71	3.70	3.70
$As\text{-}As_1$	–	4.11	4.13
$As\text{-}As_2$	–	4.51	4.58
$As\text{-}O_1$	1.69	1.68	1.69

Annex 1

ORGANISING COMMITTEE

T. Reich (FZR, Germany)

D.K. Shuh (LBNL, USA)

G. Bernhard (FZR, Germany)

C. Madic (CEA, France)

C. Kunz (ESRF, France)

C. Nordborg, (OECD/NEA, France)

Annex 2

LIST OF PARTICIPANTS

AUSTRALIA

Mr. Ned BLAGOJEVIC
Australian Nuclear Science and Technology Organisation
Private Mail Bag 1
Menai
New South Wales 2234
Australia

Tel: +61-2-9717-3660
Fax: +61-2-9717-9260
Eml: nbx@ansto.gov.au

FINLAND

Mr. Jussi JERNSTRÖM
University of Helsinki
Department of Chemistry
Laboratory for Radiochemistry
P.O. Box 55
00014 University of Helsinki

Tel: +358-9-191-40120
Fax: +358-9-191-40121
Eml: jussi.jernstrom@helsinki.fi

FRANCE

Dr. Isabelle BONHOURE
Laboratoire Lure
Centre Universitaire Paris-Sud
Bat 209 D
F-91898 Orsay

Tel: +33-(0)164-468099
Fax: +33-(0)164-464148
Eml: bonhoure@lure.u-psud.fr

Dr. Michael DRAKOPOULOS
European Synchrotron Radiation Facility
6 rue Jules Horowitz
B.P. 220
F-38043 Grenoble Cedex

Tel: +33-(0)476-882127
Fax: +33-(0)476-882785
Eml: drako@esrf.fr

Prof. François FARGES
Université de Marne la Vallée
Laboratoire de géomatériaux
5 blvd Descartes – Champ-sur-Marne
F-77454 Marne la Vallée Cedex 2

Tel: +33-(0)149-329057
Fax: +33-(0)149-329137
Eml: farges@univ-mlv.fr

Dr. Massoud FATTAHI
Laboratoire Subatech
4 rue Alfred Kastler
F-44307 Nantes, Cedex 3

Tel: +33-(0)251-838407
Fax: +33-(0)251-838452
Eml: fattahi@subatech.in2p3.fr

Dr. Konstantin GUERMAN
Centre National de la Recherche Scientifique
U.M.R. 5084-CNRS
Domaine du Haut Vigneau
B.P.120
F-33175 Gradignan Cedex

Tel: +33-(0)557-120907
Fax: +33-(0)557-120900
Eml: guerman@cenbg.in2p3.fr

Dr. Christoph HENNIG
Forschungszentrum Rossendorf
ESRF
B.P. 220
F-38043 Grenoble Cedex

Tel: +33-(0)476-882005
Fax: +33-(0)476-882505
Eml: hennig@esrf.fr

Dr. Lilian JACQUAMET
European Synchrotron Radiation Facility
ESRF, PLUO B 206
B.P. 220
6 rue Jules Horowitz
F-38043 Grenoble Cedex

Tel: +33-(0)476-882922
Fax: +33-476-882784
Eml: jacquame@esrf.fr

Prof. Dr. Christof KUNZ
European Synchrotron Radiation Facility
6 rue Jules Horowitz
B.P. 220
F-38043 Grenoble Cedex

Tel: +33-(0)476-882160
Fax: +33-(0)476-882508
Eml: ckunz@esrf.fr

Dr. Tristan LE BIHAN
European Synchrotron Radiation Facility
6 rue Jules Horowitz
B.P. 220
F-38043 Grenoble Cedex

Tel: +33-(0)476-882775
Fax: +33-(0)476-882907
Eml: lebihan@esrf.fr

Mrs. Claire LOMENECH
Institut de Physique Nucléaire
Groupe de Radiochemie
15 rue Clémenceau, Bât. 100
F-91406 Orsay Cedex

Tel: +33-(0)169-158144
Fax: +33-(0)196-157150
Eml: lomenech@ipno.in2p3.fr

Prof. Charles MADIC
Commissariat à l'Énergie Atomique
Fuel Cycle Division
DCC/dir. BP450
CEA/Saclay
F-91191 Gif-sur-Yvette

Tel: +33-(0)169-088207
Fax: +33-(0)169-088538
Eml: madic@amandin.cea.fr

Dr. Pascale MALDIVI
Commissariat à l'Énergie Atomique
DRFMC/LCIB (UMR CEA-CNRS-UJF 5046)
CEA-Grenoble
17 Rue des Martyrs
F-38054 Grenoble Cedex 9
Tel: +33-(0)476-885303
Fax: +33-(0)476-885090
Eml: pmaldivi@cea.fr

Dr. Gills MONTAVON
Laboratoire Subatech
4 rue Alfred Kastler
F-44307 Nantes, Cedex 3
Tel: +33-(0)251-858420
Fax: +33-(0)251-858452
Eml: montavon@subatech.in2p3.fr

Dr. Pierre-Emmanuel PETIT
European Synchrotron Radiation Facility
6 rue Jules Horowitz
B.P. 220
F-38043 Grenoble Cedex
Tel: +33-(0)476-882602
Fax: +33-(0)476-882160
Eml: ppetit@esrf.fr

Dr. Tobias REICH
Forschungszentrum Rossendorf
ROBL – CRG
ESRF PLUOE 217
B.P. 220
F-38043 Grenoble Cedex
Tel: +33-(0)476-88-2339
Fax: +33-(0)476-88-2505
Eml: reich@esrf.fr

Mr. André ROSSBERG
Forschungszentrum Rossendorf
ROBL – CRG
ESRF PLUOE 217
B.P. 220
F-38043 Grenoble Cedex
Tel: +33-(0)476-882849
Fax: +33-(0)476-88-2505
Eml: rossberg@esrf.fr

Dr. Eric SIMONI
Institut de Physique Nucléaire
Groupe de Radiochemie
15 rue Clémenceau
F-91406 Orsay Cedex
Tel: +33-(0)169-157343
Fax: +33-(0)169-157150
Eml: simoni@ipno.in2p3.fr

Dr. Jean SUSINI
European Synchrotron Radiation Facility
6 rue Jules Horowitz
B.P. 220
F-38043 Grenoble Cedex
Tel: +33-(0)476-882124
Fax: +33-(0)476-882542
Eml: susini@esrf.fr

Dr. Satoru TSUSHIMA
University of Tokyo
ROBL – CRG
ESRF PLUOE 217
B.P. 220
F-38043 Grenoble Cedex
Tel: +33-(0)476-88-2849
Fax: +33-(0)476-88-2505
Eml: tsushima@esrf.fr

Dr. Laurent VICHOT
Laboratoire Subatech
4 rue Alfred Kastler
44307 Nantes, Cedex 3

Tel: +33-(0)251-858477
Fax: +33-(0)251-858452
Eml: vichot@subatech.fn2p3.fr

GERMANY

Mr. Samer AMAYRI
Forschungszentrum Rossendorf
P.O. Box 510 119
D-01314 Dresden

Tel: +49-(0)351-2602432
Fax: +49-(0)351-2603553
Eml: amayri@fz-rossendorf.de

Prof.Dr. Gert BERNHARD
Forschungszentrum Rossendorf
P.O. Box 510 119
D-01314 Dresden

Tel: +49-(0)351-2603280
Fax: +49-(0)351-2603553
Eml: G.Bernhard@fz-rossendorf.de

Dr. Maria BETTI
Institute for Transuranium Elements
Joint Research Centre
Postfach 2340
D-76125 Karlsruhe

Tel: +49-(0)7247-951-363
Fax: +49-(0)7247-951-595
Eml: betti@itu.fzk.de

Dr. Kathy DARDENNE
Forschungszentrum Karlsruhe
Institut für Nukleare Entsorgungstechnik
Postfach 3640
D-76021 Karlsruhe

Tel: +49-7247-82-6669
Fax: +49-7242-82-3927
Eml: dardenne@ine.fzk.de

Dr. Melissa DENECKE
Forschungszentrum Karlsruhe
Institut für Nukleare Entsorgungstechnik
Postfach 3640
D-76021 Karlsruhe

Tel: +49-7247-825536
Fax: +49-7247-823927
Eml: melissa@ine.fzk.de

Prof. Thomas FANGHÄNEL
Forschungszentrum Rossendorf
P.O. Box 510 119
D-01314 Dresden

Tel: +49-(0)351-2603210
Fax: +49-(0)351-2603553
Eml: Th.Fanghaenel@fz-rossendorf.de

Dr. Harald FUNKE
Forschungszentrum Rossendorf
Postfach 510119
D-01314 Dresden

Tel: +49-(0)351-2603138
Fax: +49-(0)351-2603553
Eml: H.Funke@fz-rossendorf.de

Dr. Thomas GOUDER
Institute for Transuranium Elements
Joint Research Centre
Postfach 2340
D-76125 Karlsruhe

Tel: +49-(0)7247-951243
Fax: +49-(0)7247-951593
Eml: gouder@itu.fzk.de

Ms. Monique IDIRI
Institute for Transuranium Elements
Joint Research Centre
Postfach 2340
D-76125 Karlsruhe

Tel: +49-(0)7247-951-256
Fax: +49-(0)7247-951-531
Eml: idiri@itu.fzk.de

Dr. Günter KAINDL
Freie Universität Berlin
Institut für Experimentalphysik
Arnimallee, 14
D-14195 Berlin

Tel: +49-(0)30-8382977
Fax: +49-(0)30-8386560
Eml: kaindl@physik.fu-berlin.de

Prof. Dr. Jae-Il KIM
Forschungszentrum Karlsruhe
Institut für Nukleare Entsorgungstechnik
Postfach 3640
D-76021 Karlsruhe

Tel: +49-(0)7247-722230/31
Fax: +49-(0)7247-824308
Eml: kim@ine.fzk.de

Mr. Jens-Uwe KÜNSTLER
Forschungszentrum Rossendorf
Institut für Bioanorganische und
Radiopharmazeutische Chemie
P.O. Box 510 119
D-01314 Dresden

Tel: +49-(0)351-2603170
Fax: +49-(0)351-2603232
Eml: kuenstler@fz-rossendorf.de

Prof. Gerard LANDER
Institute for Transuranium Elements
Joint Research Centre
Postfach 2340
D-76125 Karlsruhe

Tel: +49-(0)724-7951-382
Fax: +49-(0)7247-951599
Eml: lander@ill.fr

Mr. Stefan MANGOLD
Technische Universität Hamburg-Harburg
Eissendorfer Strasse 40
D-21073 Hamburg

Tel: +49-(0)40-42878-2608
Fax: +49-(0)40-42878-2315
Eml: mangold@tu-harburg.de

Dr. Mohamed Larbi MERROUN
Forschungszentrum Rossendorf
Institute of Radiochemistry
P.O. Box 510 119
D-01314 Dresden

Tel: +49-(0)351-2602958
Fax: +49-(0)351-2603553
Eml: m.merroun@fz-rossendorf.de

Dr. Henry MOLL
Forschungszentrum Rossendorf
Institute of Radiochemistry
P.O. Box 510 119
D-01314 Dresden

Tel: +49-(0)351-2602895
Fax: +49-(0)351-2603553
Eml: moll@fz-rossendorf.de

Dr. Susanne POMPE
Forschungszentrum Rossendorf
Institute of Radiochemistry
P.O. Box 510 119
D-01314 Dresden
Tel: +49-(0)351-2602436
Fax: +49-(0)351-2603553
Eml: s.pompe@fz-rossendorf.de

Dr. Katja SCHMEIDE
Forschungszentrum Rossendorf
Institute of Radiochemistry
P.O. Box 510 119
D-01314 Dresden
Tel: +49-(0)351-2602436
Fax: +49-(0)351-2603553
Eml: schmeide@fz-rossendorf.de

Dr. Christian SCHÜSSLER-LANGEHEINE
Freie Universität Berlin
Institut für Experimentalphysik
Arnimallee, 14
D-14195 Berlin
Tel: +49-(0)30-838-52988
Fax: +49-(0)30-838-56560
Eml: christian.schuessler@physik.fu-berlin.de

Dr. Kai STARKE
Freie Universität Berlin
Institut für Experimentalphysik
Arnimallee, 14
D-14195 Berlin
Tel: +49-(0)30-8385-3336
Fax: +49-(0)30-8385-6560
Eml: starke@phyzik.fu-berlin.de

Ms. Caterina TOMMASEO
Johannes Gutenberg-Universität
Institut für Geowissenschaft
FB 22 Mineralogie
Becherweg 21
D-55099 Mainz
Tel: +49-(0)6131-3924780
Fax: +49-(0)6131-3923070
Eml: tommc000@mail.uni-mainz.de

Mr. Edmund WELTER
Hasylab at DESY
Notkestrasse 85
D-22607 Hamburg
Tel: +49-(0)40-89984510
Fax: +49-(0)40-8998
Eml: edmund.welter@desy.de

GREECE

Dr. Evagelia MOSHOPOULOU
National Center for Scientific Research
“Demokritos”
Institute for Materials Science
15310 Agia Paraskevi
Tel: +30-1-6503320
Fax: +30-1-6519430
Eml: evagelia@ims.demokritos.gr

JAPAN

Dr. Tsuyoshi YAITA
Japan Atomic Energy Research Institute
Tokai-mura, Naka-gun
Ibaraki-ken 319-1195
Tel: +81-29-282-6162
Fax: +81-29-282-6723
Eml: yaita@mummy.tokai.jaeri.go.jp

NORWAY

Dr. Ole Christian LIND
Agricultural University of Norway
Laboratory for Analytical Chemistry
P.O. Box 5026
N-1432 AAS

Tel: +47-64948351
Fax: +47-64948359
Eml: Ole-Christian.Lind@ikb.nlh.no

Prof. Dr. Brit SALBU
Agricultural University of Norway
Laboratory for Analytical Chemistry
P.O. Box 5026
N-1432 AAS

Tel: +47-64948355
Fax: +47-64958359
Eml: brit.salbu@ikb.nlh.no

RUSSIAN FEDERATION

Dr. Marina CHUKALINA
Russian Academy of Science
Institute of Microelectronics Technology
142432 Chernogolovka
Moscow District

Tel: +7-096-524-42-56
Fax: +7-095-962-80-47
Eml: marina@ipmt-hpm.ac.ru

Prof.Dr. Yu. A. BABANOV
Russian Academy of Sciences
Institute of Metal Physics
S. Kovalevskaya 18
620219 Ekaterinburg GSP-170

Tel: +7-(0)3432-499363
Fax: +7-(0)3432-745244
Eml: babanov@imp.uran.ru

Dr. Kirill Evgenjevich IVANOV
Russian Research Centre “Kurchatov Institute”
I.V. Kurchatov Square 1
123182 Moscow

Tel: +7-(0)95-196-9252
Fax: +7-(0)95-882-5804
Eml: ivanov@ignph.kiae.ru

Prof. Dr. Victor L. KRAIZMAN
Rostov State University
Institute of Physics
194 Stachky Ave.
344090 Rostov-on-Don

Tel: +7-8632-223756
Fax: +7-8632-285044
Eml: saleks@icomm.ru

Mr. Konstantin MASLAKOV
Russian Research Centre “Kurchatov Institute”
1, Kurchatov Square
Moscow 123182

Tel: +7-(0)95-196-7286
Fax: +7-(0)95-882-5804
Eml: utkin@ignph.kiae.ru

Dr. Yuri Alexandrovich TETERIN
Russian Research Centre “Kurchatov Institute”
I.V. Kurchatov Square 1
123182 Moscow

Tel: +7-(0)95-196-9252
Fax: +7-(0)95-882-5804
Eml: teterin@ignph.kiae.ru

Dr. Igor O. UTKIN
Russian Research Centre “Kurchatov Institute”
I.V. Kurchatov Square 1
123182 Moscow
Tel: +7-(0)95-196-9252
Fax: +7-(0)95-882-5804
Eml: utkin@ignph.kiae.ru

Ms. Tatyana ZAYARNAYA
Russian Academy of Sciences
Institute of Metal Physics
S. Kovalevskaya 18
620219 Ekaterinburg GSP-170
Tel: +7-(0)34-3249-9044
Fax: +7-(0)34-3274-5244
Eml: zayarnaya@imp.uran.ru

SPAIN

Dr. Tiziana MISSANA
CIEMAT
Dpto de Impacto Ambiental de la Energia
Avenida Complutense, 22
E-28040 Madrid
Tel: +91-3466185
Fax: +91-3466542
Eml: tiziana.missana@ciemat.es

SWEDEN

Dr. Patric LINDQVIST-REIS
Royal Institute of Technology
Deptartment of Inorganic Chemistry
Teknikringen 26
S-10044 Stockholm
Tel: +46-8-7908156
Fax: +46-8-212626
Eml: plr@inorg.kth.se

Dr. Zoltan SZABO
The Royal Institute of Technology
Department of Inorganic Chemistry
Teknikringen 30
S-10044 Stockholm
Tel: +46-8-7908144
Fax: +46-8-212626
Eml: zoltan@inorchem.kth.se

SWITZERLAND

Mr. Rainer DÄHN
Paul Scherrer Institute
Waste Management Laboratory
O.H.L.B./411
CH-5232 Villigen
Tel: +41-56310-2175
Fax: +41-56310-4438
Eml: rainer.daehn@psi.ch

UNITED KINGDOM

Dr. Deborah BUNKER
University of Manchester
Department of Chemistry
Oxford Road
Manchester M13 9PL
Tel: +44-(0)161-275-4647
Fax: +44-(0)161-275-4598
Eml: debbie.bunker@man.ac.uk

Mr. Benjamin ATKINS
University of Manchester
Department of Chemistry
Oxford Road
Manchester M13 9PL
Tel: +44-(0)161-275-4647
Fax: +44-(0)161-275-4598
Eml: benatkins33@hotmail.com

Mr. Mark JONES
University of Manchester
Department of Chemistry
Manchester M13 9PL
Tel: +44-(0)161-275-4647
Fax: +44-(0)161-275-4598
Eml: mark.j.jones@stud.man.ac.uk

UNITED STATES OF AMERICA

Dr. Patrick ALLEN
Seaborg Institute LLNL
MS L-231, P.O. BOX 808
Livermore CA 94551-9900
Tel: +1-925-423-8953
Fax: +1-925-422-3160
Eml: allen42@llnl.gov

Dr. Gordon E. BROWN
Stanford University
Department of Geological and Environmental Sciences
Green Earth Sci.
309 Stanford
CA 94305-2115
Tel: +1-650-723-9168
Fax: +1-650-725-2199
Eml: gordon@pangea.Stanford.EDU

Dr. David L. CLARK
Los Alamos National Laboratory
Seaborg Institute
NMT-DO, MS E500
Los Alamos, NM 87545
Tel: +1-505-665-6690
Fax: +1-505-665-7895
Eml: dlclark@lanl.gov

Dr. Steven CONRADSON
Los Alamos National Laboratory
MST MS G755
Los Alamos, NM 87595
Tel: +1-505-667-9589
Fax: +1-505-667-8021
Eml: conradson@lanl.gov

Dr. Noman EDELSTEIN
US Department of Energy
Office of Science
SC-142
19901 Germantown Road
Germantown, MD 20874-1290
Tel: +1-301-903-9311
Fax: +1-301-903-0271
Eml: norman.edelstein@science.doe.gov

Dr. Richard HAIRE
Oak Ridge National Laboratory
P.O. Box 7008
MS 6375
Oak Ridge, TN 37831-6375
Tel: +1-865-574-5007
Fax: +1-865-574-4987
Eml: hairer@ornl.gov

Dr. David K. SHUH
Lawrence Berkeley National Laboratory
MS 70A-1150
1 Cyclotron Road
Berkeley CA 94720
Tel: +1-510-486-6937
Fax: +1-510-406-5596
Eml: dkshuh@lbl.gov

Dr. Lynda SODERHOLM
Argonne National Laboratory
9600 South Cass Avenue
Argonne IL 60439
Tel: +1-630-252-4364
Fax: +1-630-252-9289
Eml: ls@anl.gov

Dr. Stephen WASSERMAN
Argonne National Laboratory
9700 S. Cass Avenue
Building 438
Argonne, IL 60439
Tel: +1-630-252-3527
Fax: +1-630-252-0855
Eml: SRW@ANL.GOV

INTERNATIONAL ORGANISATIONS

Mr. Claes NORDBORG
OECD Nuclear Energy Agency
Le Seine St. Germain
12, Bld. des Iles
F-92130 Issy-les-Moulineaux
France
Tel: +33-(0)145-241090
Fax: +33-(0)145-241110
Eml: nordborg@oecd.org

OECD PUBLICATIONS, 2 rue André-Pascal, 75775 PARIS CEDEX 16
Printed in France.